IntechOpen

Thermodynamics

Kinetics of Dynamic Systems

Edited by Juan Carlos Moreno Piraján

THERMODYNAMICS – KINETICS OF DYNAMIC SYSTEMS

Edited by **Juan Carlos Moreno-Piraján**

Thermodynamics - Kinetics of Dynamic Systems
http://dx.doi.org/10.5772/1433
Edited by Juan Carlos Moreno Piraján

Contributors

Burkhard Bechinger, Christopher Aisenbrey, Gordon Holcomb, Zhen-Bang Kuang, Roland Pascal Borghi, Helio Dos Santos, Wagner De Almeida, Lai-Chang Zhang, Ozkan Demirbas, Mahir Alkan, Hiromi Saida, Srboljub Simić, Shawn Wettig, Tranum Kaur, Roderick A. Slavcev, Naser Tavakoli, Yong Duan, Hongxing Lei, Wenlong Jia, Xia Wu, Changjun Li, Francisco Uribe, Leopoldo Garcia-Colin, Jose Ines Jimenez-Aquino, G. Reza Vakili-Nezhaad, Ibrahim Ashour, Nabeel Al-Rawahi, Seyed Amin Fatemi, Thomas Boehme, Ralf Drautz, Thomas Hammerschmidt, Thomas Pretorius, Jack Denur

Notice

First published in Croatia, 2011 by INTECH d.o.o.
eBook (PDF) Published by IN TECH d.o.o.
Place and year of publication of eBook (PDF): Rijeka, 2019.
IntechOpen is the global imprint of IN TECH d.o.o.
Printed in Croatia

Legal deposit, Croatia: National and University Library in Zagreb

Additional hard and PDF copies can be obtained from orders@intechopen.com

Thermodynamics - Kinetics of Dynamic Systems
Edited by Juan Carlos Moreno Piraján
p. cm.
ISBN 978-953-307-627-0
eBook (PDF) ISBN 978-953-51-6056-4

Meet the editor

Dr. Juan Carlos Moreno-Piraján is a Full Professor, Department of Chemistry at the Universidad de los Andes (Bogotá, Colombia) and a Director of the Research Group of Porous Solids and Calorimetry. He is a chemist by profession who obtained his Ph.D. from the Universidad Nacional de Colombia, where his work was concentrated on the construction of the Tian-Calvet microcalorimeter, which was used for the characterization of activated carbons. Professor Moreno has spent his research career developing new materials for water purification. These interesting materials have been synthesized and he has also designed several microcalorimeters that have contributed to these studies. As a result of his research, Professor Moreno-Piraján has 160 publications. His main contributions can be found in the thermodynamic interpretation of solids and liquids, and in the information obtained from calorimetric measurements.

Contents

Preface

Thermodynamics is one of the most exciting branches of physical chemistry which has greatly contributed to the modern science. Since its inception, great minds have built their theories of thermodynamics. One should name those of Sadi Carnot, Clapeyron Claussius, Maxwell, Boltzman, Bernoulli, Leibniz etc. Josiah Willard Gibbs had perhaps the greatest scientific influence on the development of thermodynamics. His attention was for some time focused on the study of the Watt steam engine. Analysing the balance of the machine, Gibbs began to develop a method for calculating the variables involved in the processes of chemical equilibrium. He deduced the phase rule which determines the degrees of freedom of a physicochemical system based on the number of system components and the number of phases. He also identified a new state function of thermodynamic system, the so-called free energy or Gibbs energy (G), which allows spontaneity and ensures a specific physicochemical process (such as a chemical reaction or a change of state) experienced by a system without interfering with the environment around it. The essential feature of thermodynamics and the difference between it and other branches of science is that it incorporates the concept of heat or thermal energy as an important part in the energy systems. The nature of heat was not always clear. Today we know that the random motion of molecules is the essence of heat. Some aspects of thermodynamics are so general and deep that they even deal with philosophical issues. These issues also deserve a deeper consideration, before tackling the technical details. The reason is a simple one - before one does anything, one must understand what they want.

In the past, historians considered thermodynamics as a science that is isolated, but in recent years scientists have incorporated more friendly approach to it and have demonstrated a wide range of applications of thermodynamics.

These four volumes of applied thermodynamics, gathered in an orderly manner, present a series of contributions by the finest scientists in the world and a wide range of applications of thermodynamics in various fields. These fields include the environmental science, mathematics, biology, fluid and the materials science. These four volumes of thermodynamics can be used in post-graduate courses for students and as reference books, since they are written in a language pleasing to the reader.

They can also serve as a reference material for researchers to whom the thermodynamics is one of the area of interest.

Juan Carlos Moreno-Piraján
Department of Chemistry
University of the Andes
Colombia

1

Some Thermodynamic Problems in Continuum Mechanics

Zhen-Bang Kuang
Shanghai Jiaotong University, Shanghai
China

1. Introduction

Classical thermodynamics discusses the thermodynamic system, its surroundings and their common boundary. It is concerned with the state of thermodynamic systems at equilibrium, using macroscopic, empirical properties directly measurable in the laboratory (Wang, 1955; Yunus, Michael and Boles, 2011). Classical thermodynamics model exchanges of energy, work and heat based on the laws of thermodynamics. The first law of thermodynamics is a principle of conservation of energy and defines a specific internal energy which is a state function of the system. The second law of thermodynamics is a principle to explain the irreversibile phenomenon in nature. The entropy of an isolated non-equilibrium system will tend to increase over time, approaching a maximum value at equilibrium. Thermodynamic laws are generally valid and can be applied to systems about which only knows the balance of energy and matter transfer. The thermodynamic state of the system can be described by a number of state variables. In continuum mechanics state variables usually are pressure p, volume V, stress $\boldsymbol{\sigma}$, strain $\boldsymbol{\varepsilon}$, electric field strength $\boldsymbol{E}$, electric displacement $\boldsymbol{D}$, magnetic induction density $\boldsymbol{B}$, magnetic field strength $\boldsymbol{H}$, temperature $\boldsymbol{T}$, entropy per volume s, chemical potential per volume μ and concentration c respectively. Conjugated variable pairs are $(p,V),(\boldsymbol{\sigma},\boldsymbol{\varepsilon}),(\boldsymbol{E},\boldsymbol{D}),(\boldsymbol{H},\boldsymbol{B}),(T,S),(\mu,c)$. There is a convenient and useful combination system in continuum mechanics: variables $V,\boldsymbol{\varepsilon},\boldsymbol{E},\boldsymbol{H},T,\mu$ are used as independent variables and variables $p,\boldsymbol{\sigma},\boldsymbol{D},\boldsymbol{B},S,c$ are used as dependent variables. In this chapter we only use these conjugated variable pairs, and it is easy to extend to other conjugated variable pairs. In the later discussion we only use the following thermodynamic state functions: the internal energy $\mathcal{U}$ and the electro-magneto-chemical Gibbs free energy $g_{e\mu}(\boldsymbol{\varepsilon},\boldsymbol{E},\boldsymbol{H},T,\mu)$ per volume in an electro-magneto-elastic material. They are taken as

$$\begin{aligned}&\mathrm{d}\mathcal{U}(\boldsymbol{\varepsilon},\boldsymbol{D},\boldsymbol{B},s,c)=\boldsymbol{\sigma}:\mathrm{d}\boldsymbol{\varepsilon}+\boldsymbol{E}\cdot\mathrm{d}\boldsymbol{D}+\boldsymbol{H}\cdot\mathrm{d}\boldsymbol{B}+T\mathrm{d}s+\mu\mathrm{d}c\ ;\quad \boldsymbol{\sigma}:\mathrm{d}\boldsymbol{\varepsilon}=\sigma_{ij}\mathrm{d}\varepsilon_{ij}\\&\mathrm{d}g_{e\mu}(\boldsymbol{\varepsilon},\boldsymbol{E},\boldsymbol{H},T,\mu)=\mathrm{d}\left(\mathcal{U}-\boldsymbol{E}\cdot\boldsymbol{D}-\boldsymbol{H}\cdot\boldsymbol{B}-Ts-\mu c\right)=\boldsymbol{\sigma}:\mathrm{d}\boldsymbol{\varepsilon}-\boldsymbol{D}\cdot\mathrm{d}\boldsymbol{E}-\boldsymbol{B}\cdot\mathrm{d}\boldsymbol{H}-s\mathrm{d}T-c\mathrm{d}\mu\end{aligned}\tag{1}$$

Other thermodynamic state functions and their applications can be seen in many literatures (Kuang, 2007, 2008a, 2008b, 2009a, 2009b, 2010, 2011a, 2011b). For the case without chemical potential $g_{e\mu}=g_e$ is the electromagnetic Gibbs free energy. For the case without electromagnetic field $g_{e\mu}=g_\mu$ is the Gibbs free energy with chemical potential. For the case without chemical potential and electromagnetic field $g_{e\mu}=g$ is the Helmholtz free energy.

In this chapter two new problems in the continuum thermodynamics will be discussed. The first is that in traditional continuum thermodynamics including the non-equilibrium theory the dynamic effect of the temperature is not fully considered. When the temperature T is varied, the extra heat or entropy should be input from the environment. When c is varied, the extra chemical potential μ is also needed. So the general inertial entropy theory (Kuang, 2009b, 2010) is introduced into the continuum thermodynamics. The temperature and diffusion waves etc. with finite phase velocity can easily be obtained from this theory. The second is that usually we consider the first law only as a conservation law of different kinds of energies, but we found that it is also containing a physical variational principle, which gives a true process for all possible process satisfying the natural constrained conditions (Kuang, 2007, 2008a, 2008b, 2009a 2011a, 2011b). Introducing the physical variational principle the governing equations in continuum mechanics and the general Maxwell stress and other theories can naturally be obtained. When write down the energy expression, we get the physical variational principle immediately and do not need to seek the variational functional as that in the usual mathematical methods. The successes of applications of these theories in continuum mechanics are indirectly prove their rationality, but the experimental proof is needed in the further.

2. Inertial entropy theory

2.1 Basic theory in linear thermoelastic material

In this section we discuss the linear thermoelastic material without chemical reaction, so in Eq. (1) the term $-\boldsymbol{D}\cdot\mathrm{d}\boldsymbol{E}-\boldsymbol{B}\cdot\mathrm{d}\boldsymbol{H}-\mathrm{d}c\mu$ is omitted. It is also noted that in this section the general Maxwell stress is not considered. The classical thermodynamics discusses the equilibrium system, but when extend it to continuum mechanics we need discuss a dynamic system which is slightly deviated from the equilibrium state. In previous literatures one point is not attentive that the variation of temperature should be supplied extra heat from the environment. Similar to the inertial force in continuum mechanics we modify the thermodynamic entropy equation by adding a term containing an inertial heat or the inertial entropy (Kuang, 2009b), i.e.

$$\begin{aligned}
&T\dot{s}+T\dot{s}^{(a)}=\dot{r}-q_{i,i}=\dot{r}-(T\dot{\eta}_i)_{,i},\quad \dot{s}^{(a)}=\rho_s\ddot{T},\quad s^{(a)}=\rho_s\dot{T}=\rho_{s0}\left(C/T_0\right)\dot{T}\\
&\dot{s}=\dot{s}^{(r)}+\dot{s}^{(i)};\quad \dot{s}^{(r)}+\dot{s}^{(a)}=\dot{r}/T-\dot{\eta}_{i,i};\quad \dot{\boldsymbol{\eta}}=\boldsymbol{q}/T\\
&T\dot{s}^{(i)}=T\dot{s}-T\dot{s}^{(r)}=T\dot{s}+T\dot{s}^{(a)}-\dot{r}+T\dot{\eta}_{i,i}=-\dot{\eta}_iT_{,i}\geq 0;\quad \dot{s}^{(i)}=-\dot{\eta}_iT_{,i}/T
\end{aligned}\tag{2}$$

where $s^{(a)}$ is called the reversible inertial entropy corresponding to the inertial heat; ρ_s is called the inertial entropy coefficient, ρ_{s0} is also a constant having the dimension of the time; s is the entropy saved in the system, $\dot{s}^{(r)}$ and $\dot{s}^{(i)}$ are the reversible and irreversible parts of the s, $T\dot{s}$ is the absorbed heat rate of the system from the environment, $T\dot{s}^{(a)}=\rho_sT\ddot{T}$ is the inertial heat rate and $\dot{s}^{(a)}$ is proportional to the acceleration of the temperature; r is the external heat source strength, $\boldsymbol{q}$ is the heat flow vector per interface area supplied by the environment, $\boldsymbol{\eta}$ is the entropy displacement vector, $\dot{\boldsymbol{\eta}}$ is the entropy flow vector. Comparing Eq. (2) with the classical entropy equation it is found that in Eq. (2) we use $T\dot{s}+T\dot{s}^{(a)}$ to instead of $T\dot{s}$ in the classical theory. In Eq. (2) s is still a state function because $s^{(a)}$ is

reversible. As in classical theory the dissipative energy $\dot{h}'$ and its Legendre transformation or "the complement dissipative energy" h are respectively

$$\dot{h}' = \mathrm{d}h'/\mathrm{d}t = T\dot{s}^{(i)} = -T_{,i}\dot{\eta}_i, \quad \dot{h} = -T_{,i}\dot{\eta}_i + \left(T_{,i}\eta_i\right)^{\bullet} = \eta_i\dot{T}_{,i} \tag{3}$$

Using the theory of the usual irreversible thermodynamics (Groet, 1952; Gyarmati, 1970; Jou, Casas-Vzquez, Lebon, 2001; Kuang, 2002) from Eq. (3) we get

$$\begin{aligned} &\dot{\eta}_i = \dot{\eta}_i(T_{,j}), \quad \text{or} \quad \dot{\eta}_i = -\lambda_{ij}T^{-1}T_{,j}, \quad T\dot{\eta}_i = q_i = -\lambda_{ij}T_{,j} \\ &T_{,j} = -\hat{\lambda}_{ij}T\dot{\eta}_i = -\hat{\lambda}_{ij}q_i, \quad \hat{\lambda}_{ij} = \lambda_{ij}^{-1} \end{aligned} \tag{4}$$

where $\boldsymbol{\lambda}$ is the usual heat conductive coefficient. Eq. (4) is just the Fourier's law.

2.2 Temperature wave in linear thermoelastic material

The temperature wave from heat pulses at low temperature propagates with a finite velocity. So many generalized thermoelastic and thermopiezoelectric theories were proposed to allow a finite velocity for the propagation of a thermal wave. The main generalized theories are: Lord−Shulman theory (1967), Green−Lindsay theory (1972) and the inertial entropy theory (Kuang, 2009b).

In the Lord−Shulman theory the following Maxwell-Cattaneo heat conductive formula for an isotropic material was used to replace the Fourier's law, but the classical entropy equation is kept, i.e. they used

$$q_i + \tau_0\dot{q}_i = -\lambda T_{,i}, \quad T\dot{s} = \dot{r} - q_{i,i} \tag{5}$$

where τ_0 is a material parameter with the dimension of time. After linearization and neglecting many small terms they got the following temperature wave and motion equations for an isotropic material:

$$\begin{aligned} &\lambda T_{,ii} = C(\dot{T} + \tau_0\ddot{T}) + \left[2G(1+\nu)/(1-2\nu)\right]\alpha T_0(\dot{\varepsilon}_{jj} + \tau_0\ddot{\varepsilon}_{jj}) \\ &\left[G/(1-2\nu)\right]u_{j,ij} + Gu_{i.jj} - \left[2G(1+\nu)/(1-2\nu)\right]\alpha T_{,i} = \rho\ddot{u}_i \end{aligned} \tag{6}$$

where C is the specific heat, α is the thermal expansion coefficient, G and ν are the shear modulus and Poisson's ratio respectively. From Eq.（5）we can get

$$T\dot{s} - \tau_0 T\ddot{s} = \lambda T_{,ii} + \left(\dot{r} + \tau_0\ddot{r}\right)$$

From above equation it is difficult to consider that s is a state function.

The Green−Lindsay theory with two relaxation times was based on modifying the Clausius-Duhemin inequality and the energy equation; In their theory they used a new temperature function $\phi(T,\dot{T})$ to replace the usual temperature T. They used

$$\begin{aligned} &\int_V \dot{s}\mathrm{d}V - \int_V (r/\phi)\mathrm{d}V + \int_a (q_i/\phi)n_i\mathrm{d}a \geq 0, \quad \phi = \phi(T,\dot{T}), \quad T = \phi(T,0) \\ &g = \mathcal{U} - \phi s, \quad g = g\left(T,\dot{T},\varepsilon_{ij}\right) \end{aligned} \tag{7}$$

After linearization and neglecting small terms, finally they get (here we take the form in small deformation for an isotropic material)

$$\begin{aligned} &\lambda T_{,ii} = C(\dot{T} + \tau_0 \ddot{T}) + \gamma T_0 \dot{\varepsilon}_{jj}, \qquad \sigma_{ji,j} + \rho f_i = \rho \ddot{u}_i \\ &\sigma_{ij} = \left[2G\nu/(1-2\nu)\right]\varepsilon_{kk}\delta_{ij} + 2G\varepsilon_{ij} - \gamma(\theta + \tau_1 \dot{\theta}) \end{aligned} \tag{8}$$

where τ_0, τ_1 and γ are material constants.

Now we discuss the inertial entropy theory (Kuang, 2009b). The Helmholtz free energy g and the complement dissipative energy h assumed in the form

$$\begin{aligned} &g(\varepsilon_{kl}, \vartheta) = (1/2)C_{ijkl}\varepsilon_{ji}\varepsilon_{lk} - \alpha_{ij}\varepsilon_{ij}\vartheta - (1/2T_0)C\vartheta^2 \\ &\delta h = -\left[\int_0^t (\lambda_{ij}/T)\vartheta_{,i} d\tau)\right]\delta\vartheta_{,j}, \quad \vartheta = T - T_0 \\ &C_{ijkl} = C_{jikl} = C_{ijlk} = C_{klij}, \quad \alpha_{ij} = \alpha_{ji}, \quad \lambda_{ij} = \lambda_{ji} \end{aligned} \tag{9a}$$

where T_0 is the reference (or the environment) temperature, C_{ijkl}, α_{ij} are material constants. In Eq. (9a) it is assumed that $s = 0$ when $T = T_0$ or $\vartheta = 0$. It is obvious that $T_{,j} = \vartheta_{,j}, \dot{T} = \dot{\vartheta}$. The constitutive (or state) and evolution equations are

$$\begin{aligned} &\sigma_{ij} = \partial g/\partial \varepsilon_{ij} = C_{ijkl}\varepsilon_{kl} - \alpha_{ij}\vartheta, \quad s = -\partial g/\partial \vartheta = \alpha_{ij}\varepsilon_{ij} + C\vartheta/T_0 \\ &\eta_i = \partial h/\partial \vartheta_{,i} = -\int_0^t (\lambda_{ij}/T)\vartheta_{,j} \mathrm{d}\tau, \quad T\dot{\eta}_i = q_i = -\lambda_{ij}\vartheta_{,j} \end{aligned} \tag{10}$$

Using Eq. (10), Eq. (9a) can be rewritten as

$$g = (1/2)C_{ijkl}\varepsilon_{ji}\varepsilon_{lk} + g^{(T)}, \quad g^{(T)} = -(1/2)s\vartheta - (1/2)\alpha_{ij}\varepsilon_{ij}\vartheta \tag{9b}$$

where $g^{(T)}$ is the energy containing the effect of the to temperature.

Substituting the entropy s and $T\dot{\eta}_i$ in Eq. (10) and $s^{(a)}$ in (2) into $T\dot{s} + T\dot{s}^{(a)} = \dot{r} - (T\dot{\eta}_i)_{,i}$ in Eq. (2) we get

$$T(\alpha_{ij}\varepsilon_{ij} + C\vartheta/T_0)^{\bullet} + \rho_s T\ddot{\vartheta} = \dot{r} + (\lambda_{ij}\vartheta_{,j})_{,i} \tag{11}$$

When material coefficients are all constants from（11）we get

$$\rho_s T\ddot{\vartheta} + CT\dot{\vartheta}/T_0 - \lambda_{ij}\vartheta_{,ji} = \dot{r} - \alpha_{ij}T\dot{\varepsilon}_{ij} \tag{12a}$$

Eq. (12a) is a temperature wave equation with finite phase velocity. For an isotropic elastic material and the variation of the temperature is not large, from Eq. (12a) we get

$$\begin{aligned} &(C/T_0)(\rho_{s0}\ddot{\vartheta} + \dot{\vartheta}) - (\lambda/T)\vartheta_{,ii} = \dot{r}/T - \alpha\dot{\varepsilon}_{ii} \quad or \\ &\lambda\vartheta_{,ii} = C(\rho_{s0}\ddot{\vartheta} + \dot{\vartheta}) + \alpha T_0\dot{\varepsilon}_{ii} - \dot{r} \end{aligned} \tag{12b}$$

Comparing the temperature wave equation Eq. (12b) with the Lord－Shulman theory (Eq. (6)) it is found that in Eq. (12b) a term $\tau_0\ddot{\varepsilon}_{jj}$ is lacked (in different notations),but with that in

the Green−Lindsay theory (Eq. (8)) is similar (in different notations). For the purely thermal conductive problem three theories are fully the same in mathematical form.
The momentum equation is

$$\sigma_{ij,j} + f_i = \rho \ddot{u}_i \tag{13}$$

where $\boldsymbol{f}$ is the body force per volume, ρ is the density. Substituting the stress $\boldsymbol{\sigma}$ in Eq. (10) into (13) we get

$$\left(C_{ijkl}\varepsilon_{kl} - \alpha_{ij}\vartheta\right)_{,j} + f_i = \rho \ddot{u}_i, \quad or \quad \rho \ddot{u}_i = C_{ijkl}u_{k,lj} - \alpha_{ij}\vartheta_{,j} + f_i \tag{14}$$

Comparing the elastic wave equation Eq. (14) with the Green−Lindsay theory (Eq. (8)) it is found that in Eq. (14) a term $\gamma\tau_1\dot{\vartheta}_{,i}$ is lacked (in different notations), but with the Lord−Shulman theory (Eq. (6)) is similar (in different notations).

2.3 Temperature wave in linear thermo - viscoelastic material

In the pyroelectric problem (without viscous effect) through numerical calculations Yuan and Kuang（2008, 2010）pointed out that the term containing the inertial entropy attenuates the temperature wave, but enhances the elastic wave. For a given material there is a definite value of ρ_{s0}^*, when $\rho_{s0} > \rho_{s0}^*$ the amplitude of the elastic wave will be increased with time. For $BaTio_3$ ρ_{s0}^* is about 10^{-13}s. In the Lord−Shulman theory critical value τ_0^* is about 10^{-8}s. In order to substantially eliminate the increasing effect of the amplitude of the elastic wave the viscoelastic effect is considered as shown in this section.
Using the irreversible thermodynamics (Groet, 1952; Kuang, 1999, 2002) we can assume

$$\begin{aligned}
&g = (1/2)C_{ijkl}\varepsilon_{ji}\varepsilon_{lk} - \alpha_{ij}\varepsilon_{ij}\vartheta - (1/2T_0)C\vartheta^2 \\
&\sigma_{ij}^{(r)} = \partial g/\partial \varepsilon_{ij} = C_{ijkl}\varepsilon_{kl} - \alpha_{ij}\vartheta, \quad s = -\partial g/\partial \vartheta = \alpha_{ij}\varepsilon_{ij} + C\vartheta / T_0 \\
&\delta h = \beta_{ijkl}\dot{\varepsilon}_{ji}\delta\dot{\varepsilon}_{lk} + \eta_j\delta\vartheta_{,j} = \beta_{ijkl}\dot{\varepsilon}_{ji}\delta\dot{\varepsilon}_{lk} - \left[\int_0^t \left(\lambda_{ij}/T\right)\vartheta_{,i}d\tau)\right]\delta\vartheta_{,j}, \\
&\sigma_{ij}^{(i)} = \partial h/\partial \dot{\varepsilon}_{ij} = \beta_{ijkl}\dot{\varepsilon}_{kl}, \ \eta_i = \partial h/\partial \vartheta_{,i} = -\int_0^t \left(\lambda_{ij}/T\right)\vartheta_{,j}\mathrm{d}\tau, \ T\dot{\eta}_i = q_i = -\lambda_{ij}\vartheta_{,j} \\
&\sigma_{ij} = \sigma_{ij}^{(r)} + \sigma_{ij}^{(i)} = C_{ijkl}\varepsilon_{kl} + \beta_{ijkl}\dot{\varepsilon}_{kl} - \alpha_{ij}\vartheta
\end{aligned} \tag{15}$$

where $\sigma_{ij}^{(r)}$ and $\sigma_{ij}^{(i)}$ are the reversible and irreversible parts of the stress σ_{ij}, $\dot{\varepsilon}_{ij} = \mathrm{d}\varepsilon_{ij}/\mathrm{d}t$. Comparing Eqs. (9) and (10) with (15) it is found that only a term $\beta_{ijkl}\dot{\varepsilon}_{ji}\delta\dot{\varepsilon}_{lk}$ is added to the rate of the complement dissipative energy in Eq. (15) . Substituting the entropy s and $T\dot{\eta}_i$ in Eq. (15) and $s^{(a)}$ in (2) into $T\dot{s} + T\dot{s}^{(a)} = \dot{r} - (T\dot{\eta}_i)_{,i}$ in Eq. (2) we still get the same equation (12). Substituting the stress $\boldsymbol{\sigma}$ in Eq. (15) into (13) we get

$$\left(C_{ijkl}\varepsilon_{kl} + \beta_{ijkl}\dot{\varepsilon}_{kl} - \alpha_{ij}\vartheta\right)_{,j} + f_i = \rho \ddot{u}_i, \quad or \quad \rho \ddot{u}_i = C_{ijkl}u_{k,lj} + \beta_{ijkl}\dot{u}_{k,lj} - \alpha_{ij}\vartheta_{,j} + f_i \tag{16}$$

In one dimensional problem for the isotropic material from Eq. (15) we have

$$\sigma = Y\varepsilon + \beta\dot{\varepsilon} - \alpha\vartheta, \quad s = \alpha\varepsilon + C\vartheta / T_0 \tag{17}$$

where Y is the elastic modulus, β is a viscose coefficient, α is the temperature coefficient. When there is no body force and body heat source, Eqs. (12) and (16) are reduced to

$$\begin{aligned} &C\left(\rho_{s0}\ddot{\vartheta}+\dot{\vartheta}\right)-\lambda\vartheta''+\alpha T_0\dot{u}'=0 \\ &\rho\ddot{u}-Yu''-\beta\dot{u}''+\alpha\vartheta'=0 \end{aligned} \tag{18}$$

where $\dot{\varphi}=\partial\varphi/\partial t, \varphi'=\partial\varphi/\partial x$ for any function φ. For a plane wave propagating along direction x we assume

$$u=U\exp\left[\mathrm{i}\left(kx-\omega t\right)\right], \quad \theta=\Theta\exp\left[\mathrm{i}\left(kx-\omega t\right)\right] \tag{19}$$

where U,Θ are the amplitudes of u and ϑ respectively, k is the wave number and ω is the circular frequency. Substituting Eq. (19) into (18) we obtain

$$\begin{aligned} &\left[\left(Y-\mathrm{i}\beta\omega\right)k^2-\rho\omega^2\right]U+\mathrm{i}\alpha k\Theta=0 \\ &\alpha T_0 k\omega U+\left[\lambda k^2-C\left(\rho_{s0}\omega^2+\mathrm{i}\omega\right)\right]\Theta=0 \end{aligned} \tag{20}$$

In order to have nontrivial solutions for U,Θ, the coefficient determinant of Eq. (20) should be vanished:

$$\begin{vmatrix} \left(Y-\mathrm{i}\beta\omega\right)k^2-\rho\omega^2 & \mathrm{i}\alpha k \\ \alpha T_0 k\omega & \lambda k^2-C\left(\rho_{s0}\omega^2+\mathrm{i}\omega\right) \end{vmatrix} = \begin{vmatrix} ak^2-\rho\omega^2 & \mathrm{i}\alpha k \\ \alpha T_0 k\omega & \lambda k^2-Cb \end{vmatrix} = 0 \tag{21a}$$

where

$$\begin{aligned} &a=Y-\mathrm{i}\beta\omega=r_Y e^{\mathrm{i}\theta_Y}, \quad r_Y=\sqrt{a\bar{a}}=\sqrt{Y^2+\beta^2\omega^2}, \quad \sin\theta_Y=-\beta\omega/r_Y \\ &b=\rho_{s0}\omega^2+\mathrm{i}\omega=r_T e^{\mathrm{i}\theta_T}, \quad r_T=\sqrt{b\bar{b}}=\omega\sqrt{\rho_{s0}^2\omega^2+1}, \quad \sin\theta_T=\omega/r_T \end{aligned} \tag{21b}$$

From Eq. (21) we get

$$\begin{aligned} &\lambda ak^4-\left(Cab+\lambda\rho\omega^2+\mathrm{i}\alpha^2T_0\omega\right)k^2+\rho\omega^2Cb=0 \\ &k=\left\{\frac{1}{2\lambda r_Y}\left[\left(Cr_Yr_T\,\mathrm{e}^{\mathrm{i}\theta_T}+\lambda\rho\omega^2\,\mathrm{e}^{-\mathrm{i}\theta_Y}+\mathrm{i}\alpha^2T_0\omega\mathrm{e}^{-\mathrm{i}\theta_Y}\right)\right.\right. \\ &\left.\left.\pm\sqrt{\left(Cr_Yr_T\,\mathrm{e}^{\mathrm{i}\theta_T}-\lambda\rho\omega^2\,\mathrm{e}^{-\mathrm{i}\theta_Y}+\mathrm{i}\alpha^2T_0\omega\mathrm{e}^{-\mathrm{i}\theta_Y}\right)^2+4\mathrm{i}\alpha^2T_0\omega r_Yr_Te^{\mathrm{i}\left(\theta_T-\theta_Y\right)}}\right]\right\}^{1/2}\!\!/2 \end{aligned} \tag{22}$$

where the symbol "+" is applied to the wave number k_T of the temperature wave and the symbol " – " is applied to the wave number of the viscoelastic wave k_Y. If the temperature wave does not couple with the elastic wave, then α is equal to zero. In this case we have

$$\begin{aligned} &k=\sqrt{\left(2\lambda r_Y\right)^{-1}\left\{\left(Cr_Tr_Ye^{\mathrm{i}\theta_T}+\lambda\rho\omega^2e^{-\mathrm{i}\theta_Y}\right)\pm\left(Cr_Tr_Ye^{\mathrm{i}\theta_T}-\lambda\rho\omega^2e^{-\mathrm{i}\theta_Y}\right)\right\}} \\ &k_Y=\omega\sqrt{\rho/r_Y}e^{-\mathrm{i}\theta_Y/2}, \quad k_T=\sqrt{Cr_T/\lambda}e^{\mathrm{i}\theta_T/2} \end{aligned} \tag{23}$$

Because $-\theta_Y > 0$ due to $\beta > 0$ and $\theta_T > 0$ due to $\rho_{s0} > 0$, a pure viscoelastic wave or a pure temperature waves is attenuated. The pure elastic wave does not attenuate due to $\beta = 0$.
For the general case in Eq. (22) a coupling term $i\alpha^2 T_0 \omega k^2$ is appeared. It is known that

$$\left|\mathrm{Im}\left(Cr_Y r_T \mathrm{e}^{\mathrm{i}\theta_T} + \lambda\rho\omega^2 \mathrm{e}^{-\mathrm{i}\theta_Y} + \mathrm{i}\alpha^2 T_0 \omega \mathrm{e}^{-\mathrm{i}\theta_Y}\right)\right| > \left|\mathrm{Im}\left(Cr_Y r_T \mathrm{e}^{\mathrm{i}\theta_T} - \lambda\rho\omega^2 \mathrm{e}^{-\mathrm{i}\theta_Y} + \mathrm{i}\alpha^2 T_0 \omega \mathrm{e}^{-\mathrm{i}\theta_Y}\right)\right|$$

It means that $\mathrm{Im}\, k_T > 0$ or the temperature wave is always an attenuated wave. If

$$\begin{aligned} &\mathrm{Im}\left[\left(Cr_Y r_T \mathrm{e}^{\mathrm{i}\theta_T} - \lambda\rho\omega^2 \mathrm{e}^{-\mathrm{i}\theta_Y} + \mathrm{i}\alpha^2 T_0 \omega \mathrm{e}^{-\mathrm{i}\theta_Y}\right)^2 + 4\mathrm{i}\alpha^2 T_0 \omega r_Y r_T e^{\mathrm{i}\left(\theta_T - \theta_Y\right)}\right] \\ &< \mathrm{Im}\left(Cr_Y r_T \mathrm{e}^{\mathrm{i}\theta_T} + \lambda\rho\omega^2 \mathrm{e}^{-\mathrm{i}\theta_Y} + \mathrm{i}\alpha^2 T_0 \omega \mathrm{e}^{-\mathrm{i}\theta_Y}\right)^2 \end{aligned} \tag{24}$$

we get $\mathrm{Im}\, k_Y > 0$ or in this case the elastic wave is an attenuated wave, otherwise is enhanced.
Introducing the viscoelastic effect in the elastic wave as shown in this section can substantially eliminate the increasing effect of the amplitude of the elastic wave with time.

2.4 Temperature wave in thermo-electromagneto-elastic material

In this section we discuss the linear thermo-electromagneto-elastic material without chemical reaction and viscous effect, so the electromagnetic Gibbs free energy g_e in Eq. (1) should keep the temperature variable. The electromagnetic Gibbs free energy g_e and the complement dissipative energy h_e in this case are assumed respectively in the following form

$$\begin{aligned} &g_e\left(\varepsilon_{kl}, E_k, H_k, \vartheta\right) = (1/2) C_{ijkl}\varepsilon_{ji}\varepsilon_{lk} - e^e_{kij}E_k\varepsilon_{ij} - (1/2)\epsilon_{ij}E_iE_j - \tau^e_i E_i\vartheta \\ &\quad - e^m_{kij}H_k\varepsilon_{ij} - (1/2)\mu_{ij}H_iH_j - \tau^m_i H_i\vartheta - \alpha_{ij}\varepsilon_{ij}\vartheta - (1/2T_0)C\vartheta^2 \\ &\delta h_e = -\left(\int_0^t \left(\lambda_{ij}/T\right)\vartheta_{,i}d\tau\right)\delta\vartheta_{,j}\ (=\eta_j\delta\vartheta_{,j}), \quad \vartheta = T - T_0 \\ &C_{ijkl} = C_{jikl} = C_{ijlk} = C_{klij},\ e^e_{kij} = e^e_{kji},\ \epsilon_{kl} = \epsilon_{lk},\ e^m_{kij} = e^m_{kji},\ \mu_{kl} = \mu_{lk},\ \alpha_{ij} = \alpha_{ji} \end{aligned} \tag{25}$$

where $e^e_{kij}, \epsilon_{kl}, \tau^e_i, e^m_{kij}, \mu_{kl}, \tau^m_i$ are material constants. The constitutive equations are

$$\begin{aligned} &\sigma_{ij} = C_{ijkl}\varepsilon_{kl} - e^e_{kij}E_k - e^m_{kij}H_k - \alpha_{ij}\vartheta,\ D_i = \epsilon_{ij}E_j + e^e_{ijk}\varepsilon_{jk} + \tau^e_i\vartheta \\ &B_i = \mu_{ij}H_j + e^m_{ijk}\varepsilon_{jk} + \tau^m_i\vartheta,\ s = \alpha_{ij}\varepsilon_{ij} + \tau^e_i E_i + \tau^m_i H_i + C\vartheta/T_0 \\ &\eta_i = \partial h_v/\partial\vartheta_{,i} = -\int_0^t \left(\lambda_{ij}/T\right)\vartheta_{,j}\mathrm{d}\tau,\ T\dot{\eta}_i = q_i = -\lambda_{ij}\vartheta_{,j} \end{aligned} \tag{26}$$

Similar to derivations in sections 2.2 and 2.3 it is easy to get the governing equations:

$$T\left(\alpha_{ij}\varepsilon_{ij} + \tau^e_i E_i + \tau^m_i H_i + C\vartheta/T_0\right)^{\bullet} + \rho_s T\ddot{T} = \dot{r} + \left(\lambda_{ij}\vartheta_{,j}\right)_{,i} \tag{27}$$

$$\begin{aligned}&\left(C_{ijkl}\varepsilon_{kl}-e^{e}_{kij}E_k-e^{m}_{kij}H_k-\alpha_{ij}\vartheta\right)_{,j}+f_i=\rho\ddot{u}_i,\\&\left(\epsilon_{ij}\,E_j+e^{e}_{kij}\varepsilon_{kl}+\tau^{e}_{i}\vartheta\right)_{,i}=\rho_e,\quad\left(\mu_{ij}H_j+e^{m}_{kij}\varepsilon_{kl}+\tau^{m}_{i}\vartheta\right)_{,i}=0\end{aligned}\tag{28}$$

where ρ_e is the density of the electric charge. The boundary conditions are omitted here.

2.5 Thermal diffusion wave in linear thermoelastic material

The Gibbs equation of the classical thermodynamics with the thermal diffusion is:

$$\begin{aligned}&T\dot{s}=\dot{r}-q_{i,i}+\mu d_{i,i},\quad T\dot{s}+\mu\dot{c}=\dot{r}-q_{i,i}=\dot{r}-\left(T\dot{\eta}_i\right)_{,i},\quad d_{i,i}=-\dot{c}\\&\mathcal{U}\dot{\ell}=\boldsymbol{\sigma}:\dot{\boldsymbol{\varepsilon}}+T\dot{s}+\mu\dot{c},\quad \dot{g}_{\mu}=\boldsymbol{\sigma}:\dot{\boldsymbol{\varepsilon}}-s\dot{T}-c\dot{\mu}\end{aligned}\tag{29}$$

where μ is the chemical potential, $\boldsymbol{d}$ is the flow vector of the diffusing mass, c is the concentration. In discussion of the thermal diffusion problem we can also use the free energy $\dot{g}_c=\boldsymbol{\sigma}:\dot{\boldsymbol{\varepsilon}}-s\dot{T}+\mu\dot{c}$ (Kuang, 2010), but here it is omitted. Using relations

$$T^{-1}q_{i,i}=\left(T^{-1}q_i\right)_{,i}+T^{-2}q_iT_{,i},\qquad T^{-1}\mu d_{i,i}=\left(T^{-1}\mu d_i\right)_{,i}-d_i\left(T^{-1}\mu\right)_{,i}$$

From Eq. (29) (Kuang, 2010) we get:

$$\begin{aligned}&\dot{s}=\dot{s}^{(r)}+\dot{s}^{(i)};\quad T\dot{s}^{(r)}=\dot{r}-T\left(q_i/T-\mu d_i/T\right)_{,i}\\&T\dot{s}^{(i)}=T\dot{s}-T\dot{s}^{(r)}=-T_{,i}\dot{\eta}_i-\mu'_i\dot{\xi}'_i=\geq 0,\quad \mu'_{,i}=\left(\mu/T\right)_{,i},\ \dot{\xi}'_i=Td_i\end{aligned}\tag{30}$$

where $T\dot{s}^{(i)}$ is the irreversible heat rate. According to the linear irreversible thermodynamics the irreversible forces are proportional to the irreversible flow (Kuang, 2010; Gyarmati, 1970; De Groet, 1952), we can write the evolution equations in the following form

$$T\dot{\eta}_i=-\lambda_{ij}\left(T\right)T_{,i}-L_{ij}\left(T\right)T\mu'_{,i},\qquad T^{-1}\dot{\xi}'_i=-D_{ij}\left(T\right)T\mu'_{,i}-L_{ij}\left(T\right)T_{,i}\tag{31a}$$

where D_{ij} is the diffusing coefficients and L_{ij} is the coupling coefficients. The linear irreversible thermodynamics can only give the general form of the evolution equation, the concrete exact formula should be given by experimental results. Considering the experimental facts and the simplicity of the requirement for the variational formula, when the variation of T is not too large, Eq. (31a) can also be approximated by

$$\begin{aligned}&T\dot{s}^{(i)}\approx-T_{,i}\dot{\eta}_i-\mu_{,i}\dot{\xi}_i\geq 0;\quad \dot{\xi}_i=d_i\\&T\dot{\eta}_i=-\lambda_{ij}\left(T\right)T_{,i}-L_{ij}\left(T\right)\mu_{,i},\quad \dot{\xi}_i=-D_{ij}\left(T\right)\mu_{,i}-L_{ij}\left(T\right)T_{,i}\\&T_{,i}=-\hat{\lambda}_{ij}\left(T\right)T\dot{\eta}_i-\hat{L}_{ij}\left(T\right)\dot{\xi}_i,\quad \mu_{,i}=-\hat{D}_{ij}\left(T\right)\dot{\xi}_i-\hat{L}_{ij}\left(T\right)T\dot{\eta}_i\end{aligned}\tag{31b}$$

Especially the coefficients $\lambda_{ij},L_{ij},D_{ij},\hat{\lambda}_{ij},\hat{L}_{ij},\hat{D}_{ij}$ in Eq. (31b) can all be considered as symmetric constants which are adopted in following sections. Eq. (31) is the extension of the Fourier's law and Fick's law.

Eq. (29) shows that in the equation of the heat flow the role of $T\dot{s}$ is somewhat equivalent to $\mu\dot{c}$. So analogous to the inertial entropy $s^{(a)}$ we can also introduce the inertial

concentration $c^{(a)}$ and introduce a general inertial entropy theory of the thermal diffusion problem. Eq. (29) in the general inertial entropy theory is changed to (Kuang, 2010)

$$\begin{aligned} &T\left(\dot{s}+\dot{s}^{(a)}\right)+\mu\left(\dot{c}+\dot{c}^{(a)}\right)=\dot{r}-q_{i,i}=\dot{r}-\left(T\dot{\eta}_i\right)_{,i}; \quad \dot{c}+\dot{c}^{(a)}=-\dot{d}_{i,i} \\ &s^{(a)}=\int_0^t \dot{s}^{(a)}\mathrm{d}\tau, \quad \dot{s}^{(a)}=\rho_s\ddot{T}; \quad c^{(a)}=\int_0^t \dot{c}^{(a)}\mathrm{d}\tau, \quad \dot{c}^{(a)}=\rho_c\ddot{\mu} \end{aligned} \tag{32}$$

where ρ_c is the inertial concentration coefficient. Applying the irreversible thermodynamics we can get the Gibbs free energy g_μ and the complement dissipative energy h_μ as

$$\begin{aligned} &g_\mu\left(\varepsilon_{kl},\vartheta,\mu\right)=\frac{1}{2}C_{ijkl}\varepsilon_{ji}\varepsilon_{lk}-\alpha_{ij}\varepsilon_{ij}\vartheta-\frac{1}{2T_0}C\vartheta^2-\frac{1}{2}b\mu^2-b_{ij}\varepsilon_{ij}\mu-a\mu\vartheta \\ &\delta h_\mu=-T_{,i}\delta\eta_i-\mu_{,i}\delta\xi_i+\delta\left(T_{,i}\eta_i\right)+\delta\left(\mu_{,i}\xi_i\right)=\eta_j\delta\vartheta_{,j}+\xi_j\delta\mu_{,j} \\ &\quad=-\delta\vartheta_{,j}\int_0^t\left(\lambda_{ij}T^{-1}\vartheta_{,i}+L_{ij}T^{-1}\mu_{,i}\right)d\tau-\delta\mu_{,j}\int_0^t\left(L_{ij}\vartheta_{,i}+D_{ij}\mu_{,i}\right)d\tau \end{aligned} \tag{33a}$$

where a,b,b_{ij} are also material constants. The constitutive and evolution equations are:

$$\begin{aligned} &\sigma_{ij}=\partial g_\mu/\partial\varepsilon_{ij}=C_{ijkl}\varepsilon_{kl}-\alpha_{ij}\vartheta-b_{ij}\mu, \\ &s=-\partial g_\mu/\partial\vartheta=\alpha_{ij}\varepsilon_{ij}+C\vartheta/T_0+a\mu, \quad c=-\partial g_\mu/\partial\mu=b\mu+b_{ij}\varepsilon_{ij}+a\vartheta \\ &\eta_i=\partial h_\mu/\partial\vartheta_{,i}=-\int_0^t\left(\lambda_{ij}T^{-1}\vartheta_{,j}+L_{ij}T^{-1}\mu_{,j}\right)d\tau, \quad \xi_i=\partial h_\mu/\partial\mu_{,i}=-\int_0^t\left(L_{ij}\vartheta_{,j}+D_{ij}\mu_{,j}\right)d\tau \end{aligned} \tag{34}$$

Using Eq. (34) g_μ in Eq. (33a) can also be rewritten as

$$g_\mu\left(\varepsilon_{kl},\vartheta,\mu\right)=(1/2)C_{ijkl}\varepsilon_{ji}\varepsilon_{lk}+g_\mu^{(T)}, \quad g_\mu^{(T)}=-(1/2)\left(s\vartheta+c\mu+\alpha_{ij}\varepsilon_{ij}\vartheta+b_{ij}\varepsilon_{ij}\mu\right) \tag{33b}$$

where $g_\mu^{(T)}$ is the energy containing the effects of temperature and concentration. Substituting Eq. (34) into Eq. (32) we get

$$\begin{aligned} &T\left(\alpha_{ij}\varepsilon_{ij}+C\vartheta/T_0+a\mu\right)^{\bullet}+T\rho_s\ddot{\vartheta} \\ &\quad+\mu\left(b\mu+b_{ij}\varepsilon_{ij}+a\vartheta\right)^{\bullet}+\mu\rho_s\ddot{\vartheta}=\dot{r}+\left(\lambda_{ij}\vartheta_{,j}+L_{ij}\mu_{,j}\right)_{,i} \\ &\left(b\mu+b_{ij}\varepsilon_{ij}+a\vartheta\right)^{\bullet}+\rho_c\ddot{\mu}=L_{ji}\vartheta_{,ij}+D_{ji}\mu_{,ij}; \qquad \textit{In medium} \end{aligned} \tag{35}$$

If we neglect the term in second order $\mu d_{i,i}$ in Eq. (29), i.e. we take $T\dot{s}=\dot{r}-q_{i,i}$ and assume that $T_{,i}$ and $\mu_{,j}$ are not dependent each other, i.e. in Eq. (31b) we assume $\dot{\eta}_i=-\lambda_{ij}T^{-1}T_{,j}, \dot{\xi}_i=-D_{ij}\mu_{,j}$, then for $\dot{r}=0$, Eq. (35) becomes

$$\begin{aligned} &T\left(\alpha_{ij}\dot{u}_{i,j}+C\dot{\vartheta}/T_0+a\dot{\mu}+\rho_s\ddot{\vartheta}\right)=\lambda_{ij}\vartheta_{,j} \\ &b\dot{\mu}+b_{ij}\dot{u}_{i,j}+a\dot{\vartheta}+\rho_c\ddot{\mu}=D_{ij}\mu_{,ji}; \qquad \textit{In medium} \end{aligned} \tag{36}$$

The formulas in literatures analogous to Eq. (34) can be found, such as in Sherief, Hamza, and Saleh's paper (2004), where they used the Maxwell-Cattaneo formula.
The momentum equation is

$$\left(C_{ijkl}u_{k,l}-\alpha_{ij}\vartheta-b_{ij}\mu\right)_{,j}+f_i=\rho\ddot{u}_i \tag{37}$$

The above theory is easy extended to more complex materials.

3. Physical variational principle

3.1 General theory

Usually it is considered that the first law of thermodynamics is only a principle of the energy conservation. But we found that the first law of thermodynamics is also a physical variational principle (Kuang, 2007, 2008a, 2008b, 2009a 2011a, 2011b). Therefore the first law of the classical thermodynamics includes two aspects: energy conservation law and physical variational principle:

$$\begin{aligned}&\text{Classical Energy conservation:}\quad \int_V \mathrm{d}\mathcal{U}\mathrm{d}V-\mathrm{d}W-\mathrm{d}Q=0\\&\text{Classical physical variational principle:}\quad \delta\Pi=\int_V\delta\mathcal{U}\mathrm{d}V-\delta W-\delta Q=0\end{aligned} \tag{38}$$

where $\mathcal{U}$ is the internal energy per volume, W is the work applied on the body by the environment, Q is the heat supplied by the environment . According to Gibbs theory when the process is only slightly deviated from the equilibrium state $\mathrm{d}Q$ can be substituted by $\int_V T\mathrm{d}s\mathrm{d}V$. In practice we prefer to use the free energy g :

$$\begin{aligned}&g=\mathcal{U}-Ts,\quad \mathrm{d}g=\mathrm{d}\mathcal{U}-s\mathrm{d}T-T\mathrm{d}s\\&\text{Energy Principle:}\qquad \int_V \mathrm{d}g\mathrm{d}V-dW^*-\int_V s\mathrm{d}T\mathrm{d}V=0\\&\text{Physical Variational Principle:}\quad \delta\Pi=\int_V\delta g\mathrm{d}V-\delta W^*-\int_V s\delta T\mathrm{d}V=0\end{aligned} \tag{39}$$

Here the physical variational principle is considered to be one of the fundamental physical law, which can be used to derive governing equations in continuum mechanics and other fields. We can also give it a simple explanation that the true displacement is one kind of the virtual displacement and obviously it satisfies the variational principle. Other virtual displacements cannot satisfy this variational principle, otherwise the first law is not objective. The physical variational principle is different to the usual mathematical variational method which is based on the known physical facts. In many problems the variation of a variable ϕ different with displacement $\boldsymbol{u}$, should be divided into local variation and migratory variation, i.e. the variation $\delta\phi=\delta_\phi\phi+\delta_u\phi$, where the local variation $\delta_\phi\phi$ of ϕ is the variation duo to the change of ϕ itself and the migratory variation $\delta_u\phi$ of ϕ is the variation of change of ϕ due to virtual displacements. In Eqs. (38) and (39) the new force produced by the migratory variation $\delta_u\phi$ will enter the virtual work δW or δW^* as the same as the external mechanical force. But in the following sections we shall modify Eq. (39) or (38) to deal with this problem. The physical variational principle is inseparable with energy conservation law, so when the expressions of energies are given we get physical variational principle immediately. We need not to seek the variational functional as that in

usual mathematical methods. In the following sections we show how to derive the governing equations with the general Maxwell stress of some kind of materials by using the physical variational principle. From this physical variational principle all of the governing equations in the continuum mechanics and physics can be carried out and this fact can be considered as the indirect evidence of the physical variational principle.

3.2 Physical variational principle in thermo-elasticity

In the thermo-elasticity it is usually considered that only the thermal process is irreversible, but the elastic process is reversible. So the free energy g and the complement dissipative energy can be assumed as that in Eq. (9). The corresponding constitutive and evolution equations are expressed in Eq. (10). As shown in section 3.1, the variation of the virtual temperature ϑ is divided into local variation $\delta_\vartheta\vartheta$ due to the variation of ϑ itself and the migratory variation $\delta_u\vartheta$ due to $\delta\mathbf{u}$:

$$\delta\vartheta = \delta_\vartheta\vartheta + \delta_u\vartheta, \quad \delta_u\vartheta = \vartheta_{,i}\delta u_i \tag{40}$$

In previous paper (Kuang, 2011a) we showed that the migratory variation of virtual electric and magnetic potentials will produce the Maxwell stress in electromagnetic media, which is also shown in section 3.4 of this paper. Similarly the migratory variation $\delta_u\vartheta$ will also produce the general Maxwell stress which is an external temperature stress. The effective general Maxwell stress can be obtained by the energy principle as that in electromagnetic media.

Under assumptions that the virtual mechanical displacement $\boldsymbol{u}$ and the virtual temperature ϑ $(or\ T)$ satisfy their own boundary conditions $u_i = u_i^*, \vartheta = \vartheta^*$ on a_u and a_T respectively. The physical variational principle using the free energy in the inertial entropy theory for the thermo-elasticity can be expressed as:

$$\begin{aligned}
&\delta\Pi_T = \int_V \delta(g+h)\mathrm{d}V + \int_V g^{(T)}\delta u_{k,k}\mathrm{d}V - \delta Q^* - \delta W = 0\\
&\delta Q^* = -\int_V\int_0^t (\dot{r}/T)\delta\vartheta\mathrm{d}\tau\mathrm{d}V - \int_V\int_0^t \dot{s}^{(i)}\delta\vartheta\mathrm{d}\tau\mathrm{d}V + \int_{a_q}\int_0^t \dot{\eta}^*\delta\vartheta\mathrm{d}\tau\mathrm{d}a + \int_V\int_0^t \rho_s\ddot{\vartheta}\delta\vartheta\mathrm{d}\tau\mathrm{d}V\\
&\delta W = \int_V (f_k - \rho\ddot{u}_k)\delta u_k dV + \int_{a_\sigma} T_k^*\delta u_k da
\end{aligned} \tag{41}$$

where f_k, T_k^* and $\dot{\eta}^* = \dot{\eta}_i^* n_i$ are the given mechanical body force, surface traction and surface entropy flow respectively. Eq. (41) is an alternative form of Eq. (39). In Eq. (41) the term $-\int_0^t \dot{s}^{(i)}\delta\vartheta\mathrm{d}\tau = \int_0^t \eta_i\delta T_{,i}\mathrm{d}\tau$ is the complement dissipative heat rate per volume corresponding to the inner complement dissipation energy rate δh. The entropy s includes the contribution of $-\int_0^t \dot{s}^{(i)}\delta\vartheta\mathrm{d}\tau$. The fact that the complement dissipation energy rate $\int_V \delta h dV$ in $\delta\Pi_T$ and the internal irreversible complement heat rate $-\int_V\int_0^t \dot{s}^{(i)}\delta\vartheta\mathrm{d}\tau\mathrm{d}V$ in δQ^* are simultaneously included in Eq. (41) allows us to get the temperature wave equation and the boundary condition of the heat flow from the variational principle. In Eq. (41) there are two kinds of variational formulas. The first is $\int_V \delta g dV + \int_V g^{(T)}\delta u_{k,k}\mathrm{d}V - \delta W$, in which the integrands contain variables themselves. The second is $\int_V \delta h dV - \delta Q^*$, in which the integrands contain the time derivatives of variables, so it needs integrate with time t. This is the common feature of the irreversible process because in the irreversible process the integral is dependent to the integral path.

It is noted that

$$\begin{aligned}
\int_V \delta g dV &= \int_V (C_{ijkl}\varepsilon_{kl} - \alpha_{ij}\vartheta)\delta u_{i,j} dV - \int_V (\alpha_{ij}\varepsilon_{ij} + C\vartheta / T_0)\delta\vartheta dV \\
&= \int_a \sigma_{ij} n_j \delta u_i da - \int_V \sigma_{ij,j}\delta u_i dV - \int_V s\delta\vartheta dV \\
\int_V g^{(T)}\delta u_{k,k}\mathrm{d}V &= -(1/2)\int_V \left(s + \alpha_{ij}\varepsilon_{ij}\right)\vartheta\delta u_{k,k}\mathrm{d}V \\
&= -(1/2)\int_a \left(s + \alpha_{ij}\varepsilon_{ij}\right)\vartheta n_k \delta u_k \mathrm{d}V + (1/2)\int_V \left[\left(s + \alpha_{ij}\varepsilon_{ij}\right)\vartheta\right]_{,k}\delta u_k \mathrm{d}V \\
\int_V \delta h dV &= -\int_a (\int_0^t \lambda_{ij} T^{-1}\vartheta_{,i} n_j \mathrm{d}\tau)\delta\vartheta da + \int_V [\int_0^t (\lambda_{ij} T^{-1}\vartheta_{,i})_{,j}\mathrm{d}\tau]\delta\vartheta dV
\end{aligned} \tag{42}$$

Finishing the variational calculation, we have

$$\begin{aligned}
\delta\Pi = &\int_{a_\sigma} (\tilde{\sigma}_{ij} n_j - T_i^*)\delta u_i da \\
&- \int_V (\tilde{\sigma}_{ij,j} + f_i - \rho\ddot{u}_i)\delta u_i dV - \int_{a_q} [\int_0^t T^{-1}\lambda_{ij}\vartheta_{,i} n_j \mathrm{d}\tau + \eta^*]\delta\vartheta \mathrm{d}a \\
&- \int_V \{s + \int_0^t [-T^{-1}\dot{r} - (\lambda_{ij} T^{-1}\vartheta_{,i})_{,j} - \dot{s}^{(i)}]\mathrm{d}\tau\}\delta\vartheta \mathrm{d}V - \int_V \int_0^t \rho_s \ddot{\vartheta}\mathrm{d}\tau \mathrm{d}V\}\delta\vartheta \mathrm{d}V = 0 \\
\tilde{\sigma}_{ij} = \sigma_{ij} + \sigma_{ij}^T, \quad &\sigma_{ij}^T = -(1/2)\left(s + \alpha_{ij}\varepsilon_{ij}\right)\vartheta\delta_{ij} \approx -(1/2)s\vartheta\delta_{ij}
\end{aligned} \tag{43}$$

where $\boldsymbol{\sigma}^T$ is the effective or equivalent general Maxwell stress which is the external equal axial normal temperature stress. This general Maxwell stress is first introduced and its rationality should be proved by experiments. Obviously $\boldsymbol{\sigma}^T$ can be neglected for the case of the small strain and small change of temperature. In Eq. (43) it is seen that $\delta\vartheta = \delta_\vartheta\vartheta + \delta_u\vartheta$ is appeared in a whole. Using

$$-T(\lambda_{ij} T^{-1}\vartheta_{,i})_{,j} - T\dot{s}^{(i)} = T\dot{\eta}_{j,j} - T\dot{s}^{(i)} = T\dot{\eta}_{j,j} + \dot{\eta}_i T_{,i} = \left(T\dot{\eta}_i\right)_{,i} = q_{i,i}$$

and the arbitrariness of δu_i and $\delta\vartheta$, from Eq. (43) we get

$$\begin{aligned}
&\tilde{\sigma}_{ij,j} + f_i = \rho\ddot{u}_i; \quad T\left(\dot{s} + \rho_s\ddot{\vartheta}\right) = \dot{r} - q_{i,i} \quad \textit{in medium} \\
&\tilde{\sigma}_{kl} n_l = T_k^*, \quad \textit{on} \quad a_\sigma; \quad \dot{\eta}_i = -T^{-1}\lambda_{ij}\vartheta_{,i}, \ \dot{\eta}_i n_i = \dot{\eta}_i^*, \ \textit{or} \quad q_n = q_n^*, \quad \textit{on } a_q
\end{aligned} \tag{44}$$

Here $\boldsymbol{\nabla}\cdot\boldsymbol{\sigma}^T$ is the external temperature body force and $\boldsymbol{n}\cdot\boldsymbol{\sigma}^T$ is the surface traction.
The above variational principle requests prior that displacements and the temperature satisfy the boundary conditions, so in governing equations the following equations should also be added

$$\mathbf{u} = \mathbf{u}^*, \quad \text{on } a_u; \quad \vartheta = \vartheta^* (or\ T = T^*), \quad \text{on } a_T \tag{45}$$

Eqs. (44) and (45) are the governing equations of the thermo-elasticity derived from the physical variational principle.

3.3 Physical variational principle in thermo-diffusion theory

The electro-chemical Gibbs free energy g_μ and the complement dissipative energy h_μ are expressed in Eq. (33) and the constitutive and evolution equations are expressed in Eq. (34).

Under assumptions that the mechanical displacement $\boldsymbol{u}$, the temperature ϑ and the chemical potential μ satisfy their own boundary conditions $\boldsymbol{u}=\boldsymbol{u}^*$, $\vartheta=\vartheta^*$ and $\mu=\mu^*$ on a_u, a_T and a_μ respectively. When the variation of temperature is not large the physical variational principle for the thermo-elasto-diffusive problem is

$$\begin{aligned}
&\delta\Pi_\mu=\int_V\delta(g_\mu+h_\mu)dV+\int_V g_\mu^{(T)}\delta u_{k,k}\mathrm{d}V-\delta Q^*-\delta\Phi^*-\delta W=0\\
&\delta Q^*=-\int_V\left(\int_0^t T^{-1}\dot{r}d\tau\right)\delta\vartheta\mathrm{d}V+\int_V s^{(a)}\delta\vartheta\mathrm{d}V+\int_{a_q}\eta^*\delta\vartheta\mathrm{d}a\\
&\qquad+\int_V\int_0^t T^{-1}\left(T_{,i}\dot{\eta}_i+\mu_{,i}\dot{\xi}_i\right)\delta\vartheta\,\mathrm{d}\tau\mathrm{d}V-\int_a\int_0^t T^{-1}\mu\dot{\xi}_i n_i\delta\vartheta\,\mathrm{d}\tau\mathrm{d}a\\
&\delta\Phi^*=\int_V c^{(a)}\delta\mu\mathrm{d}V+\int_{a_d}\xi^*\delta\mu\mathrm{d}a\\
&\delta W=\int_V(f_k-\rho\ddot{u}_k)\delta u_k dV+\int_{a_\sigma}T_k^*\delta u_k da
\end{aligned}\tag{46}$$

In Eqs. (46) f_k, T_k^* $\dot{\eta}^*=\dot{\eta}_i^* n_i$ and $\dot{\xi}^*=\dot{\xi}_i^* n_i$ are given values. In Eq. (46) δQ^* is related to heat (including the heat produced by the irreversible process in the material), $\delta\Phi^*$ is related to the diffusion energy. Eq. (46) shows that there is no term in $\int_V\delta h_\mu dV$ corresponding to the term $-\int_a\int_0^t T^{-1}\mu\dot{\xi}_n\delta\vartheta\,\mathrm{d}\tau\mathrm{d}a$, so it should not be included in δQ^* and $\int_V\int_0^t T^{-1}\mu_{,i}\dot{\xi}_i\delta\vartheta\,\mathrm{d}\tau\mathrm{d}V-\int_a\int_0^t T^{-1}\mu\dot{\xi}_i n_i\delta\vartheta\,\mathrm{d}\tau\mathrm{d}a=-\int_V\int_0^t T^{-1}\mu\dot{\xi}_{i,i}\delta\vartheta\,\mathrm{d}\tau\mathrm{d}V$.
It is noted that we have the following relations

$$\begin{aligned}
&\int_V\delta g_\mu dV=\int_a\sigma_{ij}n_j\delta u_i da-\int_V\sigma_{ij,j}\delta u_i dV-\int_V s\delta\vartheta dV-\int_V c\delta\mu dV\\
&\int_V g_\mu^{(T)}\delta u_{k,k}\mathrm{d}V=-(1/2)\int_V\left(s\vartheta+c\mu+\alpha_{ij}\varepsilon_{ij}\vartheta+b_{ij}\varepsilon_{ij}\mu\right)\delta u_{k,k}\mathrm{d}V\\
&\qquad=-(1/2)\int_a\left(s\vartheta+c\mu+\alpha_{ij}\varepsilon_{ij}\vartheta+b_{ij}\varepsilon_{ij}\mu\right)n_k\delta u_k\mathrm{d}V\\
&\qquad+(1/2)\int_V\left(s\vartheta+c\mu+\alpha_{ij}\varepsilon_{ij}\vartheta+b_{ij}\varepsilon_{ij}\mu\right)_{,k}\delta u_k\mathrm{d}V\\
&\delta h_\mu=-\int_V\left\{\delta\vartheta_{,i}\int_0^t\left(\lambda_{ij}T^{-1}T_{,i}+L_{ij}T^{-1}\mu_{,i}\right)d\tau+\delta\mu_{,i}\int_0^t\left(L_{ij}T_{,i}+D_{ij}\mu_{,i}\right)d\tau\right\}dV
\end{aligned}\tag{47}$$

The further derivation is fully similar to that in the thermo-elasticity. Combining Eqs. (46) and (47) we get

$$\begin{aligned}
&\delta\Pi_\mu=\int_{a_\sigma}(\tilde{\sigma}_{ij}n_j-T_i^*)\delta u_i da-\int_V(\tilde{\sigma}_{ij,j}+f_i-\rho\ddot{u}_i)\delta u_i dV-\int_V s\delta\vartheta dV-\int_V c\delta\mu dV\\
&\quad-\int_a\left\{\delta\vartheta n_j\int_0^t\left(\lambda_{ij}T^{-1}T_{,i}+L_{ij}T^{-1}\mu_{,i}\right)d\tau+\delta\mu n_j\int_0^t\left(L_{ij}T_{,i}+D_{ij}\mu_{,i}\right)d\tau\right\}da\\
&\quad+\int_V\left\{\delta\vartheta\int_0^t\left(\lambda_{ij}T^{-1}T_{,i}+L_{ij}T^{-1}\mu_{,i}\right)_{,j}d\tau+\delta\mu\int_0^t\left(L_{ij}T_{,i}+D_{ij}\mu_{,i}\right)_{,j}d\tau\right\}dV\\
&\quad+\int_V\left(\int_0^t T^{-1}\dot{r}d\tau\right)\delta\vartheta\mathrm{d}V-\int_V s^{(a)}\delta\vartheta\mathrm{d}V-\int_V c^{(a)}\delta\mu\mathrm{d}V\\
&\quad-\int_{a_q}\eta^*\delta\vartheta\mathrm{d}a-\int_{a_d}\xi^*\delta\mu\mathrm{d}a-\int_V\int_0^t\left(T^{-1}T_{,i}\dot{\eta}_i-T^{-1}\mu\dot{\xi}_{i,i}\right)\delta\vartheta\,\mathrm{d}\tau\mathrm{d}V=0
\end{aligned}\tag{48}$$

where

$$\tilde{\sigma}_{ij}=\sigma_{ij}+\sigma_{ij}^{T\mu},\quad \sigma_{ij}^{T\mu}=-(1/2)\left(s\vartheta+c\mu+\alpha_{ij}\varepsilon_{ij}\vartheta+b_{ij}\varepsilon_{ij}\mu\right)\delta_{ij}\approx-(1/2)(s\vartheta+c\mu) \tag{49}$$

Due to the arbitrariness of $\delta\boldsymbol{u}$, $\delta\vartheta$ and $\delta\mu$, from Eq. (48) we get

$$\tilde{\sigma}_{kl,l}+f_k=\rho\ddot{u}_k,\quad in\ medium;\quad \tilde{\sigma}_{kl}n_l=T_k^*,\quad on\ a_\sigma \tag{50}$$

and

$$\begin{aligned}
&\int_V\int_0^t\left(\dot{s}+\rho_s\ddot{\vartheta}\right)d\tau dV=\int_V\int_0^t T^{-1}\left(\dot{r}-q_{j,j}+\mu\dot{\xi}_{j,j}\right)\mathrm{d}\tau dV\\
&\int_V\int_0^t\left(\dot{c}+\rho_c\ddot{\mu}\right)d\tau dV=-\int_V\int_0^t\dot{\xi}_{j,j}d\tau dV\quad In\ medium\\
&\dot{\eta}_j=-T^{-1}\left(\lambda_{ij}T_{,i}+L_{ij}\mu_{,i}\right),\quad \dot{\eta}_jn_j=\dot{\eta}^*,\quad or\quad q_n=q_n^*\quad on\ a_q\\
&\dot{\xi}_j=-\left(L_{ij}T_{,i}+D_{ij}\mu_{,i}\right),\quad \dot{\xi}_jn_j=\dot{\xi}^*,\quad or\quad d_n=d_n^*\quad on\ a_d
\end{aligned} \tag{51}$$

where $T^{-1}\left(\lambda_{ij}T_{,i}+L_{ij}\mu_{,i}\right)_{,j}-T^{-1}\left(T_{,i}\dot{\eta}_i-\mu\dot{\xi}_{i,i}\right)=-T^{-1}\left(q_{j,j}+\mu\dot{\xi}_{i,i}\right)$ has been used.

The first two formulas in Eq. (51) can be rewritten as

$$\begin{aligned}
&T\left(\dot{s}+\rho_s\ddot{\vartheta}\right)=\dot{r}-q_{j,j}+\mu\dot{\xi}_{j,j};\quad \dot{c}+\rho_c\ddot{\mu}=-\dot{\xi}_{j,j}\\
&T\left(\dot{s}+\rho_s\ddot{\vartheta}\right)+\mu\left(\dot{c}+\rho_c\ddot{\mu}\right)=\dot{r}-q_{j,j};\quad In\ medium
\end{aligned} \tag{52}$$

The last equation in Eq. (52) is just the same as that in Eq. (32).

The above variational principle requests prior that the $\mathbf{u},\vartheta$ and μ satisfy their own boundary conditions, so in governing equations the following equations should also be added

$$\mathbf{u}=\mathbf{u}^*,\quad \text{on } a_u;\quad \vartheta=\vartheta^*,\quad \text{on } a_T;\quad \mu=\mu^*,\quad \text{on } a_\mu \tag{53}$$

Eqs. (49)-(53) are the governing equations of the generalized thermodiffusion theory.

If we neglect the term $\mu\left(\dot{c}+\dot{c}^{(a)}\right)$ in Eq. (32), or $T\left(\dot{s}+\dot{s}^{(a)}\right)=\dot{r}-q_{i,i}$ is adopted, then we easily get

$$\begin{aligned}
&T\left(\dot{s}+\rho_s\ddot{\vartheta}\right)=\dot{r}-q_{j,j},\quad \dot{c}+\rho_c\ddot{\mu}=-\dot{\xi}_{j,j};\quad In\ medium\\
&\dot{\eta}_jn_j=\dot{\eta}^*,\quad or\quad q_n=q_n^*\quad on\ a_q\\
&\dot{\xi}_jn_j=\dot{\xi}^*,\quad or\quad d_n=d_n^*\quad on\ a_d\ and\ a_q
\end{aligned} \tag{54}$$

If we also assume that $T_{,i}$ and $\mu_{,j}$ are not dependent each other, then for $\dot{r}=0$, the Eq. (54) becomes Eq. (36), i.e.

$$\begin{aligned}
&T\left(\alpha_{ij}\dot{u}_{i,j}+C\dot{\vartheta}/T_0+a\dot{\mu}+\rho_s\ddot{\vartheta}\right)=\lambda_{ij}\vartheta_{,j}\\
&b\dot{\mu}+b_{ij}\dot{u}_{i,j}+a\dot{\vartheta}+\rho_c\ddot{\mu}=D_{ij}\mu_{,j};\qquad In\ medium
\end{aligned} \tag{55}$$

3.4 Physical variational principle in electro-magneto-elastic analysis

In this section we discuss the nonlinear electro-magneto-elastic media. Here we extend the theory in previous paper (Kuang, 2011) to the material with the electromagnetic body couple. Because the asymmetric part of the stress is introduced by the electromagnetic body couple, the specific electromagnetic Gibbs free energy g_{em} is taken as

$$\begin{aligned} g_{em}(\varepsilon_{kl},E_k,H_k) &= (1/2)C_{ijkl}\varepsilon_{ji}\varepsilon_{lk} - \left(e^e_{kij}E_k + e^m_{kij}H_k\right)\varepsilon_{ij} - (1/2)\left(\in_{ij} E_iE_j + \mu_{ij}H_iH_j\right) \\ &\quad - (1/2)\left(l^e_{ijkl}E_iE_j + l^m_{ijkl}H_iH_j\right)\varepsilon_{kl} - \left(\in_{km} E_mE_l + \mu_{km}H_mH_l\right)\varepsilon_{kl} \\ \left(C_{ijkl},l^e_{ijkl},l^m_{ijkl}\right) &= \left(C_{jikl},l^e_{jikl},l^m_{jikl}\right) = \left(C_{ijlk},l^e_{ijlk},l^m_{ijlk}\right) = \left(C_{klij},l^e_{klij},l^m_{klij}\right),\ e^e_{kij} = e^e_{kji},\ e^m_{kij} = e^m_{kji} \end{aligned} \tag{56a}$$

where l^e_{ijkl} and l^m_{ijkl} are the electrostrictive and megnetostrictive constants respectively; $\boldsymbol{\in}$ and $\boldsymbol{\mu}$ may be asymmetric. The corresponding constitutive equations are

$$\begin{aligned} \sigma_{kl} &= \partial g_{em}/\partial\varepsilon_{kl} = C_{ijkl}\varepsilon_{ij} - e^e_{jkl}E_j - e^m_{jkl}H_j - (1/2)l^e_{ijkl}E_iE_j - (1/2)l^m_{ijkl}H_iH_j \\ &\quad - \in_{km} E_mE_l - \mu_{km}H_mH_l \\ D_k &= -\partial g_{em}/\partial E_k = \left[\in_{kl} + l^e_{ijkl}\varepsilon_{ij} + \left(\in_{ml}\varepsilon_{mk} + \in_{mk}\varepsilon_{ml}\right)\right]E_l + e^e_{kij}\varepsilon_{ij} \approx \in_{kl} E_l \\ B_k &= -\partial g_{em}/\partial H_k = \left[\mu_{kl} + l^m_{ijkl}\varepsilon_{ij} + \left(\alpha^m_{ml}\varepsilon_{mk} + \alpha^m_{mk}\varepsilon_{ml}\right)\right]H_l + e^m_{kij}\varepsilon_{ij} \approx \mu_{kl}H_l \end{aligned} \tag{57}$$

Let $\boldsymbol{\sigma}^s$ and $\boldsymbol{\sigma}^a$ be the symmetric and asymmetric parts of $\boldsymbol{\sigma}$ respectively, we have

$$\begin{aligned} \sigma^s_{kl} &= (1/2)(\sigma_{kl} + \sigma_{lk}) = C_{ijkl}\varepsilon_{ji} - e^e_{jkl}E_j - (1/2)l^e_{ijkl}E_iE_j - e^m_{jkl}H_j - (1/2)l^m_{ijkl}H_iH_j \\ &\quad - (1/2)(\in_{km} E_l + \in_{lm} E_k)E_m - (1/2)(\mu_{km}H_l + \mu_{lm}H_k)H_m \\ \sigma^a_{kl} &= (1/2)(\sigma_{kl} - \sigma_{lk}) = -(1/2)(\in_{km} E_l - \in_{lm} E_k)E_m - (1/2)(\mu_{km}H_l - \mu_{lm}H_k)H_m \\ D_kE_l - D_lE_k &= P_kE_l - P_lE_k \approx (\in_{km} E_l - \in_{lm} E_k)E_m \\ B_kH_l - B_lH_k &= \mu_0(M_kH_l - M_lH_k) \approx (\mu_{km}H_l - \mu_{lm}H_k)H_m \end{aligned} \tag{58}$$

where $\boldsymbol{D} = \in_0 \boldsymbol{E} + \boldsymbol{P}, \boldsymbol{B} = \mu_0(\boldsymbol{H} + \boldsymbol{M})$ have been used, $\boldsymbol{P}$ and $\boldsymbol{M}$ are the polarization density and magnetization density, $\in_0$ and μ_0 are the dielectric constant and magnetic permeability in vacuum respectively. The terms containing $\boldsymbol{\varepsilon}$ in $\boldsymbol{D}$ and $\boldsymbol{B}$ in Eq. (58) have been neglected. In the usual electromagnetic theory the electromagnetic body couple is $\boldsymbol{P}\times\boldsymbol{E} + \mu_0\boldsymbol{M}\times\boldsymbol{H}$. From Eq. (58) it is seen that $2\sigma^a_{kl} + (D_kE_l - D_lE_k) + (B_kH_l - B_lH_k) = 0$ or the electromagnetic body couple is balanced by the moment produced by the asymmetric stresses.

Using Eq. (57), Eq. (56a) can be reduced to

$$\begin{aligned} g_{em} &= (1/2)C_{ijkl}\varepsilon_{ji}\varepsilon_{lk} + g^{em},\ g^{em} = -(1/2)(D_kE_k + B_kH_k + \Delta_{kl}\varepsilon_{lk}) \approx -(1/2)(D_kE_k + B_kH_k) \\ \Delta_{kl} &= e^e_{mkl}E_m + e^m_{mkl}H_m = -e^e_{mkl}\varphi_{,m} - e^m_{mkl}\psi_{,m} \end{aligned} \tag{56b}$$

Because the value of the term $\boldsymbol{\Delta}:\boldsymbol{\varepsilon}$ is much less than that of other terms, it can be neglected.

In the nonlinear electro-magneto-elastic analysis the medium and its environment should be considered together as shown in Fig. 1 (Kuang, 2011a, 2011b), because the electromagnetic field exists in all space. Under the assumption that $\mathbf{u},\varphi,\psi,\mathbf{u}^{env},\varphi^{env},\psi^{env}$ satisfy their

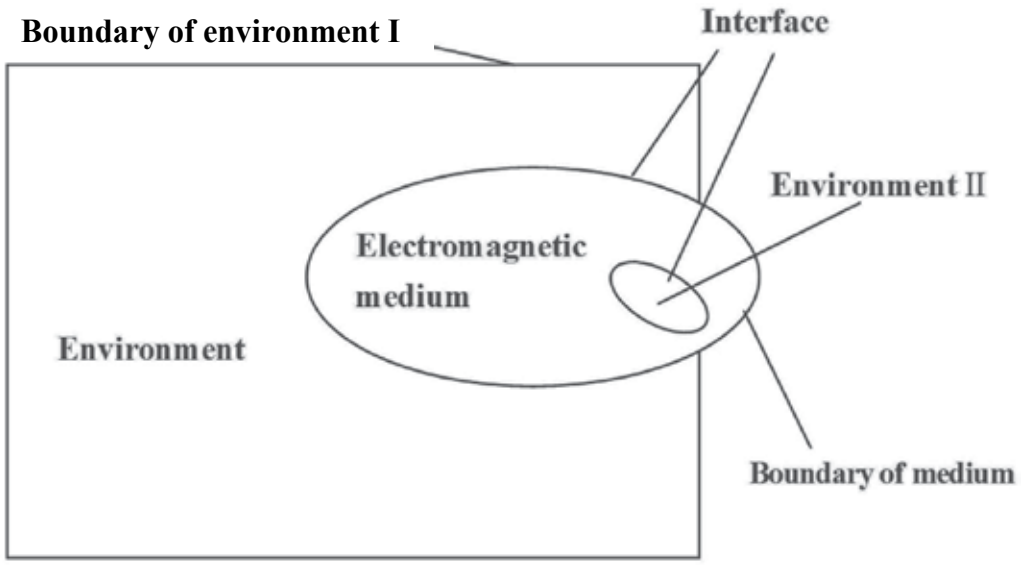

Fig. 1. Electromagnetic medium and its environment

boundary conditions on their own boundaries $a_u, a_\varphi, a_\psi, a_u^{env}, a_\varphi^{env}, a_\psi^{env}$ and the continuity conditions on the interface a^{int}. The Physical variational principle in the nonlinear electro-magneto-elastic analysis is

$$\begin{aligned}
&\delta\Pi = \delta\Pi_1 + \delta\Pi_2 - \delta W^{*int} = 0\\
&\delta\Pi_1 = \int_V \delta g_{em} dV + \int_V g^{em}\delta u_{i,i} dV - \delta W^*\\
&\delta\Pi_2 = \int_{V^{env}} \delta g_{em}^{env} dV + \int_{V^{env}} g^{em\,env}\delta u_{i,i}^{env} dV - \delta W^{*env}\\
&\delta W^* = \int_V (f_k - \rho\ddot{u}_k)\delta u_k dV - \int_V \rho_e \delta\varphi dV + \int_{a_\sigma} T_k^*\delta u_k da - \int_{a_q} \sigma^*\delta\varphi da + \int_{a_\mu} B_i^* n_i \delta\psi da\\
&\delta W^{*int} = \int_{a^{\text{int}}} T_k^{*\text{int}}\delta u_k da - \int_{a^{\text{int}}} \sigma^{*\text{int}}\delta\varphi da + \int_{a_\mu^{\text{int}}} B_i^{*\text{int}} n_i \delta\psi^{env} da\\
&g_{em}^{env},\ g^{em\,env}, \delta W^{*env} \text{ are similar and omited here}
\end{aligned} \tag{59}$$

where the superscript "env" means the variable in environment, "int" means the variable on the interface, $f_k, T_k^*, \sigma^*, B_n{}^* = B_i{}^* n_i;\ T_k^{*env}, \sigma^{*env}, B_n{}^{*env}; T_k^{*int}, \sigma^{*int}, B_n{}^{*int}$ are the given values on the corresponding surfaces. Eq. (59) is an alternative form of Eq. (39) and the electromagnetic force is directly enclosed in the formula (Kuang, 2008a, 2009a).
As shown in previous paper (Kuang, 2011a, 2011b) and in section 3.1 the variations of $\varphi, \psi, \boldsymbol{E}, \boldsymbol{H}$ will be distinguished into local and migratory variations, i.e.

$$\begin{aligned}
&\delta(\varphi,\psi,E_i,H_i) = \delta_{(\varphi,\psi,E_i,H_i)}(\varphi,\psi,E_i,H_i) + \delta_u(\varphi,\psi,E_i,H_i)\\
&\delta_u(\varphi,\psi) = (\varphi,\psi)_{,p}\,\delta u_p = -(E_p,H_p)\delta u_p\\
&\delta_u(E_i,H_i) = -\delta_u(\varphi,\psi)_{,i} = -(\varphi,\psi)_{,ip}\,\delta u_p = (E_{p,i},H_{p,i})\delta u_p = (E_{i,p},H_{i,p})E_{i,p}\delta u_p
\end{aligned} \tag{60}$$

Noting that in Eq. (59) we have

$$\begin{aligned}
&\int_V \delta g_{em} dV + \int_V g^{em} \delta u_{k,k} dV = \int_V \sigma_{ij} \delta \varepsilon_{ij} dV - \int_V D_i \delta E_i dV - \int_V B_i \delta H_i dV \\
&\quad - (1/2) \int_V (D_k E_k + B_k H_k) \delta u_{j,j} dV = \int_a \left[\sigma_{ij} - (1/2)(D_k E_k + B_k H_k) \delta_{ij} \right] n_j \delta u_i \mathrm{d}a \\
&\quad - \int_V \left[\sigma_{ij} - (1/2)(D_k E_k + B_k H_k) \delta_{ij} \right]_{,j} \delta u_i \mathrm{d}V + \int_a D_i n_i \delta_\varphi \varphi \mathrm{d}a - \int_V D_{i,i} \delta_\varphi \varphi \mathrm{d}V \\
&\quad - \int_V D_i E_{p,i} \delta u_p \mathrm{d}V + \int_a B_i n_i \delta_\psi \psi \mathrm{d}a - \int_V B_{i,i} \delta_\psi \psi \mathrm{d}V - \int_V B_i H_{p,i} \delta u_p \mathrm{d}V
\end{aligned}$$

So $\delta \Pi_1$ in Eq. (59) is reduced to

$$\begin{aligned}
&\delta \Pi_1 = \delta \Pi_1' + \delta \Pi_1'' \\
&\delta \Pi_1' = \int_{a_\sigma} \left(\sigma_{kj} n_j - T_k^* \right) \delta u_k \mathrm{d}a + \int_{a^{\mathrm{int}}} \sigma_{kj} n_j \delta u_k \mathrm{d}a \\
&\quad - \int_V \left(\sigma_{kj,j} + f_k - \rho \ddot{u}_k \right) \delta u_k \mathrm{d}V - \int_V \left(D_{i,i} - \rho_e \right) \delta_\varphi \varphi \mathrm{d}V + \int_{a_D} \left(D_i n_i + \sigma^* \right) \delta_\varphi \varphi \mathrm{d}a \\
&\quad + \int_{a^{\mathrm{int}}} D_i n_i \delta_\varphi \varphi \mathrm{d}a - \int_V B_{i,i} \delta_\psi \psi \mathrm{d}V + \int_{a_\mu} \left(B_i - B_i^* \right) n_i \delta_\psi \psi \mathrm{d}a + \int_{a^{\mathrm{int}}} B_i n_i \delta_\psi \psi \mathrm{d}a \qquad (61) \\
&\delta \Pi_1'' = (1/2) \int_{a_\sigma} \left(D_m \varphi_{,m} + B_m \psi_{,m} \right) n_k \delta u_k \mathrm{d}a + (1/2) \int_{a^{\mathrm{int}}} \left(D_m \varphi_{,m} + B_m \psi_{,m} \right) n_k \delta u_k \mathrm{d}a \\
&\quad - (1/2) \int_V \left(D_m \varphi_{,m} + B_m \psi_{,m} \right)_{,k} \delta u_k \mathrm{d}V - \int_V D_i E_{p,i} \delta u_p \mathrm{d}V - \int_V \rho_e E_p \delta u_p dV \\
&\quad - \int_{a_D} \sigma^* E_p \delta u_p da - \int_V B_i H_{p,i} \delta u_p \mathrm{d}V + \int_{a_\mu^{env}} B_i^* n_i H_p \delta u_p da
\end{aligned}$$

where $\delta \Pi_1'$ is the part of $\delta \Pi_1$ due to the local variations of $\mathbf{u}, \varphi, \psi$; $\delta \Pi_1''$ is the part of $\delta \Pi_1$ due to the migratory variations of φ, ψ . Substituting the following identity

$$\begin{aligned}
&- \int_V D_i E_{p,i} \delta u_p \mathrm{d}V - \int_V \rho_e E_p \delta u_p dV - \int_{a_D} \sigma^* E_p \delta u_p da - \int_V B_i H_{p,i} \delta u_p \mathrm{d}V \\
&+ \int_{a_\mu} B_i^* n_i H_p \delta u_p da = \int_{a_D} (D_i n_i + \sigma^*) \delta_u \varphi da + \int_{a^{\mathrm{int}}} D_i n_i \delta_u \varphi da + \int_a \left(D_i E_p \right) n_i \delta u_p da \\
&- \int_V \left(D_i E_p \right)_{,i} \delta u_p dV - \int_V (D_{i,i} - \rho_e) \delta_u \varphi dV + \int_{a_\mu} \left(B_i - B_i^* \right) n_i \delta_u \psi da \\
&+ \int_{a^{\mathrm{int}}} B_i n_i \delta_u \psi da + \int_a \left(B_i H_p \right) n_i \delta u_p da - \int_V \left(B_i H_p \right)_{,i} \delta u_p dV - \int_V B_{i,i} \delta_u \psi dV
\end{aligned} \qquad (62)$$

into $\delta \Pi_1''$ in Eq. (61) we get

$$\begin{aligned}
\delta \Pi_1'' &= - \int_V (D_{i,i} - \rho_e) \delta_u \varphi dV + \int_{a_D} (D_i n_i + \sigma^*) \delta_u \varphi da + \int_{a^{\mathrm{int}}} D_i n_i \delta_u \varphi da \\
&\quad - \int_V B_{i,i} \delta_u \psi dV + \int_{a_\mu} \left(B_i - B_i^* \right) n_i \delta_u \psi da + \int_{a^{\mathrm{int}}} B_i n_i \delta_u \psi da \qquad (63) \\
&\quad + \int_{a_\sigma} \sigma_{ik}^M n_i \delta u_k da + \int_{a^{\mathrm{int}}} \sigma_{ik}^M n_i \delta u_k da - \int_V \sigma_{ik,i}^M \delta u_k dV
\end{aligned}$$

where $\boldsymbol{\sigma}^M$ is the Maxwell stress:

$$\sigma_{ik}^M = D_i E_k + B_i H_k - (1/2)(D_n E_n + B_n H_n) \delta_{ik} \qquad (64)$$

Substituting Eq. (63) into Eq. (61) we get

$$
\begin{aligned}
\delta \Pi_1 &= \int_{a_\sigma} (\tilde{\sigma}_{ij} n_i - T_j^*)\delta u_j \mathrm{d}a + \int_{a^{\mathrm{int}}} \tilde{\sigma}_{ij} n_i \delta u_j \mathrm{d}a - \int_V (\tilde{\sigma}_{ij,i} + f_j - \rho \ddot{u}_j)\delta u_j \mathrm{d}V \\
&+ \int_{a_D} (D_{i,i} + \sigma^*)\delta\varphi \mathrm{d}a + \int_{a^{\mathrm{int}}} D_i n_i \delta\varphi \mathrm{d}a - \int_V (D_{i,i} - \rho_e)\delta\varphi dV \\
&+ \int_{a_\mu} \left(B_i - B_i^*\right) n_i \delta\psi da + \int_{a^{\mathrm{int}}} B_i n_i \delta\psi da - \int_V B_{i,i}\delta\psi dV \\
\tilde{\sigma}_{kl} &= \sigma_{kl} + \sigma_{kl}^M = C_{ijkl}\varepsilon_{ij} - e_{jkl}^e E_j - e_{jkl}^m H_j - (1/2) l_{ijkl}^e E_i E_j - (1/2) l_{ijkl}^m H_i H_j \\
&- (1/2)(D_m E_m + B_m H_m)\delta_{kl}
\end{aligned}
\tag{65}
$$

where $\tilde{\boldsymbol{\sigma}}$ is the pseudo total stress (Jiang and Kuang, 2004), which is not the true stress in electromagnetic media. From the expression of $\tilde{\boldsymbol{\sigma}}$ it is known that $\tilde{\boldsymbol{\sigma}}$ is symmetric though $\boldsymbol{\sigma}$ and $\boldsymbol{\sigma}^M$ are asymmetric. Due to the arbitrariness of $\delta u_i, \delta\varphi$ and $\delta\psi$, from Eq. (65) we get

$$
\begin{aligned}
&\tilde{\sigma}_{jk,j} + f_k = \rho \ddot{u}_k, \quad D_{i,i} = \rho_e, \quad B_{i,i} = 0, \quad \text{in } V \\
&\tilde{\sigma}_{jk} n_j = T_k^*, \quad on\ a_\sigma; \quad D_i n_i = -\sigma^*, \quad on\ a_D; \quad \left(B_i - B_i^*\right) n_i = 0, \quad on\ a_\mu \\
&\delta \Pi_1 = \int_{a^{\mathrm{int}}} \tilde{\sigma}_{ij} n_i \delta u_j \mathrm{d}a + \int_{a^{\mathrm{int}}} D_i n_i \delta\varphi da + \int_{a^{\mathrm{int}}} B_i n_i \delta\psi da
\end{aligned}
\tag{66}
$$

For the environment we have the similar formula:

$$
\begin{aligned}
&\tilde{\sigma}_{ij,i}^{env} + f_j^{env} = \rho^{env} \ddot{u}_j^{env}, \quad D_{i,i}^{env} = \rho_e^{env}, \quad B_{i,i} = 0, \quad \text{in } V^{env} \\
&\tilde{\sigma}_{ij}^{env} n_i^{env} = T_j^{*env}, \ \text{on } a_\sigma^{env}; \ D_i^{env} n_i^{env} = -\sigma^{*env}, \ on\ a_D^{env}; \ B_i^{env} n_i^{env} = B_i^{*env} n_i^{env}, \ on\ a_\mu^{env} \\
&\delta \Pi_2 = \int_{a^{\mathrm{int}}} \tilde{\sigma}_{ij}^{env} n_i^{env} \delta u_j^{env} da + \int_{a^{\mathrm{int}}} D_i^{env} n_i^{env} \delta\varphi^{env} da + \int_{a^{\mathrm{int}}} B_i^{env} n_i^{env} \delta\psi^{env} da \\
&\tilde{\sigma}_{jk}^{env} = \sigma_{jk}^{env} + \sigma_{jk}^{M\,env}
\end{aligned}
\tag{67}
$$

Using $n_i = -n_i^{env}, u_i = u_i^{env}, \varphi = \varphi^{env}, \psi = \psi^{env}$ and $\delta\Pi_1 + \delta\Pi_2 = \delta W^{*int}$ on the boundary surface we get

$$
(\tilde{\sigma}_{ij} - \tilde{\sigma}_{ij}^{env}) n_i = T_j^{*\mathrm{int}}, \ (D_i - D_i^{env}) n_i = -\sigma^{*\mathrm{int}}, \ (B_i - B_i^{env}) n_i = B_i^{*\mathrm{int}} n_i, \ \text{on } a^{\mathrm{int}} \tag{68}
$$

The above variational principle requests prior that the displacements, the electric potential and the magnetic potential satisfy their own boundary conditions and the continuity conditions on the interface, so the following equations should also be added to governing equations

$$
\begin{aligned}
&u_i = u_i^*, \ \text{on } a_u; \ \varphi = \varphi^*, \ \text{on } a_\varphi; \ \psi = \psi^*, \ \text{on } a_\mu \\
&u_i^{env} = u_i^{*env}, \ \text{on } a_u^{env}; \ \varphi^{env} = \varphi^{*env}; \ on\ a_\varphi^{env}; \ \psi^{env} = \psi^{*env}, \ on\ a_\mu^{env} \\
&u_i = u_i^{env}, \ \varphi = \varphi^{env}, \ \psi = \psi^{env}; \ on\ a^{\mathrm{int}}
\end{aligned}
\tag{69}
$$

Eqs. (66)—(69) are the governing equations. It is obvious that the above physical variational principle is easy to extend to other materials.

3.5 Materials with static magnetoelectric coupling effect

In this section we discuss the electro-magneto-elastic media with static magnetoelectric coupling effect shortly. For these materials the constitutive equations are

$$\begin{aligned}
\sigma_{kl} &= C_{ijkl}\varepsilon_{ij} - e^{e}_{jkl}E_j - e^{m}_{jkl}H_j - (1/2)l^{e}_{ijkl}E_iE_j - (1/2)l^{m}_{ijkl}H_iH_j \\
&\quad - \epsilon_{km}E_mE_l - \mu_{km}H_mH_l - \beta_{km}H_mE_l - \beta_{km}E_mH_l \\
D_k &= \left[\epsilon_{kl} + l^{e}_{ijkl}\varepsilon_{ij} + (\epsilon_{ml}\varepsilon_{mk} + \epsilon_{mk}\varepsilon_{ml})\right]E_l + e^{e}_{kij}\varepsilon_{ij} + \beta_{kl}H_l \\
B_k &= \left[\mu_{kl} + l^{m}_{ijkl}\varepsilon_{ij} + 2(\alpha^{m}_{ml}\varepsilon_{mk} + \alpha^{m}_{mk}\varepsilon_{ml})\right]H_l + e^{m}_{kij}\varepsilon_{ij} + \beta_{kl}E_l
\end{aligned} \tag{70}$$

where $\beta_{ij} = \beta_{ji}$ is the static magnetoelectric coupling coefficient. The electromagnetic body couple is still balanced by the asymmetric stress, i.e.

$$\begin{aligned}
D_kE_l - D_lE_k + B_kH_l - B_lH_k &= \left[(\epsilon_{km}E_l - \epsilon_{lm}E_k)E_m + (\mu_{km}H_l - \mu_{lm}H_k)H_m\right] \\
&\quad + \left[(\beta_{km}E_l - \beta_{lm}E_k)H_m + (\beta_{km}H_l - \beta_{lm}H_k)E_m\right] = -2\sigma^{a}_{kl}
\end{aligned}$$

In this case though the constitutive equations are changed, but the electromagnetic Gibbs free energy g_e in Eq. (56b), governing equations (66)—(69) and the Maxwell stress (64) are still tenable.

4. Conclusions

In this chapter some advances of thermodynamics in continuum mechanics are introduced. We advocate that the first law of the thermodynamics includes two contents: one is the energy conservation and the other is the physical variational principle which is substantially the momentum equation. For the conservative system the complete governing equations can be obtained by using this theory and the classical thermodynamics. For the non-conservative system the complete governing equations can also be obtained by using this theory and the irreversible thermodynamics when the system is only slightly deviated from the equilibrium state. Because the physical variational principle is tensely connected with the energy conservation law, so we write down the energy expressions, we get the physical variational principle immediately and do not need to seek the variational functional as that in usual mathematical methods.

In this chapter we also advocate that the accelerative variation of temperature needs extra heat and propose the general inertial entropy theory. From this theory the temperature wave and the diffusion wave with finite propagation velocities are easily obtained. It is found that the coupling effect in elastic and temperature waves attenuates the temperature wave, but enhances the elastic wave. So the theory with two parameters by introducing the viscous effect in this problem may be more appropriate.

Some explanation examples for the physical variational principle and the inertial entropy theory are also introduced in this chapter, which may indirectly prove the rationality of these theories. These theories should still be proved by experiments.

5. References

Christensen, R M, 2003, Theory of Viscoelasticity, Academic Press, New York.

De Groet, S R, 1952, Thermodynamics of Irreversible Processes, North-Holland Publishing Company,

Green, A E, Lindsay, K A, 1972, Thermoelasticity, Journal of Elasticity, 2: 1-7.

Gyarmati, I, 1970, Non-equilibrium thermodynamics, Field theory and variational principles, Berlin, Heidelberg, New York, Springer-Verlag.

Kuang, Z-B, 1999, Some remarks on thermodynamic theory of viscous-elasto-plastic media, in IUTAM symposium on rheology of bodies with defects, 87-99, Ed. By Wang, R., Kluwer Academic Publishers.

Kuang, Z-B, 2002, Nonlinear continuum mechanics, Shanghai Jiaotong University Press, Shanghai. (in Chinese)

Kuang, Z-B, 2007, Some problems in electrostrictive and magnetostrictive materials, Acta Mechanica Solida Sinica, 20: 219-217.

Kuang, Z-B,. 2008a, Some variational principles in elastic dielctric and elastic magnetic materials, European Journal of Mechanics - A/Solids, 27: 504-514.

Kuang, Z-B, 2008b, Some variational principles in electroelastic media under finite deformation, Science in China, Series G, 51: 1390-1402.

Kuang, Z-B, 2009a, Internal energy variational principles and governing equations in electroelastic analysis, International journal of solids and structures, 46: 902-911.

Kuang, Z-B, 2009b, Variational principles for generalized dynamical theory of thermopiezoelectricity, Acta Mechanica, 203: 1-11.

Kuang Z-B. 2010, Variational principles for generalized thermodiffusion theory in pyroelectricity, Acta Mechanica, 214: 275-289.

Kuang, Z-B, 2011a, Physical variational principle and thin plate theory in electro-magneto-elastic analysis, International journal of solids and structures, 48: 317-325.

Kuang, Z-B, 2011b, Theory of Electroelasticity, Shanghai Jiaotong University Press, Shanghai (in Chinese).

Jou, D, Casas-Vzquez, J, Lebon, G, 2001, Extended irreversible thermodynamics (third, revised and enlarged edition), Springer-Verlag, Berlin, Heidelberg, New York.

Lord, H W, Shulman, Y, A, 1967, generalized dynamical theory of thermoelasticity, Journal of the Mechanics and Physics of Solids, 15: 299-309.

Sherief, H H, Hamza, F A, Saleh, H A. 2004, The theory of generalized thermoelastic diffusion, International Journal of engineering science, 42: 591－608.

Wang Z X, 1955, Thermodynamics, Higher Education Press, Beijing. (in Chinese).

Yuan X G, Kuang Z-B. 2008, Waves in pyroelectrics[J], Journal of thermal stress, 31: 1190-1211.

Yuan X G, Kuang Z-B. 2010, The inhomogeneous waves in pyroelectrics [J], Journal of thermal stress, 33: 172-186.

Yunus A. Çengel, Michael A. Boles, 2011, Thermodynamics : an engineering approach, 7th ed, McGraw-Hill , New York.

2

First Principles of Prediction of Thermodynamic Properties

Hélio F. Dos Santos[1] and Wagner B. De Almeida[2]
[1]*NEQC: Núcleo de Estudos em Química Computacional, Departamento de Química, ICE*
Universidade Federal de Juiz de Fora (UFJF),
Campus Universitário Martelos, Juiz de Fora
[2]*LQC-MM: Laboratório de Química Computacional e Modelagem Molecular*
Departamento de Química, ICEx, Universidade Federal de Minas Gerais (UFMG)
Campus Universitário, Pampulha, Belo Horizonte
Brazil

1. Introduction

The determination of the molecular structure is undoubtedly an important issue in chemistry. The knowledge of the tridimensional structure allows the understanding and prediction of the chemical-physics properties and the potential applications of the resulting material. Nevertheless, even for a pure substance, the structure and measured properties reflect the behavior of many distinct geometries (conformers) averaged by the Boltzmann distribution. In general, for flexible molecules, several conformers can be found and the analysis of the physical and chemical properties of these isomers is known as *conformational analysis* (Eliel, 1965). In most of the cases, the conformational processes are associated with small rotational barriers around single bonds, and this fact often leads to mixtures, in which many conformations may exist in equilibrium (Franklin & Feltkamp, 1965). Therefore, the determination of temperature-dependent conformational population is very much welcomed in conformational analysis studies carried out by both experimentalists and theoreticians.

There is a common interest in finding an efficient solution to the problem of determining conformers for large organic molecules. Experimentally, nuclear magnetic resonance (NMR) spectroscopy is considered today to be one of the best methods available for conformational analysis (Franklin & Feltkamp, 1965). Besides NMR, other physical methods, including infrared (IR) spectroscopy (Klaeboe, 1995) and gas phase electron diffraction (ED) experiments (De Almeida, 2000), have been employed in an attempt to determine the geometries and relative energies of conformers. Experimental studies conducted in the gas and condensed phases under a given temperature can yield information on structural parameters and conformational populations, and so Gibbs free energy difference values. On the other side, theoretical calculations employing standard quantum chemical methods can be performed in the search for stationary points on the potential energy surface (PES) enabling the determination of equilibrium geometries, relative energies, spectroscopic and thermodynamic properties of minimum energy and transition state structures (Dos Santos &

De Almeida, 1995; Dos Santos, Taylor-Gomes, De Almeida, 1995; Dos Santos, O´Malley & De Almeida, 1995; Dos Santos, De Almeida & Zerner, 1998; Dos Santos et al., 1998; Rocha et al., 1998; Dos Santos, Rocha & De Almeida, 2002; Anconi et al., 2006; Ferreira, De Almeida & Dos Santos, 2007; Franco et al., 2007, 2008). As a considerable amount of experimental and theoretical work has been already reported addressing the conformational analysis, an assessment of the performance of distinct theoretical approaches for predicting the conformational population as a function of the temperature can be made. In this Chapter we discuss theoretical approaches used for the calculation of thermodynamic quantities, with particular attention paid to the role played by the *ab initio* level of theory and an assessment of the performance of the standard statistical thermodynamics formalism for the evaluation of the entropy contribution to the Gibbs free energy for large molecular systems. The next Sections include the theoretical backgrounds with emphasis in the statistical thermodynamics formalism and some case studies focused on conformational analysis, which we consider as good benchmarks for setting up the methodology due to the low energy change involved in such processes. We believe this contribution will be useful to illustrate most of the essential ideas on first principle calculations of thermodynamic properties generalizing the formalism to handle more complicated situations.

2. Theoretical background

Ab initio quantum mechanical methods have been broadly used for prediction of thermodynamic properties of chemicals and chemical processes with the aid of the well established statistical thermodynamics formalism. The final quantities, namely internal energy (E_{int}), enthalpy (H), entropy (S), Gibbs free energy (G), etc., are actually calculated from *ab initio* data for a single and isolate molecule using the set of quantum states available. These include electronic (normally the ground state), translational (ideal gas and particle in a box model), rotational (rigid-rotor) and vibrational (harmonic oscillator) states, which are the basis for construction of the molecular partition functions (Q). The Gibbs free energy is the primary property in thermodynamics. From the first principle methods it can be calculated by adding two energy quantities (Eq. 1)

$$\Delta G = \Delta E_{ele-nuc} + \Delta G_T \tag{1}$$

where the first term on the right side is the total energy difference within the Born-Oppenheimer approximation (electronic-nuclear attraction, electronic-electronic repulsion plus nuclear-nuclear repulsion potential energy terms) obtained by solving the time-independent Schrödinger equation and the second term is the temperature-pressure dependent thermal correction to the Gibbs free energy, which accounts for enthalpy and entropy contributions (Eq. 2).

$$\Delta G_T = \Delta H_T - T\Delta S \tag{2}$$

where ΔH_T is the thermal correction to enthalpy. In analogy to Eq. (1) we can write the relative enthalpy as Eq. (3).

$$\Delta H = \Delta E_{ele-nuc} + \Delta H_T \tag{3}$$

The $\Delta E_{ele-nuc}$ depends essentially on the approach used to solve the electronic time-independent Schrödinger equation (Eq. 4) that includes the simplest Hartree-Fock (HF)

level up to the very sophisticated *post*-HF Coupled-Cluster approximation (CC). We define $E_{ele-nuc}$ as a sum of the pure electronic energy (E_{ele}) given by Eq. (4) and the nuclear-nuclear repulsion energy (V_{NN}) at equilibrium positions on the PES, in the light of the Born-Oppenheimer approximation ($E_{ele-nuc} = E_{ele} + V_{NN}$).

$$\hat{H}\Psi_{ele} = E_{ele}\Psi_{ele} \tag{4}$$

All these methods are based on solid quantum mechanics foundations, thus it might be thought that the use of the state of the art CC with single, double and perturbative triple excitations (CCSD(T)), employing a sufficient large basis set (triple-zeta quality), for the calculation of the quantum mechanical terms necessary for the evaluation of the Gibbs free energy would always lead to a perfect agreement with experimental findings. Our recent theoretical results from conformational population studies of cycloalkanes (Rocha et al., 1998; Dos Santos, Rocha & De Almeida, 2002; Anconi et al., 2006; Ferreira, De Almeida & Dos Santos, 2007; Franco et al., 2007) and small substituted alkanes (Franco et al., 2008), where highly correlated *ab initio* calculations are computational affordable, showed that this is not always the case.

According to the standard statistical thermodynamics the partition function of the molecular system is given by Eq. (5), where ε_i is the energy of the distinct allowed quantum states, k the Boltzmann constant and T the absolute temperature (Mcquarrie, 1973). The full molecular partition function ($Q^{tot}(T)$) can be written as a product of electronic, translational, rotational and vibrational contributions (Eq. 6). We found that the vibrational partition function (Eqs. 7 and 8), derived in the light of the statistical thermodynamics approach, is significantly affected by the presence of low frequency vibrational modes (less than approx. 625 cm^{-1} at room temperature) leading to considerable deviation between theoretical and experimental predictions for thermodynamic properties. It is important to remind that a low frequency mode is defined as one for which more than 5% of an assembly of molecules are likely to exist in excited vibrational states at room temperature. In other units, this corresponds to about 625 cm^{-1}, 1.9×10^{13} Hz, or a vibrational temperature ($\theta_K = \frac{h\nu_K}{k_B}$, for the kth vibrational mode) of 900 K.

$$Q(T) = \sum_i e^{-\varepsilon_i/kT} \tag{5}$$

$$Q^{tot}(T) = Q_{ele} \times Q_{trans} \times Q_{rot} \times Q_{vib} \tag{6}$$

$$Q_{vib}^{\nu}(T) = \frac{e^{-h\nu/2kT}}{1-e^{-h\nu/kT}} \tag{7}$$

$$Q_{vib} = \prod_{j=1}^{Nlow} Q_{vib}^{\nu_j} \cdot \prod_{j=Nlow+1}^{3N-6} Q_{vib}^{\nu_j} \tag{8a}$$

$$Q_{vib} = Q_{vib}^{NHO} \cdot Q_{vib}^{HO} \tag{8b}$$

In Eq. (8a) the first product on the right side accounts for the contribution due to the low frequency vibrational modes (*Nlow*), which are not true harmonic oscillators. So they can be treated separately as indicated in Eq. (8b). As a first assumption we can exclude these frequencies (*Nlow* modes) from vibrational partition function, which is equivalent to set up the first product in Eq. 8a to unity (hereafter called HO approach). This approach was firstly introduced in our paper on cyclooctane (Dos Santos, Rocha & De Almeida, 2002).

According to the statistical thermodynamics formalism (see Mcquarrie, 1973) the vibrational contribution to internal energy and entropy are given by Eqs. (9) and (10), respectively, with similar equations holding for the electronic, translational and rotational terms ($Q_{ele}, Q_{trans}, Q_{rot}$). Assuming that the first electronic excitation energy is much greater than kT, and so the first and higher excited states can be considered to be inaccessible, the electronic partition function is simply the electronic spin multiplicity of the molecule ($Q_{ele} = 2S + 1$), with the energy of the electronic ground state set to zero. The translational and rotational partition functions are given by the particle in a box (Q_{trans}) and rigid rotor (Q_{rot}) models respectively (Mcquarrie, 1973).

$$E_{int,vib} = RT^2 \left(\frac{\partial lnQ_{vib}}{\partial T}\right)_V \tag{9}$$

$$S_{vib} = R + RlnQ_{vib} + RT \left(\frac{\partial lnQ_{vib}}{\partial T}\right)_V \tag{10}$$

In the HO approach introduced previously (Dos Santos, Rocha & De Almeida, 2002), the Q_{vib}^{NHO} partition function is made equal to unity, and so, following Eqs. (8b), (9) and (10), the low frequency modes do not make a contribution to the evaluation of thermodynamic properties (null value). It is also possible, for very simple molecules, as will be shown latter, to use other empirical approaches such as hindered rotor analysis and including anharmonic treatment of the low frequency modes (see for example Truhlar, 1991; Ayala & Schlegel, 1998). The way that the low frequency modes are treated is crucial for the correct evaluation of conformational population. For large cycloalkanes, other macrocycles and supramolecular systems there will be a great number of low frequency modes and so the uncertainty in the theoretical determination of relative values of Gibbs free energy tends to naturally increase.

It is opportune to clarify the notation we have been using for thermodynamic quantities, which may differ from that commonly used in many textbooks on thermodynamics. In the way that the vibrational partition function is calculated using the Gaussian package, which we used to perform quantum chemical calculations, the zero of energy is choosen as the bottom of the internuclear potential well. Then, the vibratonal partition function, for the specific frequency ν, is given by Eq. (7) and the zero-point energy (ZPE) contribution ($h\nu/2kT$ or ZPE/kT) is added to the internal energy, which we called E_{int}. In addition, the thermal energy correction to enthalpy (ΔH_T) within the ideal gas model is given by $E_{int} + nRT$. In conformation analysis studies for a given process A →B, the nRT term cancelled out and so the thermal correction to enthalpy is just ΔE_{int} ($\Delta H_T = \Delta E_{int}$) . The thermal correction to Gibbs free energy (named here ΔG_T) is given by Eq. (2).

In the next Sections we will present theoretical thermodynamic quantity results for substituted alkanes and cycloalkanes, where experimental conformational population data are available, which can illustrate the performance of theoretical approaches available for the calculation of thermodynamic properties.

3. Conformational analysis of 1,2-substituted alkanes

There have been a considerable number of investigations on substituted alkanes such as 1,2-dichlroethane (Ainsworth & Karle, 1952; Orville-Thomas, 1974; Youssoufi, Herman & Lievin, 1998; Roberts, 2006; Freitas & Rittner, 2007) and 1,2-difluoroethane (Orville-Thomas,

1974; Hirano et al., 1986; Wiberg & Murcko, 1987; Durig et al., 1992; Roberts, 2006; Freitas & Rittner, 2007) motivated by the interest in its restricted internal rotation. The recent literature for the simple non-substituted ethane molecule also shows that the reason for the rotational barrier leading to the experimentally observed staggered structure (Pophristic & Goodman, 2001; Bickelhaupt & Baerends, 2003) has also been investigated. It is well known that for 1,2-dichloroethane the *anti* form predominates over the *gauche* conformer. However the opposite is observed for the 1,2-difluoroethane, where both experimental and theoretical investigations have shown that this molecule prefer the *gauche* conformation, what has been successfully rationalized in terms of a hyperconjugation model (Goodman, Gu & Pophristic, 2005). So, in the case of the 1,2-difluoroethane molecule, the stability of the *gauche* conformation has been attributed to the high electronegative character of the fluorine atom denominated the *gauche effect*, where the equilibrium geometry is a result of charge transfer from C-H electron to the C-F* antibonds (Goodman & Sauers, 2005). Investigation of the far IR (50-370 cm^{-1}) and low frequency Raman (70-300 cm^{-1}) spectra (Durig et al., 1992) of the gas phase sample of 1,2-difluoroethane showed that the *gauche* conformer is 0.81±0.13 kcal mol^{-1} more stable than the *anti* form, and it has been one of the most discussed case of intramolecular interaction over the past decades.

The very simple ethane molecule has called the attention of many researchers with a number of work reported addressing restricted internal rotation (Kemp & Pitzer, 1936; Ainsworth & Karle, 1952; Pitzer, 1983; Pophristic & Goodman, 2001; Bickelhaupt & Baerends, 2003; Goodman, Gu & Pophristic, 2005). The experimental gas phase spectroscopic and thermodynamic data available for ethane and ethane substituted molecules provide useful information to assess the capability of available theoretical methods used to calculate temperature-dependent macroscopic properties. In order to investigate the performance of theoretical approaches for predicting relative gas phase conformational population values, as compared to observed experimental data, two distinct points must be considered: the adequacy of the theoretical model employed, which is reflected in the pertinence of the mathematical equations developed, and the quality of the calculated energy values used to feed the mathematical functions to produce numerical values for the population ratio, which is dictated by the *ab initio* level of theory employed. Regarding the calculation of Gibbs conformational population, on one side we have the statistical thermodynamic formalism which makes use of molecular partition functions based on Boltzmann distributions and also additional corrections for hindered rotation through the use of empirical formulae, and on the other side the quantum mechanical methods available for the resolution of the time independent Schrödinger equation for an isolated molecule in the vacuum, which produce the various energy values (electronic, rotational, vibrational) and structural data to feed the thermodynamic partition functions. At this point the validity of the theoretical approaches is attested by comparison with experimental conformational population data within experimental uncertainties.

The theoretical methods available for the determination of thermodynamic properties are based on quantum mechanics and statistical thermodynamics formalism and are quite sound, from a methodological point of view. We can reach the state of the art of a quantum mechanical calculation by using a highly correlated *ab initio* method and a basis set close to completeness, and therefore any disagreement with experimentally observed quantities cannot be blamed only on the level of theory used to calculated geometrical parameters, vibrational frequencies and relative electronic plus nuclear-nuclear repulsion energy values ($\Delta E_{ele-nuc}$). However, the evaluation of thermal corrections (ΔG_T) that lead to the

calculation of relative ΔG values (Eq. 1) for a given temperature may not be improved in the same manner as $\Delta E_{ele-nuc}$, which is dictated by the level of electron correlation and size of basis set. The thermal correction is calculated using the statistical thermodynamics partition functions with the vibrational (Q_{vib}) and rotation (Q_{rot}) contributions playing a key role. The rotation and vibrational partition functions are commonly evaluated in the light of the rigid rotor (RR) and harmonic oscillator (HO) approximation, usually denominated RR-HO partition function. To account for deviation from the RR-HO approximation centrifugal distortion effect and anharmonicity correction must be addressed and this is not a simple matter for large molecules. We have observed in our recent studies on substituted alkanes (Franco et al., 2008) that the vibrational contribution to the thermal correction given by Q_{vib} (see Eq. 7) plays a major role for the evaluation of relative ΔG values, and so we have concentrated our attention on the analysis of effect of the low frequency modes on the calculation of the vibrational thermal correction given by Eq. (11) (remember we use $\Delta E_{int} = \Delta H_T$ for conformational interconversion processes). As the internal energy and entropy quantities are given by a logarithmic function (see eqs. 9 and 10), the total thermal correction can be written as a sum of four contributions according to Eq. (12), where only the last term on the right side of Eq. (12) affects significantly the calculation of relative Gibbs free energies and so conformational population values.

$$\Delta G_{T,vib} = \Delta E_{int,vib} - T\Delta S_{vib} \tag{11}$$

$$\Delta G_T = \Delta G_{T,ele} + \Delta G_{T,trans} + \Delta G_{T,rot} + \Delta G_{T,vib} \tag{12}$$

A treatment of low frequency vibrational modes, which are not true vibrations, as hindered rotations, is well known to be required to describe the thermodynamics of ethane and ethane substituted molecules. In (Ayala & Schlegel, 1998) a treatment of low frequency modes as internal hindered rotation is described in details, with an automatic procedure for the identification of low frequency modes as hindered rotor, requiring no user intervention (implemented in the Gaussian® computer code), being reported. Following early works of Pitzer et al. (Pitzer & Gwinn, 1942) tabulating thermodynamic functions, formulas became available to interpolate the partition function between that of a free rotor, hindered rotor and harmonic oscillators (Pitzer & Gwinn, 1942; Li & Pitzer, 1956; Truhlar, 1991; Mcclurg, Flagan & Goddard, 1997), with the approximation by Truhlar (Truhlar, 1991) being used in many studies in recent years. In (Ayala & Schlegel, 1998) a modified approximation to the hindered rotor partition function for the ith low frequency mode (named here $Q_i^{Hind-Rot}$) was given. These formulas (see (Pitzer & Gwinn, 1942) are for one normal vibrational mode involving a single rotating group with clearly defined moment of inertia. The thermal corrections to enthalpy and Gibbs free energy, including hindered rotation and anharmonic correction to vibrational frequencies are calculated according to Eqs. (13) and (14) below, using the Mϕller-Plesset second-order perturbation theory (MP2) and good quality basis sets. The symbols *Hind-Rot* and *Anh* indicate the use of hindered rotation and anharmonicity correction to vibrational frequencies treatments respectively, to account for deviations from the RR-HO partition function. For more details of mathematical treatments see a recent review by Ellingson et al. (Ellingson et al., 2006).

$$\Delta E_{int}^{Hind-Rot-Anh} = \Delta E_{int} + \Delta E_{int}^{Hind-Rot} + \Delta E_{int}^{Hind-Anh} \tag{13}$$

$$\Delta G_T^{Hind-Rot-Anh} = \Delta G_T + \Delta G_T^{Hind-Rot} + \Delta G_T^{Hind-Anh} \tag{14}$$

Table 1 reports the calculation of absolute entropy for ethane at room temperature, using the MP2 level of theory and the 6-311++G(3df,3pd) triple zeta quality basis set, with the aid of the standard statistical thermodynamics formalism with the inclusion of a treatment of the hindered-rotation effects and anharmonicity correction to vibrational frequencies. From the results reported in Table 1 it can be seen that the combination of anharmonic correction to vibrational frequencies and a hindered rotor treatment of the lowest-frequency modes provides a perfect description of the entropy of ethane at room temperature, when a large basis set is used (at least of triple zeta quality) with a MP2 calculation. The deviation from the experimental value is only 0.3% which is within the experimental uncertainty of ±0.19 cal mol^{-1} K^{-1}. The percent error for the aug-cc-pVTZ basis set is only 0.2% (Franco et al., 2008). Therefore, for the ethane molecule, the approach given by Eqs. (13) and (14) works very well.

	S [a]	S^{HO} [b]	S^{Anh} [c]	$S^{Hind-Ror}$ [d]	$S^{Hind-Rot-Anh}$ [e]
Calculated	54.29	52.99	54.45	54.54	54.70
Entropy	{1.0%} [f]	{3.4%} [f]	{0.7%} [f]	{0.6%} [f]	{0.3%} [f]
Expt. [g]					54.85±0.19[g]

[a] $S = S_{trans} + S_{rot} + S_{vib}$ (S_{trans} = 36.13 and S_{rot} = 16.26 cal mol^{-1} K^{-1}). 1 cal = 4.184 J. [b]The low frequency mode was excluded from the evaluation of the vibrational partition function for the calculation of the absolute entropy (HO approach) so, 3N-7 normal modes were used. The low frequency contribution to entropy (S_{vib}^{NHO}) is 1.30 cal mol^{-1} K^{-1}. [c]Absolute entropy value calculated with the inclusion of anharmonicity correction. [d]Absolute entropy value calculated with the inclusion of hindered internal rotation correction. [e]Absolute entropy value calculated with the inclusion of anharmonicity and hindered internal rotation corrections for the evaluation of the vibrational partition function. Contributions to the total entropy value: $S_{vib}^{HO} = 0.60$; $S_{vib}^{NHO} = 1.30$; $S_{vib}^{Hind-Rot} = 0.25$; $S_{vib}^{Anh} = 0.16$ cal mol^{-1} K^{-1}. $S_{vib}^{Hind-Rot-Anh} = S_{vib}^{HO} + S_{vib}^{NHO} + S_{vib}^{Hind-Rot} + S_{vib}^{Anh} = 2.31$ cal mol^{-1} K^{-1}. [f]Percent error relative to the experimental entropy value obtained at 298.15 K from (Kemp & Pitzer, 1937). The corresponding error for the TS value are only 0.04 kcal mol^{-1}. [g]Experimental entropy value from (Kemp & Pitzer, 1937).

Table 1. MP2/6-311++G(3df,3pd) absolute entropy (cal mol^{-1} K^{-1}) of the ethane molecule in the staggered form (T = 298 K, p = 1 atm) calculated using standard statistical thermodynamics partition function (particle in a box, rigid rotor and harmonic oscillator approximations for translational, rotational and vibrational contributions) including all 3N-6 vibrational modes as harmonic oscillators.

MP2 thermal quantities (ΔE_{int} and ΔG_T) results using various basis sets for the *anti→gauche* process for 1,2-difluorethane (Figure 1) are shown in Figure 2 (a similar behavior was found for 1,2-dichloroethane).

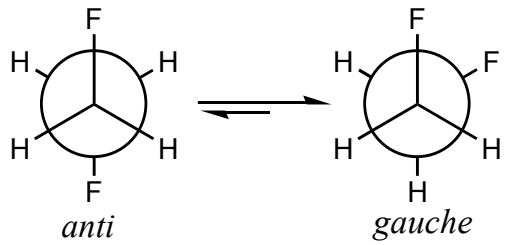

Fig. 1. Schematic representation of the *anti→gauche* process for the 1,2-difluorethane molecule.

It can be seen from Figure 2 that the thermal corrections reached nearly unchanged values within 0.02 kcal mol^{-1} at the MP2/6-311++G(3df,3pd) level of theory, a variation that would cause a change on the calculated conformational population of less than 1%. Figure 3 shows $\Delta E_{ele-nuc}$ results for 1,2-difluorethane (a similar pattern was obtained for 1,2-dicloroethane), where the effect of the electronic correlation and size of the basis set on relative energy values can be analyzed. It can be seen that the MP4(SDTQ) and CCSD(T) relative energies for the *anti→gauche* process agree within less than 0.05 kcal mol^{-1}, showing a welcome smooth behavior of the energy values as a function of the level of theory and basis set quality. We may say that the MP4(SDTQ) and CCSD(T) conformational energies might be trusted with a rough uncertainty estimated at ±0.05 kcal mol^{-1} based on the pattern shown in Figure 3, with a corresponding uncertainty in the conformational population of approximately 1%. The reported uncertainties for experimental conformational populations are in the range of ±2–5%, and the uncertainty value for experimental enthalpy determination is within ±0.10–0.19 kcal mol^{-1}. Therefore, we are confident in using these *ab initio* data to analyze the performance of the theoretical models for calculating thermal corrections through the evaluation of molecular partition functions, making use of the statistical thermodynamics formalism and, therefore, enthalpy and Gibbs free-energy values, leading to the theoretical determination of conformational population ratios.

The Gibbs population results for the *anti→gauche* processes (see Figure 1) for 1,2-difluoroethane and 1,2-dichloroethane at 25°C are reported in Table 2. It can be seen that the effect of the anharmonic correction to the vibrational frequencies on the thermal energies is quite small (±0.01 kcal mol^{-1}) and so it can be neglected; therefore, only the treatment of the low-frequency modes need to be considered. It is important to make it clear that the anharmonicity effect was not included explicitly in the vibrational partition function, which can easily be done for diatomic molecules (Mcquarrie, 1973); however, much more work is required for polyatomic molecules. In the present case, the harmonic oscillator functional dependence was used for the vibrational partition function, but the anharmonic frequencies are utilized instead of harmonic values. As far as enthalpy calculations are concerned, it was found that the *ab initio* and experimental enthalpy values for the *anti→gauche* process exhibit a very fair agreement, for both 1,2-dichloroethane and 1,2-difluorethane, independent of the way that the low-frequency modes are treated (see Table 3). In other words, the internal energy contribution is not so sensitive to the model used to treat the low-frequency modes in the calculation of relative enthalpy values, with the $\Delta E_{ele-nuc}$ contribution being of major relevance (Franco et al., 2008).

When the agreement between theoretical and experimental populations is analyzed, an assessment of the performance of the hindered-rotor approach can be made. From Table 2, the effectiveness of the hindered-rotor approach to describe the 1,2-dichloroethane species is promptly seen, leading to a good agreement with gas-phase electron diffraction conformational population data. The simple procedure of neglecting the low-frequency modes (three modes at room temperature) in the evaluation of the vibrational partition function, which may be considered as a rough but simple approximation also works well for 1,2-dichloroethane. For 1,2-difluorethane, a satisfactory agreement with experimental conformational population data was not obtained. An interesting feature that can be seen from Table 2 is the fact that the procedure of treating the lowest-frequency modes as a hindered rotor leads to a very small correction, compared to the corresponding value obtained for 1,2-dichloroethane, providing virtually the same conformational population as the consideration of all 3N-6 modes as harmonic oscillators. So, in this case, the procedure

was useless. The alternative of ignoring the three lowest-frequency modes also does not work well here.

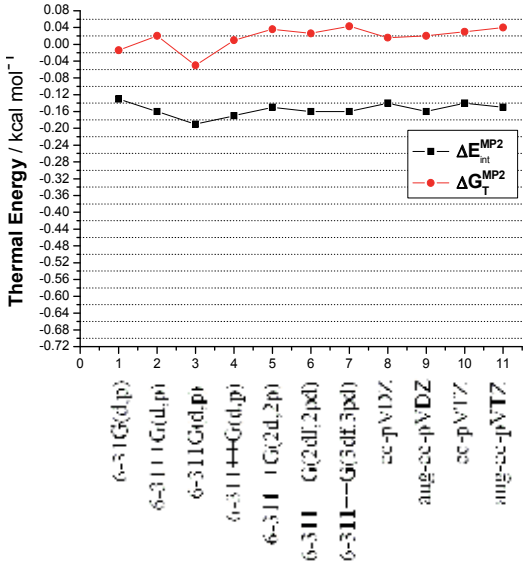

Fig. 2. *Anti→gauche* MP2 thermal energy variation (at room temperature) for 1,2-difluorethane as a function of the basis set quality. The MP2/6-311++G(3df,3pd) and MP2/aug-cc-pVTZ TΔS values (entropic contribution) are respectively -0.20 and -0.19 kcal mol-1 (see Eq. 2).

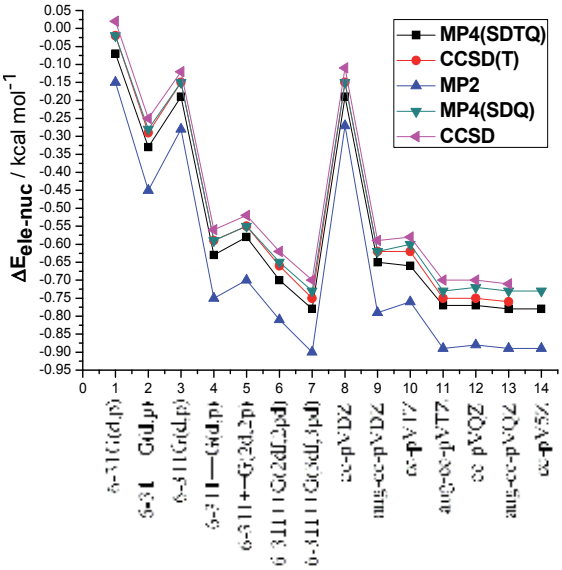

Fig. 3. *Anti→gauche* energy ($\Delta E_{ele-nuc}$ in the vacuum) variation for 1,2-difluorethane as a function of the level of calculation. The CCSD(T)/6-311++G(3df,3pd)//MP2/6-311++G(3df,3pd) and CCSD(T)/aug-cc-pVQZ//MP2/aug-cc-pVTZ relative energy values are respectively -0.75 and -0.76 kcal mol-1. The corresponding MP4(SDTQ) values are respectively -0.78 and -0.78 kcal mol-1 (The MP4(SDTQ)/cc-pV5Z//MP2/aug-cc-pVTZ value is -0.78 kcal mol-1).

	1,2-dichloroethane	1,2-difluorethane
$T\Delta S$ [a]	-0.11	-0.17
$T\Delta S^{HO}$ [b]	0.13	0.05
$T\Delta S^{Anh}$ [c]	0.01	-0.003
$T\Delta S^{Hind-Rot}$ [d]	0.40	-0.04
$T\Delta S^{Hint-Rot-Anh}$ [e]	0.41	-0.04
ΔG [% *anti*]	1.30 [90%]	-0.73 [23%]
ΔG^{HO} [b] [% *anti*]	0.95 [83%]	-1.03 [15%]
$\Delta G^{Hint-Rot-Anh}$ [f] [% *anti*]	0.90 [82%]	-0.70 [23%]
[% *anti*] *expt*	[78±5%][g]	[37±5%][h]

[a]The MP2/aug-cc-pVTZ TΔS values for 1,2-dichloroethane and 1,2-difluorethane and are respectively -0.11 and -0.20 kcal mol^{-1} at 25 °C. The room temperature MP2/6-311++G(3df,3pd) rotational entropy ($T\Delta S_{rot}$) contributions are 0.11 and 0.05 kcal mol^{-1} for 1,2-dichloroethane and 1,2-difluorethane, respectively (identical to the MP2/aug-cc-pVTZ values). [b] Calculated using the vibrational partition function evaluated excluding the low frequency normal vibrational modes (three modes at room temperature). [c]Anharmonicity correction evaluated at the MP2/6-311++G(2d,2p) level and room temperature. [d]Internal rotation correction to the MP2/6-311++G(3df,3pd) entropy term ($T\Delta S$) value (one internal rotation was identified for all four species). [e]Anharmonicity and hindered internal rotation corrections. [f]$\Delta G^{Hind-Rot-Anh} = \Delta E_{ele-nuc} + \Delta G_T + \Delta G_T^{Hind-Rot} + \Delta G_T^{Anh}$, with $\Delta G_T = \Delta H_T - T\Delta S$. Value obtained including the anharmonicity and hindered internal rotation correction to calculation of the thermal energy correction (ΔG_T). This should be our best Gibbs free energy value. [g]Experimental value from (Ainsworth & Karle, 1952). See also (Bernstein, 1949). [h]Experimental value from (Durig et al., 1992). There are other two population data obtained from electron diffraction experiment that differ considerably from the more recent reported value in (Durig et al., 1992) based on the vibrational spectroscopy analysis: 9% of the *anti* form from (Fernholt & Kveseth, 1980) at room temperature and 4.0±1.8% at 22 °C from (Friesen & Hedberg, 1980).

Table 2. Temperature-dependent Gibbs population and relative Gibbs free energy (ΔG) values calculated including anharmonicity and hindered-rotation effects on the entropy contribution ($T\Delta S$) to the thermal energy correction (ΔG_T) calculated at the MP2/6-311++G(3df,3pd) level, for the *anti→gauche* interconversion process for 1,2-dichloroethane and 1,2-difluorethane. CCSD(T)/6-311++G(3df,3pd)//MP2/6-311++G(3df,3pd) $\Delta E_{ele-nuc}$ values (1.31 and -0.75 kcal mol^{-1} for 1,2-dichloroethane and 1,2-difluorethane, respectively) were used. All values are in kcal mol^{-1}. T = 298.15 K.

In an attempt to better understand the reason for the disagreement between theoretical and experimental gas phase conformational population for 1,2-difluorethane we decided to use the experimental entropy for the *anti→gauche* process. It was obtained from the analysis of the vibrational spectral data dependence with temperature reported in (Durig et al., 1992), where by applying the van't Hoff isochore equation, $ln(I_{anti}/I_{gauche}) = \Delta H/RT - \Delta S/R$, with the value in parenthesis being the ration of the intensities of the Raman lines due to the *anti* and *gauche* conformers, the entropy change for the process could be evaluated (assuming that ΔH is not a function of the temperature). The enthalpy is determined through the $ln(I_{anti}/I_{gauche})$ versus $1/T$ plot, where $\Delta H/R$ is the slope of the line. The experimental entropy contribution at room temperature is: $T\Delta S^{Expt}$ = -0.49 kcal mol^{-1}. Our MP2/6-311++G(3df,3pd) best value is -0.17 kcal mol^{-1} (a quite sizeable 65% difference). Using the experimental entropy and our *ab initio* CCSD(T)/6-311++G(3df,3pd) relative energy ($\Delta E_{ele-nuc}$) and MP2/6-311++G(3df,3pd) internal energy (ΔE_{int}) we obtain a room

temperature Gibbs population of 33% of the *anti* form, in good agreement with the experimental value of 37±5%. Therefore, it is quite evident that our calculated entropy for the *anti→gauche* process of 1,2-difluorethane, using the combined quantum mechanical/statistical thermodynamic approach, is in serious error. It is also opportune to emphasize here that, as already pointed out by Ayala and Schlegel (Ayala & Schlegel, 1998), in principle most of the problem resides in the identification of the internal rotation modes. Large molecules can have a large number of low frequency modes which can include not only internal rotations but also large amplitude collective bending motions of atoms. Moreover, some of the low frequency modes can be a mixture of such motions. For large cyclic molecules there are ring torsional modes, and similar to internal rotations ring torsions can cause problems in the evaluation of thermodynamic functions, as will be shown in the next Section.

	1,2-dichloroethane	1,2-difluorethane
ΔH	1.19	-0.90
ΔH^{HO} [a]	1.08	-0.98
$\Delta H^{Hint-Rot-Anh}$ [b]	1.17	-0.93
ΔH^{Expt}	[1.20±0.19][c]	[-0.81±0.13][d]

[a]Calculated using the vibrational partition function evaluated excluding the low frequency normal vibrational modes (three modes at room temperature). [b] $\Delta H^{Hint-Rot-Anh} = \Delta E_{ele-nuc} + \Delta E_{int} + \Delta E_{int}^{Hint-Rot} + \Delta E_{int}^{Anh}$. Value obtained including the anharmonicity and hindered internal rotation correction to calculation of the internal energy correction. The anharmonic correction to internal energy (ΔE_{int}^{Anh}) is -0.01 kcal mol^{-1} for both 1,2-dichloro and 1,2-difluorethane, evaluated at the MP2/6-311++G(2d,2p) level and room temperature. This should be our best enthalpy value. [c]Experimental value from (Bernstein, 1949). [d]Experimental value from (Durig et al., 1992).

Table 3. Enthalpy (ΔH in kcal mol^{-1}) values calculated including anharmonicity and hindered-rotation effects on the internal energy correction (ΔE_{int}) evaluated at the MP2/6-311++G(3df,3pd) level, corresponding to the *anti→gauche* interconversion process for 1,2-dichloroethane and 1,2-difluorethane. CCSD(T)/6-311++G(3df,3pd)//MP2/6-311++G(3df,3pd). $\Delta E_{ele-nuc}$values (1.31 and -0.75 kcal mol^{-1} for 1,2-dichloroethane and 1,2-difluorethane respectively) were used. T = 298.15 K.

It is well known that the vibrational entropy term ($T\Delta S_{vib}$) has a much higher sensibility to the low frequency mode than the internal energy ($\Delta E_{int,vib}$), what can be easily seen from Figure 4 where the variation of the respective thermodynamic functions with the vibrational frequency is shown. $\Delta E_{int,vib}$ is very monotonically dependent on the frequency in the low frequency region, what explain why our calculated enthalpies are in good agreement with the experimental ones. On the contrary, the entropy counterpart is strongly dependent of the frequency, particularly in the region of 0-200 cm^{-1}, therefore, the treatment of low frequency modes definitively has a pronounced effect on the entropy evaluation.

4. Conformational analysis of cycloalkanes

Despite a rather simple carbon–hydrogen cyclic skeleton structure, the cycloalkanes have indeed attracted the interest of several research investigations in the experimental and theoretical fields. These studies are mainly concerned with the conformational analysis as a

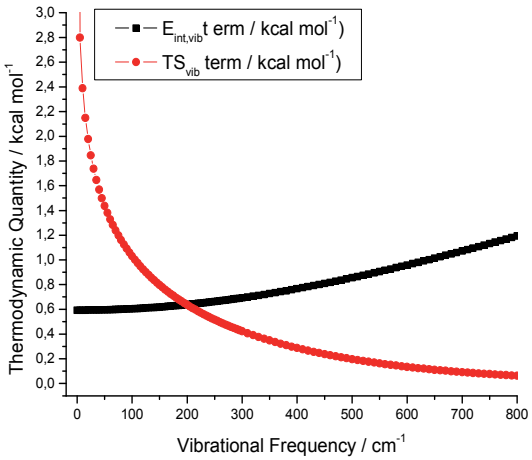

Fig. 4. Thermodynamic energy or internal thermal energy ($E_{int,vib}$) and entropic (TS_{vib}) vibrational contributions (in units of kcal mol-1) represented as a function of the vibrational frequency, calculated with the aid of the statistical thermodynamics formulae, within the harmonic oscillator (HO) approximation (HO vibrational partition function), at room temperature and normal pressure.

function of the temperature and pressure conditions. Electron diffraction experiments have been of great aid to provide population data for cycloalkanes for gas phase samples, as reported for cycloheptane (Dillen & Geise, 1979), cyclooctane (Dorofeeva et al., 1985), cyclodecane (Hilderbrandt, Wieser & Montgomery, 1973) and cyclododecane (Atavin et al., 1989). For solution and solid state samples NMR spectroscopy have provided valuable information for temperature-dependent conformational analysis as given for cyclononane (Anet & Krane, 1980), cyclodecane (Pawar et al., 1998), cycloundecane (Brown, Pawar & Noe, 2003), and cyclododecane (Anet & Rawdah, 1978). In all these experimental investigation a population conformation with an uncertainty of ±5% was reported, and so the preferred conformation for each cycloalkane containing 7 to 12 carbon atoms precisely determined.

In this Section we report a comprehensive conformational analysis for a series of cycloalkanes containing seven to ten carbon atoms (cycloheptane, cyclooctane, cyclononane and cyclodecane) using *ab initio* molecular orbital theory, with the aim to analyze the performance of available theoretical methods to describe large cycloalkanes and also other macrocycles. An investigation of the influence of low frequency vibrational modes in the calculation of thermodynamic properties as a function of temperature, employing standard statistical thermodynamics, was carried on. The main focus of this work is to explore this subject and extend the discussion on the calculation of thermodynamic quantities for other large molecular systems or molecular clusters that are relevant for many areas of chemistry, in particular supramolecular chemistry, and present a challenge for available theoretical methods. Our ultimate goal is a clear understanding of the efficaciousness of standard quantum chemical procedures for the calculation of conformational population of large molecular systems usually containing macrocycle units. This is a relevant academic problem that has not received much attention in the literature so far, which has also important consequences in the application of theoretical methods to solve problems of general and applied chemical interest, such as biological application and material science.

We will present first separate results for each cycloalkane and in the end a global analysis of the cycloalkanes investigated, what can shed some light on the performance of available theoretical methods for the calculation of conformational population of large macrocycles. The mathematical equations necessary for the calculation of relative Gibbs free energy values, with the explicit consideration of low frequency normal modes, were given in Section 2 and we provide now some example to illustrate the application of theoretical methods. In Section 3 we showed the effect of including anharmonicity and hindered-rotation corrections to ΔE_{int} and ΔG_T for 1,2-dichloro and 1,2-difluorethane, which are very simple molecules where available empirical models can be applied. In the case of cycloalkanes we found not appropriate an attempt to include such corrections to the calculation of ΔG_T and our proposal was to separate the vibrational thermal correction in two main contributions given by Eq. (15), where low and high frequency normal modes are included in the NHO and HO terms respectively, since the thermodynamic statistical formalism allowed us to write ΔG_T as a sum of terms.

$$\Delta G_{T,vib} = \Delta G_{T,vib}^{NHO} + \Delta G_{T,vib}^{HO} \tag{15}$$

In this Section we make use of a very simple approach, already introduced in Section 3 of this Chapter named HO approach, that is assuming the vibrational partition function contribution due to the low frequency modes given by equation (8b), Q_{vib}^{NHO}, to be unitary what is equivalent to exclude the corresponding vibrational frequencies from the calculation of the thermal correction, i.e., $\Delta G_{T,vib}^{NHO} = 0$. We will discuss the applicability of this approximation for the series of cycloalkanes where experimental conformational populations are available for comparison. The proposal of another Q_{vib}^{NHO} partition function that is not unitary and so can describe more realistically the effect of the low frequency modes that are no harmonic oscillator is indeed a big challenge in what large molecules are concerned. The most recently reported treatments have been reviewed recently by Ellingson and collaborators (Ellingson et al., 2006) with results for hydrogen peroxide model system presented.

4.1 Cycloheptane

The conformational analysis of cycloheptane has been well documented in the literature (Hendrickson, 1961; Hendrickson, 1967a, 1967b; Dowd et al., 1970; Pickett & Strauss, 1971; Hendrickson et al., 1973; Bocian et al., 1975; Cremer & Pople, 1975; Flapper & Romers, 1975; Brookeman & Rushworth, 1976; Bocian & Strauss, 1977a, 1977b; Flapper et al., 1977; Snyderman et al., 1994; Senderowitz, Guarnieri & Still, 1995; Wiberg, 2003) so it is known that there are five possible distinct conformers being two true minima (twist-chair (TC) and boat (B)) and three first-order transition state (TS) structure, (chair (C), twist-boat (TB) and a third structure named TS3) (Wiberg, 2003). The TC, B and C conformers are depicted in Figure 5. The TC conformer is the global minimum energy structure and is connected to the local minimum B (which is ca. 3 kcal mol^{-1} energetically higher (Wiberg, 2003)) through the TS3 structure, with a reasonable energy barrier of ca. 8 kcal mol^{-1} (Wiberg, 2003). The only experimental conformational data available is from an electron diffraction study (Dillen & Geise, 1979), where a mixture of TC and C conformers was proposed, in order to explain the electron diffraction patterns. In this Section we present a discussion on the performance of the standard quantum chemical methods to describe the structure, energetic and thermodynamic properties of the TC and C conformers of cycloheptane with a special

attention being paid to the role played by the low frequency vibrational modes in the calculation of thermodynamic quantities. By writing the enthalpy and Gibbs free energy as a sum of two independent contributions (see Eqs. (1) and (3)) it is implied that we can use different levels of theory to evaluate each term. Therefore, it is common to use a lower cost computational method for geometry optimization and vibrational frequency calculations, which are need for the determination of ΔG_T, with *post*-HF methods being employed to evaluate the $\Delta E_{ele-nuc}$ counterpart. It is important to assess the performance of theoretical methods for the determination of structural parameters.

(a) TC (b) B (c) C

Fig. 5. MP2 fully optimized structures of the relevant conformers of cycloheptane: (a) TC; (b) B; (c) C. The numbering scheme is included in the Figure 5a.

We report in Table 4 a summary of theoretical and experimental dihedral angles for the global minimum structure located on the PES for cycloheptane (TC), with experimental gas phase electron diffraction data being also quoted for reason of comparison. It can be seen that there is a nice agreement with the MP2 optimized values for the TC structure, with all basis sets employed. It is interesting to see that all fully optimized MP2 dihedral angles agree very well, independent of the basis set used, showing the strength of the MP2 level of theory for structural determination. It can also be seen from Table 4 that DFT (B3LYP functional) torsion angles also agree very well with experimental data. It can be inferred that DFT and MP2 geometrical parameters for cycloalkanes are very satisfactory described and so, the rotational partition function (Q_{rot}), which depends essentially on the structural data through the moment of inertia within the rotor rigid approximation, is also well predicted by DFT and MP2 methods.

	d1 [1,2,3,4]	d2 [2,3,4,5]	d3 [3,4,5,6]	d4 [4,5,6,7]	d5 [5,6,7,1]	d6 [6,7,1,2]	d7 [7,1,2,3]
B3LYP/6-31G(d,p)	38.0	-84.4	70.1	-53.8	70.1	-84.4	38.0
MP2/6-31G(d,p)	39.3	-87.1	70.3	-52.5	70.3	-87.1	39.3
MP2/6-311++G(2d,2p)	39.6	-87.9	70.6	-52.5	70.6	-87.9	39.6
MP2/cc-pVDZ	39.2	-87.0	70.4	-52.8	70.4	-87.0	39.2
MP2/aug-cc-pVDZ	39.7	-88.2	70.6	-52.3	70.6	-88.2	39.7
Expt. [b]	38.3	-86.5	70.8	-52.4	70.8	-86.5	38.3

[a]The labels are defined in Figure 5. [b]Experimental values from (Dillen & Geise, 1979).

Table 4. Dihedral angles[a] (in degrees) calculated for the global minimum TC form of the cycloheptane molecule at different levels of theory.

The energy differences ($\Delta E_{ele-nuc}$) for the conformational interconversion process TC→C, using various methods of calculation, are shown in Tables 5 and 6 (MP4 and CCSD values). It can be seen that, despite the fact of providing reasonable structural data, the B3LYP functional cannot be used for the evaluation energy of differences, compared to MP2, in what cycloheptane is concerned. An extensive investigation of the behavior of other DFT functional is required. Also in Table 5 are internal energy (ΔE_{int}), entropy contribution ($T\Delta S$) and thermal correction (ΔG_T) evaluated at distinct levels of calculation showing a relative good agreement between B3LYP and MP2 results. It can be seen from Table 5 that the vibrational contribution plays the major role in the evaluation of thermal quantities, stressing the importance of using an adequate treatment of the low frequency vibrational modes. It can also be seen from Tables 5 and 6 that the MP2 relative energies are larger than the MP4 and CCSD values, showing the importance of a better description of electron correlation and how the way it is evaluated, and the basis set employed, affects the $\Delta E_{ele-nuc}$ value. The difference between the MP4(SDTQ) and CCSD(T) energy is 0.03 kcal mol^{-1} for both cc-pVDZ and 6-311G(d,p) basis sets. The same result is observed for the smaller 6-31G(d,p) basis set. Therefore, it can be said that the computational more feasible high correlated level of theory, MP4(SDTQ), would lead to a Gibbs conformational population value virtually the same as the CCSD(T) prediction, within the same basis set, and so can be safely used to account for the electronic correlation energy in conformational analysis studies. It can also be seen that the uncertainty in the *post*-HF energy values for the TC→C process is stabilized to less than ~0.1 kcal mol^{-1}. This would lead to a variation of less than 2% in the TC/C conformational population, which is less than the experimental reported uncertainty (Dillen & Geise, 1979). The behavior of the thermal quantities as a function of the level of theory employed can also be analyzed from the results reported in Table 5. It can be seen that the uncertainty in the MP2 entropy and thermal energy values (ΔG_T) is within ~0.05 kcal mol^{-1}, so we can assume that the MP2 thermodynamic quantities reached a converged value within 0.05 kcal mol^{-1}, which would cause a small variation of less than 1% in TC/C conformational population.

Level of theory	$\Delta E_{ele-nuc}$	ΔE_{int}	$T\Delta S$	ΔG_T
B3LYP/6-31G(d,p)	0.69	-0.60	-1.05	0.45
MP2/6-31G(d,p)	1.24 {0.87}[a]	-0.60	-0.92	0.32
MP2/6-31++G(d,p)	1.22 {0.87}[a]	-0.61	-0.92	0.31
MP2/6-311G(d,p)	1.22 {0.83}[a]	-0.57 (-0.60)[b]	-0.93 (-1.01)[c]	0.36 (0.41)[d]
MP2/6-311++G(d,p)	1.21 {0.84}[a]	-0.57	-0.94	0.37
MP2/6-311++G(2d,2p)	1.28 {0.85}[a]	-	-	-
MP2/cc-pVDZ	1.18 {0.87}[a]	-0.58 (0.03)[b]	-0.93 (-0.0002)	0.35 (0.03)[d]
MP2/aug-cc-pVDZ	1.31 {0.89}[a]	-	-	-

[a]Hartree-Fock (HF) contribution to the MP2 fully optimized geometry energy difference. [b]$\Delta E_{int,vib}$. [c]$T\Delta S_{vib}$. [d]$\Delta G_{T,vib}$.

Table 5. Relative total energy ($\Delta E_{ele-nuc}$) and thermodynamic properties calculated for the TC→C equilibrium at T=310 K and 1 atm (values in kcal mol^{-1}).

Single Point Energy Calculations	$\Delta E_{ele-nuc}$ /kcal mol^{-1}
MP4(SDQ)/6-31G(d,p)//MP2/6-31G(d,p)	1.12
MP4(SDTQ)/6-31G(d,p)//MP2/6-31G(d,p)	1.16
CCSD/6-31G(d,p)//MP2/6-31G(d,p)	1.11
CCSD(T)/6-31G(d,p)//MP2/6-31G(d,p)	1.14
MP4(SDQ)/6-311G(d,p)//MP2/6-311G(d,p)	1.10
MP4(SDTQ)/6-311G(d,p)//MP2/6-311G(d,p)	1.15
CCSD/6-311G(d,p)//MP2/6-311G(d,p)	1.08
CCSD(T)/6-311G(d,p)//MP2/6-311G(d,p)	1.12
MP4(SDQ)/cc-pVDZ//MP2/cc-pVDZ	1.07
MP4(SDTQ)/cc-pVDZ//MP2/cc-pVDZ	1.11
CCSD/cc-pVDZ//MP2/cc-pVDZ	1.06
CCSD(T)/cc-pVDZ//MP2/cc-pVDZ	1.08

Table 6. *Post*-HF relative electronic plus nuclear repulsion energy values for cycloheptane: TC→C. The double slash means a single point energy calculation using the geometry optimized at the level indicated after the double slash.

Conformational population values for the TC conformer are given in Figure 6, where the thermodynamic quantities were partitioned into a harmonic contribution (HO) and a low frequency mode part, considered as non-harmonic (NHO), so the total value is a sum of these two contributions. Some of the low frequency modes (eight for TC) may be internal rotations, and so may need to be treated separately, depending on the temperatures and barriers involved. Following the Eq. (15) we can write:

$$\Delta E_{int,vib} = \Delta E_{int,vib}^{NHO} + \Delta E_{int,vib}^{HO} \tag{16}$$

$$T\Delta S_{vib} = T\Delta S_{vib}^{NHO} + T\Delta S_{vib}^{HO} \tag{17}$$

The rotational contribution to the entropic term is also quoted in the caption of Figure 6 (the corresponding contribution for the internal energy $\Delta E_{int,rot}$ is null, as well as the translational term). It can also be seen that the $T\Delta S_{rot}$ term is negligible, and so only the vibrational contributions need to be considered, i.e., $T\Delta S \cong T\Delta S_{vib}$. It can be seen from Figure 6 that the MP4(SDTQ) and CCSD(T) conformational population results agree nicely within 1%, so we are confident that the *ab initio* correlated level of calculation employed is sufficient for the description of the temperature-dependent thermodynamic properties.

The experimental conformational population data for cycloheptane comes from the electron diffraction study, at T = 310 K, reported in (Dillen & Geise, 1979), where a TC/C mixture, with 76±6% of TC, was proposed in order to explain the diffraction intensities. If we take the upper limit of the experimental uncertainty, 82%, this value is still 10% away from Gibbs population conformational value of 92%, evaluated using the 3N-6 vibrational modes. However, ignoring the low frequency modes for the calculation of thermal correction the agreement improves substantially (86–87% of TC/C, compared to the experimental upper limit of 82%). The results reported here provide a substantial support for a separate treatment of the low frequency modes and also stress the role they play for the determination of the conformational population. In order to better understand the effect of the vibrational modes, especially the low frequency ones, on the thermal correction, we present in Figure 7 the MP2/6-311G(d,p) ΔG_T value as a function of the vibrational mode (ν_i).

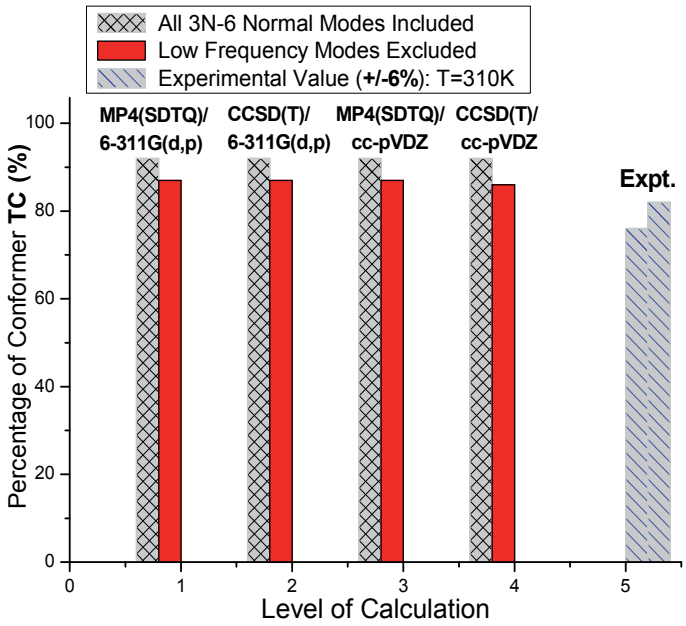

Fig. 6. Conformational population values (TC→C process) for cycloheptane at T = 310 K. Thermal correction ($\Delta G_T = \Delta H_T - T\Delta S$) was evaluated using structural parameters and vibrational frequencies calculated at the MP2/6-311G(d,p) and MP2/cc-pVDZ levels ($\Delta E_{int,trans} = T\Delta S_{trans} = 0$; $\Delta E_{int,rot} = 0$; $T\Delta S_{rot} = 0.0091$ kcal mol^{-1}; $\Delta G_T = 0.41$ *and* $\Delta G_T^{HO} = 0.03$ kcal mol^{-1}: MP2/6-311G(d,p) values).

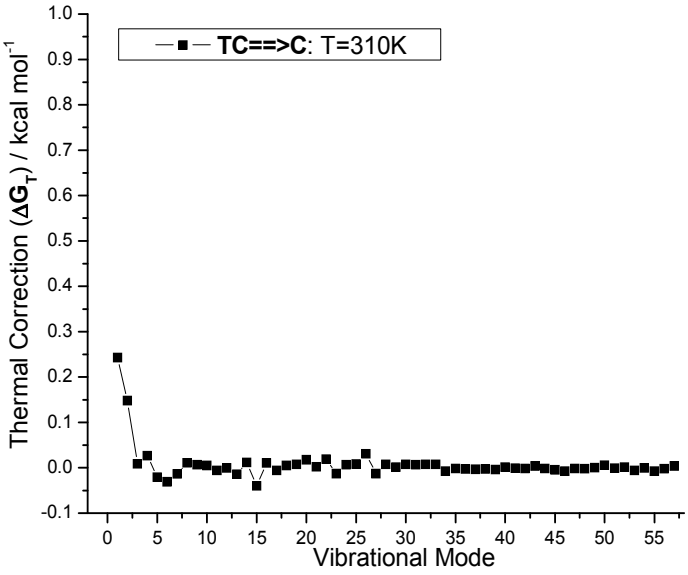

Fig. 7. MP2/6-311G(d,p) thermal correction difference (ΔG_T) as function of each normal mode for the TC→C interconversion process of cycloheptane (T = 310 K).

As can be easily seen from Figure 7, on calculating the thermal correction difference for the TC→C interconversion process the first two vibrational modes make the major contribution accounting for 93% (0.38 kcal mol^{-1}) of the total ΔG_T value of 0.41 kcal mol^{-1}. In the light of these results we decided to re-calculate the thermal correction excluding only the first two low frequency modes of conformers TC and C. The corresponding CCSD(T)/6-311G(d,p)//MP2/6-311G(d,p) and CCSD(T)/cc-pVDZ//MP2/cc-pVDZ TC population values ignoring only the first two normal modes in the evaluation of the vibrational partition function are respectively 86% and 85%, virtually the same as the value obtained excluding all ten low frequency modes from the evaluation of the vibrational partition function (87%) differently by approx. only 1%.
It can be seen that the $\Delta E_{int,vib}^{HO}$ and $\Delta G_{T,vib}^{HO}$ values calculated neglecting all the low frequency modes or only the first two modes are virtually the same, stressing the point that only these two vibrational modes must be treated separately, not as harmonic-oscillators. We then found that a proper treatment of these two low frequency modes for cycloheptane (and also for cyclooctane addressing in the next Section), should yield as a result a thermal correction very close to the values we reported in this work, using the simple procedure of ignoring the first two low frequency modes in the calculation of the thermodynamic quantities.

4.2 Cyclooctane

A considerable amount of experimental and theoretical work has been reported addressing the conformational analysis of the cyclooctane molecule, therefore, an assessment of the performance of distinct theoretical approaches for predicting the conformational population as a function of the temperature can be made. The molecular structure of cyclooctane has been widely discussed since the early 1960s (Eliel et al., 1965). The central point of the discussion is the conformation of the molecule as investigated by a variety of experimental and theoretical methods (see reviews in Anet, 1974; Burkert, 1982 and Brecknell, Raber & Ferguson, 1985; Saunders, 1987; Lipton & Still, 1988; Chang, Guida & Still, 1989; Ferguson et al., 1992; Rocha et al., 1998; De Almeida, 2000). It is important to mention the pioneering work of Hendrickson (Hendrickson, 1964), who reported nine conformations of cyclooctane belonging to three families; CROWN, boat-chair (BC) and boat-boat (BB), concluding that cyclooctane will form a very mobile conformational mixture at ordinary temperature in the gas phase. Almenningen et al. (Almenningen, Bastiansen & Jensen, 1966), in a subsequent electron diffraction study of cyclooctane in the gas phase at 40°C, gave support to Hendrickson's conclusion. At the same time, X-ray studies of cyclooctane derivatives showed that in the crystal the BC conformer is certainly preferred (Dobler, Dunitz & Mugnoli, 1966; Burgi & Dunitz, 1968; Srinivasan & Srikrishnan, 1971). Later, various studies (Anet & Basus, 1973; Meiboom, Hewitt & Luz, 1977; Pakes, Rounds & Strauss, 1981; Dorofeeva et al., 1985, 1990) indicated the exclusive or predominant existence of the BC form of the cyclooctane in the liquid and gas phase.
In this Section we discuss the gas phase conformational analysis of cyclooctane, including the BC and CROWN forms (see Figure 8). We show that the role played by the entropic contribution to the energy balance, which defines the preferable conformer, is very sensitive to the presence of low vibrational modes and the level of calculation used for its determination.
The calculated dihedral angles for the BC form of the cyclooctane molecule, are given in Table 7. There is a good agreement for all *ab initio* and DFT values, being the maximum deviation of ca. 2°. Since the cc-pVDZ basis set is believed to be more appropriated for

correlated *ab initio* calculations we take the MP2/cc-pVDZ as our best level for geometry optimization. Therefore, it can be seen that electron diffraction dihedral angle values reported for the BC conformer agree with our best theoretical result within ca. 2°. The corresponding X-ray data from (Egmond & Romers, 1969) show also a close agreement with our MP2/cc-pVDZ optimized values. The B3LYP dihedral angles are in good agreement with the MP2 ones, being also quite similar to the HF/6-31G(d,p) ones. From the results reported in Table 7 it can be seen that the calculated HF/6-31G(d,p) dihedral angles agree with the MP2/cc-pVDZ optimized values by ca. 1°, showing that, indeed, it is not necessary a high correlated level of theory for a satisfactory prediction of equilibrium structures. A similar behavior was found for cycloheptane as shown in the previous Section.

(a) **BC** (b) **CROWN**

Fig. 8. MP2 fully optimized structures of the BC (a) and CROWN (b) conformers of cyclooctane. The numbering scheme is included in the Figure 8a.

As already mentioned, statistical thermodynamics can be used to calculate temperature-dependent quantities, using equilibrium structures and harmonic frequencies evaluated from quantum mechanical calculations, which in turn are employed in the generation of partition functions. However, the occurrence of low frequency modes that may represent hindered internal rotation, can cause significant errors when the harmonic approximation is used for the calculation of partition functions. For the case of cyclic molecules featuring rings bigger than six-member, as the cyclooctane, the situation is more complicated and treating the internal rotation modes is still a big challenge. Therefore, as discussed in the previous Section, we decided just to remove the low frequency internal rotational modes from the calculations of the partition functions, minimizing the error of using the harmonic approximation for generating vibration partition functions. By comparing the conformational population calculated using vibrational partition functions neglecting the low frequency torsion modes contribution with the experimental predictions we can assess the validity of our assumption.

The results for the thermodynamic analysis, eliminating the low frequency modes from the evaluation of the vibrational partition function, are reported in Table 8, along with the thermal data evaluated considering all 3N-6 harmonic frequency values. It can be seen that the agreement with experiment is much more uniform after the internal rotation modes are excluded from the partition functions for the calculation of the thermal correction. If the low frequency modes are not removed from the thermodynamic analysis a rather non-uniform behavior is predicted.

So, it can be concluded that the low frequency modes, which may be internal rotation modes, have to be treated separately or at least removed. Zero point energy corrections (ΔZPE), internal thermal energy (ΔE_{int}) and entropy term ($-T\Delta S$) contributions to the

thermal energies (ΔG_T) for the BC and CROWN conformers (BC→CROWN interconversion process) for T=298 K are reported in Table 9. The second and third columns of Table 9 contain the values calculated using the harmonic oscillator partition function including all 3N–6 normal modes. In the last two columns of Table 9 are reported the corresponding values obtained by neglecting the low frequency torsion modes in the evaluation of the partition functions. It can be seen that the average deviation for the two sets of calculation (using all 3N-6 frequencies and omitting the low frequency torsion modes), obtained by subtracting the values from columns four and two, and columns five and three, respectively, is ca. 0.2 kcal mol^{-1} for ΔE_{int} and ca. 2 kcal mol^{-1} (MP2 value) for the $T\Delta S$ term. Therefore, the largest effect of the low frequency torsion modes is in the evaluation of the entropy term, which can have a significant effect on the calculation of conformational populations.

	D1	D2	D3	D4
HF/6-31G(d,p)	-65.6	65.6	-99.6	43.6
B3LYP/6-31G(d,p)	-65.2	65.2	-99.6	43.7
B3LYP/6-311G(d,p)	-65.2	65.2	-99.7	43.7
MP2/6-31G(d,p)	-65.2	65.2	-100.7	44.4
MP2/cc-pVDZ	-64.8	64.8	-100.9	44.5
MP2/6-311G(d,p)	-64.8	64.8	-101.1	44.5
Expt. [a]	-63.1	63.1	-98.4	42.0
X-Ray	-70.3 [b] (-60.3)[c]	70.8 [b] (62.6)[c]	-105.9 [b] (-100.0)[c]	46.8 [b] (40.9)[c]
	D5	D6	D7	D8
HF/6-31G(d,p)	63.9	-63.9	-44.6	99.6
B3LYP/6-31G(d,p)	64.1	-64.1	-43.7	99.6
B3LYP/6-311G(d,p)	64.1	-64.1	-43.7	99.7
MP2/6-31G(d,p)	64.9	-64.9	44.3	100.7
MP2/cc-pVDZ	65.1	-65.1	-44.5	100.9
MP2/6-311G(d,p)	65.4	-65.4	-44.5	101.1
Expt. [a]	68.3	-68.3	-42.0	98.4
X-Ray	62.0 [b] (67.5)[c]	-63.0 [b] (-62.2)[c]	-43.4 [b] (-48.2)[c]	100.9[b] (100.6)[c]

[a]Electron diffraction results from (Almenningen, Bastiansen & Jensen, 1966). [b]See (Dobler, Dunitz & Mugnoli, 1966). [c]See (Egmond & Romers, 1969).

Table 7. Dihedral angles (D_i in degrees) for the BC form of the cyclooctane molecule. D1=C_1-C_2-C_3-C_4, D2=C_2-C_3-C_4-C_5, D3=C_3-C_4-C_5-C_6, D4=C_4-C_5-C_6-C_7, D5=C_5-C_6-C_7-C_8, D6=C_6-C_7-C_8-C_1, D7=C_7-C_8-C_1-C_2, D8=C_8-C_1-C_2-C_3.

To ease the analysis of the performance of theoretical methods for calculating population values for cyclooctane, Figure 9 shows DFT, MP2 and MP4(SDTQ) results for the temperature of 332 K, corresponding to the experimental gas phase electron diffraction condition, along with the corresponding experimental data, in the range of 91 to 98% of BC conformer.

T = 298.15 K, p = 1atm	$\Delta E_{ele-nuc}$ [%BC]	ΔG_T	ΔG_T^{HO}	ΔG_T	ΔG_T^{HO}	%BC^{HO} [%BC]
Full Geometry Optimization						
HF/6-31G(d,p)	0.49 [69]	-1.56	-0.18	-1.07	0.31	64 [14]
HF/6-311G(d,p)	0.37 [65]	-1.43	-0.20	-1.06	0.17	58 [14]
B3LYP/6-31G(d,p)	0.32 [63]	-0.82	-0.037	-0.499	0.29	64 [30]
B3LYP/6-311G(d,p)	0.34 [64]	-0.77	-0.01	-0.433	0.33	65 [32]
BLYP/6-31G(d,p)	-0.09 [46]	-0.65	-0.017	-0.740	-0.108	45 [25]
BLYP/6-311G(d,p)	-0.06 [48]	-0.66	-0.03	-0.711	-0.086	46 [23]
MP2/6-31G(d,p)	2.31 [98]	-2.44	-0.20	-0.138	2.11	97 [44]
MP2/cc-pVDZ	2.25 [98]	-2.10	-0.18	0.154	2.07	97 [56]
MP2/6-311G(d,p)	2.59 [99]	-2.45	-0.26	0.143	2.33	98 [96]
Experimental data [+]					1.39/2.20	91-98
Single Point Energy						
CCSD//MP2/cc-pVDZ	1.61 [94]	-2.10	-0.18	-0.49	1.43	92 [30]
MP4//MP2/cc-pVDZ	1.67 [94]	-2.10	-0.18	-0.43	1.49	93 [33]
MP4/cc-pVDZ//HF/631G(d,p)	1.57 [93]	-1.56	-0.18	0.01	1.39	91 [50]

[+]Experimentally, at the temperature of 59°C (332 K), and also room temperature, the boat-chair is either the exclusive or at least the strongly predominant form in the gas phase (See Dorofeeva et al., 1985).
ΔE^0 correction is included in ΔE_{int}.

Table 8. Energy differences ($\Delta E_{ele-nuc}$), thermal energies (ΔG_T) and the corresponding values corrected for errors due to internal rotations (ΔG_T^{HO}), Gibbs free energy differences (ΔG) and the values corrected for internal rotation (ΔG^{HO}) and Gibbs populations (values calculated using 3N-6 normal modes as harmonic oscillators are in brackets). The Boltzmann populations are given in brackets in the second column. All energy values are in units of kcal mol^{-1}.

A result that calls our attention is the bad performance of the B3LYP and BLYP DFT functionals for predicting the relative conformational population of the BC and CROWN conformers of cyclooctane. The B3LYP functional (and also calculations with other functional not reported here) produces a very poor result. It can be clearly seen that the problem is in the evaluation of the electronic energy term ($\Delta E_{ele-nuc}$), with the B3LYP thermal correction being at least reasonable. The B3LYP functional underestimates the electronic plus nuclear repulsion energy difference between the CROWN and BC conformers by more than 1 kcal mol^{-1}, which causes a remarkable effect on the conformational population evaluated with the exponential Gibbs free energy. It is hard to say if this is a particular misbehavior for the specific case of cyclooctane molecule or maybe other macrocyclic systems.

It is informative to access explicitly how an uncertainty in the ΔG value can influence the calculation of the conformational population. The relative conformational population corresponding to the BC→CROWN interconversion process is evaluated with the equilibrium constant calculated with the well-known equation given below (Eqs. 18,19), where [BC] and [CROWN] are respectively the concentrations of the BC and CROWN conformers.

	ΔZPE	ΔE_{int}	$-T\Delta S$	ΔE_{int}^{OH}	$-T\Delta S^{HO}$
HF/6-31G(d,p)	-0.57	-0.29	-1.26	-0.13	-0.05
HF/6-311G(d,p)	-0.55	-0.30	-1.13	-0.14	-0.06
HF/6-311++G(d,p)	-0.53	-0.27	-1.18	-0.11	-0.16
MP2/6-31G(d,p)	-0.72	-0.34	-2.11	-0.14	-0.06
MP2/cc-pVDZ	-0.65	-0.31	-1.79	-0.13	-0.05
MP2/6-311G(d,p)	-0.77	-0.40	-2.05	-0.20	-0.06
B3LYP/6-31G(d,p)	-0.28	-0.12	-0.699	0.003	-0.040
B3LYP/6-311G(d,p)	-0.25	-0.10	-0.669	0.03	-0.04

All energy values are in units of kcal mol^{-1}. The values were calculated using the harmonic approximation for the generation of the thermodynamical partition functions for all vibrational modes including the low frequency modes and also, neglecting the low frequency torsion modes (HO approach).

Table 9. Zero-point energy corrections (ΔZPE), internal thermal energy (ΔE_{int}) and entropy term ($-T\Delta S$) contributions to the thermal energies for the BC and CROWN conformers (BC→CROWN interconversion process, T=298 K, p=1atm).

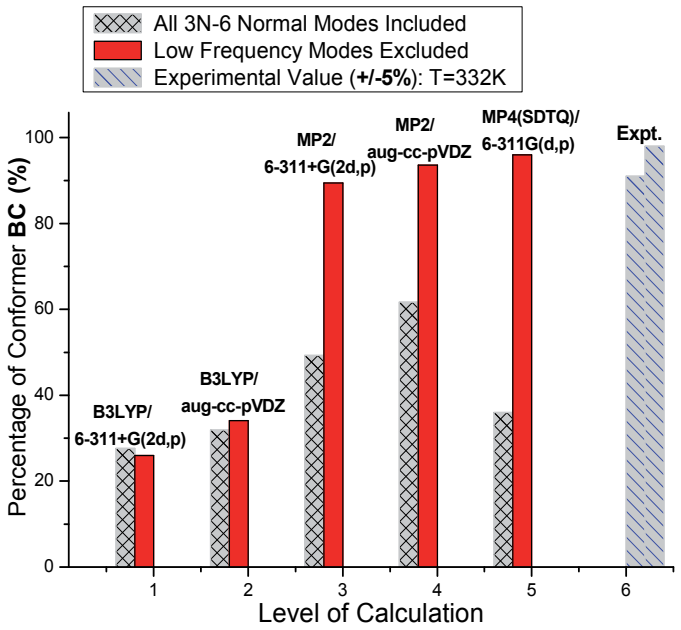

Fig. 9. Population for BC conformer of cyclooctane (BC→CROWN equilibrium process) at T=332K. The MP4(SDTQ) value was calculated using the MP2/6-311G(d,p) thermal correction.

$$\Delta G \quad = G_{CROWN} - G_{BC} \tag{18}$$

$$K_{eq} = \frac{[CROWN]}{[BC]} = \exp(-\frac{\Delta G}{RT}) \tag{19}$$

The BC population can be obtained through the equation below keeping in mind that [BC]+[CROWN]=1.

$$[BC] = \frac{1}{1+\exp(-\frac{\Delta G}{RT})} \tag{20}$$

Let us assume that the Gibbs free energy value is estimated to a precision of ±d kcal mol^{-1}. Then the exponential factor in Eq. (20) will be:

$$\exp\left(-\frac{\Delta G}{RT} \pm \frac{d}{RT}\right) = \exp(\pm\frac{d}{RT}) \times \exp\left(-\frac{\Delta G}{RT}\right)$$

Then from Eq. (20),

$$[BC] = \frac{1}{1+f_{\pm}\exp(-\frac{\Delta G}{RT})} \therefore f_{\pm} = \exp(\frac{\pm d}{RT}) \tag{21}$$

Depending on the + or – sign used for d (named d_+ or d_-) we have two possibilities for the value of the pre-exponential factor: f_+ or f_-, leading to two distinct conformational populations named, %BC(f_+) and %BC(f_-). From Eq. (21) it can be seen that the accuracy of the %BC value depend on the quality of ΔG and also the uncertainty in its evaluation d (or factor, f_+ and f_-). Assuming T = 298.15 K just for comparison, for low values of ΔG a very small uncertainty (less than 0.1 kcal mol^{-1}) is required to produce acceptable variations in the population. For ΔG higher than 3 kcal mol^{-1} an uncertainty of ca. 1 kcal mol^{-1} does not cause significant variations. However, for intermediate values of ΔG as is the case of the cycloalkanes molecule, care is needed and a high correlated level of calculation is needed for evaluating Gibbs free energies, if trustable conformational populations is desired. Then, it can be anticipated that a quite reliable value of Gibbs free energy difference would be required to calculate accurate conformational population values (having an average uncertainty of ±1%), for ΔG around 2 kcal mol^{-1} (as in the cyclooctane case). It can be seen that there is an inevitable compromise between the uncertainty d and ΔG, that is, smaller is the value of ΔG smaller should be d, in order to reach reliable predictions of conformational populations.

In the light of the comments of last paragraph we are inclined to affirm that for the cyclooctane molecule in the gas phase, the most trustable conformational population data available is the CCSD/cc-pVDZ result (or MP4(SDQ)/cc-pVDZ that differs only in 1%), that is 92% of BC and 8% of CROWN, at room temperature, with thermal corrections evaluated at the MP2 level and neglecting the low frequency torsion modes. These results are in good agreement with the experimental predictions of Dorofeeva et al. (Dorofeeva et al., 1985), which reported the population of BC to be in a range of 91–98%, at 332 K. There is indeed a contribution of ca. 8% of the CROWN form in the conformational mixture at 298 K. If the temperature is raised to 59°C (332 K), as in the experiment of Dorofeeva et al. (Dorofeeva et al., 1985), the percentage of the CROWN structure would increase to ca. 10% (CCSD/cc-pVDZ//MP2/cc-pVDZ value) and might well be detectable in the electron diffraction gas phase experiment. Therefore, the lower limit for the percentage of BC (91%) that was reported by Dorofeeva et al. (Dorofeeva et al., 1985) is definitively their best value, not the upper limit of 98%.

Lastly, **w**e aim to call the attention of people working on conformational analysis studies to the important problem of adding thermal corrections to the calculated relative energy values and also to the role played by the low frequency modes for the calculation of the thermal

energy corrections. We are not affirming here that the behavior observed for the cyclooctane molecule would be necessarily the same for other molecular systems. However, we should be alert to the fact that the use of the harmonic oscillator partition function to treat low frequency vibrational modes, that may be internal rotation modes, can lead to wrong predictions, and the simple approach that we used for cyclooctane may be a way out to obtain more trustable relative Gibbs free energy values. By using a high correlated *ab initio* level of theory with a reasonable basis set for calculating the electronic contribution to the total Gibbs free energy we eliminated the possibility of cancellation of errors in the *ab initio* electronic structure calculation. As we performed a systematic investigation our nice agreement with experiment cannot be viewed as just a lucky circumstance. Unfortunately there are not many accurate experimental gas phase conformational relative energy data available in the literature for comparison and we have to rely on theoretical highly correlated *ab* initio data.

4.3 Cyclononane

The literature with the focus on the conformational analysis of cyclononane is also substantial (Hendrickson, 1961; Hendrickson, 1967b; Anet & Krane, 1980; Kolossvary & Guida, 1993; Weinberg & Wolfe, 1994; Wiberg, 2003). Anet and Krane (Anet & Krane, 1980) carefully analyzed the conformational distribution of cyclononane as a function of the temperature using dynamic NMR spectroscopy and found two major forms in the equilibrium mixture (named TBC and TCB) with a third conformer (TCC) present on a small amount at higher temperature. More recently Wiberg (Wiberg, 2003) used quantum-mechanical methods to obtain structure and energy for this molecule with the MP2 prediction found in qualitative agreement with the experimental proposal (Anet & Krane, 1980). In our recent paper (Franco et al., 2007), eight distinct minimum energy conformers were located on the gas phase MP2/6-31G(d,p) PES, with the main structures shown in Figure 10. The first two isomers (TBC and TCB) were proposed in the pioneer works of Hendrickson (Hendrickson, 1961; Hendrickson, 1967a, 1967b), and Anet and Krane (Anet & Krane, 1980) described later the so called TCC (and also C1) structure. The conformation M4 (and also M6 and M7) has been found by Wiberg (Wiberg, 2003) in a theoretical *ab initio* analysis. The structure M8 was proposed by our group and represents a higher energy minimum point on the PES at the MP2 level. Experimentally, the conformational analysis was done by dynamic ^{13}C NMR at a broad range of temperature from -173 to -70°C (Anet & Krane, 1980). The measurements were carried out in solution of a solvent mixture of $CHFCl_2$ and vinyl chloride (1:2) using TMS (tetramethylsylane) as internal reference. The distribution of conformers in the equilibrium was obtained by fitting to a theoretical model, depending on chemical shift, conformational population and interconversion rate constant, to the experimental line shape.

The calculated relative energies ($\Delta E_{ele-nuc}$) are given in Table 10 where the TBC form was taken as reference. It can be seen from Table 10 that the HF and B3LYP relative energies are virtually the same, what has also been observed by Wiberg (Wiberg, 2003). At these levels of theory the TCB isomer was found to be the global minimum with the TBC only 0.1 kcal mol^{-1} higher in energy. The MPn methods predict the TBC form as the most stable in gas phase with the MP4 values found to be very close to the MP2 one. The DFT relative energies exhibit a sizeable disagreement with the MPn values, with the B3LYP and BLYP functionals exhibiting the poorest accordance with the MP2 and MP4 energies. The B3P86/6-31G(d,p) and PBE1PBE/6-31G(d,p) values show the smallest deviation, however being still far away from the *post*-HF description of the relative energy values.

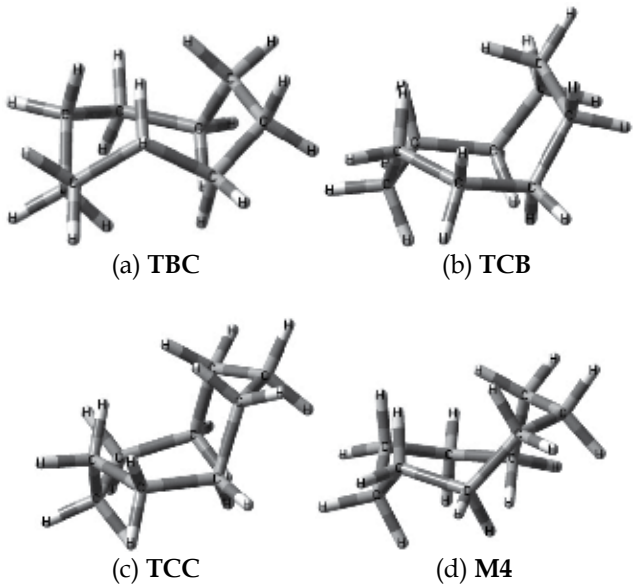

(a) **TBC** (b) **TCB**

(c) **TCC** (d) **M4**

Fig. 10. MP2/6-31G(d,p) fully optimized geometries for the main conformers of cyclononane (TBC, TCB, TCC and M4).

The thermodynamic properties for the four main minimum conformers, TBC, TCB, TCC and M4, are reported in Table 11 as calculated at distinct temperatures for what experimental data are available (Anet & Krane, 1980). All thermal corrections (ΔG_T) calculations were done using the MP2/6-31G(d,p) structural parameters and harmonic frequencies, for the calculation of the enthalpic and entropic terms, including all 3N-6 normal modes in the evaluation of the vibrational partition function.

	TBC	TCB	TCC	M4	C1	M6	M7	M8
HF/6-31G(d,p)	0.0	-0.10	1.17	-	3.3	-	10.2	-
B3LYP/6-31G(d,p)	0.0	-0.08	1.34	-	3.29	-	10.3	-
BLYP/6-31G(d,p)	0.0	-0.39	1.10					
BP86/6-31G(d,p)	0.0	0.19	1.62					
B3P86/6-31G(d,p)	0.0	0.43	1.80					
PW91/6-31G(d,p)	0.0	0.19	1.65					
PBE1PBE/6-31G(d,p)	0.0	0.48	1.80					
MP2/6-31G(d,p)	0.0	1.16	2.49	3.88	3.92	7.16	11.3	10.2
MP4(SDQ)/6-31G(d,p)// MP2/6-31G(d.p)	0.0	0.84	2.07	3.55	3.72	6.87	11.01	9.92
MP4(SDTQ)/6-31G(d,p)// MP2/6-31G(d,p)	0.0	1.00	2.28	3.68	3.75	6.88	10.99	9.94

[a]From (Anet & Krane, 1980).

Table 10. Relative energies (in kcal mol^{-1}) calculated for the distinct minimum conformers of cyclononane.

	T=100.15K	T=128.15K	T=178.15K	T=298.15K
TBC	0.0[0.0]	0.0[0.0]	0.0	0.0
	94.1%[95%]	87.6%[88%]	74.9%	52.1%[40%]
TCB	0.5497[0.6]	0.4997[0.5]	0.3975	0.1217
	5.9%[5%]	12.3%[12%]	24.4%	42.4%[50%]
TCC	1.7699	1.7307	1.6440[1.6]	1.3946
	0.0%	0.1%	0.7%[1%]	5.0%[10%]
M4	3.1949	3.1507	3.0555	2.7869
	0.0%	0.0%	0.0%	0.5%

Table 11. Relative Gibbs free energy (ΔG), obtained using all 3N-6 normal modes for the evaluation of the vibrational partition function, for the four main conformations of cyclononane molecule calculated at MP4(SDTQ)/6-31G(d,p)//MP2/6-31G(d,p) level (values in kcal mol^{-1}). The Gibbs population is also given with the experimental data in brackets.

At 100.15 K the experimental data were assigned to the TBC major form and a small amount of a second conformer. The analysis was rationalized by postulating a simple conformational mixture with the TBC→TCB equilibrium being established and strongly shifted to the TBC isomer (95%) (Anet & Krane, 1980). Our MP4 results are in excellent agreement with this proposal with the Gibbs population calculated to be 94.1% (TBC) and 5.9% (TCB). Rising the temperature to 128.15 K the experimental analysis showed the population distribution equal to 88% for the major conformation (TBC) and 12% for the minor form (TCB). The theoretical results gave 87.6, 12.4 and 0.1% for TBC, TCB and TCC, respectively supporting the experimental findings. At 178.15 K the TCC form was observed at small amount, 1.0±0.5% (Anet & Krane, 1980). The theoretical determination gives 0.7% for TCC with the TBC→TCB equilibrium being slightly shifted toward the TCB species, which is present in the medium on a relative population of 24.4%. At room temperature a rough experimental estimation of the conformational population was made with the aid of MM structural and energy data, i.e., 40% of TBC, 50% of TCB and 10% of TCC. The theoretical results obtained at MP4(SDTQ)/6-31G(d,p)//MP2/6-31G(d,p) showed the following values: 52.1% of TBC, 42.4% of TCB, 5% of TCC and 0.5% of M4, in nice agreement with the experimental estimation, but with the TBC structure still found to be the global minimum. These comparisons are better summarized in Figure 11, which shows the Gibbs conformational population for the four relevant conformers of cyclononane as a function of the temperature, along with the available experimental data. The apparent disagreement between our theoretical and experimental populations at room temperature regarding to the TBC→TCB equilibrium position is certainly due to the fact that the experimental population at this temperature was not directly based on the NMR data, but a rough extrapolation (Anet & Krane, 1980). By looking at Figure 11a, where the MP4(SDTQ)/6-31G(d,p)//MP2/6-31G(d,p) Gibbs conformational population for the four relevant conformers of cyclononane is represented as a function of the temperature considering all 3N-6 harmonic frequencies, we can clearly see that in the region where the NMR spectrum was recorded (100-180K), the theoretical and experimental predictions are in excellent agreement. In Figure 11b the common sense of increasing the population of conformers having higher energy as the temperature raise is observed, with the equilibrium being shifted to TCB just above room temperature.

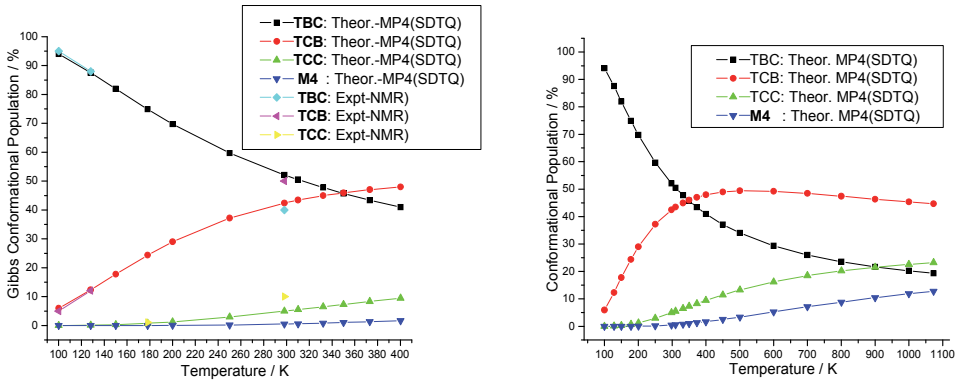

Fig. 11. MP4(SDTQ)/6-31G(d,p)//MP2/6-31G(d,p) Gibbs population for the four most relevant conformers of cyclononane as a function of the temperature. (a) All 3N-6 normal modes included in the evaluation of the vibrational partition function (available experimental data are also shown). (b) Calculated values, using the 3N-6 normal modes, on the range of 100-1073K are included.

The effect of the low frequency modes on the calculation of conformational population values is shown in Figure 12, where MP4(SDTQ)/6-31G(d,p)//MP2/6-31G(d,p) conformational population data evaluated at various temperatures are reported. In Figure 12 experimental values and theoretical results calculated including all 3N-6 normal modes and also excluding the low frequency modes from the evaluation of the vibrational partition function (HO approach) are given. It can be promptly seen the best agreement with experimental population data is obtained using all 3N-6 normal modes for the determination of the thermal correction, quite different from the behavior found for cycloheptane and cyclooctane discussed in the previous Sections.
To illustrate the dependence of thermodynamic quantities with the temperature Figure 13 shows the vibrational internal energy and entropy contributions to the thermal energy as a function of the temperature considering all 3N-6 normal modes and excluding the low frequency modes from the evaluation of the vibrational partition function. It can be easily seen that only the low frequency modes contributions are affected by the increase in the temperature.

4.4 Cyclodecane

Cyclodecane has considerably more conformational flexibility (Hendrickson, 1964; Eliel et al., 1965; Almenningen, Bastiansen & Jensen, 1966; Rounds & Strauss, 1978; Dobler, Dunitz & Mugnoli, 1966; Burgi & Dunitz, 1968; Egmond & Romers, 1969; Srinivasan & Srikrishnan, 1971; Anet & Basus, 1973; Anet, 1974; Meiboom, Hewitt & Luz, 1977; Pakes, Rounds & Strauss, 1981; Burkert, 1982; Brecknell, Raber & Ferguson, 1985; Saunders, 1987; Lipton & Still, 1988; Chang, Guida & Still, 1989; Dorofeeva et al., 1990; Ferguson et al., 1992; Kolossvary & Guida, 1993; Weinberg & Wolfe, 1994; Wiberg, 2003) than the smaller C7–C9 cycloalkanes discussed in the previous Sections. The structures of the lower-energy conformations have been studied via electron diffraction (Hilderbrandt, Wieser & Montgomery, 1973), X-ray crystallography (Shenhav & Schaeffer, 1981) and dynamic NMR spectroscopy (Pawar et al., 1998). The boat-chair-boat (BCB) conformation for the

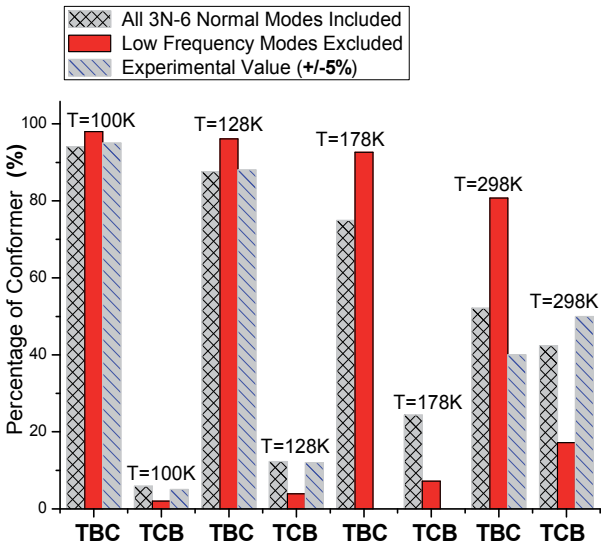

Fig. 12. MP4(SDTQ)/6-31G(d,p)//MP2/6-31G(d,p) conformational population data for cyclononane evaluated at various temperatures. Experimental values and theoretical results calculated including all 3N-6 normal modes and also excluding the low frequency modes from the evaluation of the vibrational partition function (HO approach) are shown.

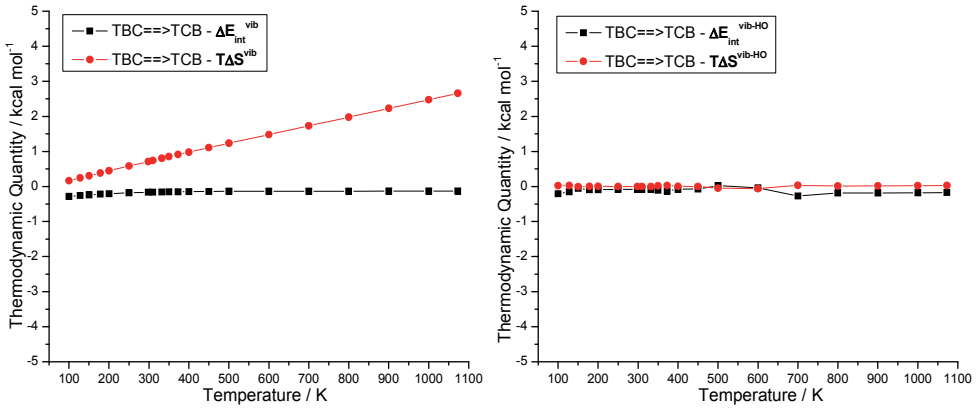

(a) (b)

Fig. 13. MP2/6-31G(d,p) thermodynamic quantities ($\Delta E_{int,vib}$, $T\Delta S_{vib}$, in units of kcal mol^{-1}) as a function of the temperature. (a) All 3N-6 normal modes included in the evaluation of the vibration partition function. (b) Low frequency modes excluded from the calculations.

cyclodecane has been found in the solid state by X-ray diffraction (Shenhav & Schaeffer, 1981) near 173 K and assigned as the most stable form.

The low-temperature ^{13}C NMR spectra of cyclodecane showed a minor presence of a conformation assigned to the twist-boat-chair–chair (TBCC), besides the expected boat-chair-boat (BCB) conformer (Pawar et al., 1998)]. A conformational distribution having 89.6%, 5.2% and 5.2% of BCB, TBC and TBCC conformations, respectively was proposed by

Pawar and collaborators (Pawar et al., 1998) for cyclodecane based on the analysis of dynamic NMR spectroscopy carried out at 127.05 K and theoretical calculations using *ab initio* level of theory. Cyclodecane has also been studied in the gas phase at 403.15 K by means of a combination of electron diffraction and MM calculations (Hilderbrandt, Wieser & Montgomery, 1973). In this case, least square analysis of the experimental radial distribution curve, utilizing the theoretical predictions for the four lowest-energy conformations, indicated a more complex equilibrium composition: BCB, 49±3%, TBC, 35±3%, TBCC, 8±4 and BCC, 8±4%. In the present Section we discuss an accurate analysis of the thermodynamic properties and conformational populations in order to assess the influence of the low frequency vibrational modes on the calculation of thermodynamic quantities as a function of temperature for the cyclodecane molecule.

Among all possible conformers, 15 true minima were located on the PES (named S1, S2, . . . , S15), with the boat-chair-boat, BCB (S1), being the lowest energy structure, and characterized through harmonic frequency analysis. In Table 12, relative energies are shown for all conformers obtained from HF, B3LYP and MP2 levels of theory. As can be seen from Table 12, the conformations S1, S2, S3, S4 and S5, also called BCB, TBCC, TBC, BCC and TCCC, respectively, were found as the more stable forms, with relative energies within 3 kcal mol^{-1}. Based on these results, we can assume that only these five conformations are present in the equilibrium in significant amounts. The structures of the main conformers are depicted in Figure 14.

	$\Delta E_{ele-nuc}$		
	HF/6-31G(d,p)	B3LYP/6-31G(d,p)	MP2/6-31G(d,p)
S1 (BCB)	0.00	0.00	0.00
S2 (TBCC)	1.04	1.24	1.22
S3 (TBC)	0.92	0.93	1.06
S4 (BCC)	2.38	2.46	2.18
S5 (TCCC)	2.64	3.09	2.54
S6	3.15	3.23	3.54
S7	4.30	4.10	4.84
S8	4.08	3.80	4.54
S9	4.56	4.22	5.03
S10	4.64	4.43	5.65
S11	5.21	5.11	6.30
S12	6.78	6.61	6.89
S13	6.99	7.02	7.94
S14	10.94	9.01	11.23
S15	19.23	17.47	19.45

Table 12. Relative energies ($\Delta E_{ele-nuc}$ in kcal mol^{-1}) for distinct minimum energy conformers of cyclodecane

With the aim to describe the effect of electronic correlation on the relative energy, we carried out single point calculations at the MP4(SDTQ) and CCSD(T) levels, using MP2/6-31G(d,p) geometries. The results are given in Table 13, where the double slashes indicate a single point energy calculation at the geometry specified after the slash. As can be seen in Table 13, the energy variation observed at the MP2/6-31G(d,p), MP4(SDTQ)/6-31G(d,p) and

CCSD(T)/6-31G(d,p) calculations was smaller than 0.1 kcal mol^{-1}. Thus, we can conclude that the electron correlation effect accounted for at the MP2 level is satisfactory for the description of cyclodecane. A variety of DFT-based methods were also tested, including BLYP, PW91 and BP86 GGA functionals and the B3LYP, B3P86 and PBE1PBE hybrid functionals employing the 6-31G(d,p) basis set (see Table 13). Analyzing these results and having as reference the MP2/6-31G(d,p) values, it was observed that all functionals provide satisfactory relative energies, with the B3P86 and PBE1PBE functionals giving the best agreement with MP2 data. Therefore, the DFT approaches can be viewed as a feasible alternative for studying larger cycloalkanes where MP2 and higher *post*-HF calculations are computationally prohibitive.

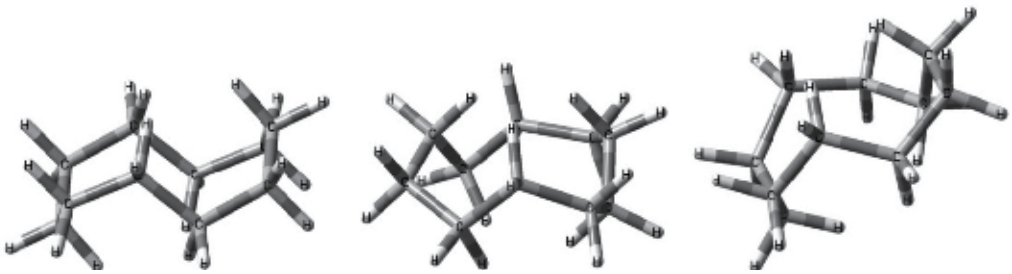

(a) BCB (b) TBCC (c) TBC

Fig. 14. MP2/6-31G(d,p) fully optimized geometries for the main conformations of the cyclodecane molecule. (a) BCB (b) TBCC (c) TBC

	$\Delta E_{elec-nuc}$				
	BCB	TBC	TBCC	BCC	TCCC
MP2/6-31G(d,p)	0.00	1.06	1.22	2.18	2.54
MP4(SDQ)/6-31G(d,p)// MP2/6-31G(d,p)	0.00	1.00	1.14	2.20	2.48
MP4(SDQT)/6-31G(d,p)// MP2/6-31G(d,p)	0.00	1.03	1.19	2.17	2.50
CCSD/ 6-31G(d,p)// MP2/6-31G(d,p)	0.00	1.00	1.10	2.17	2.42
CCSD(T)/ 6-31G(d,p)// MP2/6-31G(d,p)	0.00	1.01	1.14	2.14	2.44
BLYP/6-31G(d,p)	0.00	0.90	1.29	2.46	3.19
B3LYP/6-31G(d,p)	0.00	0.93	1.24	2.46	3.09
BP86/6-31G(d,p)	0.00	0.96	1.25	2.41	3.07
PW91PW91/6-31G(d,p)	0.00	0.96	1.28	2.44	3.15
PBE1PBE/6-31G(d,p)	0.00	0.96	1.18	2.35	2.87

Table 13. Electronic plus nuclear relative energies ($\Delta E_{elec-nuc}$ in kcal mol^{-1}) calculated for the main conformers of cyclodecane molecule.

The effect of the quality of the basis set on the MP2 relative energies for the five main cyclodecane conformations was also investigated. In Figure 15, the relative energies for the four equilibrium processes (BCB→TBCC, BCB→TBC, BCB→BCC and BCB→TCCC) are

plotted as a function of distinct basis sets. It is noted that the relative energies are more sensitive to the basis set than to the electron correlation effect (see Table 13). The basis-set effect is more pronounced for the equilibrium involving the lower-energy conformers, for which $\Delta E_{elec-nuc}$ values are within 1 kcal mol^{-1}. The TBC isomer is more stable than TBCC at lower levels of theory (MP2/6-31G(d,p)), and the enhancement of basis set up to 6-311+G(d,p) changes the stability order, with the TBCC found as more stable. Further improvement of the basis set with inclusion of two sets of polarization functions (MP2/6-311++G(2d,2p)) predicts both forms as being almost degenerate. These calculations revealed the importance of using extended basis sets (triple-zeta) with diffuse functions, which improves significantly the description of the electronic plus nuclear-nuclear repulsion energy.

Conformational analysis for cyclodecane was performed, with the CCSD(T)/6-31G(d,p)// MP2/6-31G(d,p) results reported in Table 14 at distinct temperatures in which experimental data are available. The Gibbs populations calculated at the MP2/6-311G(d,p) level predicted the population of TBCC slightly higher than TBC, respectively 4% and 2% at T = 102.05 K. As in the previous sections the thermal correction term (ΔG_T), necessary for the calculation of thermodynamic quantities, was also partitioned into two contributions: non-harmonic (NHO) and harmonic (HO), differing by whether the low frequency modes are included or not, respectively. The total thermal correction corresponds to the sum of these two contributions. Therefore, the Gibbs free energy can be evaluated using all 3N-6 normal modes (ΔG) or ignoring the low frequency modes that corresponds to the inclusion of only the harmonic contribution (ΔG^{HO}), neglecting the ΔG_T^{NHO} term.

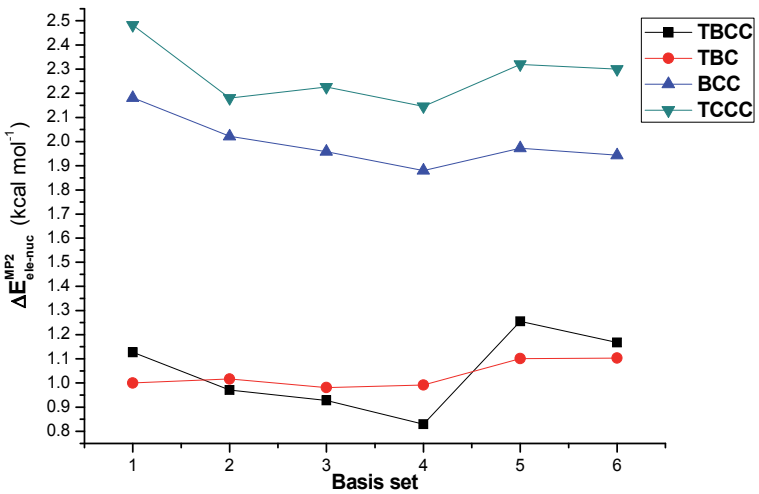

Fig. 15. Variation of the relative energy for the main conformers of cyclodecane as a function of the basis set. The BCB form was taken as reference. Basis set: 1: 6-31G(d,p); 2: 6-311G(d,p); 3: 6-31++G(d,p); 4: 6-311+G(d,p); 5: 6-311G(2d,2p); 6: 6-311++G(2d.2p).

The CCSD(T)/6-31G(d,p)//MP2/6-31G(d,p) population for the main conformers are summarized in Figure 16a, evaluated at various temperatures. Experimental values and theoretical results calculated including all 3N-6 normal modes and also excluding the low frequency modes from the evaluation of the vibrational partition function (HO approach) are

shown. It can be seen that in the case of cyclodecane the low frequency modes do not play a major role as in the case of cyclooctane, and so similar agreement with experiment is obtained excluding or not the low frequency modes from the evaluation of the vibrational partition function. As can be observed in Table 14, the thermal energy contribution due to the low frequency modes (ΔG_T^{NHO}) is small, leading to a maximum variation of ~2% in the conformational population. The variation of the conformational population as a function of the temperature is shown in Figure 16b. A similar pattern obtained previously for cyclononane is observed, however, at higher temperatures conformer BCB is the predominant.

	T=102.05K			*T=127.05K*			*T=403.15K*		
	ΔG	ΔG^{HO}	pop[b]	ΔG	ΔG^{HO}	pop[b]	ΔG	ΔG^{HO}	pop[b]
BCB	0.00 (97%)	0.00 (97%)	95%	0.00 (92%)	0.00 (91%)	90%	0.00 (41%)	0.00 (43%)	49±3%
TBC	0.81 (2%)	0.80 (2%)	3%	0.78 (4%)	0.75 (5%)	5.%	0.40 (25%)	0.43 (25%)	35±3%
TBCC	0.87 (1%)	0.92 (1%)	3%	0.83 (3%)	0.79 (4%)	5%	0.36 (26%)	0.51 (23%)	8±4%
BCC	1.96 (0%)	1.96 (0%)		1.92 (0%)	1.87 (0%)		1.51 (6%)	1.54 (6%)	8±4%
TCCC	2.30 (0%)	2.38 (0%)		2.30 (0%)	2.26 (0%)		2.19 (3%)	2.24 (3%)	

[a]Gibbs population from CCSD(T)/6-31G(d,p)//MP2/6-31G(d,p) given in parenthesis. [b]Values from (Pawar et al., 1998). [c]Values from (Hilderbrandt, Wieser & Montgomery, 1973). These are rough estimates using empirical MM data (not genuinely from spectroscopic analysis).

Table 14. Relative Gibbs free energy (ΔG) for the five main conformations of cyclodecane molecule calculated at CCSD(T)/6-31G(d,p)//MP2/6-31G(d,p) (values in kcal mol^{-1}) level at distinct temperatures[a].

Another important factor to be taken into account in the evaluation of the Gibbs free energy is the multiplicity (m) for each form present in the equilibrium mixture. This is the number of ways of realizing each type of conformation and can be different from unity. Thus the ΔG should be corrected for the additional term $-RTln(m_j/m_i)$, with m_j and m_i being the multiplicity for the isomers j and i respectively. According to Pawar (Pawar et al., 1998), it is necessary to assign a statistical weight of 2 to the free energies of TBCC and TBC cyclodecane conformation, since these forms may exist as two enantiomers, therefore, the factor $-RTln2$ must be included to compute the final Gibbs free energy difference. In our paper on cyclodecane (Ferreira, De Almeida & Dos Santos, 2007), the vibrational circular dichroism (VCD) spectra for the distinct forms were calculated at the B3LYP/6-31G(d,p) level. The analysis of the VCD spectra for BCB, TBC, TBCC, BCC and TCCC forms confirmed the existence of enantiomers only for TBCC, TBC and BCC structures. These results support the proposal of Pawar et al. (Pawar et al., 1998) and Kolossváry and Guida (Kolossvary & Guida, 1993), showing the existence of chiral isomers for these three forms of the cyclodecane. Therefore, the $-RTln2$ factor must be

included to compute the relative Gibbs free energy for the following equilibria BCB→TBCC, BCB→TBC and BCB→BCC.

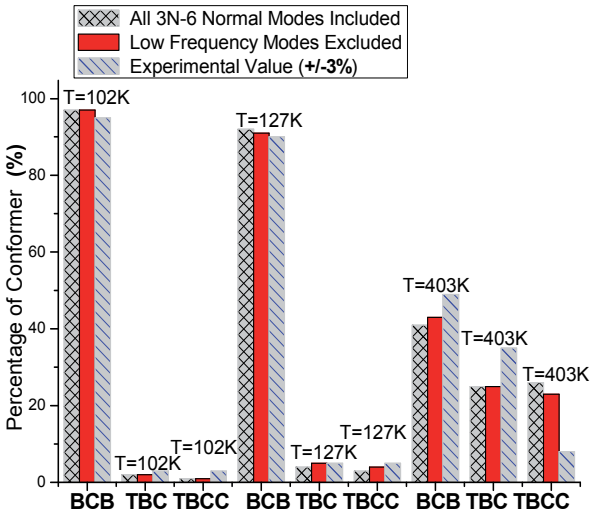

(a)

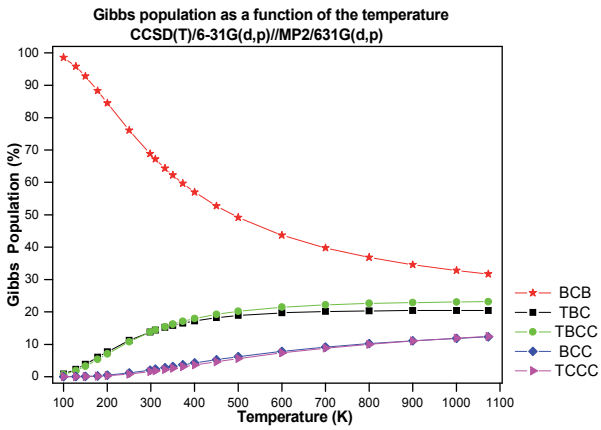

(b)

Fig. 16. (a) CCSD(T)/6-31G(d,p)//MP2/6-31G(d,p) conformational population data for cyclodecane evaluated at various temperatures. Experimental values and theoretical results calculated including all 3N-6 normal modes and also excluding the low frequency modes from the evaluation of the vibrational partition function (HO approach) are shown. (b) Variation of population, calculated using all 3N-6 normal modes, as a function of temperature.

It is opportune to compare the conformational population values reported in Figure 16a for cyclodecane and Figure 9 for cyclooctane. A rather different behavior was observed for the cyclooctane molecule, where the exclusion of the low frequency modes (below ~650 cm^{-1}, at room temperature) has promoted a good improvement between the experimental and

theoretical data. The inclusion of all 3N-6 vibrational modes for the calculation of the vibrational partition function for cyclooctane, different from the cyclodecane case, proved to be an inadequate procedure for calculating the thermodynamic properties, leading to a total disagreement with the experimental findings. In the light of the *post*-HF *ab initio* calculations reported for cycloheptane, cyclooctane, cyclononane and cyclodecane, we can say that there is indeed an important participation of the low frequency modes for the determination of the vibrational partition function, which are used within the framework of the statistical thermodynamics formalism for the evaluation of free energies. We have so far proposed a simple and satisfactory procedure to treat these cycloalkanes; however, this approach is not meant to be a more general procedure to be applied for cycloalkanes of any size. The disagreement between the experimental and calculated conformational populations for cyclodecane was more pronounced at higher temperature (403 K). The theoretical calculation predicted the equilibrium slightly shifted toward the TBCC isomer, which is found in a ratio close to 26%. Experimentally, the TBCC population was only 8%. This disagreement may be attributed in part to the fact that at this temperature the experimental conformation distribution was not directly obtained from experiment, as in the case of low temperature measurements (Hilderbrandt, Wieser & Montgomery, 1973), but using additional information from molecular mechanics calculations. Therefore, in view of the good agreement with the experimental conformational population obtained from the low temperature NMR experiment, and also the nice agreement between *ab initio* and experimental electron diffraction population data for cycloheptane (Anconi et al., 2006) and cyclooctane (Dos Santos, Rocha & De Almeida, 2002), we believe that the CCSD(T)/6-31G(d,p)//MP2/6-31G(d,p) calculations at the temperatures range considered here can be taken as reliable within experimental uncertainties.

4.5 Large cycloalkanes

In previous Sections we reported conformational analysis of cycloheptane, cyclooctane, cyclononane and cyclodecane, where experimental population data are available, using quantum chemical methods and statistical thermodynamic formalism for the determination of conformational populations, with the main focus on conformational distribution and its dependence on the level of theory and the effect of low-frequency vibrational modes for the evaluation of entropy contribution. In these studies it was shown that for some derivatives (cycloheptane and cyclooctane), low frequency vibrations may not be considered as harmonic oscillators, having a great effect on the partition function, which leads to a significant deviation in the calculated thermodynamic properties with respect to experimental data

Our best level of calculation for relative Gibbs free energy, used as reference value, is obtained with the Eq. (22) below, where the double slash means that single point CCSD(T) energy calculations were performed using MP2 fully optimized geometries. We have also found that the use of the MP4(SDTQ) correlated level of theory leads to conformational population results very similar to CCSD(T), which consumes much more computer time, and so it can safely replace the CCSD(T) energy calculations.

$$\Delta G = \Delta E_{ele-nuc}^{CCSD(T)//MP2} + \Delta G_T^{MP2} \tag{22}$$

We can also apply Eq. (22) using the same level of calculation for the first and second terms, or other combination of levels, what may even result in a fortuitous agreement with experiment but not based on fundamental justification, only by a cancellation of errors.

Certainly, it would be ideal to use the MP4(SDTQ) or CCSD(T) level for the evaluation of relative energy and thermal correction that is undoubtedly theoretical sound, however, this is computationally prohibitive.

Aiming a better understanding of the deviation from a harmonic oscillator behavior we extended this investigation to larger cycloalkanes: cycloundecane, cyclododecane and cyclotridecane (unpublished results). According to the analysis of experimental low temperature NMR data obtained at 90.1 K (Brown, Pawar & Noe, 2003) cycloundecane exist as a mixture of two main conformers, named here 11a and 11b, being 59% of 11a and 41% of 11b. Cyclododecane has also been investigated by gas phase electron diffraction experiment at 120 ^{0}C (Atavin et al., 1989) and X-ray diffraction for a solid sample (Pickett & Strauss, 1971), both predicting the predominance of a single conformer, named 12a. The largest cycloalkane that we have been investigating is the cyclotridecane. A conformation study of a saturated 13-membered ring macrocycle, which lies on the borderline between medium and large ring systems and are generally considered very complex with a variety of conformational possibilities, has been reported by Rubin and collaborators (Rubin et al., 1984). Cyclotridecane that is placed in this borderline has defied ^{13}C NMR analysis (Dunitz & Shearer, 1960) because fast pseudorotation processes lead to a single peak, even at -135 ^{0}C, and so experimental conformational population data are not yet available. In Rubin at al. paper (Rubin et al., 1984) X-ray elucidation of the structure of a 13-atom heteromacrocycle combined with force field calculations carried out on cyclotridecane and 1,1-dimethylcyclotridecane pointed out to the existence of a main conformer denominated [33331] and a contribution of approx. 20% of minor conformers. We named this main conformer 13a. Following the structural data published by Rubin et al. (Rubin et al., 1984), just over two years ago, Valente et al. (Valente et al., 2008) reported the synthesis and X-ray structure of cyclotridecanone 2,4-dinitrophenylhydrazone, $C_{19}H_{28}N_4O_4$, a 13-membered carbocycle that was predicted to exists in the triangular [337] conformation (Valente et al., 2008). The reported molecular structure, in combination with additional evidence, indicates that [337] should be the preferred conformation of cyclotridecane and other simple 13-membered rings. We named this structure 13b. We have used the ring dihedral angles for structure 13b reported by Valente et al. (Valente et al., 2008) as an input for DFT full geometry optimization, without any geometrical constraint, and found that this is indeed a true minimum energy structure (having no imaginary frequencies) on the PES for cyclotridecane. We found that an agreement with conformational population data reported for cycloundecane and cyclododecane is obtained when all 3N-6 normal modes are used in the evaluation of the vibrational partition function (unpublished results), similar to the results reported in previous sections for cyclononane and cyclodecane. For cyclotridecane the analysis of the theoretical results are not yet conclusive, regarding the use of the HO approach. Therefore, in the light of these results it seems that for larger cycloalkanes the usual procedure of considering all 3N-6 normal modes in the calculation of relative Gibbs free energy values, implemented in most of the quantum chemical computer packages, would probably lead to satisfactory agreement with experimental population data. This is likely to hold for other macrocycles and supramolecular systems.

5. Concluding remarks

In this Chapter the theoretical formalism behind de calculation of temperature-dependent conformational population, an important subject in the area of physical organic chemistry, is

briefly reviewed, with the emphasis placed on the role played by vibrational partition function evaluated with the aid of standard statistical thermodynamics formulae. We identified which contributions to the Gibbs free energy differences (ΔG) between conformers of a given molecule are likely to be more sensitive to the level of *ab initio* theory employed for its evaluation and also the level of calculation required for an adequate description of the thermodynamic properties. The results reported here strength the validity of the procedure outlined previously to evaluate the distinct contributions to ΔG, $\Delta E_{ele-nuc}$ and ΔG_T, employing different computational procedures. The size of the molecules treated in this chapter enable the calculation of the first contribution at the MP4(SDTQ)//MP2 and CCSD(T)//MP2 single point levels and the thermal correction (ΔG_T) at the MP2 fully optimized geometry level of theory. For larger molecular systems we may use a more approximate procedure, as for exemple DFT or even DFT//PM3 level of calculation which was recently shown to produce very satisfactory results for the calculation of the Gibbs free energy of hydration of α-cyclodextrin (Nascimento et al., 2004). The less sensitivity of the thermal energy correction to the quantum chemical method employed, compared to the electronic plus nuclear-nuclear repulsion energy counterpart, is the basic reason for the suitability of this computational procedure which enables us to study large molecular systems of biological and technological interest.

Results for two classes of molecules, for which experimental conformational population data are available, were presented: substituted alkanes and cycloalkanes. In the case of substituted alkanes we found that a treatment of low frequency vibrational as hindered rotor and anharmonicity correction leads to a fine agreement between experimental gas phase population data for 1,2-dichloro ethane and theoretical predictions, as also found for the ethane molecule. However, for 1,2-difluor ethane such procedure did not work at all, and an alternative description of the vibrational partition function must be found. The main results for the substituted alkanes discussed in this Chapter are shown in Figure 17a. For cycloalkanes a similar decomposition of the vibrational partition function was made (see equation (8b)). The very simple procedure of considering the contribution due to the low frequency modes (Q_{vib}^{NHO}) set to unity, named HO approach, was used, which is equivalent to exclude these normal modes from the evaluation of the thermal energy (ΔG_T). Such procedure worked very well for cycloheptane and cyclooctane. However, for cyclononane and cyclodecane a good agreement with experimental conformational population data is achieved considering all 3N-6 normal modes, including the low frequency modes, as harmonic oscillators, a procedure commonly used in the computational chemistry community and readily implemented in any quantum chemical computer package. Very recently we have shown that this standard procedure also worked for larger cycloalkanes containing eleven and twelve carbon atoms (unpublished results). Figure 17b show a summary of theoretical and experimental conformational population results for the cycloalkanes addressed here.

Figure 17 gives a very clear account and a quite transparent view of the importance of a separate treatment of the low frequency modes for the evaluation of the vibrational partition function, within the statistical thermodynamics formalism, according to Eq. (8b) ($Q_{vib} = Q_{vib}^{NHO}.Q_{vib}^{HO}$) which leads to the calculation of the thermal correction following Eq. (15) ($\Delta G_{T,vib} = \Delta G_{T,vib}^{NHO} + \Delta G_{T,vib}^{HO}$).

When the low frequency modes are excluded from the calculation of thermal correction it means the $Q_{vib}^{NHO} = 1$, and so, $\Delta G_{T,vib}^{NHO} = 0$, otherwise the last term is evaluated using the

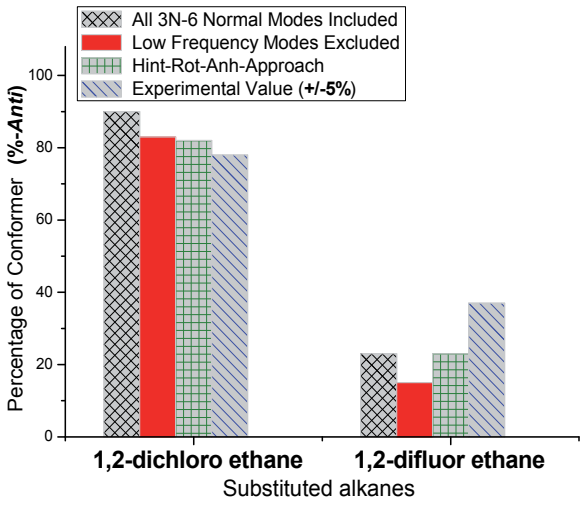

(a)

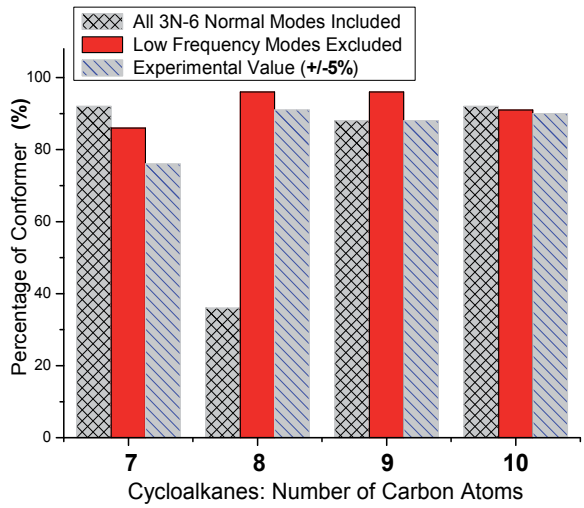

(b)

Fig. 17. A summary of conformational population values (percentage of the predominant conformer A for a generic interconversion process: A→B) obtained from Gibbs free energy results (ΔG) calculated at the MP4(SDTQ)//MP2 or CCSD(T)//MP2 level of theory. The 3N-6 superscript means that all normal modes were included in the calculations, and the HO label indicate that the low frequency modes were ignored for calculation of the thermal correction (HO Approach). The *Hint-Rot-Anh* superscript means that the internal rotation (a treatment of low frequency modes as hindered rotor) and anharmonicity correction was included. (a) Susbtituted alkanes, 1,2-dichloro ethane and 1,2-difluor ethane. (b) Cycloheptane (TC→C); Cyclooctane (BC→CROWN); Cyclononane (TBC→TCB); Cyclodecane (BCB→TBC).

harmonic approximation. It can be seen from Figure 17 that the behavior for small cycloalkanes, as also substituted alkanes, is distinct from cycloalkanes containing more than eight atoms of carbon. This shows that, in the series of cycloalkanes investigated, there is no

overall agreement with experiment when the low frequency modes are excluded or not from the evaluation of the vibrational partition function. It seems that each case must be considered individually, since it may really not be possible to find a "general" vibrational partition function that precisely mimic the behavior of all cycloalkanes represented in Figure 17b, and very likely many other macrocycles and supramolecular structures. The results reported by our group on the series of cycloalkanes provide an indication that the usual procedure of considering all 3N-6 normal modes in the vibrational partition function appears to work very satisfactorily for larger macrocycles and also supramolecular systems.

6. Acknowlegment

The authors would like to thank the Brazilian agencies CNPq (Conselho Nacional de Desenvolvimento Científico e Tecnológico) and FAPEMIG (Fundação de Amparo à Pesquisa do Estado de Minas Gerais) for financial support. This work is a collaboration research project of members of the Rede Mineira de Química (RQ-MG) supported by FAPEMIG. Many people have contributed to the work described in this Chapter. We particularly would like to thank Prof. Willian Rocha (UFMG), Prof. Cleber Anconi (UFLA), Prof. Mauro Franco (UFVJM) and Prof. Dalva Ferreira (UFVJM). We also thank Dr. Diego Paschoal (UFJF) for his helpful assistance on the reference checking. Finally, the authors are greatly indebted to their families for their constant support and understanding.

7. List of symbols and abbreviations

Anh	Anharmonicity correction
B3LYP	Becke three-parameter, Lee-Yang-Parr exchange-correlation functional
B3P86	Becke three-parameter, Perdew 86 exchange-correlation functional
BLYP	Becke, Lee-Yang-Parr exchange-correlation functional
BP86	Becke, Perdew 86 exchange-correlation functional
CC	Coulpled-Cluster method
CCSD(T)	Coulpled-Cluster method with single-double and perturbative triple excitation
DFT	Density Functional Theory
ED	Electron Diffraction
$E_{ele\text{-}nuc}$	Electronic plus nuclear-nuclear repulsion energy
E_{int}	Internal energy
G	Gibbs free energy
G_T	Thermal correction to the Gibbs free energy
H	Enthalpy
HF	Hartree-Fock method
Hind-Rot	Hindered-Rotor approach
HO	Harmonic Oscillator approximation
H_T	Thermal correction for enthalpy
IR	Infrared
MM	Molecular Mechanics
MP2	Mϕller-Plesset second-order perturbation theory

MP4(SDTQ)	Mϕller-Plesset forth-order perturbation theory with single, double, triple and quadruple excitation
ν	Vibrational frequency (or wavenumber in cm^{-1})
NHO	Non-Harmonic Oscillator approach
Nlow	Number of low frequency vibrational modes
NMR	Nuclear Magnetic Resonance
PBE1PBE	Hybrid Perdew, Burke and Ernzerhof exchange-correlation functional
PES	Potential Energy Surface
PW91	Perdew and Wang's 1991 gradient-corrected correlation functional
Q	Partition function
RR	Rigid-Rotor approach
S	Entropy
TMS	Tetramethylsylane
TS	Transition State
VCD	Vibrational Circular Dichroism
V_{NN}	Nuclear-Nuclear repulsion energy
ZPE	Zero-Point Energy

8. References

Ainsworth, J. & Karle, J. (1952). The Structure and Internal Motion of 1,2-Dichloroethane. *Journal of Chemical Physics*, vol. 20, No. 3, pp. 425-427, 0021-9606

Almenningen, A., Bastiansen, O. & Jensen, H. (1966). An Electron Diffraction Investigation of Cyclooctane and Cyclotetradeca-1,8-Diyne. *Acta Chemica Scandinavica*, vol. 20, No. 10, pp. 2689-&, 0904-213X

Anconi, C. P. A., Nascimento, C. S., Dos Santos, H. F. & De Almeida, W. B. (2006). A highly correlated ab initio investigation of the temperature-dependent conformational analysis of cycloheptane. Chemical Physics Letters, vol. 418, No. 4-6, pp. 459-466, 0009-2614

Anet, F. A. L. & Basus, V. J. (1973). Detection of a Crown Family Conformation in Cyclooctane by Proton and C-13 Nuclear Magnetic-Resonance. *Journal of the American Chemical Society*, vol. 95, No. 13, pp. 4424-4426, 0002-7863

Anet, F. A. L. (1974) Dynamics of eight-membered rings in the cylooctane class, In: *Topics in Current Chemistry : Dynamic Chemistry*, (Ed.) vol. 45, 169-220, Berlim, German.

Anet, F. A. L. & Rawdah, T. N. (1978). Cyclododecane - Force-Field Calculations and H-1 NMR-Spectra of Deuterated Isotopomers. *Journal of the American Chemical Society*, vol. 100, No. 23, pp. 7166-7171, 0002-7863

Anet, F. A. L. & Krane, J. (1980). The Conformations of Cyclononane Dynamic Nuclear Magnetic-Resonance and Force-Field Calculations. *Israel Journal of Chemistry*, vol. 20, No. 1-2, pp. 72-83, 0021-2148

Atavin, E. G., Mastryukov, V. S., Allinger, N. L., Almenningen, A. & Seip, R. (1989). Molecular-Structure of Cyclododecane, C12h24, as Determined by Electron-Diffraction and Molecular Mechanics. *Journal of Molecular Structure*, vol. 212, No. pp. 87-95, 0022-2860

Ayala, P. Y. & Schlegel, H. B. (1998). Identification and treatment of internal rotation in normal mode vibrational analysis. *Journal of Chemical Physics*, vol. 108, No. 6, pp. 2314-2325, 0021-9606

Bernstein, H. J. (1949). Internal Rotation .2. the Energy Difference between the Rotational Isomers of 1,2-Dichloroethane. *Journal of Chemical Physics*, vol. 17, No. 3, pp. 258-261, 0021-9606

Bickelhaupt, F. M. & Baerends, E. J. (2003). The case for steric repulsion causing the staggered conformation of ethane. *Angewandte Chemie-International Edition*, vol. 42, No. 35, pp. 4183-4188, 1433-7851

Bocian, D. F., Pickett, H. M., Rounds, T. C. & Strauss, H. L. (1975). Conformations of Cycloheptane. *Journal of the American Chemical Society*, vol. 97, No. 4, pp. 687-695, 0002-7863

Bocian, D. F. & Strauss, H. L. (1977a). Conformational Structure and Energy of Cycloheptane and Some Related Oxepanes. *Journal of the American Chemical Society*, vol. 99, No. 9, pp. 2876-2882, 0002-7863

Bocian, D. F. & Strauss, H. L. (1977b). Vibrational-Spectra, Conformations, and Potential Functions of Cycloheptane and Related Oxepanes. *Journal of the American Chemical Society*, vol. 99, No. 9, pp. 2866-2876, 0002-7863

Brecknell, D. J., Raber, D. J. & Ferguson, D. M. (1985). Structures of Lanthanide Shift-Reagent Complexes by Molecular Mechanics Computations. *Journal of Molecular Structure,* vol. 25, No. 3-4, pp. 343-351, 0166-1280

Brookeman, J. R. & Rushworth, F. A. (1976). Nuclear Magnetic-Resonance in Solid Cycloheptane. *Journal of Physics C-Solid State Physics*, vol. 9, No. 6, pp. 1043-1054, 0022-3719

Brown, J., Pawar, D. M. & Noe, E. A. (2003). Conformational study of 1,2-cycloundecadiene by dynamic NMR spectroscopy and computational methods. *Journal of Organic Chemistry*, vol. 68, No. 9, pp. 3420-3424, 0022-3263

Burgi, H. B. & Dunitz, J. D. (1968). Sturctures of Medium-Sized Ring Compounds .16. Cyclooctane-Cis-1,2-Dicarboxylic Acid. *Helvetica Chimica Acta*, vol. 51, No. 7, pp. 1514-&, 0018-019X

Burkert, U., Allinger, N. L. (1982) Molecular Mechanics, *American Chemical Society*, Washington, DC.

Chang, G., Guida, W. C. & Still, W. C. (1989). An Internal Coordinate Monte-Carlo Method for Searching Conformational Space. *Journal of the American Chemical Society*, vol. 111, No. 12, pp. 4379-4386, 0002-7863

Cremer, D. & Pople, J. A. (1975). General Definition of Ring Puckering Coordinates. *Journal of the American Chemical Society*, vol. 97, No. 6, pp. 1354-1358, 0002-7863

De Almeida, W. B. (2000). Molecular structure determination of cyclootane by ab initio and electron diffraction methods in the gas phase. *Quimica Nova*, vol. 23, No. 5, pp. 600-607, 0100-4042

Dillen, J. & Geise, H. J. (1979). Molecular-Structure of Cycloheptane - Electron-Diffraction Study. *Journal of Chemical Physics*, vol. 70, No. 1, pp. 425-428, 0021-9606

Dobler, M., Dunitz, J. D. & Mugnoli, A. (1966). Die Strukturen Der Mittleren Ringverbindungen .11. Cyclooctan-1,2-Trans-Dicarbonsaure. *Helvetica Chimica Acta*, vol. 49, No. 8, pp. 2492-&, 0018-019X

Dorofeeva, O. V., Mastryukov, V. S., Allinger, N. L. & Almenningen, A. (1985). The Molecular-Structure and Conformation of Cyclooctane as Determined by Electron-

Diffraction and Molecular Mechanics Calculations. *Journal of Physical Chemistry*, vol. 89, No. 2, pp. 252-257, 0022-3654

Dorofeeva, O. V., Mastryukov, V. S., Siam, K., Ewbank, J. D., Allinger, N. L. & Schafer, L. (1990). Conformational State of Cyclooctane, C8h14, in the Gas-Phase. *Journal of Structural Chemistry*, vol. 31, No. 1, pp. 153-154, 0022-4766

Dos Santos, H. F. & De Almeida, W. B. (1995). MNDO/AM1/PM3 quantum mechanical semiempirical and molecular mechanics barriers to internal rotation: a comparative study. *Journal of Molecular Structure*, vol. 335, No. 1-3, pp. 129-139,

Dos Santos, H. F., De Almeida, W. B., Taylor-Gomes, J. & Booth, B. L. (1995). AM1 study of the conformational equilibrium and infrared spectrum for 1,2,4- and 1,3,5-substituted benzenes. *Vibrational Spectroscopy*, vol. 10, No. 1, pp. 13-28,

Dos Santos, H. F., O´Malley, P. J. & De Almeida, W. B. (1995). A molecular mechanics and semiempirical conformational analysis of the herbicide diuron inhibitor of photosystem II. *Structural Chemistry*, vol. 6, No. 6, pp. 383-389, 1040-0400

Dos Santos, H. F., De Almeida, W. B. & Zerner, M. C. (1998). Conformational analysis of the anhydrotetracycline molecule: A toxic decomposition product of tetracycline. *Journal of Pharmaceutical Sciences*, vol. 87, No. 2, pp. 190-195, 0022-3549

Dos Santos, H. F., O'Malley, P. J. & De Almeida, W. B. (1998). Gas phase and water solution conformational analysis of the herbicide diuron (DCMU): an ab initio study. *Theoretical Chemistry Accounts*, vol. 99, No. 5, pp. 301-311, 1432-881X

Dos Santos, H. F., Rocha, W. R. & De Almeida, W. B. (2002). On the evaluation of thermal corrections to gas phase ab initio relative energies: implications to the conformational analysis study of cyclooctane. *Chemical Physics*, vol. 280, No. 1-2, pp. 31-42, 0301-0104

Dowd, P., Dyke, T., Neumann, R. M. & Klempere.W. (1970). On Existence of Polar Conformations of Cycloheptane, Cyclooctane, and Cyclodecane. *Journal of the American Chemical Society*, vol. 92, No. 21, pp. 6325-&, 0002-7863

Dunitz, J. D. & Shearer, H. M. M. (1960). Die Strukturen der mittleren Ringverbindungen III. Die Struktur des Cyclododecans. *Helvetica Chimica Acta*, vol. 43, No. 1, pp. 18-35,

Durig, J. R., Liu, J., Little, T. S. & Kalasinsky, V. F. (1992). Conformational-Analysis, Barriers to Internal-Rotation, Vibrational Assignment, and Abinitio Calculations of 1,2-Difluoroethane. *Journal of Physical Chemistry*, vol. 96, No. 21, pp. 8224-8233, 0022-3654

Egmond, J. V. & Romers, C. (1969). Conformation of non-aromatic ring compounds--LI : The crystal structure of trans-1,4-dichlorocyclooctane at -180°. *Tetrahedron*, vol. 25, No. 13, pp. 2693-2699,

Eliel, E. L. (1965). Conformational Analysis in Mobile Cyclohexane Systems. *Angewandte Chemie-International Edition*, vol. 4, No. 9, pp. 761-&, 1433-7851

Eliel, E. L., Allinger, N. L., Angyal, S. J., Morrison, G. A. (1965) Conformational Analysis, Wiley-Interscience, New York.

Ellingson, B. A., Lynch, V. A., Mielke, S. L. & Truhlar, D. G. (2006). Statistical thermodynamics of bond torsional modes: Tests of separable, almost-separable, and improved Pitzer-Gwinn approximations. *Journal of Chemical Physics*, vol. 125, No. 8, pp. 0021-9606

Ferguson, D. M., Gould, I. R., Glauser, W. A., Schroeder, S. & Kollman, P. A. (1992). Comparison of Abinitio, Semiempirical, and Molecular Mechanics Calculations for the Conformational-Analysis of Ring-Systems. *Journal of Computational Chemistry*, vol. 13, No. 4, pp. 525-532, 0192-8651

Fernholt, L. & Kveseth, K. (1980). Conformational-Analysis - the Temperature Effect on the Structure and Composition of the Rotational Conformers of 1,2-Difluoroethane as

Studied by Gas Electron-Diffraction. *Acta Chemica Scandinavica Series a-Physical and Inorganic Chemistry*, vol. 34, No. 3, pp. 163-170, 0302-4377

Ferreira, D. E. C., De Almeida, W. B. & Dos Santos, H. F. (2007). A theoretical investigation of structural, spectroscopic and thermodynamic properties of cyclodecane. *Journal of Theoretical & Computational Chemistry*, vol. 6, No. 2, pp. 281-299, 0219-6336

Flapper, W. M. J. & Romers, C. (1975). Pseudorotation of Cycloheptane .1. *Tetrahedron*, vol. 31, No. 15, pp. 1705-1713, 0040-4020

Flapper, W. M. J., Verschoor, G. C., Rutten, E. W. M. & Romers, C. (1977). Pseudorotation of Cycloheptane .2. Crystal-Structure of Calcium Cycloheptanecarboxylate Pentahydrate. *Acta Crystallographica Section B-Structural Science*, vol. 33, No. JAN15, pp. 5-10, 0108-7681

Franco, M. L., Ferreira, D. E. C., Dos Santos, H. F. & De Almeida, W. B. (2007). Temperature-dependent conformational analysis of cyclononane: An ab initio study. *International Journal of Quantum Chemistry*, vol. 107, No. 3, pp. 545-555, 0020-7608

Franco, M. L., Ferreira, D. E. C., Dos Santos, H. F. & De Almeida, W. B. (2008). Ab initio highly correlated conformational analysis of 1,2-difluorethane and 1,2-dichloroethane. *Journal of Chemical Theory and Computation*, vol. 4, No. 5, pp. 728-739, 1549-9618

Franklin, N. C. & Feltkamp, H. (1965). Conformational Analysis of Cyclohexane Derivatives by Nuclear Magnetic Resonance Spectroscopy. *Angewandte Chemie-International Edition*, vol. 4, No. 9, pp. 774-&, 1433-7851

Freitas, M. P. & Rittner, R. (2007). Is there a general rule for the gauche effect in the conformational isomerism of 1,2-disubstituted ethanes? J*ournal of Physical Chemistry A*, vol. 111, No. 30, pp. 7233-7236, 1089-5639

Friesen, D. & Hedberg, K. (1980). Conformational-Analysis .7. 1,2-Difluoroethane - an Electron-Diffraction Investigation of the Molecular-Structure, Composition, Trans-Gauche Energy and Entropy Differences, and Potential Hindering Internal-Rotation. *Journal of the American Chemical Society*, vol. 102, No. 12, pp. 3987-3994, 0002-7863

Goodman, L., Gu, H. B. & Pophristic, V. (2005). Gauche effect in 1,2-difluoroethane. Hyperconjugation, bent bonds, steric repulsion. *Journal of Physical Chemistry A*, vol. 109, No. 6, pp. 1223-1229, 1089-5639

Goodman, L. & Sauers, R. R. (2005). 1-fluoropropane. Torsional potential surface. *Journal of Chemical Theory and Computation*, vol. 1, No. 6, pp. 1185-1192, 1549-9618

Hendrickson, J. B. (1961). Molecular Geometry. I. Machine Computation of the Common Rings. *Journal of the American Chemical Society*, vol. 83, No. 22, pp. 4537-4547,

Hendrickson, J. B. (1964). Molecular Geometry .4. Medium Rings. *Journal of the American Chemical Society*, vol. 86, No. 22, pp. 4854-&, 0002-7863

Hendrickson, J. B. (1967a). Molecular Geometry .7. Modes of Interconversion in Medium Rings. *Journal of the American Chemical Society*, vol. 89, No. 26, pp. 7047-&, 0002-7863

Hendrickson, J. B. (1967b). Molecular Geometry .V. Evaluation of Functions and Conformations of Medium Rings. *Journal of the American Chemical Society*, vol. 89, No. 26, pp. 7036-&, 0002-7863

Hendrickson, J. B., Boeckman, R. K., Glickson, J. D. & Grunwald, E. (1973). Molecular Geometry .8. Proton Magnetic-Resonance Studies of Cycloheptane Conformations. *Journal of the American Chemical Society*, vol. 95, No. 2, pp. 494-505, 0002-7863

Hilderbrandt, R. L., Wieser, J. D. & Montgomery, L. K. (1973). Conformations and Structures of Cyclodecane as Determined by Electron-Diffraction and Molecular Mechanics Calculations. *Journal of the American Chemical Society*, vol. 95, No. 26, pp. 8598-8605, 0002-7863

Hirano, T., Nonoyama, S., Miyajima, T., Kurita, Y., Kawamura, T. & Sato, H. (1986). Gas-Phase F-19 and H-1 High-Resolution Nmr-Spectroscopy - Application to the Study of Unperturbed Conformational Energies of 1,2-Difluorethane. *Journal of the Chemical Society-Chemical Communications*, vol. No. 8, pp. 606-607, 0022-4936

Kemp, J. D. & Pitzer, K. S. (1936). Hindered Rotation of the Methyl Groups in Ethane. *The Journal of Chemical Physics*, vol. 4, No. 11, pp. 749-749,

Kemp, J. D. & Pitzer, K. S. (1937). The Entropy of Ethane and the Third Law of Thermodynamics. Hindered Rotation of Methyl Groups. *Journal of the American Chemical Society*, vol. 59, No. 2, pp. 276-279,

Klaeboe, P. (1995). Conformational Studies by Vibrational Spectroscopy - a Review of Various Methods. Vibrational Spectroscopy, vol. 9, No. 1, pp. 3-17, 0924-2031

Kolossvary, I. & Guida, W. C. (1993). Comprehensive conformational analysis of the four- to twelve-membered ring cycloalkanes: identification of the complete set of interconversion pathways on the MM2 potential energy hypersurface. *Journal of the American Chemical Society*, vol. 115, No. 6, pp. 2107-2119,

Li, J. C. M. & Pitzer, K. S. (1956). Energy Levels and Thermodynamic Functions for Molecules with Internal Rotation .4. Extended Tables for Molecules with Small Moments of Inertia. *Journal of Physical Chemistry*, vol. 60, No. 4, pp. 466-474, 0022-3654

Lipton, M. & Still, W. C. (1988). The Multiple Minimum Problem in Molecular Modeling - Tree Searching Internal Coordinate Conformational Space. *Journal of Computational Chemistry*, vol. 9, No. 4, pp. 343-355, 0192-8651

Mcclurg, R. B., Flagan, R. C. & Goddard, W. A. (1997). The hindered rotor density-of-states interpolation function. *Journal of Chemical Physics*, vol. 106, No. 16, pp. 6675-6680, 0021-9606

Mcquarrie, D. A. (1973) Statistical Thermodynamics, University Science Books, 129-143, Mill Valley, CA

Meiboom, S., Hewitt, R. C. & Luz, Z. (1977). Conformation of Cyclooctane - Experimental-Determination by Nmr in an Oriented Solvent. *Journal of Chemical Physics*, vol. 66, No. 9, pp. 4041-4051, 0021-9606

Nascimento, C. S., Dos Santos, H. F. & De Almeida, W. B. (2004). Theoretical study of the formation of the alpha-cyclodextrin hexahydrate. *Chemical Physics Letters*, vol. 397, No. 4-6, pp. 422-428, 0009-2614

Orville-Thomas, W. J. (1974) Internal Rotation in Molecules, John Wiley & Sons, 101, London, England.

Pakes, P. W., Rounds, T. C. & Strauss, H. L. (1981). Vibrational-Spectra and Potential Functions of Cyclooctane and Some Related Oxocanes. *Journal of Physical Chemistry*, vol. 85, No. 17, pp. 2476-2483, 0022-3654

Pawar, D. M., Smith, S. V., Mark, H. L., Odom, R. M. & Noe, E. A. (1998). Conformational study of cyclodecane and substituted cyclodecanes by dynamic NMR spectroscopy and computational methods. *Journal of the American Chemical Society*, vol. 120, No. 41, pp. 10715-10720, 0002-7863

Pickett, H. M. & Strauss, H. L. (1971). Symmetry and Conformation of Cycloalkanes. *Journal of Chemical Physics*, vol. 55, No. 1, pp. 324-&, 0021-9606

Pitzer, K. S. & Gwinn, W. D. (1942). Energy Levels and Thermodynamic Functions for Molecules with Internal Rotation I. Rigid Frame with Attached Tops. *Journal of Chemical Physics*, vol. 10, No. 7, pp. 428-440,

Pitzer, R. M. (1983). The Barrier to Internal-Rotation in Ethane. *Accounts of Chemical Research*, vol. 16, No. 6, pp. 207-210, 0001-4842

Pophristic, V. & Goodman, L. (2001). Hyperconjugation not steric repulsion leads to the staggered structure of ethane. *Nature*, vol. 411, No. 6837, pp. 565-568, 0028-0836

Roberts, J. D. (2006). Fascination with the conformational analysis of succinic acid, as evaluated by NMR spectroscopy, and why. *Accounts of Chemical Research*, vol. 39, No. 12, pp. 889-896, 0001-4842

Rocha, W. R., Pliego, J. R., Resende, S. M., Dos Santos, H. F., De Oliveira, M. A. & De Almeida, W. B. (1998). Ab initio conformational analysis of cyclooctane molecule. *Journal of Computational Chemistry*, vol. 19, No. 5, pp. 524-534, 0192-8651

Rounds, T. C., Strauss, H. L. (1978). Vibrational Spectroscopy of the medium rings. In *Vibrational Spectra and Structure*, Elsevier, vol. 7, 237-268, Amsterdam, Netherlands

Rubin, B. H., Williamson, M., Takeshita, M., Menger, F. M., Anet, F. A. L., Bacon, B. & Allinger, N. L. (1984). Conformation of a Saturated 13-Membered Ring. *Journal of the American Chemical Society*, vol. 106, No. 7, pp. 2088-2092, 0002-7863

Saunders, M. (1987). Stochastic Exploration of Molecular Mechanics Energy Surfaces - Hunting for the Global Minimum. *Journal of the American Chemical Society*, vol. 109, No. 10, pp. 3150-3152, 0002-7863

Senderowitz, H., Guarnieri, F. & Still, W. C. (1995). A Smart Monte-Carlo Technique for Free-Energy Simulations of Multiconformational Molecules, Direct Calculations of the Conformational Populations of Organic-Molecules. *Journal of the American Chemical Society*, vol. 117, No. 31, pp. 8211-8219, 0002-7863

Shenhav, H. & Schaeffer, R. (1981). Cyclodecane - C10h20. *Crystal Structure Communications*, vol. 10, No. 4, pp. 1181-1182, 0302-1742

Snyderman, D. M., Adams, J. M., Mcdowell, A. F., Conradi, M. S. & Bunnelle, W. H. (1994). Solid-Phases and Phase-Transitions of Cycloheptane. *Journal of Physical Chemistry*, vol. 98, No. 24, pp. 6234-6236, 0022-3654

Srinivasan, R. & Srikrishnan, T. (1971). Studies in Molecular Structure, Symmetry and Conformation .4. Conformation of Cyclooctane Ring System from X-Ray Studies. *Tetrahedron*, vol. 27, No. 5, pp. 1009-&, 0040-4020

Truhlar, D. G. (1991). A Simple Approximation for the Vibrational Partition-Function of a Hindered Internal-Rotation. *Journal of Computational Chemistry*, vol. 12, No. 2, pp. 266-270, 0192-8651

Valente, E. J., Pawar, D. M., Fronczek, F. R. & Noe, E. A. (2008). Cyclotridecanone 2,4-dinitrophenylhydrazone. *Acta Crystallographica Section C-Crystal Structure Communications*, vol. 64, No. pp. O447-O449, 0108-2701

Weinberg, N. & Wolfe, S. (1994). A Comprehensive Approach to the Conformational-Analysis of Cyclic-Compounds. *Journal of the American Chemical Society*, vol. 116, No. 22, pp. 9860-9868, 0002-7863

Wiberg, K. B. & Murcko, M. A. (1987). Rotational Barriers .1. 1,2-Dihaloethanes. *Journal of Physical Chemistry*, vol. 91, No. 13, pp. 3616-3620, 0022-3654

Wiberg, K. B. (2003). The C7-C10 cycloalkanes revisited. *Journal of Organic Chemistry*, vol. 68, No. 24, pp. 9322-9329, 0022-3263

Youssoufi, Y. E., Herman, M. & Lievin, J. (1998). The ground electronic state of 1,2-dichloroethane - I. Ab initio investigation of the geometrical, vibrational and torsional structure. *Molecular Physics*, vol. 94, No. 3, pp. 461-472, 0026-8976

3

Modeling and Simulation for Steady State and Transient Pipe Flow of Condensate Gas

Li Changjun, Jia Wenlong and Wu Xia
School of Petroleum Engineering, Southwest Petroleum University
China

1. Introduction

Condensate gas is mainly demonstrated by methane. However, it also contains a lot of heavier contents like C_5 or C_5+ and some non-hydrocarbon mixture as well (Mokhatab *et al*, 2006). After recovering from gas wells, condensate gas needs liquid separation, gas purification and condensate stabilization treatment in the processing plant to meet the quality requirements. Processing plants far away from the gas well with long distances of two-phase flow in one condensate gas pipeline will take less investment than adjacent process plant with two single phase pipelines which are dry gas pipeline and liquid phase pipeline (Li, 2008).

If the operation temperature somewhere in the condensate gas pipeline is lower than the gas dew point, liquid condensation would occur, subjecting the pipeline to two phase flow (Potocnik, 2010). While gas and its condensate flow simultaneously, mass transfer takes place continuously due to the change in pressure and temperature conditions. This leads to compositional changes and associated fluid property changes and also makes the hydraulic and thermal calculations of condensate gas more complex than normal gas. The condensate gas pipeline model which is established and solved based on the principle of fluid mechanics can simulate hydraulic and thermal parameters under various operation conditions. By means of technical support, this model is of great importance in the pipeline design and safety operation aspects (Mokhatab, 2009).

2. Thermodynamic model

The purpose of the thermodynamic model is three-fold. First, it defines the transition between single phase/two phase conditions (point of condensate inception in the pipeline or gas dew point). Second, it is used for the prediction of properties for the flowing fluids (gas and its condensate). And lastly, it derives the mass exchange between the flowing phases (Adewumi *et al*, 1990 ; Estela-Uribe *et al*, 2003). This work uses the BWRS equation of state (EOS) to implement the thermodynamic model as it has proven reliable for gas condensate system (McCain *et al*, 1990). Most property predictions are derived from the equation of state (i.e., densities values, densities values and their derivatives with respect to pressure and temperature, departure enthalpies, heat capacities, and Joule-Thompson coefficients). Additionally, phase equalibria are calculated on the basis of flash calculation method. Expressions for such parameters as fugacity are elaborated in

standard textbooks, where the theory and relevant procedures for flash calculation are well documented (API, 2005).

3. General model of condensate gas pipeline

3.1 Basic assumptions

One of the most fundamental approaches used to model two phase flow is the two-fluid model (Ayala *et al*, 2003). It consists of separate mass, momentum and energy conservation equations written for each of the phases. This results in up to six differential equations. Furthermore, the model is more complicate as relating parameters in the equations vary with the fluid flowing. Thus, simple and reasonable assumptions could help to reduce the unknowns in the model (Hasan *et al*, 1992). The hydrodynamic model has three major inherent assumptions:

1. Gas and liquid average flow velocities are calculated according to the section area occupied by each phase respectively.
2. Mass transfer takes place between gas and liquid phase. However, two phases are assumed to be at thermodynamic equilibrium at every point within the pipe.
3. In the transient process, the pipeline assumed to be isothermal. The liquid hold up within pipeline, the wall friction force of each phase, the drag force between two phases are assumed to be the same as steady state.

3.2 Description of general model

The general model for two phase flow is built on the basis of mass, momentum and energy conservation equations of each phase (Li *et al*, 2009; Ayala *et al*, 2003).
Gas phase continuity equation:

$$\frac{\partial}{\partial t}\left(\rho_g \varphi A\right)+\frac{\partial}{\partial x}\left(\rho_g \varphi A w_g\right)=\Delta \dot{m}_{gl} \tag{1}$$

Liquid phase continuity equation:

$$\frac{\partial}{\partial t}\left(\rho_l H_L A\right)+\frac{\partial}{\partial x}\left(\rho_l H_L A w_l\right)=\Delta \dot{m}_{lg} \tag{2}$$

Where, $\Delta \dot{m}_{gl}$ is mass rate of phase change from gas to liquid, (kg/s.m); $\Delta \dot{m}_{lg}$ is mass rate of phase change from liquid to gas, (kg/s.m). H_L is liquid hold up; φ is gas hold up; .. ρ_g ..is density of the gas phase, kg/m^3; ρ_l is density of the liquid phase, kg/m^3; A is pipe cross sectional area, m^2; t is time, s; x is length along the pipe length, m; w_g is velocity of the gas phase, m/s; w_l is velocity of the liquid phase, m/s.
$\Delta \dot{m}_{gl}$ is defined as (3).

$$\Delta \dot{m}_{gl}=\left[\left(\frac{\partial Y_s}{\partial P}\right)_T \frac{\partial P}{\partial x}+\left(\frac{\partial Y_s}{\partial P}\right)_T \frac{\partial P}{\partial t}\frac{\partial t}{\partial x}\right]\cdot\left(m_g+m_l\right)+\left[\left(\frac{\partial Y_s}{\partial T}\right)_P \frac{\partial T}{\partial x}+\left(\frac{\partial Y_s}{\partial T}\right)_P \frac{\partial T}{\partial t}\frac{\partial t}{\partial x}\right]\cdot\left(m_g+m_l\right) \tag{3}$$

$$Y_s=\frac{m_g}{m_g+m_l}\,. \tag{4}$$

$$m_g = \rho_g w_g \varphi A \tag{5}$$

$$m_l = \rho_l w_g H_L A \tag{6}$$

Where, P is pressure, Pa; T is temperature, K; m_g is gas mass fraction in two-phase fluid system; m_l is liquid mass fraction in two-phase fluid system; Y_s is mass fraction of gas.
Gas phase momentum equation.

$$\frac{\partial}{\partial t}\left(\rho_g \varphi w_g A\right) + \frac{\partial}{\partial x}\left(\rho_g \varphi w_g^2 A\right) + A_g \frac{\partial P}{\partial x} = \Delta \dot{m}_{gl} w_a - F_{gw} - F_{gi} - \rho_g g \varphi A \sin\theta \tag{7}$$

Where, A_g is pipe cross sectional area occupied by gas phase, m^2;F_{gw} is wall shear force of gas phase, N/m^3; F_{gi} is interfacial drag force on gas phase, N/m^3; g is acceleration of gravity, m/s^2; θ is pipeline slope, rad.
Liquid phase momentum equation.

$$\frac{\partial}{\partial t}\left(\rho_l H_L w_l A\right) + \frac{\partial}{\partial x}\left(\rho_l H_L w_l^2 A\right) + A_l \frac{\partial P}{\partial x} = \Delta \dot{m}_{lg} w_a - F_{lw} - F_{li} - \rho_l g H_L A \sin\theta \tag{8}$$

Where, A_l is pipe cross sectional area occupied by liquid phase, m^2; F_{lw} is wall shear force of liquid phase, N/m^3; F_{li} is interfacial drag force on liquid phase, N/m^3; w_a is transition velocity between the gas phase and liquid phase, m/s.
Gas-liquid phase mixture energy equation

$$\begin{aligned}&\frac{\partial}{\partial t}\left[A\rho_g\varphi\left(h_g + \frac{w_g^2}{2} + gz\right) + A\rho_l H_L\left(h_l + \frac{w_l^2}{2} + gz\right)\right] \\ &+\frac{\partial}{\partial x}\left[A\rho_g\varphi w_g\left(h_g + \frac{w_g^2}{2} + gz\right) + A\rho_l H_L w_l\left(h_l + \frac{w_l^2}{2} + gz\right)\right] + K\pi D\left(T - T_0\right) = 0\end{aligned} \tag{9}$$

Where, K is overall heat transfer co-efficiency, W/(m^2· K); D is external diameter, m; T_0 is environmental temperature, K; h_l is enthalpy of liquid phase in pipeline, kJ/kg; h_g is enthalpy of the gas phase in pipeline, kJ/kg; z is pipeline elevation, m.
Add (7) and (8), obtain:

$$\begin{aligned}&\frac{\partial}{\partial t}\left(\rho_g \varphi w_g A\right) + \frac{\partial}{\partial t}\left(\rho_l H_L w_l A\right) + \frac{\partial}{\partial x}\left(\rho_g \varphi w_g^2 A\right) + \frac{\partial}{\partial x}\left(\rho_l H_L w_l^2 A\right) + A\frac{\partial P}{\partial x} \\ &= -F_{gw} - F_{lw} - \left(\rho_g \varphi + \rho_l H_L\right) g A \sin\theta\end{aligned} \tag{10}$$

Equation (10) is transformed into (11) through eliminating the pressure terms.

$$\begin{aligned}&\frac{\partial}{\partial t}\left(\rho_g w_g\right) - \frac{\partial}{\partial t}\left(\rho_l w_l\right) + \frac{\partial}{\partial x}\left(\rho_g w_g^2\right) - \frac{\partial}{\partial x}\left(\rho_l w_l^2\right) = \\ &\Delta \dot{m}_{gl} w_a\left(\frac{1}{A_g} + \frac{1}{A_l}\right) - \frac{F_{gw}}{A_g} - \frac{F_{gi}}{A_g} + \frac{F_{lw}}{A_l} + \frac{F_{li}}{A_l} - \left(\rho_l H_L - \rho_g \varphi\right) g \sin\theta\end{aligned} \tag{11}$$

In view of the slow transient behaviour in condensate gas pipeline, we can obtain equation (12) by ignoring velocity variation terms in equation (11)(Li *et al*, 1998):

$$-\frac{F_{gw}}{A_g}-F_{gi}\left(\frac{1}{A_g}+\frac{1}{A_l}\right)+\frac{F_{lw}}{A_l}-\left(\rho_l H_L-\rho_g\varphi\right)g\sin\theta=0 \tag{12}$$

Equations (1), (2), (9), (10), (12) construct the basic model for condensate gas pipe flow simulation.

4. Constitutive equations

The condensate gas flow model is one dimensional two-fluid multiphase hydrodynamic model which adapts to different flow patterns in pipeline. According to Cindric and Shoham, the flow patterns in horizontal pipeline are stratified flow, intermittent flow, annular flow, dispersed flow and these in vertical pipeline are bubble flow, slug flow, churn flow, annular flow (Mokhatab *et al*, 2006). Because of the constitutive equations is dependent on the flow pattern, one of the greatest difficulties in the analysis of two-phase flow in pipeline is defining appropriate constitutive equations for relating relevant forces-such as the steady drag force and interfacial force.

Considering low liquid hold up, the flow pattern in the condensate gas pipeline is stratified flow which has explicit interface between the liquid and gas phase, as depicted in Fig.1. Then, we can obtain the calculation methods of unknowns which dependent on the constitutive equations (Taitel *et al*, 1995 ; Chen *et al*, 1997).

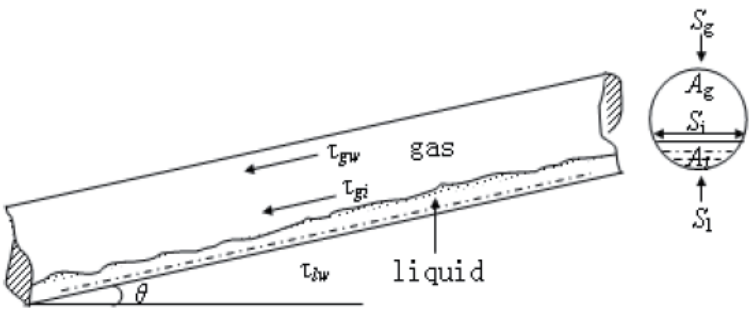

Fig. 1. Stratified flow in condensate gas pipeline

Wall shear force of each phase is expressed as follow.

$$F_{kw}=-\tau_{kw}S_k \tag{13}$$

Where, k=g when the equation is applied for the gas phase; k=l when the equation is applied for the liquid phase; S_k is defined as follow:

$$S_k=\frac{\text{total wall area wetted by phase } k}{\text{Totoal volume}} \tag{14}$$

τ_{kw} is defined as:

$$\tau_{kw} = \frac{1}{2}\lambda_k \rho_k |w_k| w_k \tag{15}$$

In which, λ is Fanning factor which is calculated by Colebrook & White empirical correlation.
If Reynolds Number $Re \leq 2000$

$$\lambda = \frac{16}{Re} \tag{16}$$

If $Re \geq 2000$

$$\frac{1}{\sqrt{\lambda}} = 3.48 - 4\lg\left(\frac{2\varepsilon}{D} + \frac{9.35}{Re\sqrt{\lambda}}\right) \tag{17}$$

Where, ε is absolute roughness of pipeline wall, m.
Interfacial force between phases is defined as follow:

$$F_{gi} = -F_{li} = -\tau_i S_i \tag{18}$$

Where

$$S_i = \frac{\text{Total surface area of contact between phases}}{\text{Totoal volume}} \tag{19}$$

$$\tau_i = \frac{1}{2}\lambda_i \rho_g |w_g - w_l|(w_g - w_l) \tag{20}$$

The interfacial friction factor λ_i is calculated with Hanrrity correlation.
If $w_{sg} \leq w_{sg \cdot t}$

$$\lambda_i = \lambda_g \tag{21}$$

If $w_{sg} \geq w_{sg \cdot t}$

$$\lambda_i = \lambda_g \left[1 + 15\sqrt{\frac{h_l}{D}}\left(\frac{w_{sg}}{w_{sg \cdot t}} - 1\right)\right] \tag{22}$$

Where,

$$w_{sg} = \frac{Q_G}{A} \tag{23}$$

$$w_{sg \cdot t} = 5\sqrt{\frac{101325}{P}} \tag{24}$$

Where, w_{sg} is reduced velocity of the gas phase, m/s; $w_{sg \cdot t}$ is reduced velocity for indentifying the transition from stratified flow pattern to smooth stratified flow pattern, m/s; Q_G is flow rate of the gas phase, m^3/s.

5. Steady state analysis of condensate gas pipeline

5.1 Basic equations

While steady operation, the variation of each parameter in equations (1), (2), (9), (10) with time can be ignored. Expand the equations above and the following equations used for steady state simulation can be obtained (Li *et al*, 2009):

Gas phase continuity equation:

$$Aw_g\varphi(\frac{\partial\rho_g}{\partial P})_T\frac{dP}{dx}+Aw_g\varphi(\frac{\partial\rho_g}{\partial T})_P\frac{dT}{dx}+A\rho_g\varphi\frac{dw_g}{dx}+A\rho_g w_g\frac{d\varphi}{dx}=\Delta\dot{m}_{gl} \tag{25}$$

Liquid phase continuity equation:

$$Aw_lH_L(\frac{\partial\rho_l}{\partial P})_T\frac{dP}{dx}+Aw_lH_L(\frac{\partial\rho_l}{\partial T})_P\frac{dT}{dx}+A\rho_lH_L\frac{dw_l}{dx}+A\rho_lw_l\frac{dH_L}{dx}=\Delta\dot{m}_{lg} \tag{26}$$

Gas-liquid phase mixture momentum equation:

$$A\frac{dP}{dx}+\rho_gw_g\varphi A\frac{dw_g}{dx}+\rho_lw_lH_LA\frac{dw_l}{dx}=-F_{gw}-F_{lw}-\left(\rho_g\varphi+\rho_lH_L\right)gA\sin\theta \tag{27}$$

Gas-liquid phase mixture energy equation:

$$\begin{aligned}&\left[\rho_gw_g\varphi A\left(\frac{\partial h_g}{\partial P}\right)_T+\rho_lw_lH_LA\left(\frac{\partial h_l}{\partial P}\right)_T\right]\frac{dP}{dx}\\&+\left[\rho_gw_g\varphi A\left(\frac{\partial h_g}{\partial T}\right)_P+\rho_lw_lH_LA\left(\frac{\partial h_l}{\partial T}\right)_P\right]\frac{dT}{dx}+\rho_gw_g^2\varphi A\frac{dw_g}{dx}+\rho_lw_l^2H_LA\frac{dw_l}{dx}\\&=-\left(\rho_ggw_g\varphi A+\rho_lgw_lH_LA\right)\frac{dz}{dx}-K\pi D\left(T-T_0\right)-\Delta\dot{m}_{gl}\left(h_g-h_l+\frac{w_g^2-w_l^2}{2}\right)\end{aligned} \tag{28}$$

The system of simultaneous differential equations composed of (25)-(28) can be written in their non-conservative form.

$$A\frac{dU}{dx}=D \tag{29}$$

Where

$$A=\begin{bmatrix}a_{11}&a_{12}&a_{13}&a_{14}\\a_{21}&a_{22}&a_{23}&a_{24}\\a_{31}&a_{32}&a_{33}&a_{34}\\a_{41}&a_{42}&a_{43}&a_{44}\end{bmatrix},D=\begin{bmatrix}D_1\\D_2\\D_3\\D_4\end{bmatrix},U=\begin{bmatrix}P\\T\\w_g\\w_l\end{bmatrix},$$

$$a_{11}=Aw_g\varphi(\frac{\partial\rho_g}{\partial P})_T,\ a_{12}=Aw_g\varphi(\frac{\partial\rho_g}{\partial T})_P,\ a_{13}=A\rho_g\phi,\ a_{14}=0,\ a_{21}=Aw_lH_L(\frac{\partial\rho_l}{\partial P})_T,$$

$$a_{22} = Aw_l H_L(\frac{\partial \rho_l}{\partial T})_P, a_{23} = 0 \quad , a_{24} = A\rho_l H_L, a_{31} = A \quad , a_{32} = 0 \quad , a_{33} = \rho_g w_g \varphi A, a_{34} = \rho_l w_l H_L A,$$

$$a_{41} = \rho_g w_g \varphi A(\frac{\partial h_g}{\partial P})_T + \rho_l w_l H_L A(\frac{\partial h_l}{\partial P})_T \quad a_{42} = \rho_g w_g \varphi A(\frac{\partial h_g}{\partial T})_P + \rho_l w_l H_L A(\frac{\partial h_l}{\partial T})_P, a_{43} = \rho_g w_g^2 \varphi A,$$

$$a_{44} = \rho_l w_l^2 H_L A$$

$$D_1 = \Delta \dot{m}_{gl} - A\rho_g w_g \frac{d\varphi}{dx}, D_2 = \Delta \dot{m}_{lg} - A\rho_l w_l \frac{dH_L}{dx} \quad , D_3 = -F_{gw} - F_{lw} - \left(\rho_g \varphi + \rho_l H_L\right) gA \sin\theta$$

$$D_4 = -(\rho_g g w_g \varphi A + \rho_l g w_l H_L A)\frac{dz}{dx} - K\pi D(T - T_0) - \Delta \dot{m}_{gl}(h_g - h_l + \frac{w_g^2 - w_l^2}{2})$$

5.2 Model solving

Steady state condensate gas model is formed by 5 equations which are (29) and (12). There are five unknowns, liquid holdup (H_L), pressure (P), temperature (T), gas and liquid velocity (w_g and w_l), in the model. Thus, the closure of the model is satisfied.

To solve the model, the liquid hold up is obtained by solving (12) firstly. And then, pressure (P), temperature (T), velocity of the gas phase (w_g), and the velocity of the liquid phase (w_l) are obtained by solving (29). The procedures for solving (29) are presented in details as follow:

Step 1. Suppose the pipeline is composed of a lot of pipes with different slope. Divide each pipe into small blocks with the step length of Δx and input the start point data.

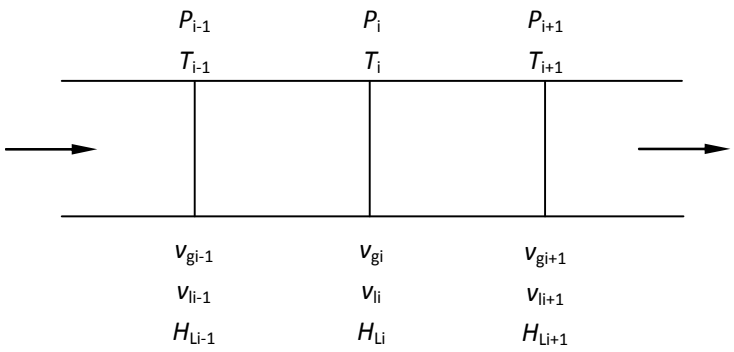

Fig. 2. Pipeline blocks for steady-state simulation

Step 2. Establish steady equation (29) on each block section. Input the boundary conditions at the initial point of pipeline (pressure, temperature, gas velocity, and liquid velocity). According to the thermodynamic model, calculate the thermophysic parameters such as density of the gas and liquid phase, gas fraction. Because there is no slip between the two phases at initial point, the liquid hold up can be gained by its relationship with mass flow rate of the gas phase and liquid phase.

Step 3. Set dU/dx as unknowns, and simplify (29) with Gaussian elimination method, then we can obtain more explicit form of (29).

$$\begin{cases} \dfrac{dP}{dx} = f_1\left(P, T, \upsilon_g, \upsilon_l\right) \\ \dfrac{dT}{dx} = f_2\left(P, T, \upsilon_g, \upsilon_l\right) \\ \dfrac{d\upsilon_g}{dx} = f_3\left(P, T, \upsilon_g, \upsilon_l\right) \\ \dfrac{d\upsilon_l}{dx} = f_4\left(P, T, \upsilon_g, \upsilon_l\right) \end{cases} \tag{30}$$

Step 4. Work out pressure (P_i), temperature (T_i), gas and liquid velocity (w_{gi} and w_{li}) by four-order Runge - Kutta Method.
Step 5. Figure out liquid holdup (H_{Li}) by equation (12).
Step 6. Resolve equations (29) by Adams predictor-corrector formula until the reasonable unknowns of this grid section are all gotten.
Step 7. Repeat the second step to the sixth step until reach the last block section which is also the end of this pipeline.

In order to make the numerical calculation converges more quickly, the Adams predictor-corrector and Runge - Kutta Method should be applied simultaneous. As the two methods have four-order accuracy, the desired accuracy also can be improved. The flow chart of the whole solving procedures is depicted in Fig.3.

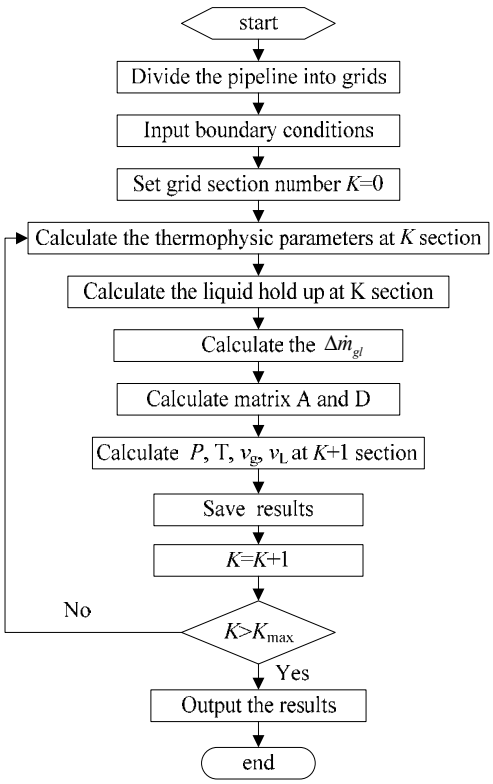

Fig. 3. Solving procedures of steady state model

6. Transient analysis of condensate gas pipeline

6.1 Basic equations of transient analysis

Opposite to the steady state simulation, the parameters in the general model are dependent on time. Expand (1), (2) and (10), and the following equations can be obtained (Masella et al, 1998).

Gas phase continuity equation:

$$A\varphi(\frac{\partial \rho_g}{\partial P})_T \frac{\partial P}{\partial t} + A\rho_g \frac{\partial \varphi}{\partial t} + Aw_g\varphi(\frac{\partial \rho_g}{\partial P})_T \frac{\partial P}{\partial x} + A\rho_g\varphi\frac{\partial w_g}{\partial x} + A\rho_g w_g \frac{\partial \varphi}{\partial x} = \Delta \dot{m}_{gl} \tag{31}$$

Liquid phase continuity equation:

$$AH_L(\frac{\partial \rho_l}{\partial P})_T \frac{\partial P}{\partial t} + A\rho_l \frac{\partial H_L}{\partial t} + Aw_l H_L(\frac{\partial \rho_l}{\partial P})_T \frac{\partial P}{\partial x} + A\rho_l H_L \frac{\partial w_l}{\partial x} + A\rho_l w_l \frac{\partial H_L}{\partial x} = \Delta \dot{m}_{lg} \tag{32}$$

Momentum equation

$$\begin{aligned} &\rho_g\varphi A\frac{\partial w_g}{\partial t} + \rho_l H_L A\frac{\partial w_l}{\partial t} + A\frac{\partial P}{\partial x} + \rho_g w_g\varphi A\frac{\partial w_g}{\partial x} + \rho_l w_l H_L A\frac{\partial w_l}{\partial x} \\ &= -F_{gw} - F_{lw} - \left(\rho_g\varphi + \rho_l H_L\right)gA\sin\theta \end{aligned} \tag{33}$$

The transient flow model can be represented by (31) ~ (33) and (12). The unknowns are the pressure P, flow velocity of the gas phase w_g, flow velocity of the liquid phase w_l and liquid holdup H_L. Notice that (31) ~ (33) are a set of partial differential equations so that they can be recast to the following matrix form.

$$B\frac{\partial U}{\partial t} + A\frac{\partial U}{\partial x} = D \tag{34}$$

Where,

$$A = \begin{bmatrix} a_{11} & a_{12} & a_{13} \\ a_{21} & a_{22} & a_{23} \\ a_{31} & a_{32} & a_{33} \end{bmatrix}, B = \begin{bmatrix} b_{11} & b_{12} & b_{13} \\ b_{21} & b_{22} & b_{23} \\ b_{31} & b_{32} & b_{33} \end{bmatrix}, D = \begin{bmatrix} D_1 \\ D_2 \\ D_3 \end{bmatrix}, U = \begin{bmatrix} P \\ w_g \\ w_l \end{bmatrix}$$

$$a_{11} = Aw_g\varphi(\frac{\partial \rho_g}{\partial P})_T,\ a_{12} = A\rho_g\phi\ ,\ a_{13} = 0,\ a_{14} = A\rho_g w_g,\ a_{21} = Aw_l H_L(\frac{\partial \rho_l}{\partial P})_T,\ a_{22} = 0\ ,$$

$$a_{23} = A\rho_l H_L\ ,\ a_{24} = A\rho_l w_l,\ a_{31} = A\ ,\ a_{32} = \rho_g w_g\varphi A,\ a_{33} = \rho_l w_l H_L A,\ .\ a_{34} = 0\ .,\ b_{11} = A\phi(\frac{\partial \rho_g}{\partial P})_T,$$

$$b_{12} = 0,\ b_{13} = 0,\ b_{14} = A\rho_g,\ b_{21} = AH_L(\frac{\partial \rho_l}{\partial P})_T,\ b_{22} = 0,\ b_{23} = 0,\ b_{24} = A\rho_l,\ b_{31} = 0,\ b_{32} = \rho_g\phi A,$$

$$b_{33} = \rho_l H_L A,\ b_{34} = 0\ D_1 = \Delta \dot{m}_{gl} - b_{14}\frac{\partial \phi}{\partial t} - a_{14}\frac{\partial \phi}{\partial x},\ D_2 = \Delta \dot{m}_{lg} - \mathrm{b}_{24}\frac{\partial \varphi}{\partial t} - a_{24}\frac{\partial H_L}{\partial x}\ ,$$

$$D_3 = -F_{gw} - F_{lw} - \left(\rho_g\phi + \rho_l H_L\right)gA\sin\theta$$

The characteristic determinant of (34) is as follow:

$$\begin{vmatrix} \lambda_0 w_g \varphi\left(\frac{\partial \rho_g}{\partial P}\right)_T + \lambda_1 \varphi\left(\frac{\partial \rho_g}{\partial P}\right)_T & \lambda_0 & 0 \\ \lambda_0 w_l H_L\left(\frac{\partial \rho_l}{\partial P}\right)_T + \lambda_1 H_L\left(\frac{\partial \rho_l}{\partial P}\right)_T & 0 & \lambda_0 \\ \lambda_0 & \lambda_0 w_g + \lambda_1 & \lambda_0 w_l + \lambda_1 \end{vmatrix} = 0 \tag{35}$$

Where, λ_0 and λ_1 are the eigenvalues of A and B. If $\lambda = \lambda_0 / \lambda$ established, one solution of λ is 0 and the other two non-zero solutions should be expressed as follow:

$$\begin{aligned} &\left[\varphi\left(\frac{\partial \rho_g}{\partial P}\right)_T + H_L\left(\frac{\partial \rho_L}{\partial P}\right)_T\right]\lambda^2 + 2\left[\varphi w_g\left(\frac{\partial \rho_g}{\partial P}\right)_T + H_L w_l\left(\frac{\partial \rho_l}{\partial P}\right)_T\right]\lambda \\ &+ w_l^2 H_L\left(\frac{\partial \rho_l}{\partial P}\right)_T + w_g^2 \varphi\left(\frac{\partial \rho_g}{\partial P}\right)_T - 1 = 0 \end{aligned} \tag{36}$$

The condition for having real solutions of (36) is:

$$\left|w_g - w_l\right| < \sqrt{\frac{1}{H_L}\left(\frac{\partial P}{\partial \rho_l}\right)_T + \frac{1}{\varphi}\left(\frac{\partial P}{\partial \rho_g}\right)_T} \tag{37}$$

In (37), $\left(\frac{\partial P}{\partial \rho_l}\right)_T$ and $\left(\frac{\partial P}{\partial \rho_g}\right)_T$ represent square of liquid and gas isothermal wave velocities separately. Thus the right side of (37) is greater than the wave velocity, which means (37) can be established for raw gas pipelines.

According to the analysis above, it can be concluded that under the giving range of operation conditions, all the eigenvaluse of (35) are real different number. Therefore, (34) is strictly hyperbolic and this type will not change as its well posedness.

6.2 Boundary conditions

The boundary conditions include the input and output conditions as well as conditions, such as valves shut off, compressors shut down and etc., which will lead to operating changes. For this transient model, the boundary conditions are considered as: the starting pressure and flow rate over time, ending pressure and flow rate over time.

$$P\big|_{x=0} = f_{p1}(t) \tag{38}$$

$$Q\big|_{x=0} = f_{q1}(t) \tag{39}$$

$$P\big|_{x=L} = f_{p2}(t) \tag{40}$$

$$Q|_{x=L} = f_{q2}(t) \tag{41}$$

6.3 Solutions of the transient model

Equation (34) is a set of non-liner partial differential equations and the method of characteristic (MOC) and implicit difference method are always adopted to gain numerical solutions. By both methods have advantages and disadvantages. There is strict restriction with the time length of each step (Fig.4), thus the stability of the implicit difference method is better. But at each time layer, differential equations of all the grids should be solved simultaneously, which causes the computing time is large. Different with the implicit difference method, for MOC, the time length of each step is restricted in a relatively short range by its stability conditions. The advantage of MOC is the unknowns of each grid at each time layer can be solved dependently, and the amount of equations solved simultaneously is reduced. Considering the transient feature of low-liquid loading multiphase flow in pipeline is slow transient behaviour which means the transient process lasts long time, the former method is adopted.

Mesh the length variable x and time variable t into grids as shown in Fig. 4. In each block, the differential equations of (31) ~ (33) can be obtained by the implicit different method (Li *et al*, 2011).

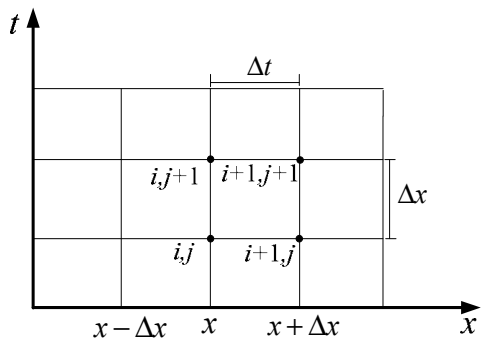

Fig. 4. Differential blocks of pipelines

Gas phase continuity equation:

$$\begin{aligned}
&b_{11}^n \frac{P_i^{n+1} + P_{i-1}^{n+1} - P_i^n - P_{i-1}^n}{2\Delta t} - b_{14}^n \frac{H_{Li}^{n+1} + H_{Li-1}^{n+1} - H_{Li}^n - H_{Li-1}^n}{2\Delta t} + \\
&+a_{11}^n \frac{\xi(P_i^{n+1} - P_{i-1}^{n+1}) + (1-\xi)(P_i^n - P_{i-1}^n)}{\Delta x} \\
&+a_{12}^n \frac{\xi(w_{gi}^{n+1} - w_{gi-1}^{n+1}) + (1-\xi)(w_{gi}^n - w_{gi-1}^n)}{\Delta x} - \\
&-a_{14}^n \frac{\xi(H_{Li}^{n+1} - H_{Li-1}^{n+1}) + (1-\xi)(H_{Li}^n - H_{Li-1}^n)}{\Delta x} = \Delta \dot{m}_{gl}
\end{aligned} \tag{42}$$

In which ξ is the weight coefficient. Set $\lambda = \frac{2\Delta t}{\Delta x}$, then above equation reduces to:

$$(b_{11}^n - a_{11}^n\lambda\xi)P_{i-1}^{n+1} - a_{12}^n\lambda\xi w_{gi-1}^{n+1} - (b_{14}^n - a_{14}^n\lambda\xi)H_{Li-1}^{n+1} + (b_{11}^n + a_{11}^n\lambda\xi)P_i^{n+1} + a_{12}^n\lambda\xi w_{gi}^{n+1}$$
$$-(b_{14}^n + a_{14}^n\lambda\xi)H_{Li}^{n+1} = 2\Delta t\Delta\dot{m}_{gl} + b_{11}^n(P_i^n + P_{i-1}^n) - b_{14}^n(H_{Li}^n + H_{Li-1}^n) - a_{11}^n\lambda(1-\xi)(P_i^n - P_{i-1}^n) \quad (43)$$
$$-a_{12}^n\lambda(1-\xi)(w_{gi}^n - w_{gi-1}^n) + a_{14}^n\lambda(1-\xi)(H_{Li}^n - H_{Li-1}^n)$$

Similarly, liquid phase continuity equation is as follow:

$$(b_{21}^n - a_{21}^n\lambda\xi)P_{i-1}^{n+1} - a_{23}^n\lambda\xi w_{li-1}^{n+1} + (b_{24}^n - a_{24}^n\lambda\xi)H_{Li-1}^{n+1} + (b_{21}^n + a_{21}^n\lambda\xi)P_i^{n+1} + a_{23}^n\lambda\xi w_{li}^{n+1}$$
$$+(b_{24}^n + a_{24}^n\lambda\xi)H_{Li}^{n+1} = 2\Delta t\Delta\dot{m}_{lg} + b_{21}^n(P_i^n + P_{i-1}^n) + b_{24}^n(H_{Li}^n + H_{Li-1}^n) \quad (44)$$
$$-a_{21}^n\lambda(1-\xi)(P_i^n - P_{i-1}^n) - a_{23}^n\lambda(1-\xi)(v_{li}^n - v_{li-1}^n) - a_{24}^n\lambda(1-\xi)(H_{Li}^n - H_{Li-1}^n)$$

Momentum equation:

$$(b_{32}^n - a_{32}^n\lambda\xi)w_{gi-1}^{n+1} + (b_{33}^n - a_{33}^n\lambda\xi)w_{li-1}^{n+1} - a_{31}^n\lambda\xi P_{i-1}^{n+1} + (b_{32}^n + a_{32}^n\lambda\xi)w_{gi}^{n+1} + (b_{33}^n + a_{33}^n\lambda\xi)w_{li}^{n+1}$$
$$+a_{31}^n\lambda\xi P_i^{n+1} = 2\Delta tD_3^n + b_{32}^n(w_{gi}^n + w_{gi-1}^n) + b_{33}^n(w_{li}^n + w_{li-1}^n) - \lambda a_{32}^n(1-\xi)(w_{gi}^n - w_{gi-1}^n) \quad (45)$$
$$-a_{33}^n\lambda(1-\xi)(w_{li}^n - w_{li}^n) - \lambda a_{31}^n(1-\xi)(P_i^n - P_{i-1}^n)$$

Based on the above three differential equations, the pressure, flow velocity of the gas phase as well as that of the liquid phase can be obtained. The solution procedures are as follow:

Step 1. Divide pipeline system into series of pipeline segments with different angles. Mesh each segment into blocks with the step length of Δx;

Step 2. Get the operation parameters on each grid node by steady state solutions;

Step 3. Put the parameters on 0 time layer into (43) ~ (45) and get the solutions of operation parameters (the pressure P, gas flow rate w_g and liquid flow rate w_l) at 1 time layer;

Step 4. Get the solution of liquid holdup H_L at 1 time layer by (12);

Step 5. Repeat step 3 ~ step 4 until reach the giving time layer;

The flow chart of the solution procedures is shown in Fig. 5.

7. Application

7.1 Steady state simulation

Table 1 is the basic data of a condensate gas pipeline. The pressure at starting point is 11.0MPa and the temperature is 330K. The mass of gas flow rate is 29.0kg/s and liquid flow is 0kg/s. The components of the condensate gas are shown in Table 2. Calculate the operation parameters of the pipeline by steady state model and determine the location where phase change occurs.

Segments	Length (km)	Diameter (mm)	Absolute roughness (mm)	Total diathermanous factor (W/m2.K)	Ambient temperature (K)	Step length (m)
30	40.0	355.6	0.0457	6.05	330	1333.33

Table 1. Basic data of the condensate gas pipeline

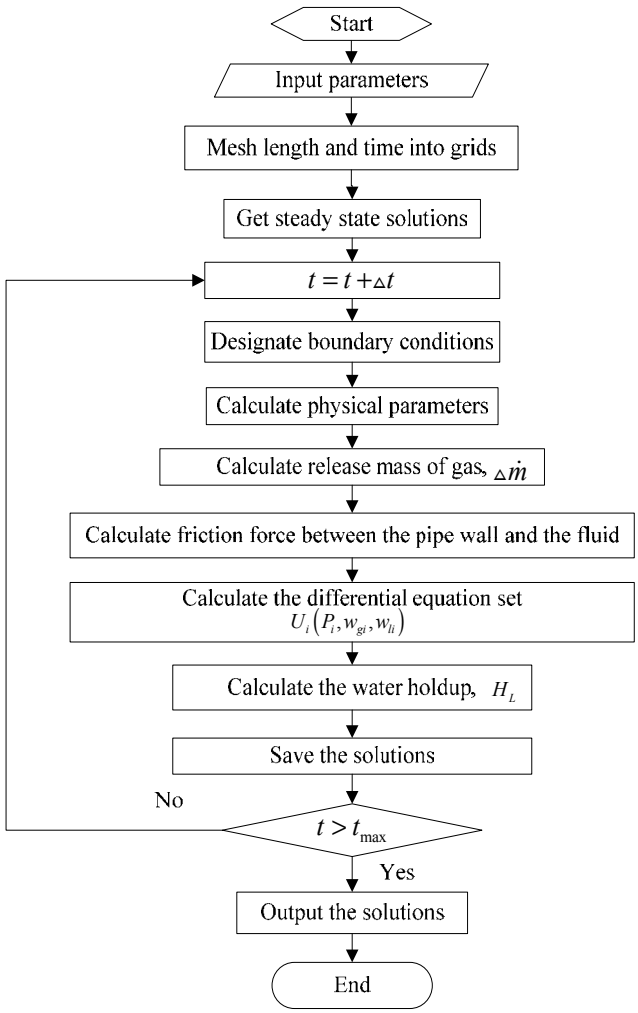

Fig. 5. Solving procedures of transient model

Component	Fraction	Component	Fraction
C1	0.841454	C6	0.002818
C2	0.075518	C7	0.001535
C3	0.039954	C8	0.001442
C4	0.009476	CO_2	0.012166
C5	0.007121	N_2	0.008517

Table 2. Basic data of the condensate gas pipeline

The solutions can be illustrated as Fig. 6. According to the solutions above, the liquid begins to condensate from the section of 12.3km because the hydrocarbons enter the anti-condensate region.

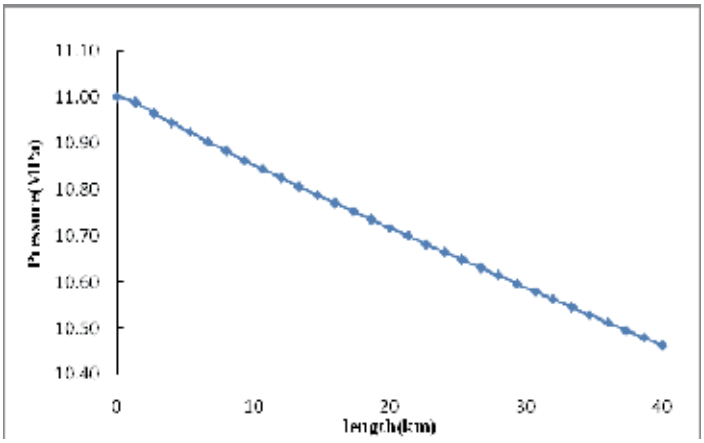

Fig. 6. The steady state pressure variations of the condensate gas pipeline

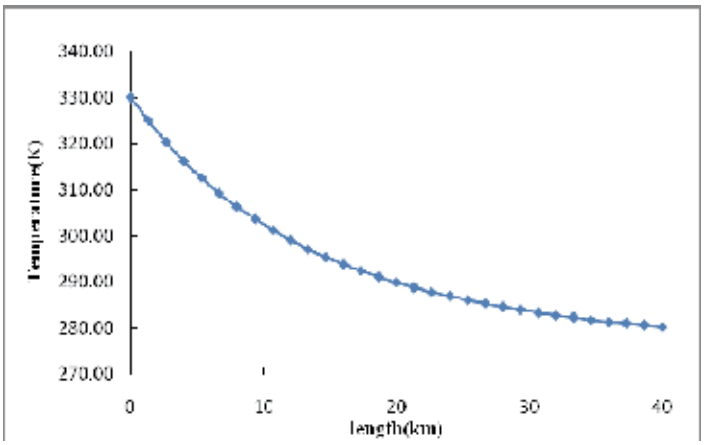

Fig. 7. The steady state temperature variations of the condensate gas pipeline

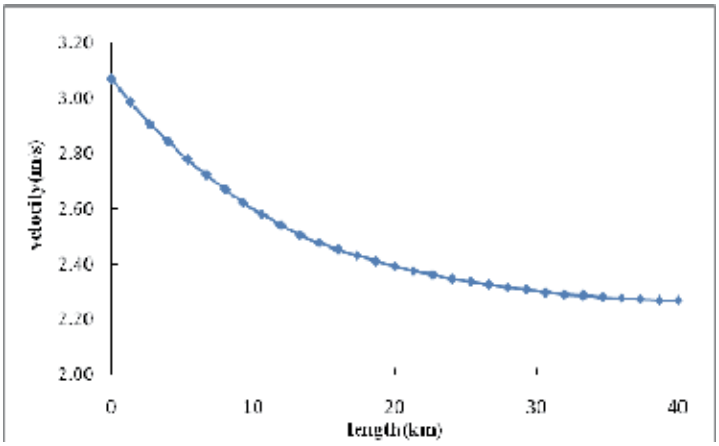

Fig. 8. The steady state gas velocity variations of the condensate gas pipeline

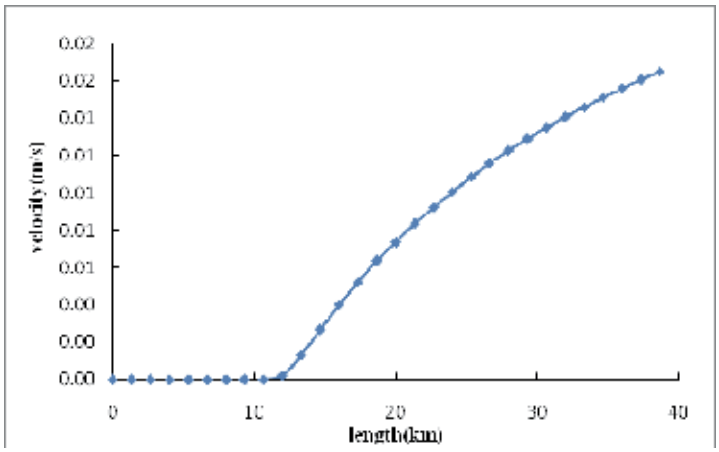

Fig. 9. The steady state liquid velocity variations of the condensate gas pipeline

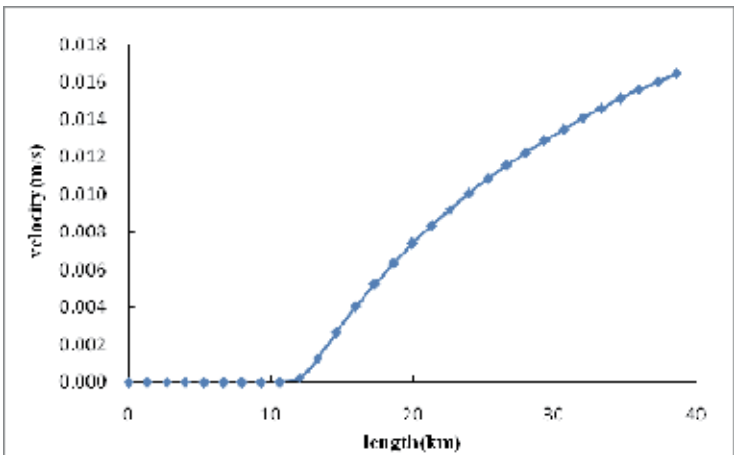

Fig. 10. The steady state liquid holdup variations of the condensate gas pipeline

The feature of condensate gas pipelines is phase change may occur during operating. This leads to a lot of new phenomena as follow:

1. It can be seen from Fig.6 that the pressure drop curve of two phase flow is significantly different from of gas flow even the liquid holdup is quite low. The pressure drop of gas flow is non-linear while the appearance of liquid causes a nearly linear curve of the pressure drop. This phenomenon is expressed that the relatively low pressure in the pipeline tends to increase of the gas volume flow; the appearance of condensate liquid and the temperature drop reduce the gas volume flow.
2. It can be seen from Fig. 7 that the temperature drop curve of two phase flow is similar to single phase flow. The temperature drop gradient of the first half is greater than the last half because of larger temperature difference between the fluid and ambient.

3. It can be seen from Fig. 8 and Fig.9 that the appearance of two phase flow lead to a reduction of gas flow velocity as well as an increase of liquid flow velocity. The phenomenon also contributes to the nearly linear drop of pressure along the pipeline.
4. The sharp change of liquid flow velocity as shown in Fig. 9 is caused by phase change. The initial flow velocity of liquid is obtained by flash calculation which makes no consideration of drag force between the phases. Therefore, an abrupt change of the flow rate before and after the phase change occurs as the error made by the flash calculation cannot be ignored. The two-fluid model which has fully considerate of the effect of time is adopted to solve the flow velocity after phase change and the solutions are closer to realistic. It is still a difficulty to improve the accuracy of the initial liquid flow rate at present. The multiple boundaries method is adapted to solve the steady state model. But the astringency and steady state need more improve while this method is applied to non-linear equations.
5. As shown in Fig.10, the liquid hold up increases behind the phase transition point (two-phase region). Due to the increasing of the liquid hold up is mainly constraint by the phase envelope of the fluid, increasing amount is limited.

The steady state model can simulate the variation of parameters at steady state operation. Actually, there is not absolute steady state condition of the pipeline. If more details of the parameters should be analyzed, following transient simulation method is adopted.

7.2 Transient simulation

Take the previous pipeline as an example, and take the steady state steady parameters as the initial condition of the transient simulation. The boundary condition is set as the pressure at the inlet of pipeline drops to 10.5MPa abruptly at the time of 300s after steady state. The simulation results are shown in Fig11-Fig.15.

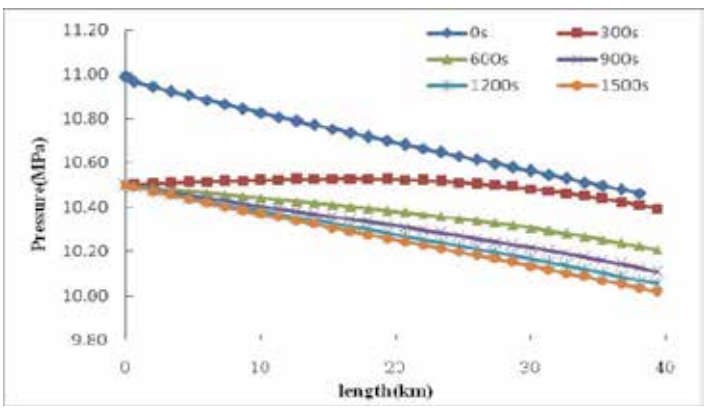

Fig. 11. Pressure variation along the pipeline

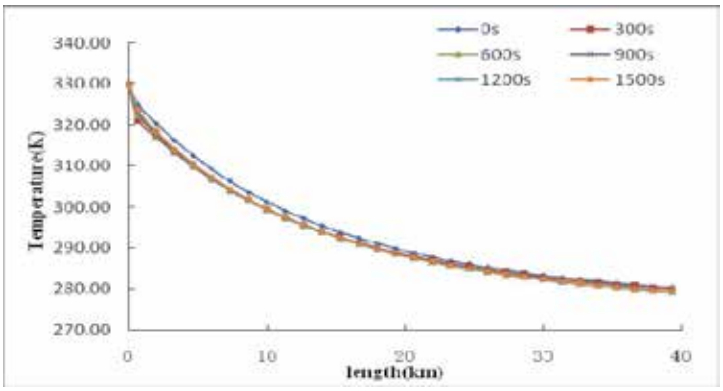

Fig. 12. Temperature variation along the pipeline

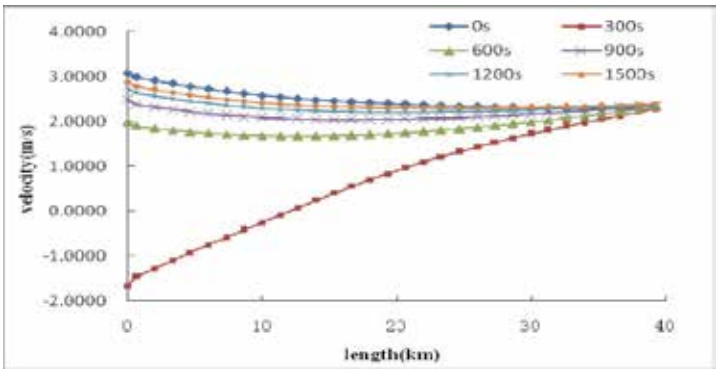

Fig. 13. Velocity of the gas phase variation along the pipeline

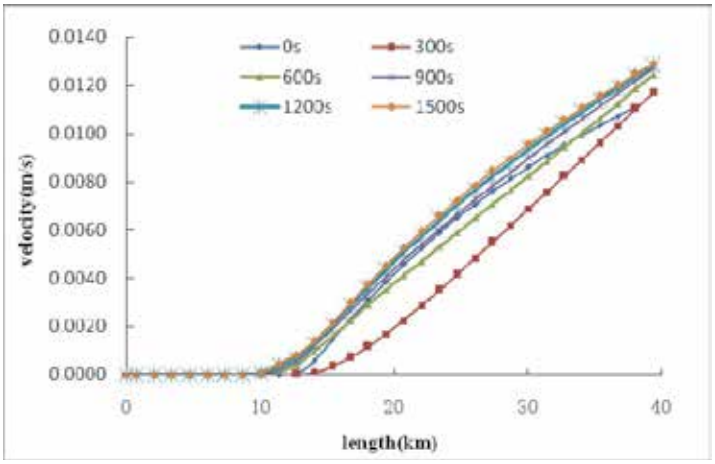

Fig. 14. Velocity of the liquid phase variation along the pipeline

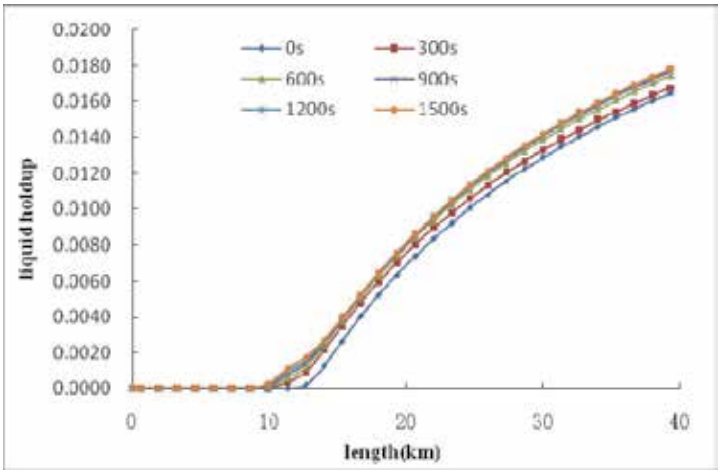

Fig. 15. Liquid hold up variation along the pipeline

Compared with steady state, the following features present.

1. Fig.11 depicts the pressure along the pipeline drops continuously with time elapsing after the inlet pressure drops to 10.5MPa at the time of 300s as the changing of boundary condition.
2. Fig.12 shows the temperature variation tendency is nearly the same as steady state. The phenomenon can be explained by the reason that the energy equation is ignored in order to simplify the transient model. The approximate method is reasonable because the temperature responses slower than the other parameters.
3. As depicted in Fig.13, there are abrupt changes of the gas phase velocity at the time of 300s. The opposite direction flow occurs because the pressure at the inlet is lower than the other sections in the pipeline. However, with the rebuilding of the new steady state, the velocity tends to reach a new steady state.
4. Fig.14 shows the velocity variation along the pipeline. Due to the loss of pressure energy at the inlet, the liquid velocity also drops simultaneously at the time of 300s. Similar to gas velocity, after 300s, the liquid velocity increases gradually and tends to reach new steady state with time elapsing.
5. Due to the same liquid hold up equation is adopted in the steady state and transient model, the liquid hold up simulated by the transient model and steady state mode has almost the same tendency (Fig.15). However, the liquid hold up increases because of the temperature along the pipeline after 300s is lower than that of initial condition.

Sum up, the more details of the results and transient process can be simulated by transient model. There are still some deficiencies in the model, which should be improved in further work.

8. Conclusions

In this work, a general model for condensate gas pipeline simulation is built on the basis of BWRS EOS, continuity equation, momentum equation, energy equation of the gas and liquid phase. The stratified flow pattern and corresponding constitutive equation are adopted to simplify the model.

By ignoring the parameters variation with time, the steady state simulation model is obtained. To solve the model, the four-order Runge - Kutta method and Gaussian

elimination method are used simultaneously. Opposite to steady state model, the transient model is built with consideration of the parameters variation with time, and the model is solved by finite difference method. Solving procedures of steady-state and transient models are presented in detail.

Finally, this work simulated the steady-state and transient operation of a condensate gas pipeline. The pressures, temperatures, velocity of the gas and liquid phase, liquid hold up are calculated. The differences between the steady-state and transient state are discussed. The results show the model and solving method proposed in this work are feasible to simulate the steady state and transient flow in condensate gas pipeline. Nevertheless, in order to expand the adaptive range the models, more improvements should be implemented in future work (Pecenko *et al*, 2011).

9. Acknowledgment

This paper is a project supported by sub-project of National science and technology major project of China (No.2008ZX05054) and China National Petroleum Corporation (CNPC) tackling key subject: Research and Application of Ground Key Technical for CO_2 flooding, JW10-W18-J2-11-20.

10. References

S. Mokhatab ; William A. Poe & James G. Speight. (2006).*Handbook of Natural Gas Transmission and Processing*, Gulf Professional Publishing, ISBN 978-0750677769

Li, C. J. (2008). *Natural Gas Transmission by Pipeline*, Petroleum Industry Press, ISBN 978-7502166700, Beijing, China

S. Mokahatab.(2009). Explicit Method Predicts Temperature and Pressure Profiles of Gas-condensate Pipelines . *Energy Sources, Part A*. 2009(29): 781-789.

P. Potocnik. (2010). *Natural Gas*, Sciyo, ISBN 978-953-307-112-1, Rijeka, Crotla.

M. A. Adewumi. & Leksono Mucharam. (1990). Compostional Multiphase Hydrodynamic Modeling of Gas/Gas-condensate Dispersed Flow. *SPE Production Engineering*, Vol.5, No.(2), pp.85-90 ISSN 0885-9221

McCain, W.D. (1990). *The Properties of Petroleum Fluids(2nd Edition)*. Pennwell Publishing Company, ISBN978-0878143351,Tulsa, OK., USA

Estela-Uribe J.F.; Jaramillo J., Salazar M.A. & Trusler J.P.M. (2003). Viriel equation of statefor natural gas systems. *Fluid Phase Equilibria*, Vol. 204, No. 2, pp. 169--182.ISSN 0378-3812

API. (2005). *API Technical Databook (7th edition)*, EPCON International and The American Petroleum Institite, TX,USA

Luis F. Ayala; M. A. Adewumi.(2003). Low liquid loading Multiphase Flow in Nature Gas Pipelines.*Journal of Energy Resources and Technology*, Vol.125, No.4, pp. 284-293, ISSN 1528-8994

Li, Y. X., Feng, S. C.(1998). Studying on transient flow model and value simulation technology for wet natural gas in pipeline tramsmission. *OGST,* vol.17, no.5, pp.11-17, ISSN1000-8241

Hasan, A.R. & Kabir, C.S.(1992). Gas void fraction in two-phase up-flow in vertical and inclined annuli. *International Journal of Multiphase Flow*, Vol.18, No.2, pp.279 – 293. ISSN0301-9322

Li, C. J., Liu E.B. (2009) .The Simulation of Steady Flow in Condensate Gas Pipeline，*Proceedings of 2009 ASCE International Pipelines and Trenchless Technology Conference*, pp.733-743, ISBN 978-0-7844-1073-8, Shanghai, China, October 19-21,2009.

Taitel, Y. & Barnea (1995). Stratified three-phase flow in pipes. *International Journal of Multiphase flow*, Vol.21, No.2, pp.53-60. ISSN0301-9322

Chen, X. T., Cai, X. D. & Brill, J. P. (1997). Gas-liquid Stratified Wavy Flow in Horizontal Pipelines, .*Journal of Energy Resources and Technology,*Vol.119, No.4, pp.209-216 ISSN 1528-8994.

Masella, J.M., Tran, Q.H., Ferre, D., and Pauchon, C.(1998). Transient simulation of two-phase flows in pipes. *Oil Gas Science Technology*. Vol. 53, No.6, pp.801 – 811 ISSN 1294-4475.

Li, C. J., Jia, W. L., Wu, X.(2010). Water Hammer Analysis for Heated Liquid Transmission Pipeline with Entrapped Gas Based on Homogeneous Flow Model and Fractional Flow Model, *Proceedings of 2010 IEEE Asia-Pacific Power and Energy Engineering Conference*, ISBN978-1-4244-4813-5, Chengdu, China, March28-21.2010.

A. Pecenko,; L.G.M. van Deurzen. (2011). Non-isothermal two-phase flow with a diffuse-interface model. *International Journal of Multiphase Flow* ,Vol.37,No.2,PP.149-165. ISSN0301-9322

4

Extended Irreversible Thermodynamics in the Presence of Strong Gravity

Hiromi Saida
Daido University
Japan

1. Introduction

For astrophysical phenomena, especially in the presence of strong gravity, the causality of any phenomena must be preserved. On the other hand, dissipations, e.g. heat flux and bulk and shear viscosities, are necessary in understanding transport phenomena even in astrophysical systems. If one relies on the Navier-Stokes and Fourier laws which we call *classic laws of dissipations*, then an infinite speed of propagation of dissipations is concluded (14). (See appendix 7 for a short summary.) This is a serious problem which we should overcome, because the infinitely fast propagation of dissipations contradicts a physical requirement that the propagation speed of dissipations should be less than or equal to the speed of light. This means the breakdown of causality, which is the reason why the dissipative phenomena have not been studies well in relativistic situations. Also, the infinitely fast propagation denotes that, even in non-relativistic case, the classic laws of dissipations can not describe dynamical behaviors of fluid whose dynamical time scale is comparable with the time scale within which non-stationary dissipations relax to stationary ones.
Moreover note that, since Navier-Stokes and Fourier laws are independent phenomenological laws, interaction among dissipations, e.g. the heating of fluid due to viscous flow and the occurrence of viscous flow due to heat flux, are not explicitly described in those classic laws. (See appendix 7 for a short summary.) Thus, in order to find a physically reasonable theory of dissipative fluids, it is expected that not only the finite speed of propagation of dissipations but also the interaction among dissipations are included in the desired theory of dissipative fluids.
Problems of the infinite speed of propagation and the absence of interaction among dissipations can be resolved if we rely not on the classic laws of dissipations but on the *Extended Irreversible Thermodynamics* (EIT) (13; 14). The EIT, both in non-relativistic and relativistic situations, is a causally consistent phenomenology of dissipative fluids including interaction among dissipations (9). Note that the non-relativistic EIT has some experimental grounds for laboratory systems (14). Thus, although an observational or experimental verification of relativistic EIT has not been obtained so far, the EIT is one of the promising hydrodynamic theories for dissipative fluids even in relativistic situations. [1]

[1] One may refer to the relativistic hydrodynamics proposed by Israel (11), which describes the causal propagation of dissipations. However, since the Israel's hydrodynamics can be regarded as one approximate formalism of EIT as reviewed in Sec.3, we dare to use the term EIT rather than Israel's theory.

In astrophysics, the recent advance of technology of astronomical observation realizes a fine observation whose resolution is close to the view size of celestial objects which are candidates of black holes (1; 20; 24). (Note that, at present, no certain evidence of the existence of black hole has been extracted from observational data.) The light detected by our telescope is emitted by the matter accreting on to the black hole, and the energy of the light is supplied via the dissipations in accreting matter. Therefore, those observational data should include signals of dissipative phenomena in strong gravitational field around black hole. We expect that such general relativistic dissipative phenomena is described by the EIT.

EIT has been used to consider some phenomena in the presence of strong gravity. For example, Peitz and Appl (23) have used EIT to write down a set of evolution equations of dissipative fluid and spacetime metric (gravitational field) for stationary axisymmetric situation. However the Peitz-Appl formulation looks very complicated, and has predicted no concrete result on astrophysics so far. Another example is the application of EIT to a dissipative gravitational collapse under the spherical symmetry. Herrera and co-workers (6–8) constructed some models of dissipative gravitational collapse with some simplification assumptions. They rearranged the basic equations of EIT into a suitable form, and deduced some interesting physical implications about dissipative gravitational collapse. But, at present, there still remain some complexity in Herrera's system of equations for gravitational collapse, and it seems not to be applicable to the understanding of observational data of black hole candidates (1; 20; 24). These facts imply that, in order to extract the signals of strong gravity from the observational data of black hole candidates, we need a more sophisticated strategy for the application of EIT to general relativistic dissipative phenomena. In order to construct the sophisticated strategy, we need to understand the EIT deeply.

Then, this chapter aims to show a comprehensive understanding of EIT. We focus on basic physical ideas of EIT, and give an important remark on non-equilibrium radiation field which is not explicitly recognized in the original works and textbook of EIT (9–14). We try to understand the EIT from the point of view of non-equilibrium physics, because the EIT is regarded as dissipative hydrodynamics based on the idea that the thermodynamic state of each fluid element is a non-equilibrium state. (But thorough knowledge of non-equilibrium thermodynamics and general relativity is not needed in reading this chapter.) As explained in detail in following sections, the non-equilibrium nature of fluid element arises from the dissipations which are essentially *irreversible processes*. Then, non-equilibrium thermodynamics applicable to each fluid element is constructed in the framework of EIT, which includes the interaction among dissipations and describes the causal entropy production process due to the dissipations. Furthermore we point out that the EIT is applicable also to radiative transfer in optically *thick* matters (4; 27). However, radiative transfer in optically *thin* matters can not be described by EIT, because the non-self-interacting nature of photons is incompatible with a basic requirement of EIT. This is not explicitely recognized in standard references of EIT (9–14).

Here let us make two comments: Firstly, note that the EIT can be formulated with including not only heat and viscosities but also electric current, chemical reaction and diffusion in multi-component fluids (13; 14). Including all of them raises an inessential mathematical confusion in our discussions. Therefore, for simplicity of discussions in this paper, we consider the *simple dissipative fluid*, which is electrically neutral and chemically inert single-component dissipative fluid. This means to consider the heat flux, bulk viscosity and shear viscosity as the dissipations in fluid.

As the second comment, we emphasize that the EIT is a *phenomenology* in which the transport coefficients are parameters undetermined in the framework of EIT (11; 13; 14). On the other hand, based on the Grad's 14-moment approximation method of molecular motion, Israel and Stewart (12) have obtained the transport coefficients of EIT as functions of thermodynamic variables. The Israel-Stewart's transport coefficients are applicable to the molecular kinematic viscosity. However, it is not clear at present whether those coefficients are applicable to other mechanisms of dissipations such as fluid turbulent viscosity and the so-called magneto-rotational-instability (MRI) which are usually considered as the origin of viscosities in accretion flows onto celestial objects (5; 15; 26). Concerning the MRI, an analysis by Pessah, Chan, and Psaltis (21; 22) seems to imply that the dissipative effects due to MRI-driven turbulence can be expressed as some transport coefficients, whose form may be different from Israel-Stewart's transport coefficients. Hence, in this chapter, we do not refer to the Israel-Stewart's coefficients. We re-formulate the EIT simply as the phenomenology, and the transport coefficients are the parameters determined empirically through observations or by underlying fundamental theories of turbulence and/or molecular dynamics. The determination of transport coefficients and the investigation of micro-processes of transport phenomena are out of the aim of this chapter. The point of EIT in this chapter is the causality of dissipations and the interaction among dissipations.
In Sec.2, the basic ideas of EIT is clearly summarized into four assumptions and one supplemental condition, and a limit of EIT is also reviewed. Sec.3 explains the meanings of basic quantities and equations of EIT, and also the derivation of basic equations are summarized so as to be extendable to fluids which are more complicated than the simple dissipative fluid. Sec.4 is for a remark on a non-equilibrium radiative transfer, of which the standard references of EIT were not aware. Sec.5 gives a concluding remark on a tacit understanding which is common to EIT and classic laws of dissipations.
In this chapter, the semicolon " ; " denotes the covariant derivative with respect to spacetime metric, while the comma " , " denotes the partial derivative. The definition of covariant derivative is summarized in appendix 7. (Thorough knowledge of general relativity is not needed in reading this chapter, but experiences of calculation in special relativity is preferable.) The unit used throughout is

$$c = 1 \quad , \quad G = 1 \quad , \quad k_B = 1 \, . \tag{1}$$

Since the quantum mechanics is not used in this paper, we do not care about the Planck constant.

2. Basic assumptions and a supplemental condition of EIT

For the first we summarizes the basis of perfect fluid and classic laws of dissipations. The theory of perfect fluid is a phenomenology assuming the *local equilibrium*; each fluid element is in a thermal equilibrium state. Here note that, exactly speaking, dissipations can not exist in thermal equilibrium states. Thus the local equilibrium assumption is incompatible with the dissipative phenomena which are essentially the irreversible and entropy producing processes. By that assumption, the basic equations of perfect fluid do not include any dissipation, and any fluid element in perfect fluid evolves adiabatically. No entropy production arises in the fluid element of perfect fluid (19). Furthermore, recall that the classic laws of dissipations (Navier-Stokes and Fourier laws) are also the phenomenologies assuming

the local equilibrium. Therefore, the classic laws of dissipations lead inevitably some unphysical conclusions, one of which is the infinitely fast propagation of dissipations (13; 14). From the above, it is recognized that we should replace the local equilibrium assumption with the idea of *local non-equilibrium* in order to obtain a physically consistent theory of dissipative phenomena. This means to consider that the fluid element is in a non-equilibrium state. A phenomenology of dissipative irreversible hydrodynamics, under the local *non*-equilibrium assumption, is called the *Extended Irreversible Thermodynamics* (EIT). [2] The basic assumptions of EIT can be summarized into four statements. As discussed above, the first one is as follows:

Assumption 1 (Local Non-equilibrium)**.** *The dissipative fluid under consideration is in "local" non-equilibrium states. This means that each fluid element is in a non-equilibrium state, but the non-equilibrium state of one fluid element is not necessarily the same with the non-equilibrium state of the other fluid element.* □

Due to this assumption, it is necessary for the EIT to formulate a non-equilibrium thermodynamics to describe thermodynamic state of each fluid element. In order to formulate it, we must specify the state variables which are suitable for characterizing non-equilibrium states. The second assumption of EIT is on the specification of suitable state variables for non-equilibrium states of fluid elements:

Assumption 2 (Non-equilibrium thermodynamic state variables)**.** *The state variables which characterize the non-equilibrium states are distinguished into two categories;*

1st category (Non-equilibrium Vestiges) *The state variables in this category do not necessarily vanish at the local equilibrium limit of fluid. These are the variables specified already in equilibrium thermodynamics, e.g. the temperature, internal energy, pressure, entropy and so on.*

2nd category (Dissipative Fluxes) *The state variables in this category should vanish at the local equilibrium limit of fluid. These are, in the framework of EIT of simple dissipative fluid, the "heat flux", "bulk viscosity", "shear viscosity" and their thermodynamic conjugate state variables. (e.g. thermodynamic conjugate to entropy S is temperature $T \equiv \partial E/\partial S$, where E is internal energy. Similarly, thermodynamic conjugate to bulk viscosity Π can be given by $\partial E/\partial \Pi$, where E is now "non-equilibrium" internal energy.)* □

Note that the terminology "non-equilibrium vestige" is a coined word introduced by the present author, and not a common word in the study on EIT. But let us dare to use the term "non-equilibrium vestige" to explain clearly the idea of EIT.
Next, recall that, in the ordinary equilibrium thermodynamics, the number of independent state variables is two for closed systems which conserve the number of constituent particles, and three for open systems in which the number of constituent particles changes. For non-equilibrium states of dissipative fluid elements, it seems to be natural that the number of independent non-equilibrium vestiges is the same with that of state variables in ordinary equilibrium thermodynamics. On the other hand, in the classic laws of dissipations which are summarized in Eq.(46) in appendix 7, the dissipative fluxes such as heat flux and viscosities were not independent variables, but some functions of fluid velocity and local equilibrium state variables such as temperature and pressure. However in the EIT, the dissipative fluxes

[2] Although the EIT is a dissipative "hydrodynamics", it is named "thermodynamics". This name puts emphasis on the replacement of local equilibrium idea with local non-equilibrium one, which is a revolution in thermodynamic treatment of fluid element.

are assumed to be independent of fluid velocity and non-equilibrium vestiges. Then, the third assumption of EIT is on the number of independent state variables:

Assumption 3 (Number of Independent State Variables)**.** *The number of independent non-equilibrium vestiges is the same with the ordinary thermodynamics (two for closed system and three for open system). Furthermore, EIT assumes that the number of independent dissipative fluxes are three. For example, we can regard the heat flux, bulk viscosity and shear viscosity are independent dissipative fluxes.* □ [3]

Mathematically, the independent state variables can be regarded as a "coordinate system" in the space which consists of thermodynamic states. A set of values of the coordinates corresponds to a particular non-equilibrium state. This means that the set of values of independent state variables is uniquely determined for each non-equilibrium state, and different non-equilibrium states have different sets of values of independent state variables.
Assumption 3 implies the existence of non-equilibrium equations of state, from which we can obtain "dependent" state variables. Concrete forms of non-equilibrium equations of state should be determined by experiments or micro-scopic theories of dissipative fluids. Given the non-equilibrium equations of state, we can consider a case that the non-equilibrium entropy, $S_{\rm ne}$, is a dependent state variable. In this case, $S_{\rm ne}$ depends on an independent dissipative flux, e.g. the bulk viscosity Π. Obviously, since Π is one of the dissipative fluxes, the partial derivative, $\partial S_{\rm ne}/\partial\Pi$, has no counter-part in ordinary equilibrium thermodynamics. This implies that $\partial S_{\rm ne}/\partial\Pi$ is a member not of non-equilibrium vestiges but of dissipative fluxes. Hence, by the assumption 2, we find that the partial derivative of dependent state variable by an independent dissipative flux should vanish at local equilibrium limit of fluid,

$$\frac{\partial[\text{non-equilibrium dependent state variable}]}{\partial[\text{independent dissipative flux}]} \to 0 \quad \text{as [independent dissipative fluxes]} \to 0\,. \tag{2}$$

The assumptions 1, 2 and 3 can be regarded as the zeroth law of non-equilibrium thermodynamics formulated in the EIT, which prescribes the existence and basic properties of local non-equilibrium states of dissipative fluids. In the relativistic formulation of EIT, the state variables are gathered in the energy-momentum tensor, $T^{\mu\nu}$. The definition of $T^{\mu\nu}$ will be shown in next section.
Here note that, because EIT is a "hydrodynamics", we should consider not only non-equilibrium thermodynamic state variables but also a *dynamical variable*, the fluid velocity. As will be shown in next section, the basic equations of EIT determine not only non-equilibrium state variables but also the dynamical variable (velocity) of fluid element, when initial and boundary conditions are specified. Hence, via the basic equations, *the fluid velocity can be regarded as a function of thermodynamic state variables of fluid elements.*
The evolution equations of fluid velocity and non-equilibrium vestiges are given by the conservation laws of mass current vector and energy-momentum tensor as will be shown

[3] As an advanced remark, recall that, in ordinary equilibrium thermodynamics, if there is an external field such as a magnetic field applied on a magnetized gas, then the number of independent state variables increases for both closed and open systems. Usually, the external field itself can be regarded as an additional independent state variable. The same is true of the number of independent non-equilibrium vestiges. In this paper, we consider no external field other than the external gravity (the metric), and the metric can be regarded as an additional independent non-equilibrium vestige. However, for simplicity and in order to focus our attention to *intrinsic* state variables of non-equilibrium states, we do not explicitly show the metric as an independent state variable in all discussions in this paper.

in next section. Then, in order to obtain the evolution equations of dissipative fluxes, we need guiding principles. In the EIT, such guiding principles are the second law of thermodynamics and the phenomenological requirement based on laboratory experiments summarized in appendix 7. The fourth assumption of EIT is on these guiding principles:

Assumption 4 (Second Law and Phenomenology)**.** *The self-production rate of entropy by a fluid element at spacetime point x, $\sigma_{\rm s}(x)$, is defined by the divergence of non-equilibrium entropy current vector, $\sigma_{\rm s} := S_{\rm ne}^{\ \mu}{}_{;\mu}$, where the detail of $S_{\rm ne}^{\ \mu}$ is not necessary at present and shown in Sec.3.2. Concerning $\sigma_{\rm s}$, EIT assumes the followings:*

(4-a) *Entropy production rate is non-negative, $\sigma_{\rm s} \geq 0$ (2nd law).*

(4-b) *Entropy production rate is expressed by the bilinear form,*

$$\sigma_{\rm s} = [\text{Dissipative Flux}] \times [\text{Thermodynamic force}]\,, \tag{3}$$

where, as explained below, the "thermodynamic force" is given by some gradients of state variables which raises a dissipative flux, and the functional form of thermodynamic force should be consistent with existing phenomenologies summarized in appendix 7. Concrete forms of them are derived in Sec.3.2. □

The notion of thermodynamic force in requirement (4-b) is not a particular property of EIT. Indeed, the thermodynamic force has already been known in classic laws of dissipations. For example, the Fourier law, $\vec{q} = -\lambda\vec{\nabla}T$, implies that the temperature gradient, $-\vec{\nabla}T$, is the thermodynamic force which raises the heat flux, $\vec{q}$, where λ is the heat conductivity. Also, it is already known for the Fourier law that the entropy production rate is given by the bilinear form, $\vec{q}\cdot(-\vec{\nabla}T) = q^2/\lambda \geq 0$, where $\vec{q}$ and $-\vec{\nabla}T$ corresponds respectively to the dissipative flux and thermodynamic force in the above requirement (4-b) (13; 14). The assumption 4 is a simple extension of the local equilibrium theory to the local non-equilibrium theory. The causality of dissipative phenomena is not retained by solely the assumption 4. Also, the inclusion of interaction among dissipative fluxes is not achieved by solely the assumption 4.
The point of preservation of causality and inclusion of interaction among dissipations is the definition of non-equilibrium entropy current, $S_{\rm ne}^{\ \mu}$. As explained in next section, once an appropriate definition of $S_{\rm ne}^{\ \mu}$ is given, the assumption 4 together with the other three assumptions yields the evolution equations of dissipative fluxes which retain the causality of dissipative phenomena and includes the interaction among dissipative fluxes.
To find the appropriate definition of $S_{\rm ne}^{\ \mu}$, it should be noted that, unfortunately, some critical problems have been found for the cases of strong dissipative fluxes; e.g. the uniqueness of non-equilibrium temperature, $T_{\rm ne}$, and non-equilibrium pressure, $p_{\rm ne}$, can not be established in the present status of EIT (13; 14). These problems are the very difficult issues in non-equilibrium physics. At present, the EIT seems not to be applicable to a non-equilibrium state with strong dissipations. However, we can expect that, by restricting our discussion to the case of weak dissipative fluxes, the difficult problems in non-equilibrium physics is avoided and a well-defined entropy current, $S_{\rm ne}^{\ \mu}$, is obtained. This expectation is realized by adopting a perturbative method summarized in the following supplemental condition:

Supplemental Condition 1 (Second Order Approximation of Equations of State)**.** *Restrict our interest to the non-equilibrium states which are not so far from equilibrium states. This means that the dissipative fluxes are not very strong. Quantitatively, we consider the cases that the strength of dissipative fluxes is limited so that the "second order approximation of equations of state" is appropriate:*

Some examples about non-equilibrium specific entropy, $s_{\rm ne}$, and non-equilibrium temperature, $T_{\rm ne}$, are (13; 14)

$$s_{\rm ne}(\varepsilon_{\rm ne}, V_{\rm ne}, q^\mu, \Pi, \overset{\circ}{\Pi}{}^{\mu\nu}) = s_{\rm eq}(\varepsilon_{\rm eq}, V_{\rm eq}) + [\text{2nd order terms of } q^\mu, \Pi \text{ and } \overset{\circ}{\Pi}{}^{\mu\nu}] \quad (4a)$$

$$T_{\rm ne}(\varepsilon_{\rm ne}, V_{\rm ne}, q^\mu, \Pi, \overset{\circ}{\Pi}{}^{\mu\nu}) = T_{\rm eq}(\varepsilon_{\rm eq}, V_{\rm eq}) + [\text{2nd order terms of } q^\mu, \Pi \text{ and } \overset{\circ}{\Pi}{}^{\mu\nu}], \quad (4b)$$

where we choose $\varepsilon_{\rm ne}$, $V_{\rm ne}$, q^μ, Π and $\overset{\circ}{\Pi}{}^{\mu\nu}$ as the independent state variables of non-equilibrium state of each fluid element, and suffix "ne" denotes "non-equilibrium". The quantities $\varepsilon_{\rm ne}$ and $V_{\rm ne}$ are respectively the non-equilibrium specific internal energy and specific volume which are non-equilibrium vestiges, and q^μ, Π and $\overset{\circ}{\Pi}{}^{\mu\nu}$ are respectively the heat flux, bulk viscosity and shear viscosity which are dissipative fluxes. In Eq.(4)*, the quantities with suffix "*eq*" are the state variables of "fiducial equilibrium state", which is defined as the equilibrium state of fluid element of an imaginary perfect fluid (non-dissipative fluid) possessing the same value of fluid velocity and rest mass density with our actual dissipative fluid. Then, $s_{\rm eq}(\varepsilon_{\rm eq}, V_{\rm eq})$ and $T_{\rm eq}(\varepsilon_{\rm eq}, V_{\rm eq})$ in Eq.*(4) *are given by the equations of state for fiducial equilibrium state. Note that, under the second order approximation* (4)*, the "non-equilibrium vestiges" are reduced to the state variables of fiducial equilibrium state. Also note that, because of Eq.*(2)*, no first order term of independent dissipative flux appears in Eq.*(4)*. In summary, Eq.*(4) *is the expansion of non-equilibrium equations of state about the fiducial equilibrium state up to the second order of independent dissipative fluxes. Thus, the dissipative fluxes under this condition are regarded as a non-equilibrium thermodynamic perturbation on the fiducial equilibrium state.* □

As will be shown in Sec.3.2, the basic equations of EIT is derived using not only the assumptions 1 $\sim$ 4 but also the supplemental condition 1. Then, one may regard the supplemental condition 1 as one of basic assumptions of EIT. However, in the study on non-equilibrium physics, there seem to be some efforts to go beyond the second order approximation required in supplemental condition 1 (13; 14). Thus, in this paper, let us understand that the supplemental condition 1 is not a basic assumption but a supplemental condition to make the four basic assumptions work well.

A quantitative estimate of the strength of dissipative fluxes for a particular situation has been examined by Hiscock and Lindblom (10). They investigated an ultra-relativistic gas including only a heat flux under the planar symmetry. We can recognize from the Hiscock-Lindblom's analysis that, for the system they investigated, the second order approximation of equations of state such as Eq.(4) is valid for the heat flux, q^μ, satisfying the inequality,

$$\frac{q}{\rho_{\rm eq}\,\varepsilon_{\rm eq}} \lesssim 0.08898\,, \quad (5)$$

where $q := \sqrt{q^\mu q_\mu}$. Note that the density of internal energy of fiducial equilibrium state, $\rho_{\rm eq}\,\varepsilon_{\rm eq}$, includes the rest mass energy of the fluid. Therefore, the inequality (5) implies that the supplemental condition 1 is appropriate when the heat flux is less than a few percent of the internal energy density including mass energy.

3. Basic quantities and basic equations of EIT

3.1 Meanings of basic quantities and equations

The basic quantities of dissipative fluid in the framework of EIT:

$u^\mu(x)$: velocity field of dissipative fluid (four-velocity of dissipative fluid element)
$\rho_{\rm ne}(x)$: rest mass density for non-equilibrium state
$\varepsilon_{\rm ne}(x)$: non-equilibrium *specific* internal energy (internal energy *per unit rest mass*)
$p_{\rm ne}(x)$: non-equilibrium pressure

$T_{\rm ne}(x)$: non-equilibrium temperature
$q^\mu(x)$: heat flux vector
$\Pi(x)$: bulk viscosity
$\overset{\circ}{\Pi}{}^{\mu\nu}(x)$: shear viscosity tensor
$g_{\mu\nu}(x)$: spacetime metric tensor .

The specific volume, $V_{\rm ne}$ (volume per unit rest mass), which is one of non-equilibrium vestiges, is defined by

$$V_{\rm ne}(x) := \rho_{\rm ne}(x)^{-1} . \tag{6}$$

These quantities will appear in the basic equations of EIT. [4] All of the above quantities are the "field" quantities defined on spacetime manifold, and x denotes the coordinate variables on spacetime. Quantities $\rho_{\rm ne}$, $\varepsilon_{\rm ne}$, $p_{\rm ne}$ and $T_{\rm ne}$ are non-equilibrium vestiges, and quantities q^μ, Π and $\overset{\circ}{\Pi}{}^{\mu\nu}$ are the dissipative fluxes (see assumption 2).
Note that, it is possible to determine the values of u^μ and $\rho_{\rm ne}$ without referring to the other thermodynamic state variables. The fluid velocity, u^μ, is simply defined as the average four-velocity of constituent particles in a fluid element. This definition of fluid velocity is called the N-frame by Israel (11). The rest mass density, $\rho_{\rm ne}$, is simply defined by the rest mass per unit three-volume perpendicular to u^μ. Because u^μ and $\rho_{\rm ne}$ are determined without the knowledge of local non-equilibrium state, the fiducial equilibrium state is defined with referring to u^μ and $\rho_{\rm ne}$ as explained in the supplemental condition 1.
Then, the rest mass current vector, J^μ, is defined as

$$J^\mu := \rho_{\rm ne}\, u^\mu . \tag{7}$$

The relations between the basic quantities and energy-momentum tensor, $T^{\mu\nu}$, of dissipative fluid are

$$\rho_{\rm ne}\,\varepsilon_{\rm ne} = u_\alpha\, u_\beta\, T^{\alpha\beta} \tag{8a}$$

$$q^\mu = -\Delta^{\mu\alpha}\, u^\beta\, T_{\alpha\beta} \tag{8b}$$

$$p_{\rm ne} + \Pi = \frac{1}{3}\,\Delta_{\alpha\beta}\, T^{\alpha\beta} \tag{8c}$$

$$\overset{\circ}{\Pi}{}^{\mu\nu} = \left[\Delta^{\mu\alpha}\,\Delta^{\nu\beta} - \frac{1}{3}\,\Delta^{\mu\nu}\,\Delta^{\alpha\beta}\right] T_{\alpha\beta} , \tag{8d}$$

[4] In this paper, following the textbook of EIT (13; 14), we use the *specific* scalar quantities, which are defined *per unit rest mass*. On the other hand, some references of EIT (9–12) use the *density* of those scalar quantities, which are defined *per unit three-volume* perpendicular to u^μ.

where $\Delta^{\mu\nu}$ is a projection tensor on perpendicular direction to u^μ defined as

$$\Delta^{\mu\nu} := u^\mu\, u^\nu + g^{\mu\nu}\,. \tag{9}$$

These relations (8) are simply the mathematically general decomposition of symmetric tensor $T^{\mu\nu}$. For the observer comoving with the fluid, $\rho_{\rm ne}\varepsilon_{\rm ne}$ is the temporal-temporal component of $T^{\mu\nu}$, q^μ the temporal-spatial component of $T^{\mu\nu}$, $p_{\rm ne}+\Pi$ the trace part of spatial-spatial component of $T^{\mu\nu}$, and $\overset{\circ}{\Pi}{}^{\mu\nu}$ the trace-less part of spatial-spatial component of $T^{\mu\nu}$. Here, note that $p_{\rm ne}$ and Π can not be distinguished by solely the relation (8c). However, we can distinguish $p_{\rm ne}$ and Π, when the equations of state are specified in which the pressure and bulk viscosity play different roles. Furthermore, as explained below, the basic equations of EIT are formulated so that $p_{\rm ne}$ and Π are distinguished and obey different evolution equations. Thus, we find that, given the basic quantities of dissipative fluid, the energy-momentum tensor can be defined as

$$T^{\mu\nu} := \rho_{\rm ne}\,\varepsilon_{\rm ne}\,u^\mu\,u^\nu + 2\,u^{(\mu}q^{\nu)} + (p_{\rm ne}+\Pi)\,\Delta^{\mu\nu} + \overset{\circ}{\Pi}{}^{\mu\nu}\,, \tag{10}$$

where the symmetrization $u^{(\mu}q^{\nu)}$ is defined as

$$u^{(\mu}q^{\nu)} := \frac{1}{2}\,\left(\,u^\mu\,q^\nu + u^\nu\,q^\mu\,\right)\,. \tag{11}$$

From the normalization of u^μ, symmetry $T^{\mu\nu}=T^{\nu\mu}$ and relations (8), we find some constraints on basic quantities of dissipative fluid (11; 12):

$$u^\mu u_\mu \;=\; -1 \tag{12a}$$

$$u^\mu q_\mu \;=\; 0 \tag{12b}$$

$$\overset{\circ}{\Pi}{}^{\mu\nu} \;=\; \overset{\circ}{\Pi}{}^{\nu\mu} \tag{12c}$$

$$u_\nu\,\overset{\circ}{\Pi}{}^{\mu\nu} \;=\; 0 \tag{12d}$$

$$\overset{\circ}{\Pi}{}^{\mu}{}_{\mu} \;=\; 0\,. \tag{12e}$$

Of course, the metric is symmetric $g_{\mu\nu}=g_{\nu\mu}$. These constraints denote that the independent quantities are ten components of $g_{\mu\nu}$, three components of u^μ, three components of q^μ, five components of $\overset{\circ}{\Pi}{}^{\mu\nu}$, five scalars $\rho_{\rm ne}$, $\varepsilon_{\rm ne}$, $p_{\rm ne}$, $T_{\rm ne}$ and Π. Here recall that, according to assumption 3, some non-equilibrium equations of state should exist in order to guarantee the number of independent state variables. Such equations of state may be understood as constraints on state variables.

The ten components of metric $g_{\mu\nu}$ are determined by the Einstein equation,

$$G_{\mu\nu} = 8\pi\,T_{\mu\nu}\,, \tag{13}$$

where $G_{\mu\nu} := R_{\mu\nu} - (1/2)\,R^\alpha{}_\alpha\,g_{\mu\nu}$ is the Einstein tensor, and $R_{\mu\nu}$ is the Ricci curvature tensor. Hence, in the framework of EIT, we need evolution equations to determine the remaining independent sixteen quantities u^μ, q^μ, $\overset{\circ}{\Pi}{}^{\mu\nu}$, $\rho_{\rm ne}$, $\varepsilon_{\rm ne}$, $p_{\rm ne}$, $T_{\rm ne}$ and Π.

Next, let us summarize the sixteen basic equations of EIT other than the Einstein equation. Hereafter, for simplicity, we omit the suffix "eq" of the state variables of fiducial equilibrium state,

$$\rho := \rho_{\rm eq} \quad,\quad \varepsilon := \varepsilon_{\rm eq} \quad,\quad p := p_{\rm eq} \quad,\quad T := T_{\rm eq} \quad,\quad s := s_{\rm eq}\,. \tag{14}$$

The five of the desired sixteen equations of EIT are given by the conservation law of rest mass, $J^{\mu}{}_{;\mu} = 0$, and that of energy-momentum, $T^{\mu\nu}{}_{;\nu} = 0$:

$$\overset{\bullet}{\rho} + \rho\, u^{\mu}{}_{;\mu} = 0 \tag{15a}$$

$$\rho \left[\overset{\bullet}{\varepsilon} + (p+\Pi)\, \overset{\bullet}{V} \right] = -q^{\mu}{}_{;\mu} - q^{\mu}\, \overset{\bullet}{u}_{\mu} - \overset{\circ}{\Pi}{}^{\mu\nu}\, u_{\mu\,;\,\nu} \tag{15b}$$

$$(\rho\,\varepsilon + p + \Pi)\, \overset{\bullet}{u}{}^{\mu} = -\overset{\bullet}{q}{}^{\mu} + q_{\alpha}\, \overset{\bullet}{u}{}^{\alpha}\, u^{\mu} - u^{\alpha}{}_{;\alpha}\, q^{\mu} - q^{\alpha}\, u^{\mu}{}_{;\alpha} - \left[(p+\Pi)_{,\alpha} + \overset{\circ}{\Pi}{}_{\alpha}{}^{\beta}{}_{;\beta} \right] \Delta^{\alpha\mu}\,, \tag{15c}$$

where the non-equilibrium vestiges are reduced to the state variables of fiducial equilibrium state due to the supplemental condition 1, and Eqs.(15) retain only the first order dissipative corrections to the evolution equations of perfect fluid. Here, $\overset{\bullet}{Q}$ is the Lagrange derivative of quantity Q defined by

$$\overset{\bullet}{Q} := u^{\mu}\, Q_{;\mu}\,. \tag{16}$$

And, Eq.(15a) is given by $J^{\mu}{}_{;\mu} = 0$ which is the continuity equation (mass conservation) , Eq.(15b) is given by $u_{\mu} T^{\mu\nu}{}_{;\nu} = 0$ which is the energy conservation and corresponds to the first law of non-equilibrium thermodynamics in the EIT, and Eq.(15c) is given by $\Delta^{\mu\alpha} T_{\alpha}{}^{\beta}{}_{;\beta} = 0$ which is the Euler equation (equation of motion of dissipative fluid).

Here, let us note the relativistic effects and number of independent equations. The relativistic effects are $q^{\mu}\, \overset{\bullet}{u}_{\mu}$ in Eq.(15b), and $(p+\Pi)\, \overset{\bullet}{u}{}^{\mu}$ and the terms including q^{μ} in Eq.(15c). Those terms do not appear in non-relativistic EIT (13; 14). And, due to the constraint of normalization (12a), three components of Euler equation (15c) are independent, and one component is dependent. Totally, the five equations are independent in the set of equations (15).

The nine of desired sixteen equations of EIT are the evolution equations of dissipative fluxes, whose derivation are reviewed in next subsection using the assumptions $1 \sim 4$ and supplemental condition 1. According the next subsection or references of EIT (9; 11; 13; 14), the evolution equations of dissipations are

$$\begin{aligned}
\tau_{\mathrm{h}}\, \overset{\bullet}{q}{}^{\mu} \;=\; & -\left[1 + \lambda\, T^2 \left(\frac{\tau_{\mathrm{h}}}{2\lambda T^2}\, u^{\nu} \right)_{;\nu} \right] q^{\mu} - \lambda\, T\, \overset{\bullet}{u}{}^{\mu} + \tau_{\mathrm{h}} (q^{\nu} \overset{\bullet}{u}_{\nu})\, u^{\mu} \\
& - \lambda\, \Delta^{\mu\nu} \left[T_{,\nu} - T^2 \left\{ \beta_{\mathrm{hb}}\, \Pi_{,\nu} + (1-\gamma_{\mathrm{hb}})\, \Pi\, \beta_{\mathrm{bh}\,,\nu} + \beta_{\mathrm{hs}}\, \overset{\circ}{\Pi}{}_{\nu}{}^{\alpha}{}_{;\alpha} \right.\right. \\
& \left.\left. + (1-\gamma_{\mathrm{hs}})\, \beta_{\mathrm{hs}\,,\alpha}\, \overset{\circ}{\Pi}{}^{\alpha}{}_{\nu} \right\} \right]
\end{aligned} \tag{17a}$$

$$\tau_{\mathrm{b}}\, \overset{\bullet}{\Pi} \;=\; -\left[1 + \zeta\, T \left(\frac{\tau_{\mathrm{b}}}{2\zeta T}\, u^{\mu} \right)_{;\mu} \right] \Pi - \zeta\, u^{\mu}{}_{;\mu} + \zeta\, T \left(\beta_{\mathrm{hb}}\, q^{\mu}{}_{;\mu} + \gamma_{\mathrm{hb}}\, q^{\mu}\, \beta_{\mathrm{hb}\,,\mu} \right) \tag{17b}$$

$$\begin{aligned}
\tau_{\mathrm{s}} \left(\overset{\circ}{\Pi}{}^{\mu\nu} \right)^{\bullet} \;=\; & -\left[1 + 2\,\eta\, T \left(\frac{\tau_{\mathrm{s}}}{4\eta T}\, u^{\alpha} \right)_{;\alpha} \right] \overset{\circ}{\Pi}{}^{\mu\nu} + 2\,\tau_{\mathrm{s}}\, \overset{\bullet}{u}_{\alpha}\, \overset{\circ}{\Pi}{}^{\alpha\,(\mu}\, u^{\nu)} \\
& - 2\,\eta \left[\!\!\left[u^{\mu;\nu} - T \left\{ \beta_{\mathrm{hs}}\, q^{\mu;\nu} + \gamma_{\mathrm{hs}}\, \beta_{\mathrm{hs}}{}^{,\mu}\, q^{\nu} \right\} \right]\!\!\right]^{\circ}\,,
\end{aligned} \tag{17c}$$

where the symbolic operation $[\![A^{\mu\nu}]\!]^{\circ}$ in the last term in Eq.(17c) denotes the traceless symmetrization of a tensor $A^{\mu\nu}$ in the perpendicular direction to u^{μ},

$$[\![A^{\mu\nu}]\!]^{\circ} := \Delta^{\mu\alpha}\,\Delta^{\nu\beta}\,A_{(\alpha\beta)} - \frac{1}{3}\,\Delta^{\mu\nu}\,\Delta^{\alpha\beta}A_{\alpha\beta}\,. \tag{18}$$

We find $\overset{\circ}{\Pi}{}^{\mu\nu} = [\![T^{\mu\nu}]\!]^{\circ}$ by Eq.(8d), and $[\![\overset{\circ}{\Pi}{}^{\mu\nu}]\!]^{\circ} = \overset{\circ}{\Pi}{}^{\mu\nu}$.
The meanings of coefficients appearing in Eq.(17) are:

$$\begin{array}{lcl} \lambda & : & \text{heat conductivity} \\ \zeta & : & \text{bulk viscous rate} \\ \eta & : & \text{shear viscous rate} \\ \tau_{\rm h} & : & \text{relaxation time of heat flux } q^{\mu} \\ \tau_{\rm b} & : & \text{relaxation time of bulk viscosity } \Pi \\ \tau_{\rm s} & : & \text{relaxation time of shear viscosity } \overset{\circ}{\Pi}{}^{\mu\nu}\,, \end{array} \tag{19a}$$

and

$$\begin{array}{lcl} \beta_{\rm hb} & : & \text{interaction coefficient between dissipative fluxes } q^{\mu} \text{ and } \Pi \\ \beta_{\rm hs} & : & \text{interaction coefficient between dissipative fluxes } q^{\mu} \text{ and } \overset{\circ}{\Pi}{}^{\mu\nu} \\ \gamma_{\rm hb} & : & \text{interaction coefficient between thermodynamic forces of } q^{\mu} \text{ and } \Pi \\ \gamma_{\rm hs} & : & \text{interaction coefficient between thermodynamic forces of } q^{\mu} \text{ and } \overset{\circ}{\Pi}{}^{\mu\nu}\,, \end{array} \tag{19b}$$

where the thermodynamic forces of q^{μ}, Π and $\overset{\circ}{\Pi}{}^{\mu\nu}$, which we express respectively by symbols $X^{\mu}_{\rm h}$, $X_{\rm b}$ and $X^{\mu\nu}_{\rm s}$, are the quantities appearing in the bilinear form (3) as $\sigma_{\rm s} = q_{\mu}\,X^{\mu}_{\rm h} + \Pi\,X_{\rm h} + \overset{\circ}{\Pi}_{\mu\nu}\,X^{\mu\nu}_{\rm s}$.
In general, the above ten coefficients are functions of state variables of fiducial equilibrium state. Those functional forms should be determined by some micro-scopic theory or experiment of dissipative fluxes, but it is out of the scop of this paper.
The coefficients in list (19a) are already known in the classic laws of dissipations and Maxwell-Cattaneo laws summarized in appendix 7. Note that the existence of relaxation times of dissipative fluxes make the evolution equations (17) retain the causality of dissipative phenomena. The relaxation time, $\tau_{\rm h}$, is the time scale in which a non-stationary heat flux relaxes to a stationary heat flux. The other relaxation times, $\tau_{\rm b}$ and $\tau_{\rm s}$, have the same meaning for viscosities. These are positive by definition,

$$\tau_{\rm h} > 0 \quad , \quad \tau_{\rm b} > 0 \quad , \quad \tau_{\rm s} > 0\,. \tag{20}$$

Concerning the transport coefficients, λ, ζ and η, the non-negativity of them is obtained by the requirement (4-a) in assumption 4 as explained in next subsection,

$$\lambda \geq 0 \quad , \quad \zeta \geq 0 \quad , \quad \eta \geq 0\,. \tag{21}$$

The coefficients in list (19b) denotes that the EIT includes the interaction among dissipative fluxes, while the classic laws of dissipations and Maxwell-Cattaneo laws do not. (See appendix 7 for a short summary.) Concerning the interaction among dissipative fluxes, Israel (11) has introduced an approximation into the evolution equations (17). Israel ignores the gradients of fiducial equilibrium state variables, as summarized in the end of next

subsection. Then, Eq.(17) can be slightly simplified by discarding terms including the gradients. Those simplified equations are shown in Eq.(34).
Given the meanings of all quantities which appear in Eq.(17), we can recognize a thermodynamical feature of Eq.(17). Recall that the dissipative phenomena are thermodynamically *irreversible processes*. Then, reflecting the irreversible nature, the evolution equations of dissipative fluxes (17) are not time-reversal invariant, i.e. Eq. (17) are not invariant under the replacement, $u^\mu \to -u^\mu$ and $q^\mu \to -q^\mu$.
Here, let us note the relativistic effects and number of independent evolution equations of dissipative fluxes. The relativistic effects are three terms including $\overset{\bullet}{u}{}^\mu$ and three terms of the form $(\bigcirc u^\mu)_{;\mu}$ in right-hand sides of Eq.(17). Those terms disappear in non-relativistic EIT (13; 14). And, due to the constraints in Eqs.(12) except Eq.(12a), the three components of evolution equation (17a) and five components of evolution equation (17c) are independent. Totally, nine equations are independent in the set of equations (17).
From the above, we have fourteen independent evolution equations in Eqs.(15) and (17). We need the other two equations to determine the sixteen quantities which appear in Eqs.(15) and (17). Those two equations, under the supplemental condition 1, are the equations of state of fiducial equilibrium state. They are expressed, for example, as

$$p = p(\varepsilon, V) \quad , \quad T = T(\varepsilon, V)\,. \tag{22}$$

The concrete forms of Eq.(22) can not be specified unless the dissipative matter composing the fluid is specified.
In summary, the basic equations of EIT, under the supplemental condition 1, are Eqs.(15), (17) and (22) with constraints (12), and furthermore the Einstein equation (13) for the evolution of metric. With those basic equations, it has already been known that the causality is retained for dissipative fluids which are thermodynamically stable. Here the "thermodynamic stability" means that, for example, the heat capacity and isothermal compressibility are positive (9). The positive heat capacity and positive isothermal compressibility are the very usual and normal property of real materials. We recognize that *the EIT is a causal hydrodynamics for dissipative fluids made of ordinary matters*.

3.2 Derivation of evolution equations of dissipations

Let us proceed to the derivation of Eqs.(17). In order to obtain them, we refer to the assumption 4 and need the non-equilibrium entropy current vector, $S_{\rm ne}^{\ \mu}$. The entropy current, $S_{\rm ne}^{\ \mu}$, is a member of dissipative fluxes (see assumption 2). Hereafter, we choose q^μ, Π and $\overset{\circ}{\Pi}{}^{\mu\nu}$ as the three independent dissipative fluxes (see assumption 3). Then $S_{\rm ne}^{\ \mu}$ is a dependent state variable and should be expanded up to the second order of independent dissipative fluxes under the supplemental condition 1 (11; 13; 14),

$$S_{\rm ne}^{\ \mu} := \rho_{\rm ne}\, s_{\rm ne}\, u^\mu + \frac{1}{T}\, q^\mu + \beta_{\rm hb}\, \Pi\, q^\mu + \beta_{\rm hs}\, q_\nu\, \overset{\circ}{\Pi}{}^{\nu\mu}\,, \tag{23}$$

where we assume the *isotropic* equations of state which will be explained below, the factor $\rho_{\rm ne}\, s_{\rm ne}$ in the first term is expanded up to the second order of independent dissipative fluxes due to the supplemental condition 1, the second term $T^{-1}q^\mu$ is the first order term of heat flux due to the meaning of "heat" already known in the ordinary equilibrium thermodynamics, and the third and fourth terms express the interactions between heat flux and viscosities as noted in list (19b). These interactions between heat and viscosities are one of significant

properties of EIT, while classic laws of dissipations and Maxwell-Cattaneo laws summarized in appendix 7 do not include these interactions.

Before proceeding to the discussion on the bilinear form of entropy production rate, we should give two remarks on Eq.(23): First remark is on the first order term of heat flux, $T^{-1}q^\mu$. One may think that this term is inconsistent with Eq.(2), since the differential, $\partial(T^{-1}q^\mu)/\partial q^\mu = T^{-1}$, does not vanish at local equilibrium limit. However, recall that the fluid velocity, u^μ, depends on the dissipative fluxes. Then, we expect a relation, $\rho_{\rm ne}\, s_{\rm ne}\,(\partial u^\mu/\partial q^\mu) = -T^{-1}$, by which Eq.(2) is satisfied. The evolution equations of EIT should yield u^μ so that $S_{\rm ne}^{\ \mu}$ satisfies Eq.(2).

Second remark is on the second order terms of dissipative fluxes in Eq.(23), which reflect the notion of isotropic equations of state. Considering a general form of those terms relates to considering a general form of non-equilibrium equations of state. In general, there may be a possibility for non-equilibrium state that equations of state depend on a special direction, e.g. a direction of spinor of constituent particles, a direction of defect of crystal structure in a solid or liquid crystal system, a direction originated from some turbulent structure, and so on, which reflect a rather micro-scopic structure of the system under consideration. If a dependence on such a special direction arises in non-equilibrium equations of state, then the entropy current, $S_{\rm ne}^{\ \mu}$, may depend on some tensors reflecting the special direction, and its most general form up to the second order of independent dissipative fluxes is (9; 12–14)

$$\begin{aligned} S_{\rm ne}^{\ \mu} :=\ & \text{Eq.(23)} + \beta'_{\rm hb}\,\Pi\, A^{\mu\alpha}q_\alpha + \beta'_{\rm hs}\, B_{\alpha\beta}q^\alpha \overset{\circ}{\Pi}{}^{\beta\mu} + \beta''_{\rm hs}\, C^{\alpha\beta\gamma\mu}q_\alpha \overset{\circ}{\Pi}_{\beta\gamma} + \beta'''_{\rm hs}\, D^{\alpha\beta}\overset{\circ}{\Pi}_{\alpha\beta}q^\mu \\ & + \beta'_{\rm bs}\,\Pi\overset{\circ}{\Pi}{}^{\mu\alpha}E_\alpha + \beta''_{\rm hs}\Pi\overset{\circ}{\Pi}_{\alpha\beta}F^{\alpha\beta\mu} + \beta'_{\rm bb}\,\Pi^2\, G^\mu + \beta'_{\rm hh}\, H^\alpha q_\alpha q^\mu + \beta''_{\rm hh}\, I^{\alpha\beta\mu}q_\alpha q_\beta \\ & + \beta'_{\rm ss}\, J_{\alpha\beta\gamma}\overset{\circ}{\Pi}{}^{\alpha\beta}\overset{\circ}{\Pi}{}^{\gamma\mu} + \beta''_{\rm ss}\, K^\mu\overset{\circ}{\Pi}{}^{\alpha\beta}\overset{\circ}{\Pi}_{\alpha\beta}\,, \end{aligned} \tag{24}$$

where $A^{\mu\nu}\cdots K^\mu$ are the tensors reflecting the special direction. Although Eq.(24) is the most general form of $S_{\rm ne}^{\ \mu}$, the inclusion of such a special direction raises an inessential mathematical confusion in following discussions. [5] Furthermore, recall that, usually, such a special direction of *micro*-scopic structure does not appear in ordinary equilibrium thermodynamics which describes the *macro*-scopic properties of the system. Thus, under the supplemental condition 1 which restricts our attention to non-equilibrium states *near* equilibrium states, it may be expected that such a special direction does not appear in non-equilibrium equations of state. Let us assume the *isotropic equations of state* in which the directional dependence does not exist, and adopt Eq.(23) as the equation of state for $S_{\rm ne}^{\ \mu}$. [6]

Here, since a non-equilibrium factor, $\rho_{\rm ne}\, s_{\rm ne}$, appears in Eq.(23), we need to show the non-equilibrium equation of state for it. Adopting the isotropic assumption, the non-equilibrium equation of state (4a) for $s_{\rm ne}$ becomes (13; 14),

$$\rho_{\rm ne}\, s_{\rm ne}(\varepsilon_{\rm ne}, V_{\rm ne}, q^\mu, \Pi, \overset{\circ}{\Pi}{}^{\mu\nu}) = \rho\, s(\varepsilon, V) - a_{\rm h}\, q^\mu\, q_\mu - a_{\rm b}\,\Pi^2 - a_{\rm s}\overset{\circ}{\Pi}{}^{\mu\nu}\overset{\circ}{\Pi}_{\mu\nu}\,, \tag{25}$$

[5] There may be a possibility that the factor tensors are gradients of fiducial equilibrium state variable, e.g. $K^\mu \propto \varepsilon_{\rm ne}^{\prime\mu}$. Those gradients are not micro-scopic quantity. However, in thermodynamics, it is naturally expected that equations of state do not depend on gradients of state variables but depend only on the state variables themselves. Furthermore, if complete nonequilibrium equations of state do not include gradients of state variables, their Tayler expansion can not include gradients in the expansion factors.

[6] When one specifies the material composing the dissipative fluid, and if its non-equilibrium equations of state have some directional dependence, then the same procedure given in Sec. 3.2 provides the basic equations of EIT depending on a special direction.

where the suffix "eq" of state variables of fiducial equilibrium state in right-hand side are omitted as noted in Eq.(14), the expansion coefficients, $a_{\rm h}$, $a_{\rm b}$ and $a_{\rm s}$, are functions of fiducial equilibrium state variables, and the minus sign in front of them expresses that the non-equilibrium entropy is less than the fiducial equilibrium entropy. Concrete forms of those coefficients will be obtained below.

On the specific entropy of fiducial equilibrium state, $s(\varepsilon, V)$, the first law of thermodynamics for fiducial equilibrium state is important in calculating the bilinear form of entropy production rate (3), $T\overset{\bullet}{s} = \overset{\bullet}{\varepsilon} + p\,\overset{\bullet}{V}$. Combining the first law of fiducial equilibrium state with the energy conservation (15b), we find

$$\rho\overset{\bullet}{s} + \frac{1}{T}\,q^{\mu}_{\ ;\mu} = -\frac{1}{T}\left(\,u^{\mu}_{\ ;\mu}\,\Pi + \overset{\bullet}{u}_{\mu} q^{\mu} + u_{\mu;\nu}\,\overset{\circ}{\Pi}{}^{\mu\nu}\,\right), \tag{26}$$

where Eq.(15a) is used in deriving the first term in right-hand side. This relation is used in following calculations.

Given the above preparation, we can proceed to calculation of the bilinear form of entropy production rate. The entropy production rate is defined as the divergence, $\sigma_{\rm s} := S_{\rm ne}{}^{\mu}_{\ ;\mu}$, as already given in assumption 4. Then, according to Eq.(3), $\sigma_{\rm s}$ should be rearranged to the bilinear form (13; 14),

$$\sigma_{\rm s} := S_{\rm ne}{}^{\mu}_{\ ;\mu} = q_{\mu}\,X^{\mu}_{\rm h} + \Pi\,X_{\rm b} + \overset{\circ}{\Pi}_{\mu\nu}\,X^{\mu\nu}_{\rm s}\,, \tag{27}$$

where the factors, $X^{\mu}_{\rm h}$, $X_{\rm b}$ and $X^{\mu\nu}_{\rm s}$, are the thermodynamic forces. To determine the concrete forms of thermodynamic forces, let us carry out the calculation of the divergence, $S_{\rm ne}{}^{\mu}_{\ ;\mu}$ of Eq.(23). We find immediately that the divergence includes the differentials of $\beta_{\rm hb}$ and $\beta_{\rm hs}$ as, $S_{\rm ne}{}^{\mu}_{\ ;\mu} = \Pi\,q^{\mu}\beta_{{\rm hb},\mu} + \overset{\circ}{\Pi}{}^{\mu\nu} q_{\nu}\beta_{{\rm hs},\mu} + \cdots$. The assumptions $1 \sim 4$ can not determine whether the term $\Pi\,q^{\mu}\beta_{{\rm hb},\mu}$ should be put into $q_{\mu}\,X^{\mu}_{\rm h}$ or $\Pi\,X_{\rm b}$ in Eq.(27), and whether the term $\overset{\circ}{\Pi}{}^{\mu\nu} q_{\nu}\beta_{{\rm hs},\mu}$ should be put into $q_{\mu}\,X^{\mu}_{\rm h}$ or $\overset{\circ}{\Pi}_{\mu\nu}\,X^{\mu\nu}_{\rm s}$ in Eq.(27). Hence, we introduce additional factors, $\gamma_{\rm hb}$ and $\gamma_{\rm hs}$, to divide those terms so that the three terms in Eq.(27) become (9)

$$\begin{aligned}
q_{\mu}\,X^{\mu}_{\rm h} &= q_{\mu}\left[\,(1-\gamma_{\rm hb})\,\Pi\,\beta_{\rm hb}{}^{,\mu} + (1-\gamma_{\rm hs})\,\overset{\circ}{\Pi}{}^{\mu\nu}\beta_{{\rm hs},\nu} + \cdots\right] \\
\Pi\,X_{\rm b} &= \Pi\left[\,\gamma_{\rm hb}\,q^{\mu}\beta_{{\rm hb},\mu} + \cdots\right] \\
\overset{\circ}{\Pi}_{\mu\nu}\,X^{\mu\nu}_{\rm s} &= \overset{\circ}{\Pi}_{\mu\nu}\left[\,\gamma_{\rm hs}\,q^{\nu}\beta_{\rm hs}{}^{,\mu} + \cdots\right].
\end{aligned} \tag{28}$$

Note that $\gamma_{\rm hb}$ and $\gamma_{\rm hs}$ are included in thermodynamic forces. The factor $\gamma_{\rm hb}$ connects $X^{\mu}_{\rm h}$ and $X_{\rm b}$, and $\gamma_{\rm hs}$ connects $X^{\mu}_{\rm h}$ and $X^{\mu\nu}_{\rm s}$. Therefore, we can understand that these factors, $\gamma_{\rm hb}$ and $\gamma_{\rm hs}$, are the kind of interaction coefficients among thermodynamic forces as noted in list (19b). Then, using Eqs.(25) and (26), we obtain the concrete forms of X's,

$$\begin{aligned}
X^{\mu}_{\rm h} &= -2\,a_{\rm h}\,\overset{\bullet}{q}{}^{\mu} - \left(a_{\rm h}u^{\alpha}\right)_{;\alpha}\,u^{\mu} - \frac{1}{T}\,\overset{\bullet}{u}{}^{\mu} - \frac{1}{T^2}\,T^{,\mu} \\
&\quad + \beta_{\rm hb}\,\Pi^{,\mu} + (1-\gamma_{\rm hb})\,\beta_{\rm hb}{}^{,\mu}\,\Pi + \beta_{\rm hs}\,\overset{\circ}{\Pi}{}^{\mu\alpha}{}_{;\alpha} + (1-\gamma_{\rm hs})\,\beta_{{\rm hs},\alpha}\,\overset{\circ}{\Pi}{}^{\alpha\mu} \\
X_{\rm b} &= -2\,a_{\rm b}\,\overset{\bullet}{\Pi} - \left(a_{\rm b}u^{\alpha}\right)_{;\alpha}\,\Pi - \frac{1}{T}\,u^{\mu}_{\ ;\mu} + \beta_{\rm hb}\,q^{\mu}_{\ ;\mu} + \gamma_{\rm hb}\,\beta_{{\rm hb},\mu}\,q^{\mu} \\
X^{\mu\nu}_{\rm s} &= -2\,a_{\rm s}\left(\overset{\circ}{\Pi}{}^{\mu\nu}\right)^{\bullet} - \left(a_{\rm s}u^{\alpha}\right)_{;\alpha}\,\overset{\circ}{\Pi}{}^{\mu\nu} - \frac{1}{T}\,u^{\mu;\nu} + \beta_{\rm hs}\,q^{\mu;\nu} + \gamma_{\rm hb}\,\beta_{\rm hb}{}^{,\mu}\,q^{\nu}\,.
\end{aligned} \tag{29}$$

Obviously these thermodynamic forces include $\overset{\bullet}{q}{}^{\mu}$, $\overset{\bullet}{\Pi}$ and $(\overset{\circ}{\Pi}{}^{\mu\nu})^{\bullet}$. Then, as reviewed bellow, making use of this fact and assumption 4 enables us to obtain the evolution equations of dissipative fluxes in the form, $[\text{dissipative flux}]^{\bullet} = \cdots$.
Thermodynamic forces, $X_{\rm h}^{\mu}$ and $X_{\rm s}^{\mu\nu}$ shown in Eq.(29), have some redundant parts. For $X_{\rm h}^{\mu}$, its component parallel to u^{μ} is redundant, because we find $q_{\mu} X_{\rm h}^{\mu} = q^{\mu} (\Delta_{\mu\nu} X_{\rm h}^{\nu})$ due to the constraint (12b). For $X_{\rm s}^{\mu\nu}$, its trace part and components parallel to u^{μ} are redundant, because we find $\overset{\circ}{\Pi}_{\mu\nu} X_{\rm s}^{\mu\nu} = \overset{\circ}{\Pi}_{\mu\nu} [\![X_{\rm s}^{\mu\nu}]\!]^{\circ}$ due to the relation $\overset{\circ}{\Pi}{}^{\mu\nu} = [\![\overset{\circ}{\Pi}{}^{\mu\nu}]\!]^{\circ}$, where the operation $[\![\cdot]\!]^{\circ}$ are defined in Eq.(18). Therefore, Eq.(27) becomes

$$\sigma_{\rm s} := S_{\rm ne}{}^{\mu}{}_{;\mu} = q^{\mu} (\Delta_{\mu\nu} X_{\rm h}^{\nu}) + \Pi X_{\rm b} + \overset{\circ}{\Pi}_{\mu\nu} [\![X_{\rm s}^{\mu\nu}]\!]^{\circ} . \tag{30}$$

This is understood as an equation of state for $\sigma_{\rm s}$. Hence, we obtain the following relations due to supplemental condition 1 and Eq.(2),

$$\Delta_{\mu\nu} X_{\rm h}^{\nu} = b_{\rm h} q_{\mu} \quad , \quad X_{\rm b} = b_{\rm b} \Pi \quad , \quad [\![X_{\rm s}^{\mu\nu}]\!]^{\circ} = b_{\rm s} \overset{\circ}{\Pi}{}^{\mu\nu} , \tag{31}$$

where the coefficients, $b_{\rm h}$, $b_{\rm b}$ and $b_{\rm s}$, are functions of fiducial equilibrium state variables. Concrete forms of them are determined as follows: According to the requirement (4-b) in assumption 4, Eq.(31) should be consistent with existing phenomenologies even in non-relativistic cases. As such reference phenomenologies, we refer to the *Maxwell-Cattaneo laws*, which are summarized in appendix 7. By comparing Eq.(31) with the Maxwell-Cattaneo laws in Eq.(48), the unknown coefficients are determined (13; 14),

$$a_{\rm h} = \frac{\tau_{\rm h}}{2\lambda T^2}, \quad a_{\rm b} = \frac{\tau_{\rm b}}{2\zeta T}, \quad a_{\rm s} = \frac{\tau_{\rm s}}{4\eta T}, \quad b_{\rm h} = \frac{1}{\lambda T^2}, \quad b_{\rm b} = \frac{1}{\zeta T}, \quad b_{\rm s} = \frac{1}{2\eta T} , \tag{32}$$

where λ, ζ, η, $\tau_{\rm h}$, $\tau_{\rm b}$ and $\tau_{\rm s}$ are shown in list (19a). By Eq.(3), non-negativity of coefficients (21) is obtained.
Then, by substituting those coefficients (32) into the concrete forms of thermodynamic forces given in Eq.(29), Eq.(31) are rearranged to the form of evolution equations, $\tau_{\rm h} \overset{\bullet}{q}{}^{\mu} = \cdots$, $\tau_{\rm b} \overset{\bullet}{\Pi} = \cdots$ and $\tau_{\rm s} (\overset{\circ}{\Pi}{}^{\mu\nu})^{\bullet} = \cdots$ (9; 13; 14). These are the evolution equations of dissipative fluxes shown in Eq.(17).
Finally in this section, summarize a discussion given in an original work of EIT (11): Under the supplemental condition 1, the dissipative fluxes appearing in Eqs.(15) and (17) are not so strong. Then, there may be many actual situations that the gradients of fiducial equilibrium state variables are also week. Motivated by this consideration, Israel (11) has introduced an additional supplemental condition:

Supplemental Condition 2 (A strong restriction by Israel)**.** *The order of gradient of any state variables of fiducial equilibrium state is at most the same order with dissipative fluxes,*

$$k \frac{\partial [\text{fiducial equilibrium state variables}]}{\partial x^{\mu}} \lesssim O([\text{dissipative fluxes}]) , \tag{33}$$

where k is an appropriate numerical factor to make the left- and right-hand sides have the same dimension. □

This condition restricts the applicable range of EIT narrower than the supplemental condition 1. However, as discussed by Israel (11), if one adopts this condition, then the evolution equations of dissipative fluxes (17) are simplified by discarding the terms of [dissipative fluxes]×[gradients of fiducial equilibrium state variable],

$$\tau_{\rm h}\,\overset{\bullet}{q}{}^{\mu} = -q^{\mu} - \lambda T\,\overset{\bullet}{u}{}^{\mu} - \lambda\,\Delta^{\mu\nu}\left[\,T_{,\nu} - T^2\left(\,\beta_{\rm hb}\,\Pi_{,\nu} + \beta_{\rm hs}\,\overset{\circ}{\Pi}{}_{\nu}{}^{\alpha}{}_{;\alpha}\,\right)\right] \tag{34a}$$

$$\tau_{\rm b}\,\overset{\bullet}{\Pi} = -\Pi - \zeta\,u^{\mu}{}_{;\mu} + \beta_{\rm hb}\,\zeta\,T\,q^{\mu}{}_{;\mu} \tag{34b}$$

$$\tau_{\rm s}\left(\,\overset{\circ}{\Pi}{}^{\mu\nu}\right)^{\bullet} = -\overset{\circ}{\Pi}{}^{\mu\nu} - 2\,\eta\,[\![\,u^{\mu;\nu} - T\,\beta_{\rm hs}\,q^{\mu;\nu}\,]\!]^{\circ}\,. \tag{34c}$$

However, Hiscock and Lindblom (9) point out that the condition 2 may not necessarily be acceptable, for example, for the stellar structure in which the gradients of temperature and pressure play the important role. Furthermore, as implied by Eq.(17), when the interaction coefficients among thermodynamic forces, $\gamma_{\rm hb}$ and $\gamma_{\rm hs}$, are very large, the terms including differentials $\beta_{{\rm hb},\mu}$ and $\beta_{{\rm hs},\mu}$ can not necessarily be ignored.

4. EIT and radiative transfer

4.1 Overview of one limit of EIT

As mentioned at the end of Sec.3.1, if and only if the dissipative fluid is made of thermodynamically normal matter with positive heat capacity and positive isothermal compressibility (the "ordinary matter"), then the EIT is a causally consistent phenomenology of the dissipative fluid with including interactions among dissipations (9). Then, it is necessary to make a remark on the *hydrodynamic and/or thermodynamic treatment of non-equilibrium radiation field*, because, as will be explained below, a radiation field changes its character according to the situation in which the radiation field is involved. Here the "radiation field" means the matters composed of non-self-interacting particles such as gravitons, neutrinos (if it is massless) and photons (with neglecting the quantum electrodynamical pair creation and annihilation of photons in very high temperature states). Hereafter, the "photon"means the constituent particle of radiation field.

Some special properties of non-equilibrium state of radiation field have been investigated: Wildt (28) found some strange property of entropy production process in the radiation field, and Essex (2; 3) recognized that the bilinear form of $\sigma_{\rm s}$ given in Eq.(3) is incompatible with the non-equilibrium state of radiation field in *optically thin matters*. This denotes that the EIT can not be applied to non-equilibrium radiation fields in optically thin matters. In other words, the formalism of EIT becomes applicable to non-equilibrium radiative transfer at the limit of *vanishing mean-free-path of photons* as considered by Udey and Israel (27) and by Fort and Llebot (4). And no thermodynamic formulation of non-equilibrium radiation field in optically thin matters had not been constructed until some years ago. Then, one of present authors constructed explicitely a *steady state* thermodynamics for a stationary non-equilibrium radiation field in optically thin matters (25), where the energy flow in the non-equilibrium state is stationary. As shown in this section, the steady state thermodynamics for a radiation field, which is different from EIT, is inconsistent with the bilinear form of entropy production rate. Inconsistency of EIT with optically thin radiative transfer is not explicitly recognized in the standard references of EIT (11–14).

Before showing a detailed discussion on non-equilibrium radiation in optically thin matters, let us summarize the point of radiation theory in optically thick matters: The collisionless

nature of photons denotes that, when photons are in vacuum space in which no matter except photons exists, any dissipative flux never arises in the gas of photons (e.g. see §63 in Landau-Lifshitz's textbook (18)). Hence, the traditional theory of radiative energy transfer (17) has been applied to a mixture of a radiation field with a matter such as a dense gas or other continuous medium. In the traditional theory, it is assumed that the medium matter is dense (optically thick) enough to ignore the vacuum region among constituent particles of the matter. Then, the successive absorptions and emissions of photons by constituent particles of medium matter make it possible to assume that the photons are as if in local equilibrium states whose temperatures equal those of local equilibrium states of the dense medium matter. Some extensions of this traditional (local equilibrium) theory to local non-equilibrium radiative transfer in *optically thick* matters have already been considered by, for example, Udey-Israel (27) and Fort-Llebot (4) in the framework of EIT. In their formulations, the local non-equilibrium state of radiation at a spacetime point is determined with referring to the local non-equilibrium state of dense medium matter at the same point, and the successive absorptions and emissions of photons by constituent particles of medium matter mimics the dissipation for radiation field. Due to this mimic dissipation, the EIT's formalism becomes applicable to non-equilibrium radiation field in continuous medium matter (4; 27).

Then, consider a non-equilibrium radiation in optically thin matters: When the mean-free-path of photons is long and we can not neglect the effect of free streaming of photons, the notion of mimic dissipation becomes inappropriate, because photons in the free streaming do not interact with other matters. Then, the evolution of non-equilibrium radiation field with long mean-free-path can never be described in the framework of EIT, since the EIT is the theory designed for *dissipative* fluids. This appears as the inconsistency of bilinear form of entropy production rate (3) with non-equilibrium radiation in optically thin matter, which can be concretely explained with using the steady state thermodynamics for a radiation field (25). The remaining of this section is for the explanation of such inconsistency.

4.2 Inconsistency of EIT with optically thin radiative transfer

A significant case of radiation field in optically thin matters is the radiation field in *vacuum* space, where the "vacuum" means that there exists no matter except a radiation field. As an example of a non-equilibrium radiation in vacuum space or with long mean-free-path of photons, let us investigate the system shown in Fig.1. For simplicity, we consider the case that any effect of gravity is neglected, and our discussion is focused on non-equilibrium physics without gravity. Furthermore, we approximate the speed of light to be infinity, which means that the size of the system shown in Fig.1 is small enough.

In the system shown in Fig.1, a black body is put in a cavity. The inner and outer black bodies are individually in thermal equilibrium states, but those equilibrium states are different, whose equilibrium temperatures are respectively $T_{\rm in}$ and $T_{\rm out}$. In the region enclosed by the two black bodies, there exists no matter except the radiation fields emitted by those black bodies. The photons emitted by the inner black body to a spatial point $\vec{x}$, which propagate through the shaded circle shown in Fig.1, have the temperature $T_{\rm in}$. The other photons emitted by the outer black body have the temperature $T_{\rm out}$. Therefore, although the inner and outer black bodies emit thermal radiation individually, the radiation spectrum observed at a point $\vec{x}$ is not thermal, since the spectrum has different temperatures according to the direction of observation. Furthermore, the directions and solid-angle around a point $\vec{x}$ covered by the photons emitted by inner black body, which is denoted by the shaded circle shown in Fig.1, changes from point to point in the region enclosed by the two black bodies. Hence, the

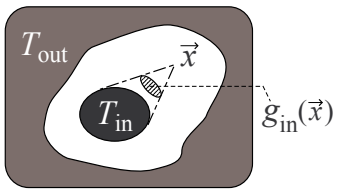

Fig. 1. A steady state of radiation field, which possesses a stationary (steady) energy flow in fixing temperatures $T_{\rm in}$ and $T_{\rm out}$. The non-equilibrium nature of this radiation field arises from the temperature difference. This is a typical model for non-equilibrium radiations in vacuum space or with long mean-free-path of photons. Even if the temperature difference is so small that the energy flux is weak and satisfies Eq.(5), the time evolution of *quasi-steady* processes of this radiation field can not be described by the EIT.

radiation field is in *local* non-equilibrium sates, whose radiation spectrum at one point is not necessarily the same with that at the other point. However, differently from Udey-Israel and Fort-Llebot theories (4; 27), there exists no reference non-equilibrium state of medium matter for the local non-equilibrium states of radiation shown in Fig.1, since the non-equilibrium radiation is in the vacuum region between two black bodies. The non-equilibrium radiation shown in Fig1 is essentially different from those in optically thick medium. The system shown in Fig.1, which is composed of two black bodies and non-equilibrium radiation field between them, can be regarded as a representative toy model of radiative transfer with long mean-free-path of photons, and, when we focus on the non-equilibrium radiation field, it is a typical model of non-equilibrium radiation in vacuum space. Note that, when the temperatures $T_{\rm in}$ and $T_{\rm out}$ are fixed to be constant, the local non-equilibrium state of radiation at $\vec{x}$ has a stationary (steady) energy flux, $\vec{j}(\vec{x})$, due to the temperature difference. A non-equilibrium thermodynamic formulation has already been constructed for those *steady* states of radiation field by one of present authors (25).

When the steady non-equilibrium radiation system shown in Fig.1 is compared with the heat conduction in continuum matters, one may expect that the energy flux in non-equilibrium radiation field, $\vec{j}$, corresponds to the heat flux in non-equilibrium continuum. Hence, according to the assumptions 2, 3 and 4, one may think it natural to assume that $\vec{j}$ is the dissipative flux which is the state variable characterizing non-equilibrium nature of steady states of radiation field in vacuum, and its entropy production rate is expressed by the bilinear form (3). However, from steady state thermodynamics for a radiation field (25), it is concluded that the bilinear form of entropy production rate fails to describe an evolution of the system shown in Fig.1.

In order to review this fact, we need three preparations. First one is that the energy flux, $\vec{j}$, is not a state variable of the system shown in Fig.1. To explain it, recall that, in any thermodynamic theory, there exists a *thermodynamic conjugate* state variable to any state variable. Therefore, if $\vec{j}$ is a state variable, there should exist a conjugate variable to $\vec{j}$. Here, for example, the temperature T which is conjugate to entropy S has a conjugate relation, $T = -\partial F/\partial S$, where F is the free energy. In general, thermodynamic conjugate variable can be obtained as a partial derivative of an appropriate thermodynamic functions such as internal energy, free energy, enthalpy and so on, which are related to each other by Legendre transformations. However, the following relation is already derived in the steady state

thermodynamics for a radiation field (25),

$$\frac{\partial F_{\rm rad}}{\partial j} = 0\,, \tag{35}$$

where $j = |\vec{j}|$ and $F_{\rm rad}$ is the free energy of steady non-equilibrium radiation field. This denotes that thermodynamic conjugate variable to $\vec{j}$ does not exit, and $\vec{j}$ can never be a state variable of the system shown in Fig.1. Hence, if we apply the EIT's formalism to the steady non-equilibrium radiation field, the energy flux, $\vec{j}$, can not appear as a dissipative flux in the assumptions 2, 3 and 4.

Second preparation is to show the steady state entropy and two non-equilibrium state variables which are suitable to characterize the steady non-equilibrium radiation field instead of energy flux. The steady state thermodynamics for a radiation field (25) defines the density of steady state entropy, $s_{\rm rad}(\vec{x})$, as

$$s_{\rm rad}(\vec{x}) := g_{\rm in}(\vec{x})\, s_{\rm eq}(T_{\rm in}) + g_{\rm out}(\vec{x})\, s_{\rm eq}(T_{\rm out})\,, \tag{36}$$

where $g_{\rm in}(\vec{x})$ is the solid-angle of the shaded circle shown in Fig.1 divided by 4π, $g_{\rm out}(\vec{x})$ is the same for the remaining part of solid-angle around $\vec{x}$ satisfying $g_{\rm in} + g_{\rm out} = 1$ by definition, and $s_{\rm eq}(T)$ is the density of equilibrium entropy of thermal radiation with equilibrium temperature T,

$$s_{\rm eq}(T) := \frac{16\,\sigma_{\rm sb}}{3}\, T^3\,, \tag{37}$$

where $\sigma_{\rm sb} := \pi^2/60\hbar^3$ is the Stefan-Boltzmann constant. And, the other two state variables characterizing the steady states are a temperature difference and a kind of entropy difference, defined as

$$\tau_{\rm rad} := T_{\rm in} - T_{\rm out} \tag{38a}$$

$$\psi_{\rm rad}(\vec{x}) := g_{\rm in}(\vec{x})\, g_{\rm out}(\vec{x}) \left[\, s_{\rm eq}(T_{\rm in}) - s_{\rm eq}(T_{\rm out}) \,\right]\,, \tag{38b}$$

where we assume $T_{\rm in} > T_{\rm out}$ without loss of generality. If we apply the EIT's formalism to the system shown in Fig.1, the state variables characterizing the steady non-equilibrium radiation, $\tau_{\rm rad}$ and $\psi_{\rm rad}$, should be understood as the dissipative fluxes in the assumptions 2, 3 and 4.

Third preparation is the notion of *quasi-steady process*. When the temperatures of inner and outer black bodies, $T_{\rm in}$ and $T_{\rm out}$, are kept constant, the non-equilibrium state of radiation field shown in Fig.1 is stationary. However, if the whole system composed of two black bodies and radiation field between them is isolated from the outside of outer black body, then the whole system should relax to an equilibrium state in which the two black bodies and radiation field have the same equilibrium temperature. If the relaxation process proceeds so slowly, it is possible to approximate the time evolution of the slow relaxation as follows: The inner black body is in thermal equilibrium state of equilibrium temperature $T_{\rm in}(t)$ at *each* moment of time t during the relaxation process. This means that the thermodynamic state of inner black body evolves on a sequence of equilibrium states in the space of thermodynamic states. This is the so-called quasi-static process in the ordinary equilibrium thermodynamics. Therefore, we can approximate the evolution of inner body by a quasi-static process. Also the evolution of outer black body is a quasi-static process on a sequence of equilibrium states which is different from that of inner black body's evolution. Then, at each moment of the slow relaxation process, the thermodynamic state of radiation field between two black bodies

is regarded as a steady non-equilibrium state which possesses the state variables given in Eqs.(36) and (38). This implies that, during the slow relaxation process of the whole system, the non-equilibrium radiation field evolves on a sequence of steady non-equilibrium states in the space of thermodynamic states. This is the quasi-steady process of non-equilibrium radiation field.

Given the above three preparations, we can show the inconsistency of EIT's formalism with non-equilibrium radiation fields in vacuum or with long mean-free-path of photons: To show it, we try to apply the EIT's formalism to the system shown in Fig.1, and will result in a failure. In order to satisfy the supplemental condition 1, which requires a sufficiently weak energy flux such as the inequality (5) for dissipative matters, we consider the case with a sufficiently small temperature difference between two black bodies,

$$T_{\rm in} = T_{\rm out} + \delta T\,, \tag{39}$$

where $\tau_{\rm rad} = \delta T \ll e_{\rm rad}$, and $e_{\rm rad}$ is the energy density of steady non-equilibrium radiation field whose explicit definition (25) is not necessary here. Then, let us isolate the whole system composed of two black bodies and non-equilibrium radiation field from the outside of outer black body. The isolated whole system relaxes to an equilibrium state. Here, we focus our attention to the case of slow evolution of the relaxation process, which is regarded as a quasi-steady process. In this case, the time evolutions of temperatures are described by quantities, $T_{\rm out}(t)$ and $\delta T(t)$, where t is the time during the relaxation process. Under the assumption that the EIT's formalism works well for non-equilibrium radiation fields in vacuum or with long mean-free-path of photons, the time evolutions of $T_{\rm out}(t)$ and $\delta T(t)$ should be determined by the EIT's formalism, in which the evolution equations of dissipative fluxes are obtained from the entropy production rate as reviewed in Sec. 3.2. Due to the requirement (4-b) in assumption 4, the entropy production rate of the relaxation process at time t at point $\vec{x}$, $\sigma_{\rm rad}(t,\vec{x})$, should be expressed by the bilinear form with using $\tau_{\rm rad}$ and $\psi_{\rm rad}$,

$$\sigma_{\rm rad} = \tau_{\rm rad}\, X_\tau + \psi_{\rm rad}\, X_\psi\,, \tag{40}$$

where X_τ and X_ψ are respectively thermodynamic forces of $\tau_{\rm rad}$ and $\psi_{\rm rad}$. Then, because Eq.(40) is a non-equilibrium equation of state for $\sigma_{\rm rad}$, the supplemental condition 1 together with Eq.(2) gives the relations,

$$\begin{aligned} X_\tau(t,\vec{x}) &= \lambda_\tau(t,\vec{x})\,\tau_{\rm rad}(t), \\ X_\psi(t,\vec{x}) &= \lambda_\psi(t,\vec{x})\,\psi_{\rm rad}(t,\vec{x})\,, \end{aligned} \tag{41}$$

where λ_τ and λ_ψ are functions of fiducial equilibrium state variables which depend on t and $\vec{x}$, and their non-negativity, $\lambda_\tau \geq 0$ and $\lambda_\psi \geq 0$, are obtained by the requirement (4-a) in assumption 4.

On the other hand, using the explicit form of $s_{\rm rad}$ in Eq.(36), $\sigma_{\rm rad}$ is given by

$$\begin{aligned} \sigma_{\rm rad}(t,\vec{x}) &:= \frac{\partial s_{\rm rad}(t,\vec{x})}{\partial t} \\ &= 16\,\sigma_{\rm sb}\left[\, g_{\rm in}(\vec{x})\,T_{\rm in}(t)^2\,\frac{{\rm d}T_{\rm in}(t)}{{\rm d}t} + g_{\rm out}(\vec{x})\,T_{\rm out}(t)^2\,\frac{{\rm d}T_{\rm out}(t)}{{\rm d}t}\,\right], \end{aligned} \tag{42}$$

where $T_{\rm in}(t) = T_{\rm out}(t) + \delta T(t)$. Here, one may think that $\sigma_{\rm rad}$ should include an entropy production due to the evolution of two black bodies. But, at the point $\vec{x}$ in the region enclosed

by two black bodies, there exists only the non-equilibrium radiation field and the entropy production at that point should be due only to the non-equilibrium radiation field. Therefore, $\sigma_{\rm rad}$ does not include contributions of entropies of black bodies.
In order to obtain the explicit forms of X_τ and X_ψ from $\sigma_{\rm rad}$ in Eq.(42), we need to replace the pair of quantities $(T_{\rm out} , \delta T)$ in Eq.(42) with the pair $(\tau_{\rm rad} , \psi_{\rm rad})$. This replacement is carried out with the relations, $\tau_{\rm rad} = \delta T$ and $\psi_{\rm rad} \simeq 16 \sigma_{\rm sb} g_{\rm in} g_{\rm out} [T_{\rm out}^2 \delta T + T_{\rm out} \delta T^2]$ up to $O(\delta T^2)$ due to supplemental condition 1. Then, Eq.(42) is rearranged to

$$\sigma_{\rm rad} = \frac{1}{D} \left[\tau_{\rm rad} Z_\tau + \psi_{\rm rad} Z_\psi + \tau_{\rm rad} \psi_{\rm rad} Z_{\tau\psi} \right] , \tag{43a}$$

where

$$Z_\tau := 16 \sigma_{\rm sb} g_{\rm in} g_{\rm out} \tau_{\rm rad}^3 \left(A - 2 \sigma_{\rm sb} g_{\rm in} g_{\rm out} \tau_{\rm rad}^2 \right) \left[\frac{\partial \psi_{\rm rad}}{\partial t} + 16 \sigma_{\rm sb} g_{\rm in} g_{\rm out} \tau_{\rm rad}^2 \frac{{\rm d}\tau_{\rm rad}}{{\rm d}t} \right] \tag{43b}$$

$$Z_\psi := - A \psi_{\rm rad} \frac{{\rm d}\tau_{\rm rad}}{{\rm d}t} \tag{43c}$$

$$Z_{\tau\psi} := \left[A + 2 \sigma_{\rm sb} g_{\rm in} g_{\rm out} (1 - 4 g_{\rm out}) \tau_{\rm rad}^2 \right] \left[\frac{\partial \psi_{\rm rad}}{\partial t} + 16 \sigma_{\rm sb} g_{\rm in} g_{\rm out} \tau_{\rm rad}^2 \frac{{\rm d}\tau_{\rm rad}}{{\rm d}t} \right] + 2 \sigma_{\rm sb} g_{\rm in} g_{\rm out} \tau_{\rm rad} \psi_{\rm rad} \frac{{\rm d}\tau_{\rm rad}}{{\rm d}t} \tag{43d}$$

$$D := 8 g_{\rm in} g_{\rm out} \tau_{\rm rad}^2 A (A - 2 \sigma_{\rm sb} g_{\rm in} g_{\rm out} \tau_{\rm rad}^2) \tag{43e}$$

$$A := \sqrt{\sigma_{\rm sb} g_{\rm in} g_{\rm out} \tau_{\rm rad} (4 \sigma_{\rm sb} g_{\rm in} g_{\rm out} \tau_{\rm rad}^3 + \psi_{\rm rad})} . \tag{43f}$$

Therefore, with introducing an supplemental factor $\gamma_{\rm rad}$, we obtain explicit forms of thermodynamic forces as

$$X_\tau = \frac{1}{D} \left[Z_\tau + \gamma_{\rm rad} \psi_{\rm rad} Z_{\tau\psi} \right] \quad , \quad X_\psi = \frac{1}{D} \left[Z_\psi + (1 - \gamma_{\rm rad}) \tau_{\rm rad} Z_{\tau\psi} \right] , \tag{44}$$

where $\gamma_{\rm rad}$ should be generally a function of fiducial equilibrium state variables which depend on t and $\vec{x}$.
Hence, from Eqs.(41) and (44), we obtain two equations,

$$D \lambda_\tau \tau_{\rm rad} = Z_\tau + \gamma_{\rm rad} \psi_{\rm rad} Z_{\tau\psi} \quad , \quad D \lambda_\psi \psi_{\rm rad} = Z_\psi + (1 - \gamma_{\rm rad}) \tau_{\rm rad} Z_{\tau\psi} . \tag{45}$$

Here, recall that we are now seeking the evolution equations of $T_{\rm out}(t)$ and $\delta T(t) = \tau_{\rm rad}(t)$, which should be ordinary differential equations about time t. However, it is improbable to adjust the factors, $\gamma_{\rm rad}(t, \vec{x})$, $\lambda_\tau(t, \vec{x})$ and $\lambda_\psi(t, \vec{x})$, so as to exclude the $\vec{x}$-dependence from Eq.(45) and yield the ordinary differential equations about t. Thus, evolution equations of $T_{\rm out}(t)$ and $\delta T(t)$ can not be obtained in the framework of EIT. We conclude that the EIT's formalism fails to describe non-equilibrium radiation field in vacuum or with long mean-free-path of photons.
As explained above, EIT is not applicable to optically thin radiative transfer. However, a thermodynamic formulation for a stationary non-equilibrium radiation field in optically thin matters, which is different from EIT, has been constructed (25). On the other hand, some efforts for describing non-equilibrium radiative transfer in optically thin astrophysical systems are now under the challenge, in which the so-called equation of radiative transfer is solved numerically under suitable approximations and assumptions (e.g. see a

spatially tree-dimensional simulation for pseudo-Newtonian model by Kato, Umemura and Ohsuga (16)). However, thermodynamic and/or hydrodynamic formulation of *non-stationary* non-equilibrium radiation field in optically thin matters remains as an open and challenging issue.

5. Concluding remark

We have provided a comprehensive understanding of EIT, which is summarized in the basic assumptions and additional supplemental conditions shown in Sec.2. Also the limit of EIT, which is not explicitly recognized in standard references of EIT (11; 13; 14), has been summarized in Sec.4. Then, we end this chapter with the following remark on a tacit understanding common to EIT and classic laws of dissipations (Navier-Stokes and Fourier laws).

In the EIT, while thermodynamic state variables are treated via the second order dissipative perturbation as shown in supplemental condition 1, the dynamical variable (fluid velocity) is not subjected to the dissipative perturbation and remains as a function of independent thermodynamic state variables, $u^\mu(\varepsilon_{\rm ne}, V_{\rm ne}, q^\alpha, \Pi, \overset{\circ}{\Pi}{}^{\alpha\beta})$. This implies that we have a tacit understanding as follows: Weak dissipative fluxes under supplemental condition 1 can raise a dissipative flow whose fluid velocity is essentially different from any fluid velocity of a perfect fluid's flow and can not be regarded as a perturbation of a perfect fluid's flow. If such a dissipative flow exits, then it can be described by the evolution equations (15) and (17). However, if some dissipative flow with weak dissipative fluxes is a perturbative flow of a perfect fluid's flow, then we should subject $u^\mu(\varepsilon_{\rm ne}, V_{\rm ne}, q^\alpha, \Pi, \overset{\circ}{\Pi}{}^{\alpha\beta})$ to the dissipative perturbation, $u^\mu = u^\mu_{\rm (p)}(\varepsilon_{\rm eq}, V_{\rm eq}) + \delta u^\mu$, where δu^μ is the velocity perturbation due to weak dissipative fluxes and $u^\mu_{\rm (p)}$ is the flow of a back-ground perfect fluid determined independently of dissipative fluxes. In this case, the EIT's basic equations (15) and (17) should also be rearranged into a perturbative form. (The present author is writing a paper of the dissipative perturbation of fluid velocity.)

Note that the classic laws of dissipations are extracted from EIT's basic equations (15) and (17) by the limiting operation, $\tau_{\rm h,b,s} \to 0$ and $\beta_{\rm hb,hs} \to 0$ (vanishing relaxation time and interaction among dissipative fluxes). This means that the classic laws are also restricted to weak dissipations (in non-relativistic case). Thus, the remark given in previous paragraph is also true of the classic laws of dissipations.

6. Acknowledgement

This work is supported by the grant of Daiko Foundation [No.9130], and partly by the Grant-in-Aid for Scientific Research Fund of the Ministry of Education, Culture, Sports, Science and Technology, Japan [Young Scientists (B) 19740149].

7. Appendix

A. Non-relativistic phenomenology of heat flux and viscosities

This appendix summarizes non-relativistic phenomenology of heat flux and viscosities. In this appendix, tensors are expressed as three dimensional quantities on three dimensional Euclidean space. The classic laws of dissipations for heat flux and viscosities are summarized

by the following three relations:

$$\text{Fourier law} \ : \ \vec{q} = -\lambda \vec{\nabla} T \tag{46a}$$

$$\text{Stokes law} \ : \ \Pi = -\zeta \vec{\nabla} \cdot \vec{v} \tag{46b}$$

$$\text{Newton law} \ : \ \overset{\circ}{\Pi}_{ij} = -2\eta \overset{\circ}{v}_{ij} , \tag{46c}$$

where T is the local equilibrium temperature, $\vec{q}$ and λ are respectively the heat flux and heat conductivity, Π and ζ are respectively the bulk viscosity and bulk viscous rate, $\overset{\circ}{\Pi}_{ij}$ and η are respectively the shear viscosity and shear viscous rate, and $\vec{v}$ and $\overset{\circ}{v}_{ij}$ are respectively the fluid velocity and shear velocity tensor defined as

$$\overset{\circ}{v}_{ij} := \partial_{(i} v_{j)} - \frac{1}{3} (\vec{\nabla} \cdot \vec{v}) \, g_{ij} , \tag{47}$$

where g_{ij} is the metric of Euclidean space. Navier-Stokes equation is obtained by substituting Stokes and Newton laws into the non-relativistic version of Euler equation (15c), in which the second and third terms in left-hand side and the terms including q^μ in right-hand side are the relativistic effects and disappear in non-relativistic case.

It should be emphasized that time derivatives of dissipative fluxes $\vec{q}$, Π and $\overset{\circ}{\Pi}_{ij}$ are not included in Eq.(46). This means that the classic laws of dissipations are phenomenological relations under the assumption that relaxation times of dissipative fluxes are zero. For example, it is assumed in the Fourier law that a non-stationary heat flux, $\vec{q}(t, \vec{x})$, relaxes *instantaneously* to a stationary one, $\vec{q}(\vec{x})$, where $\vec{x}$ is the spatial coordinates. Therefore, the retarded effects of dissipative fluxes are ignored in the classic laws of dissipations. This results in an infinitely fast propagation of perturbation of dissipative fluxes (13; 14). Hence, Eq.(46) can not describe dynamical dissipative phenomena whose dynamical time scale is comparable to the relaxation time scale of dissipative fluxes. This is the limit of Eq.(46) in either non-relativistic and relativistic cases. Especially in relativistic cases, Eq.(46) violates the causality of dissipative phenomena.

In order to consider the retarded effects of dissipative fluxes, the simplest modification of Eq.(46) is to introduce the time derivative (Lagrange derivative) of dissipative fluxes. This simple modification yields the phenomenological relations, which is called *Maxwell-Cattaneo* laws (13; 14):

$$\tau_{\rm h} \frac{{\rm d}\vec{q}}{{\rm d}t} + \vec{q} \, = \, -\lambda \vec{\nabla} T \quad , \quad \tau_{\rm b} \frac{{\rm d}\Pi}{{\rm d}t} + \Pi \, = \, -\zeta \vec{\nabla} \cdot \vec{v} \quad , \quad \tau_{\rm s} \frac{{\rm d}\overset{\circ}{\Pi}_{ij}}{{\rm d}t} + \overset{\circ}{\Pi}_{ij} \, = \, -2\eta \overset{\circ}{v}_{ij} , \tag{48}$$

where ${\rm d}Q/{\rm d}t \, = \, \partial Q/\partial t + (\vec{v} \cdot \vec{\nabla}) Q$ is the Lagrange derivative in three dimensions, τ's are the relaxation times of dissipative fluxes. The finite speed of propagation of dissipative perturbation can be obtained by these laws. However, note that the three phenomenological relations in Maxwell-Cattaneo laws (48) are independent each other. Therefore, the heating of fluid due to viscous flow and the occurrence of viscous flow due to heat flux can not be described by Eq.(48). This means that the interactions among dissipative fluxes are not introduced in the Maxwell-Cattaneo laws. On the other hand, the EIT includes not only the finite propagation speed of dissipative effects but also the interactions among dissipative fluxes, which are represented by the coefficients in lists (19). Furthermore, it is theoretically important to emphasize that, while the Maxwell-Cattaneo laws in Eq.(48) lack a systematic

way how to add time derivative (Lagrange derivative) of dissipative fluxes, *the framework of EIT gives the systematic method of introducing the Lagrange derivative of dissipative fluxes into their evolution equations*. The EIT is extendible to the other dissipation mechanisms such as diffusion among several components of fluid particles and electro-magnetic dissipation in plasma fluid (13; 14). Accepting EIT seems to be more promising than accepting Maxwell-Cattaneo laws.

B. Covariant derivative

On flat space, e.g. two dimensional Euclidean space $\mathbf{R}^2$, the derivative of a vector field V^a ($a = 1, 2$ expressing the coordinates on $\mathbf{R}^2$),

$$\frac{\partial V^a}{\partial x^b} := \lim_{\delta x^b \to 0} \frac{V^a(x^b + \delta x^b) - V^a(x^b)}{\delta x^b}\,, \tag{49}$$

is defined with using the notion of "parallel transport" along x^b-axis. In Eq.(49), the vector at point of $x^b + \delta x^b$ is parallel transported to the point of x^b along x^b-axis, then the difference between the transported vector and the original vector at x^b is calculated.
On curved spacetime, the "parallel transport" is defined so as to match with the "curved shape" of spacetime. The metic, which is the tensor field $g_{\mu\nu}$ of second rank, expresses the curved shape of the spacetime, where μ and ν denote the components of metric like V^a of a vector in the previous paragraph. The length, ds, of the spacetime between infinitesimally near points x^μ and $x^\mu + dx^\mu$ is given as,

$$ds^2 = g_{\mu\nu}\, dx^\mu\, dx^\nu\,, \tag{50}$$

where left-hand side is the square of length ds^2, and x^μ denotes the coordinates on the spacetime. (For example, for two dimensional Minkowski spacetime, $ds^2 = -dt^2 + dx^2$ with "rectangular coordinates" (t, x), which denotes the components of metric, $g_{\mu\nu} = \mathrm{diag.}(-1, 1)$ where diag. means the "diagonal matrix form".) Then, in following the standard consideration in differential manifold, the covariant derivative of a vector field W^μ is given as,

$$W^\mu_{;\nu} := \lim_{\delta x^\nu \to 0} \frac{\mathcal{T}_{x^\nu}[W^\mu(x^\nu + \delta x^\nu)] - W^\mu(x^\nu)}{\delta x^\nu}\,, \tag{51}$$

where $\mathcal{T}_{x^\nu}[W^\mu]$ is the parallel transport of W^μ to point x^ν along x^ν-axis in curved spacetime. The parallel transport is explicitly expressed with using the metric, and results in

$$W^\mu_{;\nu} = W^\mu_{,\nu} + \Gamma^\mu_{\nu\alpha} W^\alpha\,, \tag{52}$$

where the Einstein's rule of contraction (the same indices appearing in upper and lower positions are summed, e.g. $W^\mu X_\mu = W^0 X_0 + W^1 X_1 + W^2 X_2 + W^3 X_3$ for coordinates (x^0, x^1, x^2, x^3)) is used, $\Gamma^\mu_{\nu\alpha}$ is the so-called Christoffel symbol given as

$$\Gamma^\mu_{\nu\alpha} := \frac{1}{2}\, g^{\mu\beta} \left(g_{\nu\beta\,,\alpha} + g_{\beta\alpha\,,\nu} - g_{\nu\alpha\,,\beta} \right), \tag{53}$$

and the comma denotes the formal calculation of partial derivative,

$$W^\mu_{,\nu} := \lim_{\delta x^\nu \to 0} \frac{W^\mu(x^\nu + \delta x^\nu) - W^\mu(x^\nu)}{\delta x^\nu}\,. \tag{54}$$

In flat spacetime, $\Gamma^{\alpha}_{\mu\nu} = 0$, and the covariant derivative (52) reduces to the partial derivative (49). Some important results of calculation in differential geometry are

$$W_{\mu\,;\nu} := g_{\mu\alpha}W^{\alpha}_{\ ;\nu} = W_{\mu\,,\nu} - \Gamma^{\beta}_{\mu\nu}W_{\beta} \quad (\, W_{\mu} := g_{\mu\alpha}W^{\alpha}\,) \tag{55a}$$

$$Y^{\mu\nu}_{\ \ ;\lambda} = Y^{\mu\nu}_{\ \ ,\lambda} + \Gamma^{\mu}_{\lambda\alpha}Y^{\alpha\nu} + \Gamma^{\nu}_{\lambda\alpha}Y^{\mu\alpha} \tag{55b}$$

$$Y^{\mu}_{\ \nu\,;\lambda} := g_{\nu\alpha}Y^{\mu\alpha}_{\ \ ;\lambda} = Y^{\mu}_{\ \nu\,,\lambda} + \Gamma^{\mu}_{\beta\lambda}Y^{\beta}_{\ \nu} - \Gamma^{\beta}_{\nu\lambda}Y^{\mu}_{\ \beta} \tag{55c}$$

$$Y_{\mu\nu\,;\lambda} := g_{\mu\alpha}Y^{\alpha}_{\ \nu;\lambda} = Y_{\mu\nu\,,\lambda} - \Gamma^{\beta}_{\mu\lambda}Y_{\beta\nu} - \Gamma^{\beta}_{\nu\lambda}Y_{\mu\beta}\,, \tag{55d}$$

and the metric is invariant under covariant derivative,

$$g_{\mu\nu\,;\lambda} = 0\,. \tag{55e}$$

8. References

[1] Doeleman S.S. et al (2008). Event-horizon-scale structure in the supermassive black hole candidate at the Galactic Centre, *Nature* 455: 78

[2] Essex C. (1984). Radiation and the violation of bilinearity in the thermodynamics of irreversible processes, *Planet.Space.Sci.* 32: 1035

[3] Essex C. (1990). Radiation and the Continuing Failure of the Bilinear Formalism, *Advances in Thermodynamics* 3: 435

[4] Fort J. & Llebot J.E. (1996). Radiative transfer in the framework of extended irreversible thermodynamics, *J.Phys.A:Math.Gen.* 29: 3427

[5] Frank J., King A. & Raine D. (2002). *Accretion Power in Astrophysics (3rd Edition)*, Cambridge Univ. Press

[6] Herrera L. & Santos N.O. (1997). Thermal evolution of compact objects and relaxation time, *Man.Not.R.Astron.Soc.* 287: 161

[7] Herrera L., Prisco A.Di & Ospino J. (2006). Some analytical models of radiating collapsing spheres, *Phys.Rev.* D74: 044001

[8] Herrera L., Prisco A.Di, Fuenmayor E. & Troconis O. (2009). Dynamics of viscous dissipative gravitational collapse: A full causal approach, *Int.J.Mod.Phys.* D18: 129

[9] Hiscock W.A. & Lindblom L. (1983). Stability and Causality in Dissipative Relativistic Fluids, *Ann.Phys.* 151: 466

[10] Hiscock W.A. & Lindblom L. (1988). Nonlinear pathologies in relativistic heat-conducting fluid theories, *Phys.Lett.* A131: 509

[11] Israel W. (1976). Nonstationary Irreversible Thermodynamics: A Causal Relativistic Theory, *Ann.Phys.* 100: 310

[12] Israel W. & Stewart J.M. (1979). Transient Relativistic Thermodynamics and Kinetic Theory, *Ann.Phys.* 118: 341

[13] Jou D., Casas-Vazquez J. & Lebon G. (1988). Extended Irreversible Thermodynamics, *Rep.Prog.Phys.* 51: 1105

[14] Jou D., Casas-Vazquez J. & Lebon G. (2001). *Extended Irreversible Thermodynamics, 3rd Edition*, Springer Verlag, Berlin

[15] Kato S., Fukue J. & Mineshige S. (2008) *Black-Hole Accretion Disks*, Kyoto Univ. Press

[16] Kato Y., Umemura M. & Ohsuga K. (2009). Three-dimensional Radiative Properties of Hot Accretion Flows on to the Galactic Center Black Hole, *Mon.Not.R.Astron.Soc.* 400: 1742

[17] Kippenhahn R. & Weigert A. (1994). *Stellar Structure and Evolution*, Springer
[18] Landau L.D. & Lifshitz E.M. (1980). *Statistical Physics. Part I*, Pergamon
[19] Landau L.D. & Lifshitz E.M. (1987). *Fluid Mechanics (2nd Edition)*, Butterworth-Heinemann
[20] Miyoshi M., Kameno S. & Horiuchi S. (2007). An Approach Detecting the Event Horizon of Sgr.A*, *Publ. Natl. Astron. Obs. Japan* 10: 15
[21] Pessah M.E., Chan C. & Psaltis D. (2006). The signature of the magnetorotational instability in the Reynolds and Maxwell stress tensors in accretion discs, *Mon.Not.R.Astron.Soc.* 372: 183
[22] Pessah M.E., Chan C. & Psaltis D. (2006). A Local Model for Angular Momentum Transport in Accretion Disks Driven by the Magnetorotational Instability, *Phys.Rev.Lett.* 97: 221103
[23] Peitz J. & Appl S. (1988). 3+1 formulation of non-ideal hydrodynamics, *Mon.Not.R.Astron.Soc.* 296: 231
[24] Psaltis D. (2008). Probes and Tests of Strong-Field Gravity with Observations in the Electromagnetic Spectrum, *Living Rev.Rel.* 11: 9
[25] Saida H. (2005). Two-temperature steady state thermodynamics for a radiation field, *Physica* A356: 481
[26] Shakura N.I. & Sunyaev R.A. (1973). Black Holes in Binary Systems. Observational Appearance, *Astron.Astrophys.* 24: 337
[27] Udey N. & Israel W. (1982). General relativistic radiative transfer: the 14-moment approximation, *Mon.Not.R.Astron.Soc.* 199: 1137
[28] Wildt R. (1972). Thermodynamics of the gray atmosphere. IV. Entropy transfer and production, *Astrophys.J.* 174: 69

5

Kinetics and Thermodynamics of Protein Folding

Hongxing Lei[1,2] and Yong Duan[2,3]
[1]*Beijing Institute of Genomics, Chinese Academy of Sciences, Beijing*
[2]*UC Davis Genome Center and Department of Applied Science, One Shields Avenue, Davis*
[3]*College of Physics, Huazhong University of Science and Technology, Wuhan*
[1,3]*China*
[2]*USA*

1. Introduction

Proteins are the major functional elements in the living cells. Genetic information is stored in DNA. To release this information, DNA needs to be transcribed into mRNA which in turn is translated into protein. The alphabets are four bases for DNA and twenty amino acids for protein. The genetic code was revealed in 1950s with every amino acid coded by three consecutive bases. However, the amino acid sequence is only the primary structure of proteins. For proteins to be functional, the primary structure needs to fold into tertiary structure which is the optimal packing of secondary structures, namely alpha-helix and beta-sheet. In some cases, the tertiary structures of several proteins or subunits need to come together and form quaternary structure. The so-called "protein folding" problem mainly concerns the detailed physical transition process from primary structure to tertiary structure.

Protein folding mechanism consists of two major issues: kinetics and thermodynamics. Thermodynamically, the native state is the dominant and most stable state for proteins. Kinetically, however, nascent proteins take very different routes to reach the native state. Both issues have been extensively investigated by experimental as well as theoretical studies. The pioneering work by Christian Anfinsen in 1957 led to the creation and dominance of the "thermodynamic hypothesis" (also called "Anfinsen's dogma") which states that the native state is unique, stable and kinetically accessible free energy minimum(Anfinsen 1973). Under this guidance, many works have been done to pursue the illusive kinetically accessible folding pathways. One of the most famous earlier example is the "Levinthal's paradox" presented by Cyrus Levinthal in 1968, which states that the conformational space of proteins is so large that it will take forever for proteins to sample all the possible conformations before finding the global minimum(Levintha.C 1968). This essentially eliminated the possibility of global conformational search and pointed to the optimized folding pathways.

Towards this end, several well-known theories have been presented. The "framework theory" or similar "diffusion-collision theory" states that the formation of secondary structures is the first step and foundation of the global folding(Karplus and Weaver 1994). The "nucleation condensation theory", on the other hand, emphasizes the contribution from

specific global contact as the initiation point of both secondary structure formation and global folding(Fersht 1995). In contrast to the emphasis on native contacts -- global or local— in these two theories, the "hydrophobic hydration theory" states that the general repulsion between hydrophobic residues and water environment drives the spatial redistribution of polar and non-polar residues and the eventual global folding(Dill 1990). In the more recent "funnel theory", the kinetics and thermodynamics of protein folding are better illustrated as funnel-shaped where both conformational space (entropy) and energy (enthalpy) gradually decrease and numerous kinetic traps exist en route to the global folding(Bryngelson, Onuchic et al. 1995). However, the driving force for protein folding is not specified in this theory.

In order to prove or disprove any theory, experimental evidence is needed. There are several techniques developed or applied to protein folding problem. First, the structure of the investigated protein needs to be solved by X-ray crystallography or NMR (nuclear magnetic resonance). High resolution X-ray structure is preferred. However, many of the model proteins can not be crystallized, therefore only NMR structures are available. Circular dichroism (CD) is one of the classical techniques for protein folding study. The proportion of secondary structures can be reflected in CD spectrum. The change of CD spectrum under different temperature or denaturant concentration can be used to deduce melting temperature or unfolding free energy. To study the fast folding process, however, CD itself is insufficient. Fast, time-resolved techniques include ultrafast mixing, laser temperature jump and many others. Other than CD, natural or designed fluorescence probes can be used to monitor the folding process. It should be noted that the "real" folding process may not be reflected with high fidelity in these folding experiments due to the artificial folding environment. In the living cells, proteins are synthesized on ribosome one residue at a time and the final products exist in a crowded physiological condition. In the folding experiments, however, proteins stay in free artificial solution and undergo various perturbations such as denaturation. In addition, fluorescence signal of specific probes can not be simply interpreted as the global protein folding, rather it only reflects the distance between the two selected residues.

Apart from experiments, computer simulation is another approach to study protein folding mechanism. In the early days, due to the limited computing resources, protein folding simulations were performed with extremely simplified models such as lattice models and off-lattice models where each residue is represented as a bead and the movement of the residues is restricted. This gradually evolved into models with more and more realistic main chain and side chain representations including the popular all-atom models in the present era. The treatment of the solvent environment has also been evolving. The solvent was ignored in the earlier simulations (*in vacuo* simulations). Continuum models with different levels of sophistication have been developed over the years, including the most simple linear distance dependent model and the modern generalized Born (GB) models and Poisson Boltzmann (PB) models(Onufriev, Bashford et al. 2004). With the continuous growing of computing power, explicit representation of water atoms has also been used in many folding simulations.

The first ever microsecond folding simulation was performed with explicit solvent in 1998(Duan and Kollman 1998). With the help from a super computer cluster, this simulation was 100-1000 times longer than any other folding simulation at that time, thus stimulated great interest from the general public. In this simulation, the folding pathway to an intermediate state was observed. The folding rate of 4.2 μs predicted based on the simulation was highly consistent with later experimental finding of 4.3 μs. The success of

this milestone work was followed by the highly publicized folding@home project and IBM blue gene project among many other works(Zagrovic, Snow et al. 2002). It should be noted that thousands or more simulation trajectories are utilized in the folding@home project which so far can not reach the time scale for protein folding. The limitation is due to the use of idle personal desktop computers which has far less computing power than super computers. The IBM blue gene project can overcome this problem by building extremely powerful computers that can cover millisecond folding simulation. However, it has yet to make a significant progress in protein folding. In a recently published work, a specially designed super computer succeeded in the folding of two small proteins(Shaw, Maragakis et al.). Although computing power does not seem to be the greatest hurdle from now on, this success is unlikely to extend broadly in the near future. The greater challenge lies in the accuracy of simulation force fields which will be discussed later.

In this chapter, we focus on theoretical studies of protein folding by molecular dynamics simulations. The kinetics of protein folding can be studies by conventional molecular dynamics (CMD). But the insufficient sampling in current CMD simulations prevents the extraction of thermodynamic information. This has prompted the development of enhanced sampling techniques, among which the most widely adopted technique is replica exchange molecular dynamics (REMD), otherwise called parallel tempering. In the past few years, we have applied both CMD and REMD to the *ab initio* folding – meaning folding from extended polypeptide chain without any biased force towards the native contacts – of several model proteins, including villin headpiece subdomain (HP35), B domain of protein A (BdpA), albumin binding domain (ABD), and a full sequence design protein (FSD). To enhance the conformational sampling, we used an implicit solvent model GB/SA (surface area) implemented in the AMBER simulation package. The accuracy of protein folding reached sub-angstrom in most of these simulations, a significant improvement over previous simulations. Based on these high accuracy simulations, we were able to investigate the kinetics and thermodynamics of protein folding. The summary of our findings will be presented here in details. Finally, we will stress the critical role of force filed development in studying folding mechanism by simulation.

2. Kinetics and thermodynamics from *ab initio* folding simulations

2.1 Villin headpiece subdomain: Traditional analysis

Villin headpiece subdomain (HP35) is a small helical protein (35 residues) with a unique three helix architecture (Fig 1). Helix I is nearly perpendicular to the plane formed by helices II and III. The three-dimensional structure was solved earlier by an NMR experiment and more recently by a high resolution X-ray experiment(Chiu, Kubelka et al. 2005). Due to the small size and rich structural information, HP35 has attracted a lot of attention from both experimentalists and theoreticians.

In our previous works, we have conducted CMD to study the folding pathway and REMD to study the thermodynamics of HP35(Lei and Duan 2007; Lei, Wu et al. 2007). In the CMD work, we observed two intermediate states from the twenty folding trajectories (1μs each), one with the well-folded helix II/III segment (defined as the major intermediate state) and the other with the well-folded helix I/II segment (defined as the minor intermediate state). The best folded structure had C_α-RMSD of 0.39 Å and the most representative folded structure had C_α-RMSD of 1.63 Å. The productive folding always went through the major intermediate state while no productive folding was observed through the minor

intermediate state. Further examination revealed that the initiation of the folding was around the second turn between Phe17 and Pro21 rather than the hydrophobic core formed by Phe6/Phe10/Phe17. On the other hand, Gly11 was likely most accountable for the flexibility of helix I. In addition, the high occupancy of short-distance native contacts and low occupancy of long-distance native contacts pointed to the importance of local native contacts to the fast folding kinetics of HP35.

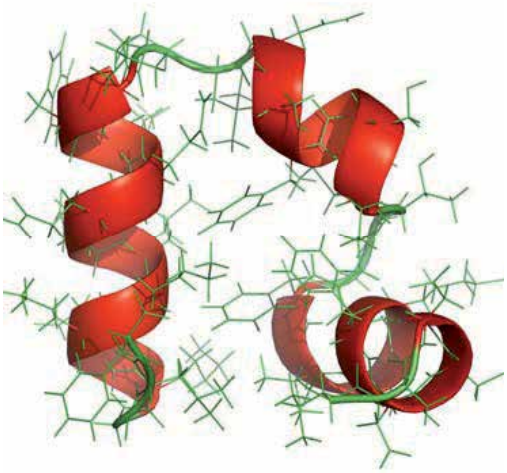

Fig. 1. Structure of villin headpiece subdomain (HP35)

In the REMD work, we conducted two sets of REMD simulations (20 replicas and 200 ns for each replica) with convergent results. The best folded structure had C_α-RMSD of 0.46 Å and the most representative folded structure had C_α-RMSD of 1.78 Å. The folding landscape of HP35 was partitioned into four thermodynamic states, namely the denatured state, native state, and the two aforementioned intermediate states. The dynamic feature of the folding landscape at selected temperatures (300 K, 340 K and 360 K) was consistent in both REMD simulations and the corresponding CMD simulations. A major free energy barrier (2.8 kcal/mol) existed between the denatured state and the major intermediate state, while a minor free energy barrier (1.3 kcal/mol) existed between the major intermediate state and the native state. In addition, a melting temperature of 339 K was predicted from the heat capacity profile, very close to the experimentally determined melting temperature of 342 K.
Because of the small size, HP35 has been considered as a classical two-state folder. This notion is supported by some earlier folding experiments. However, our simulation clearly pointed to the existence of folding intermediates. Our two-stage folding model is supported by some more recent folding experiments. In a laser temperature-jump kinetic experiment, the unfolding kinetics was fit by a bi-exponential function, with slow (5 μs) and fast (70 ns) phases. The slower phase corresponds to the overall folding/unfolding, and the fast phase was due to rapid equilibration between the native and nearby states. In a solid-state NMR study, three residues (Val9, Ala16, and Leu28) from the three helices exhibited distinct behavior during the denaturation process, and a two-step folding mechanism was proposed. In an unfolding study using fluorescence resonance energy transfer, Glasscock and co-workers demonstrated that the turn linking helices II and III remains compact under the

denaturation condition(Glasscock, Zhu et al. 2008), suggesting that the unfolding of HP35 consists of multiple steps and starts with the unfolding of helix I. In a mutagenesis experiment, Bunagan et al. showed that the second turn region plays an important role in the folding rate of HP35(Bunagan, Gao et al. 2009). A recent freeze-quenching experiment by Hu and co-workers revealed an intermediate state with native secondary structures and nonnative tertiary contacts(Hu, Havlin et al. 2009). These experiments are highly consistent with our observations in terms of both the stepwise folding and the rate-limiting step. Kubelka et al. proposed a three-state model in which the interconversion between the intermediate state and folded state is much faster than that between the intermediate state and the unfolded state(Kubelka, Henry et al. 2008). Therefore, the intermediate state lies on the folded side of the major free energy barrier, which is consistent with the separation of the unfolded state from the other states in our folding simulation. The estimation of 1.6–2.0 kcal/mol for the major free-energy barrier is also consistent with the estimation from our previous REMD simulation.

Nevertheless, controversy still exists regarding the folding mechanism of this small protein. In a recent work by Reiner et al., a folded segment with helices I/II was proposed as the intermediate state(Reiner, Henklein et al.), which corresponds to the off-pathway minor intermediate state in our work. It should be noted that different perturbations to the system, including high concentrations of denaturant, high temperatures, and site mutagenesis, have been utilized in different folding experiments. Because of the small size of HP35, the folding process may be sensitive to some of these perturbations. With the continuous development of experimental techniques that allow minimal perturbation and monitoring of the folding process at higher spatial and temporal resolution, the protein-folding mechanism will become more and more clear.

2.2 Villin headpiece subdomain: Network analysis

REMD is one of the most efficient sampling techniques for protein folding. However, due to the non-physical transitions from the exchange of conformations at different temperatures, its usage is mostly restricted to thermodynamics study. To get better understanding of the kinetics, we decided to extend the CMD simulations from the previous 1 μs to 10 μs in five selected simulation trajectories(Lei, Su et al.). Consistent with REMD, the folding free energy landscape displayed four folding states (Fig 2), the denatured state on the upper right region, the native state on the lower left region, the major intermediate state on the lower right region, and the minor intermediate state on the upper left region. The construction of the 2D landscape was based on two selected reaction coordinates, RMSD of segment A (helix I/II) and segment B (helix II/III). All five trajectories were combined together, and the population of each conformation in a small zone was converted to free energy by log transformation. From the folding landscape, we can see focused sampling in the native state, sparse sampling in the minor intermediate states, and heterogeneous sampling in the denatured state and the major intermediates state. The heavy sampling in the denatured state was likely due to the limited simulation trajectories. Ideally, thousands of trajectories are needed to reach good sampling. However, long simulations like this one are computer intensive beyond the capacity of a typical institution.

The above-described 2D landscape is only an overall display of the conformational sampling. To get more details, we performed conformational clustering based on the combined five trajectories. We here use the top ten most populated conformational clusters to describe the conformational sampling (Fig 3). The center of each conformational cluster

was used to represent the cluster. Among the top ten clusters, we can see three conformations in the native state (clusters 2, 3 and 10, colored in purple), three conformations in the major intermediate state (clusters 5, 6 and 9, colored in green), and four conformations in the denatured state (clusters 1, 4, 7 and 8, colored in blue), while the minor intermediate state did not show up due to small overall population. The overall energy (enthalpy) was not a good indication of the folding. In fact, the energy of the native state conformations was the highest and that of the denatured state conformations was the lowest. This observation did not violate the "thermodynamics hypothesis" because the conformational entropy was not included in the energy calculation. Entropy evaluation has long been a difficult subject in the field of computational biochemistry. A breakthrough will extend the application of force fields to protein structure prediction.

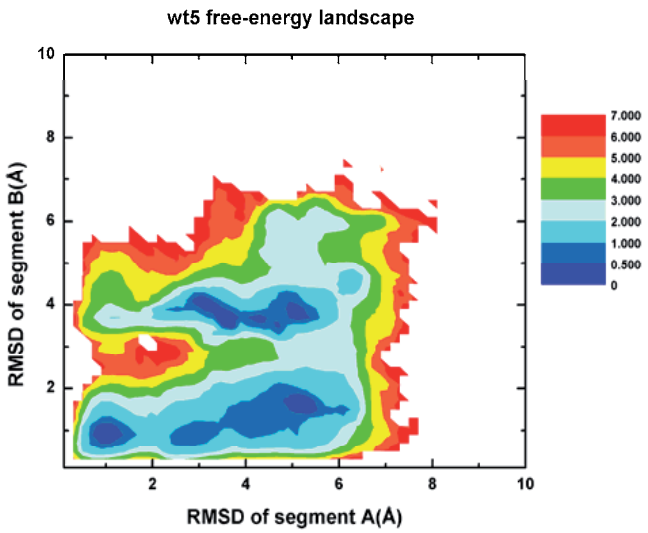

Fig. 2. Folding free energy landscape of HP35

Based on conformational clustering, we can study the kinetics and thermodynamics of protein folding using a new technique called network analysis. Traditionally, protein folding is illustrated by 1D profiles such as RMSD (global or partial), energy, solvent accessible surface area, radius of gyration and selected distances. The hyper-dimensional nature of protein folding makes none of these 1D profiles adequate to reflect the folding process. The emergence of 2D maps such as the one in Fig 2 greatly alleviate the problem by combining two independent profiles in one map. However, 2D maps are still insufficient to represent the hyper-dimensional process. Under this circumstance, several novel approaches have been applied to protein folding in recent years, including the disconnectivity graph by Karplus and network analysis pioneered by Caflisch(Krivov and Karplus 2004; Caflisch 2006).

Network analysis has gained popularity in protein folding recently(Bowman, Huang et al.; Jiang, Chen et al.). In network analysis, protein conformations are represented as nodes and the transitions among different conformations are represented as edges. Both nodes and edges can be colored based on a specified property, and analysis can be done based on the topological distribution of conformations with a specified property. In the folding network

of the combined five trajectories (Fig 4), we painted the nodes according to the state identity of the conformation and displayed the structure of the top ten populated conformations. From this network, we can see the clear separation of the denatured state from the native state and major intermediate state. The minor intermediate state was also connected to the denatured state. These findings were consistent with the observation from the 2D maps. A new finding is the mixing of the native state and major intermediate state which were clearly separated in the 2D map. The implication of this new finding is that the barrier between these two states is so small that they can easily convert to each other, which is supported by experimental evidence. This study demonstrated the power of network analysis and suggested more caution on interpreting 2D maps of protein folding.

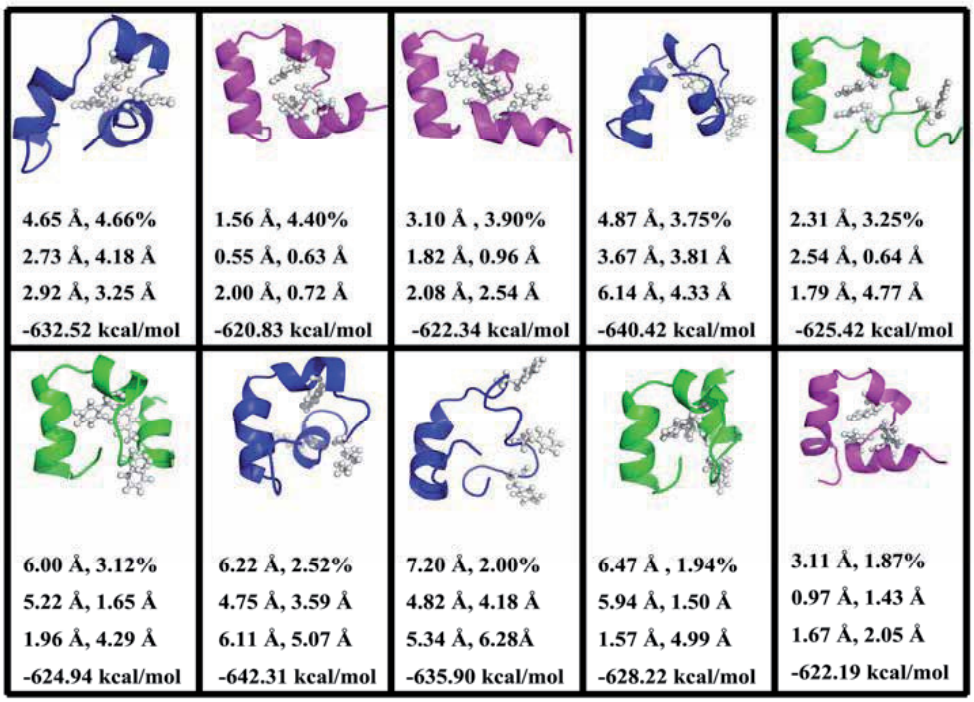

Fig. 3. Representative structures of the top ten populated clusters of HP35

The global folding network better reflect the thermodynamics of protein folding. To understand the kinetics of protein folding better, a simplified network with shortest path can be constructed (Fig 5). In this network, the shortest path connecting the denatured state, the major intermediate state and the native state was extracted from the global network. A clear flow of conformational transition from the denatured state to the major intermediate state and then to the native state was demonstrated in this network. Even the number of transitions between any neighboring conformations can be labeled on the network. In the denatured state, there were three short paths from the four top conformations to the major intermediate state, suggesting multiple folding pathways. Two conformations in the minor intermediate state were embedded in the denatured state, suggesting them as off-pathway intermediate. In the major intermediate state, the two top conformations close to the denatured state (clusters 6 and 9 in Fig 3) had wrongly folded segment A, while the top

conformation close to the native state (cluster 5 in Fig 3) had a near native structure. This information on the intra-state conformational transition is also helpful to reveal the details in the protein folding process. In the native state, the high connectivity among the conformations within the state and also with the major intermediate state suggests the relative independence of the native state and the low barrier between the native state and the major intermediate state.

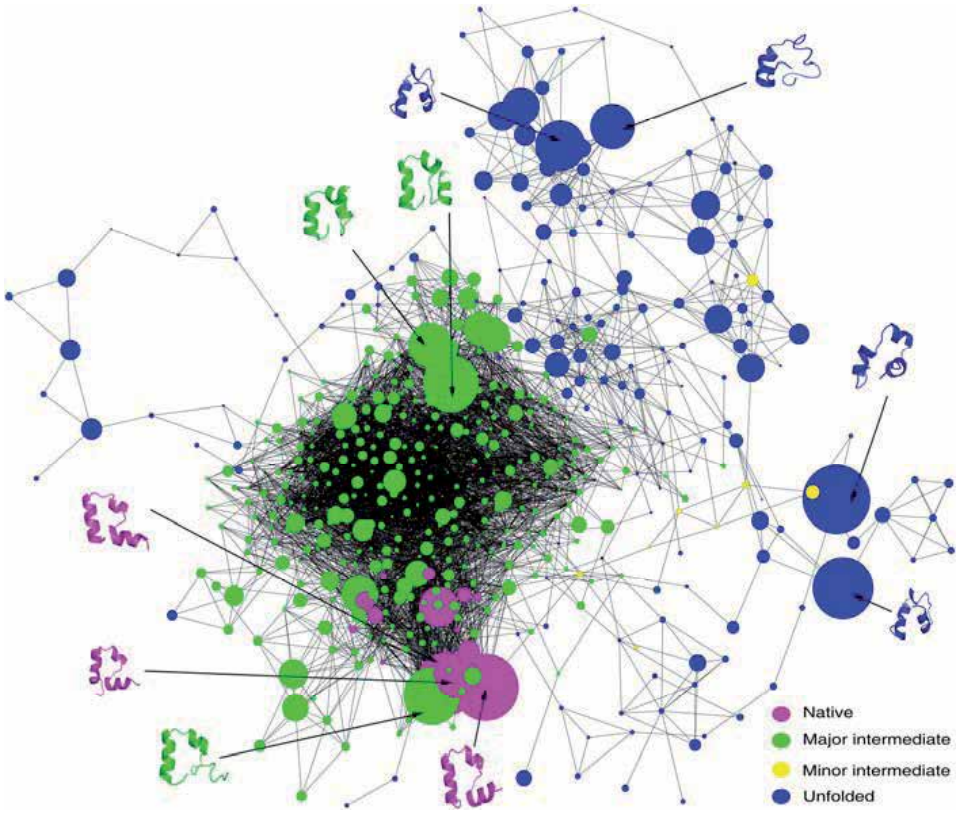

Fig. 4. Folding network of HP35

In the above two sub-sections, we have presented our study of folding mechanism for HP35 wild type. A challenging problem in this field is whether mutational effect can be reproduced in simulation. To enhance the folding rate of HP35 wild type, a mutant was designed to replace two partially buried lysine residues with non-natural neutral residues which resulted in the sub-microsecond folding. We conducted similar simulations for this HP35 mutant and compared with that of the wild type. Similar to the wild type, the mutant simulation also reached sub-angstrom accuracy(Lei, Deng et al. 2008). The folding free energy landscape also displayed similar feature with four folding states. However, some difference was also observed, especially the increased population of the native state, the decreased population of the denatured state, higher melting temperature, and the lower free energy barrier between the denatured state and the major intermediate state. These pointed to higher stability of the native state and faster folding which is consistent with the experiment. A surprising finding is the folding pathways through both intermediate states.

Therefore, the two mutated residues not only stabilized the local secondary structure (helix III), but also reshaped the folding landscape in several different ways. This kind of detailed information can not be obtained from folding experiment as yet. Thus, computer simulation will play a complimentary role in the understanding of folding mechanism in the foreseeable future.

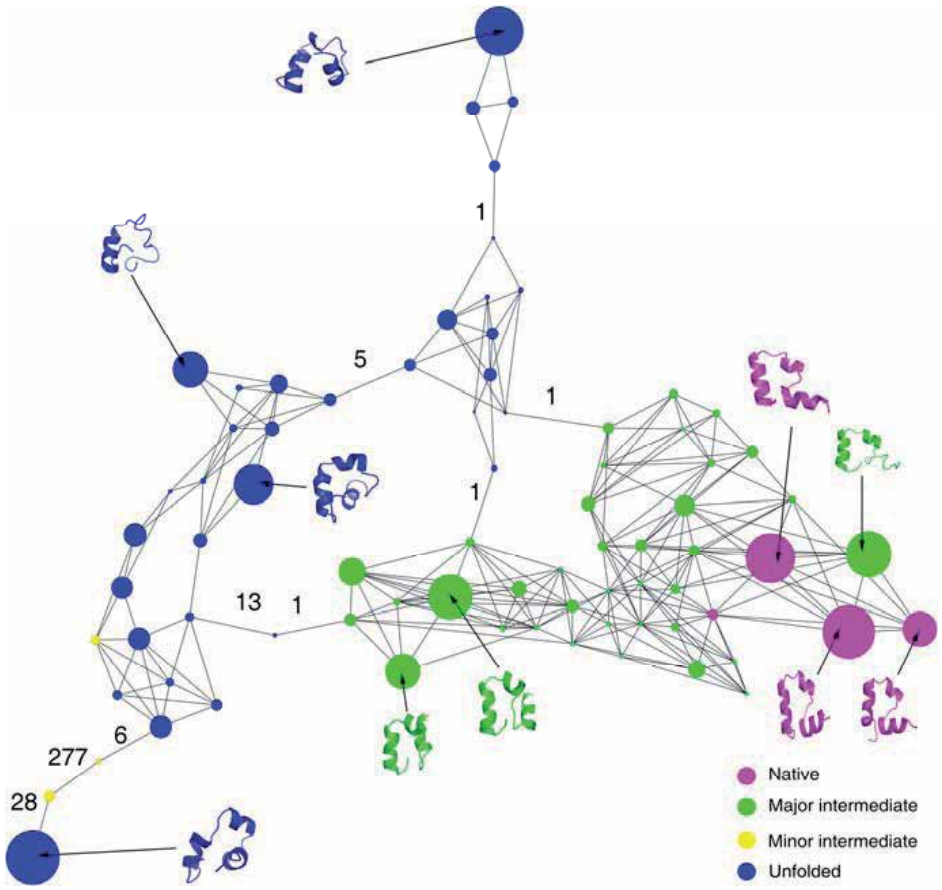

Fig. 5. A simplified folding network of HP35

2.3 Folding of three other model proteins

In addition to the folding studies of HP35 wild type and mutant, we also conducted ab initio folding on three other model proteins, namely B domain of protein A (BdpA), albumin binding domain (ABD), and a full sequence design protein (FSD). Here we will briefly describe our results. For detailed information, please refer to the original publications. BdpA is another three-helix protein with a different tertiary architecture (Fig 6). Helices II and III are relatively parallel to each other and form a plane. Helix I docks to this plane with a tilt angle relative to the other two helices. BdpA has 60 residues in the full length version and 47 residues in the truncated version (residues 10-56) where the unstructured terminal residues are trimmed off. In our simulation work, ab initio folding on both versions has been conducted.

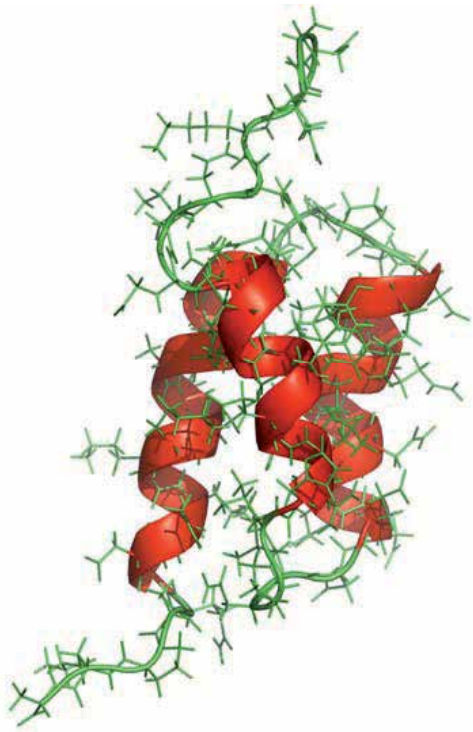

Fig. 6. Structure of B domain of protein A (BdpA)

Successful folding was achieved in our simulation(Lei, Wu et al. 2008). The best folded structure was 0.8 Å RMSD in the CMD of truncated version and 1.3 Å in the REMD of full length version. In the CMD simulations, the folding initiated from the formation of helix III, followed by the folding of a intermediate state with well folded helix II/III segment, and completed with the docking of helix I to the helix II/III segment. The folding pathway was similar to that of HP35 except for the initiation step, where it was the formation of helix III for BdpA and formation of the second turn for HP35. In the REMD simulations, the most populated conformation was a folded conformation with 64.1% population. The melting temperature of 362 K from the heat capacity profile was also close to the experimentally derived melting temperature of 346 K. From the calculated potential of mean force, the native state was 0.8 kcal/mol favored over the denatured state, and the free energy barrier from the denatured state to the native state was 3.7 kcal/mol. These findings were in qualitative agreement with folding experiments of BdpA. In addition, we tested the structure prediction performance based on AMBER potential energy and DFIRE statistical energy. Both gave similar performance with most predicted structures near 3.0-3.5 Å RMSD, while the structure with the lowest AMBER potential energy was only 2.0 Å RMSD.

Albumin binding domain (ABD) is yet another three helix protein with different topological feature from both HP35 and BdpA (Fig 7). Helices I and III are relatively long and parallel with each other, while the shorter helix II serves as linker. NMR studies revealed high uncertainty in the first loop and dynamics around helix II. The experimentally determined folding rate for wild type ABD is 6 μs. Enhanced folding rate was achieved in two mutants (2.5 μs for K5I and 1.0 μs for K5I/K39V).

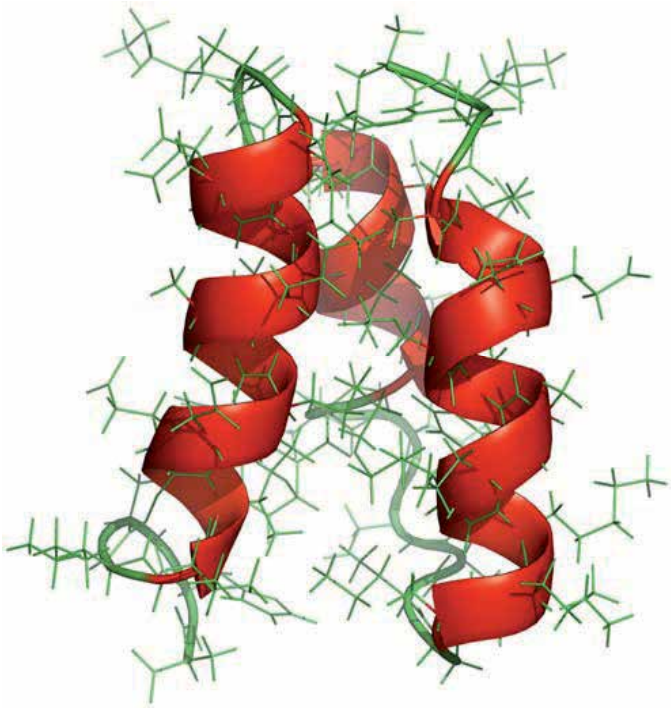

Fig. 7. Structure of albumin binding domain (ABD)

We conducted 20 CMD simulations (400 ns each) for each of the above mentioned three ABD variants. Although the size of ABD is comparable to the truncated BdpA (both 47 residues), no successful folding of ABD was reported prior to our study. In our simulations, the best folded structure reached 2.0 Å RMSD, indicating the first ever successful folding of ABD(Lei and Duan 2007). The folding started from the formation of helix I, followed by the formation of the other two helices, and completed by the optimal packing of the three helices. Although two hydrophobic cores exist in the middle, their formation was late in the simulation, suggesting that they are not the driving force of the global folding. Examination of conformational sampling revealed that the folded conformation was the most populated and significant formation of helices also appeared in other populated conformations. Compared to HP35 and BdpA, the accuracy of folding was lower for ABD. This was likely coming from several sources. First, ABD is highly dynamic according to NMR experiments which makes it difficult to choose a reference structure to determine folding accuracy. Second, the trajectory length for ABD (400 ns) was significantly shorter than that of HP35 and BdpA (both 1 μs). Third and likely most importantly, some features in ABD can not be modeled well in the current simulation force fields. The hydrophobic core in ABD may play important role in the folding mechanism, while it may play minor role in the folding of HP35 and BdpA. Therefore, inaccurate modeling of hydrophobic interaction will lead to less accurate folding of ABD than that of HP35 and BdpA. In addition, helix boundaries were slightly shifted in the simulation compared with the NMR structure, which may be partially due to the inaccurate parameterization of certain amino acids such as Valine.

The three model proteins described above are all helical proteins. A more challenging task is to fold proteins with both alpha-helix and beta-sheet secondary structures. Full sequence

design protein (FSD) is a designed 28- residue α/β protein. Our previous attempts on the ab initio folding of FSD were unsuccessful with the same simulation force field (AMBER FF03) used in the successful folding of the three helical proteins. Therefore, we decided to re-parameterize the force field under the same solvation scheme (GB/SA) for a better balance of the two major secondary structures.

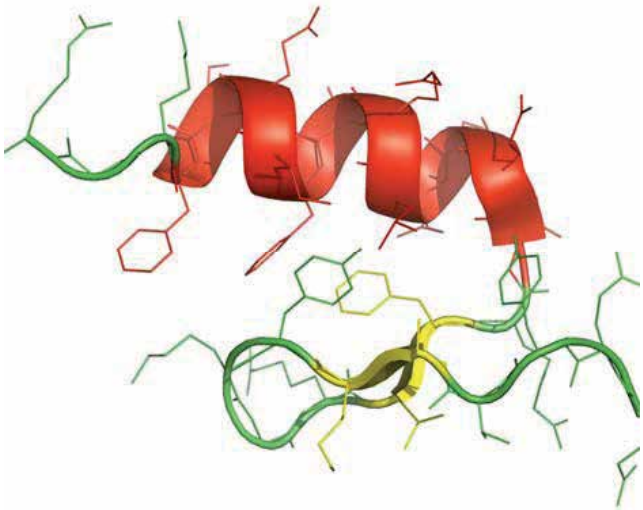

Fig. 8. Structure of a full sequence design protein (FSD)

Using the newly developed force field, we conducted ab initio folding of FSD with both CMD and REMD(Lei, Wang et al. 2009). High accuracy folding was achieved in terms of both the best folded structure (0.8 Å RMSD) and the population of the folded conformation (64.2%). High diversity was observed in the sampled denatured conformations, including a long helix, a helix hairpin and a long beta-hairpin, indicating good balance of the two major secondary structures. The folding of FSD followed two distinctive pathways. The major pathway began with the formation of the helix, while the minor pathway started with the formation of the beta-hairpin. More specifically, the initiation of the helix started from the C-terminal and propagated to the N-terminal. The free energy profiles showed different stability for the two structural elements. For the helix segment, the native helical structure had significantly lower free energy than other conformations. For the hairpin segment, however, 2-3 non-native conformations existed with similar free energy, which led to several local traps on the free energy landscape. Kinetically, the free energy barrier was similar for the folding of both segments (2-3 kcal/mol), but it was a single barrier for the helix and multiple barriers for the hairpin. The melting temperature extracted from the heat capacity profile was 360 K. However, this temperature merely reflected the melting of the helix (~50% helicity at 360 K), while the population of globally folded conformation was close to 0% at 360 K. Therefore, caution should be taken when interpreting the "melting temperature" extracted from the heat capacity profile.

3. Kinetics and thermodynamics from unfolding simulations

Ideally, protein folding mechanism should be studied by ab initio folding. However, due to the limited access of super computers by most research groups, ab initio folding simulations

are limited to very few small model proteins such as listed in Section 2. For most other proteins, an alternative approach is unfolding simulation where the native starting structures gradually unfold under the high temperature. A major assumption with this approach is that folding pathway is the reverse of unfolding pathway. To validate this approach, we conducted unfolding simulations on HP35, BdpA and FSD and compared the unfolding pathways with the folding pathways from ab initio simulations. Here we mainly use the unfolding of HP35 as an example.

We conducted ten unfolding simulations of HP35 at 350 K (100 ns each) and used the average properties from these simulations to describe the unfolding process. One of the main findings from the ab initio folding simulations was the major intermediate state with well-folded helix II/III segment. Thus, we first examined the unfolding of the two structural segments (Fig 9). We can clearly see the faster unfolding of the helix I/II segment which reached complete unfolding before 20 ns. On the other hand, the unfolding of helix II/III segment was much slower and was still fluctuating after unfolding. The slower unfolding and higher stability of helix II/III segment suggest that it folds earlier than helix I/II segment, which is consistent with the finding from ab initio folding.

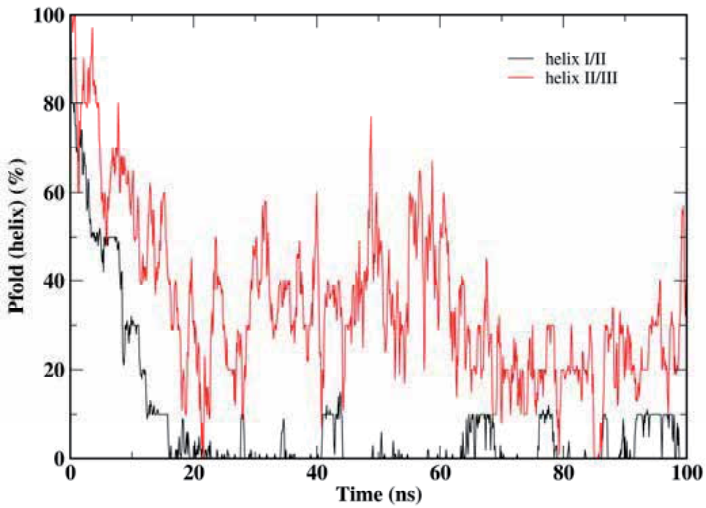

Fig. 9. Unfolding of the two segments of HP35

Second, we examined the unfolding of the three individual helices using a simple helicity measurement (Fig 10). The three helices showed distinctive unfolding features. Helix I was the fastest to unfold and the least stable one, down to 50% within 10 ns and towards 25% near 100 ns. On the other hand, helix III was the slowest to unfold and the most stable one, fluctuating between 70% and 85% during the whole simulation time. This suggests that helix III is the first to fold and helix I is the last to fold, which is also consistent with the ab initio folding simulation.

Further evaluation of the unfolding can be performed at the residue level. We calculated the root mean square fluctuation (RMSF) for each residue during the entire unfolding process (Fig 11). Overall, the two terminal regions displayed highest fluctuation and the second half of the protein was significantly more stable than the first half. Heterogeneity was observed

within the helices. Within helix I (residues 3-9), the middle residues 6 and 5 had the lowest fluctuation. Within helix II (residues 14-19), the C-terminal residues 17-19 had the lowest fluctuation. Within helix III (residues 22-31), most residues had the low fluctuation especially residues 24-30. Another interesting observation is the low fluctuation of residue 20 at the second turn. All these observations were consistent with the folding mechanism from the ab initio folding simulations.

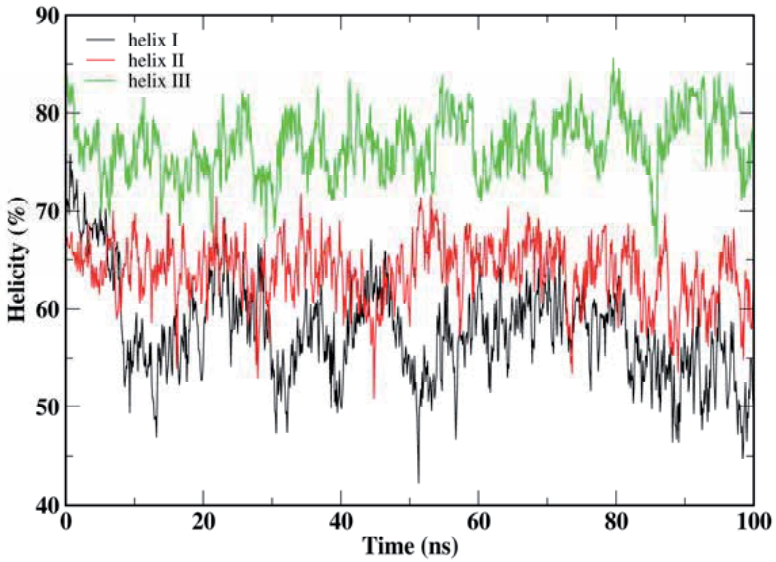

Fig. 10. Unfolding of the three helices of HP35

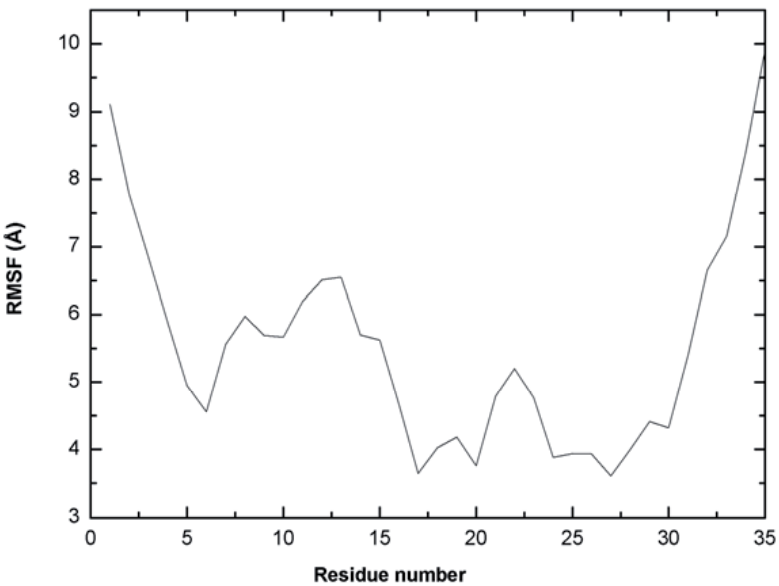

Fig. 11. Dynamic feature of each residue in the unfolding of HP35

A more intuitive way to visualize the folding pathways is by constructing the folding landscape. We divided the 100 ns unfolding time into five time frames and constructed folding landscape during each time frame (the first and last time frames shown in Fig 12). During the first time frame (0-20 ns), the native state was the most dominant one, while unfolding to the major intermediate state and denatured state was also observed. During the last time frame (80-100 ns), the denatured state became the most dominant one, while the major intermediate state was observed but the native state and the minor intermediate state were almost undetectable. The reverse of this observed process was exactly what we observed in the ab initio folding of HP35.

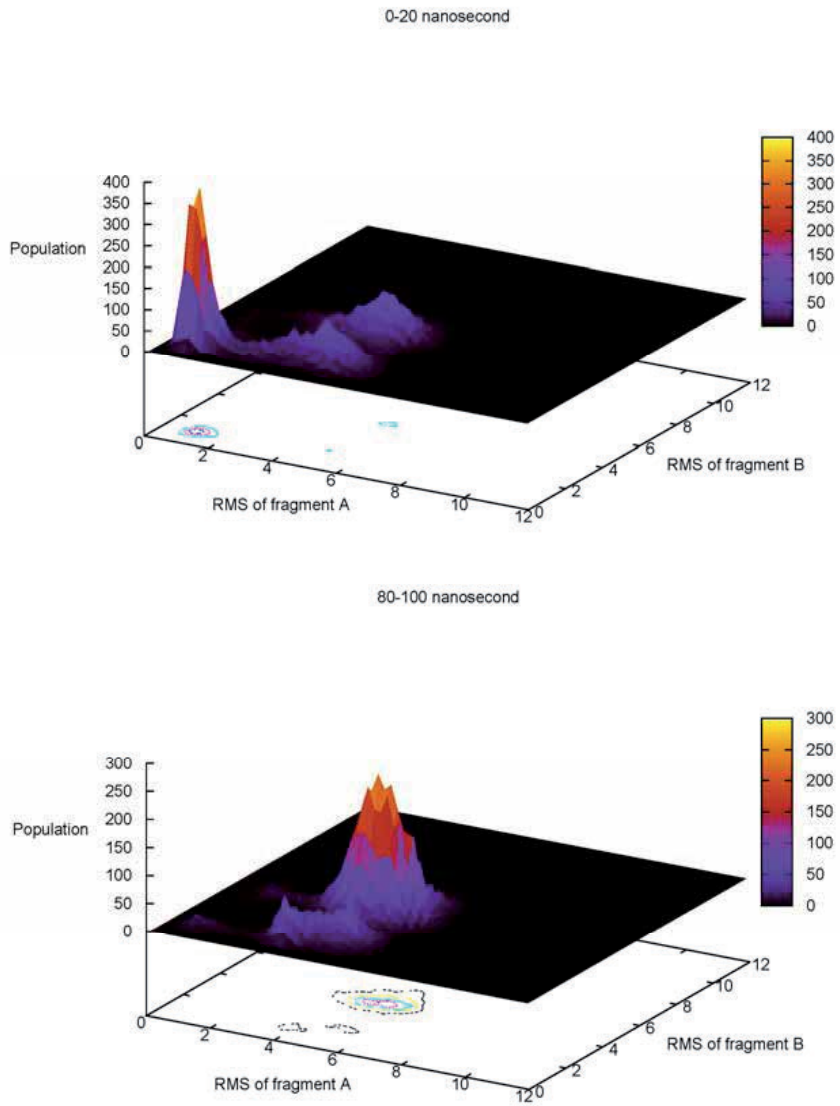

Fig. 12. Shifting of structural ensembles during the unfolding of HP35

In addition to the unfolding of HP35, we also conducted unfolding simulations on BdpA and FSD, all with ten trajectories of 100 ns simulations at 350 K. The unfolding mechanism from these two sets of simulations was also consistent with the folding mechanism from previously described ab initio folding simulations. In summary, our comparison between unfolding and ab initio folding suggests that unfolding is a valuable approach to study folding mechanism when ab initio folding is unfeasible. However, our comparison was based on three small model proteins, whether this conclusion can be extended to other proteins remains to be a question for future investigation.

4. Simulation force field development

At this point, we should stress the importance of force field in protein folding simulation. Under appropriate protocol, a simulation is as good as the underlying force field is. Currently, the main stream force fields, namely AMBER, CHARMM, GROMOS and OPLS, are all point charge models(Duan, Wu et al. 2003). Under this philosophy, a partial charge is assigned to every atom of a specific amino acid with the overall charge reflecting the charge nature of the amino acid (+1, -1 or 0). In some schemes, the main chain atoms (N, H, CA, C and O) are restricted to have the same set of partial charges for every amino acid, while this restriction was not applied in some other schemes. The partial charges can be derived from fitting to the electrostatic potential calculated by quantum mechanics, or can be assigned by chemical intuition. Another major parameterization of force field is the torsion angles, both main chain and side chain, which is usually fitted to reflect the potential energy surface of amino acid analogs especially Alanine dipeptide calculated by quantum mechanics. The major advantage of the current generation force field is the speed. However, as longer and longer simulations being conducted, more and more problems have been revealed regarding the accuracy of these force fields, including significant bias towards a specific secondary structure (alpha-helix or beta-sheet). In light of these problems, the concept of polarizable force field has emerged. The major philosophical difference from point charge models is the dynamics in charge distribution. Polarizable force fields are being developed and will likely become the next generation force field soon.

5. Conclusion

Computer simulation is a powerful tool to study the kinetics and thermodynamics of protein folding. Here we summarized our study of folding mechanism on four model proteins by CMD an REMD. We have reached sub-angstrom folding on HP35, BdpA and FSD and 2.0 Å RMSD folding on ABD. From the high quality folding simulations, we extracted a plethora of information regarding the folding mechanism, including folding pathways, folding states, free energy barriers, melting temperature and folding landscape. We have also applied network analysis to the study of folding mechanism and revealed new information about the folding of HP35. In addition, the high consistency between unfolding simulations and *ab initio* folding simulations suggest that unfolding simulations can be used as an alternative.

6. Acknowledgement

This work was supported by research grants from NIH (Grants GM79383 and GM67168 to YD), NSFC (Grant 30870474 to HL) and SRF for ROCS, SEM (to HL). Usage of AMBER and Pymol, GRACE, VMD, Matlab and Rasmol graphics packages are gratefully acknowledged.

7. References

Anfinsen, C. B. (1973). "Principles that govern the folding of protein chains." *Science* 181(96): 223-30.

Bowman, G. R., X. Huang, et al. (2010). "Network models for molecular kinetics and their initial applications to human health." *Cell Res* 20(6): 622-30.

Bryngelson, J. D., J. N. Onuchic, et al. (1995). "Funnels, Pathways, and the Energy Landscape of Protein-Folding - a Synthesis." *Proteins-Structure Function and Genetics* 21(3): 167-195.

Bunagan, M. R., J. Gao, et al. (2009). "Probing the folding transition state structure of the villin headpiece subdomain via side chain and backbone mutagenesis." *J Am Chem Soc* 131(21): 7470-6.

Caflisch, A. (2006). "Network and graph analyses of folding free energy surfaces." Current *Opinion in Structural Biology* 16(1): 71-78.

Chiu, T. K., J. Kubelka, et al. (2005). "High-resolution x-ray crystal structures of the villin headpiece subdomain, an ultrafast folding protein." *Proc Natl Acad Sci U S A* 102(21): 7517-22.

Dill, K. A. (1990). "Dominant forces in protein folding." *Biochemistry* 29(31): 7133-55.

Duan, Y. and P. A. Kollman (1998). "Pathways to a protein folding intermediate observed in a 1-microsecond simulation in aqueous solution." *Science* 282(5389): 740-4.

Duan, Y., C. Wu, et al. (2003). "A point-charge force field for molecular mechanics simulations of proteins based on condensed-phase quantum mechanical calculations." *J Comp Chem* 24(16): 1999-2012.

Fersht, A. R. (1995). "Optimization of rates of protein folding: the nucleation-condensation mechanism and its implications." *Proc Natl Acad Sci U S A* 92(24): 10869-73.

Glasscock, J. M., Y. Zhu, et al. (2008). "Using an amino acid fluorescence resonance energy transfer pair to probe protein unfolding: application to the villin headpiece subdomain and the LysM domain." *Biochemistry* 47(42): 11070-6.

Hu, K. N., R. H. Havlin, et al. (2009). "Quantitative determination of site-specific conformational distributions in an unfolded protein by solid-state nuclear magnetic resonance." *J Mol Biol* 392(4): 1055-73.

Jiang, X., C. Chen, et al. (2010). "Improvements of network approach for analysis of the folding free-energy surface of peptides and proteins." *J Comput Chem* 31(13): 2502-9.

Karplus, M. and D. L. Weaver (1994). "Protein folding dynamics: the diffusion-collision model and experimental data." *Protein Sci* 3(4): 650-68.

Krivov, S. V. and M. Karplus (2004). "Hidden complexity of free energy surfaces for peptide (protein) folding." *Proceedings of the National Academy of Sciences of the United States of America* 101(41): 14766-14770.

Kubelka, J., E. R. Henry, et al. (2008). "Chemical, physical, and theoretical kinetics of an ultrafast folding protein." *Proc Natl Acad Sci U S A* 105(48): 18655-62.

Lei, H., X. Deng, et al. (2008). "The fast-folding HP35 double mutant has a substantially reduced primary folding free energy barrier." *J Chem Phys* 129(15): 155104.

Lei, H. and Y. Duan (2007). "Ab initio folding of albumin binding domain from all-atom molecular dynamics simulation." *J Phys Chem* B 111(19): 5458-63.

Lei, H. and Y. Duan (2007). "Two-stage folding of HP-35 from Ab initio simulations." *J Mol Biol* 370(1): 196-206.

Lei, H., Y. Su, et al. (2010). "Folding network of villin headpiece subdomain." *Biophys J* 99(10): 3374-84.

Lei, H., C. Wu, et al. (2007). "Folding free-energy landscape of villin headpiece subdomain from molecular dynamics simulations." *Proc Natl Acad Sci U S A* 104(12): 4925-30.

Lei, H. X., Z. X. Wang, et al. (2009). "Dual folding pathways of an alpha/beta protein from all-atom ab initio folding simulations." *Journal of Chemical Physics* 131(16): -.

Lei, H. X., C. Wu, et al. (2008). "Folding processes of the B domain of protein A to the native state observed in all-atom ab initio folding simulations." *Journal of Chemical Physics* 128(23): -.

Levintha.C (1968). "Are There Pathways for Protein Folding." *Journal De Chimie Physique Et De Physico-Chimie Biologique* 65(1): 44-45.

Onufriev, A., D. Bashford, et al. (2004). "Exploring protein native states and large-scale conformational changes with a modified generalized born model." *Proteins* 55(2): 383-394.

Reiner, A., P. Henklein, et al. (2010). "An unlocking/relocking barrier in conformational fluctuations of villin headpiece subdomain." *Proc Natl Acad Sci U S A* 107(11): 4955-60.

Shaw, D. E., P. Maragakis, et al. (2010). "Atomic-level characterization of the structural dynamics of proteins." *Science* 330(6002): 341-6.

Zagrovic, B., C. D. Snow, et al. (2002). "Simulation of folding of a small alpha-helical protein in atomistic detail using worldwide-distributed computing." *J Mol Biol* 323(5): 927-37.

6

Closing the Gap Between Nano- and Macroscale: Atomic Interactions vs. Macroscopic Materials Behavior

T. Böhme[1], T. Hammerschmidt[2], R. Drautz[2] and T. Pretorius[1]
[1]*Dept. Research and Development, ThyssenKrupp Steel Europe AG, Duisburg*
[2]*Interdisciplinary Centre for Advanced Materials Simulation (ICAMS), Ruhr-Universität Bochum*
Germany

1. Introduction

In order to meet the continuously increasing requirements in nearly all fields of technology, an ongoing development and optimization of new and existing materials, components and manufacturing facilities is necessary. The rapidly growing demand on the application side implies a constant acceleration of the complete development process. In the past, development and optimization were often based on experiments. Indeed, the efforts for this approach are mostly extensive, time consuming and expensive, which significantly restricts the development speed.
The development of numerical methods and physical models as well as steadily increasing computer capacities allow for the employment of numerical simulations during materials development and optimization. Thus the experimental efforts can be considerably reduced. Moreover, the application of computational methods allows for the investigations of physical phenomena, which are "inaccessible" from the experimental point-of-view, such as trapping behaviour of hydrogen or carbon at different lattice defects (vacancies, dislocations, grain boundaries, etc.) within an Fe-based matrix, see e.g. (Desai et al., 2010; Hristova et al., 2011; Lee, 2006; Lee & Jang, 2007; Nazarov et.al., 2010).
In steel production for example, the goal is pursued to set up a so-called 'digital plant', in which it is possible to calculate the behavior of material and components up to the application level, see Figure 1. Such a digital production line provides deep insight into the materials response and the involved physical effects at each step of the process chain. Furthermore material parameters can be calculated, which will be used as input data to perform calculations of subsequently following process steps. In fact, if the production process chain can be completely reproduced, a backwards approach will be possible, which allows for the transfer from application requirements to the materials design (computer aided material design).
A fully theoretical, sufficiently accurate reproduction of all steps of materials processing is - as far as we know - still not possible. To achieve reliable simulation results in manageable computational times, (semi-)empirical models are widely used at nearly all production

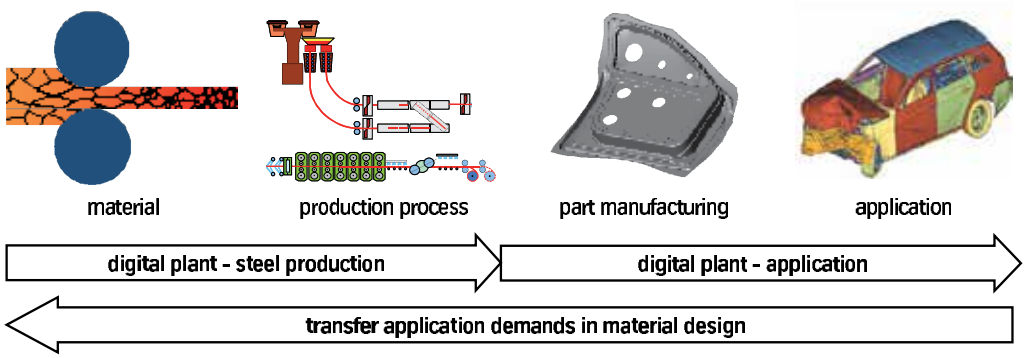

Fig. 1. Continuous full-length models of all production steps from material to application, exemplarily demonstrating materials design by simulation, e.g. during steel production.

steps. Such models make use of empirically introduced parameters, which must be fitted to experiments. For example, the description of deformation or fatigue in materials with complex microstructures, such as in multiphase steels or compound materials (e.g. fiber reinforced plastics), requires models for various physical effects on a large length- and timescale. Here, additional to macroscopic finite element analysis on the (centi-)meter scale, calculations on the microstructure (microscale) down to atomistic models (nanoscale) are necessary, cf. Figure 2.

To handle the resulting multi-scale problem, different approaches are possible. The classical approach typically starts at the application level. Here macroscopic calculations are performed, which may presuppose more detailed investigations. Such details could lead to smaller length-scales, which mainly result in an increasing number of model-parameters (input data). On the microstructure level parameters must be taken into account, in particular to describe morphology and composition as well as the temporal and spatial behaviour of the microstructures. For instance, for multiphase steels materials data of each phase and information about its shape and spatial distribution must be known. In case of compound materials the same arguments hold for the different materials fractions. Moreover, in some cases an additional description of internal interfaces (e.g. between phases or grains) must be taken into account, see for example (Artemev et al., 2000; Cahn, 1968; Kobayashi et al., 2000). By starting from the macro level, all parameters on smaller levels must be available. The efforts for the measurement of these parameters increase with decreasing length scales. Therefore, some of the required parameters cannot be measured and must be treated as fitting parameters or estimated ad hoc.

The ongoing improvement of algorithms and modeling methods accompanying the continuously rising computer capacities, allow for the use of an alternative approach to deal with the aforementioned multi-scale problems. Atomistic or even electronic level calculations can be carried out totally parameter-free (ab-initio calculations) by considering the interactions between the elemental components of matter. In this context no measurements are necessary to perform calculations at this level. Experimental data is only used for validation purposes. By following this theoretical approach, difficult experiments for the determination of required model parameters on the microscale are supplemented or partially substituted by adequate calculations. Thus, the need of fitting parameters is drastically reduced and experimental efforts are minimized, which - in turns - lead to cheaper and faster development processes.

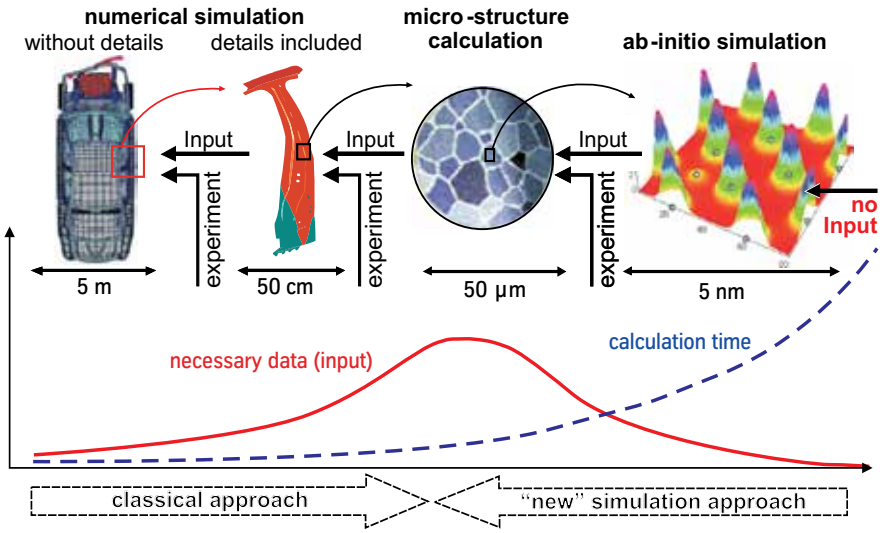

Fig. 2. Modelling on different length scales using different techniques.

However, regardless of the increasing computational capacities, most modern materials - unfortunately - are still too complex for reliable, purely-theoretical estimations of materials behaviour. Advanced high-strength steels, in particular, consist of more than 10 components (e.g. Nb, V, Al, Cr, Mn, etc.) and show different, coexisting lattice structures (e.g., martensite or austenite), orientations (texture) or precipitates (e.g., carbon nitrides). Moreover, final properties are often adjusted during advanced materials processing beyond the classical production line (e.g. annealing during surface galvanizing or hardening during hot stamping of blanks for automotive light-weight structures).

In order to understand basic mechanisms determining the specific mechanical and thermodynamic materials characteristics it is necessary to reduce the above-mentioned complexity. For this reason simple model-systems are considered to study various effects on the atomistic scale, which crucially determine the macroscopic materials properties. Recent examples in literature are e.g. binary systems such as Fe-H (Desai et al., 2010; Lee & Jang, 2007; Nazarov et.al., 2010; Psiachos et al., 2011), Fe-C (Hristova et al., 2011; Lee, 2006) or the eutectic, binary brazing alloy Ag-Cu (Böhme et al., 2007; Feraoun et al., 2001; Najababadi et al, 1993; Williams et al., 2006). Here atomistic methods allow to study the impact of interstitial elements, mostly without any a-priori assumptions, or to derive required materials data for microscopic theories (such as phase field studies), which cannot be simply measured by experiments.

The present work starts with an overview and classification of different interactions models, beginning with electronic structure theories and ending with empirical atomic potentials. In order to calculate different thermodynamic and thermo-mechanical materials properties we consider in Section 3 and 4 the above mentioned alloy Ag-Cu as well as the corresponding pure components. Two reasons are worth-mentioning for this choice: **(a)** Ag-Cu is of high technical relevance and often employed for high-stressed or high-temperature, brazing connections, e.g. for gas pipe joints. **(b)** According to the high relevance the materials behaviour is well-known and a lot of reference data are available; thus all performed calculations can be easily evaluated. But there is also materials behaviour, which cannot

be directly analyzed by the equations of Sections 3 and 4. In this context mean values and collective behaviour following from the investigation of many particle systems must be considered. One possibility for such an analysis is given by molecular dynamics simulations, which are explained in Section 5. Here we start with a brief description of the basic idea and framework and then exemplarily present simulations subjected to the temporal evolution of a misoriented grain in Titanium at finite temperature. The article ends with concluding remarks and a discussion of future tasks and challenges.

2. Atomic interactions

A central task of atomistic simulation in materials science is to calculate the cohesive energy for a given set of atoms. The many approaches to achieve this goal differ to a great extent in accuracy and computational effort. The common aspect, however, is that the calculated cohesive energy can be utilised to determine a variety of material properties: **(i)** Differences in the cohesive energies of stable structures are the basis for determining the relative stability of different structures or the formation energy of defects and and surfaces. **(ii)** Differences in the cohesive energy of metastable and unstable structures are required to calculate e.g. the energy barriers for diffusion or phase transformation. **(iii)** Gradients of the cohesive energy determine the forces acting on the atoms that are needed to carry out structural relaxation or dynamic simulations. **(iv)** Derivatives of the cohesive energy are required to calculate e.g. elastic properties. In the remainder of this section we describe the approaches that span the regime from highly accurate but computationally expensive electronic-structure calculations to less accurate but computationally cheap empirical interaction potentials.

2.1 Electronic structure theory

One of the most accurate, yet tractable theoretical approaches in materials science is electronic structure theory that we will briefly introduce here. For further information we refer the reader to one of the review papers, e.g. (Bockstedte et al., 1997; Kohn, 1998; Payne et al., 1992), or textbooks, e.g. (Dreizler & Gross, 1990; Parr & Yang, 1989). The starting point of electronic structure theory in materials science is the quantum-mechanical description of the material by the SCHRÖDINGER equation[1]

$$(\widehat{\mathrm{H}} - E)\Psi = (\widehat{\mathrm{T}}_\mathrm{e} + \widehat{\mathrm{T}}_\mathrm{i} + \widehat{\mathrm{V}}_{\mathrm{e-e}} + \widehat{\mathrm{V}}_{\mathrm{e-i}} + \widehat{\mathrm{V}}_{\mathrm{i-i}} - E)\Psi = 0. \tag{1}$$

for ions (i.e. the atomic nuclei) and electrons with a many-body wavefunction Ψ. The terms $\widehat{\mathrm{V}}_{\mathrm{e-e}}$, $\widehat{\mathrm{V}}_{\mathrm{e-i}}$ and $\widehat{\mathrm{V}}_{\mathrm{i-i}}$ describe the COULOMB interactions between electrons/electrons, electrons/ions, as well as ions/ions. The terms $\widehat{\mathrm{T}}_\mathrm{e}$ and $\widehat{\mathrm{T}}_\mathrm{i}$ denote the kinetic energies of the electrons and ions. The structure and properties of many-body systems can then be determined by solving the SCHRÖDINGER equation. Most practical applications simplify this matter by assuming a decoupled movement of electrons and ions (BORN-OPPENHEIMER approximation (Born & Oppenheimer, 1927)) and thereby reducing the problem to the interaction of the electrons among each other. This interaction is determined by the COULOMB

[1] Without loss of generality we refer through the work to Cartesian coordinates. Scalar quantities are written in italic letters (s); vectors are single underlined ($\underline{\mathbf{v}}$); tensors or matrices of second or higher order are double underlined ($\underline{\underline{\mathbf{T}}}$) or marked by blackboard capital letters ($\mathbb{M}$). Operators are indicated by the $\widehat{(\cdot)}$-symbol. Scalar products between vectors and tensors are marked with $(\cdot)$ or $(\cdot\cdot)$, respectively. Greek indices refer to atoms ($\alpha\beta\gamma$) or electrons ($\mu\nu\xi$).

potential and the PAULI principle. There are several approaches to solve the remaining quantum-mechanical problem, the most successful one being density-functional theory that can be considered the today standard method of calculating material properties accurately.

2.2 Density-functional theory

Density-functional theory originates from the KOHN-SHAM formalism (Hohenberg & Kohn, 1964; Kohn & Sham, 1965) that is based on the electron density ρ of a system which describes the number of electrons per unit volume:

$$\rho(\underline{\mathbf{r}}_1) = N \int ... \int |\Psi(\underline{\mathbf{x}}_1, ..., \underline{\mathbf{x}}_N)|^2 \, \mathrm{d}\underline{\mathbf{x}}_2 \, \mathrm{d}\underline{\mathbf{x}}_N. \tag{2}$$

The volume-integral of this quantity is the total number of electrons

$$\int \rho(\underline{\mathbf{r}}) \, \mathrm{d}\underline{\mathbf{r}} = N \tag{3}$$

in the system. KOHN and SHAM mapped the problem of a system of N interacting electrons onto the problem of a set of systems of non-interacting electrons in the effective potential v_{eff} of the other electrons. The SCHRÖDINGER equation for electrons in the non-interacting system is then

$$\left[-\frac{1}{2}\nabla^2 + v_{\mathrm{eff}}(\underline{\mathbf{r}}) \right] \psi_n(\underline{\mathbf{r}}) = \varepsilon_n \psi_n(\underline{\mathbf{r}}), \qquad n = 1 \ldots N \tag{4}$$

with the electronic density of N electrons of spin s

$$\rho(\underline{\mathbf{r}}) = \sum_{n=1}^{N} \sum_{s} |\psi_n(\underline{\mathbf{r}}, s)|^2. \tag{5}$$

The effective potential v_{eff}

$$v_{\mathrm{eff}}(\underline{\mathbf{r}}) = v(\underline{\mathbf{r}}) + v_{\mathrm{H}}(\underline{\mathbf{r}}) + v_{\mathrm{xc}}(\underline{\mathbf{r}}), \tag{6}$$

includes the Hartree-potential v_{H} and the so-called exchange-correlation energy functional $v_{\mathrm{xc}}(\underline{\mathbf{r}})$ that is not known a priori and that needs to be approximated. The most widely used approximations to the exchange-correlation functional are the *local-density approximation* (LDA) and the *generalized-gradient approximation* (GGA).

2.3 Tight-binding and bond-order potentials

The limitation of DFT to small systems (few 100 atoms) due to the numerical cost can be overcome by taking the description of the electronic structure to an approximate level. This can be carried out rigorously by approximating the density functional theory (DFT) formalism in terms of physically and chemically intuitive contributions within the tight-binding (TB) bond model (Sutton et al., 1988). The TB approximation is sufficiently accurate to predict structural trends as well as sufficiently intuitive for a physically meaningful interpretation of the bonding. The tight-binding model is a coarse-grained description of the electronic structure that expresses the eigenfunctions ψ_n of the KOHN-SHAM equation in a minimal basis

$$\psi_n = \sum_{\alpha\mu} c_{\alpha\mu}^{(n)} \alpha\mu \tag{7}$$

on atoms α with orbitals μ. With an orthonormal basis the solution of the secular equation

$$\sum_{\beta\nu} H_{\alpha\mu\beta\nu} c_{\beta\nu}^{(n)} = E_n c_{\alpha\mu}^{(n)} \tag{8}$$

gives eigenvalues E_n and coefficients $c_{\alpha\mu}^{(n)}$ of the eigenfunctions ψ_n. Here, the elements of the Hamiltonian matrix $\underline{\underline{\mathbf{H}}}$ are denoted as $H_{\alpha\mu\beta\nu}$. The dependence of these matrix elements from interatomic distance and atomic environment can be parametrised on the basis of DFT calculations. In the tight binding bond model, the binding energy E_B of the system is given as the sum over covalent bond energy E_bond, repulsive energy E_rep and promotion energy E_prom

$$E_\mathrm{B} = E_\mathrm{bond} + E_\mathrm{prom} + E_\mathrm{rep} \tag{9}$$

that allows to also include additional contributions from magnetism and charge transfer. The repulsive energy E_rep is empirical and often approximated as pairwise term. The change in orbital occupation with respect to the atomic reference state is accounted for by the promotion energy E_prom. Both, atom-based information and bond-based information can be used to express the bond energy E_bond. These are the so-called onsite and intersite representations that are equivalent but different perspectives of bond formation in materials. The basis of both representations is the set of eigenfunctions ψ_n. The central entity of the atom-based representation is the atomic local density of states (DOS) $n_{\alpha\mu}$ on atom α

$$n_{\alpha\mu}(E) = \sum_n \left| c_{\alpha\mu}^{(n)} \right|^2 \delta(E - E_n) \tag{10}$$

whereas the bond-based representation is footed on the bond-order $\Theta_{\alpha\mu\beta\nu}$ or the density matrix $\rho_{\alpha\mu\beta\nu}$ between orbital μ on atom α and orbital ν on atom β over the occupied states

$$\Theta_{\alpha\mu\beta\nu} = 2\rho_{\alpha\mu\beta\nu} = 2\sum_n^{\mathrm{occ}} c_{\alpha\mu}^{*(n)} c_{\beta\nu}^{(n)} \tag{11}$$

The bond energy in the equivalent representations is given by

$$E_\mathrm{bond} = 2\sum_{\alpha\mu} \int^{E_\mathrm{F}} \left(E - E_{\alpha\mu}\right) n_{\alpha\mu}(E)\, \mathrm{d}E = \sum_{\alpha\mu \neq \beta\nu} \Theta_{\alpha\mu\beta\nu} H_{\alpha\mu\beta\nu} \tag{12}$$

with the FERMI level E_F. The diagonalisation of the HAMILTONIAN matrix $H_{\alpha\mu\beta\nu}$ is the most demanding part of a tight-binding calculation and the limiting factor for its computational efficiency. Compared to DFT, a TB calculation is several orders of magnitude faster and can handle up to a few 10000 atoms.

This limitation can be overcome by bond-order potentials that lead a step further in coarse-graining the description of the electronic structure. Instead of the diagonalisation of the HAMILTON matrix as in the tight-binding problem, the problem is solved locally in terms of the atom-based DOS or the bond-based bond-order. This is computationally more efficient. Moreover, the involved relation of the electronic structure to the local topology and coordination of the material leads to a physically transparent description of local bond formation. Detailed reviews of bond-order potentials for transition metals,

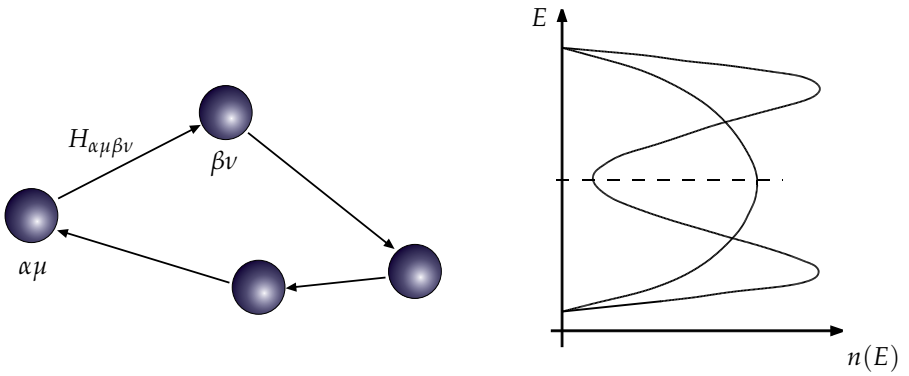

Fig. 3. A self-returning path of length 4 (left) that contributes to the 4-th moment of the DOS (right) on atom i.

semiconductors and hydrocarbons are given elsewhere (Aoki et al., 2007; Drautz et al., 2007; Finnis, 2007a; Mrovec et al., 2007). Some of us recently compiled a more tutorial-like approach to bond-order potentials (Hammerschmidt & Drautz, 2009) and an overview of applications (Hammerschmidt et al., 2009).

A central point in the theory of bond-order potentials is the moments theorem, cf. (Cryot-Lackmann, 1967). It relates the local density of states $n_{\alpha\mu}(E)$ of orbital μ on atom α to products of the HAMILTONIAN matrix elements $H_{\alpha\mu\beta\nu}$:

$$\int E^N n_{\alpha\mu}(E)\,\mathrm{d}E = m_{\alpha\mu}^{(N)} = \sum_{\beta\nu\gamma\xi\cdots} H_{\alpha\mu\beta\nu}H_{\beta\nu\gamma\xi}H_{\gamma\xi\ldots}\cdots H_{\ldots\alpha\mu} \tag{13}$$

This establishes a direct connection between the electronic structure and the local crystal structure. For the N-th moment of atom α, $m_{\alpha}^{(N)}$, the environment is sampled by self-returning paths of length N as illustrated in Figure 3. The higher the moment, the longer the length of the hopping paths and hence the more farsighted the sampling of the atomic environment of atom α. With an infinite number of moments one would recapture the exact solution of the tight-binding problem. The locality of calculating the bond energy is established by terminating the expansion beyond a certain number of moments. This local expansion of the electronic structure using truncated GREEN's function expansion can be carried out in different flavors that are described in detail in, *e.g.*, Refs. (Finnis, 2007b; Horsfield et al., 1996; Pettifor, 1989). The resulting functional form of the bond energy is derived as a function of the atomic positions, where the different ways of integrating the DOS lead to the numerical bond-order potentials (Aoki et al., 2007) and the analytic bond-order potentials for semiconductors (Pettifor & Oleinik, 1999; 2000) and transition metals (Drautz & Pettifor, 2006).

The latter use an expansion of the DOS in terms of CHEBYSHEV polynomials

$$n_{\alpha\mu}(\varepsilon) = \frac{2}{\pi}\sqrt{1-\varepsilon^2}\left(\sigma_0 + \sum_{n=1}\sigma_n P_n(\varepsilon)\right), \tag{14}$$

where the expansion coefficients σ_n are related to the moments of the DOS by expressing the CHEBYSHEV polynomials explicitly in polynomials with coefficients p_{mk},

$$P_m(\varepsilon) = \sum_{k=0}^{m} p_{mk}\varepsilon^k \,. \tag{15}$$

This links the expansion coefficients σ_m to the moments $\mu_{i\alpha}^{(k)}$

$$\sigma_m = \sum_{k=0}^{m} p_{mk} \frac{1}{(2b_{\alpha\infty})^k} \sum_{l=0}^{k} \binom{k}{l} (-a_{\alpha\infty})^{(k-l)} m_{\alpha\mu}^{(l)} \,. \tag{16}$$

which leads to a closed-form approximation of the DOS by calculating the moments $m_{\alpha\mu}^{(k)}$ and inserting σ_n into the DOS expansion of Eq. (14).
In this scheme, the integration of the DOS can be carried out analytically and yields an analytic expression for the bond energy, viz.

$$E_{\mathrm{bond},\alpha\mu} = \int^{E_\mathrm{F}} \left(E - E_{\alpha\mu}\right) n_{\alpha\mu}(\varepsilon)\, \mathrm{d}\varepsilon = \sum_n \sigma_n \left[\tilde{\chi}_{n+2}(\phi_\mathrm{F}) - \gamma\tilde{\chi}_{n+1}(\phi_\mathrm{F}) + \tilde{\chi}_n(\phi_\mathrm{F})\right] . \tag{17}$$

Here we introduced the so-called response functions

$$\tilde{\chi}_n\left(\phi_\mathrm{F}\right) = \frac{1}{\pi}\left(\frac{\sin(n+1)\phi_\mathrm{F}}{n+1} - \frac{\sin(n-1)\phi_\mathrm{F}}{n-1}\right) , \tag{18}$$

and the FERMI phase $\phi_\mathrm{F} = \cos^{-1}(E_\mathrm{F}/2b_{\alpha\infty})$. The bond energy can be taken analytically to an arbitrary number of moments. Therefore the BOPs provide an effective interatomic interaction scheme that converges systematically to the exact solution of the TB HAMILTONIAN. The number of moments required in practice depends on the investigated quantity and is approximately six for identifying qualitative features of structural stability in transition metals (Hammerschmidt et al., 2008) to nine for reproducing quantitative features of defects and transformation paths (Mrovec et al., 2004).

2.4 Empirical potentials

The lowest order approximation of the analytic bond-order potential that includes only two moments is similar to the earlier developed potentials of the FINNIS-SINCLAIR (Finnis & Sinclair, 1984) type or embedded-atom method (EAM) type (Daw & Baskes, 1983; 1984; Foiles et al., 1986). In that sense, the analytic BOP expansion may be viewed as a systematic extension of the FINNIS-SINCLAIR potential to include higher moments. By means of EAM potentials the energy of atom α is expressed as[2]:

$$E^\alpha = \frac{1}{2} \sum_{\substack{\beta \\ (\alpha\neq\beta)}} \phi^{\alpha\beta}(R^{\alpha\beta}) + F_\alpha(\bar{\rho}_\alpha) \quad \text{with} \quad \bar{\rho}_\alpha = \sum_{\substack{\beta \\ (\alpha\neq\beta)}} \rho_\beta(R^{\alpha\beta}) \quad . \tag{19}$$

[2] The factor $\frac{1}{2}$ appears to avoid double-counting of bonds for $E^\mathrm{tot} = \sum E^\alpha$.

The main idea consists of adding a nonlinear function[3], F_α, to the pairwise interaction term $\phi^{\alpha\beta}$. This so-called embedding function depends on the electronic density $\bar{\rho}_\alpha$ at the position of atom α, whereas $\phi^{\alpha\beta}$ only depends on the scalar distance $R^{\alpha\beta}$ between atom α and β. In this manner $\bar{\rho}_\alpha$ can be interpreted as a constant background electronic density, that atom α feels due to the superposition of the atomic charge densities ρ_β of its neighbors separated by the distance $R^{\alpha\beta}$. Moreover, F_α can be understood as the energy to put an atom α into a homogeneous electron gas with the density $\bar{\rho}_\alpha$. Here the embedding function itself only depends on the type of the embedded atom and the argument of F_α refers to the medium in which the atom is embedded. Typically the first term of Eq. (19) stands for the purely repulsive ion-ion interaction; the second term characterizes the ion-electron interaction, see also Figure 4. Especially for metals such a decomposition is mostly justified since the valence electrons can nearly free move within the lattice of metallic ions.

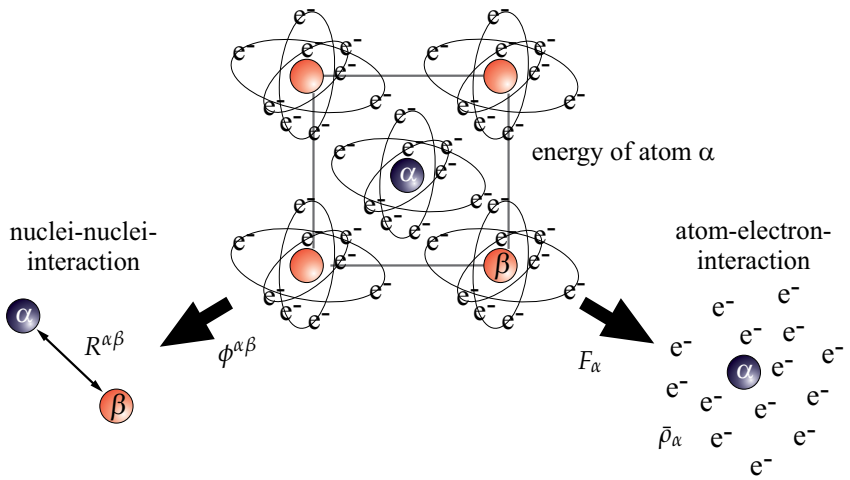

Fig. 4. Illustration of the two contributions to the atom-specific energy according to the EAM framework.

A central aspect of these types of potentials is their tendency to always favor close-packed systems over more open systems due to the purely distant dependent character of interactions. Despite this limitation to purely metallic bonding in fcc/hcp environments, simulations with this class of potentials gave a lot of insight because they are computationally cheap and are routinely applied to very large systems with millions of atoms. The efforts to extend the transferability of these potentials to covalent bonding by introducing additional directional terms (Baskes, 1992) are subsummised as modified embedded-atom methods (MEAM).
Complementary approaches that focus on covalently bound structures, semiconductors particularly, are e.g. the potentials of ABELL-TERSOFF (Abell, 1985; Tersoff, 1986) type. Just as the EAM potentials they were defined ad hoc with the goal to stabilise the diamond/zincblend structure over close-packed crystal structures for systems like C, Si, Ge, and GaAs. The functional form of the ABELL-TERSOFF potential is a combination of a repulsive (R) and an

[3] The nonlinear character remedies e.g. artifacts like the CAUCHY paradox $C_{1122} = C_{2323}$ or $C_{12} = C_{44}$ (VOIGT notation).

attractive (A) term

$$E^{\alpha} = \sum_{\beta} \left[V_{\mathrm{R}}(R^{\alpha\beta}) - B^{\alpha\beta} V_{\mathrm{A}}(R^{\alpha\beta}) \right] \tag{20}$$

mediated by a term $B^{\alpha\beta}$ that accounts for the local environment in terms of a non-linear dependence on angular terms. Later it turned out, that the particular choice of the angular term in the ABELL-TERSOFF potential has a similar correspondence in bond-order potentials for sp-valent systems (Alinaghian et al., 1993). The ABELL-TERSOFF potentials are slightly more expensive than EAM potentials and can treat similar systems sizes. There are many more empirical potentials available in literature, most notably the LENNARD-JONES potential (Jones, 1924) that is important not only as generic case for algorithm/method development, but also as add-on potential for an empirical description of VAN-DER-WAALS interactions.

For all these empirical potentials, the parametrisation and transferability is a major issue. Many effects of the electronic structure (hybridisation, magnetism, charge transfer) are difficult to be incorporated in the explicit formulation of empirical potentials. The resulting limited transferability gives rise to a dependence of the parametrisation on the considered reference data. Hence the optimal parametrisation for a given element depends often on the envisaged application. This can be partly overcome by giving up a fixed functional form and instead using an interpolating scheme with an open set of functions in the spirit of neural networks (Behler & Parrinello, 2007) or a closed set of functions in the spirit of a reactive force field (van Duin et al., 2001).

2.5 Example: Excess enthalpy of carbon in iron

Several empirical potentials have been proposed for the Fe-C system, due to the great technological relevance for steel production. These models include different parametrisations of the EAM type but also of the MEAM type that incorporates directional bonding. The advantage of using such a comparably simple potential would be the ability to describe microstructural effects that are known to be relevant for fabrication. In the following we will focus on one of the central aspects, the dependence of the solution energy of carbon in α-iron on external volumetric strain. An understanding of this is a prerequisite for predicting the distribution of C within the microstructure of the material. The relation between solubility and strain is also relevant to the interaction of carbon with extended defects such as grain boundaries and dislocations. It can therefore be seen as a critical test to assess if a model of the atomic interactions is applicable to the description of carbon near dislocations.

The solution energy (or excess enthalpy) is calculated by subtracting the cohesive energies of the elemental systems from the cohesive energy of the mixed system at volume V, i.e.

$$\Delta H(V) = E^{\mathrm{Fe}_N\mathrm{C}}(V) - E^{\mathrm{Fe}_N}(V) - E^{\mathrm{C}}(V) \tag{21}$$

where the number of iron atoms N is a variable in the calculations that defines the carbon concentration per unit volume. The calculation of each of these contributions includes a relaxation of the internal degrees of freedom at a fixed volume of the simulation cell.

A recent assessment (Hristova et al., 2011) compared the results of DFT and (M)EAM calculations for the strain-dependent solution energy. These calculations were carried out for a carbon atom in the energetically preferable octahedral interstitial site of a $3\times3\times3$ unit-cell of α-iron as shown in the left panel of Figure 5. This study showed that DFT calculations

predict a mostly linear decrease of the solution energy with increasing volumetric strain. This

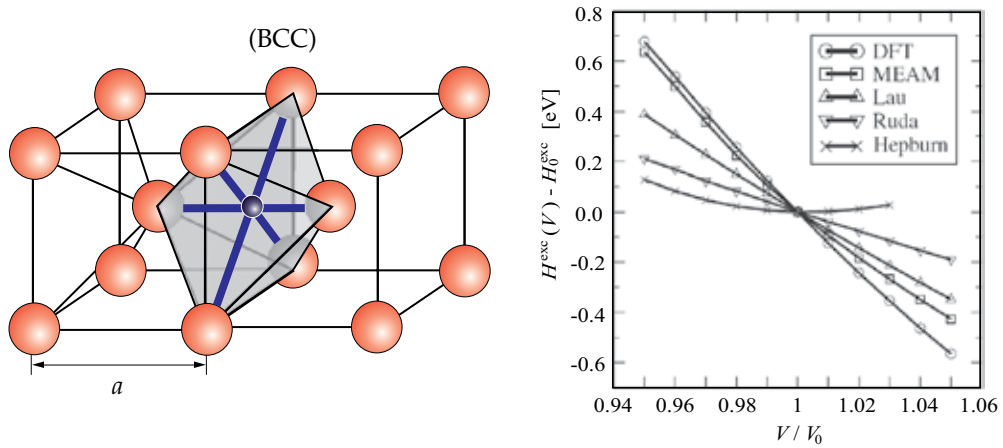

Fig. 5. Calculations of the strain-dependent solubility of C in an octahedral position in α-iron (indicated as the blue atom in left panel) show that only few empirical potentials are able to reproduce the results of corresponding DFT calculations (Hristova et al., 2011) (right panel).

can be understood intuitively in terms of the additional volume of the supercell that can be accommodated by the carbon atom. Despite this comparably simple intuitive picture, the majority of investigated EAM and MEAM potentials deviate noticeably from the DFT results. The overall trend, a decreasing solution energy with increasing strain, is present in all cases. However, the error in the slope ranges from qualitatively wrong to quantitatively reasonable. This example shows the need for developing predictive atomistic models. Once they are available, they can be employed in determining effective material properties as outlined in the next sections.

3. Lattice kinematics and energy

Beyond the task of more or less accurate description of atomic interactions presented in the previous section, the question remains, how to quantify macroscopic materials data and behaviour by considering the energy of an atom. The example in Section 2.5 already indicates the strategy to predict the (un-)mixing behaviour. However, in order to investigate further mechanical and thermodynamic materials properties a "more sophisticated analysis" of the atomic energy is necessary, which will be done in the subsequent Sections.

3.1 Crystal deformations

We start with the consideration of bulk material (no surfaces) and assume a perfect, periodic lattice. The current positions $\underline{\mathbf{X}}^\alpha$, $\underline{\mathbf{X}}^\beta$, $\underline{\mathbf{X}}^\gamma$, ... of all atoms α, β, γ, ... are described by the reference positions $\underline{\mathbf{X}}_0^\alpha$, $\underline{\mathbf{X}}_0^\beta$, $\underline{\mathbf{X}}_0^\gamma$, ... and the discrete displacements $\underline{\xi}^\alpha$, $\underline{\xi}^\beta$, $\underline{\xi}^\gamma$, ..., namely $\underline{\mathbf{X}}^\alpha = \underline{\mathbf{X}}_0^\alpha + \underline{\xi}^\alpha$, $\underline{\mathbf{X}}^\beta = \underline{\mathbf{X}}_0^\beta + \underline{\xi}^\beta$, ... (c.f., Figure 6). By introducing the distance vectors:

$$\underline{\mathbf{R}}_0^{\alpha\beta} = \underline{\mathbf{X}}_0^\beta - \underline{\mathbf{X}}_0^\alpha \quad , \quad \underline{\mathbf{R}}^{\alpha\beta} = \underline{\mathbf{X}}^\beta - \underline{\mathbf{X}}^\alpha = \underline{\mathbf{R}}_0^{\alpha\beta} + \underline{\xi}^\beta - \underline{\xi}^\alpha \tag{22}$$

between atom α and β the continuous displacement function $\underline{\mathbf{u}}$ can be defined as follows:

$$\underline{\xi}^{\alpha} \equiv \underline{\mathbf{u}}(\underline{\mathbf{X}}_0^{\alpha}) \equiv \underline{\mathbf{u}}(\underline{\mathbf{X}}_0) \quad , \quad \underline{\xi}^{\beta} = \underline{\mathbf{u}}(\underline{\mathbf{X}}_0^{\beta}) = \underline{\mathbf{u}}(\underline{\mathbf{X}}_0) + \frac{\partial \underline{\mathbf{u}}}{\partial \underline{\mathbf{X}}_0} \cdot \underline{\mathbf{R}}_0^{\alpha\beta} + \dots \quad , \tag{23}$$

$$\underline{\mathbf{R}}^{\alpha\beta} = \underline{\mathbf{R}}_0^{\alpha\beta} + \frac{\partial \underline{\mathbf{u}}}{\partial \underline{\mathbf{X}}_0} \cdot \underline{\mathbf{R}}_0^{\alpha\beta} = \underline{\underline{\mathbf{F}}} \cdot \underline{\mathbf{R}}_0^{\alpha\beta} \quad . \tag{24}$$

Here the symbol $\underline{\underline{\mathbf{F}}} = \underline{\underline{\mathbf{I}}} + \frac{\partial \underline{\mathbf{u}}}{\partial \underline{\mathbf{X}}_0}$ stands for the deformation gradient well known from macroscopic continuum mechanics. In order to describe the potential, temperature-independent energy of a lattice the deformed configuration is expanded into a TAYLOR series around the undeformed lattice state. If terms of higher order would be neglected, the energy of an atom α, $E^{\alpha}(\underline{\mathbf{R}}^{\alpha 1}, \dots, \underline{\mathbf{R}}^{\alpha N})$, within a deformed lattice consisting of N atoms can be written as:

$$E^{\alpha}(\underline{\mathbf{R}}^{\alpha 1}, \dots, \underline{\mathbf{R}}^{\alpha N}) = E^{\alpha}(\underline{\mathbf{R}}_0^{\alpha 1}, \dots, \underline{\mathbf{R}}_0^{\alpha N}) + \sum_{\substack{\beta \\ (\alpha \neq \beta)}} \frac{\partial E^{\alpha}}{\partial \underline{\mathbf{R}}^{\alpha\beta}}\Big|_{\underline{\mathbf{R}}_0^{\alpha\beta}} \cdot \left(\underline{\mathbf{R}}^{\alpha\beta} - \underline{\mathbf{R}}_0^{\alpha\beta}\right) +$$

$$+ \frac{1}{2} \sum_{\substack{\beta \\ (\alpha \neq \beta)}} \frac{\partial^2 E^{\alpha}}{\partial \underline{\mathbf{R}}^{\alpha\beta} \partial \underline{\mathbf{R}}^{\alpha\beta}}\Big|_{\underline{\mathbf{R}}_0^{\alpha\beta}} \cdot\cdot \left(\underline{\mathbf{R}}^{\alpha\beta} - \underline{\mathbf{R}}_0^{\alpha\beta}\right) \left(\underline{\mathbf{R}}^{\alpha\beta} - \underline{\mathbf{R}}_0^{\alpha\beta}\right) . \tag{25}$$

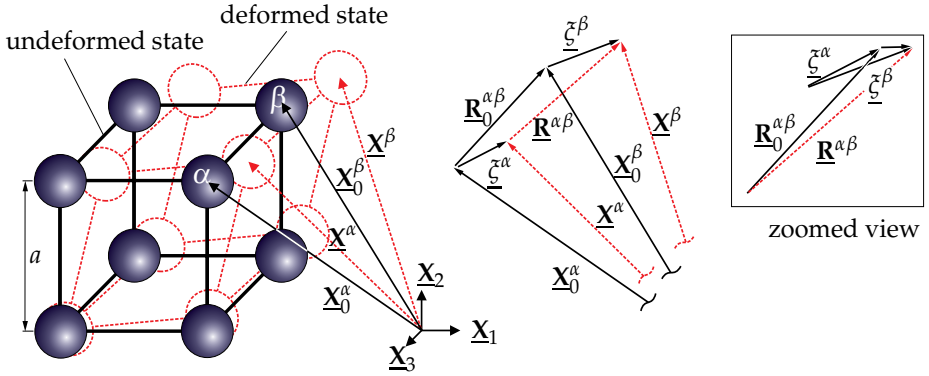

Fig. 6. Kinematic quantities of the undeformed and deformed lattice.

Within standard literature dealing with lattice kinematics, e.g. (Johnson, 1972; 1974; Leibfried, 1955), the linearized strains are introduced by using the approximation $\nabla \underline{\mathbf{u}} \equiv \frac{\partial \underline{\mathbf{u}}}{\partial \underline{\mathbf{X}}_0} \approx \frac{1}{2}(\nabla \underline{\mathbf{u}} + (\nabla \underline{\mathbf{u}})^{\mathrm{T}}) = \underline{\underline{\boldsymbol{\mathcal{E}}}}$. Substituting $\underline{\mathbf{R}}^{\alpha\beta} - \underline{\mathbf{R}}_0^{\alpha\beta}$ by Eq. (24) yields:

$$E^{\alpha}(\underline{\mathbf{R}}^{\alpha 1}, \dots, \underline{\mathbf{R}}^{\alpha N}) = E^{\alpha}(\underline{\mathbf{R}}_0^{\alpha 1}, \dots, \underline{\mathbf{R}}_0^{\alpha N}) + \underline{\underline{\boldsymbol{\mathcal{E}}}} \cdot \sum_{\substack{\beta \\ (\alpha \neq \beta)}} \frac{\partial E^{\alpha}}{\partial \underline{\mathbf{R}}^{\alpha\beta}}\Big|_{\underline{\mathbf{R}}_0^{\alpha\beta}} \underline{\mathbf{R}}_0^{\alpha\beta} +$$

$$+ \frac{1}{2} \underline{\underline{\boldsymbol{\mathcal{E}}}} \cdot\cdot \Big(\sum_{\substack{\beta \\ (\alpha \neq \beta)}} \underline{\mathbf{R}}_0^{\alpha\beta} \frac{\partial^2 E^{\alpha}}{\partial \underline{\mathbf{R}}^{\alpha\beta} \partial \underline{\mathbf{R}}^{\alpha\beta}}\Big|_{\underline{\mathbf{R}}_0^{\alpha\beta}} \underline{\mathbf{R}}_0^{\alpha\beta} \Big) \cdot\cdot \underline{\underline{\boldsymbol{\mathcal{E}}}}^{\mathrm{T}} \quad . \tag{26}$$

An alternative formulation of E^α is given by considering the scalar product of the atomic distance vector $\underline{\mathbf{R}}^{\alpha\beta}$, viz.

$$R^{\alpha\beta\,2} = \underline{\mathbf{R}}^{\alpha\beta} \cdot \underline{\mathbf{R}}^{\alpha\beta} = (\underline{\underline{\mathbf{F}}} \cdot \underline{\mathbf{R}}_0^{\alpha\beta}) \cdot (\underline{\underline{\mathbf{F}}} \cdot \underline{\mathbf{R}}_0^{\alpha\beta}) = R_0^{\alpha\beta\,2} + \underline{\mathbf{R}}_0^{\alpha\beta} \cdot (\underline{\underline{\mathbf{C}}} - \underline{\underline{\mathbf{I}}}) \cdot \underline{\mathbf{R}}_0^{\alpha\beta} \quad , \tag{27}$$

in which GREEN's strain tensor $\underline{\underline{\mathbf{G}}} = \frac{1}{2}(\underline{\underline{\mathbf{C}}} - \underline{\underline{\mathbf{I}}})$ with $\underline{\underline{\mathbf{C}}} = \underline{\underline{\mathbf{F}}}^{\mathrm{T}} \cdot \underline{\underline{\mathbf{F}}}$ is used to quantify the deformation (for small deformations holds $\underline{\underline{\mathbf{G}}} \approx \underline{\underline{\boldsymbol{\mathcal{E}}}}$). Now the energy of Eq. (26) can be rewritten as follows:

$$E^\alpha(R^{\alpha 1\,2}, \ldots, R^{\alpha N\,2}) = E^\alpha(R_0^{\alpha 1\,2}, \ldots, R_0^{\alpha N\,2}) + 2\underline{\underline{\mathbf{G}}} \cdot\cdot \sum_{\substack{\beta \\ (\alpha \neq \beta)}} E^{\alpha\prime} \underline{\mathbf{R}}_0^{\alpha\beta} \underline{\mathbf{R}}_0^{\alpha\beta} +$$

$$+ \frac{4}{2}\underline{\underline{\mathbf{G}}} \cdot\cdot \Big(\sum_{\substack{\beta \\ (\alpha \neq \beta)}} E^{\alpha\prime\prime} \underline{\mathbf{R}}_0^{\alpha\beta} \underline{\mathbf{R}}_0^{\alpha\beta} \underline{\mathbf{R}}_0^{\alpha\beta} \underline{\mathbf{R}}_0^{\alpha\beta} \Big) \cdot\cdot \underline{\underline{\mathbf{G}}} \tag{28}$$

with the abbreviation $E^{\alpha\prime} = \partial E^\alpha / \partial R^{\alpha\beta\,2}|_{R^{\alpha\beta 2} = R_0^{\alpha\beta 2}}$. Since first derivatives of the energy must vanish for equilibrium (minimum of energy) this expression allows to directly identify the equilibrium condition, which - in turn - provides an equation for calculating the lattice parameter a. Furthermore the last term of Eq. (28) can be linked to the stiffness matrix $\mathbb{C} = [C_{ijkl}]$, which contains the elastic constants of the solid. However, the atomic energy E^α in Eq. (28) must be formulated in terms of the square of the scalar distances $R^{\alpha\beta}$ between the atoms $\alpha, \beta = 1, \ldots, N$.

3.2 Brief survey of JOHNSON's analytical embedded-atom method

The specific form of E^α, $E^{\alpha\prime}$ and $E^{\alpha\prime\prime}$ in Eq. (28) strongly depends on the chosen interaction model and the corresponding parametrization, i.e., the chosen form of the function(s), which contribute(s) to the potential energy. Therefore we restrict the following explanations to so-called EAM potentials, which were developed in the mid-1980s years by DAW & BASKES and which were successfully applied to a wide range of metals, see also Section 2.4.

In order to quantify the different interaction terms in Eq. (19) parametrizations for $\phi^{\alpha\beta}$, F_α and ρ_β are required. Here JOHNSON (Johnson, 1988; 1989) published an analytical version of the EAM, which incorporates nearest-neighbors-interactions, i.e. atoms only interact with direct neighbors separated by the nearest neighbor distance $R_0 = a^{(\mathrm{e})}/\sqrt{2}$ or $R = a\sqrt{2}$ (in case of an FCC lattice), respectively. Here the symbol a denotes the lattice parameter and the index (e) stands for "equilibrium". By considering the pure substance "A" the following, monotonically decreasing form for the atomic charge density[4] and the pairwise interaction term holds[5]

$$\rho_{\mathrm{A}}(R^2) = \rho^{(\mathrm{e})} \exp\Big[-\beta\Big(\frac{R^2}{R_0^2} - 1\Big)\Big] \quad , \quad \phi^{\mathrm{AA}}(R^2) = \phi^{(\mathrm{e})} \exp\Big[-\gamma\Big(\frac{R^2}{R_0^2} - 1\Big)\Big] \quad . \tag{29}$$

[4] This form corresponds the spherical s-orbitals; consequently this method mainly holds for isotropic structures, such as FCC (Face-Centered-Cubic), cf. Figure 7. For more anisotropic configurations, such as BCC (Body-Centered-Cubic) or HCP (Hexagonal-Closed-Packed), $\bar{\rho}_\alpha$ must be varied for different directions, which lead to the Modified-EAM (Bangwei et al., 1999; Baskes, 1992; Zhang et al., 2006).

[5] For convenience we omit the index "A" at the parameters $\rho^{(\mathrm{e})}$, β, $\phi^{(\mathrm{e})}$, γ and R. The same parametrizations hold for another pure substance "B". However ρ_{A} and ρ_{B} as well as ϕ^{AA} and ϕ^{BB} have different fitting parameters.

Originally, JOHNSON used the scalar distance R within the above equations, but due to the explanations in Section 3.1 the present formulation in terms of R^2 is used by simple substitution (Böhme et al., 2007). By using the universal equation of state derived by ROSE and COWORKERS (Rose et al., 1984) the embedding function reads:

$$F_{\mathrm{A}}(\rho_{\mathrm{A}}) = -E_{\mathrm{sub}}\left[1+\alpha\left(\sqrt{1-\frac{1}{\beta}\ln\frac{\bar{\rho}_{\mathrm{A}}}{\bar{\rho}_{\mathrm{A}}^{(\mathrm{e})}}}-1\right)\right]\exp\left[\alpha\left(1-\sqrt{1-\frac{1}{\beta}\ln\frac{\bar{\rho}_{\mathrm{A}}}{\bar{\rho}_{\mathrm{A}}^{(\mathrm{e})}}}\right)\right]-6\phi^{(\mathrm{e})}\left(\frac{\bar{\rho}_{\mathrm{A}}}{\bar{\rho}_{\mathrm{A}}^{(\mathrm{e})}}\right)^{\frac{\gamma}{\beta}} \tag{30}$$

with $\alpha = \sqrt{\kappa\Omega^{(\mathrm{e})}/E_{\mathrm{sub}}}$; ($\Omega^{(\mathrm{e})}$: volume per atom). Hence three functions ϕ^{AA}, ρ_{A}, and F_{A} must be specified for the pure substance "A", which is done by fitting the five parameters $\alpha, \beta, \gamma, \phi^{(\mathrm{e})}, \rho^{(\mathrm{e})}$ to experimental data such as bulk modulus κ, shear modulus G, unrelaxed vacancy formation energy $E_{\mathrm{v}}^{\mathrm{u}}$, and sublimation energy E_{sub} (Böhme et al., 2007). For mixtures additional interactions must be considered and, therefore, the number of required fit-parameters considerably increases. For a binary alloy "A-B" seven functions $\phi^{\mathrm{AA}}, \phi^{\mathrm{BB}}, \phi^{\mathrm{AB}}, \rho_{\mathrm{A}}, \rho_{\mathrm{B}}, F_{\mathrm{A}}, F_{\mathrm{B}}$ must be determined. Here the pairwise interaction, ϕ^{AB}, between atoms of different type is defined by "averaging" as follows:

$$\phi^{\mathrm{AB}} = \frac{1}{2}\left(\frac{\rho_{\mathrm{B}}}{\rho_{\mathrm{A}}}\phi^{\mathrm{AA}} + \frac{\rho_{\mathrm{A}}}{\rho_{\mathrm{B}}}\phi^{\mathrm{AA}}\right) \quad . \tag{31}$$

Consequently all functions are calculated from information of the pure substances; however 10 parameter must be fitted. In Figure 8 the different functions according to Eq. (19) are illustrated for both FCC-metals Ag and Cu. The experimental data used to fit the EAM parameters are shown in Table 1.

atom	a in Å	E_{sub} in eV	$E_{\mathrm{v}}^{\mathrm{u}}$ in eV	κ in eV/Å^3	G in eV/Å^3
Ag	4.09	2.85	1.10	0.65	0.21
Cu	3.61	3.54	1.30	0.86	0.34

Table 1. Experimental data for silver and copper (the volume occupied by a single atom is calculated via $\Omega = a^3/4$).

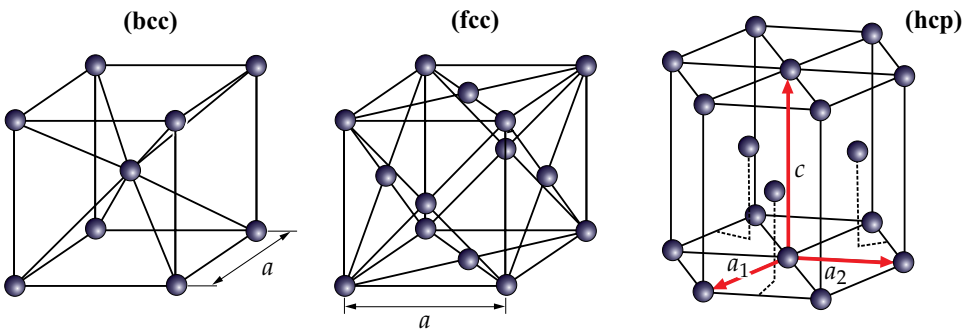

Fig. 7. Elementary cell of the BCC, FCC and HCP lattice.

3.3 Equilibrium condition, elastic constants, and lattice energy

A. Pure substances

By means of Eq. (19) the atomic energy in Eq. (28) can be further specified. For this reason we use the relation $R^{\alpha\beta\,2} = R_0^{\alpha\beta\,2} + \underline{\mathbf{R}}_0^{\alpha\beta} \cdot \underline{\underline{\mathbf{G}}} \cdot \underline{\mathbf{R}}_0^{\alpha\beta}$ derived in Section 3.1 and expand $\phi^{\alpha\beta}(R^{\alpha\beta\,2}), \rho_\beta(R^{\alpha\beta\,2})$ as well as $F_\alpha(\sum \rho_\beta(R^{\alpha\beta\,2}))$ around $R_0^{\alpha\beta\,2}$. Then the energy of atom α reads:

$$E^\alpha = \frac{1}{2}\sum_\beta \phi^{\alpha\beta}(R_0^{\alpha\beta\,2}) + F_\alpha(\bar{\rho}_\alpha^{(\mathrm{e})}) + \underline{\underline{\mathbf{G}}} \cdot \cdot \left[\underline{\underline{\mathbf{A}}}^\alpha + 2F'_\alpha(\bar{\rho}_\alpha^{(\mathrm{e})})\underline{\underline{\mathbf{V}}}^\alpha\right] + \\ + \underline{\underline{\mathbf{G}}} \cdot \cdot \left[\mathbb{B}^\alpha + 2F'_\alpha(\bar{\rho}_\alpha^{(\mathrm{e})})\mathbb{W}^\alpha + 2F''_\alpha(\bar{\rho}_\alpha^{(\mathrm{e})})\underline{\underline{\mathbf{V}}}^\alpha\underline{\underline{\mathbf{V}}}^\alpha\right] \cdot \cdot \underline{\underline{\mathbf{G}}} \tag{32}$$

in which the following abbreviations hold:

$$\begin{aligned}
\underline{\underline{\mathbf{A}}}^\alpha &= \sum_\beta \phi'^{\alpha\beta}(R_0^{\alpha\beta\,2})\underline{\mathbf{R}}_0^{\alpha\beta}\underline{\mathbf{R}}_0^{\alpha\beta} \\
\mathbb{B}^\alpha &= \sum_\beta \phi''^{\alpha\beta}(R_0^{\alpha\beta\,2})\underline{\mathbf{R}}_0^{\alpha\beta}\underline{\mathbf{R}}_0^{\alpha\beta}\underline{\mathbf{R}}_0^{\alpha\beta}\underline{\mathbf{R}}_0^{\alpha\beta} \quad , \\
\underline{\underline{\mathbf{V}}}^\alpha &= \sum_\beta \rho'_\beta(R_0^{\alpha\beta\,2})\underline{\mathbf{R}}_0^{\alpha\beta}\underline{\mathbf{R}}_0^{\alpha\beta} \\
\mathbb{W}^\alpha &= \sum_\beta \rho''_\beta(R_0^{\alpha\beta\,2})\underline{\mathbf{R}}_0^{\alpha\beta}\underline{\mathbf{R}}_0^{\alpha\beta}\underline{\mathbf{R}}_0^{\alpha\beta}\underline{\mathbf{R}}_0^{\alpha\beta} \quad .
\end{aligned} \tag{33}$$

Note that in case of equilibrium the nearest neighbor distance is equal for all neighbors β, viz. $R_0^{\alpha\beta} = R_0 = \text{const}$. By considering an FCC lattice with 12 nearest neighbors one finds $\frac{1}{2}\sum_\beta \phi^{\alpha\beta}(R_0^{\alpha\beta\,2}) = 6\phi^{(\mathrm{e})}$ and $\bar{\rho}_\alpha^{(\mathrm{e})} = 12\rho_\alpha^{(\mathrm{e})}$.

Three parts of Eq. (33) are worth-mentioning: The first two terms represent the energy of atom α within an undeformed lattice. The term within the brackets $[\ldots]$ of the third summand denotes the slope of the energy curves in Figure 8 (a). If lattice dynamics is neglected, the relation $\underline{\underline{\mathbf{A}}}^\alpha + 2F'_\alpha(\bar{\rho}_\alpha^{(\mathrm{e})})\underline{\underline{\mathbf{V}}}^\alpha = 0$ will identify the *equilibrium condition* and defines the nearest neighbor distance in equilibrium. The expression within the brackets $\underline{\underline{\mathbf{G}}} \cdot \cdot [\ldots] \cdot \cdot \underline{\underline{\mathbf{G}}}$ of the last term can be linked to the macroscopic constitutive equation $E_{\mathrm{elast}}/V = \frac{1}{2}\underline{\underline{\boldsymbol{\mathcal{E}}}} \cdot \cdot \mathbb{C} \cdot \cdot \underline{\underline{\boldsymbol{\mathcal{E}}}}$ with $\underline{\underline{\mathbf{G}}} \approx \underline{\underline{\boldsymbol{\mathcal{E}}}}$ (HOOKE's law). Here $\mathbb{C}$ stands for the *stiffness matrix* and the coefficients $[C_{ijkl}]$ represent the *elastic constants*. In particular we note: $\mathbb{C}^\alpha = \frac{2}{\Omega^{(\mathrm{e})}}[\mathbb{B}^\alpha + 2F'_\alpha(\bar{\rho}_\alpha^{(\mathrm{e})})\mathbb{W}^\alpha + 2F''_\alpha(\bar{\rho}_\alpha^{(\mathrm{e})})\underline{\underline{\mathbf{V}}}^\alpha\underline{\underline{\mathbf{V}}}^\alpha]$. Thus, in case of the above analyzed metals Ag and Cu, we obtain the following atomistically calculated values[6] (for comparison the literature values (Kittel, 1973; Leibfried, 1955) are additionally noted within the parenthesis):

$$\begin{aligned}
C_{1111}^{\mathrm{Ag}} &= 132.6\ (124)\ \mathrm{GPa} \quad , \quad C_{1122}^{\mathrm{Ag}} = 90.2\ (94)\ \mathrm{GPa} \quad , \quad C_{2323}^{\mathrm{Ag}} = 42.4\ (46)\ \mathrm{GPa} \quad , \\
C_{1111}^{\mathrm{Cu}} &= 183.7\ (168)\ \mathrm{GPa} \quad , \quad C_{1122}^{\mathrm{Cu}} = 115.1\ (121)\ \mathrm{GPa} \quad , \quad C_{2323}^{\mathrm{Cu}} = 68.7\ (75)\ \mathrm{GPa} \quad ,
\end{aligned}$$

with $C_{1111} = C_{2222} = C_{3333}$; $C_{1122} = C_{1133} = C_{2233}$; $C_{2323} = C_{1313} = C_{1212}$ and $C_{ijkl} = C_{klij}$. Obviously the discrepancy between the theoretical calculations and experimental findings is

[6] There are three non-equivalent elastic constants for cubic crystals (Leibfried, 1955).

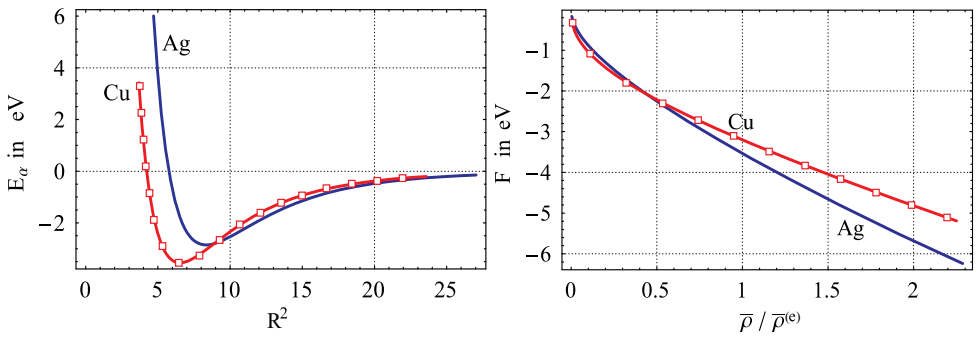

(a) energy of atom α (b) embbeding function

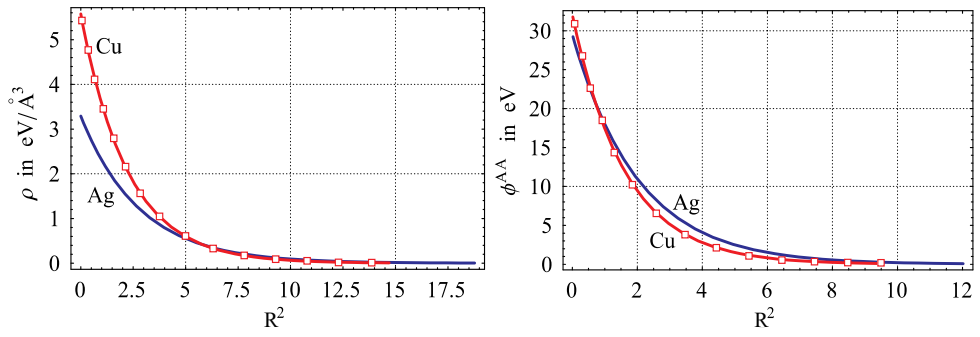

(c) atomic electronic density (d) pairwise, repulsive interaction

Fig. 8. Different contributions to the EAM potential for silver ($\alpha = 5.92$, $\beta = 2.98$, $\gamma = 4.13$, $\phi^{(e)} = 0.48$ eV/Å^3, $\rho^{(e)} = 0.17$ eV/Å^3) and copper ($\alpha = 5.08$, $\beta = 2.92$, $\gamma = 4.00$, $\phi^{(e)} = 0.59$ eV/Å^3, $\rho^{(e)} = 0.30$ eV/Å^3).

reasonably good; the relative error range is 4.1 (C_{1111}^{Ag}) - 9.3 (C_{1111}^{Cu}) percent.

B. Alloys

Up to now we only discussed atomic interactions between atoms of the same type. Consequently the question arises, how to exploit the energy expression in Eq. (32) for solid mixtures. To answer this question we have to clarify, how different "types of atoms" can be incorporated within the above set of equations. For this reason let us consider a non-stoichiometric (the occupation of lattice sites by solute substance takes place stochastically, no reactions occur) *binary alloy* "A-B" with the atomic concentration y. Hence we must distinguish the following interactions: A⇔A, B⇔B, A⇔B. Following DE FONTAINE (De Fontaine, 1975) we introduce the discrete concentration $\hat{y}_\gamma = \delta_{\gamma B}$; $\gamma = \{1, \ldots, N\}$, where δ_{ij} is the KRONECKER symbol. Then $\phi^{\alpha\beta}$ and $\bar{\rho}_\alpha^{(e)}$ can be written as:

$$\phi^{\alpha\beta} = \phi^{AA} + \left[\hat{y}_\alpha + (1 - 2\hat{y}_\alpha)\hat{y}_\beta\right]\phi + (\hat{y}_\alpha + \hat{y}_\beta)\tilde{\phi}\,, \tag{34}$$

$$\bar{\rho}_\alpha^{(e)} = \sum_\beta \left[\hat{y}_\beta(\rho_B - \rho_A) + \rho_A\right] \tag{35}$$

with the definitions $\phi = \phi^{\mathrm{AB}} - \frac{1}{2}(\phi^{\mathrm{AA}} + \phi^{\mathrm{BB}})$ and $\tilde{\phi} = \frac{1}{2}(\phi^{\mathrm{BB}} - \phi^{\mathrm{AA}})$. Here $\hat{y}_\gamma$ acts as a "selector", which provides the corresponding interaction terms depending on which pair of atoms is considered. Thus, in particular, $\hat{y}_{\alpha/\beta}$ are both zero, if two "A" atoms are considered and $\phi^{\alpha\beta} = \phi^{\mathrm{AA}}$ and $\bar{\rho}_\alpha^{(\mathrm{e})} = \sum_\beta \rho_{\mathrm{A}}$ would follow. Replacing the discrete concentrations by its continuous counterpart:

$$\hat{y}_\alpha = y(\underline{\mathbf{X}}_0^\alpha) \equiv y(\underline{\mathbf{X}}_0) \quad , \quad \hat{y}_\beta = y(\underline{\mathbf{X}}_0) + \frac{\partial y}{\partial \underline{\mathbf{X}}_0} \cdot \underline{\mathbf{R}}_0^{\alpha\beta} + \frac{1}{2}\frac{\partial^2 y}{\partial \underline{\mathbf{X}}^2} \cdot \cdot \underline{\mathbf{R}}_0^{\alpha\beta}\underline{\mathbf{R}}_0^{\alpha\beta} \tag{36}$$

yields the so-called mean-field limit[7], viz.

$$\phi^{\alpha\beta} = \phi^{\mathrm{AA}} + 2y(1-y)\phi + 2y\tilde{\phi} + \mathcal{O}\Big(\nabla y, \nabla^2 y\Big) \,, \tag{37}$$

$$\bar{\rho}_\alpha^{(\mathrm{e})} = \bar{\rho}_{\mathrm{A}} + y\bar{\rho}_\Delta + \mathcal{O}\Big(\nabla y, \nabla^2 y\Big) \quad \text{with} \quad \bar{\rho}_\Delta = \sum_\beta (\bar{\rho}_{\mathrm{B}} - \bar{\rho}_{\mathrm{A}}) \,. \tag{38}$$

In a similar manner the embedding function F_α in Eq. (32) is decomposed:

$$F_\alpha(\bar{\rho}_\alpha^{(\mathrm{e})}) = (1-y)F_{\mathrm{A}} + yF_{\mathrm{B}} \,, \tag{39}$$

but note that the argument of $F_{\mathrm{A/B}}$ is also defined by a decomposition according to Eq. (38). Therefore F_{A} and F_{B} are separately expanded into a TAYLOR series around the weighted averaged electron density $\bar{\rho}_{\mathrm{av}} = (1-y)\bar{\rho}_{\mathrm{A}} + y\bar{\rho}_{\mathrm{B}}$, namely $F_{\mathrm{A/B}}(\bar{\rho}_\alpha^{(\mathrm{e})}) = F_{\mathrm{A/B}}(\bar{\rho}_{\mathrm{av}}) + \mathcal{O}(\nabla^2 y)$. Moreover, the quantities $\underline{\underline{\mathbf{A}}}^\alpha$, $\mathbb{B}^\alpha$, $F'_\alpha \underline{\underline{\mathbf{V}}}^\alpha$, $F''_\alpha \underline{\underline{\mathbf{V}}}^\alpha \underline{\underline{\mathbf{V}}}^\alpha$, and $F'_\alpha \mathbb{W}^\alpha$ can be also treated analogously to Eqs. (39-37). Finally, one obtains for the energy of an atom α within a binary alloy, see also (Böhme et al., 2007) for a detailed derivation:

$$\begin{aligned}
E^\alpha(y) = {} & \frac{1}{2}g^{\mathrm{AA}} + F_{\mathrm{A}} + yg^{\tilde{\phi}} + y(F_{\mathrm{B}} - F_{\mathrm{A}}) + y(1-y)g^{\phi} + \\
& + \underline{\underline{\mathbf{G}}} \cdot \cdot \Big[\underline{\underline{\mathbf{A}}}^{\mathrm{A}} + 2y\underline{\underline{\mathbf{A}}}^{\tilde{\phi}} + 2y(1-y)\underline{\underline{\mathbf{A}}}^{\phi} + 2\Big(\underline{\underline{\mathbf{V}}}^{\mathrm{A}} + y\underline{\underline{\mathbf{V}}}^{\Delta}\Big)\Big(F'_{\mathrm{A}} + y(F'_{\mathrm{B}} - F'_{\mathrm{A}})\Big)\Big] + \\
& + \frac{1}{2}\underline{\underline{\mathbf{G}}} \cdot \cdot \Big[2\mathbb{B}^{\mathrm{A}} + 4y\mathbb{B}^{\tilde{\phi}} + 2y(1-y)\mathbb{B}^{\phi} + 4\Big(\mathbb{W}^{\mathrm{A}} + y\mathbb{W}^{\Delta}\Big)\Big(F'_{\mathrm{A}} + y(F'_{\mathrm{B}} - F'_{\mathrm{A}})\Big) + \\
& + 4\Big(\underline{\underline{\mathbf{V}}}^{\mathrm{A}} + y\underline{\underline{\mathbf{V}}}^{\Delta}\Big)\Big(\underline{\underline{\mathbf{V}}}^{\mathrm{A}} + y\underline{\underline{\mathbf{V}}}^{\Delta}\Big)\Big(F''_{\mathrm{A}} + y(F''_{\mathrm{B}} - F''_{\mathrm{A}})\Big)\Big] \cdot \cdot \underline{\underline{\mathbf{G}}} + \mathcal{O}(\nabla y, \nabla^2 y)
\end{aligned} \tag{40}$$

with the abbreviations: $g^{\mathrm{AA}} = \sum_\beta \phi^{\mathrm{AA}}$, $g^{\phi} = \sum_\beta \phi$, $g^{\tilde{\phi}} = \sum_\beta \tilde{\phi}$. The remaining abbreviations $\underline{\underline{\mathbf{A}}}^{\mathrm{A}}$, $\underline{\underline{\mathbf{A}}}^{\phi}$, $\underline{\underline{\mathbf{A}}}^{\tilde{\phi}}$, $\mathbb{B}^{\phi}$, $\mathbb{B}^{\tilde{\phi}}$, $\underline{\mathbf{V}}^{\Delta}$, and $\mathbb{W}^{\Delta}$ are defined correspondingly to Eq. (33); here the indices A, ϕ, $\tilde{\phi}$, and Δ refer to the first argument within the sum, i.e. $\phi^{\mathrm{AA}\prime}$; ϕ' or ϕ''; $\tilde{\phi}'$ or $\tilde{\phi}''$, and $(\rho'_{\mathrm{B}} - \rho'_{\mathrm{A}})$ or $(\rho''_{\mathrm{B}} - \rho''_{\mathrm{A}})$. Eq. (40) indicates various important conclusions:

- The terms of the **first row** stand for the energy of the undeformed lattice. Here no mechanical effects contributes to the energy of the (homogeneous) solid. These energy

[7] For homogeneous mixtures concentration gradients can be neglected; for mixtures with spatially varying composition terms with $\nabla y = \partial y/\partial \underline{\mathbf{X}}_0$ and $\nabla^2 y = \partial y^2/\partial \underline{\mathbf{X}}_0^2$ contribute e.g. to phase kinetics, cf. (Böhme et al., 2007).

terms are typically used in equilibrium thermodynamics to determine GIBBS free energy and phase diagrams.

- The **second row**, in particular the expression within the brackets $[\ldots]$, identifies the *equilibrium condition* since first derivatives of the energy must vanish in equilibrium. Analyzing the root

$$\underline{\underline{\mathbf{A}}}^{\mathrm{A}} + 2y\underline{\underline{\mathbf{A}}}^{\tilde{\phi}} + 2y(1-y)\underline{\underline{\mathbf{A}}}^{\phi} + 2\Big(\underline{\underline{\mathbf{V}}}^{\mathrm{A}} + y\underline{\underline{\mathbf{V}}}^{\Delta}\Big)\Big(F'_{\mathrm{A}} + y(F'_{\mathrm{B}} - F'_{\mathrm{A}})\Big) \equiv 0 \tag{41}$$

yields $a^{(\mathrm{e})}(y)$ as a function of the concentration, cf. example below.

- The term of the **third and last row** denotes the elastic energy $E^{\mathrm{elast}} = \frac{1}{2}\underline{\underline{\boldsymbol{\mathcal{E}}}} \cdot\cdot\, \mathbb{C}(y) \cdot\cdot\, \underline{\underline{\boldsymbol{\mathcal{E}}}}$ with $\underline{\underline{\boldsymbol{\mathcal{E}}}} \approx \underline{\underline{\mathbf{G}}}$ of an atom in the lattice system. Consequently, the bracket term characterizes the *stiffness matrix* of the solid mixture, viz.

$$\mathbb{C}(y) = \frac{1}{\Omega^{(\mathrm{e})}(y)}\Big[2\mathbb{B}^{\mathrm{A}} + 4y\mathbb{B}^{\tilde{\phi}} + 2y(1-y)\mathbb{B}^{\phi} + 4\Big(\mathbb{W}^{\mathrm{A}} + y\mathbb{W}^{\Delta}\Big)\Big(F'_{\mathrm{A}} + y(F'_{\mathrm{B}} - F'_{\mathrm{A}})\Big) + \\ + 4\Big(\underline{\underline{\mathbf{V}}}^{\mathrm{A}} + y\underline{\underline{\mathbf{V}}}^{\Delta}\Big)\Big(\underline{\underline{\mathbf{V}}}^{\mathrm{A}} + y\underline{\underline{\mathbf{V}}}^{\Delta}\Big)\Big(F''_{\mathrm{A}} + y(F''_{\mathrm{B}} - F''_{\mathrm{A}})\Big)\Big] . \tag{42}$$

Note that $\Omega^{(\mathrm{e})}(y)$ is calculated by $a^{(\mathrm{e})}(y)$ following from Eq. (41).

Figure 9 (left) displays the left hand side of Eq. (41) as a function of R^2 for different concentrations $y = y_{\mathrm{Cu}}$ in Ag-Cu. The root defines the equilibrium lattice parameter, which is illustrated in Figure 9 (right). Obviously, $a^{(\mathrm{e})}(y)$ does not follow VEGARD's law. However, by using the mass concentration $c(y) = yM_{\mathrm{Cu}}/(yM_{\mathrm{Cu}} + (1-y)M_{\mathrm{Ag}})$ instead of y the linear interpolation $a^{(\mathrm{e})}(c) = (1-c)a_{\mathrm{Ag}} + ca_{\mathrm{Cu}}$ holds.

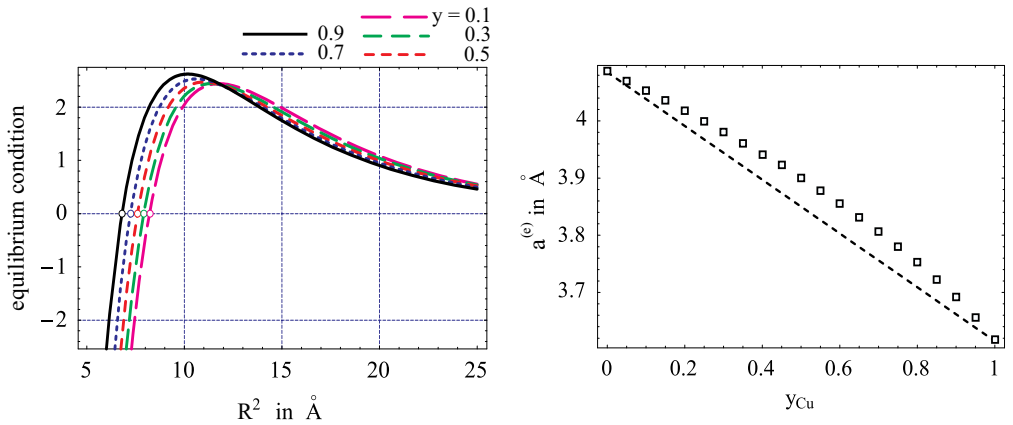

Fig. 9. *Left*: Left hand side of the equilibrium condition for different, exemplarily chosen concentrations ($R^2_{0,\mathrm{Ag}} = 8.35$, $R^2_{0,\mathrm{Cu}} = 6.53$). *Right*: Calculated equilibrium lattice parameter as a function of concentration.

The three independent elastic constants for the mixture Ag-Cu are calculated by Eq. (42) and illustrated in Figure 10. Here we used $a^{(\mathrm{e})}(y_i)$, with $y_i = 0, 0.05, \ldots, 0.95, 1$ correspondingly to Figure 9 (right). It is easy to see, that for $y = 0$ (Ag) and $y = 1$ (Cu) the elastic constants of

silver and copper, illustrated on page 15, result. However, for $0 < y < 1$ the elements of the stiffness matrix do not follow the linear interpolation as indicated in Figure 10.

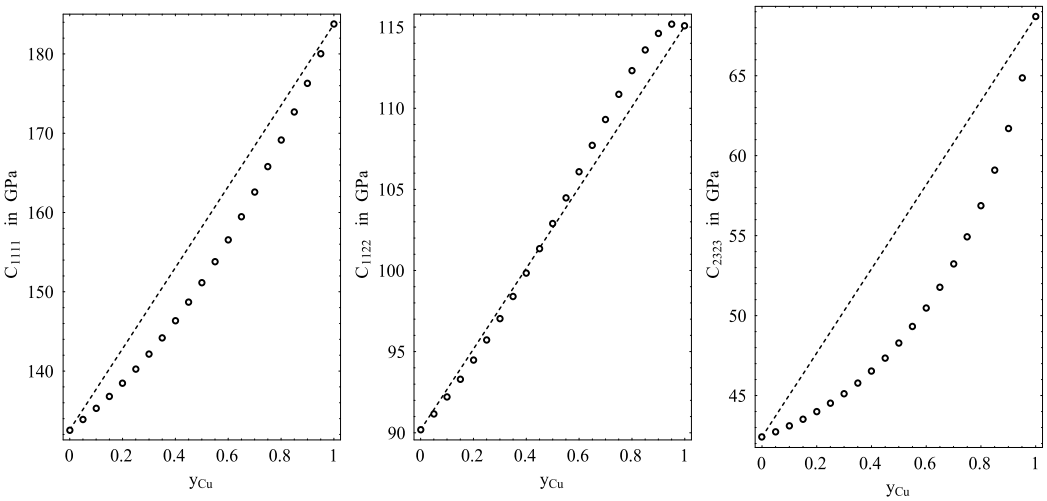

Fig. 10. Calculated elastic constants for Ag-Cu as function of concentration.

Finally, Eq. (40) allows to analyze the so-called *excess enthalpy* g^{exc} of the solid system, which characterizes the (positive or negative) heat of mixing. It represents the deviation of the resulting energy of mixture with concentration y from the linear interpolation of the pure-substance-contributions, cf. Section 2.5. By considering the so-called regular solution model introduced by HILDEBRANDT in 1929, see for example the textbook of (Stølen & Grande, 2003):

$$g^{\text{exc}} = \Lambda\, y(1-y) \quad \text{with} \quad y = y_{\text{B}}\,,\; y_{\text{A}} = 1-y \quad \text{(binary alloys)}\,. \tag{43}$$

the excess term can be directly identified in Eq. (40) as the coefficient of $y(1-y)$. However, the above regular solution model only allows symmetric curves $g^{\text{exc}}(y)$, with the maximum at $y = 0.5$. This shortcoming originates from the constant Λ-value and is remedied within the above energy expression of Eq. (40). In particular holds:

$$\Lambda = \Lambda(y) = g^{\phi}(y) + \underline{\underline{\mathbf{G}}}(y) \cdot\cdot\, \mathbb{B}^{\phi} \cdot\cdot\, \underline{\underline{\mathbf{G}}}\,. \tag{44}$$

Here g^{ϕ} as well as $\mathbb{B}^{\phi}$ are given by the interatomic potentials[8] and must be evaluated at the concentration dependent nearest neighbor distance $R_0(y) = a^{(\text{e})}(y)/\sqrt{2}$, which - in turn - follows from the equilibrium condition. Thus, symmetry of Eq. (43) does not necessarily exist. Moreover, further investigations of Eq. (44) may allow a deeper understanding of non-ideal energy-contributions to solid (and mechanically stressed) mixtures.

[8] Note, that Λ exclusively depends on the pairwise interaction terms; contributions from the embedding functions naturally cancel.

4. Thermodynamic properties

Atomistic approaches for calculating interaction energies cannot only be used to quantify deformation and mechanical equilibrium but may also serve as the basis for accessing thermodynamic and thermo-mechanical properties as we will show in the following section.

4.1 Phase diagram construction

In macroscopic thermodynamics the molar GIBBS free energy of an undeformed binary mixture is typically written as (pressure $P = \text{const.}$):

$$\tilde{g}(y,T) = (1-y_\mathrm{B})\tilde{g}_\mathrm{A}(T) + y_\mathrm{B}\tilde{g}_\mathrm{B}(T) + N_A k_B T\Big[y_\mathrm{B}\ln y_\mathrm{B} + (1-y_\mathrm{B})\ln(1-y_\mathrm{B})\Big] + \tilde{g}^{\mathrm{exc}}(y,T)\,. \tag{45}$$

The first and second term represent the contributions from the pure substances; the third summand denotes the entropic part of an ideal mixture $-T\tilde{s}(y) = -N_A k_B T \sum_{i=1}^{2} y_i \ln y_i$ with $N_A = 6.022 \cdot 10^{23}$ mol^{-1} (AVOGADRO constant) and $k_B = 1.38 \cdot 10^{-23}$ J/K (BOLTZMANN constant) and the last term stands for the molar excess enthalpy.
By using the identity $\tilde{g}(y,T) = N_A g(y,T) = N_A[E^\alpha - Ts(y)]$ the atom-specific GIBBS free energy can be directly calculated from the expression in Eq. (40), viz.

$$g(y,T) = (1-y_\mathrm{B})(6\phi^{\mathrm{AA}} + F_\mathrm{A}) + y(6\phi^{\mathrm{BB}} + F_\mathrm{B}) + k_B T\Big[y_\mathrm{B}\ln y_\mathrm{B} + (1-y_\mathrm{B})\ln(1-y_\mathrm{B})\Big] + \\ + 12y(1-y)\phi\,. \tag{46}$$

Obviously, the GIBBS free energy curve is superposed by three, characteristic parts, namely **(a)** a linear function interpolating the energy of the pure substances; **(b)** a convex, symmetric entropic part, which has the minimum at $y = 0.5$ and vanishes for $y = \{0,1\}$ and **(c)** an excess term, which - in case of binary solids with miscibility gap - has a positive, concave curve shape, cf. Figure 11 (right). Hence, a double-well function results, as illustrated in Figure 11 (left) for the cases of Ag-Cu at 1000 K. Here the concave domain $y \in [0.19, 0.79]$ identifies the unstable regime, in which any homogeneous mixture starts to decompose into two different equilibrium phases (α) and (β) with the concentrations $y_{(\alpha)}$, $y_{(\beta)}$, cf. (Cahn, 1968).
In order to determine the equilibrium concentrations the so-called *common tangent rule* must be applied. According to this rule the mixture decomposes such, that the slope of the energy curve at $y_{(\alpha)/\beta}$ is equal to the slope of the connecting line through these points, as illustrated in Figure 11 (left), i.e.

$$\left.\frac{\partial g(y,T)}{\partial y}\right|_{y=y_{(\alpha)}} = \left.\frac{\partial g(y,T)}{\partial y}\right|_{y=y_{(\beta)}} = \frac{g(y_{(\beta)},T) - g(y_{(\alpha)},T)}{y_{(\beta)} - y_{(\alpha)}}\,. \tag{47}$$

Eq. (47) provides two equations for the two unknown variables $y_{(\alpha)/(\beta)}$. The quantity $g(y,T)$ as well as its derivatives can be directly calculated from the atomistic energy expression in Eq. (46).
Figure 12 (squared points) displays the calculated equilibrium concentrations for different temperatures. Here the dashed lines represent experimental data adopted from the database MTData$^{\mathrm{TM}}$. As one can easily see, there is good agreement between the experimental

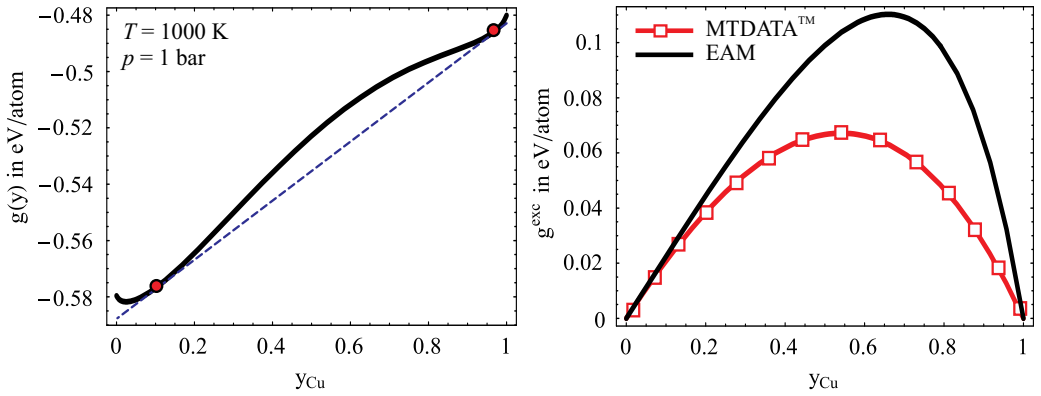

Fig. 11. *Left*: Atomic GIBBS free energy curve for Ag-Cu at 1000 K, adopted from the program package MTDATA™ (MTDATA, 1998) including the common tangent (dashed line) for defining the equilibrium concentration. *Right*: Comparison of the theoretically and experimentally obtained atomic excess enthalpy.

and theoretical results. Deviations mainly occur for the high temperature regime and - in particular - for the (β)-phase. Two reasons are worth-mentioning:

(a) The temperature only enters via the entropic part in Eq. (46); lattice dynamics are neglected up to now. Adding a vibrational term to the energy expression yields an explicitly temperature-depending equilibrium condition and lattice parameter $a^{(e)}(T, y)$, which increases the agreement between experiment and atomistic model, cf. (Najababadi et al, 1993; Williams et al., 2006).

(b) As indicated in Figure 11 (right) the excess enthalpy crucially determines the concave area of the g-curve and, therefore, $y_{(\alpha)/(\beta)}$. Obviously, the applied, analytical nearest-neighbor EAM model, cf. Section 3.2, leads to overestimated excess data, as illustrated in Figure 11 (right). Here better results can be found by incorporating more neighbors or increased interaction models, such as MEAM potentials (Feraoun et al., 2001).

However, the calculated solid part of the phase diagram qualitatively and also in a wide range quantitatively reproduces the experimental values and confirms the applicability of the present model for thermodynamic calculations.

4.2 Lattice vibrations, heat capacity, and thermal expansion

Up to now no contributions to the energy resulting from lattice dynamics are considered. Indeed, temperature and (mean) velocity of the particle system are directly coupled and, thus, temperature-depending materials properties can only be precisely determined on the atomistic scale by incorporating lattice vibrations, i.e. phonons.

To this end the lattice is modelled as a 3D-many-body-system, consisting of mass points (atoms) and springs (characterized by interatomic forces). Thus, the equation of motion of atom α can easily be found by the framework of classical mechanics. By considering $m_\alpha \ddot{\underline{\xi}}_\alpha = \underline{\mathbf{F}}_\alpha = -\nabla E^\alpha$ and Eq. (25) one can write the following equation of motion for the

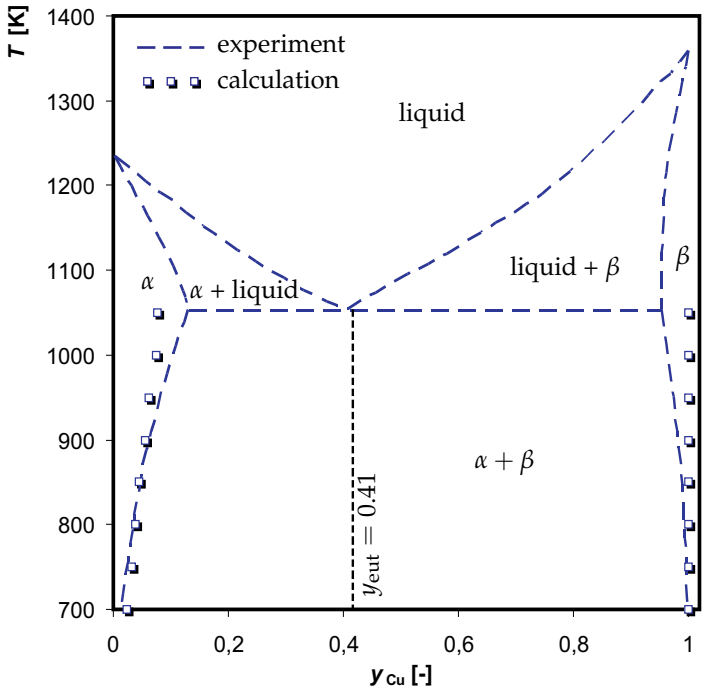

Fig. 12. On the phase diagram construction. Atomistically calculated data (squared points) vs. experimental data (dashed line), adopted from MTDATA^{TM}, (MTDATA, 1998).

discrete displacement $\underline{\xi}_\alpha$ of atom α:

$$m_\alpha \ddot{\underline{\xi}}_\alpha = -\sum_\beta \frac{\partial^2 E^\alpha}{\partial \underline{\mathbf{R}}^{\alpha\beta} \partial \underline{\mathbf{R}}^{\alpha\beta}}\Big|_{\underline{\mathbf{R}}_0^{\alpha\beta}} \cdot (\underline{\mathbf{R}}^{\alpha\beta} - \underline{\mathbf{R}}_0^{\alpha\beta}) \,. \tag{48}$$

In what follows we restrict ourselves to the so-called harmonic approximation, which means that terms beyond quadratic order are neglected in Eq. (25). Please note the identity $\underline{\mathbf{R}}^{\alpha\beta} - \underline{\mathbf{R}}_0^{\alpha\beta} = \underline{\xi}^\beta - \underline{\xi}^\alpha$; consequently Eq. (48) represents a partial differential equation for $\underline{\xi}^\alpha$, which can be solved by the ansatz for planar waves, (Leibfried, 1955):

$$\underline{\xi}^\alpha = \underline{\mathbf{e}}\, e^{\mathrm{i}(\underline{\mathbf{k}} \cdot \underline{\mathbf{X}}_0^\alpha - \omega t)} \quad \text{and} \quad \underline{\xi}^\beta = \underline{\mathbf{e}}\, e^{\mathrm{i}(\underline{\mathbf{k}} \cdot \underline{\mathbf{X}}_0^\beta - \omega t)} \,. \tag{49}$$

Here $\underline{\mathbf{e}}$ stands for the normalized vector parallel to the direction of the corresponding displacement. Inserting the above ansatz into Eq. (48) yields:

$$m_\alpha \omega^2\, \underline{\mathbf{e}} = \sum_\beta \frac{\partial^2 E^\alpha}{\partial \underline{\mathbf{R}}^{\alpha\beta} \partial \underline{\mathbf{R}}^{\alpha\beta}}\Big|_{\underline{\mathbf{R}}_0^{\alpha\beta}} \cdot \underline{\mathbf{e}} \left(1 - e^{\mathrm{i}\underline{\mathbf{k}} \cdot \underline{\mathbf{R}}_0^{\alpha\beta}}\right) = \sum_\beta \underline{\underline{\mathbf{D}}}^{\alpha\beta}(\underline{\mathbf{R}}_0^{\alpha\beta}) \cdot \underline{\mathbf{e}} \left(1 - e^{\mathrm{i}\underline{\mathbf{k}} \cdot \underline{\mathbf{R}}_0^{\alpha\beta}}\right) . \tag{50}$$

The symbol $\underline{\underline{\mathbf{D}}}^{\alpha\beta}$ represents the force constant matrix, the 3D-analogon to the spring constant within HOOKE's law in one dimension. By combining $\underline{\underline{\mathbf{D}}}^{\alpha\beta}$ and the exponential function yields

the dynamical matrix $\underline{\underline{\tilde{\mathbf{D}}}}^{\alpha\beta}(\underline{\mathbf{k}})$, which can be directly linked to the FOURIER transform of the force constant matrix.
In case of EAM potentials E^{α} only depends on the distance $R^{\alpha\beta}$ or $R^{\alpha\beta\,2}$, respectively. Therefore the chain rule $\partial^2 E^{\alpha}/(\partial \underline{\mathbf{R}}^{\alpha\beta})^2 = (\partial^2 E^{\alpha}/\partial x^2)(\partial x/\partial \underline{\mathbf{R}}^{\alpha\beta})^2 + (\partial E^{\alpha}/\partial x)(\partial^2 x/\partial \underline{\mathbf{R}}^{\alpha\beta\,2})$ must be applied to obtain $\underline{\underline{\mathbf{D}}}^{\alpha\beta}$.
Furthermore, ω denotes the angular velocity defining the time $\Theta = 2\pi/\omega$ required for one period of the propagating wave; $\underline{\mathbf{k}}$ identifies the wave vector, which defines the direction of wave propagation and the wave length $\lambda = 2\pi/|\underline{\mathbf{k}}|$.
Equation (50) represents an eigenvalue problem, which can be solved by the following equation:

$$\det\Big[\underbrace{\sum_{\beta}\underline{\underline{\mathbf{D}}}^{\alpha\beta}(\underline{\mathbf{R}}_0^{\alpha\beta})\left(1-e^{\mathrm{i}\underline{\mathbf{k}}\cdot\underline{\mathbf{R}}_0^{\alpha\beta}}\right)}_{=\underline{\underline{\mathring{\mathbf{D}}}}^{\alpha\beta}} - \underline{\mathbf{I}} m_{\alpha}\omega^2\Big] = 0\,. \tag{51}$$

The three eigenvalues, $\mathring{D}_{\mathrm{I/II/III}}(\underline{\mathbf{k}}) = m_{\alpha}\omega^2_{\mathrm{I/II/III}}(\underline{\mathbf{k}})$, of the 3×3 matrix $\underline{\underline{\mathring{\mathbf{D}}}}^{\alpha\beta}$ yield the eigenfrequencies $\nu_{\mathrm{I/II/III}}(\underline{\mathbf{k}}) = \omega_{\mathrm{I/II/III}}(\underline{\mathbf{k}})/(2\pi)$. Additionally, Eq. (51) defines three eigenvectors $\underline{\mathbf{e}}^{\mathrm{I/II/III}}$ with $\underline{\mathbf{e}}^{k}\,\underline{\mathbf{e}}^{l} = \underline{\mathbf{I}}$ and $k,l \in \{\mathrm{I,II,III}\}$, i.e. they form an orthonormal basis. Moreover, $\underline{\mathbf{e}}^{\mathrm{I/II/III}}$ determine the polarization of the wave - namely the oscillation direction of atoms. In particular, one longitudinal wave ($\underline{\mathbf{e}}^{k} \perp \underline{\mathbf{k}}$) and two transversal waves ($\underline{\mathbf{e}}^{k} || \underline{\mathbf{k}}$) can be typically found in an elemental system.

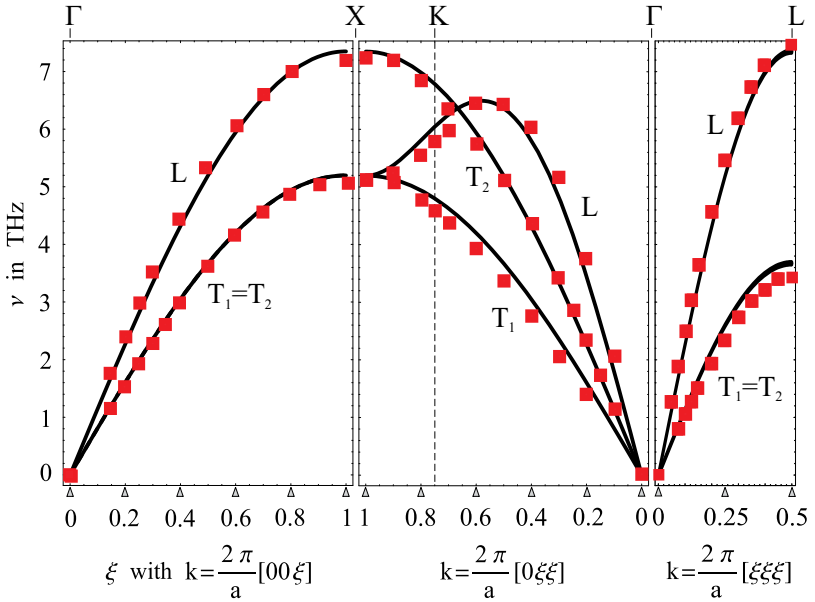

Fig. 13. Phonon dispersion of copper calculated for the three elementary FCC-symmetry directions [001], [011], and [111] with Johnson's nearest neighbor EAM potentials, (Johnson, 1989). Squared, red points identify experimental data at room temperature according to the literature, (Bian et al., 2008; Svensson et al., 1967).

At finite temperature real crystal vibrations show a wide range of wave vectors and frequencies. To quantify the dynamical characteristics of the lattice phonon dispersion curves are measured (or calculated), which displays all frequencies for the lattice-specific symmetry directions. Figure 13 illustrates the phonon dispersion curves, calculated from the atomistic model for copper. Here we considered the three elemental symmetry directions of the FCC-structure, namely $\xi[100]$, $\xi[011]$, and $\xi[111]$ with $\xi \in [0, 2\pi/a^{(e)}]$ or $\xi \in [0, \pi/a^{(e)}]$, respectively (1st BRILLOUIN zone[9]). The squared, discrete points are added for comparative purposes and identify experimental data obtained from (Bian et al., 2008; Svensson et al., 1967).
By means of quantum-mechanics and statistical physics the kinetic energy, resulting from lattice vibrations, can be written as, cf. (Leibfried, 1955):

$$E^{\alpha}_{\mathrm{kin}}(T) = \frac{1}{N}\sum_{i=1}^{3N}\sum_{\underline{\mathbf{k}}}\frac{h\,\nu_i(\underline{\mathbf{k}})}{2} + \frac{1}{N}\sum_{i=1}^{3N}\sum_{\underline{\mathbf{k}}}\frac{h\,\nu_i(\underline{\mathbf{k}})}{\exp\left[\frac{h\,\nu_i(\underline{\mathbf{k}})}{k_{\mathrm{B}}T}\right]-1} \quad , \tag{52}$$

in which the variable $h = 6.626 \cdot 10^{-34}$ Js denotes PLANCK's constant. Furthermore the summation is performed over all occurring eigenfrequencies $\nu_1, \ldots, \nu_{3N}$ of the N atoms within the lattice system and the wave vectors $\underline{\mathbf{k}}$. The relation of Eq. (52) results from considering the $6N$-dimensional phase space, well-established in statistical mechanics, and by adding the energy-contribution of each oscillator to the partition function Z. Consequently an expression for the total kinetic energy $E^{\mathrm{tot}}_{\mathrm{kin}}$ is obtained, from which $E^{\alpha}_{\mathrm{kin}}$ follows by introducing the factor $1/N$. The total energy of atom α can now be written as:

$$E^{\alpha}_{\mathrm{tot}}(T, y) = E^{\alpha}_{(\mathrm{EAM})}(y) + E^{\alpha}_{\mathrm{kin}}(T) \quad , \tag{53}$$

At this point it is worth-mentioning, that the question of which and how many frequencies ν_i and wave vectors $\underline{\mathbf{k}}$ are used to quantify $E^{\mathrm{tot}}_{\mathrm{kin}}$ may strongly determine the accuracy of all subsequently derived quantities. In (Bian et al., 2008) the authors, for example, uniformly discretized the BRILLOUIN zone by 20^3 grid points and used a weighted sum of 256 different wave vectors. However, such procedure requires considerable computational capacities since the eigenvalue-problem of Eq. (51) must be solved for each choice of $\underline{\mathbf{k}}$. In the present work we exclusively investigated a weighted sum of the eigenfrequencies of the three elemental symmetry directions [001], [011], and [111].
Equation (53) can be interpreted as the relation for the particle-specific internal energy of the solid, in which the temperature is included via the kinetic term. The heat capacity c_{v} at constant volume[10] can now be calculated by means of the partial derivative:

$$c_{\mathrm{v}}(T, y) = \frac{\partial E^{\alpha}_{\mathrm{tot}}(T, y)}{\partial T} = \frac{\mathrm{d}E^{\alpha}_{\mathrm{kin}}(T)}{\mathrm{d}T} \, . \tag{54}$$

Figure 14 compares the calculated heat capacity for copper with the experimental one constructed from the measured EINSTEIN frequency and the homonymous ansatz for c_{v}, (Fornasini et al., 2004).

[9] The first BRILLOUIN zone represents the unit cell in the reciprocal lattice, for more details see for example (Yu & Cardona, 2010).
[10] This condition can be guaranteed by setting e.g. $a = a^{(e)}$ but any volume-preserving deformation is possible.

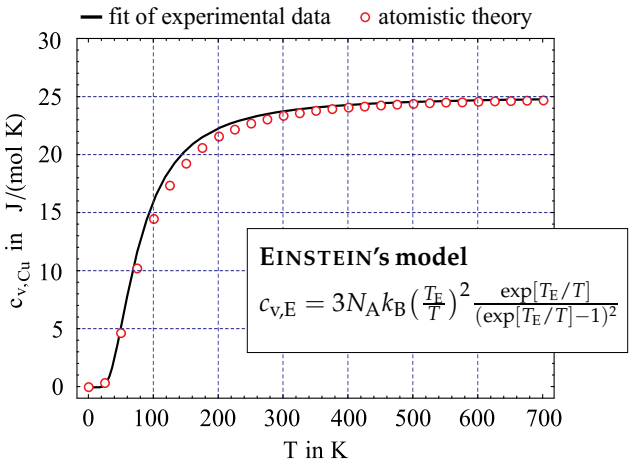

Fig. 14. Molar heat capacity c_v at constant volume, calculated from EAM potentials. The solid line denotes the fitting curve, according to EINSTEIN's model by using the EINSTEIN frequency $\nu_E = T_E k_B/h = 4.96$ THz measured by Extended X-ray-Absorption Fine-Structure (EXAFS), (Fornasini et al., 2004).

Due to the vibrational part the total energy of atom α additionally depends on T. The thermal expansion coefficient can be calculated by expanding E^{α}_{tot} into a TAYLOR series according to Eqs. (26,28), but additionally incorporating derivatives of T. A subsequent exploitation of terms of mixed derivatives yields the thermal expansion coefficient, cf. (Leibfried, 1955), pp. 235 ff..

An alternative approach for the determination of the thermal expansion coefficient is given by the following illustrative arguments, see also Figure 15 (upper left). For $T = 0$ atom α is situated in the potential energy minimum defined by the equilibrium nearest neighbor distance R_0. For $T > 0$ the atoms oscillates around the equilibrium position. Here the sum $E_{pot} + E_{kin}$ defines the oscillating distance R_- and R_+, cf. Figure 15 (upper left). The center position $R_{01} = R_- + 0.5(R_+ - R_-)$ defines the equilibrium distance for $T > 0$. Note that R_{01} is greater than R_0, due to the asymmetry of the energy curve w.r.t. the energy minimum. For increasing temperatures the kinetic energy and R_{01} increase, cf. 15 (upper right), which characterizes the thermal expansion.

Figure 15 (lower left) illustrates the oscillation range $(R_+ - R_-)$ following from both intersections of $E^*(T,R)$ with the horizontal axis and the construction of R_{01} for different temperatures. The resulting nearest neighbor distances are displayed in the lower right panel. By assuming isotropy on the macroscopic level the following equations hold for thermal expansion:

$$\underline{\underline{\boldsymbol{\varepsilon}}}^{th} = \underline{\underline{\boldsymbol{\alpha}}}^{th}(T)(T - T_{ref}) \quad , \quad \underline{\underline{\boldsymbol{\alpha}}}^{th}(T) = \alpha^{th}(T)\,\underline{\underline{\mathbf{I}}} \quad , \quad \alpha^{th}(T) = \frac{1}{R_{01}(T)}\frac{dR_{01}(T)}{dT} \,. \tag{55}$$

An exploitation of Eq. (55) at $T = 300$ K yields the thermal expansion coefficient of $\alpha^{th} = 9.1 \cdot 10^{-6}$ K^{-1}. This value is smaller than the corresponding literature value $\alpha^{th}_{Cu} \approx 15 \cdot 10^{-6}$ K^{-1} (Bian et al., 2008), whereas the temperature dependence $R_{01} = R_{01}(T) \Leftrightarrow a^{(e)} = a^{(e)}(T)$ qualitatively agrees with experimental observations.

The reasons for the deviations are different. First, no anharmonic terms or electronic contributions are considered. Therefore, deviations occur, particularly in the high temperature regime, (Kagaya et al., 1988; Wallace, 1965). Second, the limited consideration of exclusively nine eigenfrequencies according to the three elementary symmetry directions lead to a reduced description of the vibrational energy. Consequently, α^{th} is insufficiently reproduced. Indeed, incorporating more wave vectors leads to more accurate results (Bian et al., 2008; Kagaya et al., 1988), but the computational costs drastically increase.
In case of cubic lattice symmetry the heat capacity at constant pressure, c_{p}, can be easily calculated via the relation $c_{\text{p}}(T) = c_{\text{v}}(T) + 3T(C_{1111} + 2C_{1122})\alpha_{\text{th}}^2(T)$. Finally we emphasize, that the above framework can be also applied to solid mixtures. For this reason the dynamical matrix $\underline{\underline{\tilde{\mathbf{D}}}}^{\alpha\beta}(\underline{\mathbf{k}}, y)$ must be calculated by the first line of the energy expression in Eq. (40). Please note the additional argument y in $\underline{\underline{\tilde{\mathbf{D}}}}^{\alpha\beta}$, and consequently in $\nu_i(\underline{\mathbf{k}}, y)$ and $E_{\text{kin}}^{\alpha}(T, y)$. Furthermore one needs the mean field relation $m_\alpha(y) = y m_{\text{B}} + (1-y)m_{\text{A}}$ with $y = y_{\text{B}}$.

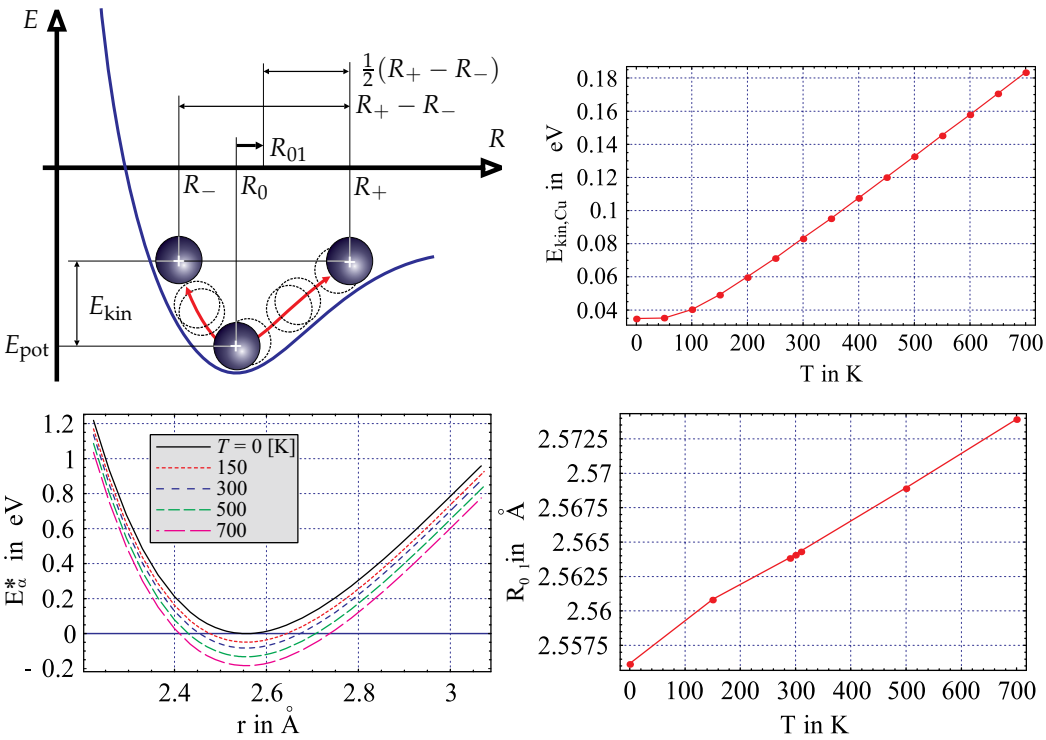

Fig. 15. *Upper left*: On the origin of thermal expansion. The shift from $R_0^{\alpha\beta}$ to $R_{01}^{\alpha\beta}$ results from the asymmetric energy curve around the minimum. *Upper right*: kinetic energy of Cu-atoms calculated for different temperatures. *Lower left*: $E^*(R,T) = E_{\text{pot}}^{\alpha}(R) + [E_{\text{pot}}^{\alpha}(R_0) - E_{\text{kin}}^{\alpha}(T)]$; the roots define R_- and R_+. *Lower right*: Theoretical nearest neighbor distance at various temperatures.

5. Molecular dynamic simulations

The application of atomistic calculations presented in the previous two sections dealt with ideal crystal lattices. In the following section we will show how to extend the range of applications to arbitrary microstructures by using molecular dynamic simulations.

5.1 Methodology

Molecular dynamics (MD) simulations play an important role in materials science. They are based on the integration of NEWTON's equation of motion and applied in order to understand the dynamic evolution of a system in time. This evolution is driven by the interaction of the particles that enter the equations of motion as forces. In contrast to the quantities calculated in the previous Sections 3 and 4 MD-simulations are particularly useful to obtain quantities that are not accessible directly such as macroscopic diffusion constants or melting temperatures. For an in-depth introduction to MD-simulations we refer the reader to one of the many textbooks (Allen & Tildesley, 1989; Frenkel & Smit, 2001).

The starting point of an MD-simulation is the choice of a thermodynamic ensemble that determines which thermodynamic variables are conserved during the runtime of the simulation. The thermodynamic variables most relevant for applications are temperature T, pressure P, volume V, internal energy E, particle number N and chemical potential μ. The most important ensembles for MD simulations are

- the microcanonical ensemble with constant N, V, E,
- the canonical ensemble with constant N, V, T, and
- the grand-canonical ensemble with constant μ, V, T.

These macroscopic thermodynamic variables are implicitly included in an atomistic simulation. Their calculation provides a direct link between the macroscopic (system-wide) properties and the microscopic (atom-resolved) MD-simulation. For example, the system-wide instantaneous temperature at a time t is calculated by equipartitioning the kinetic energy of N atoms

$$\frac{1}{2}k_{\mathrm{B}}T(t) = \frac{\sum_{\alpha=1}^{N} \frac{1}{2}m_{\alpha}[\underline{\mathbf{v}}_{\alpha}(t) \cdot \underline{\mathbf{v}}_{\alpha}(t)]}{3N} \tag{56}$$

where m_{α} and $\underline{\mathbf{v}}_{\alpha}$ are mass and velocity of particle α, respectively. The direct results of an MD-simulation are the positions, velocities and cohesive energies of the system along the simulated trajectory. An example of an NVE simulation is shown in Figure 16: the total energy is constant but the cohesive (i.e. potential) and kinetic energy and the temperature of the system are fluctuating.

The particular choice of ensemble is realised technically by the use of appropriate boundary conditions, thermostats and/or barostats. The variety of available thermostats and barostats differs mainly in the time-reversibility and in the statistic properties. An MD-simulation starts from an initial structure, i.e. atomic positions $\underline{\mathbf{X}}^{\alpha}(t = 0)$, by calculating the forces on the atoms α. Based on these forces the equations of motion are integrated for a specific timestep δt, i.e. the atomic positions are propagated in time using to new atomic positions $\underline{\mathbf{X}}^{\alpha}(t + \delta t)$. This is then repeated iteratively (Figure 17), thereby creating the trajectory of the system evolving in time. The propagation of atomic positions in time, based on derivatives of the energy landscape, is an extrapolation with an accuracy that is directly related to the timestep δt. A decrease of δt increases the accuracy of the extrapolation but at the same time decreases

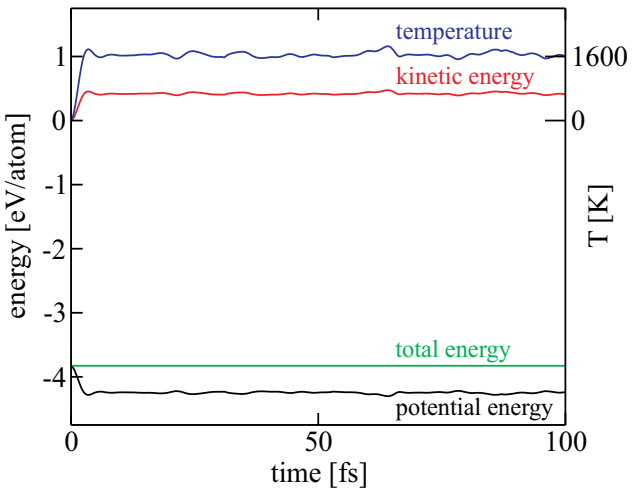

Fig. 16. Time evolution of temperature and energy contributions in an MD-simulation that employs an NVE ensemble.

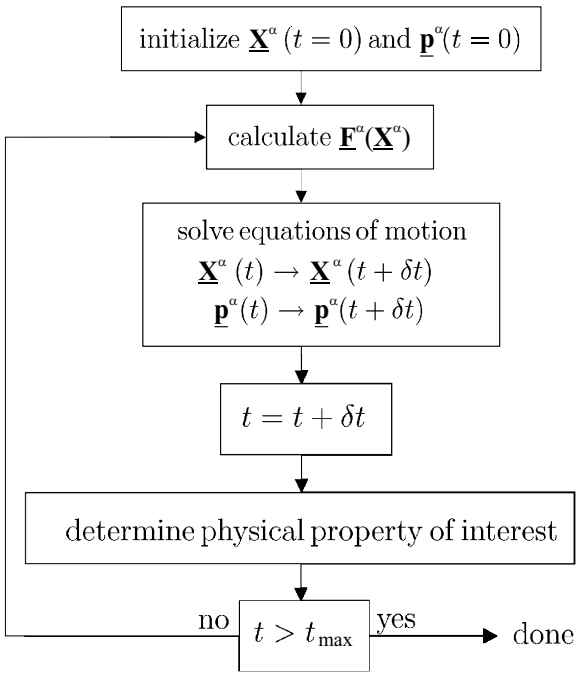

Fig. 17. Flowchart illustrating the principle of a typical MD-simulation.

the simulated system time for a given number of simulation steps. This is overcome by the different integrators that optimise the accuracy of the trajectory for a given number of force and energy calculations per unit system time. A simple approach is the VERLET algorithm that takes the difference of a TAYLOR expansion of the energy for $t - \delta t$ and $t + \delta t$. Then the

terms of even power vanish and one obtains

$$\underline{\mathbf{X}}^{\alpha}(t+\delta t) = 2\underline{\mathbf{X}}^{\alpha}(t) - \underline{\mathbf{X}}^{\alpha}(t-\delta t) + \frac{\underline{\mathbf{F}}^{\alpha}(t)}{m}\delta t^2 + \mathcal{O}(\delta t^4) \tag{57}$$

as MD-integrator scheme with an error of the order of δt^4. Due to the absence of velocities in the extrapolation of positions the VERLET algorithm cannot be coupled with thermostats/barostats and hence is suitable for NVE ensembles only. Other ensembles can be realised with, e.g., the VELOCITY-VERLET algorithm that involves both, positions and velocities

$$\underline{\mathbf{X}}^{\alpha}(t+\delta t) = \underline{\mathbf{X}}^{\alpha}(t) + \underline{\mathbf{v}}^{\alpha}(t)\delta t + \frac{1}{2}\underline{\mathbf{a}}^{\alpha}(t)\delta t^2 + \mathcal{O}(\delta t^4) \quad , \tag{58}$$

$$\underline{\mathbf{v}}^{\alpha}(t+\delta t) = \underline{\mathbf{v}}^{\alpha}(t) + \frac{1}{2}\left[\underline{\mathbf{a}}^{\alpha}(t) + \underline{\mathbf{a}}^{\alpha}(t+\delta t)\right]\delta + \mathcal{O}(\delta t^3) \quad , \tag{59}$$

where $\underline{\mathbf{a}}^{\alpha}$ denotes the acceleration of atom α. Besides the many other schemes for determining the NEWTONian trajectory (e.g. the NOSE-HOOVER scheme) there are stochastic approaches that aim to explore the phase space of a system instead of following a particular trajectory (LANGEVIN dynamics). Note that these algorithms are independent of the physical approach of the force calculation and purely classical. Treating the dynamics of the system in its full quantum-mechanical character requires more elaborate techniques (Marx & Hutter, 2009).
The structural evolution of the system can be assessed by considering averaged quantities of the atomic positions. The radial distribution function g_2 measures the correlation between the probabilities $\rho(\underline{\mathbf{X}}^{\alpha})$ and $\rho(\underline{\mathbf{X}}^{\alpha,*})$ of finding atom β in an infinitesimal volume element at $\underline{\mathbf{X}}^{\alpha}$ or $\underline{\mathbf{X}}^{\alpha,*}$, respectively, and the probability $\rho(\underline{\mathbf{X}}^{\alpha}, \underline{\mathbf{X}}^{\alpha,*})$ of finding atoms in both volume elements.

$$\rho(\underline{\mathbf{X}}^{\alpha}, \underline{\mathbf{X}}^{\alpha,*}) = \left[\rho(\underline{\mathbf{X}}^{\alpha})\rho(\underline{\mathbf{X}}^{\alpha,*})\right] g_2(\underline{\mathbf{X}}^{\alpha}, \underline{\mathbf{X}}^{\alpha,*}) \tag{60}$$

This quantity (Figure 18, left) corresponds to measuring the distance-relation between the atoms and provides a good indicator if the system is solid or liquid.

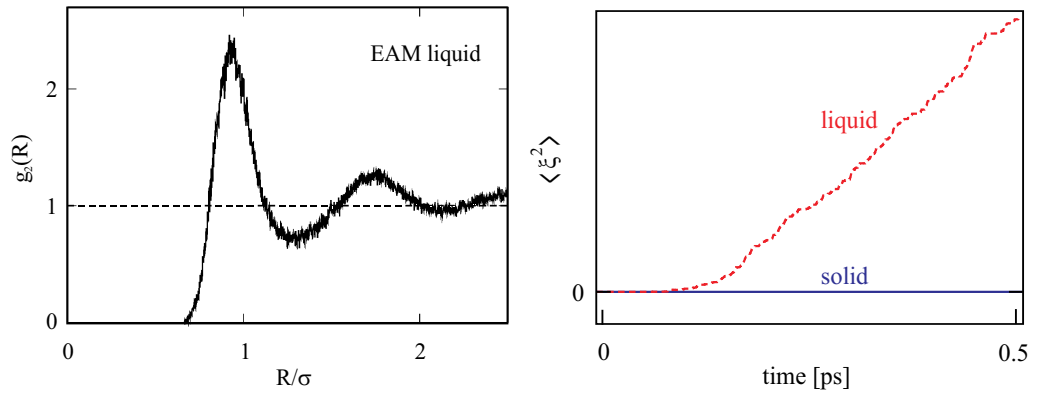

Fig. 18. Radial distribution function (left) and mean square displacement (right) as obtained from an MD simulation (here σ identifies the equilibrium lattice constant).

Another indicator in this direction is the mean square displacement

$$\frac{\partial}{\partial t}\left\langle \underline{\xi}(t)^2 \right\rangle = \frac{\partial}{\partial t}\left[\frac{1}{N}\sum_{\beta=1}^{N}\underline{\xi}^{\beta}(t)^2\right] = 6D \quad , \tag{61}$$

that relates the microscopic displacements, $\underline{\xi}^{\beta} = \underline{\mathbf{X}}^{\beta} - \underline{\mathbf{X}}_0^{\beta}$, to the macroscopic diffusion constant D. The time-evolution of this average over atoms gives an indicator of the onset of diffusion in the system. The derivative of the time-evolution of the mean square displacement (Figure 18, right) allows to deduce the macroscopic diffusion constant D. This routinely calculated quantity can be further utilised as input parameters for coarse-grained approaches such as e.g. kinetic Monte-Carlo that is described in detail in e.g. Refs. (Allen & Tildesley, 1989; Frenkel & Smit, 2001).

5.2 Application: Structural transformations

Quantities like the mean-square displacement and the radial distribution function introduced in the previous paragraph provide an overall picture of the system. They are based on atom-averages over quantities which can vary significantly throughout the system. However, such averaging causes loss of information on e.g. a heterogeneous or microstructured system. A technologically important case of a heterogeneous system is a polycrystal that contains crystal grains with different mutual orientations. In some cases the microscopic single-crystal information can be extrapolated to the macroscopic poly-crystalline correspondence, like e.g. the elastic constants (Hill et al., 1963) for randomly distributed grain orientations.
But in the case of structural transformations the spatial variation of the crystal structure and its dependence on time and temperature is the central result of the simulation. This is illustrated by the isolated grain shown in Figure 19 that one of the present authors investigated in the context of growth on microstructured substrates of HCP Titanium. Here, the description of

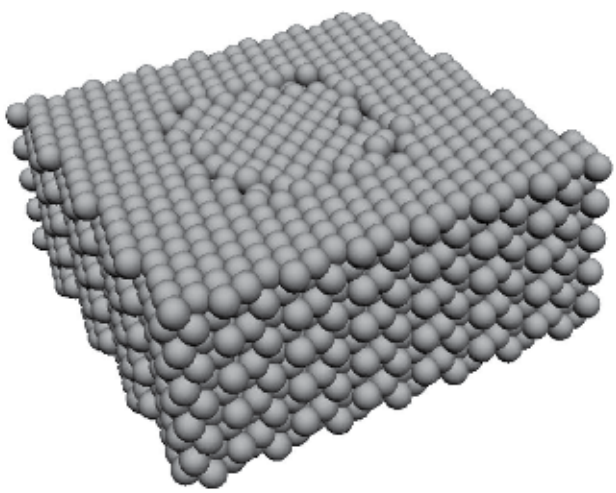

Fig. 19. Isolated grain of HCP Titanium after atomistic relaxation using an embedded-atom potential (Hammerschmidt et al., 2005). The applied angle of misorientation corresponds to a coincidence-site lattice.

interatomic interactions is carried out with an embedded-atom potential described earlier. The parametrisation of the EAM potential was particularly optimised for the description of the undercoordinated atoms at the grain boundary (Hammerschmidt et al., 2005). The atomic structure shown in Figure 19 was obtained by **(i)** determining the energetically favored atomic structure of the $\Sigma 7(0001)$ coincidence-site lattice (CSL) grain boundary, **(ii)** setting up a block of CSL cells of orientation $\mathcal{A}$ surrounded by cells of orientation $\mathcal{B}$ and **(iii)** relaxing the atoms in the interface area. The atomic relaxation of the interface region did not allow the grain to decay, but resulted in a change of the grain shape from rectangular to nearly circular. Visualising the relaxed grain (Figure 19) along the crystal axis [1000] in Figure 20 allows one to easily distinguish the misoriented grain from the surrounding. In order to investigate the

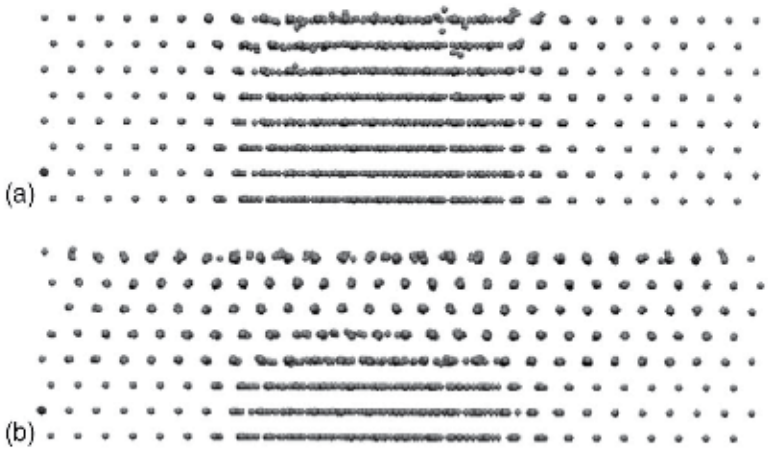

Fig. 20. Initial isolated grain (a), viewed along [0001], undergoes a structural transformation and orients itself to match the surrounding crystal directions (b). The MD-simulation was carried out for 20 ps at 300 K with the bottom three layers fixed, cf. (Hammerschmidt et al., 2005).

structural stability of the isolated grain at elevated temperatures, we carried out molecular dynamic simulations. In particular, we simulated an NVT ensemble for 20 ps at 300 K where we kept the bottom three layers fixed in order to mimic a microstructured substrate. The central finding of this simulation is the decay of the isolated grain within a very short time already at room temperature. Repeating this procedure for isolated grains of different sizes showed that the thermal stability increases with diameter. In particular, we found that grains with a diameter of at least 33Å are thermally stable over a maximum simulation time of several hundred ps. This compares well with the experimentally observed minimum grain size.

In this example, the analysis of the molecular dynamic simulation is straight-forward. However, simulations of long times and/or large systems make it hard to identify particular events due to the shear mass of data on atomic trajectories. This calls for approaches that transform the information on atomic positions to meaningful derived atom-based properties like e.g. the moments of the bond-order potentials, Eq. (13), or to even coarse-grained entities like dislocation skeletons (Begau et al., 2011).

6. Summary and outlook

In the foregoing sections various approaches were explained, which allows for the calculation of macroscopic thermodynamic data (e.g. elastic constants, phase stability data, excess enthalpy, heat capacity, and thermal expansion) or mesoscopic material properties (e.g. grain evolution) by using atomistic calculation methods. Starting with the quantum-mechanical SCHRÖDINGER equation and ending with various empirical potentials a brief hierarchical overview was given, which describes different precise possibilities to quantify atomic interactions. Subsequently, the EAM-framework was applied to derive energy expressions for the pure solid and binary alloys. Once the energy is calculated investigations of static and dynamic (vibrations) lattice deformations as well as thermodynamic and thermo-mechanical materials behaviour can be performed. For this reason different, technologically relevant materials were investigated such as Fe-C, Ag, Cu, and the binary brazing alloy Ag-Cu. In order to analyze the thermodynamics of many particle systems (such as diffusion) statistical ensembles and mean quantities (e.g. the mean displacement) were finally considered, which are derived, for example, via MD-simulations. In particular, MD-calculations were presented, which allow to predict the temporal evolution of different grain orientations in "polycrystalline" Titanium.

The presented methods can help to overcome many difficulties related to the determination of material parameters on the mesoscopic length scale. Note that there are already many examples - beyond the present work - for the successful applications of atomistic calculations to gain information about the materials behavior on micro- or macroscale, see e.g. (Begau et al., 2011; Bleda et al., 2008; Chiu et al., 2008; Kadau et al., 2004) or (Bian et al., 2008; Böhme et al., 2007; Williams et al., 2006), respectively. Two, recently published, examples are worth mentioning: calculations of the interaction of hydrogen with voids and grain boundaries in steel under the allowance of different alloying elements, (Nazarov et.al., 2010), and investigations of the influence of hydrogen on the elastic properties of α-iron, (Psiachos et al., 2011).

Nevertheless, the bridging of length- and timescales is still a big challenge for most multiscale approaches. Here information of the nano- (e.g. binding energies of different H-traps, such as dislocations and phase boundaries) and microscale (e.g. the temporal and spatial phase distribution in multiphase materials) must be incorporated in macroscopic, constitutive equations (e.g. the diffusion equation with source/sink-term for hydrogen trapping, (McNabb & Foster, 1963; Oriani, 1970)). Moreover, the ongoing increase of computational capacities and the development of suitable interfaces for considering atomistic or microstructural calculations in commercial simulation software will further establish multiscale approaches in materials engineering. The FE^2-method, for instance, described by (Balzani et.al., 2010) shows the large potential for incorporating micro- or mesoscopic information in macroscopic simulations, but also the need for further acceleration of numerical calculations and the development of optimized algorithms.

7. References

Abell, G.C. (1985). Empirical chemical pseudopotential theory of molecular and metallic bonding, *Phys. Rev. B*, Vol. 31, 6184–6196 (and references therein).

Alinaghian, P.; Gumbsch, P.; Skinner, A.J. & Pettifor, D.G. (1993). Bond order potentials: a study of s- and sp-valent systems, *J. Phys.: Cond. Mat.*, Vol. 5, 5795–5810.

Allen, M.P. & Tildesley, D.J. (1989). *Computer simulation of liquids*, Oxford University Press, ISBN: 019-8-55645-4, New York.

Aoki, M.; Nguyen-Manh, D.; Pettifor, D.G. & Vitek, V. (2007). Atom-based bond-order potentials for modelling mechanical properties of metals. *Prog. Mat. Sci.*, Vol. 52, 154–195.

Artemev, A.; Wang, Y. & Khachaturyan, A.G. (2000). Three-dimensional phase filed model and simulation of martensitic transformation in multilayer systems under applied stresses, *Acta Mater.*, Vol. 48, 2503–2518.

Balzani, D. & Schröder, J. & Brands, D. (2010). FE^2-Simulation of Microheterogeneous Steels Based on Statistically Similar RVE's, In: *IUTAM Symposium on Variational Concepts with Applications to the Mechanics of Materials*, Hackl K. (Ed.), IUTAM Bookseries, Vol. 21, 15–28, Springer, ISBN: 978-90-481-9195-6, Dordrecht Heidelberg London New York.

Bangwei, Z.; Yifang, O.; Shuzhi, L. & Zhanpeng, J. (1999). An analytic MEAM model for all BCC transition metals. *Physica B*, Vol. 262, 218–225.

Baskes, M.I. (1992). Modified embedded-atom potentials for cubic materials and impurities. *Phys. Rev. B*, Vol. 46, 2727–2742.

Begau, C.; Hartmaier, A.; George, E.P. & Pharr, G.M. (2011). Atomistic processes of dislocation generation and plastic deformation during nanoindentation. *Acta Materialia*, Vol. 59, 934–942.

Behler, J. & Parrinello, M. (2007). Generalized Neural-Network Representation of High-Dimensional Potential-Energy Surfaces. *Phys. Rev. Lett.*, Vol. 98, No. 14, 146401–146404.

Bian, Q.; Bose, S.K. & Shukla, R.C. (2008). Vibrational and thermodynamic properties of metals from a model embedded-atom potential. *J. Phys. Chem. Solids*, Vol. 69, 168-181.

Bleda, E.A.; Gao, X. & Daw, M.S. (2008). Calculations of diffusion in FCC binary alloys using on-the-fly kinetic Monte Carlo. *Comp. Mat. Sci.*, Vol. 43, 608–615.

Bockstedte, M.; Kley, A.; Neugebauer, J. & Scheffler, M. (1997). Density-functional theory calculations for poly-atomic systems: electronic structure, static and elastic properties and ab initio molecular dynamics, *Comp. Phys. Comm.*, Vol. 107, 187–222.

Böhme, T.; Dreyer, W. & Müller, W.H. (2007). Determination of stiffness and higher gradient coefficients by means of the embedded-atom method - an approach for binary alloys. *Continuum Mech. Therm.*, Vol. 18, 411–441.

Born, M. & Oppenheimer, R. (1927). Zur Quantentheorie der Molekeln, *Ann. Phys.*, Vol. 84, 457–484.

Cahn, J.W. (1968). Spinodal decomposition. *Trans. Metall. Soc. AIME*, Vol. 242, 166–180.

Cryot-Lackmann, F. (1967). On the electronic structure of liquid transition metals. *Adv. Phys.*, Vol. 16, 393–400.

Daw, M.S. & Baskes, M.I. (1983). Semiempirical, quantum mechanical calculation of hydrogen embrittlement in metals. *Phys. Rev. Lett.*, Vol. 50, 1285–1288.

Daw, M.S. & Baskes, M.I. (1984). Embedded-atom method: derivation and application to impurities, surfaces and other defects in metals. *Phys. Rev. B*, Vol. 29, 6443–6453.

De Fontaine, D. (1975). Clustering effects in solid solutions, In: *Treatise in solid state chemistry, Vol. 5: Changes of state*, N. B. Hannay (Ed.), 129-178, Plenum, New-York.

Desai, S.K.; Neeraj, T. & Gordon, P.A. (2010). Atomistic mechanism of hydrogen trapping in bcc Fe-Y solid solution: A first principles study, *Acta Mater.*, Vol. 58, 5363–5369.

Chiu, J.-T.; Lin, Y.-Y.; Shen, C.-L.; Lo, S.-P. & Wu, W.-J. (2008). Atomic-scale finite-element model of tension in nanoscale thin film, *Int. J. Adv. Manuf. Technol.*, Vol. 37, 76–82.

Drautz R. & Pettifor, D.G. (2006). Valence-dependent analytic bond-order potential for transition metals, *Phys. Rev. B*, Vol. 74, 174117/1–174117/14.

Drautz, R.; Zhou, X.W.; Murdick, D.A.; Gillespie, B.; Wadley, H.N.G. & Pettifor, D.G. (2007). Analytic bond-order potentials for modelling the growth of semiconductor thin films, *Prog. Mat. Sci.*, Vol. 52, 196–229.

Dreizler, R.M. & Gross, E.K.U. (1990). *Density Functional Theory*, Springer, ISBN: 3-540-51993-9, Berlin.

Feraoun, H.; Aourag, H.; Grosdidier, T.; Klein, D. & Coddet, C. (2001). Development of modified embedded atom potentials for the Cu-Ag system. *Superlattice Microst.*, Vol. 30, No. 5, 261–271.

Finnis, M.W. & Sinclair, J.E. (1984). A simple empirical N-body potential for transition metals, *Phil. Mag. A*, Vol. 50, 45–55.

Finnis, M.W. (2007a). Bond-order potentials through the ages. *Prog. Mat. Sci.*, Vol. 52, 133–153.

Finnis, M.W. (2007b). *Interatomic forces in condensed matter*. Oxford University Press, ISBN: 978-0-198-50977-6, New York.

Foiles, S.M.; Baskes, M.I. & Daw, M.S. (1986). Embedded-atom-method functions for the fcc metals Cu, Ag, Au, Ni, Pd, Pt, and their alloys. *Phys. Rev. B*, Vol. 33, 7983–7991.

Fornasini, P.; Beccara, S. a; Dalba, G.; Grisenti, R.; Sanson, A. & Vaccari, M. (2004). Extended x-ray-absorption fine-structure measurements of copper: Local dynamics, anharmonicity, and thermal expansion. *Phys. Rev. B*, Vol. 70, 174301/1–174301/12.

Frenkel, D. & Smit, B.J. (2001). *Understanding Molecular Simulation: From Algorithms to Applications*, Academic Press Inc., ISBN: 012-2-67370-0, Orlando, FL, USA.

Hammerschmidt, T.; Kersch, A. & Vogl, P. (2005). Embedded atom simulations of titanium systems with grain boundaries. *Phys. Rev. B*, Vol. 71, 205409/1–205409/9.

Hammerschmidt, T.; Seiser, B.; Drautz, R. & Pettifor, D.G. (2008). *Modelling topologically close-packed phases in superalloys: Valence-dependent bond-order potentials based on ab-initio calculations*, in: *Superalloys 2008*, edited by R. C. Reed (The Metals, Minerals and Materials Society, Warrendale), 847–853.

Hammerschmidt, T. & Drautz, R. (2009). Bond-Order Potentials for Bridging the Electronic to Atomistic Modelling Hierarchies. in: *NIC Series 42 - Multiscale Simulation Methods in Molecular Science*, edited by J. Grotendorst, N. Attig, S. Blügel and D. Marx. (Jülich Supercomputing Centre, 2009), 229–246.

Hammerschmidt, T.; Drautz, R. & Pettifor, D.G. (2009). Atomistic modelling of materials with bond-order potentials. *Int. J. Mat. Res.*, Vol. 100, 1479–1487.

Hill, R. (1963). Elastic properties of reinforced solids - Some theoretical principles. *J. Mech. Phys. Solids*, Vol. 11, 357–372.

Hohenberg, P. & Kohn, W. (1964). Quantum density oscillations in an inhomogeneous electron gas, *Phys. Rev.*, Vol. 137, A1697-A1705.

Horsfield, A.; Bratkovsky, A.M.; Fearn, M.; Pettifor, D.G. & Aoki, M. (1996). Bond-order potentials: Theory and implementation, *Phys. Rev. B*, Vol. 53, 12694–12712.

Hristova, E.; Janisch, R.; Drautz, R. & Hartmaier, A. (2011). Solubility of carbon in α-iron under volumetric strain and close to the Σ5(310)[001] grain boundary: Comparison of DFT and empirical potentials, *Comp. Mat. Sci.*, Vol. 50, 1088–1096.

Johnson, R.A. (1972). Relationship between two-body interatomic potentials in a lattice model and elastic constants. *Phys. Rev. B*, Vol. 6, 2094–2100.

Johnson, R.A. (1974). Relationship between two-body interatomic potentials in a lattice model and elastic constants II. *Phys. Rev. B*, Vol. 9, 1304–1308.

Johnson, R.A. (1988). Analytic nearest-neighbor model for FCC metals. *Phys. Rev. B*, Vol. 37, 3924–3931.

Johnson, R.A. (1989). Alloy model with the embedded-atom-method. *Phys. Rev. B*, Vol. 39, 12554–12559.

Jones, J.E. (1924). On the Determination of Molecular Fields. II. From the Equation of State of a Gas, *Proc. R. Soc. Lond. A*, Vol. 106, No. 738, 463–477.

Kadau, K.; German, T.C.; Lomdahl, P.S.; Holian, B.L.; Kadau, D.; Entel, P.; Kreth, M.; Westerhoff, F. & Wolf, D.E. (2004). Molecular-Dynamics Study of Mechanical Deformation in Nano-Crystalline Aluminum, *Metall. Mater. Trans. A*, Vol. 35A, 2719–2723.

Kagaya, H.-M.; Shoji, N. & Soma, T. (1988). Anharmonic effects on the thermal properties of Si and Ge. *Solid State Commun.*, Vol. 65, No. 11, 1445–1450.

Kittel, C. (1973). *Einführung in die Festkörperphysik* (3. erweiterte und verbesserte Auflage), R. Oldenbourg Verlag GmbH München Wien, John Wiley & Sons GmbH, Frankfurt, ISBN: 978-3-486-32763-2.

Kobayashi, R.; Warren, J.A. & Carter, W.C. (2000). A continuum model of grain boundaries. *Physica D*, Vol. 140, 141–150.

Kohn, W. & Sham, L.J. (1965). Self-consistent equations including exchange and correlation effects, *Phys. Rev.*, Vol. 140, A1133–A1138.

Kohn, W. (1998). An essay on condensed matter physics in the twentieth century, *Rev. Mod. Phys.*, Vol. 71, S59–S77.

Lee, B.-J. (2006). A modified embedded-atom method interatomic potential for the Fe-C system, *Acta Mater.*, Vol. 54, 701–711.

Lee, B.-J. & Jang, J.-W. (2007). A modified embedded-atom method interatomic potential for the Fe-H system, *Acta Mater.*, Vol. 55, 6779–6788.

Leibfried, G. (1955). Mechanische und thermische Eigenschaften der Kristalle, In: *Handbuch der Physik. Band VII*, S. Flügge (Ed.), 104–324, Springer, Berlin-Göttingen-Heidelberg.

Marx, D. & Hutter, J. (2009). *Ab-Initio Molecular Dynamics: Basic Theory And Advanced Methods*, Cambridge University Press, ISBN: 978-0-521-89863-8, Cambridge.

McNabb, A. & Foster, P.K. (1963). A New Analysis of the Diffusion of Hydrogen in Iron and Ferritic Steels. *Trans. Metall. Soc. AIME*, Vol. 227, 618–627.

Mrovec, M.; Nguyen-Manh, D.; Pettifor, D.G. & Vitek, V. (2004). Bond-order potential for molybdenum: Application to dislocation behaviour. *Phys. Rev. B*, Vol. 69, 094115/1–094115/16.

Mrovec, M.; Moseler, M.; Elsässer, C. & Gumbsch, P. (2007). Atomistic modeling of hydrocarbon systems using analytic bond-order potentials, *Prog. Mat. Sci.*, Vol. 52, 230–254.

MTDATA NPL database for materials thermochemistry (1998). Queens Road, Teddington, Middlesex, TW11 0LW.

Najafabadi, R.; Srolovitz, D.J.; Ma, E. & Atzmon, M. (1993). Thermodynamic properties of metastable Ag-Cu alloys. *J. Appl. Phys.*, Vol. 74, No. 5, 3144–3149.

Nazarov, R. & Hickel, T. & Neugebauer, J. (2010). First-principles study of the thermodynamics of hydrogen-vacancy interaction in fcc iron. *Phys. Rev. B*, Vol. 82, No. 22, 224104/1–224104/11

Oriani, R.A. (1970). The diffusion and trapping of hydrogen in steel. *Acta Metall.*, Vol. 18, 147–157.

Parr, R.G. & Yang, W. (1989). *Density-Functional Theory of Atoms and Molecules*, Oxford University Press, ISBN: 978-0-195-09276-9, New York.

Payne, M.C.; Teter, M.P.; Allen, D.C.; Arias, T.A. & Joannopoulos, J.D. (1992). Iterative minimization techniques for ab initio total-energy calculations: molecular dynamics and conjugate gradients, *Rev. Mod. Phys.*, Vol. 64, 1045–1097.

Pettifor, D.G. (1989). New many-body potential for the bond-order, *Phys. Rev. B*, Vol. 63, 2480–2483.

Pettifor, D.G. & Oleinik, I.I. (1999). Analytic bond-order potentials beyond Tersoff-Brenner. I. Theory, *Phys. Rev. B*, Vol. 59, 8487–8499.

Pettifor, D.G. & Oleinik, I.I. (2000). Bounded Analytic Bond-Order Potentials for σ and π Bonds. *Phys. Rev. Lett.*, 84, 4124–4127.

Psiachos, D.; Hammerschmidt, T. & Drautz, R. (2011). Ab initio study of the modification of elastic properties of α-iron by hydrostatic strain and by hydrogen interstitials. *Acta Mater.*, Vol. 59, 4255–4263.

Rose, J.H.; Smith, J.R.; Guinea, F. & Ferrante, J. (1984). Universal features of the equation of state of metals. *Phys. Rev. B*, Vol. 29, 2963–2969.

Stølen, S. & Grande, T. (2003). *Chemical thermodynamics of materials - macroscopic and microscopic aspects*, John Wiley & Sons Ltd, ISBN: 0 471 49230 2, Chichester West Sussex, England.

Sutton, A.P.; Finnis, M.W.; Pettifor, D.G. & Ohta, Y. (1988). The tight-binding bond model. *J. Phys. C*, Vol. 21, 35–66.

Svensson, E.C.; Brockhouse, B.N. & Rowe, J.M. (1984). Crystal Dynamics of Copper. *Phys. Rev.*, Vol. 155, 619–632.

Tersoff, J. (1986). New empirical model for the structural properties of silicon. *Phys. Rev. Lett.*, Vol. 56, 632–635.

van Duin, A.C.T.; Dasgupta, S.; Lorant, F. & Goddard, W.A. (2001). ReaxFF: A reactive force field for hydrocarbons. *J. Phys. Chem. A*, Vol. 105, No. 41, 9396–9409.

Wallace, D.C. (1965). Thermal Expansion and other Anharmonic Properties of Crystals. *Phys. Rev.*, Vol. 139, No. 3A, A877–A888.

Williams, P.L.; Mishin, Y. & Hamilton, J.C. (2006). An embedded-atom potential for the Cu-Ag system. *Model. Simul. Mater. Sc.*, Vol. 14, 817–833.

Yu, P.Y. & Cardona, M. (2010). *Fundamentals of Semiconductors - Physics and Materials Properties*, Springer, ISBN: 978-3-642-00710-1, Berlin Heidelberg.

Zhang, J.-M.; Wang, D.-D. & Xu, K.-W. (2006). Calculation of the surface energy of hcp metals by using the modified embedded atom method. *Appl. Surf. Sci.*, Vol. 253, 2018–2024.

7

Applications of Equations of State in the Oil and Gas Industry

Ibrahim Ashour[1], Nabeel Al-Rawahi[2], Amin Fatemi[1]
and Gholamreza Vakili-Nezhaad[1,3]
[1]*Department of Petroleum and Chemical Engineering*
College of Engineering, Sultan Qaboos University, Oman
[2]*Department of Mechanical & Industrial Engineering,*
College of Engineering, Sultan Qaboos University, Oman
[3]*Department of Chemical Engineering, Faculty of Engineering, University of Kashan, Kashan*
I. R. Iran

1. Introduction

Reservoir fluids contain a variety of substances of diverse chemical nature that include hydrocarbons and nonhydrocarbons. Hydrocarbons range from methane to substances that may contain 100 carbon atoms. The chemistry of hydrocarbon reservoir fluids is very complex. In spite of the complexity of hydrocarbon fluids found in underground reservoirs, equations of state have shown surprising performance in the phase-behavior calculations of these complex fluids. An equation of state (EOS) is an analytical expression relating pressure to the volume and temperature. The expression is used to describe the volumetric behavior, the vapor/liquid equilibria (VLE), and the thermal properties of pure substances and mixtures. Numerous EOS have been proposed since Van der Waals introduced his expression in 1873. Currently, a number of EOS are used in reservoir engineering which have shown more reliability in reservoir fluids calculations. In this chapter, a review over the most commonly used EOS in the oil and gas industry has been provided. We explore their strengths and weaknesses and to examine the predictive capability of these equations. A brief introduction to Soave-Redlich-Kwong (SRK), Peng-Robinson (PR), Patel-Teja (PT), Schmit-Wenzel (SW), and Esmaeilzadeh-Roshanfekr (ER) equations of state has been provided with intention to compare their efficiency in predicting different reservoir fluids properties. The Progress in developing EOS for the calculation of thermodynamic data and phase behavior is also reviewed. Effect of characterization on VLE predictions as well as advances in application of equations of state for heavy hydrocarbons has been considered in this work. Finally, as a case-study, phase behavior of a typical Omani crude oil as well as application of EOS with proper characterization method for this real oil sample has been examined.

2. Overview of EOS

Consider the plot of pressure versus total volume of a pure substance shown in Fig.1. An equation of state (EOS) is desired to represent the volumetric behavior of the pure substance in the entire range of volume both in the liquid and in the gaseous state.

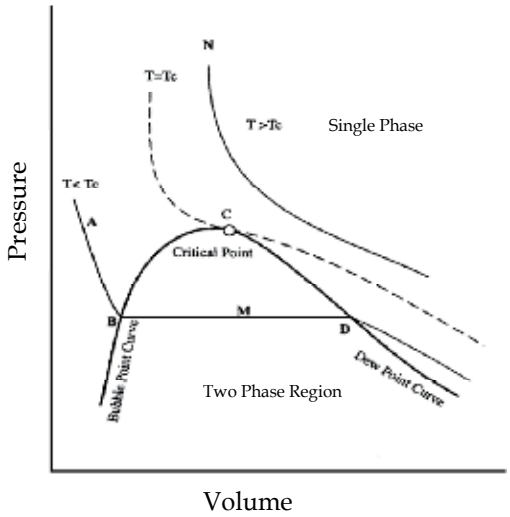

Fig. 1. Pressure volume diagram of a pure component

An EOS can represent the phase behavior of the fluid, both in the two-phase envelope (i.e., inside the binodal curve), on the two-phase envelope, and outside the binodal curve. Numerous EOS have been proposed to represent the phase behavior of pure substances and mixtures in the gas and liquid states since Van der Waals introduced his expression in 1873. These equations were generally developed for pure fluids and then extended to mixtures through the use of mixing rules. The mixing rules are simply a means of calculation mixture parameters equivalent to those of a pure substance. The equations of state are divided into two main groups: cubic and noncubic. Noncubic equations can better describe the volumetric behavior of pure substances but may not be suitable for complex hydrocarbon mixtures (Firoozabadi, 1989). For instance, the modified Benedict-Webb-Rubin equation (Starling, K.E. 1973) is admittedly more accurate than the cubic EOS (such as the Peng-Robinson EOS) for the PVT description of pure substances, but it may be less accurate than the two-constant cubic equations for VLE computation of complex reservoir fluid systems (Katz and Firoozabadi, 1978). The application of BWRS type equations demands a high computational time and effort, due to their high powers in volume and large number of parameters, hence, unsuitable for reservoir fluid studies where many sequential equilibrium calculations are required. More importantly, for multi-component systems each parameter must be determined using a mixing rule, which at best is quite arbitrary (Danesh, 1998). Although acceptable phase behavior results can be obtained by BWRS (Starling, 1966), it has been surpassed by the simpler, yet more reliable van der Waals type cubic equation of state. There are many examples in the literature where EOS are compared (Sing, 2005; Ahmed, 2004). The findings all highlight the fact that there is currently no "all in one" EOS that will give the best prediction of all thermodynamic properties of different types of reservoir fluids. It seems that some EOS can do better than the others only for certain reservoir fluid types and some EOS are advantageous for particular properties. For example, the PR-EOS for superior phase transitions (O'Reilly, 2009). This may also lead to entire PVT experiments being better represented by a particular EOS. The objective is to review literature for a number of common cubic EOS used in reservoir engineering calculations and compare their strengths and weaknesses.

2.1 Commonly used EOS in reservoir engineering calculations

Since 1949 when Redlich and Kwong (RK) formulated their two-parameter cubic equation of state (EOS), many investigators have introduced various modifications to improve ability of RK-EOS. Two other well-known cubic equations are Soave (SRK) (1972) and Peng-Robinson (PR) (1976) equations. Although many modified forms of RK-EOS are reported in the literature, but at least for hydrocarbon systems and their mixtures, only SRK and PR equations have been widely accepted. Both SRK and PR equations use Pitzer acentric factor as the third parameter to obtain parameter a in their equations. Acentric factors are calculated through critical properties; therefore, for heavy compounds where critical properties should be estimated, errors in critical properties will be contributed to acentric factor. Probably, the most successful cubic EOS for vapor liquid equilibria (VLE) calculations have been those proposed by Soave, Redlich and Kwong and Robinson and Peng (Esmaeilzadeh et al., 2005). Both of these EOS assumed a fixed value of the critical compressibility factor for all substances and as a result the predicted values for saturated liquid density differs considerably from their experimental values.

2.1.1 Soave-Redlich-Kwong (SRK) EOS

In 1972, Soave improved on the RK-EOS which represents an attempt to take molecular geometry and polarity into account by replacing the term $\frac{\alpha}{T^{0.5}}$ in RK-EOS with a more general temperature-dependent term $\alpha(T)$. He showed that a simple expression for the temperature dependency of attraction parameter "a" enabled the equation to represent vapor pressure of a wide class of substances. The proposed equation known as SRK-EOS is as follows:

$$P = \frac{RT}{v-b} - \frac{a(T)}{v(v+b)} \tag{1}$$

Where

$$a(T) = 0.42747\frac{R^2T_c^2}{P_c}\alpha(T) \tag{2}$$

$$b = 0.0867\frac{RT_c}{P_c} \tag{3}$$

Soave proposed a simple form for $\alpha \equiv \alpha(T_r, \omega)$ for all pure substances, taking advantage of the concept of the acentric factor of Pitzer (Pitzer et al., 1955) . Soave compared the predicted vapor pressure from his modification and the original RK EOS for a number of substances, showing that his modification greatly improved vapor pressure predictions. In this modification α(T) is extrapolated for the supercritical temperatures. Soave compared only the measured and computed saturation pressures of several binary systems that showed good agreement. SRK is quite capable of predicting vapour-liquid equilibria, but it does not provide reliable liquid density. (Danesh, 1998)

2.1.2 Peng-Robinson (PR) EOS

Another important variation of the van der Waals EOS was introduced in 1976 by Peng and Robinson. SRK-EOS fails to predict liquid densities accurately. Improved density prediction

was the main motivation of the authors of PR-EOS which in general is superior in density predictions of reservoir fluid systems. Although this equation improves the liquid density prediction, it cannot describe volumetric behavior around the critical point. The PR-EOS is perhaps the most popular and widely used EOS. In terms of the molar volume V_m, Peng and Robinson proposed the following two-constant cubic EOS:

$$P = \frac{RT}{V_m - b} - \frac{a(T)}{V_m(V_m + b) + b(V_m - b)} \tag{4}$$

Where

$$a(T_c) = 0.45724\ \frac{(RT_c)^2}{P_c} \tag{5}$$

$$b = 0.07780 \frac{(RT_c)}{P_c} \tag{6}$$

The generalized expression for the temperature-dependant parameter is given by

$$a(T) = a(T_c)\alpha(T) \tag{7}$$

where

$$\alpha(T) = \left\{1 + m\left[1 - \sqrt{\frac{T}{T_C}}\right]\right\}^2 \tag{8}$$

With

$$m = 0.3746 + 1.5423\omega - 0.2699\omega^2 \tag{9}$$

Comparison of the vapor-pressure prediction of several substances by the SRK EOS and the PR EOS with experimental data shows that the error is small for both equations, although the PR EOS performs better by a small margin (Firoozabadi A., 1988). Peng and Robinson also compared enthalpy departures for five pure substances from both their proposed EOS and the SRK EOS. Both equations generate enthalpy values of about the same reliability. According to different researchers' experience, PR-EOS enjoys more simplicity and reliability than many other equations. However, both PR and SRK equations break-down at C10 – C11and heavier compounds. Peneloux and Rauzy (1982) introduced a constant for each substance to be subtracted from the volume obtained in the SRK equation. Their modification greatly improves liquid density predictions, but it requires a fourth parameter beside critical temperature, critical pressure and acentric factor required by SRK equation.

2.1.2.1 Volume shift

A comparison of the predicted liquid molar volume by leading two parameter EOS with experimental data of pure compounds generally shows a systematic deviation. The deviation is almost constant over a wide pressure range away from the critical point. Hence, subtracting the predicted molar volume by a constant correction term can improve the predicted liquid density. The effect on the predicted vapor volume is generally insignificant due to its large value relative to that of liquid away from the critical point. Peneloux et al.

[26] were the first who introduced the volume shift concept, i.e. shifting the volume axis, and applied it to SRK,

$$v^c = v\text{-}c \tag{10}$$

where v^c is the corrected molar volume, and c is the correction term determined by matching the measured and predicted saturated liquid volumes at $T_r = 0.7$. The volume shift generally improves the predicted liquid density, and has a minimal effect on the vapor density at low and moderate pressures as its molar volume is relatively large compared to the value of c. At high pressure condition, the inclusion of c parameter may not necessarily improve the predicted gas density as it is just a correction term for the liquid density. However, it is advisable to adjust the gas phase volume by the third parameter to maintain consistency, particularly near the critical point where properties of the two phases approach each other. Peneloux et al. correlated the volume translation parameter c as,

$$c = 0.40768(0.29441 - Z_{RA})\, RT^c/P^c \tag{11}$$

where ZRA is the Rackett compressibility factor. For a more detailed discussion, reader is suggested to refer to Peneloux et al. (1982).

2.2 Three-parameter EOS

A two-parameter EOS predicts the same critical compressibility factor, Z, for for all substances, i.e. 0.307 and 0.333 by PR and SRK respectively, whereas Z_c varies within a range of 0.2 to 0.3 for hydrocarbons. Although the inaccuracy of predicted volume at the critical point, not necessarily leads to unreliable volumetric data at all conditions, it demonstrates the inflexibility of two-parameter EOS for matching both the vapor pressure and volume. The inclusion of a third parameter relaxes the above limitation. The third parameter is generally determined by employing volumetric data.

2.2.1 Esmaeilzadeh-Roshanfekr (ER) EOS

Both of PR and SRK equations assume a fixed value of the critical compressibility factor for all substances and, as a result, the predicted values for saturated liquid density differ considerably from their experimental values. On the other hand, some equations of state proposed by Schmit and Wenzel (Schmit G. & Wenzel H., 1980) and Patel and Teja (Patel N.C., Teja A.S., 1982) introduced a third parameter to their equations. This suggestion led to the introduction of a substance dependent critical compressibility which allowed them to reproduce more accurate the experimental saturate liquid density at a particular temperature. Their work showed that the optimum value of substance critical compressibility was not equal to the experimental critical compressibility of the fluid of interest. Using the generalized Van der Walls theory, Esmaeilzadeh and Roshanfekr used a mathematically simple cubic EOS to model attractive interactions between molecules. The proposed equation of state in their work is as follows (Esmaeilzadeh & Roshanfekr, 2006)

$$P = \frac{RT}{v - b} - \frac{a(T)}{v(v + c) + c(v - c)} \tag{12}$$

Where "a" is a function of temperature and "b" and "c" are constants. In this EOS $a(T)$ and b are derived as:

$$a(T_c) = \Omega_a \frac{(RT_c)^2}{P_c}.\alpha(T_r) \tag{13}$$

$$b = \Omega_b \frac{(RT_c)}{P_c} \tag{14}$$

$$c = \Omega_c \frac{(RT_c)}{P_c} \tag{15}$$

This EOS predicts saturated liquid density more accurately than the PT and PR EOS. The results for the calculation of vapor pressure of pure components for light hydrocarbons show that Eq. (12) has the lowest deviation and for heavy hydrocarbons the PT EOS yields the lowest deviation (for Tr < 0.75). The prediction of thermodynamic properties of light and intermediate hydrocarbons by Eq. (12) is superior to other EOS studied in this work. Moreover, It is found that Esmaeilzadeh-Roshanfekr EOS is most accurate for predicting gas-condensate properties, while the original SRK and PR equations remain reliable for oil samples. (Bonyadi et al., 2007)

2.2.2 Schmidt-Wenzel EOS (SW)

Liquid density prediction at T_r=0.7 by SRK and PR for pure substances is associated with noticeable deviation from reliable values. Note that SRK is more reliable for substances with small acentric factors, whereas PR gives reliable data for compounds with acentric factors around (1/3). Based on the above observation, Schmidt and Wenzel incorporated the acentric factor as the third parameter in the attractive term as,

$$P = \frac{RT}{v-b} - \frac{a_c\alpha}{v^2 + (1+3\omega)bv - 3\omega b^2} \tag{16}$$

Substituting acentric factor values of zero and $1/3$ in the Schmidt-Wenzel EOS (SW) will reduce it to SRK and PR respectively, where these equations predict the liquid density reliably. SW can, therefore, be considered a general form of SRK and PR (Danesh, 1998). The authors used the boundary conditions at the critical point, Eq.(4.9) to determine a_c, and b, as

$$a_c = \Omega_{ac} \frac{R^2 {T_c}^2}{P_c} \tag{17}$$

$$b = \Omega_b \frac{RT_c}{P_c} \tag{18}$$

Where

$$\Omega_{ac} = [1 - \eta(1-q)]^3 \tag{19}$$

$$\Omega_b = \eta q \tag{20}$$

In above equations η is the critical compressibility factor, and is related to the correlating parameter q, by

$$\eta = {}^{1}/_{[3(1+q\omega)]} \tag{21}$$

and q, defined as b/v_c, is the smallest positive root of the following equation,

$$(6\omega + 1)\, q^3 + 3q^2 + 3q - 1 = 0 \tag{22}$$

with an approximate value of,

$$q = 0.25989 - 0.0217\, \omega + 0.00375\omega^2 \tag{23}$$

Schmidt and Wenzel selected the same form of a as proposed by Soave, but correlated, m, with the acentric factor and reduced temperature by matching vapor pressure data of pure compounds as is discussed in details in Schmidt et al, 1980. The inclusion of ω in EOS as the third parameter by Schmidt and Wenzel resulted in a variable calculated critical compressibility, according to the value of acentric factor. The predicted values are, however, about 15% higher than the true values. This was known to the authors, but was accepted as the price for an overall optimum accuracy in predicted volumes (Danesh, 1998).

2.2.3 Patel-teja (PT) EOS

Patel N.C., Teja A.S. (1982) modified the attractive term by including a more flexible third parameter. (Patel et al., 1982) The authors found that the use of true critical compressibility factor will result in the overall loss of accuracy in predicted density, a conclusion also reached by Schmidt and Wenzel. For more details the reader is recommended to referred to Patel N.C., Teja A.S.(1982).

3. Heavy oil characterization

Heavy-oil fluids contain large concentrations of high-molecular weight components, including a large content of the plus fractions, such as C7+. For crude oils and reservoir fluids, the basic laboratory data are usually presented in the form of the composition of hydrocarbons up to hexanes and the heptane-plus fraction (C7+), with its molecular weight and specific gravity calculations (Danesh 1998; Ahmed 2007). The constituents of a hydrocarbon system are classified in two categories: the well-defined components and the undefined petroleum fractions, which are those heavy compounds lumped together and identified as the plus-fraction [i.e., C7+ (Ahmed 2007)]. Several samples of heavy oil indicate that the plus fraction C10+ contains a molar fraction close to 70% and that the fraction C80+ is also representative with values close to 2% (Pedersen et al. 2004). The importance of characterizing the plus fraction arises when the modeled fluid has high molecular weight and high density (heavy oil). Characterization of plus fraction usually consists of three parts: (1) splitting the fraction into a certain number of component groups called SCNs; (2) estimation of the physicochemical properties of the SCN; and (3) lumping of the generated SCNs (Pedersen et al. 2006).

3.1 Splitting method

Several methods have been developed to estimate the mole distribution of the compounds in the plus fraction (Katz et al. 1978; Pedersen et al. 1982; Ahmed et al. 1985; Whitson 1983). Heptanes plus (C7+) fractions are expressed by a distribution model and the fractions heavier than C6 have been lumped into pseudo-components with approximately equal weight fraction of each pseudo-component (i.e. molar averaging). Often, the exact chemical composition of a HC fraction is not known, therefore, pseudoization defines these HC fractions and allows the determination of EOS parameters Splitting and lumping are the two

main types of the pseudoization. A common feature among these methods is that components with the same number of carbon atoms are lumped in groups called SCNs with a single predefined value for properties like Pc, Tc, ω, Tb, M, and density ρ. Whitson (1983) proposed a method using the TPG distribution in order to estimate the mol fraction as a function of the molecular weight. The molecular weights used are the generalized values presented for each SCN (Katz and Firoozabadi 1978). Generalized correlations have been developed to generate critical properties for the SCN including those by Twu (1984), Ahmed (1985), Kesler-Lee (1976), Riazi-Daubert (1987), and Edmister (1958). Riazi-Daubert, and Edmister correlations are used.
Whitson (1983) used TPG distribution to estimate the mole fraction of the SCNs within the Cn+ fraction. TPG is defined (Whitson 1983) as a function of the molecular weight (M) by the following equation:

$$P(M) = \frac{(M-\eta)^{\alpha-1}\exp\left(-\frac{M-\eta}{\beta}\right)}{\beta^{\alpha}\Gamma(\alpha)} \tag{24}$$

where η is the minimum molecular weight present in the C_{n+} fraction, α is used to fit the shape of the distribution, and Γ is the gamma function. Whitson recommended Γ = 92, the molecular weight of toluene, as a good estimation of η, if C7+ is the plus fraction; for other plus fractions, following is used as approximation:

$$\eta = 14n - 6 \tag{25}$$

and

$$\beta = \frac{M_{cn+} - \eta}{\alpha} \tag{26}$$

where M_{Cn+} is the molecular weight of the Cn+ fraction. The mole fraction of an SCN is then generated by calculation of the cumulative frequency of occurrence between the limits M_{i-1} and M_i multiplied by the mole fraction of the Cn+ fraction.

$$Z_i = Z_{C_{n+}} + \int_{M_{i-1}}^{M_i} p(x)dx \tag{27}$$

where i is the SCN and M_i is the molecular weight of the SCN usually defined as the molecular weight of the normal component.

3.2 Correlations used to estimate physicochemical properties of the SCN

In a hydrocarbon mixture, the critical properties (critical pressure "Pc", critical temperature "Tc" and accentric factor "ω") must be given for each component. These properties are well known for pure compounds (like methane, ethane, etc.), but nearly all naturally occurring gas and crude oil fluids contain some heavy fractions that are not well defined. There arises the need of adequately characterizing these undefined plus fractions in terms of their critical properties (Gastón, 2007).
Several correlations have been developed to estimate the physical properties of petroleum fractions and are in principal function of the specific gravity, the boiling point temperature and the molecular weight Riazi-Daubert (1987), Twu (1984), Ahmed (1985), Kesler-Lee (1976), and Edmister (1958); in this study, the Riazi-Daubert (1986) has been used.

3.2.1 Riazi-Daubert correlation

Riazi-Daubert's correlation is utilized to obtain physical properties of the plus fraction using the laboratory reported MW and SG as heavy fraction parameters. This study uses Riazi and Daubert, since it is the one mostly used in the industry; for calculating the accentric factor, Riazi-Daubert uses the Edmister's correlation (Riazi, M. R., Daubert, T. E. (1987)). The proposed relationship is:

$$\Theta = a\mathrm{MW}^{b}\mathrm{SG}^{c} \exp\left[d\mathrm{MW} + e\mathrm{SG} + f\,(\mathrm{MW}\,.\,\mathrm{SG})\right] \tag{28}$$

Where:

Θ = some physic property.

a-f = coefficients for each physic property (Table 1).

The Edmister's correlation for the accentric factor is P_c and T_c dependent is given by (Edmister, W.C., 1958):

$$\omega = \frac{3}{7}\,\frac{\log(P_c/14.7)}{T_c/T_b - 1} - 1 \tag{29}$$

Θ	T_c	P_c	T_b
a	544.4	45203	6.77857
b	0.2998	-0.8063	0.401673
c	1.0555	1.6015	-1.58262
d	-0.00013478	-0.0018078	0.00377409
e	-0.61641	-0.3084	2.984036
f	0.0	0.0	-0.00425288

Table 1. Riazi and Daubert's coefficients

3.3 Lumping methods and mixing rules

The generation of an appropriate mole distribution that represents the plus fraction usually requires splitting the plus fraction into large number of components (SCN) with their respective mole fractions and physical properties. The use of a large number of components in a reservoir simulation is time consuming. Lumping is defined as the reduction of the number of components used in EOS calculations for reservoir fluids. After lumping many components into a minimum number of hypothetical components, it is necessary to determine the characterization parameters (critical temperature, critical pressure, and acentric factor) for each lumped hypothetical component for use in the equations of state using some mixing rules. Phase equilibrium calculations are very sensitive to the values of the characterization parameters in the equations of state. Conventional mixing rules, which are inconsistent with the equation of state itself, are usually applied to calculate the characterization parameters of the lumped pseudocomponents. The inadequacy of this characterization method often results in inaccurate predictions of phase equilibria. Another problem is that the binary interaction parameters between the lumped hypothetical components, which are often needed in the phase behavior calculations, are difficult to obtain. The common practice is to set the binary interaction parameters equal to zero for all hydrocarbon-hydrocarbon interactions, while nonzero values may be used for interactions

with non-hydrocarbons (Chorng H. Twu and John E. Coon, 1996). Pedersen et al. (2006) states that lumping consists of

- Deciding what carbon number fractions are to be lumped into same pseudocomponent.
- Deciding the mixing rules that will average T_c, P_c, ω of the individual carbon number fractions to one T_c, P_c, ω to represent the lumped pseudocomponents.

Whitson's method is described for estimating the number of MCN groups needed for adequate plus-fraction description, as well as which SCN groups belong to the MCN group. The proposed distribution model is similar to a folded log-normal distribution. The number of MCN groups, N_g , is given by

$$N_g = \text{Int}\,[\,1 + 3.3 \log_{10}(N - n)\,] \tag{30}$$

For black-oil systems, this number probably can be reduced by one (Whitson 1983).
The molecular weights separating each MCN group are taken as

$$M_l = M_n \{\text{Exp}\,[(\,1 / N_g \,.\, \ln (M_N / M_n)\,]\}^l \tag{31}$$

where M_N is the molecular weight of the last SCN group (which may actually be a plus fraction), and 1= I, 2 ... N_g. Molecular weights of SCN groups falling within the boundaries of these values are included in the MCN group, I.
Recently, Rudriguez et al. developed a method based on a modification of Whitson's approach. The approach is based on the fact that single carbon number groups (SCN), may represent hundreds of different compounds with the same number of carbon atoms. These compounds can be classified in different types: paraffins, naphtenes and aromatics. Uncertainty of the types and distribution of compounds present in each single carbon number indicates that the average value of molecular weight of a single carbon number is different from one sample to another. The modification of Whitson's method includes a simple procedure to determine the value of the fitting parameter (α); and a new definition of the limits used to calculate the frequency of occurrence for each single carbon number. The developed method is based on that the molecular weight is not uniquely related to carbon numbers due to the hidden exponential increase of number of isomers/components with increasing the carbon numbers. In the method, TPG distribution from Whitson's approach is used to characterize the plus fraction and generate molecular weight / carbon number function. It is, also used to find the best trend fit to the experimental data by solving for parameter. The limiting molecular weight, for each carbon number, is determined to fit the mole fraction that is corresponding to the carbon number. Linear extrapolation of the limiting molecular weight as a function of the carbon number is used here to extend the characterization to the missing data of the higher carbon number (Rodriguez et al., 2010). The reader is recommended to refer to Rodriguez et al. 2010, for further discussion of the proposed method.

3.4 Mixing rules

Mixing rule for calculating critical properties (including acentric factor and specific gravity) of MCN groups is discussed here. Molar and volumetric properties of MCN groups are always calculated using the mixing rules

$$M_l = \sum_i^l {}^{z_i}/_{z_l} M_i \tag{32}$$

$$\gamma_l = \frac{1}{\left[\sum_i^l \frac{\left(f_{wi}/f_{wl}\right)}{\gamma_i}\right]} \tag{33}$$

pseudocritical volume should be calculated using weight fractions

$$V_{pcl=} \sum_i^l \left(f_{wi}/f_{wl}\right).V_{ci} \tag{34}$$

where z_l and f_{wl} are the sums of z_i and f_{wi} found in MCN group l. MCN acentric factors are usually calculated using Kay's mixing rule.
In the next section, a case study is presented in order to implement correct characterization procedures using the described method in previous sections. The sample is a black oil sample collected from an Omani reservoir with specified plus fraction analyzed in the laboratory.

4. Case study: Fahud oil sample characterization

A typical reservoir oil sample collected from an Omani reservoir (Fahud) has been taken into consideration for VLE analysis and characterization scheme.

4.1 Sample selection

A set of PVT reports from different fields in north and central of Oman have been reviewed to choose a sample for our case study having an API of 37.76. The selected sample is a bottom hole sample (BHS) at the depth of 2550 m and the recorded reservoir temperature of 95 ^{0}C.

4.2 Laboratory measurement

The sample is analyzed to indentify the components through the Liquid Gas Chromatograph, AGILENT Technologies, model 7890A. The column name is DB-1 with length of 60 (m) with a diameter of 0.250 (mm) and film thickness of 0.25 (um) column temperature is -60 t0 3250C. The compositional analysis defined the mole composition of several SCN until it reaches to C7. The critical properties of these elements were obtained from Reid et al. (1986). Lastly the pseudo-component (which represents the heptanes plus-fraction of the fluid, in this case C7+) is characterized using the later described Riazi-Daubert correlation (Riazi, M. R., Daubert, T. E. (1987)). Table 2 shows the results of the compositional analysis of this crude oil sample.

4.3 Methodology

The compositional simulator utilized is reservoir simulation Eclipse (Property of Schlumberger) *PVTi* module. It uses the PR-EOS with the modifications on the volume shift, the quadratic mixing rule and Lorenz-Bray-Clark viscosity correlation. For estimation of the undefined element properties, Riazi-Daubert correlation is used (Riazi, M. R., Daubert, T. E. (1987)). This software has been used to find the phase envelop of the reservoir sample and estimation of different characteristics of the oil sample.

No.	Component	[mol %]
1	*N2*	1.67
2	*CO2*	0.24
3	*CH4*	41.2
4	*C2H6*	3.45
5	*C3H8*	1.65
6	*I-C4H10*	0.56
7	*N-C4H10*	1.75
8	*I-C5H12*	0.82
9	*N-C5H12*	1.56
10	*C6H14*	3.32
11	*C7+*	43.78

C7+ MW (gr/mol): 271
C7+ SG (gr/cm3): 0. 848

Table 2. compositional analysis of Fahud crude oil sample

4.4 Phase envelop of the Fahud oil sample

The oil sample analyzed in this study is initially composed of more than about 20 mole% heptanes and heavier compounds which is representative of Black oil type of reservoir fluid. Its phase envelope, therefore, is the widest of all types of reservoir fluids, with its critical temperature well above the reservoir temperature (T_c=828K compared to T_{res}=366K). Phase diagram of this sample is plotted using the Eclipse software as in fig. 2.

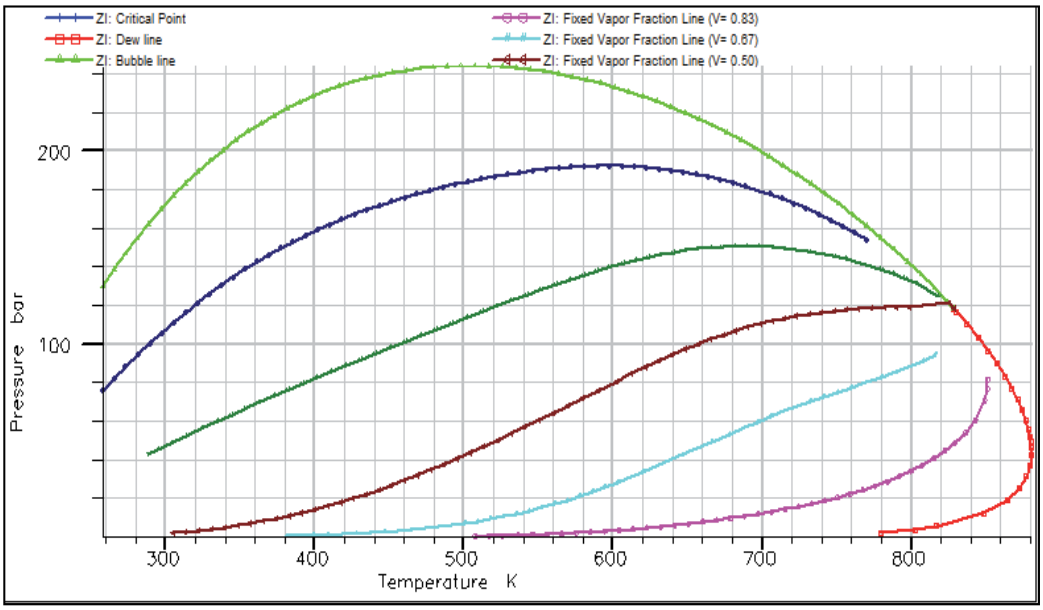

Fig. 2. Phase envelope of Fahud oil sample generated by Eclipse-*PVTi*.

5. Acknowledgment

The Research leading to these results has received funding from Petroleum Development Oman (PDO), Sultanate of Oman, through research agreement no. [CTR # 2009/111].

6. References

Ahmed T. (1997). *Hydrocarbon Phase behavior*, Gulf publishing Company, London.

Danesh A. (1998). *PVT and Phase Behavior of Petroleum Reservoir Fluids*, Elsevier Science B.V., London.

Edmister, W.C. (April 1958). Applied Hydrocarbon Thermodynamic, Part 4: Compressibility Factors and Equations of State, *Petroleum Refinery*, Vol.(37): 173-179.

Esmaeilzadeh F., Roshanfekr M. (2006). A new Cubic Equation of State for Reservoir Fluids, *Fluid Phase Equilibria* Vol.(239): 83–90

Firoozabadi A. (April 1988), Reservoir-Fluid Phase Behavior and Volumetric Prediction with Equations of State, *Journal of Petroleum Technology,* pp 397-406.

Firoozabadi A. (1989). *Thermodynamics of Hydrocarbon Reservoirs*, McGraw-Hill.

Katz, D.L. and Firoozabadi, A. (Nov. 1978). Predicting Phase Behavior of Condensate Crude-Oil Systems Using Methane Interaction Coefficients, *Journal of Petroleum Technology* 1649-55; Trans., AIME, 265.

Joffe, J., Schroeder, G.M., and Zudkevitch, D. (May 1970). Vapor-Liquid Equilibria with the Redlich-Kwong Equation of State, *AIChE J.* 496-98.

Kesler, M.G. and Lee, B.I. (1976). Improve Prediction of Enthalpy of Fractions, *Hydrocarbon Processing*: 55-59.

Krejbjerg K., Pedersen K. S. (2006). Controlling VLLE Equilibrium with a Cubic EOS in Heavy Oil Modeling, *7th Canadian International Petroleum Conference*, Calgary,Canada.

O'Reilly D.I. (2009). Comparative PVT Simulation: An application to Australian Fluid Samples, *SPE Annual Technical Conference and Exhibition*, New Orleans, Louisiana, USA.

Patel N.C., Teja A.S.(1982). A new cubic equation of state for fluids and fluid mixtures, *Chem. Eng. Sci.* Vol.(37): 463–473.

Peng, D.Y. and Robinson, D.B. (1976). A New Two-Constant Equation of State, *Ind. & Eng. Chem*. 15, No.1, 59-64.

Peneloux A., Rauzy E. and Freze, R (1982). A Consistent Correction for Redlich-Kwong-Soave Volumes. *Fluid Phase Equilibria* Vol.(8): 7-23.

Rafael A. Aguilar Zurita and William D. McCain, Jr. (2002). An Efficient Tuning Strategy to Calibrate Cubic EOS for Compositional Simulation, *SPE Annual Conference and exhibition*, San Antonio, Texas, SPE 77382.

Reid R.C., Prausnitz, J.M. and Sherwood, T.K (1986). *The Properties of Gases and Liquids*, 4th edition, McGraw Hill.

Riazi, M. R., Daubert, T. E. (1987). Characterization Parameters for Petroleum Fractions, *Ind. Eng. Chem. Res.* Vol.(26): 755-759.

Riazi M. R. (2005). *Characterization and properties of Petroleum Fractions*, ASTM Stock Number: MNL50, ISBN: 2004059586, USA.

Rodriguez I. and Hamouda A.A. (2010). An Approach for Characterization and Lumping of Plus Fractions of Heavy Oil, *SPE 117446 Reservoir Evaluation & Engineering.*

Schmit G., Wenzel H. (1980). A modified van der Waals type equation of state, *Chem. Eng. Sci.* Vol.(35): 1503-1511.

Sing, B.P. (2005): Comparison of equations of state including the generalized Rydberg EOS, *Physica B* Vol.(369): 111-116

Soave G (1972). Equilibrium Constants from a Modified Redlich-Kwong Equation of State, *Chem. Eng. Sci.* 27, 1197-1203.

Starling, K.E (1966). A New Approach for Determining Equation-of-State Parameters Using

Phase Equilibria Data, *SPE Journal Vol.(*237), 363-371, Trans. AIME.

Starling, K.E. (1973). *Fluid Thermodynamics Properties for Light Petroleum Systems,* Gulf Publishing Co., Houston.

Twu, C.H. (1984). An internally Consistent Correlation for Predicting the Critical Properties and Molecular Weights of Petroleums and Coal-Tar Liquids, *Fluid Phase Equilibria* Vol.*(*16): 137.

Twu, C.H., Coon, J.E. and Cunningham, J.R. (1995). A New Generalized Alpha Function for a Cubic Equation of State. Part 1: Peng-Robinson EOS, Fluid Phase Equilibria, Vol.(105): Number 1.

Whitson, C.H. (1982). Effect of C7+ Properties on Equation of State Predictions, *SPE Annual Technical Conference and Exhibition*, SPE 11200.

Whitson, C.H.(Aug. 1983). Characterizing Hydrocarbon Plus Fractions, *SPE Journal*: 683-94.

Zudkevitch, D. and Joffe, J. (Jan. 1970). Correlation and Prediction of Vapor Liquid Equilibrium with the Redlich-Kwong Equation of State, *AIChE J.* 112-19.

8

Shock Structure in the Mixture of Gases: Stability and Bifurcation of Equilibria

Srboljub Simić
University of Novi Sad
Serbia

1. Introduction

List of symbols

$\mathbf{A}^0, \mathbf{A}$	Jacobian matrices	$\mathbf{t}, \mathbf{t}_\alpha, \mathbf{t}_b$	stress tensor
$\mathbf{B}$	viscosity matrix	$\mathbf{u}, \mathbf{U}, \mathbf{v}$	state variables
c, c_α, c_b	concentration	u	relative velocity
c_S, c_0	local speed of sound	$\mathbf{u}_\alpha, \mathbf{u}_b$	diffusion velocity
e	internal energy density	$v, \mathbf{v}, \mathbf{v}_\alpha, \mathbf{v}_b$	velocity
$e_\alpha, e_b, \hat{e}_b$	energy density source term	x	space variable
$\mathbf{F}^0, \hat{\mathbf{F}}^0, \mathbf{f}^0, \mathbf{g}^0$	densities	*Greek symbols*	
$\mathbf{F}, \hat{\mathbf{F}}, \mathbf{f}, \mathbf{g}$	fluxes	γ	ratio of specific heats
$\mathbf{h}$	equilibrium manifold	ε	small parameter
$\mathbf{J}$	diffusion flux	$\varepsilon, \varepsilon_I, \varepsilon_\alpha, \varepsilon_b$	internal energy density
k_B	Boltzmann constant	$\varphi_{bc}, \theta_{bc}, \psi_{bc}$	phenomenological
l_0	reference length		coefficients
m	atomic mass	λ_i, Λ_j	eigenvalues
$\mathbf{m}_\alpha, \mathbf{m}_b, \hat{\mathbf{m}}_b$	momentum density	κ	heat conductivity
	source term	Θ	temperature difference
μ	viscosity	$\rho, \rho_\alpha, \rho_b$	mass density
M_0	Mach number	σ	stress
n, N	number of state variables	Σ	singular surface
p, p_α	pressure	$\tau, \tau_\sigma, \tau_q$	relaxation time
$q, \mathbf{q}, \mathbf{q}_\alpha, \mathbf{q}_b$	heat flux	$\tau_\alpha, \tau_b, \hat{\tau}_b$	mass density source term
$\mathbf{q}, \mathbf{Q}$	source terms	ξ	lumped space variable
$\mathbf{r}_i, \mathbf{R}_j$	eigenvectors	*Subscripts*	
s	shock speed	E	equilibrium
t	time variable	$0, 1$	upstream, downstream
T, T_α, T_b	temperature		

Shock waves are moving singular surfaces on which jump discontinuities of field variables occur. Such singularities are commonly related to mathematical models in the form of

hyperbolic systems of conservation laws. However, in real physical systems dissipative mechanisms of thermo-mechanical nature smear out the discontinuity and transform the shock wave into a *shock structure* – travelling wave with large gradients of field variables in the neighborhood of singular surface. Occurrence of dissipation ought to be reflected on the mathematical model. Actually, there are two common types of dissipative models: (i) a parabolic one which takes the dissipative effects into account through diffusion-like terms, and (ii) a hyperbolic system of balance laws which extends the original system with a set of hyperbolic balance laws which comprise relaxation-type source terms. Both of these models strive to capture effects which push the system out of local equilibrium state, although the mathematical structure is rather different. This chapter gives a review of recent results about the shock structure in dissipative hyperbolic systems of balance laws and provides insight into their application to recently developed hyperbolic model of gaseous mixtures.

Study of shock structure usually starts with travelling wave ansatz which transforms the original system of partial differential equations (PDE's) to a system of ordinary differential equations (ODE's). It was pointed out in a series of papers (Simić, 2008; 2009) that appearance of physically admissible shock structure can be anticipated by stability and bifurcation analysis of stationary points of the ODE system. It was recognized that these stationary points are related by Rankine-Hugoniot equations for the equilibrium subsystem which is obtained when dissipation (relaxation) is neglected. However, these results can be derived without prior knowledge of Rankine-Hugoniot conditions on singular surface and without explicit use of selection rules for physically admissible shock waves, like Lax, Liu or entropy growth condition.

Stability and bifurcation results can be easily predicted in the case of parabolic systems (with diffusion-like dissipation) since equilibrium subsystem is naturally imbedded into its structure. On the other hand, hyperbolic dissipative systems (with relaxation-type source terms) absorb the equilibrium subsystem into its structure, but also make its properties less visible. So far, the shock structure is analyzed in dissipative Burgers equation, isothermal viscoelasticity (Simić, 2008) and continuum models of gas dynamics (viscous and heat-conducting gases) (Simić, 2009). In all these models dissipation can be included in either way. Our aim is to show that methodology used in the above mentioned examples can be efficiently applied also to a rather complex hyperbolic dissipative system which models the multi-temperature mixture of gases. Thus far this model does not have its parabolic counterpart. In particular, the shock structure problem will be studied via stability and bifurcation analysis in the case of binary mixture.

The chapter will be structured as follows. First, the general framework will be given, which includes the review of dissipative mathematical models and an overview of the shock structure problem. In the sequel a review of recent results about the shock structure problem in hyperbolic systems will be given. They comprise the isothermal viscoelasticity model and continuum model of gas dynamics. Finally, the shock structure problem will be discussed in the case of binary multi-temperature mixture, a new issue which will be studied for the first time in this context.

2. General framework

2.1 The mathematical structure of dissipative models

To make the ideas more clear, a brief review of mathematical structure of dissipative models will be given. For the sake of simplicity we shall confine the exposition to one space dimension indicated by variable x.

It is well known that continuum models in physics are usually expressed in the form of conservation laws

$$\partial_t \mathbf{F}^0(\mathbf{u}) + \partial_x \mathbf{F}(\mathbf{u}) = \mathbf{0} \tag{1}$$

where $\mathbf{u}(x,t) \in \mathbf{R}^n$ is the vector of state variables, $\mathbf{F}^0(\mathbf{u})$ is the vector of densities and $\mathbf{F}(\mathbf{u})$ the vector of fluxes. When densities and fluxes are functions of state variables solely, i.e. not of their derivatives, it is expected that (1) is hyperbolic, at least in some region of the state space. In other words, the eigenvalue problem

$$\begin{aligned} &(-\lambda \mathbf{A}^0(\mathbf{u}) + \mathbf{A}(\mathbf{u}))\mathbf{r} = \mathbf{0}; \\ &\mathbf{A}^0(\mathbf{u}) = \partial \mathbf{F}^0(\mathbf{u})/\partial \mathbf{u}; \qquad \mathbf{A}(\mathbf{u}) = \partial \mathbf{F}(\mathbf{u})/\partial \mathbf{u}, \end{aligned} \tag{2}$$

has n real eigenvalues $\lambda_i(\mathbf{u})$ called characteristic speeds, and n linearly independent eigenvectors $\mathbf{r}_i(\mathbf{u})$, $i = 1, \ldots, n$; $\mathbf{A}^0(\mathbf{u})$ is assumed to be nonsingular. This property permits modelling of wave propagation through space with finite speeds.

Hyperbolicity is the main cause for non-existence of smooth solutions for all t, even when initial data are smooth. Jump discontinuities – shock waves – which are located on the singular surface $\Sigma(x,t)$, may appear in finite time interval. If $[[\cdot]] = (\cdot)_1 - (\cdot)_0$ denotes the jump of any quantity in front (upstream) $(\cdot)_0$ and behind (downstream) $(\cdot)_1$ the surface Σ which propagates with speed s, then Rankine-Hugoniot conditions relate the jump of the field variables to the shock speed

$$[[\mathbf{F}(\mathbf{u})]] = s[[\mathbf{F}^0(\mathbf{u})]]. \tag{3}$$

However, not all of the jump discontinuities which satisfy (3) are observable in reality. Along with Rankine-Hugoniot conditions, they have to satisfy additional ones which serve as selection rules for physically admissible solutions (Dafermos, 2000; Serre, 1999). For the purpose of this exposition we shall be confined with the Lax condition

$$\lambda_i(\mathbf{u}_1) \geq s \geq \lambda_i(\mathbf{u}_0). \tag{4}$$

It represents a particular form of irreversibility condition since the roles of $\mathbf{u}_0$ and $\mathbf{u}_1$ cannot be interchanged. In classical gas dynamics it is related to the fact that physically admissible shock wave has to be supersonic with respect to upstream state and subsonic with respect to downstream state.

Classical continuum thermomechanics motivates so-called viscosity approach which regularizes the system (1) by adding parabolic terms

$$\partial_t \mathbf{F}^0(\mathbf{u}) + \partial_x \mathbf{F}(\mathbf{u}) = \varepsilon \partial_x (\mathbf{B}(\mathbf{u}) \partial_x \mathbf{u}) \tag{5}$$

where $\mathbf{B}(\mathbf{u})$ is viscosity matrix and $\varepsilon > 0$ small parameter, usually related to viscosity, heat conductivity and diffusivity. This model predicts infinite speed of propagation of disturbances, and characteristic speeds, as one of the basic features of hyperbolic model (1), cannot be related to (5). However, parabolic terms regularize the shock waves which correspond to genuinely nonlinear characteristic speeds of (1). In such a way (5) comprise solutions representing the shock profile travelling uniformly with shock speed s. These models are proved to be reliable as long as the state of the system is not far from the local equilibrium one.

Another way of description of dissipative mechanisms is to take into account the relaxation effects. Formally, this assumes extension of the set of state variables $\mathbf{u} \in \mathbf{R}^n$ by $\mathbf{v} \in \mathbf{R}^k$, $n + k = N$, which are governed by the additional set of balance laws. In particular, we have

$$\partial_t \hat{\mathbf{F}}^0(\mathbf{U}) + \partial_x \hat{\mathbf{F}}(\mathbf{U}) = \frac{1}{\tau}\mathbf{Q}(\mathbf{U}), \tag{6}$$

where

$$\mathbf{U} = \begin{pmatrix} \mathbf{u} \\ \mathbf{v} \end{pmatrix}, \qquad \mathbf{Q}(\mathbf{U}) = \begin{pmatrix} \mathbf{0} \\ \mathbf{q}(\mathbf{u},\mathbf{v}) \end{pmatrix}, \tag{7}$$
$$\hat{\mathbf{F}}^0(\mathbf{U}) = \begin{pmatrix} \mathbf{f}^0(\mathbf{u},\mathbf{v}) \\ \mathbf{g}^0(\mathbf{u},\mathbf{v}) \end{pmatrix}, \qquad \hat{\mathbf{F}}(\mathbf{U}) = \begin{pmatrix} \mathbf{f}(\mathbf{u},\mathbf{v}) \\ \mathbf{g}(\mathbf{u},\mathbf{v}) \end{pmatrix},$$

and $\tau > 0$ is a small parameter – relaxation time. It is assumed that $\mathbf{q}(\mathbf{u},\mathbf{v}) = \mathbf{0}$ uniquely determines the "equilibrium manifold" $\mathbf{v}_{\mathrm{E}} = \mathbf{h}(\mathbf{u})$ as $\tau \to 0$, on which the system (6) reduces to (1) with $\mathbf{F}^0(\mathbf{u}) = \mathbf{f}^0(\mathbf{u},\mathbf{h}(\mathbf{u}))$ and $\mathbf{F}(\mathbf{u}) = \mathbf{f}(\mathbf{u},\mathbf{h}(\mathbf{u}))$. The first n equations in (6) are conservation laws, while remaining k ones are balance laws with source terms $\mathbf{q}(\mathbf{u},\mathbf{v})/\tau$ which describe dissipative effects off the equilibrium manifold.
It is customary to expect that system (6) is hyperbolic at least in some subset of the extended state space $\mathbf{R}^N$ which contains the equilibrium manifold. Corresponding characteristic speeds $\Lambda_j(\mathbf{U})$, $j = 1,\ldots,N$, and the set of linearly independent eigenvectors $\mathbf{R}_j(\mathbf{U})$ are determined from the eigenvalue problem for the differential part of (6)

$$(-\Lambda\hat{\mathbf{A}}^0(\mathbf{U}) + \hat{\mathbf{A}}(\mathbf{U}))\mathbf{R} = \mathbf{0}; \tag{8}$$
$$\hat{\mathbf{A}}^0(\mathbf{U}) = \partial\hat{\mathbf{F}}^0(\mathbf{U})/\partial\mathbf{U}; \qquad \hat{\mathbf{A}}(\mathbf{U}) = \partial\hat{\mathbf{F}}(\mathbf{U})/\partial\mathbf{U}.$$

Important property of characteristic speeds $\Lambda_j(\mathbf{U})$ is that they provide bounds for the characteristic speeds of (1) on equilibrium manifold through the subcharacteristic condition (Boillat & Ruggeri, 1997; Chen et al., 1994)

$$\min_{1\le j\le N} \Lambda_j(\mathbf{u},\mathbf{h}(\mathbf{u})) \le \lambda_i(\mathbf{u}) \le \max_{1\le j\le N} \Lambda_j(\mathbf{u},\mathbf{h}(\mathbf{u})). \tag{9}$$

However, the spectrum $\lambda_i(\mathbf{u})$ of the system (1) does not have to be contained in the spectrum $\Lambda_j(\mathbf{u},\mathbf{h}(\mathbf{u}))$ of the hyperbolic dissipative system (6), i.e. λ's may not coincide with Λ's on the equilibrium manifold. Moreover, Rankine-Hugoniot conditions for (6) have different form than for (1), and consequently may predict jump discontinuities which appear off the equilibrium manifold. These discrepancies between hyperbolic systems and their dissipative counterparts call for the answer to the question how can one relate the jump discontinuities of (1) to the shock structure solutions expected to be derived from (6). First results may be found in (Liu, 1987) for systems of two balance laws. General existence result for shock profiles has been given in (Yong & Zumbrun, 2000), under certain reasonable structural conditions.
It is important to note that dissipative character of parabolic (5) and hyperbolic (6) system comes from the compatibility with entropy inequality. In former case it imposes restrictions on viscosity matrix $\mathbf{B}(\mathbf{u})$, while in the latter one determines the structure of source terms $\mathbf{q}(\mathbf{u},\mathbf{v})$. In parabolic case Coleman-Noll procedure is usually applied (de Groot & Mazur, 1984). For hyperbolic case a systematic procedure is developed within the framework of extended thermodynamics (Müller & Ruggeri, 1998), based upon exploitation of Liu's method of multipliers (Liu, 1972) and generalized form of entropy flux.

2.2 Shock structure problem and stability analysis

The shock structure problem has long and rich history. First attempt to apply dynamical systems theory in the study of shock structure was (Gilbarg & Paolucci, 1953). This approach provided an excellent framework which persisted and still remains one of the basic tools in complex problems, e.g. shock waves in higher-order approximations (Holian et al., 2011; Uribe et al., 2000), predictions using modified Mott-Smith method (Solovchuk & Sheu, 2011) and generalizations of Navier-Stokes equations (Uribe, 2011).

However, stability and bifurcation analysis related to the shock structure problem had been mostly applied in the study of Boltzmann equation. Nicolaenko and Thurber (Nicolaenko & Thurber, 1975) showed that Boltzmann operator for hard sphere potential has nontrivial eigenvalue which changes the sign in transition from subsonic to supersonic regimes. Caflisch and Nicolaenko (Caflisch & Nicolaenko, 1982) generalized these results for hard cut-off potentials and proved the existence of shock profile solutions. Existence results for discrete velocity models of the Boltzmann equation, which also have a flavor of bifurcation theory, have been proven in (Bose et al., 1998) and (Bernhoff & Bobylev, 2007). Recently, center manifold reduction has been applied to prove the existence of weak shocks for the classical parabolic model of gas dynamics and bifurcation equation of transcritical type appeared there as a side result (Lorin, 2003).

This problem was also extensively studied within the framework of extended thermodynamics (Weiss, 1995), whose models are strongly related to ones obtained by the method of moments in kinetic theory of gases (Grad, 1949). One of the most important shortcomings of these models, recognized at the early stage (Grad, 1952), is that continuous shock structure seize to exist when shock speed exceeds certain critical value. It was proven (Boillat & Ruggeri, 1998) that this is an intrinsic property of hyperbolic systems of balance laws endowed with convex entropy, and the critical value of shock speed coincides with the highest characteristic speed. Since our study will be focused on shock speeds in the neighborhood of the highest characteristic speed of equilibrium subsystem, rather than complete hyperbolic system, we shall not be confronted with this problem.

3. Isothermal viscoelasticity

In this section we shall analyze the shock structure problem in a simple mathematical model of isothermal viscoelasticity. It will give us an idea of the method to be used in more involved situations and provide a flavor of basic results concerned with stability and bifurcation of equilibria in this problem. Underlying equilibrium system will be the so-called $p-$system

$$\begin{aligned} \partial_t u^1 - \partial_x u^2 &= 0, \\ \partial_t u^2 - \partial_x p(u^1) &= 0. \end{aligned} \tag{10}$$

Although primarily arose in the context of isothermal elastodynamics, it is paradigmatic model for nonlinear wave propagation. The system is hyperbolic provided $p'(u^1) > 0$ with characteristic speeds

$$\lambda_1(\mathbf{u}) = -\sqrt{p'(u^1)}, \quad \lambda_2(\mathbf{u}) = \sqrt{p'(u^1)}, \tag{11}$$

for the vector of equilibrium variables $\mathbf{u} = (u^1, u^2)^T$. We shall assume that eigenvalues (11) are genuinely nonlinear (see Dafermos (2000)), which implies $p''(u^1) \neq 0$ for all u^1. Our analysis will be focused on weak shocks which appear as bifurcating solution in the neighborhood of

the highest characteristic speed, i.e. when $s \to s^* = \lambda_2(\mathbf{u}_0)$ and satisfy Lax condition

$$\lambda_2(\mathbf{u}_0) < s < \lambda_2(\mathbf{u}_1).$$

They are determined as solutions of Rankine-Hugoniot equations

$$\begin{aligned} s\left(u_0^1 - u_1^1\right) + \left(u_0^2 - u_1^2\right) = 0; \\ s\left(u_0^2 - u_1^2\right) + \left(p(u_0^1) - p(u_1^1)\right) = 0. \end{aligned} \tag{12}$$

A simple way to capture nonequilibrium and dissipative effects is to extend the set of field variables by introducing nonequilibrium ones. Their evolution is governed by additional balance laws of relaxation type. In the case of $p-$system such a model has been proposed in (Suliciu, 1990)

$$\begin{aligned} &\partial_t u^1 - \partial_x u^2 = 0, \\ &\partial_t u^2 - \partial_x v = 0, \\ &\partial_t v - \nu \partial_x u^2 = -\frac{1}{\varepsilon}\left(v - p(u^1)\right), \end{aligned} \tag{13}$$

where $\nu > 0$ and ε is small positive parameter which plays the role of relaxation time. Its aim was to describe isothermal viscoelastic response of a continuum. Heuristically, the difference $v - p(u^1)$ acts as a driving agent which pushes the system towards local equilibrium state $v = p(u^1)$. On the other hand, the smaller ε is, the more rapid will be the response of the material. As a matter of fact, when $\varepsilon \to 0$ an *equilibrium manifold* $v_{\mathrm{E}} = p(u^1)$ is determined from $(13)_3$, and $(13)_{1,2}$ is reduced to the equilibrium subsystem (10). Characteristic speeds of the differential part of (13) are

$$\Lambda_1(\mathbf{U}) = -\sqrt{\nu}, \quad \Lambda_2(\mathbf{U}) = 0, \quad \Lambda_3(\mathbf{U}) = \sqrt{\nu}, \tag{14}$$

for $\mathbf{U} = (u^1, u^2, v)^T$. Since $\mathbf{U}_{\mathrm{E}} = (u^1, u^2, p(u^1))^T$, the subcharacteristic condition reads

$$\Lambda_1(\mathbf{U}_{\mathrm{E}}) \le \lambda_1(\mathbf{u}) < \lambda_2(\mathbf{u}) \le \Lambda_3(\mathbf{U}_{\mathrm{E}})$$

which is satisfied for $p'(u^1) \le \nu$. In the sequel we shall assume that strict inequality holds. Otherwise, a continuous shock structure determined by (13) will seize to exist.
Our aim is to seek for continuous travelling wave solution of the system (13) which connects two equilibrium states – one in front of the wave $\mathbf{U}_{\mathrm{E}0} = (u_0^1, u_0^2, p(u_0^1))$ reached when $x \to +\infty$, with another behind it $\mathbf{U}_{\mathrm{E}1} = (u_1^1, u_1^2, p(u_1^1))$ reached for $x \to -\infty$. We shall therefore assume the solution in the form $\mathbf{U} = \hat{\mathbf{U}}(\xi)$ for $\xi = (x - st)/\varepsilon$ which transforms (13) into a system of ODE's

$$\begin{aligned} s(u^1 - u_1^1) + (u^2 - u_1^2) = 0, \\ s(u^2 - u_1^2) + (v - p(u_1^1)) = 0, \\ s\dot{v} + \nu\dot{u}^2 = v - p(u^1), \end{aligned} \tag{15}$$

where $(\,)^{\cdot} = d(\,)/d\xi$. First two equations are integrated and downstream equilibrium state $v(-\infty) = v_{\mathrm{E}}(-\infty) = p(u_1^1)$ for v is used in the course of integration. Note that stationary points of (15), for which $\dot{\mathbf{U}} = \mathbf{0}$, lie on equilibrium manifold. For equilibrium behind the

wave ($v = p(u_1^1)$) the system is trivially satisfied, whereas for the one in front of the wave ($v = p(u_0^1)$) Rankine-Hugoniot equations (12) are recovered from $(15)_{1,2}$.
By eliminating u^2 and v from $(15)_{1,2}$ the system is reduced to a single ODE which reads

$$\dot{u}^1 = \theta(u^1, s) = \frac{s^2\left(u^1 - u_1^1\right) - p(u^1) + p(u_1^1)}{s\left(s^2 - \nu\right)}. \tag{16}$$

Two remarks are in order for (16):

1. $\theta(u_{0,1}^1, s) = 0$, i.e. stationary points lie on equilibrium manifolds related by the shock wave with speed s through Rankine-Hugoniot equations (12);
2. $\theta(u^1, s)$ has singularity for $s = \Lambda_i(\mathbf{U})$, $i = 1, 2, 3$, i.e. when shock speed coincides with characteristic speeds of the hyperbolic system (13).

It has to be noted that critical value of shock speed $s^* = \lambda_2(\mathbf{u}_1)$, which determines the bifurcation point of the equilibrium system (10), does not have anything in common with characteristic speeds (14) of the hyperbolic system (13). This inevitably motivates stability and bifurcation analysis of the stationary points of (16).
Stability of downstream equilibrium point u_1^1 is determined by the linear variational equation

$$\dot{y} = \Theta(u_1^1, s)y, \quad \Theta(u_1^1, s) = \frac{\partial\theta}{\partial u^1}(u_1^1, s) = \frac{s^2 - p'(u_1^1)}{s\left(s^2 - \nu\right)},$$

where $y = u^1 - u_1^1$ is a perturbation. Eigenvalue is equal to the coefficient $\Theta(u_1^1, s)$ and its sign depends upon the value of shock speed. The critical values of shock speed s occur for

$$\Theta(u_1^1, s_{\mathrm{h}}^*) = 0 \qquad \Rightarrow \qquad s_{\mathrm{h}}^* = \pm\sqrt{p'(u_1^1)},$$

and obviously coincide with characteristic speeds (11) of equilibrium system (10). Taking $s_{\mathrm{h}}^* = s^* = \lambda_2(u_1^1)$ it is easy to check that stability of stationary point is changed in the neighborhood of this critical value since

$$\frac{\partial\Theta}{\partial s}(u_1^1, s_{\mathrm{h}}^*) = -\frac{2}{\nu - p'(u_1^1)} \neq 0. \tag{17}$$

Since $\nu > p'(u_1^1)$, it can be concluded that stability of stationary point u_1^1 is changed in the neighborhood of the critical value of shock speed as follows:

(a) u_1^1 is unstable for $s < s_{\mathrm{h}}^* = \lambda_2(u_1^1)$;

(b) u_1^1 is stable for $s > s_{\mathrm{h}}^* = \lambda_2(u_1^1)$.

In other words, downstream equilibrium state of dissipative hyperbolic system (13) is unstable when shock speed satisfies Lax condition for equilibrium system (10), whereas it is stable when shock speed violates it.
By Taylor expansion of the right hand side of (16) up to second order terms in both variables in the neighborhood of $(u_1^1, s_{\mathrm{h}}^*)$, a bifurcation equation is revealed

$$\dot{y} \approx \frac{1}{2(\nu - p'(u_1^1))}\left(-2\mu y + \frac{p''(u_1^1)}{\sqrt{p'(u_1^1)}}y^2\right), \tag{18}$$

for a bifurcation parameter $\mu = s - s_{\mathrm{h}}^{*}$. This equation describes *transcritical bifurcation* pattern in the neighborhood of the critical value of the parameter $\mu^{*} = 0$.
Although Suliciu's hyperbolic model (13) is physically well founded, it is common in engineering practice to use parabolic models. They are reliable when the state of the system is not far from equilibrium one and nonequilibrium variables are related to equilibrium ones through nonlocal constitutive relations. In this account we shall not pursue in this direction. Interested reader could find in (Simić, 2008) that parabolic model which corresponds to (13) gives rise to the same conclusions about stability and bifurcation as hyperbolic one.
The most important conclusion, which could be drawn from the shock structure analysis in the hyperbolic model of isothermal viscoelasticity (13), is that appearance of the travelling shock profile is indicated by the change of stability of stationary points, i.e. equilibrium states. However, the critical value of the shock speed coincides with its bifurcation value for equilibrium subsystem (10) obtained from Rankine-Hugoniot equations (12). At first, this result is not surprising since stationary points determine the states which lie on equilibrium manifolds $v_{\mathrm{E}} = p(u^{1})$, determined by the source term in $(13)_3$. Nevertheless, the critical shock speed cannot be predicted from the structure of (13) since its characteristic speeds do not coincide with the ones of equilibrium subsystem. This fact emphasizes the role of equilibrium subsystem in the study of shock structure.
A complaint could be made about conclusions since they are based upon reduced system (16) instead of the full system (15) (actually, the system in which $(15)_{1,2}$ are differentiated). Namely, complete downstream equilibrium state $\mathbf{U}_1 = (u_1^1, u_1^2, p(u_1^1))^T$ is non-hyperbolic stationary point of this system for a travelling profile $\mathbf{U}(\xi)$: linearized variational equations have two zero eigenvalues. However, the remaining one has the same behaviour as predicted by linearization of (16) and the conclusion can be retained, albeit in a weaker sense in view of stability.

4. Dissipative hyperbolic model of gas dynamics

Governing equations of gas dynamics are conservation laws of mass, momentum and energy, which in one dimensional setting read

$$\begin{aligned} &\partial_t \rho + \partial_x(\rho v) = 0, \\ &\partial_t(\rho v) + \partial_x(\rho v^2 - \sigma + p) = 0, \\ &\partial_t\left(\frac{1}{2}\rho v^2 + \rho e\right) + \partial_x\left(\left(\frac{1}{2}\rho v^2 + \rho e\right)v - \sigma v + pv + q\right) = 0. \end{aligned} \tag{19}$$

The simplest case is the one in which stress σ and heat flux q are neglected ($\sigma = 0, q = 0$) and one obtains Euler equations of gas dynamics. The vector of state variables $\mathbf{u} = (\rho, v, T)^T$ is consisted of density, velocity and temperature of the gas. Pressure p and internal energy density e are determined by the constitutive equations (thermal and caloric equation of state)

$$p = p(\rho, T) = \rho\frac{k_{\mathrm{B}}}{m}T, \qquad e = e(\rho, T) = \frac{k_{\mathrm{B}}}{m}\frac{T}{\gamma - 1}, \tag{20}$$

where k_{B} is Boltzmann constant, m atomic mass of gas and γ the ratio of specific heats.
In classical approach dissipative effects are modelled through nonlocal constitutive equations for stress and heat flux

$$\sigma = \frac{4}{3}\mu\partial_x v, \qquad q = -\kappa\partial_x T. \tag{21}$$

μ and κ being viscosity and heat conductivity. Actually, (21) describe transport (or nonconvective flux) of momentum and internal energy. By inserting (21) into (19) we obtain so-called Navier-Stokes-Fourier (NSF) model of gas dynamics

$$\begin{aligned}
&\partial_t \rho + \partial_x(\rho v) = 0,\\
&\partial_t(\rho v) + \partial_x(\rho v^2 + p) = \partial_x\left(\frac{4}{3}\mu\partial_x v\right),\\
&\partial_t\left(\frac{1}{2}\rho v^2 + \rho e\right) + \partial_x\left(\left(\frac{1}{2}\rho v^2 + \rho e\right)v + pv\right)\\
&\qquad = \partial_x\left(\kappa\partial_x T + \frac{4}{3}\mu v\partial_x v\right).
\end{aligned} \tag{22}$$

Although it is commonly accepted in engineering applications, it has an intrinsic physical shortcoming: it is parabolic and predicts paradoxical infinite speed of propagation of heat pulses and shear waves.

Another way to describe dissipation is to extend the system of state variables with nonequilibrium ones, i.e. with stress and heat flux $\mathbf{U} = (\rho, v, T, \sigma, q)^T$, and to write appropriate rate-type equations (balance laws) for them. That was systematically analyzed in extended thermodynamics (Müller & Ruggeri, 1998) where the following set of equations is obtained

$$\begin{aligned}
&\partial_t \rho + \partial_x(\rho v) = 0,\\
&\partial_t(\rho v) + \partial_x(\rho v^2 - \sigma + p) = 0,\\
&\partial_t\left(\frac{1}{2}\rho v^2 + \rho e\right) + \partial_x\left(\left(\frac{1}{2}\rho v^2 + \rho e\right)v - \sigma v + pv + q\right) = 0,\\
&\partial_t\left(\rho v^2 + p - \sigma\right) + \partial_x\left(\rho v^3 + 3pv - 3\sigma v + \frac{6}{5}q\right) = \frac{1}{\tau_\sigma}\sigma,\\
&\partial_t\left(\frac{1}{2}\rho v^3 + \frac{5}{2}pv - \sigma v + q\right)\\
&\qquad + \partial_x\left(\frac{1}{2}\rho v^4 + 4pv^2 - \frac{5}{2}\sigma v^2 + \frac{16}{5}qv - \frac{7}{2}\frac{p}{\rho}\sigma + \frac{5}{2}\frac{p^2}{\rho}\right)\\
&\qquad = -\frac{1}{\tau_q}\left(q - \frac{3}{2}\sigma v\right).
\end{aligned} \tag{23}$$

This set of equations is known as *13 moments model*. Closure problem for this model is solved through compatibility with entropy inequality. It has to be noted that the same model was derived in kinetic theory of gases where the balance laws for stress tensor and heat flux came out as macroscopic equations for higher order moments of velocity distribution function (Grad, 1949). That is where the name of the model actually came from.

Small parameters τ_σ and τ_q play the role of relaxation times and, for monatomic gases, obey the relation $\tau_q = 3\tau_\sigma/2$. Although NSF and 13 moments model are principally different, they are related to each other through Chapman-Enskog expansion. Moreover, constitutive equations (21) can be recovered from balance laws of (23) by means of Maxwellian iteration procedure (see Müller & Ruggeri (1998)). Either of these methods lead to the following relations

$$\tau_\sigma = \frac{\mu}{p}, \qquad \tau_q = \frac{2}{5}\frac{\kappa}{p^2}\rho T, \qquad \kappa = \frac{15}{4}\frac{k_B}{m}\mu, \tag{24}$$

valid for monatomic gases. Note that $\mu, \kappa \to 0$, or equivalently $\tau_\sigma, \tau_q \to 0$, pushes the system towards equilibrium manifold $\sigma_{\mathrm{E}} = 0$, $q_{\mathrm{E}} = 0$, i.e. $\mathbf{U}_{\mathrm{E}} = (\rho, v, T, 0, 0)^T$, and leads to the equilibrium subsystem in the form of Euler equations (19) (with $\sigma = 0$, $q = 0$).
It is well-known that characteristic speeds of the equilibrium subsystem (19) correspond to the speed of sound

$$\lambda_1 = v - c_{\mathrm{s}}, \qquad \lambda_2 = v, \qquad \lambda_3 = v + c_{\mathrm{s}}, \tag{25}$$
$$c_{\mathrm{s}} = \left(\gamma \frac{k_B}{m} T\right)^{1/2},$$

whereas characteristic speeds of 13 moments model (23) evaluated on equilibrium manifold for monatomic gases ($\gamma = 5/3$) read

$$\begin{aligned} &\Lambda_1 = v - 1.6503 c_{\mathrm{s}} \qquad \Lambda_2 = v - 0.6297 c_{\mathrm{s}} \\ &\Lambda_3 = v, \\ &\Lambda_4 = v + 0.6297 c_{\mathrm{s}}, \qquad \Lambda_5 = v + 1.6503 c_{\mathrm{s}}. \end{aligned} \tag{26}$$

It is obvious that characteristic speeds of equilibrium subsystem are bounded by the characteristic speeds of 13 moments model

$$\Lambda_1(\mathbf{U}_{\mathrm{E}}) < \lambda_1(\mathbf{u}) < \lambda_3(\mathbf{u}) < \Lambda_5(\mathbf{U}_{\mathrm{E}}),$$

but are not contained in the corresponding spectrum. The aim of this part of the study is to show that travelling shock profile in 13 moments model appears when the shock speed exceeds the highest characteristic speed of the equilibrium subsystem and that it is indicated by the change of stability properties of equilibrium states. All details of the analysis are given in (Simić, 2009); only the main ideas and results will be given here.

4.1 Shock waves in Euler equations

The central point in this stability analysis is subtle relation between complete hyperbolic dissipative system of balance laws and its equilibrium counterpart. Therefore, in the first step it is needed to determine possible equilibrium states related by Rankine-Hugoniot equations for the equilibrium subsystem. Using standard notation and introducing relative velocity of the fluid with respect to shock wave $u = v - s$, the following Rankine-Hugoniot equations are obtained for (19)

$$\begin{aligned} &[[\rho u]] = 0, \\ &\left[\left[\rho u^2 + p\right]\right] = 0, \\ &\left[\left[\left(\frac{1}{2}\rho u^2 + \rho\varepsilon\right) u + pu\right]\right] = 0, \end{aligned}$$

whose nontrivial solution is

$$\begin{aligned} \frac{\rho_1}{\rho_0} &= \frac{M_0^2}{1 - \tilde{\mu}^2(1 - M_0^2)}, \\ \frac{u_1}{u_0} &= \frac{1}{M_0^2}\left[1 - \tilde{\mu}^2(1 - M_0^2)\right], \\ \frac{T_1}{T_0} &= \frac{1}{M_0^2}\left[(1 - \tilde{\mu}^2(1 - M_0^2))((1 + \tilde{\mu}^2)M_0^2 - \tilde{\mu}^2)\right], \end{aligned} \tag{27}$$

where $M_0 = u_0/c_0$ is Mach number in the upstream equilibrium, c_0 is corresponding sound speed and $\tilde{\mu}^2 = (\gamma-1)/(\gamma+1)$. Note that downstream equilibrium state $\mathbf{u}_1$ tends to upstream one $\mathbf{u}_0$ when $M_0 \to 1$, i.e. when the shock speed tends to the highest characteristic speed. In such a way downstream equilibrium can be regarded as bifurcation solution $\mathbf{u}_1(\mathbf{u}_0, M_0)$, and it is transverse to trivial one in the neighborhood of the critical point $M_0 = 1$. For future reference it is important to note that according to Lax condition only the supersonic nontrivial branch ($M_0 > 1$) of the solution (27) is physically admissible, whereas the trivial branch ($\mathbf{u}_1 = \mathbf{u}_0$) is physically admissible in subsonic case ($M_0 < 1$).

4.2 Shock structure in 13 moments model: stability and bifurcation of equilibria

Analysis of the shock structure in 13 moments model (23) will be performed in dimensionless form. Also, it will be assumed that viscosity of the gas is temperature dependent, $\mu = \mu_0(T/T_0)^\alpha$, where exponent α depends on the type of gas and μ_0 is viscosity in reference state. The problem will be considered in a moving reference frame with a single independent variable $\xi = x - st$, and the following dimensionless variables will be used

$$\tilde{\xi} = \frac{\xi}{l_0}, \qquad \tilde{\rho} = \frac{\rho}{\rho_0}, \qquad \tilde{u} = \frac{v-s}{c_0}, \qquad \tilde{T} = \frac{T}{T_0}, \qquad \tilde{\sigma} = \frac{\sigma}{\rho_0 \frac{k_B}{m} T_0}, \qquad \tilde{q} = \frac{q}{\rho_0 \frac{k_B}{m} T_0 c_0},$$

$$M_0 = \frac{v_0 - s}{c_0}, \qquad c_0 = \left(\frac{5}{3}\frac{k_B}{m}T_0\right)^{1/2}, \qquad l_0 = \frac{\mu_0}{\rho_0 \frac{k_B}{m} T_0} c_0.$$

The system of shock structure equations in dimensionless form derived from (23) reads (tildes are dropped for convenience)

$$\begin{aligned}
&\frac{d}{d\xi}(\rho u) = 0 \\
&\frac{d}{d\xi}\left(\frac{5}{3}\rho u^2 + \rho T - \sigma\right) = 0, \\
&\frac{d}{d\xi}\left(\frac{5}{6}\rho u^3 + \frac{5}{2}\rho T u - \sigma u + q\right) = 0, \\
&\frac{d}{d\xi}\left(\frac{5}{3}\rho u^3 + 3\rho T u - 3\sigma u + \frac{6}{5}q\right) = \rho T^{1-\alpha}\sigma, \\
&\frac{d}{d\xi}\left(\frac{5}{6}\rho u^4 + 4\rho T u^2 - \frac{5}{2}\sigma u^2 + \frac{16}{5}q u - \frac{21}{10}T\sigma + \frac{3}{2}\rho T^2\right) \\
&\qquad = -\frac{2}{3}\rho T^{1-\alpha}\left(q - \frac{3}{2}\sigma u\right).
\end{aligned} \tag{28}$$

Equations $(28)_{1-3}$ can be integrated taking into account equilibrium values for $\xi \to -\infty$

$$\rho_0 = 1, \qquad u_0 = M_0, \qquad T_0 = 1, \qquad \sigma_0 = 0, \qquad q_0 = 0,$$

and used to express ρ, σ and q in terms of u, T and M_0 as a parameter

$$\begin{aligned}
\rho &= \frac{M_0}{u}, \\
\sigma &= \frac{5}{3}M_0(u - M_0) + M_0\frac{T}{u} - 1, \\
q &= \frac{5}{6}M_0\left(M_0^2 - u^2\right) + \frac{5}{2}M_0(1 - T) + \frac{5}{3}M_0 u(u - M_0) + M_0 T - u.
\end{aligned}$$

Inserting these relations into $(28)_{4,5}$ one obtains the system of two first-order ODE's

$$\frac{du}{d\xi} = F(u, T, M_0), \qquad \frac{dT}{d\xi} = G(u, T, M_0), \tag{29}$$

whose structure will be omitted for the sake of brevity, but could be found in (Simić, 2009). Although the analytical form of (29) is quite cumbersome, it can be shown that (dimensionless) upstream equilibrium $(u_0, T_0) = (M_0, 1)$ and downstream equilibrium

$$u_1 = \frac{3 + M_0^2}{4M_0}, \qquad T_1 = \frac{1}{16}\left(14 - \frac{3}{M_0^2} + 5M_0^2\right), \tag{30}$$

determined from (27) for $\gamma = 5/3$, are the stationary points, i.e.

$$F(u_0, T_0, M_0) = F(u_1, T_1, M_0) = 0,$$
$$G(u_0, T_0, M_0) = G(u_1, T_1, M_0) = 0.$$

The main idea of stability analysis is to show that stationary points (u_0, T_0) and (u_1, T_1) change their stability properties in the neighborhood of the critical value of upstream Mach number, $M_0 = 1$. In the sense of dynamical system theory they are hyperbolic for $M_0 \neq 1$ but loose hyperbolicity for $M_0 = 1$. This can be proved by analyzing eigenvalues of the linearized system derived from (29) at stationary points. In particular, stationary points are distinct and corresponding linearized systems have nonzero eigenvalues for $M_0 \neq 1$, whereas they coincide for $M_0 = 1$ and one of the eigenvalues is equal zero.
Let $\Delta\mathbf{u} = (\Delta u, \Delta T)^T = (u - u_0, T - T_0)^T = \mathbf{u} - \mathbf{u}_0$ denote the perturbation of upstream equilibrium. Linearized variational equations in the neighborhood of $\mathbf{u}_0$, which read $d(\Delta\mathbf{u})/d\xi = \mathbf{A}_0(M_0)\Delta\mathbf{u}$, have the Jacobian matrix

$$\mathbf{A}_0(M_0) = \frac{1}{27 - 78M_0^2 + 25M_0^4}\begin{pmatrix} \frac{-9+42M_0^2-25M_0^4}{M_0} & 3(3+M_0^2) \\ \frac{54-162M_0^2+200M_0^4}{9M_0^2} & \frac{-18+114M_0^2-50M_0^4}{3M_0} \end{pmatrix},$$

and corresponding eigenvalues are

$$\lambda_{01}(M_0) = \frac{5D_{0-}}{6M_0(27 - 78M_0^2 + 25M_0^4)}, \qquad \lambda_{02}(M_0) = \frac{5D_{0+}}{6M_0(27 - 78M_0^2 + 25M_0^4)},$$
$$D_{0\mp} = -9 + 48M_0^2 - 25M_0^4 \mp \sqrt{81 - 216M_0^2 + 234M_0^4 + 72M_0^6 + 25M_0^8}.$$

Simple calculation shows

$$\lambda_{01}(1) = 0, \qquad \frac{d\lambda_{01}(1)}{dM_0} = \frac{10}{7}; \qquad \lambda_{02}(1) = -\frac{35}{39}. \tag{31}$$

By continuity argument it follows that there is a neighborhood of $M_0 = 1$ in which $\lambda_{01}(M_0) < 0$ for $M_0 < 1$ and $\lambda_{01}(M_0) > 0$ for $M_0 > 1$, while $\lambda_{02}(M_0) < 0$ in either case. Equivalent arguments, but more cumbersome analytical expressions which will be omitted here, lead to the same results in downstream equilibrium $\mathbf{u}_1$. Namely,

$$\lambda_{11}(1) = 0, \qquad \frac{d\lambda_{11}(1)}{dM_0} = -\frac{10}{7}; \qquad \lambda_{12}(1) = -\frac{35}{39}, \tag{32}$$

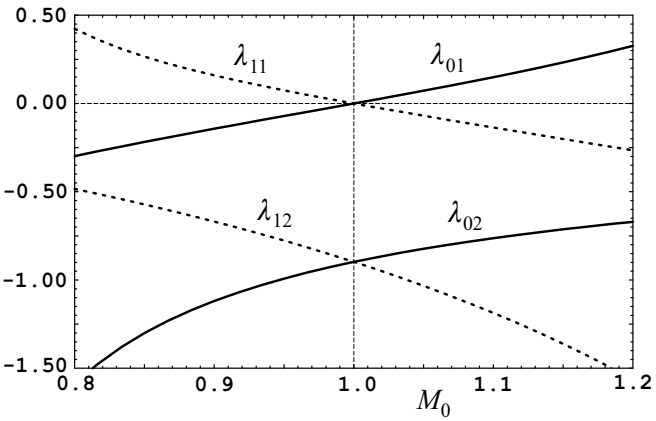

Fig. 1. Eigenvalues in upstream $\mathbf{u}_0$ and downstream $\mathbf{u}_1$ stationary points in gas dynamics shock structure.

which by continuity argument lead to a conclusion that there is a neighborhood of $M_0 = 1$ in which $\lambda_{11}(M_0) > 0$ for $M_0 < 1$ and $\lambda_{11}(M_0) < 0$ for $M_0 > 1$, while $\lambda_{12}(M_0) < 0$ in either case. In the language of dynamical system theory, $\mathbf{u}_0$ is a stable node and $\mathbf{u}_1$ is a saddle when $M_0 < 1$, while $\mathbf{u}_0$ is a saddle and $\mathbf{u}_1$ is a stable node when $M_0 > 1$. Obviously, this characterization is valid only for the reduced system of shock structure equations (29): in the complete system (28) neither of stationary points which lie on equilibrium manifold is hyperbolic, but there is always one eigenvalue which changes the sign in the neighborhood of $M_0 = 1$ and indicates the critical value of the shock speed. This property has already been observed in the hyperbolic model of isothermal viscoelasticity.

Like in the previous section, bifurcation analysis should reveal the type of bifurcation which occur in the neighborhood of the critical value of shock speed. Unlike the shock structure problem (16) which was one-dimensional, shock structure equations (29) in 13 moments model form a two-dimensional system. In such a case recognition of bifurcation pattern have to be preceded by the reduction process. In this problem the centre manifold reduction could be efficiently applied (see Guckenheimer & Holmes (1986) for a detailed account on this method). Complete procedure is given in (Simić, 2009); only essential steps will be shown in this review. First, the system (29) is extended by trivial equation $dM_0/d\xi = 0$ and analyzed in the neighborhood of the stationary point $\mathbf{u}_0$. Let $\Delta M_0 = M_0 - 1$. By means of linear transformation

$$(\Delta u, \Delta T, \Delta M_0) = (-3y/2 + 18z/23, y + z, \epsilon)$$

the extended system is transformed into normal form

$$\frac{d}{d\xi}\begin{pmatrix} y \\ z \\ \epsilon \end{pmatrix} = \begin{pmatrix} f(y,z,\epsilon) \\ g(y,z,\epsilon) \\ 0 \end{pmatrix} = \mathbf{B}_0(\epsilon)\begin{pmatrix} y \\ z \\ \epsilon \end{pmatrix} + \begin{pmatrix} Y(y,z,\epsilon) \\ Z(y,z,\epsilon) \\ 0 \end{pmatrix}, \tag{33}$$

where

$$\mathbf{B}_0(0) = \begin{pmatrix} 0 & 0 & 0 \\ 0 & -35/39 & 0 \\ 0 & 0 & 0 \end{pmatrix}, \tag{34}$$

and $Y(y,z,\epsilon)$ and $Z(y,z,\epsilon)$ are at least of the second order in y and z. Centre manifold is locally invariant manifold in the neighborhood of the critical point; it is tangent to the eigenspace

spanned by the eigenvectors corresponding to eigenvalues with zero real part. Due to the structure of (34) it has the form $z = h(y, \epsilon)$ and should satisfy conditions

$$h(0,0) = 0, \qquad \frac{\partial h(0,0)}{\partial y} = 0, \qquad \frac{\partial h(0,0)}{\partial \epsilon} = 0.$$

Determining equation for the centre manifold comes from equation for z variable in (33) and reads

$$\frac{\partial h(y,\epsilon)}{\partial y} f(y, h(y,\epsilon), \epsilon) - g(y, h(y,\epsilon), \epsilon) = 0.$$

Since it cannot be resolved analytically, the approximate solution can be found using power series expansion

$$h(y,\epsilon) \approx \frac{184}{245}\epsilon y - \frac{115}{196} y^2.$$

Insertion of this result into (33) yields the bifurcation equation

$$\frac{dy}{d\xi} \approx \frac{10}{7}\epsilon y - \frac{20}{7} y^2 \tag{35}$$

which represents the canonical form of transcritical bifurcation pattern. It is well known that (trivial) stationary point $y_0 = 0$ looses its stability for $\epsilon > 0$, while nontrivial one $y_1 \approx \epsilon/2$ becomes stable. This exchange of stability of stationary points described by the lumped variable y reflects the change of stability properties of the equilibrium states $\mathbf{u}_0$ and $\mathbf{u}_1$.

Stability and bifurcation analysis of equilibrium states in 13 moments model, related to the shock structure problem, has dominantly mathematical character. The main question is: can we draw a conclusion of thermodynamical flavor from these results? The idea will come from comparison of stability results (31)-(32) with the Lax condition. By the Lax condition, shock waves in Euler model, i.e. nontrivial bifurcating solution of Rankine-Hugoniot equations, are admissible when shock speed s satisfies the inequality

$$\lambda_3(\mathbf{u}_0) < s < \lambda_3(\mathbf{u}_1).$$

Left inequality corresponds to $M_0 > 1$. When $s < \lambda_3(\mathbf{u}_0)$, or equivalently $M_0 < 1$, shocks are not admissible. These conditions are in clear correspondence with stability results for 13 moments model. Eigenvalue $\lambda_{01}(M_0) < 0$ and determines the stable direction (eigenvector) in state space when $M_0 < 1$. On the other hand, $\lambda_{01}(M_0) > 0$ and determines the unstable direction in state space for $M_0 > 1$. Recall that another eigenvalue is not of any importance since it does not change the sign. The opposite statements are valid for the eigenvalue $\lambda_{11}(M_0)$. Therefore, we can conclude that admissible shock structure appears when

$$0 < \lambda_{01}(M_0) \qquad (\lambda_{11}(M_0) < 0), \tag{36}$$

while $\lambda_{01}(M_0) = 0$, or $\lambda_{11}(M_0) = 0$, determine the critical value of the parameter (shock speed). These conditions seem to be the natural consequence of the fact that Euler system (19) is contained in 13 moments model (23) and the properties of equilibrium system are "absorbed" by the dissipative one. As typical for selection rules, they are expressed in the form of inequality and reflect irreversible character of the process.

Although it looks like a simple and natural transfer of analysis from equilibrium to a dissipative system, the main point is that equilibrium states (stationary points), the critical value of the shock speed and stability condition (36) could be determined from the shock

structure equations *without prior knowledge* of solutions of Rankine-Hugoniot equations and exploitation of Lax condition. This self-contained analysis of the shock structure in hyperbolic dissipative systems will be the cornerstone in studying the same problem in binary mixture. It was shown in (Simić, 2009) that completely the same conclusions can be drawn even for the hyperbolic models with higher order moments (14 and 21), as well as for parabolic NSF model. This suggests that stability properties and bifurcation pattern are not the same by mere coincidence, but reflect intrinsic properties of dissipative systems.

5. Multi-temperature mixture of Euler fluids

The mixture model we shall deal with in this account arose within the framework of rational thermodynamics (Truesdell, 1969). Roughly speaking, it is based upon assumption that behavior of each fluid component is governed by the same balance laws as a single fluid, but mutual interactions among them are taken into account through appropriate source terms. On the other hand, governing equations for the mixture ought to be reconstructed from equations for components. However, these general principles allow for different levels of accuracy depending on the number of variables chosen to describe the state of each component.
Since the modelling issue is very important for the study of shock structure, the first part of this section will be devoted to the review of recent results about macroscopic multi-temperature model. The general model will then be specialized to the case of binary mixture for which the shock structure will be analyzed in the same spirit as it was done in the previous section.

5.1 The model and its properties

According to assumptions given above, the model of the mixture is consisted of balance laws of mass, momentum and energy for each component $\alpha = 1, \ldots, n$

$$\begin{aligned}
&\frac{\partial \rho_\alpha}{\partial t} + \operatorname{div}(\rho_\alpha \mathbf{v}_\alpha) = \tau_\alpha, \\
&\frac{\partial}{\partial t}(\rho_\alpha \mathbf{v}_\alpha) + \operatorname{div}(\rho_\alpha \mathbf{v}_\alpha \otimes \mathbf{v}_\alpha - \mathbf{t}_\alpha) = \mathbf{m}_\alpha, \\
&\frac{\partial}{\partial t}\left(\frac{1}{2}\rho_\alpha v_\alpha^2 + \rho_\alpha \varepsilon_\alpha\right) + \operatorname{div}\left\{\left(\frac{1}{2}\rho_\alpha v_\alpha^2 + \rho_\alpha \varepsilon_\alpha\right)\mathbf{v}_\alpha - \mathbf{t}_\alpha \mathbf{v}_\alpha + \mathbf{q}_\alpha\right\} = e_\alpha.
\end{aligned} \tag{37}$$

By ρ_α, $\mathbf{v}_\alpha$, ε_α, $\mathbf{t}_\alpha$ and $\mathbf{q}_\alpha$ we denote respectively the mass density, the velocity, the internal energy density, the stress tensor and the heat flux of each component. Source terms τ_α, $\mathbf{m}_\alpha$ and e_α describe the actions of other components which cause the change of mass, momentum and energy density of the chosen one. In the sequel it will be assumed that all the components of the mixture are Euler fluids, i.e. they are neither viscous, nor heat-conducting, so that stress tensor and heat flux are assumed as

$$\mathbf{t}_\alpha = -p_\alpha \mathbf{I}, \qquad \mathbf{q}_\alpha = \mathbf{0}, \tag{38}$$

where p_α is the partial pressure. In such a model, the state of each component is determined by its own mass density, velocity and temperature field, $(\rho_\alpha, \mathbf{v}_\alpha, T_\alpha)^T$, thus the name *multi-temperature* mixture. This approach is not a widespread one in continuum modelling of mixtures, except in the case of plasma. However, it naturally arises in macroscopic equations derived from kinetic theory of gases, i.e. Boltzmann equations for mixtures, either due to presence of distribution functions for each specie (Bisi et al., 2005), or due to violation

of equipartition of energy for translational degrees of freedom (Hoover & Hoover, 2009; Xu & Liu, 2007). In this study the temperatures of components were introduced with the aim to show that, in the absence of viscosity and heat conductivity, large mass disparity is the main driving agent for thermal nonequilibrium.
To reconstruct the governing equations for the mixture we need some more assumptions and definitions. It will be assumed that source terms satisfy the following relations

$$\sum_{\alpha=1}^{n} \tau_\alpha = 0, \qquad \sum_{\alpha=1}^{n} \mathbf{m}_\alpha = \mathbf{0}, \qquad \sum_{\alpha=1}^{n} e_\alpha = 0. \tag{39}$$

Along with them the following definitions for field variables of the whole mixture will be introduced

$$\begin{aligned}
&\rho = \sum_{\alpha=1}^{n} \rho_\alpha, && \text{mass density,}\\
&\mathbf{v} = \frac{1}{\rho} \sum_{\alpha=1}^{n} \rho_\alpha \mathbf{v}_\alpha, && \text{velocity,}\\
&\mathbf{u}_\alpha = \mathbf{v}_\alpha - \mathbf{v}, && \text{diffusion velocities,}\\
&\varepsilon_I = \frac{1}{\rho} \sum_{\alpha=1}^{n} \rho_\alpha \varepsilon_\alpha, && \text{intrinsic internal energy density,}\\
&\varepsilon = \varepsilon_I + \frac{1}{2\rho} \sum_{\alpha=1}^{n} \rho_\alpha u_\alpha^2, && \text{internal energy density}\\
&\mathbf{t} = \sum_{\alpha=1}^{n} \left(\mathbf{t}_\alpha - \rho_\alpha \mathbf{u}_\alpha \otimes \mathbf{u}_\alpha \right), && \text{stress tensor,}\\
&\mathbf{q} = \sum_{\alpha=1}^{n} \left\{ \mathbf{q}_\alpha + \rho_\alpha \left(\varepsilon_\alpha + \frac{1}{2} u_\alpha^2 \right) \mathbf{u}_\alpha - \mathbf{t}_\alpha \mathbf{u}_\alpha \right\}, && \text{flux of internal energy (heat flux).}
\end{aligned} \tag{40}$$

Summing up equations (37) one obtains the conservation laws of mass, momentum and energy for the whole mixture

$$\begin{aligned}
&\frac{\partial \rho}{\partial t} + \operatorname{div}(\rho \mathbf{v}) = 0,\\
&\frac{\partial}{\partial t}(\rho \mathbf{v}) + \operatorname{div}(\rho \mathbf{v} \otimes \mathbf{v} - \mathbf{t}) = \mathbf{0},\\
&\frac{\partial}{\partial t} \left(\frac{1}{2} \rho v^2 + \rho \varepsilon \right) + \operatorname{div} \left\{ \left(\frac{1}{2} \rho v^2 + \rho \varepsilon \right) \mathbf{v} - \mathbf{t}\mathbf{v} + \mathbf{q} \right\} = 0.
\end{aligned} \tag{41}$$

Note that assumptions (38) lead to a simplified form of the stress tensor $\mathbf{t}$ and the heat flux $\mathbf{q}$. However, they are not simple componentwise sums of corresponding quantities, but are influenced by the diffusion process through $\mathbf{u}_\alpha$

$$\mathbf{t} = -p\mathbf{I} - \sum_{\alpha=1}^{n} \left(\rho_\alpha \mathbf{u}_\alpha \otimes \mathbf{u}_\alpha \right); \qquad p = \sum_{\alpha=1}^{n} p_\alpha, \qquad \mathbf{q} = \sum_{\alpha=1}^{n} \left\{ \rho_\alpha \left(\varepsilon_\alpha + \frac{1}{2} u_\alpha^2 \right) + p_\alpha \right\} \mathbf{u}_\alpha,$$

where p denotes the total pressure of the mixture. Our concern will be even restricted class of Euler fluids – perfect gases whose constitutive equations are

$$p_\alpha = \rho_\alpha \frac{k_\mathrm{B}}{m_\alpha} T_\alpha, \qquad \varepsilon_\alpha = \frac{k_\mathrm{B}}{m_\alpha} \frac{T_\alpha}{\gamma_\alpha - 1}. \tag{42}$$

This completes the results based upon principles of rational thermodynamics.

The structure of source terms in (37) is determined using the general principles of extended thermodynamics – Galilean invariance and the entropy principle. Galilean invariance (Ruggeri, 1989) restricts the velocity dependence of source terms to the following form (Ruggeri & Simić, 2007):

$$\tau_b = \hat{\tau}_b, \qquad \mathbf{m}_b = \hat{\tau}_b \mathbf{v} + \hat{\mathbf{m}}_b, \qquad e_b = \hat{\tau}_b \frac{v^2}{2} + \hat{\mathbf{m}}_b \cdot \mathbf{v} + \hat{e}_b, \tag{43}$$

for $b = 1, \ldots, n-1$, where $\hat{\tau}_b$, $\hat{\mathbf{m}}_b$ and $\hat{e}_b$ are independent of the mixture velocity $\mathbf{v}$. The final form of velocity independent parts of source terms is determined by means of entropy inequality (Ruggeri & Simić, 2007)

$$\begin{aligned}
\hat{\tau}_b &= -\sum_{c=1}^{n-1} \varphi_{bc} \left(\frac{\mu_c - \frac{1}{2}u_c^2}{T_c} - \frac{\mu_n - \frac{1}{2}u_n^2}{T_n} \right), \\
\hat{\mathbf{m}}_b &= -\sum_{c=1}^{n-1} \psi_{bc} \left(\frac{\mathbf{u}_c}{T_c} - \frac{\mathbf{u}_n}{T_n} \right), \\
\hat{e}_b &= -\sum_{c=1}^{n-1} \theta_{bc} \left(-\frac{1}{T_c} + \frac{1}{T_n} \right),
\end{aligned}$$

where:

$$\mu_\alpha = \varepsilon_\alpha - T_\alpha S_\alpha + \frac{p_\alpha}{\rho_\alpha}, \qquad (\alpha = 1, \ldots, n)$$

are chemical potentials of the constituents and φ_{bc}, ψ_{bc} and θ_{bc}, $(b, c = 1, \ldots, n-1)$ are phenomenological symmetric positive definite matrices. Source terms are given for $n-1$ components since the last one can be determined from restrictions (39).

One of the most important properties of the mixture model (37) is its hyperbolicity. Characteristic speeds calculated from the differential part are almost trivial – they consist of independent subsets of characteristic speeds of the components

$$\lambda_\alpha^{(1)} = v_{\alpha\mathrm{n}} - c_{\mathrm{s}\alpha}, \qquad \lambda_\alpha^{(2,3,4)} = v_{\alpha\mathrm{n}}, \qquad \lambda_\alpha^{(5)} = v_{\alpha\mathrm{n}} + c_{\mathrm{s}\alpha},$$
$$c_{\mathrm{s}\alpha} = \left(\gamma_\alpha \frac{k_\mathrm{B}}{m_\alpha} T_\alpha \right)^{1/2},$$

where $v_{\alpha\mathrm{n}} = \mathbf{v}_\alpha \cdot \mathbf{n}$ are component velocities normal to the wave front and $c_{\mathrm{s}\alpha}$ are local sound speeds of the components.

It is crucial for further study to use the possibility to substitute the balance laws for one component from (37), say n, with conservation laws for the mixture (41)

$$\begin{aligned}
&\frac{\partial \rho}{\partial t} + \operatorname{div}(\rho \mathbf{v}) = 0,\\
&\frac{\partial}{\partial t}(\rho \mathbf{v}) + \operatorname{div}(\rho \mathbf{v} \otimes \mathbf{v} - \mathbf{t}) = \mathbf{0},\\
&\frac{\partial}{\partial t}\left(\frac{1}{2}\rho v^2 + \rho\varepsilon\right) + \operatorname{div}\left\{\left(\frac{1}{2}\rho v^2 + \rho\varepsilon\right)\mathbf{v} - \mathbf{t}\mathbf{v} + \mathbf{q}\right\} = 0,\\
&\frac{\partial \rho_b}{\partial t} + \operatorname{div}(\rho_b \mathbf{v}_b) = \tau_b,\\
&\frac{\partial}{\partial t}(\rho_b \mathbf{v}_b) + \operatorname{div}(\rho_b \mathbf{v}_b \otimes \mathbf{v}_b - \mathbf{t}_b) = \mathbf{m}_b,\\
&\frac{\partial}{\partial t}\left(\frac{1}{2}\rho_b v_b^2 + \rho_b \varepsilon_b\right) + \operatorname{div}\left\{\left(\frac{1}{2}\rho_b v_b^2 + \rho_b \varepsilon_b\right)\mathbf{v}_b - \mathbf{t}_b \mathbf{v}_b + \mathbf{q}_b\right\} = e_b.
\end{aligned} \tag{44}$$

These two sets of governing equations, (37) and (44), are equivalent – they are actually obtained by the change of state variables $(\rho_\alpha, \mathbf{v}_\alpha, T_\alpha)^T \rightarrow (\rho, \mathbf{v}, T, \rho_b, \mathbf{v}_b, T_b)^T$. As a consequence, their characteristic speeds are the same.

In this setting $\mathbf{v}_b$ (or $\mathbf{u}_b$) and T_b can be regarded as nonequilibrium variables. As a matter of fact, mixture theory was, in its historical development, formulated within extended thermodynamics as a single-temperature theory, but with component velocities $\mathbf{v}_b$ as state variables. That was crucial for removal of paradox of infinite speed of pulse propagation due to the presence of nonlocal constitutive equation – Fick law. The hyperbolic single-temperature system appears as a principal subsystem of (44). Complete hierarchy of principal subsystems was analyzed in (Ruggeri & Simić, 2007) and it was shown that in the case of non-reacting mixtures equilibrium condition reads

$$\mathbf{v}_1 = \ldots = \mathbf{v}_n = \mathbf{v}; \qquad (\mathbf{u}_1 = \ldots = \mathbf{u}_n = \mathbf{0}), \qquad T_1 = \ldots = T_n = T, \tag{45}$$

and leads to an equilibrium subsystem (41). Corresponding characteristic speeds are

$$\lambda_{\mathrm{E}}^{(1)} = v_{\mathrm{n}} - c_{\mathrm{sE}}, \qquad \lambda_{\mathrm{E}}^{(2,3,4)} = v_{\mathrm{n}}, \qquad \lambda_{\mathrm{E}}^{(5)} = v_{\mathrm{n}} + c_{\mathrm{sE}},$$

where $v_{\mathrm{n}} = \mathbf{v} \cdot \mathbf{n}$ and c_{sE} is equilibrium sound speed of the mixture. Since (44) is endowed with convex entropy, the following subcharactiristic condition is valid

$$\min_\alpha (v_{\alpha \mathrm{n}} - c_{\mathrm{s}\alpha}^*) \leq \lambda_{\mathrm{E}}^{(1)}, \qquad \lambda_{\mathrm{E}}^{(5)} \leq \max_\alpha (v_{\alpha \mathrm{n}} + c_{\mathrm{s}\alpha}^*)$$

where $c_{\mathrm{s}\alpha}^* = (\gamma_\alpha (k_{\mathrm{B}}/m_\alpha)T)^{1/2}$ are the sound speeds of the full system evaluated in equilibrium. Explicit form of the equilibrium sound speed of the mixture c_{sE} will be left for the case of binary mixture. It is only important to note that it is evaluated when (45) is satisfied.

5.2 Binary mixture and the shock structure problem

Analysis of the shock structure in mixtures, modelled by the hyperbolic system (44), will be restricted to a binary mixture of perfect gases without chemical reactions ($\tau_\alpha = 0$). It was

shown (Ruggeri, 2001) that governing equations (44) could be written in the following form in the case of binary mixture

$$\begin{aligned}
&\frac{\partial \rho}{\partial t} + \operatorname{div}(\rho \mathbf{v}) = 0,\\
&\frac{\partial}{\partial t}(\rho \mathbf{v}) + \operatorname{div}\left(\rho \mathbf{v} \otimes \mathbf{v} + p\mathbf{I} + \frac{1}{\rho c(1-c)}\mathbf{J} \otimes \mathbf{J}\right) = \mathbf{0},\\
&\frac{\partial}{\partial t}\left(\frac{1}{2}\rho v^2 + \rho\varepsilon\right) + \operatorname{div}\left\{\left(\frac{1}{2}\rho v^2 + \rho\varepsilon + p\right)\mathbf{v} + \left(\frac{\mathbf{v}\cdot\mathbf{J}}{\rho c(1-c)} + \frac{1}{\beta}\right)\mathbf{J}\right\} = 0,\\
&\frac{\partial}{\partial t}(\rho c) + \operatorname{div}(\rho c \mathbf{v} + \mathbf{J}) = 0,\\
&\frac{\partial}{\partial t}(\rho c \mathbf{v} + \mathbf{J}) + \operatorname{div}\left\{\rho c \mathbf{v} \otimes \mathbf{v} + \frac{1}{\rho c}\mathbf{J} \otimes \mathbf{J} + \mathbf{v} \otimes \mathbf{J} + \mathbf{J} \otimes \mathbf{v} + \nu\mathbf{I}\right\} = \mathbf{m}_1,\\
&\frac{\partial}{\partial t}\left(\frac{1}{2}\rho c\left(\mathbf{v} + \frac{\mathbf{J}}{\rho c}\right)^2 + \rho c e\right) + \operatorname{div}\left\{\left(\frac{1}{2}\rho c\left(\mathbf{v} + \frac{\mathbf{J}}{\rho c}\right)^2 + \rho c e + \nu\right)\left(\mathbf{v} + \frac{\mathbf{J}}{\rho c}\right)\right\} = e_1,
\end{aligned} \tag{46}$$

provided we introduce concentration variable c and diffusion flux vector $\mathbf{J}$

$$c = \frac{\rho_1}{\rho}, \qquad \mathbf{J} = \rho_1 \mathbf{u}_1 = -\rho_2 \mathbf{u}_2.$$

Thermal inertia β reads

$$\beta = \frac{1}{g_1 - g_2}, \qquad g_\alpha = \varepsilon_\alpha + \frac{p_\alpha}{\rho_\alpha} + \frac{u_\alpha^2}{2},$$

and $\nu = p_1$, $e = \varepsilon_1$.

Thermal and caloric equation of state for the mixture could be expressed in the form of equations for a single fluid

$$p = \rho \frac{k_B}{m} T, \qquad \varepsilon_I = \frac{k_B}{m}\frac{T}{\gamma - 1}, \tag{47}$$

provided we introduce average atomic mass m, average temperature T and average ratio of specific heats γ in the following way (Ruggeri & Simić, 2007)

$$\begin{aligned}
\frac{1}{m} &= \frac{c}{m_1} + \frac{1-c}{m_2}, \qquad T = c\frac{m}{m_1}T_1 + (1-c)\frac{m}{m_2}T_2,\\
\frac{1}{\gamma - 1} &= \frac{c}{\gamma_1 - 1}\frac{m}{m_1}\frac{T_1}{T} + \frac{1-c}{\gamma_2 - 1}\frac{m}{m_2}\frac{T_2}{T}.
\end{aligned} \tag{48}$$

Note that $\gamma_1 = \gamma_2$ implies $\gamma = \gamma_1 = \gamma_2$. It will be useful for further analysis to use the temperature difference $\Theta = T_2 - T_1$ as a nonequilibrium variable, so that component temperatures can expressed in terms of Θ and average temperature T

$$T_1 = T - \frac{m}{m_2}(1-c)\Theta, \qquad T_2 = T + \frac{m}{m_1}c\Theta. \tag{49}$$

Using these relations ν, e and β can be expressed in terms of $\mathbf{u} = (\rho, \mathbf{v}, T, c, \mathbf{J}, \Theta)^T$, a new set of state variables. Using these new quantities one may determine the sound speed for equilibrium subsystem

$$c_{\mathrm{sE}} = \left(\gamma \frac{k_{\mathrm{B}}}{m} T\right)^{1/2}. \tag{50}$$

Explicit form of source terms $\mathbf{m}_1$ and e_1 reads as follows

$$\hat{\mathbf{m}}_1 = -\psi_{11}\left(\frac{\mathbf{u}_1}{T_1} - \frac{\mathbf{u}_2}{T_2}\right) = -\psi_{11}\left(\frac{1}{\rho c T_1} + \frac{1}{\rho(1-c)T_2}\right)\mathbf{J},$$
$$\hat{e}_1 = -\theta_{11}\left(-\frac{1}{T_1} + \frac{1}{T_2}\right) = \theta_{11}\frac{\Theta}{T_1 T_2},$$

where T_1 and T_2 are given by (49). However, source terms cannot be completely described within the framework of extended thermodynamics since coefficients ψ_{11} and θ_{11} remain undetermined. They can be related either to experimental data, or to some other theory. We shall recourse to the results of kinetic theory of gases (Bose, 2004) which relate them to volumetric collision frequency Γ'_{12} in equilibrium

$$\psi_{11\mathrm{E}} = 2T_0\frac{m_1 m_2}{m_1 + m_2}\Gamma'_{12}, \qquad \theta_{11\mathrm{E}} = 3k_{\mathrm{B}}T_0^2\frac{m_1 m_2}{(m_1+m_2)^2}\Gamma'_{12}.$$

On the other hand, by linearization of source terms in the neighborhood of equilibrium they could be related to relaxation times τ_{D} and τ_{T} for diffusion and temperature in equilibrium

$$\psi_{11\mathrm{E}} = \frac{\rho_0 c_0(1-c_0)T_0}{\tau_{\mathrm{D}}}, \qquad \theta_{11\mathrm{E}} = \frac{k_{\mathrm{B}}}{m_1(\gamma_1 - 1)}\frac{\rho_0 c_0 T_0^2}{\tau_{\mathrm{T}}}. \tag{51}$$

Comparison of the last two equations yields the relation between relaxation times

$$\tau_{\mathrm{T}} = \frac{2}{3(\gamma_1 - 1)}\frac{m_1 + m_2}{(1-c_0)m_1}\tau_{\mathrm{D}}$$

and it is frank that for real gases we have an estimate $\tau_{\mathrm{T}} > \tau_{\mathrm{D}}$. This fact gives strong support to the multi-temperature assumption since thermal nonequilibrium needs more time for attenuation than mechanical (diffusion) one. In the sequel we shall adopt equilibrium values of coefficients (51): since we are dealing with states which are close to equilibrium ones, they will provide sufficiently accurate estimate.

Equilibrium state is characterized by vanishing of the entropy production. In the case of binary mixture it is equivalent to vanishing of the source terms, $\mathbf{m}_1 = \mathbf{0}$ and $e_1 = 0$ (see Ruggeri & Simić (2007)). Condition of equilibrium leads to a state without diffusion where constituents have common temperature

$$\mathbf{J} = \mathbf{J}_0 = \mathbf{0}, \qquad \Theta = \Theta_0 = 0.$$

These conditions are in agreement with (45). We shall further assume that other variables have uniform distributions in equilibrium state

$$\rho = \rho_0 = \text{const.}, \qquad \mathbf{v} = \mathbf{v}_0 = \text{const.}, \qquad T = T_0 = \text{const.}, \qquad c = c_0 = \text{const.}$$

The shock structure is assumed to be a continuous travelling wave-like solution which asymptotically connects two such equilibrium states.

The shock structure problem will be analyzed for a plane wave which propagates in x-direction with speed s. Therefore, we shall seek for a travelling wave solution in the form $\mathbf{u}(\xi) = \mathbf{u}(x - st)$ with a single independent variable $\xi = x - st$. This assumption transforms

the system of governing equations (46) to the following set of ODE's which determine the shock structure

$$\begin{aligned}
&\frac{d}{d\xi}(\rho u) = 0,\\
&\frac{d}{d\xi}\left(\rho u^2 + p + \frac{J^2}{\rho c(1-c)}\right) = 0,\\
&\frac{d}{d\xi}\left\{\left(\frac{1}{2}\rho u^2 + \rho\varepsilon + p\right)u + \left(\frac{uJ}{\rho c(1-c)} + \frac{1}{\beta}\right)J\right\} = 0,\\
&\frac{d}{d\xi}(\rho c u + J) = 0,\\
&\frac{d}{d\xi}\left\{\rho c u^2 + \frac{J^2}{\rho c} + 2uJ + \nu\right\} = \hat{m}_1,\\
&\frac{d}{d\xi}\left\{\left(\frac{1}{2}\rho c\left(u + \frac{J}{\rho c}\right)^2 + \rho c e + \nu\right)\left(u + \frac{J}{\rho c}\right)\right\} = \hat{m}_1 u + \hat{e}_1,
\end{aligned} \tag{52}$$

where $u = v - s$ is x-component of the relative mixture velocity with respect to the shock wave and J and $\hat{m}_1$ are x-components of diffusion flux and source term. Due to change of variables we shall have a standing shock profile with upstream (unperturbed) state $\mathbf{u}_0 = \lim_{\xi\to-\infty}\mathbf{u}(\xi)$ and downstream (perturbed) state $\mathbf{u}_1 = \lim_{\xi\to\infty}\mathbf{u}(\xi)$. In view of equilibrium conditions discussed above, we adjoin the system (52) with following boundary conditions

upstream		downstream	
$\rho = \rho_0,$	$c = c_0;$	$\rho = \rho_1,$	$c = c_1;$
$u = u_0,$	$J = 0;$	$u = u_1,$	$J = 0;$
$T = T_0,$	$\Theta = 0;$	$T = T_1,$	$\Theta = 0.$

(53)

Downstream boundary conditions $\mathbf{u}_1$ will be determined in the sequel.

5.3 Stability and bifurcation of equilibria in shock structure problem

Further analysis will be performed in dimensionless form using the following dimensionless variables

$$\hat{\rho} = \frac{\rho}{\rho_0}, \quad \hat{u} = \frac{u}{c_{\mathrm{sE}}}, \quad \hat{T} = \frac{T}{T_0}, \quad \hat{J} = \frac{J}{\rho_0 c_0 c_{\mathrm{sE}}}, \quad \hat{\Theta} = \frac{\Theta}{T_0}, \quad \hat{\xi} = \frac{\xi}{\tau_{\mathrm{D}} c_{\mathrm{sE}}}, \quad M_0 = \frac{u_0}{c_{\mathrm{sE}}}.$$

We shall also assume that both components have the same ratio of specific heats, equal to the average one γ. Upstream boundary data thus read

$$\hat{\rho}_0 = 1, \quad \hat{u}_0 = M_0, \quad \hat{T}_0 = 1, \quad \hat{J}_0 = 0, \quad \hat{\Theta}_0 = 0, \tag{54}$$

while c_0 is already a dimensionless quantity. For convenience hats will be dropped in the sequel.

To reduce the order of the system, as well as computational effort, conservation laws for mass and momentum of the mixture $(52)_{1,2}$ and conservation law for mass of the component $(52)_4$

will be used to express ρ, J and T in terms of c and u

$$\rho = \frac{M_0}{u}, \qquad J = M_0\left(1 - \frac{c}{c_0}\right), \tag{55}$$
$$T = \frac{m}{m_0}\frac{u}{M_0}\left\{1 + \gamma M_0^2\left[1 - \frac{u}{M_0}\left(1 + \frac{(c_0 - c)^2}{c(1-c)}\right)\right]\right\},$$

where m_0 denotes the average atomic mass evaluated in upstream equilibrium state.
There will remain three equations which will finally determine the shock structure. Although still remains one conservation law among them $(52)_3$ further elimination of state variables will cause appearance of singularities which prevent efficient numerical calculations in the sequel. Thus, inserting (55) into $(52)_{3,5,6}$ written in dimensionless form we formally obtain the following set of ODE's

$$\frac{du}{d\xi} = F(u, c, \Theta, M_0), \qquad \frac{dc}{d\xi} = G(u, c, \Theta, M_0), \qquad \frac{d\Theta}{d\xi} = H(u, c, \Theta, M_0), \tag{56}$$

The actual form of the ODE system is a bit different

$$\mathbf{B}(\mathbf{u}, M_0)\frac{d\mathbf{u}}{d\xi} = \mathbf{f}(\mathbf{u}, M_0) \tag{57}$$

for $\mathbf{u} = (u, c, \Theta)^T$. Under regularity assumption $\det \mathbf{B}(\mathbf{u}, M_0) \neq 0$ equations (56) can be reconstructed as $d\mathbf{u}/d\xi = \mathbf{F}(\mathbf{u}, M_0) = \mathbf{B}^{-1}(\mathbf{u}, M_0)\mathbf{f}(\mathbf{u}, M_0)$. However, the form (57) is much more convenient and will be used in stability analysis.
It is of utmost importance to notice that stationary points of (56), or (57), which satisfy

$$\mathbf{f}(\mathbf{u}_0, M_0) = \mathbf{f}(\mathbf{u}_1, M_0) = \mathbf{0}$$

are determined by relations

$$\mathbf{u}_0 = (u_0, c_0, \Theta_0) = (M_0, c_0, 0), \qquad \mathbf{u}_1 = (u_1, c_1, \Theta_1) = \left(\frac{3 + M_0^2}{4M_0}, c_0, 0\right). \tag{58}$$

Actually, they satisfy the Rankine-Hugoniot equations on singular surface for the equilibrium subsystem (41). This fact is far from being obvious, but it is in a full accordance with the results obtained thus far for other hyperbolic dissipative systems (isothermal viscoelasticity and gas dynamics).
Our main concern will be the stability analysis of stationary points (58). We want show that there is a critical value for the upstream Mach number M_0 for which stationary points change their stability properties. Moreover, we would like to show that we can rely on a simple criterion, related to the eigenvalues, which provides us a selection rule for admissible shock structures. To that end we shall introduce perturbation of upstream equilibrium state $\Delta\mathbf{u} = (u - u_0, c - c_0, \Theta - \Theta_0)^T = \mathbf{u} - \mathbf{u}_0$ and write the system of linearized variational equations in the form

$$\mathbf{B}(\mathbf{u}_0, M_0)\frac{d\Delta\mathbf{u}}{d\xi} = \frac{\partial \mathbf{f}}{\partial \mathbf{u}}(\mathbf{u}_0, M_0)\Delta\mathbf{u}.$$

Eigenvalue problem which corresponds to this system reads

$$\left(\frac{\partial \mathbf{f}}{\partial \mathbf{u}}(\mathbf{u}_0, M_0) - \lambda \mathbf{B}(\mathbf{u}_0, M_0)\right)\mathbf{r} = \mathbf{0}.$$

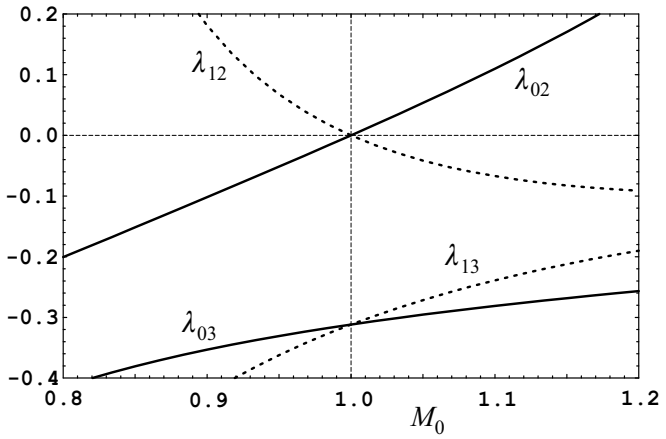

Fig. 2. Eigenvalues in upstream $\mathbf{u}_0$ and downstream $\mathbf{u}_1$ stationary points in He-Xe mixture shock structure.

Characteristic equation has generalized form

$$\det\left(\frac{\partial \mathbf{f}}{\partial \mathbf{u}}(\mathbf{u}_0, M_0) - \lambda \mathbf{B}(\mathbf{u}_0, M_0)\right) = 0$$

and gives three eigenvalues

$$\lambda_{01} \equiv 0, \qquad \lambda_{02} = \lambda_{02}(M_0), \qquad \lambda_{03} = \lambda_{03}(M_0).$$

Note that one eigenvalue is identically zero, which is a consequence of the fact that among the system of shock structure equations (57) there is one conservation law. Other two eigenvalues can be calculated in a closed form, which is rather cumbersome. More important than its closed form is the fact that one of them changes the sign in the neighborhood of $M_0 = 1$

$$\lambda_{02}(1) = 0, \qquad \frac{d\lambda_{02}(1)}{dM_0} = 1.046; \qquad \lambda_{03}(1) = -0.3118, \tag{59}$$

the conclusion which can be drawn by continuity argument. By similar calculation one may determine the eigenvalues in downstream equilibrium state $\mathbf{u}_1$

$$\lambda_{11} \equiv 0, \qquad \lambda_{12} = \lambda_{12}(M_0), \qquad \lambda_{13} = \lambda_{13}(M_0).$$

Again, one of the eigenvalues is identically zero, and among other two there is one which changes the sign in the neighborhood of the critical value of shock speed $M_0 = 1$

$$\lambda_{12}(1) = 0, \qquad \frac{d\lambda_{12}(1)}{dM_0} = -1.046; \qquad \lambda_{13}(1) = -0.3118, \tag{60}$$

Figure 2 shows the graphs of nontrivial eigenvalues calculated in the mixture of Helium and Xenon, whose ratio of atomic masses is $m_{\mathrm{Xe}}/m_{\mathrm{He}} = 32.80$, and with equilibrium concentration of Helium $c_0 = 0.3$.

Arguments which relate the results in (59) and (60) to admissibility conditions are the same as in the case of gas dynamics. Namely, admissibility of the shock wave in equilibrium subsystem reads

$$\lambda_{\mathrm{E}}^{(5)}(\mathbf{u}_0) < s < \lambda_{\mathrm{E}}^{(5)}(\mathbf{u}_1).$$

Left inequality corresponds to $M_0 > 1$. For $s < \lambda_{\mathrm{E}}^{(5)}(\mathbf{u}_0)$, or $M_0 < 1$, shocks are not admissible. Moreover, $\lambda_{02}(M_0) < 0$ determines the stable direction (eigenvector) in state space when $M_0 < 1$, while $\lambda_{02}(M_0) > 0$ determines unstable one for $M_0 > 1$. The opposite conclusions are valid for $\lambda_{12}(M_0)$. Therefore, equivalently to (36), we can conclude that admissible shock structure appears when

$$0 < \lambda_{02}(M_0) \qquad (\lambda_{12}(M_0) < 0), \tag{61}$$

while $\lambda_{02}(M_0) = 0$, or $\lambda_{12}(M_0) = 0$, determine the critical value of the parameter (shock speed). Once again, the selection rule (61) is in direct relation to the properties of equilibrium subsystem, which are absorbed in the mixture model. Inequality form of admissibility criterion strengthens its irreversible nature. Finally, it has to be stressed that equilibrium states (stationary points $\mathbf{u}_0$ and $\mathbf{u}_1$), the critical value of the shock speed and stability condition (61) are determined from the shock structure equations (57) (or equivalently (52)) without prior solution of Rankine-Hugoniot equations and usage of Lax condition.

Explicit bifurcation analysis of the system (57), in the sense of previous two sections, will be omitted here due to huge computational efforts needed. However, from (58) and (55) it is obvious that $\lim_{M_0 \to 1} \mathbf{u}_1 = \mathbf{u}_0$ and that equilibrium states form two branches in the state space which intersect for $M_0 = 1$. This fact, along with existence of a simple eigenvalue which changes the sign, resembles the structure of transcritical bifurcation pattern discovered in previously studied models.

6. Conclusions

This study was concerned with stability and bifurcation analysis of equilibrium states in hyperbolic models of dissipative thermomechanical systems. It was focused on stability properties of equilibrium states connected by the shock structure. In particular, it was shown that the critical value of the speed of a travelling shock profile in dissipative system coincides with the critical value of the shock speed in equilibrium subsystem, the one which separates admissible from inadmissible shock waves according to Lax condition. The main feature of this analysis is its independence of previous study of equilibrium subsystem: the stationary points and their stability properties reflect the structure of equilibrium subsystem contained in dissipative one, but are determined without prior knowledge of solutions of Rankine-Hugoniot relations or application of Lax condition. The stability results for the models of isothermal viscoelasticity and gas dynamics, as well as the new ones for the multi-temperature model of mixture of Euler fluids, seem to be persuasive enough that we may conjecture that exchange of stability properties of stationary points may be used as a selection rule for admissible shock structures in dissipative hyperbolic systems.

Stability results shown in this chapter may be generalized and exploited in several ways. First, it is expected that stability and bifurcation of equilibrium can be proved for a general hyperbolic system of balance laws, under reasonable physical and structural assumption. This is a natural step towards their complete verification. Another possibility for application is numerical calculation of shock profiles. Eigenvectors corresponding to eigenvalues with changing sign determine asymptotic behavior of heteroclinic orbits in the neighborhood of stationary points when $\xi \to \pm\infty$. This fact can be used in truncation of the domain, necessary

for numerical computation of the profile, and determination of initial data for solving the problem as initial value one.

7. Acknowledgment

This work was supported by the Ministry of Science of the Republic of Serbia within the project "Mechanics of nonlinear and dissipative systems – contemporary models, analysis and applications" (Project No. 174016).

8. References

Boillat, G. & Ruggeri, T. (1997). Hyperbolic principal subsystems: entropy convexity and subcharacteristic conditions. *Archive for Rational Mechanics and Analysis* Vol. 137, 305–320, ISSN 1432-0673

Boillat, G. & Ruggeri, T. (1998). On the shock structure problem for hyperbolic system of balance laws and convex entropy. *Continuum Mechanics and Thermodynamics*, Vol. 10, 285–292, ISSN 1432-0959

Bose, T.K. (2004). *High Temperature Gas Dynamics*, Springer-Verlag, ISBN 3-540-40885-1, Berlin.

Bose, C.; Illner, R. & Ukai, S. (1998). On shock wave solutions for discrete velocity models of the Boltzmann equation. *Transport Theory and Statistical Physics*, Vol. 27, 35–66, ISSN 1532-2424

Bernhoff, N. & Bobylev, A. (2007). Weak shock waves for the general discrete velocity model of the Boltzmann equation. *Communications in Mathematical Sciences*, Vol. 5, 815–832, ISSN 1539-6746

Bisi, M.; Groppi, M. & Spiga, G. (2005). Fluid-dynamic equations for reacting gas mixtures. *Applications of Mathematics*, Vol. 50, 43–62, ISSN 0862-7940

Caflisch, R.E. & Nicolaenko, B. (1982) Shock profile solutions of the Boltzmann equation. *Communications in Mathematical Physics*, Vol. 86, 161–194, ISSN 1432-0916

Chen G.-Q.; Levermore C.D. & Liu T.-P. (1994). Hyperbolic Conservation Laws with Stiff Relaxation Terms and Entropy. *Communications on Pure and Applied Mathematics*, Vol. 47, 787–830, ISSN 1097-0312

Dafermos, C.M. (2000). *Hyperbolic Conservation Las in Continuum Physiscs*, Springer-Verlag, ISBN 978-3-642-04047-4, Berlin.

Gilbarg, D. & Paolucci, D. (1953). The structure of shock waves in the continuum theory of fluids. *Journal of Rational Mechanics and Analysis*, Vol. 2, 617–642, ISSN 1943-5282

Grad, H. (1949) On the kinetic theory of rarefied gases. *Communications on Pure and Applied Mathematics*, Vol. 2, 331–407, ISSN 1097-0312

Grad, H. (1952) The profile of a steady planar shock wave. *Communications on Pure and Applied Mathematics*, Vol. 5, 257–300, ISSN 1097-0312

de Groot, S.R. & Mazur, P. (1984). *Non-equilibrium thermodynamics*, Dover, ISBN 0-486-64741-2, New York.

Guckenheimer, J. & Holmes, P. (1986). *Nonlinear Oscillations, Dynamical Systems and Bifurcations of Vector Fields*, Springer-Verlag, ISBN 978-0-387-90819-9, New York.

Holian, B.L.; Mareschal, M. & Ravelo, R. (2011). Burnett-Cattaneo continuum theory for shock waves. *Physical Review E*, Vol. 83, 026703, ISSN 1539-3755

Hoover, Wm.G. & Hoover, C.G. (2009). Tensor temperature and shock-wave stability in a strong two-dimensional shock wave. *Physical Review E*, Vol. 80, 011128, ISSN 1539-3755

Liu, I-S. (1972). Method of Lagrange Multipliers for Exploitation of the Entropy Principle. *Archive for Rational Mechanics and Analysis* Vol. 46, 131–148, ISSN 1432-0673

Liu, T.-P. (1987). Hyperbolic conservation laws with relaxation. *Communications in Mathematical Physics*, Vol. 108, 153–175, ISSN 1432-0916

Lorin, E. (2003). Existence of viscous profiles for the compressible Navier-Stokes equations. *Applicable Analysis*, Vol. 82, 645–654, ISSN 0003-6811

Müller, I. & Ruggeri, T. (1998). *Rational Extended Thermodynamics*, Springer-Verlag, ISBN 0-387-98373-2, New York.

Nicolaenko, B. & Thurber, J.K. (1975). Weak shock and bifurcating solutions of the non-linear Boltzmann equation. *Journal de Mécanique*, Vol. 14, 305–338, ISSN 0021-7832

Ruggeri, T. (1989). Galilean Invariance and Entropy Principle for Systems of Balance Laws. The Structure of the Extended Thermodynamics. *Continuum Mechanics and Thermodynamics*, Vol. 1, 3–20, ISSN 1432-0959

Ruggeri, T. (2001). The binary mixtures of Euler fluids: a unified theory of second sound phenomena, In: *Continuum Mechanics and Applications in Geophysics and the Environment*, Straughan, B.; Greve, R.; Ehrentraut, H. & Wang, Y., (Eds.), 79–91, Springer, ISBN 978-3-540-41660-9, Berlin.

Ruggeri T. & Simić S. (2007). On the hyperbolic system of a mixture of Eulerian fluids: A comparison between single- and multi-temperature models. *Mathematical Methods in the Applied Sciences*, Vol. 30, 827–849, ISSN 1099-1476

Serre, D. (1999). *Systems of Conservation Laws 1: Hyperbolicity, Entropies, Shock Waves*, Cambridge University Press, ISBN 9780521582339, Cambridge.

Simić, S.S. (2008). A note on shock profiles in dissipative hyperbolic and parabolic models. *Publication de l'Institut Mathématique*, Nouvelle série Vol. 84 (98), 97–107, ISSN 0350-1302

Simić, S.S. (2009). Shock structure in continuum models of gas dynamics: stability and bifurcation analysis. *Nonlinearity*, Vol. 22, 1337–1366, ISSN 0951-7715

Solovchuk, M.A. & Sheu, T.W.H. (2011). Prediction of strong-shock structure using the bimodal distribution function. *Physical Review E*, Vol. 83, 026301, ISSN 1539-3755

Suliciu, I. (1990). On modelling phase transitions by means of rate-type constitutive equations. Shock wave structure. *International Journal of Engineering Science* Vol. 28, 829–841, ISSN 0020-7225

Truesdell, C. (1969). *Rational Thermodynamics*, Springer-Verlag, ISBN 0-387-90874-9, New York.

Uribe, F.J.; Velasco, R.M.; García-Colín, L.S. & Díaz-Herrera E. (2000). Shock wave profiles in the Burnett approximation. *Physical Review E*, Vol. 62, 6648–6666, ISSN 1539-3755

Uribe, F.J. (2011). The Shock Wave Problem Revisited: The Navier-Stokes Equations and Brenner's Two Velocity Hydrodynamics, In: *Coping with Complexity: Model Reduction and Data Analysis*, Gorban, A.N. & Roose, D., (Eds.), 207-229, Springer-Verlag, ISBN 978-3-642-14941-2, Berlin

Weiss, W. (1995). Continuous shock structure in extended thermodynamics. *Physical Review E*, Vol. 52, R5760–R5763, ISSN 1539-3755

Xu, K. & Hongwei Liu, H. (2007). Multiple-temperature kinetic model for continuum and near continuum flows, *Physics of Fluids*, Vol. 19, 016101, ISSN 1070-6631

Yong, W.-A. & Zumbrun, K. (2000). Existence of relaxation shock profiles for hyperbolic conservation laws. *SIAM Journal on Applied Mathematics*, Vol. 60, 1565–1575, ISSN 0036-1399

9

Chromia Evaporation in Advanced Ultra-Supercritical Steam Boilers and Turbines

Gordon R. Holcomb
National Energy Technology Laboratory, United States Department of Energy, Albany, OR USA

1. Introduction

Goals of the U.S. Department of Energy's Advanced Power Systems Initiatives include power generation from coal at 60% efficiency, which requires steam conditions of up to 760 °C and 340 atm, so-called advanced ultra-supercritical (A-USC) steam conditions. Similar efforts are underway in Europe, Japan, and China to raise efficiencies by raising steam temperatures to 700 °C and above. A limitation to achieving the goal is a lack of cost-effective metallic materials that can perform at these temperatures and pressures. Some of the more important performance limitations are high-temperature creep strength, fireside corrosion resistance, and steam-side oxidation resistance. Nickel-base superalloys are expected to be the materials best suited for steam boiler and turbine applications above about 675 °C (Viswanathan et al., 2005). Specific alloys of interest include Haynes 230 and 282, Inconel 617, 625, and 740, Nimonic 263. Alloy compositions are given in Table 1 (Haynes International, 2008a, 2008b; Special Metals Corporation, 2004a, 2004b, 2005, 2006).

Steam-side oxidation can result in several adverse effects: general section loss from material thinning, deep localized section loss from internal oxidation (that may also provide crack initiation sites), reduced heat transfer due to the development of insulating oxide layers (that may lead to higher metal temperatures to maintain the same steam conditions), dimensional changes that are critical in airfoils, and downstream erosion from oxide spallation. Evaporation of protective chromia scales may also be an issue at the higher temperatures and pressures of A-USC steam turbines. The evaporation of chromia scales in steam is the focus of the research presented here.

Water vapor is known to adversely affect the oxidation behavior of chromia-forming alloys. Several explanations have been developed to explain the observed behaviors (Essuman et al., 2008; Young & Pint, 2006). Some are briefly described:

- Increased chromia growth rates from the doping of Cr_2O_3 with hydrogen species that result from the oxidation reaction between the metal and H_2O (Norby, 1993; Hänsel et al., 2003 as cited in Young & Pint, 2006). Similar increased growth rates were found for the oxidation of Cr containing dissolved hydrogen compared to Cr without dissolved hydrogen (Henry et al., 2001 as cited in Essuman et al., 2008).
- Enhanced growth stresses that lead to scale cracking (Schütze et al., 2004 as cited in Essuman et al., 2008).
- Enhanced internal oxidation of Cr by water vapor changing the solubility or diffusivity of oxygen in the alloy (Essuman et al., 2008). Increases in internal oxidation can also

lead to scales with less Cr_2O_3 formation and thus increased tendencies to breakaway oxidation (Essuman et al., 2008).

- Rapid, or "breakaway" oxidation from the depletion of Cr in the scale resulting from reactive evaporation of Cr_2O3 in the presence of O_2 and H_2O (Essuman et al., 2008; Holcomb, 2008, 2009; Young & Pint, 2006). Clear links to evaporation were shown by how increased gas flow rates led to faster breakaway oxidation and increased Fe:Cr ratios within the oxide scale (Asteman et al., 2000).

Alloy	Fe	Cr	Ni	Co	Mo	Ti	Al	Mn	Other	C_{Cr}°
Haynes 230	1.5	22	Bal	2.5	2		0.3	0.5	0.02 La 14 W 0.4 Si 0.1 C 75 B	38000
Haynes 282	0.75	19.5	Bal	10	8.5	2.1	1.5		0.15 Cu 0.075 Si 0.06 C 50 B	31000
Inconel 617	1.5	22	Bal	12.5	9	0.3	1.15	0.5	0.25 Cu 0.5 Si 0.1 C 30 B	35400
Inconel 625	2.5	21.5	Bal	0.5	9	0.2	0.2	0.25	3.65 Nb 0.25 Si 0.05 C	34900
Inconel 740	0.7	25	Bal	20	0.5	1.8	0.9	0.3	2 Nb 0.5 Si 0.03 C	38700
Nimonic 263	0.35	20	Bal	20	5.85	2.15	0.3	0.3	0.1 Cu 0.2 Si 0.06 C 25 B	32200

Table 1. Nominal alloy compositions (wt%, except for B which is in ppm) and bulk alloy Cr concentrations (C_{Cr}°, mol/m^3) for alloys of interest (Haynes International, 2008a, 2008b; Special Metals Corporation, 2004a, 2004b, 2005, 2006). Source values that were ranges are listed as the midpoint of the range. Source values that were maximums are listed as half the maximum. For economic reasons it is not unusual for actual chemical compositions of materials delivered for use in power plants to be near the lower end of the specification. Only Nb is listed for sources that gave a value or range for Nb+Ta. Source values for Pb, P, S and Bi are omitted.

This last behavior based on reactive evaporation of Cr_2O_3 is the subject of the work presented here. In prior work, a methodology to calculate the expected chromia evaporation rate as a function of temperature, pressure, gas velocity, and steam chemistry was developed for chromia forming alloys (Holcomb, 2008). The methodology was experimentally validated at low pressures and gas velocities by how well its kinetics

predictions matched atmospheric pressure oxidation experiments in air plus water vapor environments. At 760 °C and 340 atm, evaporation rates as high as 5.18×10^{-8} kg/m^2/s of $CrO_2(OH)_2(g)$ were predicted for rotating high pressure (HP) turbine blade components (Holcomb, 2008). This is equivalent to 0.08 mm per year of solid Cr loss. It was speculated that chromia evaporation upstream of the HP turbine, such as in the superheater, could partially saturate the steam with $CrO_2(OH)_2(g)$ and reduce the chromia evaporation rate.

The above efforts were expanded (Holcomb, 2009) to include 1) the use of new determinations of the thermodynamic properties of $CrO_2(OH)_2(g)$ (Opila et al., 2007), 2) expanding the methodology from flat plate components to cylindrical geometries (such as found within superheaters and steam pipes), 3) linking the chromia evaporation in steam to Cr diffusion within the alloy to predict alloy Cr concentration profiles and breakaway oxidation times, and 4) applying the breakaway oxidation predictions to a hypothetical superheater-steam pipe-HP turbine steam path, where the effects of $CrO_2(OH)_2(g)$ saturation along the steam path are applied. In many aspects this was similar to the work of Young and Pint (2006).

Presented here is further validation of the model by examining the reactive evaporation effects resulting from exposure of Haynes 230 and Haynes 282 to moist air environments as a function of flow rate and water content. These two alloys differ in Ti and Mn contents, which may form outer layers of TiO_2 or Cr-Mn spinels, which would in theory decrease the evaporation of Cr_2O_3 from the scale (Holcomb & Alman, 2006).

2. Chromia evaporation

The oxidation of alloys protected by the formation of Cr_2O_3 (chromia formers) can undergo scale loss due to reactive evaporation of chromium-containing gas species. Water vapor increases the evaporation loss by allowing the formation of $CrO_2(OH)_2(g)$, which for these conditions has a higher vapor pressure than $CrO_3(g)$. $CrO_3(g)$ is the predominate Cr gas specie in dry air or oxygen (Graham & Davis, 1971). The formation of $CrO_2(OH)_2(g)$ can be written as:

$$½Cr_2O_3(s) + H_2O(g) + ¾O_2(g) = CrO_2(OH)_2(g) \quad (1)$$

The equilibrium partial pressure of $CrO_2(OH)_2(g)$ can be found from Eq. 2, where ΔG_1° is the Gibbs energy of reaction 1, R is the gas constant, T is the absolute temperature, K_1 is the equilibrium constant of reaction 1, a_{Cr2O3} is the activity of Cr_2O_3, and P_i is the partial pressure of gas specie i.

$$\Delta G_1^\circ = -RT\ln K_1 = -RT\ln\frac{P_{Cr2(OH)2}}{a_{Cr2O3}^{1/2} P_{H2O} P_{O2}^{3/4}} \quad (2)$$

Even while maintaining a Cr_2O_3 scale, evaporation can change the overall oxidation kinetics from parabolic behavior to linear kinetics or even to breakaway oxidation. Linear kinetics can arise after scale growth from oxidation, which decreases with increasing scale thickness, matches the scale loss from reactive evaporation (Tedman, 1966). The change in scale thickness, x, with time, t, can then be described in terms of the parabolic rate constant, k_p, and the linear reactive evaporation rate, k_e, as:

$$\frac{dx}{dt} = \frac{k_p}{x} - k_e \tag{3}$$

At long times or high reactive evaporation rates, a limiting scale thickness, x_L, arises that is given by:

$$x_L = \frac{k_p}{k_e} \tag{4}$$

In this case metal loss rates are linear, but still involve diffusion through a protective scale. Rapid metal loss can occur when reactive evaporation of Cr depletes the scale (and sometimes the substrate metal) of Cr (Asteman et al., 1999, 2000). Decreased Cr in the scale or metal can lead to the formation of less protective oxides, such as Fe-Cr oxides in Fe-Cr base alloys. Unprotective scales can lead to rapid metal loss, or "breakaway" oxidation.
A detailed methodology for calculating evaporation rates in a variety of environments was presented in earlier work for gas flow over a flat plate (Holcomb, 2008). Two basic equations were developed: Eq. 5 for laminar flow and Eq. 6 for turbulent flow:

$$k_e\left(\frac{kg}{m^2 s}\right) = 0.664\, Re_L^{0.5} Sc^{0.343} \frac{D_{AB} M_{CrO_2(OH)_2}}{LRT} P_{CrO_2(OH)_2} \tag{5}$$

$$k_e\left(\frac{kg}{m^2 s}\right) = 0.0592\, Re_L^{0.8} Sc^{0.333} \frac{D_{AB} M_{CrO_2(OH)_2}}{LRT} P_{CrO_2(OH)_2} \tag{6}$$

where Re_L and Sc are the dimensionless Reynolds and Schmidt numbers, D_{AB} is the gaseous diffusion coefficient between $CrO_2(OH)_2$ and the solvent gas (m^2/s), $M_{CrO2(OH)2}$ is the molecular mass of $CrO_2(OH)_2$ (kg/g-mol), L is the length (m) in the flow direction of the flat plate, $P_{CrO2(OH)2}$ is the partial pressure of $CrO_2(OH)_2$ (atm), R is the gas constant (8.20594×10^{-5} m^3atm/K g-mol), and T is the absolute temperature (K). The dimensionless Reynolds and Schmidt numbers are defined as:

$$Re_L = \frac{\rho_s u L}{\eta} \tag{7}$$

$$Sc = \frac{\eta}{\rho_s D_{AB}} \tag{8}$$

where ρ_s is the density of the solvent gas (kg/m^3), η is the absolute viscosity (kg/m/s), and u is the gas velocity (m/s). Values for two key parameters in Eqs. 5-8 (D_{AB} and η) are not established and require estimates (Holcomb, 2008) to be made.
The diffusion coefficient, D_{AB}, was estimated with a method using a $T^{1.75}/P_T$ relationship and "diffusion volumes" (Fuller et al., 1966; Holcomb, 2008), where P_T is total pressure. This estimate was later improved (Holcomb, 2009) using a computed geometry for $Cr_2(OH)_2(g)$ (Opila et al., 2007) to estimate the "diffusion volumes". The diffusion coefficient estimate in supercritical steam was further adjusted (reduced) based on methods presented by Bird et al. (1960) and Slattery and Bird (1958).
The absolute viscosity, η, was estimated for gas mixtures using the semi empirical formulation of Wilke (Wilke, 1950 as cited in Gaskell, 1992) that combines the absolute

viscosity of the component gases. For non-polar gases, η was estimated based on the Lennard_jones potential (Gaskell, 1992). For water and steam, information of η as a function of T and P was used (Stultz & Kitto, 1992).
The Gibbs energy for reaction 1, (Opila et al., 2007), was used to determine $P_{CrO2(OH)2}$. This is a change from the prior work (Holcomb, 2008), where the thermodynamic data of Gindorf et al. (2001) was used. The differences in Gibbs energies for reaction 1 between the two transpiration studies (Gindorf et al., 2001, Opila et al., 2007) are shown in Table 2. The Opila values result in higher $P_{CrO2(OH)2}$ values (Eq. 2) and was attributed to possible undercounting of Cr loss in the Gindorf study and to the wider range in water vapor contents that allowed more precision in measurements at higher water levels (Opila et al., 2007).

Source	ΔH_x°, J mol^{-1}	ΔS_x°, J mol^{-1}	Notes
Opila et al., 2007	53500 ± 5400	-45.6 ± 6.6	Based on second law enthalpy and entropy methods from transpiration experiments to determine ΔH_{861}° = 53.5 kJ mol^{-1} and ΔS_{861}° = 45.6 J mol^{-1} K^{-1} at the average temperature of 861 K.
Gindorf et al., 2001	61400	-49.8	Based on transpiration experiments to determine $\ln P_{Cr2(OH)2}$ (Pa) to be equal to 0.442 + -7387.5T^{-1} with an average temperature of 948 K in air with 2% H_2O.

Table 2. Simplified ΔG_T° formulations based on the approximation that ΔG_T° varies linearly with temperature for most substances (Kubaschewki & Alcock, 1979), where $\Delta G_T^\circ = \Delta H_x^\circ - T\Delta S_x^\circ$ and x is an elevated temperature close to the desired T.

The above methodology for flat surfaces (Eqs. 5-6) was expanded for use in pipes and to include possible saturation effects (Holcomb, 2009). Equations 5-6 were written in more general terms that included the average Sherwood number (Sh_{Ave}) and that allowed for the value of the partial pressure of $CrO_2(OH)_2(g)$ well away from the metal surface, $P_{CrO2(OH)2}^\circ$, to slow down the evaporation (Eqs. 4-5 assumed $P_{CrO2(OH)2}^\circ$ was zero), Eq. 9. Here Sh_{Ave} is equal to $0.664Re_L^{0.5}Sc^{0.343}$ for laminar flow over flat plates and to $0.0592Re_L^{0.8}Sc^{0.333}$ for turbulent flow over flat plates.

$$k_e\left(\frac{kg}{m^2 s}\right) = Sh_{Ave}\frac{D_{AB}M_{CrO_2(OH)_2}}{LRT}\left(P_{CrO_2(OH)_2} - P^\circ_{CrO_2(OH)_2}\right) \quad (9)$$

For flow within circular tubes, Eq. 9 was used but with a different expression for Sh_{Ave}. For the analysis that follows, the Dittus-Boelter equation (Winterton, 1998; Incropera & DeWitt, 2001) was used for Sh_{Ave} for turbulent conditions:

$$Sh_{Ave} = 0.023Re_d^{0.8}Sc^{0.4} \quad (10)$$

where Re_d is the same as Re_L but with the diameter, d, instead of the plate length, L, in Eq. 7. For rough pipes the use of an expression for Sh_{Ave} that incorporates a friction factor, such as that of Petukov (Incropera & DeWitt, 2001; Petukhov, 1970) can be used.
One additional point is that the evaporation rate, k_e, from Eq. 9 is for the amount of $Cr_2(OH)_2(g)$ leaving the surface, while the mass change data will be in terms of $Cr_2O_3(s)$ lost

from the surface. The conversion is shown in Eq. 11 (Holcomb, 2008). Unless otherwise stated, k_e is on a $Cr_2(OH)_2(g)$ basis.

$$k_{e,\,Cr2O3} = \frac{M_{Cr2O3}}{2M_{CrO2(OH)2}} k_{e,\,CrO2(OH)2} = 0.644 k_{e,\,CrO2(OH)2} \tag{11}$$

3. Chromia evaporation in cyclic oxidation tests

Cyclic oxidation tests were conducted for up to 2000 hourly cycles in moist air. Each hourly cycle consisted of 55 minutes in the furnace, withdrawal from the furnace, holding for 3.4 minutes, and then placement back into the furnace. The remaining 1.6 minutes per hourly cycle was the travel time the samples took into and out of the furnace. The samples experienced rapid heating and cooling rates, and were oriented such that the gas flow was parallel to their surfaces. More experimental details can be found in prior work (Holcomb et al., 2007).

A goal of the cyclic tests was to evaluate alloys for use in A-USC boilers and turbines. Scale exfoliation, resulting in part from thermal expansion mismatch between the alloy and the scale, is an important failure mechanism in boiler tubes (Wright & Tortorelli, 2007). The use of thermal cycles is an aggressive test of scale exfoliation tendencies. While some alloys did exhibit scale exfoliation in the cyclic tests (Holcomb et al., 2007), except as noted no scale exfoliation was observed during tests on the alloys discussed below.

Results for two alloys from prior work (Holcomb, 2008, 2009), Haynes 230 and Inconel 740, are shown in Figs. 1 and 2 respectively, and also in Table 3. The Haynes 230 results show the influence of gas velocity—a factor of 4 increase in gas velocity resulted in a factor of 2 increase in evaporation, which is consistent with Eqs. 7 and 9. The dashed lines in Fig. 1 show the evaporation rate from the model, with an activity of chromia of 0.05. This low chromia activity presumably arises from chromia depletion in the outer portion of the oxide scale as chromia is lost to evaporation. The results for two different heats of Inconel 740 in Fig. 2 show two different behaviors. The heat with the □ symbols initially had a similar evaporation rate as the Haynes 230 results. The evaporation rate decreased after about 800 cycles. The other heat, with + symbols, exhibited much less chromia evaporation. One difference between the two heats was 1.6 Ti in the heat with the □ symbols compared with 1.8 Ti in the heat with + symbols.

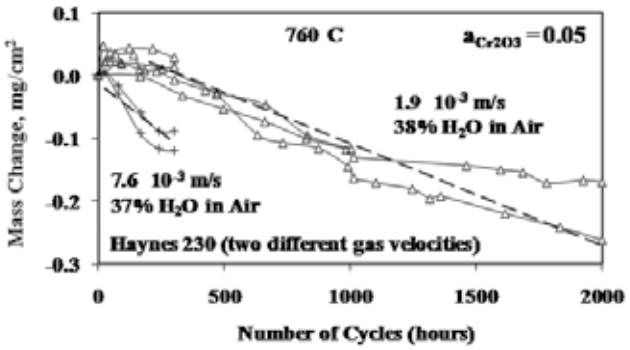

Fig. 1. Mass change measurements for Haynes 230 exposed at 760 °C in moist air at two different gas velocities. The dotted lines are the predicted mass change due to chromia evaporation with a chromia activity of 0.05. Adapted from Holcomb (2009).

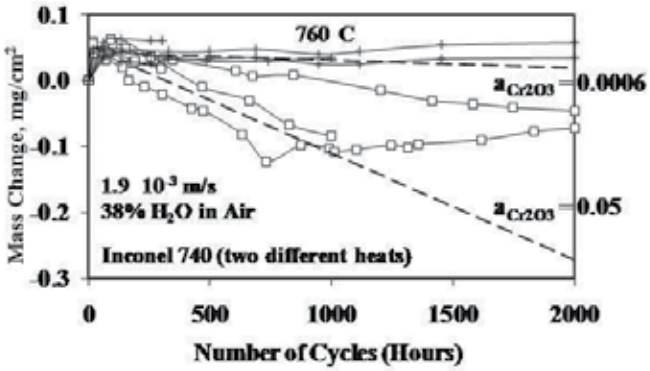

Fig. 2. Mass change measurements for two different heats of Inconel 740 exposed at 760 °C in moist air. The dotted lines are the predicted mass changes due to chromia evaporation with chromia activities of 0.05 and 0.0006. Adapted from Holcomb (2009).

Results for Haynes 230 and Haynes 282 at 800 °C are shown in Figs. 3-4 for two water vapor levels and two gas flow rates, and are also shown in Table 3. The results for Haynes 230 continue to show the same gas velocity dependence shown at 760 °C—a four-fold increase in flow rate doubles the evaporation rate. For Haynes 282, the combination of the highest flow rate and water vapor percentage changed behavior after 1000-12000 cycles. Past this point, small amounts of debris were found upon handling the sample for weighing. So the mass loss was a combination of chromia evaporation and scale spallation. A four-fold increase in flow rate increased, but did not double evaporation rate for Haynes 282. It could well be the case that steady state evaporation was not yet reached for the Haynes 282 prior to it starting to spall.

When the results in Figs. 3-4 were compared with the chromia evaporation model, chromia activities were found that matched the results—found in the last column in Table 3. One thought from prior research (Holcomb, 2009) was that chromia activities would decrease with higher rates of evaporation. As chromia leaves the surface, Mn and Ti oxides would become enriched and thus decrease the chromia activity. Table 3 shows that this is not always the case. Increasing the flow rate while maintaining a constant P_{H2O} resulted in chromia activities of Haynes 230 and Haynes 282 dropping from 0.14 to 0.11 and 0.21 to 0.07, respectively. However, raising the P_{H2O} from 0.19 to 0.57 while maintaining a constant flow rate increased the evaporation rate but also increased the chromia activity for Haynes 230 (0.06 to 0.11). The expected result was found for Haynes 282 with a decrease from 0.12 to 0.07.

Scanning electron microscopy (SEM) was used to examine the surfaces of the 800 °C samples, Fig. 5. The surface structure of Haynes 230 was finer than that found on Haynes 282. The Haynes 282 at the fastest chromia evaporation rate (lower right-hand image in Fig. 5) shows holes in the structure. One could speculate that these holes were where chromia may have evolved from and thus undercut the outer oxide. This undercutting appears to have resulted in the scale spalling in this sample.

The use of x-ray diffraction (XRD) on these surfaces showed chromia and spinels on Haynes 203 and chromia, spinels, and TiO_2 on Haynes 282. Various Cr-Ni-Mn containing spinels have very similar XRD peaks, making identification of Mn-containing spinels impossible.

Alloy	T, °C	P_{H2O}	Flow Rate, m/s	k_e [Cr_2O_3], kg/m²s	Time Range, hr	Apparent a_{cr2O3}
Haynes 230	760	0.37	1.9×10^{-3}	3.8×10^{-10}	200-2000	~0.05
Haynes 230	760	0.37	7.6×10^{-3}	11.7×10^{-10}	94-2000	~0.05
Inconel 740	760	0.38	1.9×10^{-3}	1.5×10^{-10} 5.5×10^{-10}	102-2000 18-734	~0.0006 ~0.05
Haynes 230	800	0.19	4.2×10^{-3}	3.4×10^{-10}	200-2000	0.06
Haynes 230	800	0.57	1.0×10^{-3}	4.9×10^{-10}	24-2000	0.14
Haynes 230	800	0.57	4.2×10^{-3}	9.1×10^{-10}	24-2000	0.11
Haynes 282	800	0.19	4.2×10^{-3}	4.9×10^{-10}	600-2000	0.12
Haynes 282	800	0.57	1.0×10^{-3}	6.1×10^{-10}	500-2000	0.21
Haynes 282	800	0.57	4.2×10^{-3}	7.2×10^{-10}	125-1000	0.07

Table 3. Alloys, conditions, and results for cyclic oxidation tests. Gas flow rates are at temperature. Data for 760 °C are from prior work (Holcomb, 2008). Data for Inconel 740 are from the heat with □ points in Fig. 2.

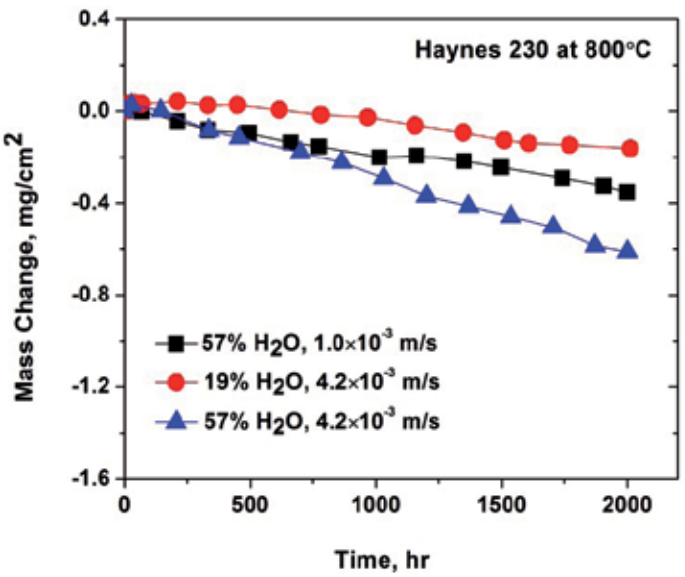

Fig. 3. Mass change measurements Haynes 230 at 800 °C in moist air at three different water vapor levels and gas flow rates.

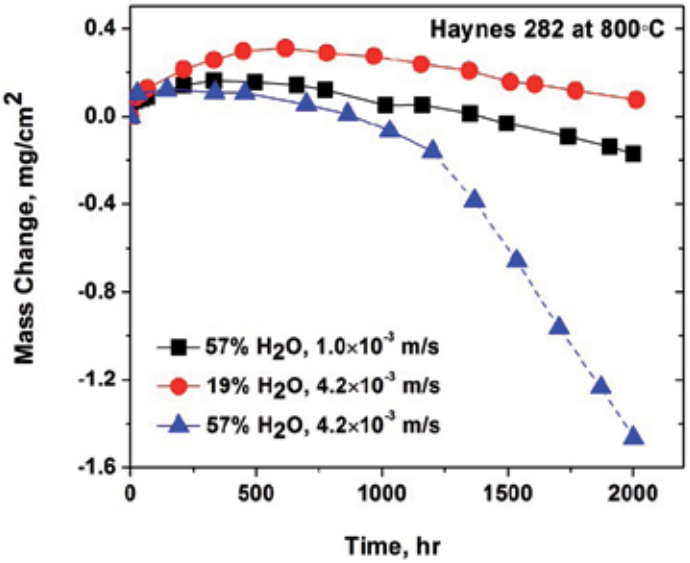

Fig. 4. Mass change measurements Haynes 282 at 800 °C in moist air at three different water vapor levels and gas flow rates. The dashed line indicates spalling.

Elemental spot analyses on the Haynes 230 surface for the slowest chromia evaporation sample (19% H_2O, 4.2×10^{-3} m/s) did not show any Mn on the surface. Analyses of the other two samples, with higher evaporation rates, showed Mn throughout the surface (along with Cr and O).

Elemental spot analyses on all of the Haynes 282 surfaces showed two distinct types of areas within a fine structure. Figure 6 shows a higher magnification image of this surface and these two types of areas. The smaller grains are primarily Cr and O (with smaller amounts of Ni and Al), and the larger grains (with flat surfaces) to be essentially pure Ti and O.

4. Chromium diffusion

After evaporation causes the overall oxidation kinetics to become linear and to have a steady state scale thickness (Eq. 4), the flux of Cr away from the scale via evaporation must equal the flux of Cr to the scale via Cr diffusion within the alloy. If there is insufficient arrival of Cr to the surface, then the chromia scale will not be maintained and breakaway oxidation would be expected to eventually occur.

To model Cr diffusion within the alloy with a constant flux of Cr leaving the surface, the transient heat transfer model of Incropera and DeWitt (Incropera & DeWitt, 2001) within a semi-infinite solid and with a constant surface heat flux was used. The underlying mathematics between heat and mass transfer are the same, so this model was used with appropriate mass transfer parameters. The overall equation for the concentration of Cr as a function of x (depth from the surface into the alloy, m) and t (time, s), $C_{Cr}(x,t)$ is:

$$C_{Cr}(x,t) = C_{Cr}^{\circ} - \frac{2k_e}{M_{CrO_2(OH)_2}}\sqrt{\frac{t}{\pi D_{Cr}}}\exp\left(-\frac{x^2}{4D_{Cr}t}\right) + \frac{k_e x}{M_{CrO_2(OH)_2}D_{Cr}}\operatorname{erfc}\left(\frac{x}{2\sqrt{D_{Cr}t}}\right) \quad (12)$$

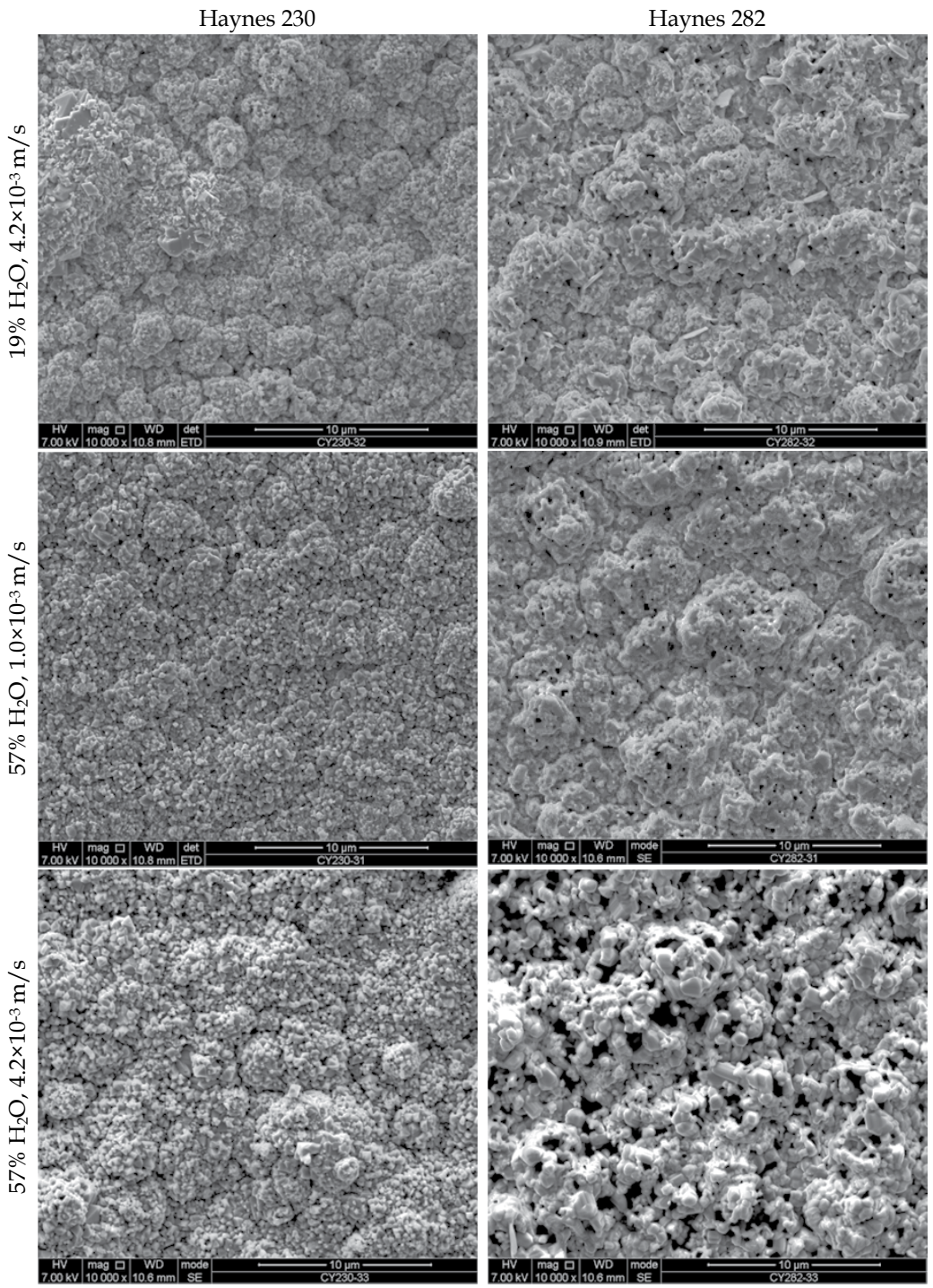

Fig. 5. Surface SEM after 2000 cycles at 800 °C in moist air.

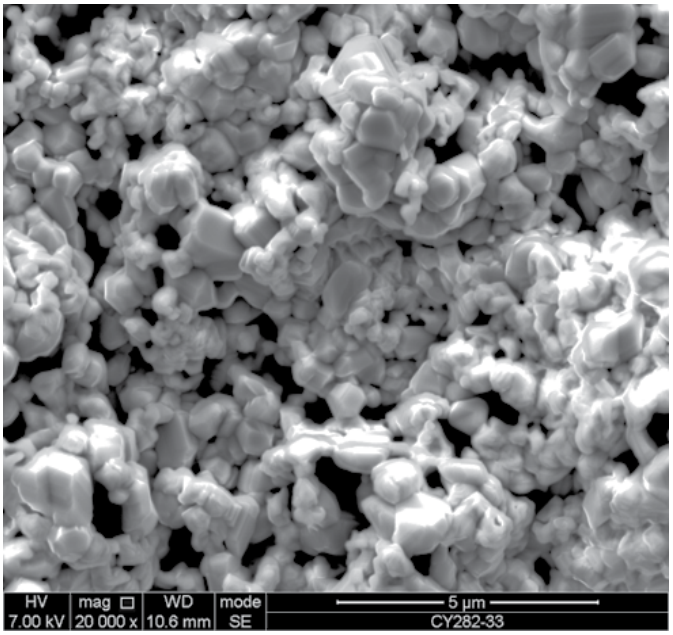

Fig. 6. Secondary electron image of Haynes 282 after 2000 hourly cycles at 800 °C in moist air (57% H_2O) and a gas flow rate of 4.2×10^{-3} m/s. Elemental spot analysis shows the smaller grains to be primarily Cr and O (with smaller amounts of Ni and Al), and the larger grains (with flat surfaces) to be essentially pure Ti and O

where C_{Cr}° is the bulk alloy Cr concentration (mol/m^3) (Table 1), D_{Cr} is the diffusion coefficient of Cr (m^2/s), and erfc is the complementary error function. For the concentration of Cr at the surface as a function of time, Eq. 12 simplifies to Eq. 13.

$$C_{Cr}(0,t) = C_{Cr}^{\circ} - \frac{2k_e}{M_{CrO_2(OH)_2}}\sqrt{\frac{t}{\pi D_{Cr}}} \tag{13}$$

And the surface concentration is equal to zero at time t^*, as shown in Eq. 14.

$$t^* = \frac{\pi D_{Cr}}{4}\left(\frac{M_{CrO_2(OH)_2}C_{Cr}^{\circ}}{k_e}\right)^2 \tag{14}$$

Breakaway oxidation is expected to occur prior to t^*, such as when the surface concentration becomes less than the critical value required to sustain a Cr_2O_3 scale. The critical value could be estimated, as was done for the critical bulk concentration of Cr in Fe-Cr alloys (Meier et al., 2010), if sufficient diffusion rates in the metal and scale are known. However, the lower bound on the critical value of the surface concentration is zero. So t^* is used as a proxy for the time until breakaway oxidation will occur.

At the temperatures in a steam turbine, the diffusion coefficient, D_{Cr}, is an effective diffusion coefficient and is a combination of lattice, D_{Cr}^{L}, and grain boundary, D_{Cr}^{gb}, diffusion. The relationship used is based on cubic grains of size λ (m) and with grain boundary width δ (m) (Peng et al., 2005):

$$D_{Cr} \cong D_{Cr}^{L} + \frac{2\delta}{\lambda} D_{Cr}^{gb} \tag{15}$$

The lattice diffusion coefficients were determined using Dictra diffusion simulation software (Thermo-Calc Software AB, 2006) with the Ni-DATA (Saunders, 2000) and MOB2 (Royal Institute of Technology, 1999) databases. Figure 7 shows lattice diffusion coefficients of Cr in the face-centered-cubic (FCC) phase for several alloys of interest as a function of Cr content at 760 °C. The right-most-point for each alloy is at the alloy Cr content. The lower Cr content values represent the alloy where it is locally depleted in Cr near the surface. Figure 7 shows that for many of the alloys an assumption of a constant value for the diffusion coefficient is a good one.

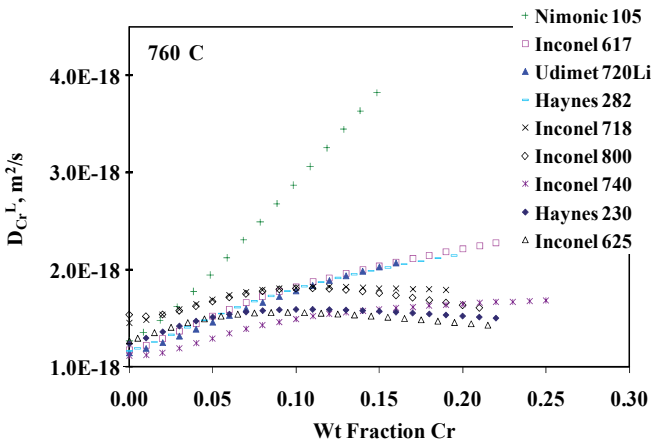

Fig. 7. Lattice diffusion coefficients at 760 °C for Cr in the FCC phase of nickel base superalloys determined using Dictra diffusion simulation software (Thermo-Calc Software AB, 2006) with the Ni-DATA (Saunders, 2000) and MOB2 (Royal Institute of Technology, 1999) databases.

The use of the FCC phase as the basis of lattice diffusion is a simplification of the rather complex nature of these alloys. All of the alloys in Fig. 7 are strengthened by the formation of one or more second phases, the amount of which depends upon heat treatment. Two of these alloys (Nimonic 105 and Udimet 720Li) have very significant amounts of a second phase (gamma prime). The ordered structure of these second phases should result an diffusivities that are much smaller than the FCC phase. So this simplification would tend to overstate the overall effective diffusion coefficients.

Further phase complications can arise from Cr depletion, where the loss of Cr can itself lead to phase changes. An example of this can be seen in Fig. 8, for Inconel 617 exposed to 2000 hourly cycles at 760 °C in air with 37% H_2O at atmospheric pressure (Holcomb, 2009). Figure 8 shows a phase transition zone near the oxide interface, presumably from Cr depletion. Internal oxidation, mainly of aluminum, is also present underneath the oxide scale along grain boundaries. Thus, a more comprehensive phase-based treatment of diffusion coefficients may be warranted. However, for the calculations that follow, the values used for the lattice diffusion coefficients are ones from the FCC phase at the Cr content of the alloy (Fig. 7).

Grain boundary diffusion coefficients are estimated based on the work of Paul *et al.* (Paul et al., 1994) where lattice and grain boundary diffusion coefficients were determined for Inconel 800 (where a grain boundary width of 0.5 nm was used). The estimate is to use the same ratio of grain boundary diffusion to lattice diffusion that was found for Inconel 800, and to use the same grain boundary width of 0.5 nm. This ratio is given by Eq. 16.

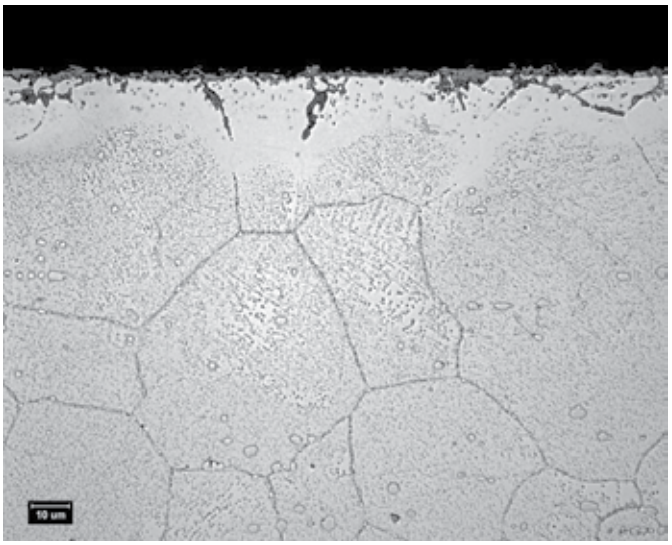

Fig. 8. Results of cyclic oxidation of Inconel 617 at 760 °C in air plus 37% H_2O after 2000 hourly cycles (Holcomb, 2009). A bright field image after etching (50% concentrated nitric acid, 50% glacial acetic acid). A precipitate free zone lies beneath internal oxidation areas.

$$\frac{D_{Cr}^{gb}}{D_{Cr}^{L}} \cong \exp\left(\frac{12412}{T} - 1.7203\right) \tag{16}$$

An example of a comparison between calculated and measured Cr diffusion profiles is given in Figs. 9-10 for Inconel 740 exposed to 2000 hourly cycles at 760 °C (under the same conditions as in Fig 8). Figure 9 is a backscattered electron image of a cross-section of the metal-scale interface. It shows a very thin oxide scale and a larger thickness of internal oxidation. The internal oxidation is primarily of aluminum and titanium. This kinetic data for this specimen are the points in Fig. 2 with the most mass loss. Figure 10 shows the Cr concentration profile measured using X-ray photoelectron spectroscopy (points) and the results of the model of Eqs. 12 and 16 with λ equal to 50 µm, δ equal to 0.5 nm (line), and k_e of 8.0×10^{-10} kg/m²s. This evaporation rate is the model prediction with an a_{Cr2O3} of 0.4. The model is a close fit to the measured points. Note that the use of 2000 hours in Fig. 10 is an approximation that overstates the time at temperature (each hourly cycle had a few minutes at lower temperatures). If the predicted evaporation rate using pure chromium is used (a_{Cr2O3} of 1), the predicted evaporation rate is 2.0×10^{-9} kg/m²s, and the model would predict too much Cr loss (a wt fraction of Cr of 0.05 at the surface).

The model curve in Fig 10 invoked an a_{Cr2O3} of 0.4. Is lowering the chromia activity valid? These alloys are not pure Ni-Cr alloys and have other alloying elements that oxidize, are mobile, and many times can be found on the outer surface of oxide scales—namely Ti and

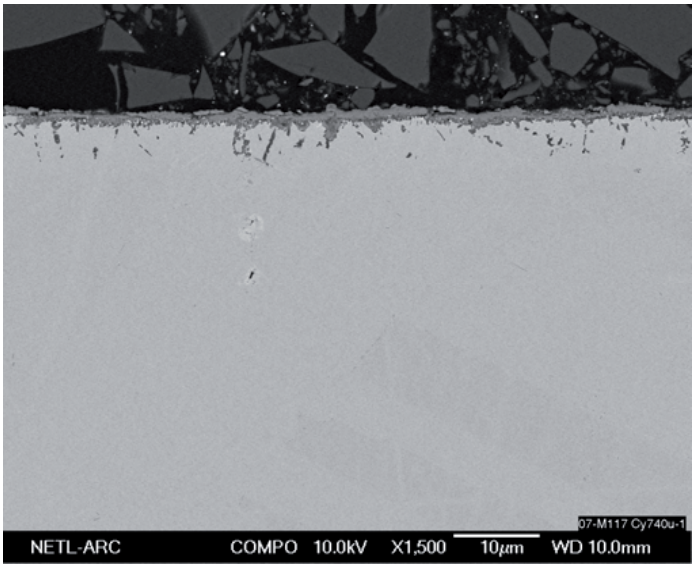

Fig. 9. Backscattered electron cross-section image after cyclic oxidation of Inconel 740 at 760 °C in air plus 37% H_2O after 2000 hourly cycles (Holcomb, 2009).

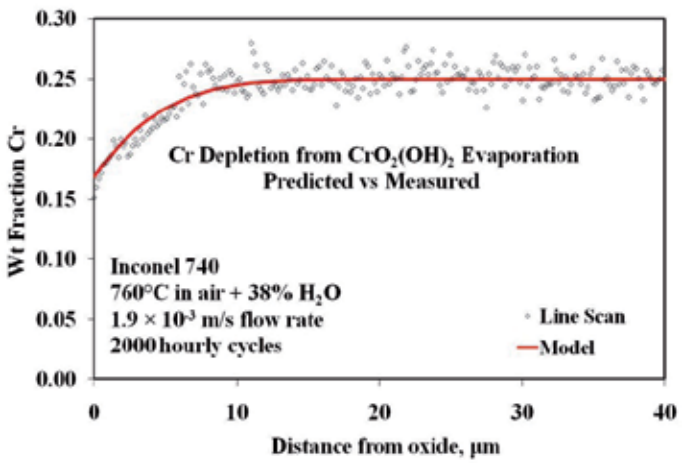

Fig. 10. Chromium depletion from cyclic oxidation of Inconel 740 at 760 °C in air plus 37% H_2O after 2000 hourly cycles. The individual points are from a line scan into the sample on the cross-section shown in Fig. 9 (Holcomb, 2009). The line results from the Eq. 12. The evaporation rate used in Eq. 12 was 8×10^{-10} kg/m^{2}s, which corresponds to an a_{Cr2O3} of 0.4.

Mn. For example, enough Mn additions to result in outer scales of Mn-Cr spinels instead of chromia is expected to reduce the evaporation of Cr by a factor of 55 at 700 °C and by a factor of 35 at 800 °C (Holcomb & Alman, 2006). This is equivalent to a chromia activity of 0.0006 at 760 °C. Prior work (Holcomb, 2009) showed that the higher evaporation rates shown by Haynes 230 and Inconel 740 corresponded to an a_{Cr2O3} value of 0.05. The use of 0.05 in the analysis used for Fig. 10 results in a predicted evaporation rate of 2.8×10^{-10}

kg/m²s, and a wt fraction of Cr of 0.22 at the surface. Since some of the Cr loss can be attributed to the non-evaporated chromia scale, the best value for a_{Cr2O3} lies between 0.05 and 0.4. Apparent a_{Cr2O3} values, based on the negative slope of the mass change data, are shown in Table 3 for each alloy and condition in this study. Most of the apparent a_{Cr2O3} values are within this range.

5. Hypothetical superheater-steam pipe-hp turbine steam path

The combination of gas evaporation of $CrO_2(OH)_2$, gas saturation of $CrO_2(OH)_2$, and Cr depletion in the alloy is illustrated in Fig. 11. Figure 11 represents one section of superheater (SH) tubing or steam pipe of cell length L. The bulk partial pressure of $CrO_2(OH)_2$ coming into the cell is $P_{CrO2(OH)2}°$ (Incoming). Evaporation within the cell at rate k_e raises the $P_{CrO2(OH)2}°$ (Outgoing) by the amount released by evaporation and is shown in Eq. 17.

$$P^{\circ}_{CrO_2(OH)_2}\,(\text{Outgoing}) = P^{\circ}_{CrO_2(OH)_2}\,(\text{Incoming}) + \frac{4k_e LRT}{duM_{CrO_2(OH)_2}} \tag{17}$$

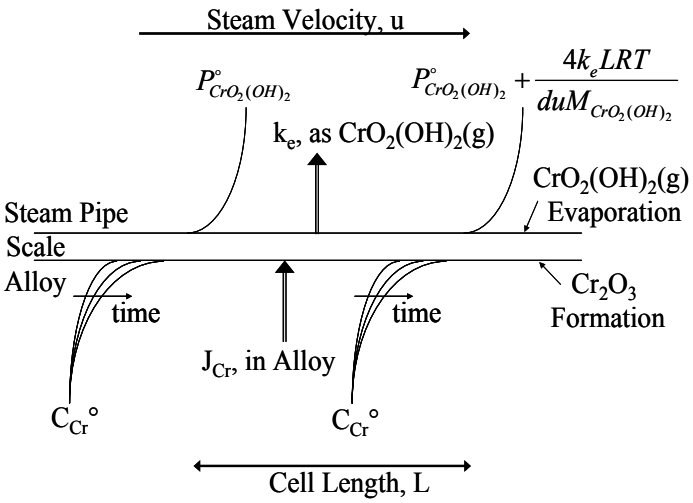

Fig. 11. The combination of gas evaporation of $CrO_2(OH)_2$, gas saturation of $CrO_2(OH)_2$, and Cr depletion in the alloy is illustrated. This represents one section of superheater tubing or steam pipe of cell length L (Holcomb, 2009).

The effects of saturating the gas phase with $CrO_2(OH)_2$ can then be calculated along the length of a SH tube or steam pipe by combining many cells together. A hypothetical arrangement of a 100 m long, 0.05 m I.D., SH that leads into a 50m long, 0.3 m I.D., steam pipe that leads to a high pressure (HP) turbine is illustrated in Fig. 12. The temperature profile and steam velocities are shown on the left-hand axis, while the evaporation rate is shown on the right-hand axis. The evaporation rate is based on an a_{Cr2O3} of 0.05. The SH and steam pipe each consisted of 160 cells of the type shown in Fig. 11. Saturation results in an 80% reduction in the evaporation rate at the HP turbine.The steam chemistry used in Fig. 12 and in subsequent calculations was based off of feedwater

treatments that are typical of once-through supercritical power plants, i.e., a pH of 8.0-8.5 controlled with ammonia additions (Babcock & Wilcox, 1992). At high temperatures, water undergoes dissociation to O_2 and H_2 to levels well above 1 ppb. To estimate the dissolved oxygen required for Eq. 1 at temperature and pressure, the program FactSage 5.5 (Bale et al., 2007) was used to first determine the amount of NH_3 required for a pH of 8.25 at 25°C: 34.5 ppb. This agreed well with the reported (Babcock & Wilcox, 1992) 20-65 ppb NH_3 used for pH control to 8.0 to 8.5. Next FactSage 5.5 was used to find the value of the fugacities of H_2O and O_2 for each temperature and pressure combination from water with 34.5 ppb NH_3. The use of fugacities instead of partial pressures made only a minor difference because the fugacity adjustments tended to cancel each other out.

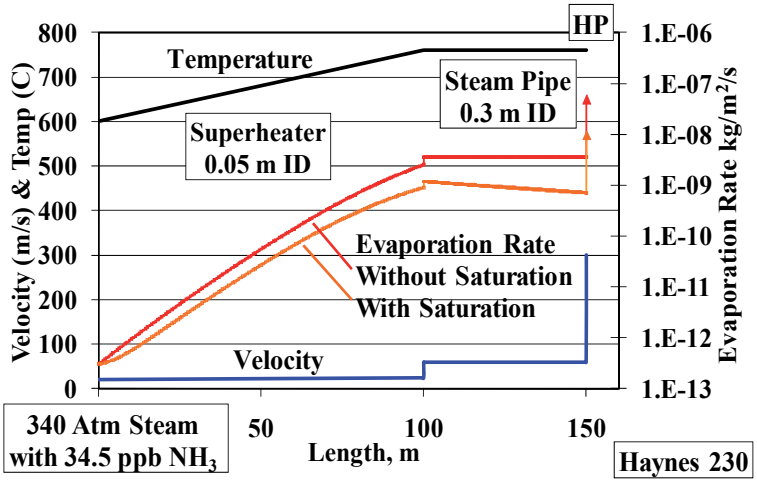

Fig. 12. The effects of gas saturation is shown for a hypothetical arrangement of a 100m long SH that leads into a 50m steam pipe that leads to a high pressure (HP) turbine. Saturation results in a 80% reduction in the evaporation rate at the HP turbine. An a_{Cr2O3} of 0.05 was used. Adapted from Holcomb (2009).

The time for the alloy Cr level to reach zero at the scale-metal interface, using Eq. 14, is shown in Fig. 13 for the same conditions as in Fig. 12 (and using saturated values for k_e). Haynes 230 was the alloy used. Under this simulation the chromia evaporation at the HP turbine blade is expected to be so great as to deplete the alloy surface of Cr in a few days. However, the very high rates of evaporation predicted at the HP turbine will likely be less than the model. The model is highly dependent upon the chromia activity term, especially in combination with the saturation effect. Should the higher evaporation rate at the HP lead to a lower chromia activity (while keeping the a_{Cr2O3} in the SH and steam pipe at 0.05) , then the equilibrium surface $P_{Cr2(OH)2}$ can easily drop below $P_{Cr2(OH)2}^{\circ}$, and thus stop chromia evaporation (Eq. 9). In this example (with the a_{Cr2O3} in the SH and steam pipe at 0.05), an a_{Cr2O3} in the HP turbine section of 0.032 would be sufficiently low enough to stop chromia evaporation in the HP turbine.

The very high temperatures and total pressures of Figs. 12-13 match that of the U. S. Department of Energy's goals of 760 °C and 340 atm. The impact of evaporation at lower temperatures and pressures can be seen in Figs. 14-15, where similar procedures are used to estimate the time it takes for the surface concentration of Cr in the alloy to reach zero. In all

cases the SH inlet temperature was taken to be 600 °C. Below 600 °C, ferritic alloys, which would not be expected to form chromia scales, would typically be used.

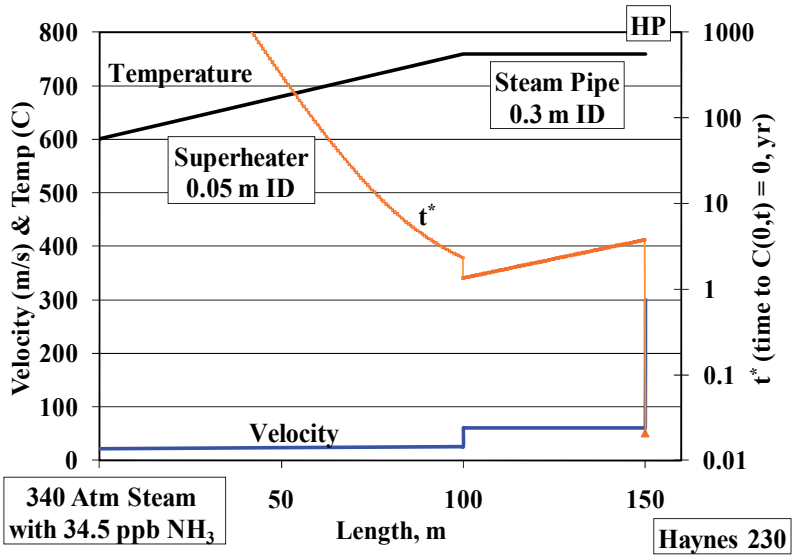

Fig. 13. The predicted time for the Cr level at the scale-metal interface to reach zero. Haynes 230 was the alloy system used in this estimate. An a_{Cr2O3} of 0.05 was used. Adapted from Holcomb (2009).

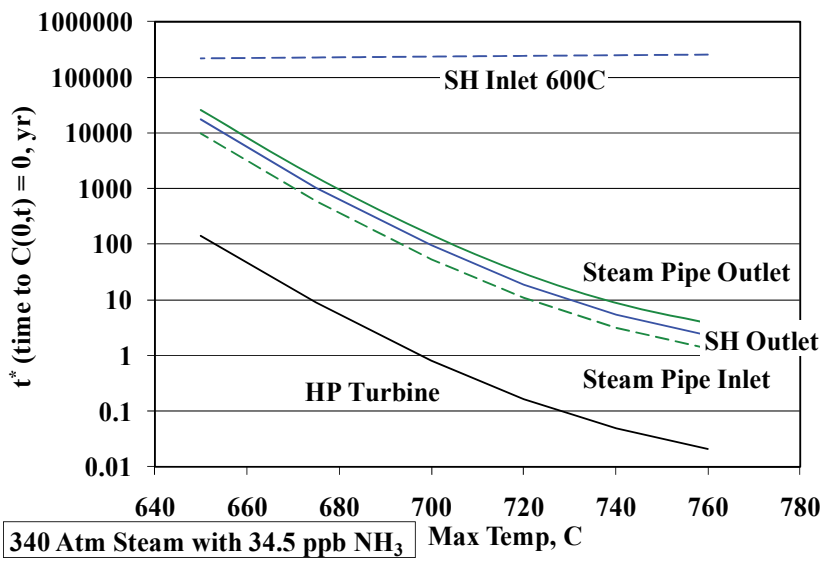

Fig. 14. The effects of temperature on the estimate of the time it takes for the surface concentration of Cr in the alloy to reach zero, at 340 atm. Haynes 230 was the alloy system used in this estimate. An a_{Cr2O3} of 0.05 was used. Adapted from Holcomb (2009).

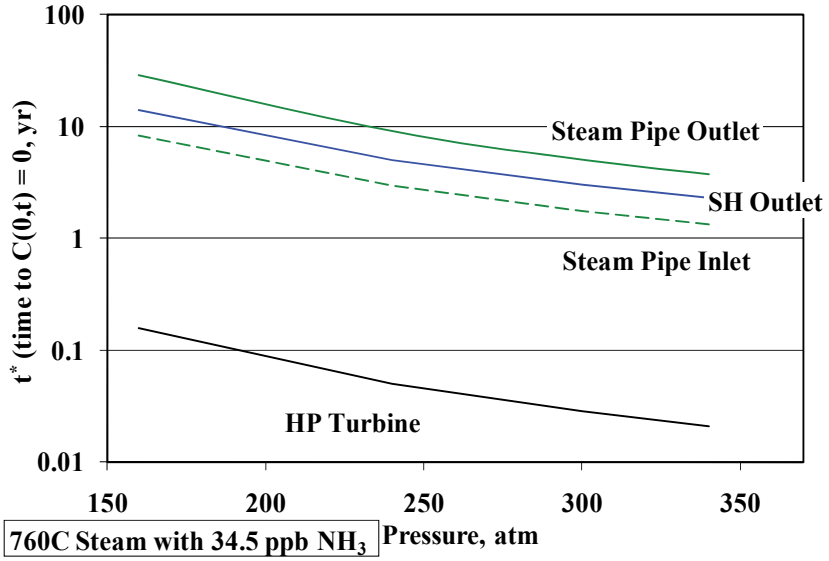

Fig. 15. The effects of pressure on the estimate of the time it takes for the surface concentration of Cr in the alloy to reach zero, at 760 °C. Haynes 230 was the alloy system used in this estimate. An a_{Cr2O3} of 0.05 was used. Adapted from Holcomb (2009).

Figure 14 shows why chromia evaporation is not considered to be of much concern in existing steam boilers and turbines. Modern advanced steam cycles are currently no higher than 630 °C, so the time to breakaway oxidation (for which the time for C(0,t) to reach 0 is being used as an estimate) is well beyond the life span of the boiler or turbine. Another factor limiting chromia evaporation in modern advance steam cycles is that ferritic steels are extensively used, and they do not form chromia scales. So the activity of Cr is lower in the scales, which from Eq. 1 lowers the partial pressure of $CrO_2(OH)_2(g)$, which in turn decreases chromia evaporation (Eq. 9).

6. Mitigation

As discussed in the Hypothetical Superheater-Steam Pipe-HP Turbine Steam Path section, relatively small changes in chromia activity at the oxide-steam interface can greatly influence the amount of chromia evaporation. For the alloys of interest, which contain Ti and/or Mn, large evaporation rates may be self-correcting as chromia is lost from the surface and concentrates Ti and Mn oxides (and thus reduces the chromia activity). Decreases in chromia activity along the steam path can result in little or no evaporation if the steam becomes saturated in $Cr_2(OH)_2$ relative to the lower surface $PCr_2(OH)_2$ that arises from the lower aCr_2O_3.

Another mitigation would be the use of a non-chromia forming coating. An example would be a thermal barrier coating (TBC), such as one based on yttria stabilized zirconia (YSZ). Such coatings are being postulated for use to reduce turbine blade erosion. This would eliminate the transport path for chromia evaporation. Even if the coating were porous, it would effectively increase the gaseous diffusion boundary layer to the thickness of the coating, thus eliminating much of the detrimental gas velocity effects.

7. Conclusions

A methodology was developed to calculate Cr evaporation rates from Cr_2O_3 with a flat planar geometry (Holcomb, 2008), was expanded upon to allow for interior cylindrical geometries, and to allow for the effects of $CrO_2(OH)_2$ saturation within the gas phase (Holcomb, 2009). This approach was combined with Cr diffusion calculations within the alloy (with a constant flux of Cr leaving the alloy from evaporation) to predict Cr concentration profiles as a function of exposure time and to predict the time until the alloy surface concentration of Cr reaches zero.

An important aspect of chromia evaporation in alloys of interest (that contain Mn and Ti) is the possibility of reduced chromia activity at the metal surface. A reduction in chromia activity will reduce chromia evaporation. It was found that increasing the gas flow rate led to increased chromia evaporation and decreased apparent chromia activity. Increasing the water content in the moist air increased the evaporation, but results were mixed with its effect on chromia activity.

A hypothetical super heater (SH) tube, steam pipe, and high pressure (HP) turbine steam path was assembled and examined with the methodology. At the U. S. Department of Energy's goals of 760 °C and 340 atm, the time until breakaway oxidation was predicted to be quite short for the turbine blade, and of concern within the steam pipe and the higher temperature portions of the SH tube. The predicted time until breakaway oxidation increases dramatically with decreases in temperature and total pressure. However, it was shown that chromia activity variability within the steam path (i.e., chromia activity in the HP lower than that in the SH/steam pipe) could reduce or eliminate chromia evaporation. The steam could become saturated in $Cr_2(OH)_2$ relative to the lower partial pressure of $Cr_2(OH)_2$ at the metal surface (lowered by the lower chromia activity). Thus the higher expected chromia evaporation rates in the HP section could be self-mitigating as the loss of chromia from the scale, which increases the relative amounts of Ti and Mn oxides) reduces the chromia activitiy at the oxide surface.

8. References

Asteman, H., Svensson, J.-E., Johansson, L.-G. & Norell, M. (1999). Indication of Chromium Oxide Hydroxide Evaporation during Oxidation of 304L at 873 K in the Presence of Water Vapor. *Oxidation of Metals*, Vol. 52, Nos. 1-2, (August 1999), pp. 95-111, ISSN 0030-770X.

Asteman, H., Svensson, J.-E., Norell, M., & Johansson, L.-G. (2000). Influence of Water Vapor and Flow Rate on the High Temperature Oxidation of 304L; Effect of Chromium Oxide Hydroxide Evaporation. *Oxidation of Metals*, Vol. 54, Nos. 1-2, (August 2000), pp. 11-26, ISSN 0030-770X.

Bale, C.W., Pelton, A.D., Thompson, W.T., Eriksson, G., Hack, K., Chartrand, P., Decterov, S., Melançon, J. & Petersen, S. (2007). FactSage 5.5, Thermfact and GTT-Technologies (2007).

Bird, R.B., Stewart, W.E. & Lightfoot, E.D. (1960). *Transport Phenomena*, John Wiley & Sons, ISBN 0-471-41077-2, New York.

Essuman, E., Meier, G.H., Żurek, J., Hänsel, M. & Quadakkers, W. J. (2008). The Effect of Water Vapor on Selective Oxidation of Fe-Cr Alloys. *Oxidation of Metals*, Vol. 69, Nos. 3-4, (April, 2008), pp. 143-162, ISSN 0030-770X.

Fuller, E.N., Schettler, P.D. & Giddings J.C. (1966). *Industrial & Engineering Chemistry*, Vol. 58, No. 5, (May, 1966), pp. 19-27, ISSN 1226-086X.

Gaskell, D.R. (1992). *An Introduction to Transport Phenomena in Materials Engineering*, Macmillan Publishing, ISBN 0-02-340720-4, New York.

Gindorf, C., Hilpert, K., & L. Singheiser, L. (2001). Determination of Chromium Vaporization Rates of Different Interconnect Alloys by Transpiration Experiments, In: *Solid Oxide Fuel Cells (SOFC VII)*, Yokokawa, H. & Singhal, S.C. (Eds.), PV 2001-16, pp. 793-802, The Electrochemical Society Proceedings Series, ISBN 978-1-56677-322-5 Pennington, NJ.

Graham, H.C. & Davis, H.H. (1971). Oxidation/Vaporization Kinetics of Cr_2O_3. *Journal of the American Ceramic Society*, Vol. 54, No. 2, (February 1971), pp. 89-93. ISSN 0002-7820.

Haynes International. (2008a). Haynes 230 Alloy, H-3135C, Haynes International, Kokomo, IN.

Haynes International. (2008b). Haynes 282 Alloy, H-3172A, Haynes International, Kokomo, IN.

Holcomb, G.R. (2008). Calculation of Reactive-Evaporation Rates of Chromia. *Oxidation of Metals*, Vol. 69, Nos. 3-4, (April 2008), pp. 163-180, ISSN 0030-770X.

Holcomb, G.R. (2009). Steam Oxidation and Chromia Evaporation in Ultrasupercritical Steam Boilers and Turbines. *Journal of the Electrochemical Society*, Vol. 156, No. 9, (September, 2009), pp. C292-C297. ISSN 0013-4651.

Holcomb, G.R. & Alman, D.E. (2006). Effect of Manganese Additions on the Reactive Evaporation of Chromium in Ni-Cr Alloys, *Scripta Materialia*, Vol. 54, No. 10, (May, 2006), pp. 1821-1825, ISSN 1059-9495.

Holcomb, G.R., Alman, D.E., Doğan, Ő.N., Rawers, J.C., Schrems, K.K. & Ziomek-Moroz, M. (2007). Steam Turbine Materials and Corrosion. *Proceedings of the 21st Annual Conference on Fossil Energy Materials*, Knoxville, TN, April 30-May 1, 2007.

Incropera, F.P. & DeWitt, D.P. (2001). *Fundamentals of Heat and Mass Transfer* (5th edition)., John Wiley & Sons, ISBN 978-0471386506, New York.

Kubaschewski, O. & Alcock, C.B. (1979). *Metallurgical Thermochemistry* (5th edition), Pergamon Press, ISBN 0080221076, New York.

Masuyama, F. (2001). History of Power Plants and Progress in Heat Resistant Steels, *ISIJ International*, Vol. 41, (June, 2001), No. 6, pp. 612-625, ISSN 0915-1559.

Meier, G.H., Jung, K., Mu, N., Yanar, N.M., Pettit, F.S., Abellán, J.P., Olszewski, T., Quadakkers, W.J. & Holcomb, G.R. (2010). Effect of Alloy Composition and Exposure Conditions on the Selective Oxidation Behavior of Ferritic Fe-Cr and Fe-Cr-X Alloys. *Oxidation of Metals*, Vol. 74, Nos. 5-6, (November-December, 2010), pp. 319-340, ISSN 0030-770X.

Opila, E.J., Myers, D.L., Jacobson, N.S., Nielsen, I.M.B., Johnson, D.F., Olminsky, J.K. & Allendorf, M. D. (2007). Theoretical and Experimental Investigation of the Thermochemistry of CrO2(OH)(2)(g). *Journal of Physical Chemistry A*, Vol. 111, No. 10, (October 2007), pp. 1971-1980, ISSN 1089-5639.

Paul, A.R., Kaimal, K.N.G., Naik, M.C. & Dharwadkar, S.R. (1994). Lattice and Grain Boundary Diffusion of Chromium in Superalloy Incoloy-800. *Journal of Nuclear Materials*, Vol. 217, (November, 1994), Nos. 1-2 pp. 75-81, ISSN 0022-3115.

Peng, X., Yan, J., Zhou, Y. & Wang, F. (2005). Effect of Grain Refinement on the Resistance of 304 Stainless Steel to Breakaway Oxidation in Wet Air. *Acta Materialia*, Vol. 53, No. 19, (November, 2005), pp. 5079-5088, ISSN 1359-6454.

Pettit, F.S. & Meier, G.H. (2006). Fundamental Studies of the Durability of Materials for Interconnects in Solid Oxide Fuel Cells, Final Report, DOE Award: DE FC26 02NT41578.

Petukhov, B.S. (1970). Heat Transfer and Friction in Turbulent Pipe Flow with Variable Physical Properties, In: *Advances in Heat Transfer*, Vol 6, Irvine, T.F. & Hartnett, J.P. (Eds.), p. 503-564, Academic Press, ISBN 978-0120200061, New York.

Royal Institute of Technology, Foundation of Computational Thermodynamics. (1999). MOB2, Mobility Database, Version 2.0, Royal Institute of Technology, Foundation of Computational Thermodynamics, Stockholm, Sweden.

Saunders, N. (2000). Ni-DATA, Version 7, Thermotech Ltd, Surrey, UK.

Slattery, J.C. & Bird, R.B. (1958). *American Institute of Chemical Engineers Journal*, Vol. 4, No. 2, (june, 1958), pp. 137-142, ISSN 0001-1541.

Special Metals Corporation. (2004a). Inconel Alloy 740, SMC-090, Special Metals Corporation, Huntington, WV.

Special Metals Corporation. (2004b). Nimonic Alloy 263, SMC-054, Special Metals Corporation, Huntington, WV.

Special Metals Corporation. (2005). Inconel Alloy 617, SMC-029, Special Metals Corporation, Huntington, WV.

Special Metals Corporation. (2006). Inconel Alloy 625, SMC-063, Special Metals Corporation, Huntington, WV.

Stultz, S.C. & Kitto, J.B. (Eds.) (1992). *Steam* (40th edition), Babcock & Wilcox, ISBN 0963457004, Barberton, Ohio.

Tedman, C.S., Jr. (1966). The Effect of Oxide Volatilization on the Oxidation Kinetics of Cr and Fe-Cr Alloys. *Journal of the Electrochemical Society*, Vol. 113, No. 8, (August 1966), pp. 766-768, ISSN 0013-4651.

Thermo-Calc Software AB. (2006). Dictra, Diffusion Simulation Software, Version 24, Thermo-Calc Software AB, Stockholm, Sweden.

Viswanathan, R., Henry, J.F., Tanzosh, J., Stanko, G., Shingledecker, J., Vitalis, B & Purgert, R. (2005). U.S. Program on Materials Technology for Ultra-Supercritical Coal power Plants. *Journal of Materials Engineering and Performance*, Vol. 14, No. 3, (June 2005), pp. 281-292, ISSN 1059-9495.

Whittle, D.P., Evans, D.J., Scully, D.B. & Wood, G.C. (1967a). Compositional Changes in the Underlying Alloy during the Protective Oxidation of Alloys. *Acta Metallurgica*. Vol. 15, No. 9, (September, 1967), pp. 1421-1430, ISSN 1359-6454.

Whittle, D.P., Wood, G.C., Evans, D.J. & Scully, D.B. (1967b). Concentration Profiles in the Underlying Alloy during the Oxidation of Iron-Chromium Alloys. *Acta Metallurgica*, Vol. 15, No. 11, (November, 1967), pp. 1747-1755, ISSN 1359-6454.

Winterton, R.H.S. (1998). Where did the Dittus and Boelter Equation Come From? *International Journal of Heat and Mass Transfer*, Vol. 41, Nos. 4-5, (February-March, 1998), pp. 809-810, ISSN 0017-9310.

Wright, A.I.G. & Tortorelli, P.F. (2007). Program on Technology Innovation: Oxide Growth and Exfoliation on Alloys Exposed to Steam, Report 1013666, EPRI, Palo Alto, CA.

Young, D.J. & Pint, B.A. (2006). Chromium Volatilization Rates from Cr_2O_3 Scales into Flowing Gases Containing Water Vapor. *Oxidation of Metals*, Vol. 66, Nos. 3-4, (October, 2006), pp. 137-153, ISSN 0030-770X.

10

Thermohydrodynamics: Where Do We Stand?

L. S. García–Colín[1,2], J. I. Jiménez–Aquino[1] and F. J. Uribe[1]
[1]*Universidad Autónoma Metropolitana – Iztapalapa*
[2]*El Colegio Nacional. Centro Histórico, México D. F.*
México

1. Introduction

The subjects selected to conform the content of this chapter have beem chosen following two main criteria. Firstly, subjects which are of great interest today in the field of thermohydrodynamics. Secondly, they are neither well understood nor we can regard them as fully developed. Many aspects in their own structure pose very deep and interesting questions whose answers are yet to be obtained. Indeed when closely examined one finds rather surprising results. Start with magnetohydrodynamics. When in a charged fluid ordinary hydrodynamics is coupled with Maxwell's equations using the conventional form of Ohm's equation an assumption lies behind which is hardly sustained with the results obtained in kinetic theory. Further, if the fluid is viscous such coupling becomes much more sophisticated a fact that it is hardly noticed in the current literature.
A similar situation occurs with shock waves when in spite of the fact Euler's equations are well known not to provide a correct description of the structure of a shock wave, they are still used in many applications. The use of the Navier–Stokes and higher order hydrodynamics equations seeking a more accurate description of shock waves is full of loopholes which we hope to bring to the attention of the reader.
On the other hand quantum hydrodynamics, a field long ignored by both physicists and hydrodynamicists is becoming more and more demanding specially due to the experimental results in relativistic heavy ion collisions (RHIC) and in the study of non–equilibrium properties of very cold Bose and Fermi gases. Indeed, one can safely assert that quantum hydrodynamics has never been correctly formulated.
The last topic we chose to discuss is currently referred to as Stochastic Thermodynamics and/or Fluctuation Theorems. This field pretends to extrapolate well established results in Thermostatics as well as in near–equilibrium thermodynamics in the study of small (nanoscale) systems. The two fundamental problems we see here is, firstly, the validity of the use of well defined macroscopic concepts to very small systems. This requires caution. Secondly, the abuse of the thermodynamic languaje in these systems is rather confusing. For instance, entropy is a state function only defined for equilibrium states of macrosystems or in near equilibrium states as required in linear non–equilibrium thermodynamics (LIT). Far away from equilibrium entropy is not defined and entropy production which is unfortunately adopted instead of Clausius uncompensated heat is only meningful in (LIT). In this part of the review we insist in placing the enormous amount of results so far obtained in a more adequate language. This will avoid misconceptions as well as misundertandings.

2. Magnetohydrodynamics

In order to get a clear picture of what we are going to understand by magnetohydrodynamics, it is convenient to recall the methodology that lies behind the derivation of the equations of ordinary hidrodynamics. We consider a single fluid whose thermodynamic states are described by five locally conserved variables, $\rho(\mathbf{r},t)$ the mass density, $\rho(\mathbf{r},t)\,\mathbf{u}(\mathbf{r},t)$ the momentum density, and $\rho(\mathbf{r},t)\,e_{_T}(\mathbf{r},t)$ the total energy density. These equations satisfy the five well-known conservation equations, needless to be written down here. These equations contain fourteen unknowns, three for the energy flux, six for the momentum flux (assuming fluid is isotropic) and the five state variables. To turn them into a complete set of equations one needs to introduce nine so called constitutive equations, expressing the fluxes in terms of the state variables. For an ideal (non-viscous) fluid one readily obtains the well known Euler equations, the lowest order equations including dissipative effects are the Navier–Stokes–Fourier equations an so on.

If one now considers that the fluid is charged, then when set in motion its charge and current densities will generate an electromagnetic field which, through Maxwell's equations couples with the fluid's own hydrodynamic equations, giving rise to what is usually referred as the equations of magnetohydrodynamics. Yet the resulting equations are not closed. Constitutive equations must be supplied for all the resulting fluxes which arise from such coupling. Further, the state variables are now enlarged in number due to the presence of the charged particles. In the simplest case, say, the fluid consisting of electrons and ions, we must account for their corresponding densities. Needless to say that the resulting equations will be far more complicated that the ones for the ordinary fluid, a reason which, in our opinion, has given rise to some misunderstandings in the rich literature on the subject Alfven (1963); Balescu (1988); Braginskii (1965); Chandrasekhar (1960); Cowling (1957); García–Colín & Dagdug (2009); Jackson (1962); Kulsrud (2005); Spitzer (1956); Van Kampen & Felderhof (1967), including their kinetic theoretical foundations.

Consider a charged fluid consisting of electrons and ions of masses m_e and m_i, respectively, whose number densities are n_i and n_e respectively. Then $\rho = n_e\, m_e + n_i\, m_i = \rho_e + \rho_i$ and the conservation equations read

$$\frac{\partial \rho}{\partial t} + \nabla\cdot(\rho\,\mathbf{u}) = 0, \tag{1}$$

$$\frac{\partial}{\partial t}(\rho\,\mathbf{u}) + \nabla\cdot(\rho\,\mathbf{u}\,\mathbf{u} + \boldsymbol{\tau}) = Q\,(\mathbf{E} + \mathbf{u}\times\mathbf{B}) + \mathbf{J}_c\times\mathbf{B}, \tag{2}$$

$$\rho\,\frac{\partial \epsilon}{\partial t} + \nabla\cdot\mathbf{J}_q + \boldsymbol{\tau} : (\nabla\mathbf{u})^s + \mathbf{J}_{_T}\times\mathbf{B} = 0, \tag{3}$$

where $\mathbf{u}(\mathbf{r},t)$ is the fluid's velocity, $\boldsymbol{\tau} = p\,\mathbb{I} + \boldsymbol{\tau}^v$, p being the hydrostatic pressure and $\boldsymbol{\tau}^v$ the symmetric viscous tensor, ϵ is the internal energy per unit mass, $\mathbf{J}_q$ the heat flux, $\mathbf{J}_c$ the conduction current, and $\mathbf{J}_{_T}$ the total current. Here $Q = n_i\,c_i + n_e\,c_e = (n_i - n_e)\,e$ and

$$\mathbf{J}_{_T} = Q\,\mathbf{u} + \mathbf{J}_c = Q\,\mathbf{u} + \frac{m_e + m_i}{m_i\,m_e}\,e\,\mathbf{J}_e^{(m)} \tag{4}$$

where $\mathbf{J}_e^{(m)}$ is the mass current for the electrons. We recall that $\mathbf{J}_e + \mathbf{J}_i = 0$. Maxwell's equations in the MKS system are,

$$\nabla\cdot\mathbf{E} = \frac{1}{\epsilon_0}\,Q, \quad \nabla\cdot\mathbf{B} = 0, \tag{5}$$

$$\nabla \times \mathbf{E} = -\frac{\partial \mathbf{B}}{\partial t}, \quad -\mu_0 \epsilon_0 \frac{\partial \mathbf{E}}{\partial t} + \nabla \times \mathbf{B} = \mu_0 \mathbf{J}_T. \tag{6}$$

Notice that the currents $\mathbf{J}_q, \boldsymbol{\tau}^v, \mathbf{J}_e^{(m)}$ (or $\mathbf{J}_c$) require to be expressed in terms of the state variables ρ_e, ρ_i, $\mathbf{u}$, and ϵ through still unknown constitutive equations through eqs. (2) and (3).
In order to simplify the problem several approximations are introduced. Firstly the temperatures of electrons and ions is taken to be the same, $T_i = T_e = T$ a fact which is readily justified Moratto & García–Colín (2011). Next we define the hydrodynamic time τ_H^α and the hydrodynamic lenght l_H as follows,

$$\frac{1}{\tau_H^\alpha} \approx \frac{v_\alpha}{l_H}, \quad v_\alpha = \sqrt{\frac{2\,k_B\,T}{m_\alpha}}, \quad \alpha = 1, e, \tag{7}$$

k_B being Boltzmann's constant and

$$l_H^{-1} = Max \frac{|\nabla A(\mathbf{r},t)|}{|A(\mathbf{r},t)|}, \tag{8}$$

where A is ρ,$\mathbf{u}$ or T.
We now assume that both l_H and τ_H are the characteristic length and time scales of $\mathbf{E}$ and $\mathbf{B}$. Then several approximations follow Balescu (1988); García–Colín & Dagdug (2009):

$$|\frac{\partial \mathbf{E}}{\partial t}| \approx \frac{u^2}{c^2} |\nabla \times \mathbf{B}| \approx 0, \quad \textit{in a non relativistic plasma.} \tag{9}$$

This is a tricky approximation. By eq. (6) it implies that

$$\nabla \times \mathbf{B} = \mu_o \mathbf{J}_T, \tag{10}$$

or that

$$\nabla \cdot \mathbf{J}_T = 0. \tag{11}$$

But since total charge is conserved, the balance equation

$$\frac{\partial Q}{\partial t} + \nabla \cdot \mathbf{J}_T = 0, \tag{12}$$

must be obeyed which implies that $\frac{\partial Q}{\partial t} = 0$. Consistency may be achieved if local neutrality is satisfied namely Balescu (1988),

$$|n_e(\mathbf{r},t) - n_i(\mathbf{r},t)| \leq \frac{1}{2}\Big(n_e(\mathbf{r},t) + n_i(\mathbf{r},t)\Big), \tag{13}$$

in which case $Q \approx 0$ in **all** hydrodynamic equations.
This leads to the so called pre–Maxwell's equations $|\frac{\partial \mathbf{E}}{\partial t}| \approx 0$ and $Q\,\mathbf{E}$ is supressed. Moreover, it is also assumed that since $Q \approx 0$ then

$$Q\,\mathbf{u} << \mathbf{J}_c, \tag{14}$$

which implies that pre–Maxwell's equations read as

$$\nabla \cdot \mathbf{E} = 0, \tag{15}$$

$$\nabla \times \mathbf{E} = -\frac{\partial \mathbf{B}}{\partial t}, \quad \nabla \times \mathbf{B} = \mu_0 \mathbf{J}_T, \tag{16}$$

subject to the condition that $\nabla \cdot \mathbf{J}_c = 0$.
This fact is very often ignored or by–passed in many treatises on the subject. If we assume that $\mathbf{J}_c$ is determined through Ohm's law, which as we will see below is already incorrect, then

$$\mathbf{J}_c = Q\left(\mathbf{E} + \frac{1}{\mu_0}\mathbf{u}\times\mathbf{B}\right) = \frac{Q}{\mu_0}(\mathbf{u}\times\mathbf{B}), \tag{17}$$

which implies that (eq. (16))

$$-\nabla\times\mathbf{B} = Q(\mathbf{u}\times\mathbf{B}) \tag{18}$$

or

$$\nabla\cdot(\mathbf{u}\times\mathbf{B}) = 0, \tag{19}$$

which is consistent with eq. (11). But also,

$$\nabla\cdot(\mathbf{u}\times\mathbf{B}) = \mathbf{B}\cdot\nabla\times\mathbf{u} - \mathbf{u}\cdot\nabla\times\mathbf{B} \tag{20}$$

or using eq. (18)

$$\mathbf{B}\cdot\nabla\times\mathbf{u} = Q\,\mathbf{u}\cdot(\mathbf{u}\times\mathbf{B}) = 0. \tag{21}$$

This implies that, in general $\nabla\times\mathbf{u} = 0$ or that the flow is always irrotational, which in turn implies the fluid is non–viscous. Whence, $\boldsymbol{\tau}^v = 0$ a fact that not always is clearly pointed out in many applications. Yet eq. (17) as such is completely incorrect. This is manifestly exhibited by kinetic theory Balescu (1988); Braginskii (1965); García–Colín & Dagdug (2009).
To avoid unnecessary and lengthy repetitions we will explicitly consider the properties of vectorial currents, $\mathbf{J}_i^{(m)}$ and $\mathbf{J}_q$ but concentrate on the former one since identical properties are associated with the second one. Notice that from eq. (4) whatever we say about $\mathbf{J}_e^{(m)}$ applies to $\mathbf{J}_c$ since $m_i >> m_e$ and $\mathbf{J}_c = (e/m_e)\mathbf{J}_e^{(m)}$. Now, consider a fluid in which the magnetic vector $\mathbf{B}$ is along the z–axis, $\mathbf{B} = |B|\hat{\mathbf{k}}$. Any vectorial current has now three different components, one along the z–axis, one lying in a plane, the xy plane perpendicular to $\mathbf{B}$ and a third one which lies on a plane perpendicular to both, the z–axis and the xy plane. The two vectorial forces associated with vectorial fluxes are ∇T and $\mathbf{d}_{ie}$ where

$$\mathbf{d}_{ie} = \nabla\left(\frac{n_e}{n}\right) + \frac{n_i n_e(m_i - m_e)}{n\,\rho}\frac{\nabla p}{p} + \frac{n_i n_e}{p\,\rho}(m_i e + m_e e)\,\mathbf{E}', \tag{22}$$

is the diffusive force and $\mathbf{E}' = \mathbf{E} + \mathbf{u}\times\mathbf{B}$. If $n_i + n_e = \frac{n}{2}$ and we neglect the term with ∇p which is usually very small,

$$\mathbf{d}_{ie} = \frac{n^2}{p\,\rho}\,m_i e\,\mathbf{E}', \tag{23}$$

ignoring also the temperature gradients which give rise to the Thomson effect systematically ignored in plasma physics. This implies that $\mathbf{J}_c$ may be written as (see refs. citemb8,mb10)

$$\mathbf{J}_c = \sigma_{\parallel}E_z\,\hat{\mathbf{k}} + \sigma_{\perp}(E_x\,\hat{\mathbf{i}} + E_y\,\hat{\mathbf{j}}) + \sigma_s(\mathbf{E} + \mathbf{u}\times\mathbf{B}), \tag{24}$$

where the three conductivities are explicitly given in terms of molecular parameters but we do not need them here explicitly. Equation (24) would be the canonical form of Ohm's law we repeat, ignoring pressure diffusion and Thomson's thermoelectric terms. Now compare eqs. (17) and (24). They would be identical if $\sigma_{\parallel} = \sigma_{\perp} = 0$ and $\sigma_s = \sigma_{\parallel}$ which is completely wrong.

Even if we neglect $\mathbf{E}$, σ_s is not by any chance the same as $\sigma_\parallel$ as clearly exhibited in refs. Balescu (1988) and García–Colín & Dagdug (2009).
A second critique arises from the use of pre-Maxwell's equations (15) and (16) subject to the condition that $\nabla \cdot \mathbf{J}_c = 0$. $\mathbf{J}_c$ is the outcome of the presence of all the thermodynamic forces present in the system ∇, ∇p, $\nabla \frac{n_i}{n}$, and $\mathbf{d}_{ie}$. To assert that in general $\nabla \cdot \mathbf{J}_c = 0$ is ridiculous. Even if $\mathbf{B} = 0$ one can show that García–Colín & Dagdug (2009)

$$\nabla \cdot \mathbf{J}_c = -\sigma_\parallel \nabla^2 \phi - \tau_\perp \nabla^2 T, \tag{25}$$

where $\tau_\perp$ is a thermal conductivity. Equation 25 set equal to zero, in general, cannot be satisfied unless $\nabla\phi$ and ∇T acted in a rather peculiar way.
As a third, and last critique we will mention here, concerns magnetohydrodynamics at the level of Euler's equations. Assuming $Q|\mathbf{E}| << 1$, Euler's equations read,

$$\frac{\partial \rho_a}{\partial t} = -\nabla \cdot (\rho_a \, \mathbf{u}), \quad a = i, e. \tag{26}$$

$$\rho \, \frac{\partial \mathbf{u}}{\partial t} = -\rho \, \mathbf{u} \cdot \nabla \mathbf{u} - \nabla p + \mathbf{J}_c \times \mathbf{B}, \tag{27}$$

$$\rho \, \frac{\partial T}{\partial t} = -\left(\mathbf{u} \cdot \nabla T + \frac{2\,p}{3\,n\,k_B} \nabla \cdot \mathbf{u} \right). \tag{28}$$

The full expression for $\mathbf{J}_c$ in the absence of viscosity is still required at this level! In this canonical form they are never used in the literature, except by setting $\mathbf{J}_c = 1/\mu_0 \nabla \times \mathbf{B}$ but even if this expression is substituted in equation (27) one still needs the complete form for Jc to obtain $\mathbf{B}$. Needless to say that if viscous effects are present the whole magnetohydrodynamic scheme becomes much more complicated and even for dilute gases, it appears that it has never been given its appropriate status. Just to mention one significative result, the stress tensor in the presence of a magnetic field is considerably modified giving rise to five viscosities, which are not always negligible when compared with the one that is not affected by the field, the standard shear viscosity of hydrodynamics. Details of these results are discussed in the literature Balescu (1988); Braginskii (1965); García–Colín & Dagdug (2009) but they have been completely ignored. The literature on magnetohydrodynamics and plasma physics is overwhelming, in the partial list here provided more references can be found.

3. Shock waves

In the previous section some problems associated with magnetohydrodynamics (MHD) have been pointed out, so the reader may get the impression that for the case when there are no electromagnetic fields the situation is different, but there are cases in which the situation is far from being solved. Turbulence, sometimes referred as the last unsolved problem in classical physics, is an example in which the Navier–Stokes equations are used and their linearization destroys the problem Holmes et al. (1998). Therefore, turbulence is a genuine non linear problem but there are others like shock waves for which it is necessary to improve hydrodynamics beyond the Navier–Stokes description. For shock waves the Euler equations do not provide a strong solution (differentiable) and mathematicians have used the theory of weak solutions; these are discontinuous solutions or solutions in the sense of the theory of distributions developed by L. Schwartz Richtmyer (1978). In the Russian literature they are known as generalized functions and, as far we know, were introduced in physics by P.

Dirac (but perhaps the original idea goes back to Fourier). The famous Dirac's delta is an example of a "distribution" and it took a while to put it in a proper mathematical context. In the introduction of a book by von Neumann (1955) the reader can find a critique about distributions *a la* Dirac. From our point of view fluids are not ideal and the introduction of transport coefficients is necessary if one is interested in modeling nature properly. Therefore, we consider the Navier–Stokes equations as more appropriate than the Euler equations. In this sense the point of considering weak solutions is not important for us and we visualize this as a manifestation of the superiority of the physical content of the Navier–Stokes equations when compared to the Euler equations [1]. The reader may argue that at low temperatures He^4 or He^3 behave as fluids without viscosity (also Bose–Einstein condensates in dilute gases) so that the Euler equations should be relevant in this case. This is indeed a true but incomplete statement since according to Tisza and Landau the proper hydrodynamic description is in terms of two fluids: the normal fluid that has viscosity, and the superfluid that has no viscosity. Tieza–Landau's two fluid hydrodynamics is discussed in the next section on quantum hydrodynamics where the connection between quantum physics and classical hydrodynamics is also mentioned.

Apart from being a non linear problem, so that the whole set of equations of a theory are tested and not only its linearizations, shock waves are interesting in other aspects. For example, in astrophysics shock waves are found in many of the most spectacular events of nature Piran (2004); Woosley et al. (2002). They are generated in: explosions and detonations Fickett & Davis (2000); Zel'dovich & Raizer (2002), shock tubes Fomin (2010); Zel'dovich & Raizer (2002), appear in: traffic flow Helbing (2001), sonoluminescence Brenner et al. (2002), inertial confinement Goncharov et al. (2006), and when vehicles enter the atmosphere of the earth or other planets Gnoffo (1999).

Classical hydrodynamics, or hydrodynamics for short in this section, was born as a continuum theory. The atomistic point of view of hydrodynamics, when available, can provide explicit expressions for the transport coefficients for an assumed interaction potential between the atoms (either analytically or numerically), so that one does not have to measure or guess them. Also, for simple systems like dilute gases the equation of state and caloric equation of state are known so that disagreement between theory and experiment (or simulations) point to inadequacies of the theory and not to incorrect transport coefficients or equations of state. This is the advantage of considering dilute gases where as a bonus the kinetic description provided by the Boltzmann equation is applicable (which, as far we know, physicists and mathematicians agree that it provides a sound description). The phenomenological derivation of the hydrodynamic equations is well documented in textbooks Currie (1974); Landau (1986), to mention just two among many others; the advantage of such derivation is that it applies to gases and liquids (fluids in general); its weakness (so to speak) is that the transport coefficients have to be determined from experiments, theory, or simulations. The most successful microscopic derivation of the Navier–Stokes equations that we know is that provided by using the Chapman–Enskog method Chapman & Cowling (1970) to solve the Boltzmann equation

[1] It should be pointed out that being in a sense simpler than the Navier–Stokes, the Euler equations have perhaps a richer (perhaps simpler) mathematical structure and therefore quite a lot can be said from them, even for the MHD case. The book by V. I. Arnold is just an example Arnold (1998). On the other hand the one million dollar prize voiced by the Clay Mathematics Institute is for the Navier–Stokes equations only, but it is important to mention that Fefferman (2000) points out the relevance of Leray's existence theorem of weak solutions to the Navier–Stokes equations for tackling the problem of their existence and smooth solutions.

[2]. Other books where one can find discussions about the Chapman-Enskog, Hilbert's method, and extensions for dilute polyatomic gases are: Cercignani (1988), Ferziger & Kaper (1972), McCourt et al. (1990), Grad (1958), Résibois & De Leener (1977), Sone (2002), and Struchtrup (2005), among others. The weakness (so to speak) of the microscopic approach is that its restriction to the very simple dilute gas leaves outside of its scope wealth of applications. In this section we will be concerned with some attempts to go beyond standard hydrodynamics using both the macroscopic and microscopic approaches.

In order to understand the aspects of the shock wave problem we consider the dilute gas where Boltzmann equation is available. For simplicity let us consider a plane shock wave so that the hydrodynamic variables are functions only of x, the position along the shock wave propagation, and time. The conservation equations for mass, momentum, and energy are the following Chapman & Cowling (1970):

$$\frac{\partial}{\partial t}\rho\left(x,t\right)+\frac{\partial}{\partial x}\left(\rho\left(x,t\right)u\left(x,t\right)\right)=0, \tag{29}$$

$$\rho\left(x,t\right)\left(\frac{\partial}{\partial t}u\left(x,t\right)+u\left(x,t\right)\frac{\partial}{\partial x}u\left(x,t\right)\right)=-\frac{\partial}{\partial x}P_{xx}\left(x,t\right), \tag{30}$$

$$\rho\left(x,t\right)\left(\frac{\partial}{\partial t}e\left(x,t\right)+u\left(x,t\right)\frac{\partial}{\partial x}e\left(x,t\right)\right)=-P_{xx}\left(x,t\right)\frac{\partial}{\partial x}u\left(x,t\right)-\frac{\partial}{\partial x}q\left(x,t\right), \tag{31}$$

respectively, where the hydrodynamic velocity is given by $\mathbf{u}(\mathbf{r},t)=u(x,t)\,\hat{\mathbf{i}}$, $\hat{\mathbf{i}}$ is a unit vector along the direction of propagation, P_{xx} is the xx component of the pressure tensor, and q the heat flux. The previous conservation equations can be obtained from the Boltzmann equation or from the standard phenomenological approach Currie (1974) so that they seem to be well established. However, Brenner (2005; 2006; 2010) has recently challenged them [3]; we will refer to his theory as the two velocity hydrodynamics. Except for this case all, the other theories that we will mention here rely on the standard conservations laws. The analysis done by Greenshields & Reese (2007) on asymmetry factors show that in its present form Brenner's approach is not good for explaining the shock wave problem. Another phenomenological approach is that by Hoover & Hoover (2010b) who propose a two temperature theory with delays to try to account for new results obtained using the smooth particle method for shock waves Hoover & Hoover (2010a), further analysis of this theory Uribe et al. (2011) reveal the existence of singularities but it is necessary to analyze it with more detail. Meanwhile Hoovers' ideas have been modified to produce the so–called Burnett–Cattaneo continuum theory for shock waves Holian et al. (2011).

The shock wave problem consists in solving the conservation equations (29)–(31), either for the non–stationary or stationary case, given the Rankine–Hugoniot jump conditions that

[2] There is no universal agreement on this statement; Truesdell & Müncaster (1980) consider the Chapman–Enskog method, as given by Chapman & Cowling Chapman & Cowling (1970), as "naive" (to say the least) and proposed the methods of stretched fields and the Maxwellian iteration to solve the kinetic problem. The mathematical aspects of the Boltzmann equation and in particular the results by DiPerna & Lions can be found in the literature Cercignani et al. (1994); Villani (2002).

[3] The modification to the conservation equations by Brenner can briefly be explained as follows: conservation of mass and momentum remain the same but in eq. (31) the heat flux $\mathbf{q}$ should be changed by the diffusive volume flux density ($\mathbf{j}_e = \mathbf{u}_m - \mathbf{u}_v$), where $\mathbf{u}_m$ is the velocity that appears in the conservation equations and $\mathbf{u}_v$ is the velocity that appears in the constitutive equations. This idea of two velocities is unusual and the reader is referred to Brenner's works for more explanations. We recommend the paper by Greenshields & Reese (2007) for additional explanations of Brenner's ideas, they analyzed Brenner's theory for the shock wave problem.

are obtained from the steady form of the conservation equations. These two conditions of pressure, velocity, etc. are identified with equilibrium thermodynamic states and the goal is to see how the equilibrium points are connected as a function of x, say. As mentioned before the Euler equations do not provide a connection between the two equilibrium points but the Navier–Stokes do. Unfortunately the way in which they are connected is not accurate when compared with experimental information Alsmeyer (1976) or simulations like the Direct Simulation Monte Carlo Method (DSMC) Bird (1994) or Molecular Dynamics (MD) Salomons & Mareschal (1992) for dilute gases [4].
In the three conservation equations (29)–(31) we have the five unknowns $\{\rho, u, e(\text{or}T), P_{xx}, q\}$ and additional equations are required. There are two main theoretical pathways that can be classified according to the way in which the additional information is provided:

- "Normal" solutions: the goal is to express the fluxes, P_{xx} and q, in terms of the conserved variable $\{\rho, u, e\}$ and their gradients. Under this category we find the Navier–Stokes equations, the Burnett equations, super–Burnett equations, and so on Burnett (1935); Chapman & Cowling (1970); Foch (1973); Foch & Simon (1977); Uribe et al. (2000; 1998). They can be obtained using the Chapman–Enskog theory to solve the Boltzmann equation and in the particular case of the Burnett equations they can be obtained also using the methods by Truesdell and Müncaster Truesdell & Müncaster (1980) (the method of stretched field and the Maxwellian iteration). Sometimes the form of the collision operator is changed, the most common model being that by Bhatnagar, Gross, and Krook (BGK) Bhatnagar et al. (1954), from which one may generate what are called BGK–Burnett equations an so on.

  Due to the problems associated with the Burnett equations *a la* Chapman–Enskog, modifications to them have been proposed. They may be classified according to;

  Subsets or supersets of the Burnett equations Fiscko & Chapman (1989)

  Regularizations Jin & Slemrod (2001); Rosenau (1989); Slemrod (1998)

  Generalizations Bobylev (2008; 2011; 2006)

  BGK-Burnett Agarwal et al. (2001); Xu & Li (2004)

  It is interesting to notice that the Burnett equations have been used recently in the field of granular material Brey et al. (1998); Jin & Slemrod (2001); Sela & Goldhirsch (1998). A review of Bunett hydrodynamics is available for the interested reader García–Colín et al. (2008), also available is the detailed work by Agarwal et al. (2001) where the reader can find futher descriptions of such equations and their variants.

- Moment methods: Here additional equations (usually of the relaxation type) for $\{P_{xx}, q\}$ are provided. The main idea is to consider an expansion of the distribution function in terms of a complete set (usually Hermite tensors as done by Grad (1958)) in the velocity space whose coefficients are the so called moments that are functions of position and time. Hence one must truncate the expansion (closure) of the distribution function to get a finite number terms. Having done this one obtains the equations for the moments by using the Boltzmann equation. The well–known Grad's 13–moment approximation provides the "minimal" approximation that contains as moments the viscous pressure tensor and

[4] There is an enormous literature on MD in dense gases, liquids, and solids but we refer to just two works Holian & Lomdahl (1998); Holian et al. (1980). Another powerful computational tool is the Smooth Particles Method (SPM) Hoover (2006), originally developed for astrophysical problems, which has been applied for the shock wave problem Hoover & Hoover (2010a).

the heat flux, so that the equations for the moments provide the additional equations to close the conservation equations for the shock wave problem. Several closures have been considered in the literature, for instance:

Grad's 13–moment approximation Grad (1958).

Regularized 13–moment approximation (R13) Struchtrup (2005).

Eu's theory Eu (1998).

Müller & Ruggeri (1993).

There are also relations between normal solutions and moments methods, in particular between the Burnett equations and Grad's 13–moment equations using the Maxwell–Truesdell–Green iteration Agarwal et al. (2001) (called Maxwellian iteration by Truesdell & Müncaster (1980)). One can also perform a Knudsen expansion of Grad's 13–moment approximation to obtain the Navier–Stokes equations.

In our opinion a main objection to moment methods concerns the problem related to the aforementioned truncation [5]. For certain cases it has been necessary to use hundreds or thousands of moments Müller & Ruggeri (1993) to get agreement with experimental data, this approach therefore lacks predictive power in the sense that while agreement with experiment can be obtained, one is never sure what should be the number of moments to consider in a situation where there is no experimental information. Nevertheless one may consider more and more moments till the results do not change anymore (this is done in computational physics). On the other hand, the goal of having only a few moments to describe the systems like the Navier–Stokes equations is lost.

In addition to the two general methods mentioned and their variants, there are at least three other approaches that have been used for shock waves. They are: the Mott–Smith anzats Mott–Smith (1951), the Holian's conjecture Holian et al. (1993), and multi–temperature methods Xu & Josyula (2005). For a critique of the former approach see García–Colín et al. (2004).

All this discussion raises an important question namely, where do we stand on the description for shock waves for a dilute monatomic gas? For the Navier–Stokes equations the situation is well understood since the works by Gilbarg (1951) and Gilbarg & Paolucci (1953). With respect to the agreement with the experiment it should be pointed out that the comparisons become more sophisticated. There are several levels of comparisons that can be performed; shock thickness [6] ($(u_0 - u_1)/|du/dx|_{max}$), profiles ($u$, T, or ρ vs. x), orbits (or their projections) of the underlying dynamical system, and the asymmetry factor (Q_F) [7]. It became clear that the Navier–Stokes equations were not good enough to provide a faithful representation of the information gathered from experiments and simulations. The consideration of the asymmetry factor provides compelling evidence of this Alsmeyer (1976) and actually in our opinion this quantity should always be evaluated. That the consideration of the profiles is not enough can be exemplified with Holian's conjecture Holian et al. (1993). This conjecture leads to better profiles but when the orbit is considered it yields the same orbit as the Navier–Stokes equations. This was noted computationally Uribe et al. (2000) and later on analytically Uribe (2001), so one is lead to the conclusion that the resulting dynamical system

[5] For other critique to moment methods see García–Colín et al. (2004); Velasco et al. (2002).

[6] u_0 and u_1 refer to the equilibrium values of the velocity given by the Rankine–Hugoniot conditions.

[7] Here we are interested in the hydrodynamic description and so we prefer not to mention the comparisons at the level of the distribution function that are available Erwin et al. (1991), another quantity of interest is the temperature–density separation Greenshields & Reese (2007).

obtained from the conjecture is just a way to parametrize the Navier–Stokes equations. Recently, it has been shown that in appropriately reduced variables the orbits resulting from the Navier–Stokes equations are the same independently of the interaction potential when one relates the viscosity and thermal conductivity according to the prediction resulting from the first Sonine expansion when the Chapman–Enskog method is considered Uribe (2011). With respect to the theories for which an evaluation of the asymmetry exists we mention the following; Navier–Stokes Alsmeyer (1976); Pham–Van–Diep et al. (1991), Brenner's Greenshields & Reese (2007), R13 Struchtrup (2005), Burnett Pham–Van–Diep et al. (1991); Uribe et al. (2000), and Fiscko & Chapman (1989). The predictions of the last three (R13, Burnett, and Fiscko & Chapman) are similar with respect to the asymmetry factor and are consistent with simulations and experimental data. However, except for the one by Fiscko & Chapman (1989), the other two lack solutions [8] for Mach numbers greater than about 5/2. Brenner's two velocity hydrodynamics predicts asymmetry factors that are too low for Mach numbers greater than about 3 and its trend is different from the experimental one. The Navier–Stokes equations provide values for the asymmetry factors that are too big for Mach numbers form one up to two.

While we have not been exhaustive with the many approaches in the literature we think that the reader can get an idea of the complexity of the field of extending the Navier–Stokes equations. In our opinion the large number of approaches available is just a manifestation that there is no theory in the field with which researchers agree. This has lead to fragmentation and no synthesis seems possible in the near future. It would be very convenient to have asymmetry factors for all the other theories mentioned since then we could have a way of discriminating among the vast number available. In our opinion the procedure of adding or eliminating terms from hydrodynamic theories to eliminate problems of a theory or to get agreement with the experimental data should not be encouraged since predictive power most likely will be lost Fiscko & Chapman (1989).

4. Quantum hydrodynamics

In 1927 the German physicist E. Madelung (1927) published a paper entitled Quantum Theory in hydrodynamical form. There he showed how Schrödinger's equation for electron systems could be cast into the form of the mass and momentum conservation equations for the system. After some pertinent comments on their properties he discussed possible applications without attempting any further efforts to derive transport equations. Curiously enough, in 1941 in his landmark paper on the theory of superfluidity Landau (1941), Landau devoted the first section of his paper to derive from quantum mechanical arguments Euler's equation describing the motion of inviscid but otherwise arbitrary fluid. These equations were written in operational form and he never referred to Madelung's work. More surprisingly, he never went beyond this stage but used general features of what he considered some basic aspects of quantum hydrodynamics to obtain the qualitative form of the energy spectrum of a quantum liquid, applying the results to $H\hat{e}^4$ and from the well known form London (1964); Wilks (1966); Yarnell et al. (1959) of such spectrum computed the temperature dependance of thermodynamic functions for this system. And further, without invoking any other quantum mechanical aspects of liquid helium he set forth, using only the form of such spectrum, his well known two–fluid theory of superfluid helium $H\hat{e}^4$. The equations of the macroscopic hydrodynamic of this fluid are all expressed in classical language, so the question arises about

[8] It is not known if solutions for Mach numbers greater than about 5/2 exist.

how, being a quantum fluid, there is no obvious presence of Planck's constant $\hbar$. This is not so and the corresponding situation has been clearly and exhaustively discussed in the literature Khalatnikov (1965); London (1964); Putterman (1974). Just to emphasize the point, the equation of state for the superfluid density ρ_S as a function of T, the temperature, p the pressure and $(\mathbf{v}_n - \mathbf{v}_s)^2$ the square of the difference between the velocities of the normal fluid $\mathbf{v}_n$ and the superfluid $\mathbf{v}_s$, contain $\hbar$. However, this is not a hydrodynamic affair. In fact, the quantum macroscopic aspects of the theory appeared explicitly when Onsager (1948) and Feynman (1955) independently proposed that in order to account for vorticity in the superfluid, the circulation in it should be quantized, namely,

$$\oint \mathbf{v}_s \cdot d\mathbf{l} = n\frac{h}{m}, \tag{32}$$

where n is an integer. Besides the many important results obtained from this proposal Khalatnikov (1965); Putterman (1974), the two fluid theory plus the quantization of vorticity may be regarded as a quantum hydrodynamical theory. Nevertheless, this is not entirely satisfactory. He^4 is a many body boson system interacting among themselves with well known potentials and therefore one could ask the question as to how can one derive the two fluids hydrodynamic equations starting from the basic principles of quantum mechanics. The answer is, up to date, a completely open one. Not even the existence of a pure quantum Boltzmann equation from which we could extract, in analogy to the classical case, the hydrodynamics of a dilute Bose gas is available. Efforts have been made in this direction but they are still incomplete. Some progress was made by K. Huang (1964) for a hard sphere Bose gas but, once more, heuristic assumptions could not be avoided.

Another route followed by some authors was based on the well known Wigner's distribution functions. Proposed in 1932, this author Wigner (1932) defined quantum mechanical distributions in phase space, an apparent contradiction with the uncertainty principle, but more as a tool to perform practical calculations than to solve the deep nature of quantum statistical mechanics. Indeed, in spite of exhibiting the possibility of generating negative values they gave rise to a scheme which in principle allowed the calculation of ensemble averages properly defined of microscopic quantities which in turn provided their macroscopic counterparts Irving & Zwanzig (1951); Mori et al. (1962). However, very few applications of practical utility were ever done although, curiously enough, for non–equilibrium dilute systems a Boltzmann like equation could be derived Mori et al. (1962) from which Euler's equations for a non–viscous fluid followed at once Irving & Kirkwood (1950). Applications to the well known correlation functions method for linear dissipative systems were also made Mori et al. (1962) but once more, the ensuing calculations never went beyond low density gases.

The reader may immediately wonder about the status of this problem in the case of Bose condensates. This system, which has been rather fashionable and subject to a great deal of attention for the past two decades, poses even more complicated features. The atoms in which it has been studied are mostly composed of alkali atoms so their potential energy is far more sophisticated than in He^4 so it is very doubtful if any systematic studies have been carried on their hydrodynamic properties. A similar comment follows for cold Fermi gases. Indeed, what one should expect is that from the N-body Schrödinger equation, using the appropriate symmetry requirements for the corresponding wave functions for fermions and bosons would lead to the conservation equation for particle, momentum and energy densities.

These equations supplied with constitutive equations, either drawn from the experiment or derived from kinetic type equations, would finally yield the transport equations together with meaningful expressions for the transport coefficients. Although an attempt has been made in the past using the quantum analogy of the classical BBGKY hierarchy for reduced density matrices progess was strongly hindered, as in the classical case, due to difficulties related to truncation criteria and explicit solutions for the equations containing the remaining density matrices. A long and rather suggestive approach following these ideas was discussed almost thirty years ago Kadanoff & Baym (1962); Putterman (1974). The interested reader should take a look of this work. In the absence of a program of this sort what we could consider the quantum mechanical approaches to the study of transport properyies of bosons and fermions are of a wide variety. A very thorough and exhaustive review of these methods has been published recently Schäfer & Teaney (2009) and the interested reader is strongly encouraged to look at it. Briefly speaking the starting point is the concept of a "good fluid" namely, a fluid characterized by a small shear viscosity. To characterize these type of fluids one takes the expression for the shear viscosity for a simple gas as derived from elementary kinetic theory Kauzmann (1966); Reif (1966)

$$\eta = \frac{1}{3} n\, p\, l, \tag{33}$$

where n is the density, p the average momentum of the particles and l the mean free path. In the strong coupling limit, l is very small so that the uncertainty relation implies that

$$p\, l \sim \hbar, \tag{34}$$

so from eqs. (33) and (34) we infer that $\eta \sim n\,\hbar/3$. Now, we know that for many fluids, bosons and fermions in the non relativistic limit, $s/n \sim k_B$ where s is the entropy density so, for good fluids we may estimate that

$$\frac{\eta}{s} \sim \frac{\hbar}{k_B}, \tag{35}$$

where k_B is Boltzmann's constant. This result has even lead to the conjecture that, using results obtained from string theory Kovtun (2005)

$$\frac{\eta}{s} \geq \frac{\hbar}{4\,\pi\, k_B}, \tag{36}$$

¡for all fluids! When the equality holds as it appears to be the case in the quark–gluon plasma obtained in relativistic heavy ion collisions (RHIC) Aad et al. (2010); Aamodt (2010) the fluid is defined as a "perfect" one. Wether eq.(36) is completely correct or not is yet an unsolved problem but most of the advances that have been reported in the literature Schäfer & Teaney (2009) are strongly bound to this question.

Just as an illustration of the ideas which are in close and deep scrutiny today, eq. (36) has been both examined experimentally and theoretically in a unitary Fermi Gas Cao et al. (2011). This gas is one in which by the use of a magnetic field the range of the interacting potential is not to be small when compared with the inter-particle spacing. Under these circumstances the properties of the gas turn out to be universal functions of the density n and the temperature T. For the equilibrium properties the details have been recently revised Horikoshi (2010); Luo (2009). For the non-equilibrium properties the studies mentioned above Schäfer & Teaney

(2009) also hint at the existence of a universal hydrodynamics which appears to be consistent with eq. (36). If the findings turn out to be also applicable to both cold Bose and Fermi liquids we shall be contemplating a formidable breakthrough in quantum hydrodynamics.
Nevertheless there are still other efforts that have been advanced in connection with the problem of quantum hydrodynamics. These are based on the pioneer work on the subject by Landau who in 1953 Landau (1953) developed a description for the evolution of dense matter at high temperatures and pressure. This description was later improved by Hwa (1974) and Bjorken (1983) and very recently, re-examined thoroughly by C. Y. Wong (2008) specifically focused to account for the experimental data that is available from RHIC. The recent results obtained by this author are also quite interesting specially because the method itself is quite independent of the methods described in the previous paragraphs and quite free from the more complicated techniques of quantum field theory.
To finish this section we must briefly mention an attempt to analyze the transport problems of dense nuclear matter at very high temperatures under conditions that not only quantum mechanical equations are required, but also their relativistic versions. The ensuing formalism may be loosely regarded as the relativistic generalization of Madelung's early attempt as described at the beginning of this section. The method itself, which has a long history Wong (2010), curiosly enough, started from the Klein-Gordon equation in spite of the fact that, as well known, has a probability density $\rho = 2\,Im\left(\Psi^{\star}\frac{\partial\Psi}{\partial t}\right)$ which is not necessarily a positive quantity. Nevertheless, Feshbach & Villars (1958) were able to overcome this inconvenience by noting that the Klein-Gordon equation constrains both, particle and antiparticle degrees of freedom. That motivated Wong to write such equation in hydrodynamic form first for a single particle and then for N-body systems with strong interactions Wong (2010). Although one can indeed obtain rather complicated equations in which there are terms which may be identified, for instance, with a quantum stress tensor the whole scheme is still too formal to allow explicit calculations that may be related with transport properties, even less with transport coefficients. The reader interested in more details about this formalism should go to the original sources, it is beyond this review to provide the details which, one must say, are rather elaborated.
Summing up, this brief review clearly reveals that a quantum hydrodynamical theory is far from being developed. Even at the level of dilute systems the quantum analogue of Boltzman's equation is not available. The study of transport phenomena in quantum systems has thus followed a variety of routes which, in spite of their success, still offer no hint as to how to solve the general problem.

5. Fluctuation theorems and stochastic thermodynamics

It is well known that equilibrium statistical mechanics is a well established theory because it can explain the properties of a broad variety of systems in equilibrium. Close to equilibrium the linear response formalism is very successful in the form of the fluctuation–dissipation theorem and Onsager's reciprocity relations. However, no such universal framework exists to study systems driven far away from equilibrium. Over the past two decades, there has been considerable interest in the study of nonequilibrium statistical mechanics of small systems in which thermal fluctuations play a very important role, and has led to the discovery of several rigorous theorems called *fluctuation theorems* (FTs) and related results for systems away from

equilibrium [9]. The fluctuation theorem (FT) deals with the relative probability that a quantity so-called "entropy" of a system which is currently away from thermodynamic equilibrium will increase or decrease over a finite time interval. The second law of thermodynamics states that the Clausius entropy of a macroscopic isolated system always increases until reaches equilibrium. The entropy and the entropy production as well, are quantities associated to macroscopic systems and they have a clear physical meaning as properties of ensembles. With the discovery of statistical mechanics it was shown that the entropy increase principle is only statistical one, (it is valid as an average over the ensemble) suggesting that there always exists some nonzero probability that the entropy of a isolated system might spontaneously decrease. The fluctuation theorem precisely quantifies this probability. So, when the thermodynamic concepts are applied to small systems and in short time intervals, it becomes clear that there exists a probability to find situations which do not match the ensemble averages. The FT was first proposed and tested using computer simulations, by Evans *et.al* Evans et al. (1993) in 1993. The first mathematical proof was given by Evans and Searles Evans & Searles (1994) in 1994. Roughly speaking, the FT is related to the probability distribution of the time-average irreversible "entropy like production", denoted as $\overline{\Sigma}_t$. The theorem states that, in systems away from equilibrium over a finite time t, the ratio between the probability that $\overline{\Sigma}_t$ takes a value A and the probability that it takes the value $-A$, will be exponential in At. In other words, for a finite non-equilibrium system in a finite time, the FT gives a precise mathematical expression for the probability that such a quantity will flow in an opposite direction. Its mathematical expression reads $P(\overline{\Sigma}_t = A)/P(\overline{\Sigma}_t = -A) = e^{At}$. Because to $\overline{\Sigma}_t$ is an extensive quantity, it can be seen from the expression that, as the time or system size increses, the probability of observing the value $-A$ in opposite direction decreases exponentially, consistently which one could expect with the increase in entropy principle. Notice that the FT does not state that the second law of thermodynamics is wrong or invalid. Thus the FT when applied to macroscopic systems, is equivalent to the increase in entropy principle. Actually, the FTs involve a wide class of systems as well as several equilibrium and nonequilibrium quantities, including Helmholtz free energy Crooks (2000; 1999); Jarzynski (1997a;b; 2007); Jayannavar & Sahoo (2007); Jiménez-Aquino et al. (2008), work Jayannavar & Sahoo (2007); Jiménez-Aquino et al. (2008); Roy & Kumar (2008); van Zon & Cohen (2003), heat van Zon & Cohen (2004), and entropy production Crooks (2000; 1999); Jiménez-Aquino (2010); Saha et al. (2009); Seifert (2005; 2008). They can be applied to steady state situations Gallavotti & Cohen (2005); Jiménez-Aquino et al. (2010); van Zon & Cohen (2003) and the transient theorems allow to go a step further Crooks (1999); Evans et al. (1993); Jiménez-Aquino et al. (2010); Jiménez-Aquino (2010); Saha et al. (2009); Seifert (2005); van Zon & Cohen (2003). The FTs have been corroborated by both computer simulations Evans et al. (1993); Lechner et al. (2006); Searles & Evans (2000); Wang et al. (2002)

[9] A short list of relevant works is the following; Evans et al. (1993), Evans & Searles (1994), Evans & Searles (2002), Jarzynski (1997a), Jarzynski (1997b), Jarzynski (2007), Liphardt et al. (2002), Esposito & Van den Broek (2010), Shargel (2010), Sevick et al. (2008), Crooks (1999), Crooks (2000), Collin et.al. (2005), Garnier & Ciliberto (2005), van Zon & Cohen (2003), van Zon & Cohen (2004), Seifert (2005), Seifert (2008), Saha et al. (2009), Gallavotti & Cohen (2005), Searles & Evans (2000), Lechner et al. (2006), Wang et al. (2002), Carberry et al. (2004), Trepagnier et al. (2004), Blickle et al. (2006), Tietz et al. (2006), Esposito et al. (2010), Saito & Dhar (2007), Campisi et al. (2009), Ritort (2009), Velasco et al. (2011), Jayannavar & Sahoo (2007), Saha & Jayannavar (2008), Roy & Kumar (2008), Jiménez-Aquino et al. (2008), Jiménez-Aquino et al. (2009), Jiménez-Aquino et al. (2010), Jiménez-Aquino (2010), Bustamante et al. (2005), Zuckerman & Wolf (2002), Procacci et al. (2006), Sekimoto (1998), Carrete et al. (2008).

and experiments Blickle et al. (2006); Carberry et al. (2004); Tietz et al. (2006); Trepagnier et al. (2004); Wang et al. (2002). The FTs are not only active areas of research in classical physics but recently also in quantum mechanics Campisi et al. (2009); Esposito et al. (2010); Saito & Dhar (2007). The first laboratory experiment performed to demonstrate the transient work-fluctuation theorem (TFT) was reported by Wang *et al.* Wang et al. (2002) in 2002, for a small system over short times. In this experiment the trajectory of a colloidal particle is followed when it is captured in an optical trap that is translated relative to surrounding water molecules (the bath at temperature T).

After the works of Evans, Searles, and colleagues, another important result for non-equilibrium properties, called the Jarzynski equality (JE) Jarzynski (1997a;b; 2007) appeared in 1997 . This equality relates averages of non-equilibrium work distribution with the equilibrium free energy differences between equilibrium states. In other words, a system in thermodynamic equilibrium with a thermal bath at temperature T can be driven out of equilibrium by time-dependent external forces. For slow enough driven forces, the process is quasistatic or reversible, then the system evolves through a succession of equilibrium states and the total amount of work W_{rev} done by the external forces is equal to the equilibrium free-energy difference ΔG between the initial and final state. For nonequilibrium situations (irreversible processes), the second law of thermodynamics tell us that the total work W is larger than the reversible work: the difference between the actual work and reversible work is equal to the net heat (noncompensated Clausius' heat) produced by dissipative forces and transferred from the system to the heat bath. Jarzynski found for arbitrary irreversible processes the relation $\langle \exp(-W/k_BT) \rangle = \exp(-\Delta G/k_BT)$, where $\langle ... \rangle$ denotes the average over an infinite number of trajectories or realizations of the irreversible process, k_B is the Botzmann constant. The reversible process is then a particular case of this realation where $W = \Delta G$. The first experimental test of the JE was performed by Bustamante and collegues Liphardt et al. (2002) at UC Berkeley in 2002. They measured the work exerted on small RNA molecules using optical tweezers. In 1999, G. Crooks Crooks (1999) also at UC Berkeley, was able to go further by generalizing the JE. The Crooks relation states that the for a given protocol, the ratio between the distribution of work $P(W)$ measured along a forward trajectory (or probabilty distribution along a forward process) and its time reverse counterpart $P(-W)$ is given by $P(W)/P(-W) = \exp[(W - \Delta G)/k_BT]$. In 2005, this flutuation relation was experimentally tested by C. Collin *el al*. Collin et.al. (2005), using RNA molecules. Coming back to the experimental demonstration by Wang *et al.* Wang et al. (2002), they succeeded to test the TFT for a colloidal particle trapped into an optical trap which interacts with an experimental vessel, and the expression for the TFT reads $P(W)/P(-W) = e^W$, where W stands for the dimensionless work delivered to the vessel, $P(W)$ is the probability of the work delivered to the vessel (or the probabilty of the work measured along a forward trajectory), and P(-W) is the probability that the vessel does work on the trap (or the probabilty of the work measured along a backward trajectory). After Wang's *et al.*, Liphardt *et al*. and Collin *et al*. experimental confirmations, others were continued with colloidal particles trapped by an optical device, for instance Blickle et al. (2006); Carberry et al. (2004); Trepagnier et al. (2004), mechanical and electrical oscillators Garnier & Ciliberto (2005), etc. For all of those statements given above, it becomes clear that the FTs are very important in the description of non-equlibrium systems within short times, and suggest that the miniaturization of machines may have inherent limitations. This means that microscopic (nanosized) machines will work not in the same way as their macroscopic counter parts. As the machines become smaller, the probability that they run in reverse

becomes greater. In general, whatever is the non-equilibrium quantity, work, heat, entropy production, etc., the FTs relate probability distribution functions along forward and backward trajectories for a small system. The specific form of the various theorems depend on which thermodynamic parameter (temperature, volume, etc.) are held constant, wheter the system is prepared in an equilibrium state, and other factors.
The FTs have also been verified for heat van Zon & Cohen (2004) and entropy like production Saha et al. (2009); Seifert (2005; 2008). In the particular case of the entropy production, it has been necessary to define an entropy–like function along a stochastic trajectory. This and other thermodynamic concepts like the first-law-like energy balance involving applied or extracted work, exchanged heat, and changes in internal energy, were consistently defined along a single stochastic trajectory in the context of stochastic thermodynamics by Seifert Seifert (2005; 2008). Stochastic thermodynamics has been developed for mesoscopic systems like colloidal particles or single (bio) molecules driven out of equilibrium by time-dependent forces but still in contact with a heat bath of well-defined temperature. Stochastic thermodynamics thus attempts to extrapolate thermodynamic concepts to single particle trajectories. But one can immediately ask, how this extrapolation can be done? First of all, it is well known from the equilibrium statistical mechanics that the thermodynamics quantities such as the internal energy, entropy, etc., are related to ensemble properties and the average over the ensemble for each one becomes its thermodynamic counterpart. A similar situation has been adopted in stochastic thermodynamics by Seifert Seifert (2005; 2008), in which that concept of ensemble is extrapolated as an ensemble of a particle's stochastic trajectories. In this sense, the average over the esemble trajectories will be its corresponding thermodynamic quantity. The subject was explicitly studied by Seifert for an over-damped Brownian particle in the one-dimensional case. In his work, he defined a first law-like balance between the applied work, the change in internal energy, and the dissipative heat along a stochastic trajectory. Seifert was able to show that the total "entropy like production" (TEP), denoted as Δs_{tot}, along a single stochastic trajectory satisfies the integral fluctuation theorem (IFT) which is expressed as $\langle e^{-\Delta s_{tot}} \rangle = 1$, for any initial condition when the particle is arbitrarily driven by time-dependent external forces over a finite time interval (*the transient case*). He also showed, in the *nonequilibrium steady state* over a finite time interval that, a stronger fluctuation theorem, called the detailed fluctuation theorem (DFT) holds, that is, $P(\Delta s_{tot})/P(-\Delta s_{tot}) = e^{\Delta s_{tot}}$; where $P(\Delta s_{tot})$ is the probability of the entropy–like function given along a forward trajectory and $P(-\Delta s_{tot})$ is that given along a backward trajectory. In this context, using the concepts of stochastic thermodynamics and the definition of the entropy–like function along a single stochastic trajectory, Saha *et al.* Saha et al. (2009) proved that, even in the *transient case* the DFT for a Brownian particle in a harmonic trap also holds for two exactly solvable models. Finally, we would like to comment that over the last three years, the FTs and the JE have also been explored and verified for a charged Brownian particle in a electromagnetic field Jayannavar & Sahoo (2007); Jiménez-Aquino et al. (2008; 2009; 2010); Jiménez-Aquino (2010); Saha & Jayannavar (2008); Roy & Kumar (2008). In this section we briefly study two transient fluctuation theorems, the work and total entropy–like production, for a Brownian harmonic oscillator in the high friction limiting case, taking also into account the presence of an electromagnetic field.

5.1 Transient work-fluctuation theorem

5.1.1 Harmonic oscillator's Langevin equation

Let us consider a charged Brownian particle with mass m in a harmonic trap with a time-dependent position vector $\mathbf{r}^*(t)$ of its center, that is $V(\mathbf{r},t) = (k/2)|\mathbf{r}-\mathbf{r}^*)|^2$, with k as a constant. It will be considered that for $t = 0$, the potential minimum is located at the origin, $\mathbf{r}_0^* = 0$, whereas for $t > 0$, it moves with arbitrary velocity $\mathbf{v}^*(t)$. For this Brownian harmonic oscillator, the corresponding Langevin equation in the over-damped approximation reads

$$\frac{d\mathbf{r}}{dt} = -\gamma\,\mathbf{r} + \gamma\,\mathbf{r}^* + \alpha^{-1}\boldsymbol{\xi}(t)\,, \tag{37}$$

where $\gamma = k/\alpha$, α is the friction coefficient, and $\boldsymbol{\xi}(t)$ represents the fluctuating force produced by the surrounding medium (the bath) at temperature T, which satisfies the properties of Gaussian white noise with zero mean value $\langle\xi_i(t)\rangle$=0 and a correlation function given by $\langle\xi_i(t)\xi_j(t')\rangle = 2\lambda\,\delta_{ij}\,\delta(t-t')$, with $i,j = x,y,z$. The parameter λ is the noise intensity and acoording to the fluctuation-dissipation theorem it is related to the friction constant by $\lambda = \alpha\,k_{_B}T$, $k_{_B}$ being Boltzmann's constant.

In this work, we adopt the definition of the dimensionless total work done on a system during a finite time interval τ as given in reference van Zon & Cohen (2003). In this case

$$W_\tau = \frac{1}{k_{_B}T}\int_0^\tau \mathbf{v}^*\cdot\mathbf{F}(\mathbf{r},\mathbf{r}^*)\,dt = -\beta k\int_0^\tau \mathbf{v}^*\cdot(\mathbf{r}-\mathbf{r}^*)\,dt\,, \tag{38}$$

where $\beta = k_{_B}T$. This definition has been shown to be consistent with the definition of Jarzynski's work in Ref. Jayannavar & Sahoo (2007); Jiménez-Aquino et al. (2008). To calculate the statistical properties of this total work, we proced further by introducing the change of variable $\mathbf{R} = \mathbf{r} - \langle\mathbf{r}\rangle$, where $\mathbf{R}$ and $\langle\mathbf{r}\rangle$ satisfy the following differential equations van Zon & Cohen (2003)

$$\frac{d\mathbf{R}}{dt} = -\gamma\,\mathbf{R} + \alpha^{-1}\,\boldsymbol{\xi}(t) \qquad \frac{d\langle\mathbf{r}\rangle}{dt} = -\gamma\,\langle\mathbf{r}\rangle + \gamma\,\mathbf{r}^*\,, \tag{39}$$

$\langle\mathbf{r}\rangle$ being the deterministic solution of Ec. (37). In terms of the $\mathbf{R}$ variable the total work reads

$$W_\tau = -\beta k\int_0^\tau [\mathbf{v}^*\cdot\mathbf{R} + \mathbf{v}^*\cdot(\langle\mathbf{r}\rangle - \mathbf{r}^*)]\,dt\,. \tag{40}$$

This equation shows that the total work done on the system is a linear function of the stochastic variable $\mathbf{R}$. Accordingly, the statistical properties of this work then correspond to a Gaussian process and therefore its probability distribution can be written as follows

$$P(W_\tau) = \frac{1}{\sqrt{2\pi V_{_T}(\tau)}}\exp\left(-\frac{[W_\tau - M_{_T}(\tau)]^2}{2V_{_T}(\tau)}\right), \tag{41}$$

where we have defined $M_{_T}(\tau) \equiv \langle W_\tau\rangle$ as the mean value of the work and $V_{_T}(\tau) \equiv \langle W_\tau^2\rangle - \langle W_\tau\rangle^2$ as its variance. The probability distribution written in Eq. (41) contains the time evolution of the total work from the initial time up to time τ. This fact means that we are studying the distribution corresponding to the transient situation. We will use the subscript T for all quantities in the transient case. Taking into account that $\langle\mathbf{R}\rangle = 0$, the work mean value now reads

$$M_{_T}(\tau) = -\beta k\int_0^\tau \mathbf{v}^*\cdot(\langle\mathbf{r}\rangle - \mathbf{r}^*)\,dt\,. \tag{42}$$

Following the algebraic steps given by van Zon and Cohen van Zon & Cohen (2003), it can be shown that the work mean valeu and its corresponding variance are given respectively by

$$M_{_T}(\tau) = \beta k \int_0^\tau dt' \int_0^{t'} e^{-\gamma(t'-t'')} \mathbf{v}^*(t') \cdot \mathbf{v}^*(t'')\, dt'' \,. \tag{43}$$

$$V_{_T}(\tau) = 2\beta k \int_0^\tau dt' \int_0^{t'} e^{-\gamma(t'-t'')} \mathbf{v}^*(t') \cdot \mathbf{v}^*(t'')\, dt'' \,, \tag{44}$$

and therefore $V_{_T}(\tau) = 2\, M_{_T}(\tau)$. Making use of Eq. (41) we get the final result

$$\frac{P(W_\tau)}{P(-W_\tau)} = e^{W_\tau} \,. \tag{45}$$

This was precisely the result corroborated experimentally by Wang *et al.* Wang et al. (2002), before the work of van Zon and Cohen van Zon & Cohen (2003).

5.1.2 Harmonic oscillator's Langevin equation in an electromagnetic field

Recently, the study of van Zon and Cohen, has been extended for an electrically charged Brownian particle in an electromagnetic field Jiménez-Aquino (2010). It is not our purpose in this section to write alegebraic details to obtain the results. We suggest the reader interested in the explicit calculations to read Ref. Jiménez-Aquino (2010). When the above Brownian particle is charged and under the action of constant magnetic field orthogonal to the electric field which lies on the x-y plane, the Langevin equation can be split into two independent processes, one is given on the x-y plane perpendicular to the magnetic field and the other one along the z-axis parallel to the magnetic field. Along the z-axis, the Langevin equation is the same z-component of the Langevin equation studied in Ref. van Zon & Cohen (2003). We can define all the vectors lying on the plane as $\mathbf{x} = (x, y)$ the position vector, $\mathbf{u} = (v_x, v_y)$ the velocity vector, $\boldsymbol{\eta}(t) = (\xi_x, \xi_y)$ the fluctuating force, and $\mathbf{E}(t) = (E_x, E_y)$ the electric field. The two-dimensional harmonic potential and its corresponding harmonic force are defined as $\mathcal{U}(\mathbf{x}, t) = (k/2)|\mathbf{x} - \mathbf{x}^*|^2$ and $\mathcal{F}(\mathbf{x}, \mathbf{x}^*) = -k(\mathbf{x} - \mathbf{x}^*)$. In this case, the electric field can be interpreted as the responsible to drag the center of the harmonic trap, hence the position vector of the center in the harmonic trap can be written as $\mathbf{x}^* = (q/k)\mathbf{E}(t)$. Again for $t = 0$, $\mathbf{x}_0^* = 0$, whereas for $t > 0$, $\mathbf{u}^*(t) \equiv \dot{\mathbf{x}}^*(t) = (q/k)\dot{\mathbf{E}}(t)$ so that. the responsible for dragging of the minimum potential is the electric field rate of change. So, the planar Langevin equation in the over-damped approximation can be written as

$$\frac{d\mathbf{x}}{dt} = -\Lambda\mathbf{x} + \Lambda\mathbf{x}^* + k^{-1}\Lambda\boldsymbol{\eta}(t) \,, \tag{46}$$

Λ is a matrix given by

$$\Lambda = \begin{pmatrix} \widetilde{\gamma} & \widetilde{\Omega} \\ -\widetilde{\Omega} & \widetilde{\gamma} \end{pmatrix} \,, \tag{47}$$

with $\widetilde{\gamma} = k/\alpha(1 + C^2)$, $\widetilde{\Omega} = kC/\alpha(1 + C^2)$, and $C = qB/c\alpha$ is a dimensionless factor. Now, the total dimensionless work will be in this case

$$W_\tau = -\beta k \int_0^\tau \mathbf{u}^* \cdot (\mathbf{x} - \mathbf{x}^*)\, dt \,, \tag{48}$$

To calculale the statistical properties of this stochastic Gaussian work we again introduce the change of variable $\mathbf{X} = \mathbf{x} - \langle \mathbf{x} \rangle$. Following the steps given in Ref. Jiménez-Aquino (2010), it is also possible to show that the work mean value and its variance are then

$$M_{_T}(\tau) = \beta k \int_0^\tau dt' \int_0^{t'} e^{-\widetilde{\gamma}(t'-t'')} \mathbf{V}^*(t') \cdot \mathbf{V}^*(t'')\, dt'' \,, \tag{49}$$

$$V_{_T}(\tau) = 2\beta k \int_0^\tau dt' \int_0^{t'} e^{-\widetilde{\gamma}(t'-t'')} \mathbf{V}^*(t') \cdot \mathbf{V}^*(t'')\, dt'' \,, \tag{50}$$

where $\mathbf{V}^*(t) \equiv \mathcal{R}(t)\mathbf{u}^*(t)$ and $\mathcal{R}(t)$ is a rotation matrix given by

$$\mathcal{R}(t) = \begin{pmatrix} \cos\widetilde{\Omega}\, t & \sin\widetilde{\Omega}\, t \\ -\sin\widetilde{\Omega}\, t & \cos\widetilde{\Omega}\, t \end{pmatrix} , \tag{51}$$

and thus $V_{_T}(\tau) = 2\, M_{_T}(\tau)$. From Eq. (41) we can conclude that the same TFT given by Eq. (45) holds. Therefore, when a system (a charged Brownian particle in a harmonic trap) in the presence of a uniform magnetic field is driven out of equilibrium by an time-varying electric field, the transient work-fluctuation theorem (TFT) also holds.

5.2 Entropy production fluctuation theorem

Using the concepts of stochastic thermodynamics established by Seifert Seifert (2005; 2008), Saha and collegues Saha et al. (2009) showed in 2009 that even in the *transient case* the DFT for a Brownian particle in a harmonic trap also holds for two exactly solvable models. These models were studied in the over-damped approximation of the Langevin Dynamics in the one variable case. Last year, Saha's *et al.* work could be extended to the case of a charged harmonic oscillator in an electromagnetic field by Jiménez-Aquino Jiménez-Aquino (2010). In this paper, also two physical situations for arbitrary time-dependent electric field driven over a finite time interval were also studied, namely: (i) the charged Brownian particle in a two-dimensional harmonic trap subjected to the action of an arbitrary time-dependent electric field and, (ii) the minimum of the harmonic trap arbitrarily dragged by the electric field. We brefly introduce a short comment of stochastic thermodynamics before establishing the entropy-production fluctuation theorem. According to stochastic thermodynamics Seifert (2005; 2008); Sekimoto (1998), the first-law-like balance between the applied work W, the change in internal energy ΔU, and the dissipated heat Q to the bath, can be calculated along a trajectory $\mathbf{x}(t)$ over a finite time interval t. This first-law-like reads as $Q = W - \Delta U$, where the work (not dimensionless work) can be calculated from the relation Jarzynski (1997a); Jayannavar & Sahoo (2007); Saha et al. (2009)

$$W = \int_0^t \frac{\partial U(\mathbf{x}, t')}{\partial t'}\, dt' \,, \tag{52}$$

where $\mathbf{x}$ is the n-dimensional position vector. On the other hand, the change in the medium's entropy Δs_m over the time interval is $\Delta s_m = Q/T$ and the nonequilibrium Gibbs entropy-like S of the system in the present problem is defined as Seifert (2005)

$$S(t) = -\int f(\mathbf{x}, t) \ln f(\mathbf{x}, t)\, d\mathbf{x} = \langle s(t) \rangle \,. \tag{53}$$

This definition suggests the definition of a trajectory–dependent entropy–like function for the particle as $s(t) = -\ln f[\mathbf{x}(t), t]$, where the probability density $f(\mathbf{x}, t)$ is obtained through the

solution of the associated Fokker-Planck equation and, it is evaluated along the stochastic trajectory. For a given trajectory $\mathbf{x}(t)$, this entropy–like $s(t)$ depends on the given initial data $f(\mathbf{x}_0) \equiv f(\mathbf{x}_0, 0)$, where $f(\mathbf{x}_0)$ is the probability density of the particle at initial time $t = 0$, and thus contains information about the whole ensemble. The change in the system's entropy for any trajectory of duration t is $\Delta s = -\ln[f(\mathbf{x}, t)/f(\mathbf{x}_0)]$. Now, the change in the total entropy–like production along a trajectory over a finite time interval t is shown to be Seifert (2005; 2008) $\Delta s_{tot} = \Delta s_m + \Delta s$. Using this definition, Seifert derived the integrated fluctuation theorem, $\langle e^{-\Delta s_{tot}} \rangle = 1$, where the angular brackets denote average over the statistical ensemble of realizations, or over the ensemble of finite time trajectories Seifert (2005; 2008). Also he showed that in the nonequilibrium steady state over a finite time interval, the DFT holds. The latter is stated as

$$\frac{P(\Delta s_{tot})}{P(-\Delta s_{tot})} = e^{\Delta s_{tot}} . \tag{54}$$

This theorem has also been proved, even in the transient case, for a Brownian particle in a harmonic trap only if the system is initially prepared in equilibrium Saha et al. (2009). This was also the case for a charged harmonic oscillator in an electromagnetic field as studied by Jiménez-Aquino (2010). In both papaers Jiménez-Aquino (2010); Saha et al. (2009), the proof of the DFT has been given for two general physical situations, when the system is initially distributed with a canonical distribution at equilibrium with the thermal bath. The relation $\sigma_s^2 = 2\langle \Delta s_{tot} \rangle$ is shown to be valid, being the main requirement for the validity of the DFT. However, as it has beeen pointed out by Saha *et al.* Saha et al. (2009), when the probability density $P(\Delta s_{tot})$ is not Gaussian the DFT for the total entropy–like producton does not hold. To this respect, it is important to take into account the recent commets of Shargel Shargel (2010) about Saha's contribution, namely: as proved by Saha *et al.*, the transient fluctuation theorem (TFT), given by Eq. (54) for a Brownian particle in a harmonic potential and driven by an arbitrary time-dependent force, is only valid if the particle is initially in thermal equilibrium. However, this is a surprising result because according to Shargel, Eq. (54) fails to distinguish between both the forward and backward path measures and the forward and backward entropy–like production, each of which are different due to the time-dependent driving. Certainly, in those works Jiménez-Aquino (2010); Saha et al. (2009), the TFT holds in a very particular case that strongly depends of the form on which the initial distribution has been constructed. The latter is constructed on the basis of a harmonic potential, but any other potential or initial distribution the TFT breaks down.

Respect to the stochastic thermodynamics concepts briefly outlined above, we must mention a critical analysis given very recently in Velasco et al. (2011): as addressed by the authors, the usual concepts of thermodynamics when extrapolated to the study of thermodynamic of small systems labelled under the strange name of "stochastic thermodynamics", some care should be taken into account when concepts of entropy and related quantities out of equilibrium are used in such a description. The authors further suggest to review the books on the *thermodynamics of small systems* formulated over fifty years ago by T. L. Hill Hill (1963; 1964; 1968). Hill's theory is formulated upon a precise and conventional theory of themodynamics of small systems, and based on the fundamental ideas of statistical mechanics. To describe non-equilibrium systems consistent with thermodynamics, the theory relies upon local equilibrium states, so that the calculation of the entropy production in irreversible processes must be the same as those available for thermodynamic systems. In this context, it seems to be the case that the connection of Hill's theory with systems described by

averaging procedure, like Jarzynski equality, has been given first by J. Carrete and collegues Carrete et al. (2008) in 2008. This pioneer work opens other possibilities to explore the FTs described by the so-called "stochastic thermodynamics" theory.

6. References

Aad, G et al. (2010). Observation of a Centrality–Dependent Dijet Asymmetry in Lead–Lead Collisions at $\sqrt{s_{NN}} = 2.76$ TeV with ATLAS Detector at the LHC, *Phys. Rev. Lett.* Vol. 105: 252303.

Aamodt, K. et al. (2010). Elliptic Flow of Charged Particles in Pb–Pb Collisions at $\sqrt{s_{NN}} = 2.76$, *Physical Review Letters* Vol. 105: 252302.

Agarwal, R. K., Yun, K. Y. & Balakrishnan, R. (2001). Beyond Navier–Stokes: Burnett equations for flows in the continuum–transition regime, *Physics of Fluids* Vol. 13: 3061–3085.

Alfven, H & Falthammar, C. G. (1963). *Cosmical Electrodynamics Fundamental Principles*, Oxford University Press.

Alsmeyer H. (1976). Density profiles in Argon and Nitrogen shock waves measured by the absorption of an electron beam, Journal of Fluid Mechanics Vol. 74: 497–513.

Arnold, V. I, (1998) *Topological Methods in Hydrodynamics*, Springer.

Balbus, S. A. & Hawley, J. F. (1998), Instability, turbulence, and enhaced transport in accretion disks, *Reviews of Modern Physics* Vol. 70: 1–53.

Balescu, R. (1988). *Transport Processes in Plasmas: Vol. 1 Classical Transport*, North Holland.

Bhatnagar, P. L., Gross, E. P., Krook, M. (1954). A model for collision processes in gases. I: Small amplitude processes in charged and neutral one–component systems, *Physical Review* Vol. 94: 511–525.

Bird, G. A. (1994). *Molecular Gas Dynamics and the Direct Simulation of Gas Flows*, Oxford–Clarendon.

Bjorken, J. D. (1983). Highly relativistic nucleus–nucleus collisions: The central rapidity region, *Physical Review D* Vol. 27: 140–151.

Blickle, V., Speck, T., Helden, L., Seifert, U. & Bechinger, C. (2006). Thermodynamics of a Colloidal Particle in a Time–Dependent Nonharmonic Potential, *Physical Review Letters* Vol. 96: 070603.

Bobylev, A. V. (2008). Generalized Burnett hydrodynamics, *Journal of Statistical Physics* Vol. 132: 569-580.

Bobylev, A. V., Bisi, Cassinari, M. P. & Spiga, G. (2001). Shock wave structure for generalized Burnett equations, *Physics of Fluids* Vol. 23: 030607.

Bobylev, A. V. (2006). Instabilities in the Chapman-Enskog expansion and hyperbolic Burnett equations, *Journal of Statistical Physics* Vol. 124: 371-399.

Braginskii, S. I. (1965) Transport Processes in a Plasma, *in* Leontouech, M. A. (ed.), *Reviews of Plasma Physics* Vol. 1, Consultants Bureau, New York, p. 45.

Brenner, H. (2005). Navier–Stokes revisited, *Physica A* Vol. 349: 60–132.

Brenner, H. (2006). Fluid mechanics revisited, *Physica A* Vol. 370: 190–224.

Brenner, H. (2010). Bi–velocity transport processes. Single–component liquid and gaseous continua, *Physica A* Vol. 389: 1297–1316.

Brenner, M. P., Hilgenfeldt, S. & Lohse, D. (2002). Single–bubble sonoluminescence, *Review of Modern Physics* Vol. 72: 425–484.

Brey, J, J., Dufty, J. W., Kim, C. S., & Santos, A. (1998). Hydrodynamics for granular flow at low density, *Physical Review E* Vol. 58: 4638–4653.

Burnett, D. (1935). The distribution of velocities in a slightly non–uniform gas, *Proccedings of the London Mathematical Society* Vol. 39: 385–430.

Bustamante, C., Liphardt, J. & Ritort, F. (2005). The Nonequilibrium Thermodynamics of Small Systems, *Physics Today* Vol. 58: 43–48.

Campisi, M., Talkner, P. & Hänggi, P. (2009). Fluctuation Theorem for Arbitrary Open Quantum Systems, *Physical Review Letters* Vol. 102: 210401.

Cao, Elliott, E., Joseph, J., Wu, H., Petricka, J., Schäfer, T. & Thomas, J. E. (2011). Universal Quantum Viscosity in a Unitary Fermi Gas, *Science* Vol. 331: 58.

Carberry, D. M., Reid, J. C., Wang, G. M., Sevick, E. M., Searles, D. J. & Evans, D. J. (2004). Fluctuations and Irreversibility: An Experimental Demonstration of a Second-Law-Like Theorem Using a Colloidal Particle Held in an Optical Trap, *Physical Review Letters* Vol. 92: 140601.

Carrete, J., Varela, L. M. & and Gallego, L. J. (2008). Nonequilibrium nanothermodynamics, *Physical Review E* Vol. 77: 022102.

Cercignani, C. (1988). *The Boltzmann Equation and its Applications*, Springer–Verlag.

Cercignani, C., Illner, R. & Pulvirenti, M. (1994). *The Mathematical Theory of Dilute Gases*, Springer–Verlag.

Chandrasekhar, S. (1960). *Plasma Physics*, University of Chicago Press.

Chapman, S. & Cowling, T. G. (1970). *The Mathematical Theory of Non–Uniform Gases*, Cambridge University Press.

Collin, D., Ritort, F., Jarzynski, C., Smith, S. B., Tinoco Jr, I., & Bustamante, C. (2005). Verification of the Crooks fluctuation theorem and recovery of RNA folding free energies, *Nature* Vol. 437: 231–234.

Cowling, T. G. (1957). *Magnetohydrodynamics*, Interscience Publ. Co..

Crooks, G. E. (2000). Path-ensemble averages in systems driven far from equilibrium, *Physical Review E* Vol. 61: 2361–2366.

Crooks, G. E. (1999). Entropy production fluctuation theorem and the nonequilibrium work relation for free energy differences, *Physical Review E* Vol. 60: 2721–2726.

Currie, L. G. (1974). *Fundamental Mechanics of Fluids*, Mc-Graw–Hill.

Erwin, D. A., G.C. Pham–Van–Diep, G. C. & E.P. Muntz, E. P. (1991). Nonequilibrium gas flows: A detailed validation of Monte Carlo direct simulation for monatomic gases, *Physics of Fluids A* Vol. 3: 697–705.

Esposito, M., Harbola, U. & Mukamel, S. (2010) Nonequilibrium fluctuations, fluctuation theorems, and counting statistics in quantum systems, *Reviews of Modern Physics* Vol. 81: 1665–1698.

Esposito, M. & Van den Broeck, C. (2010). Three Detailed Fluctuation Theorems, *Physical Review Letters* Vol. 104: 090601.

Evans, D. J. & Searles, D. J. (2002). The fluctuation theorem, Advances in Physics, Vol. 51: 1529–1585.

Evans, D. J. & Searles, D. J. (1994). Equilibrium microstates which generate second law violating steady states, *Physical Review E* Vol. 50: 1645–1648.

Evans, D. J., Cohen, E. G. D. & Morris, G. P. (1993). Probability of second law violations in shearing steady states. *Physical Review Letters* Vol. 71: 2401–2404.

Eu, B. C. (1998). *Nonequilibrium Statistical Methods*, Kluwer.

Feshbach, H. & and F. Villars, F. (1958). Elementary Relativistic Wave Mechanics of Spin 0 and Spin 1/2 Particles, *Reviews of Modern Physics* Vol. 30: 24–45.

Ferziger, J. H. & Kaper, H. P. (1972). *Mathematical Theory of Transport Processes in Gases* North-Holland.

Feynman, R. P. (1955). Applications of Quantum Mechanics to Liquid Helium, *in* Gorter, C. J. (ed.), *Progress in Low Temperature Physics, vol. I*, North Holland, Amsterdam, chapter II.

Fefferman, C. L. (2000). Existence & Smoothness of the Navier–Stokes Equations. Manuscript available at:http://www.claymath.org/millennium/.

Fickett, W, & Davis, W. C. (2000). *Detonation Theory and Experiment*, Dover.

Fiscko, K. A. & D.R. Chapman, D. R. (1989). Comparison of Burnett, Super–Burnett and Monte Carlo solutions for hypersonic shock structure, *in* Muntz, E. P., Weaver, D. P. & Campbell, D. H. (eds.), *Rarefied Gas Dynamics, vol. 18*, AIAA, Washington D. C., pp. 374–395.

Foch Jr., J. D. (1973). On higher order hydrodynamic theories of shock structure, *Acta Physica Austriaca suppl. X*: 123–140.

Foch Jr., J. D. & Simon, C. E. (1977). Numerical integration of the Burnett equations for shock structure in a Maxwell gas, *in* J. L. Potter (ed.), *Rarefied Gas Dynamics, Progress in Astronautics and Aeronautics, vol. 51*, AIAA, New York, pp. 493–500.

Fomin, N. A. (2010). 110 Years of Experiments on Shock Tubes, *Journal of Engineering and Thermophysics* Vol. 83: 1118–1135.

Gallavotti, G. & Cohen, E. G. D. (1995). Dynamical Ensembles in Nonequilibrium Statistical Mechanics, *Physical Review Letters* Vol. 74: 2694–2697.

García-Colín & Dagdug, L. (2009). *The Kinetic Theory of Inert Dilute Plasmas*, Springer-Verlag.

García-Colín, L. S., Velasco, R. M., & Uribe, F. J. (2008). Beyond the Navier–Stokes equations: Burnett hydrodynamics, *Physics Reports* Vol. 465: 149–189.

García–Colín, L. S., Velasco, R. M. & Uribe, F. J. (2004). Inconsistency in the Moment's method for solving the Boltzmann equation, *Journal of Non–Equilibrium Thermodynamics* Vol. 29: 255–277.

Garnier, E. & Ciliberto, S. (2005). Nonequilibrium fluctuations in a resistor, *Physical Review E* Vol. 71: 060101.

Gilbarg, D. & Paolucci, D. (1953). The structure of shock waves in the continuum theory of fluids, *J. Ration. Mech. Anal.* Vol. 2 617–642.

Gilbarg, D. (1951). The Existence and Limit Behavior of the One–Dimensional Shock Layer, *American Journal of Mathematics* Vol. 73: 256–274.

Gnoffo, P. A. (1999). Planetary-entry gas dynamics, *Annual Review of Fluid Mechanics* Vol. 31: 459–494.

Goncharov, V. N., Gotchev, O. V., Vianello, E., Bohely, T. R., Knauer, J. P., McKenty, P. W., Radha, P. B., Regan, S. P., Sangster, T. C., S. Skupsky, S., Smalyuk, V. A., Betti, R., McCrory, R. L., Meyerhofer, D. D. & C. Cherfils–Clérouin, C. (2006). Early stage of implosion in inertial confinement fusion: Shock timing and perturbation evolution, *Physics of Plasmas* Vol. 13: 012702.

Grad, H. (1958). Principles of the kinetic theory of gases, *in* Flügge, D. (ed.), *Handbuch der Physik*, Springer–Verlag, Berlin, pp. 205–294.

Greenshields, C. J. & and J. M. Reese, J. M. (2007). The structure of shock waves as a test of Brenner's modications to the Navier–Stokes equations, *Journal of Fluid Mechanics* Vol. 580: 407–429.

Helbing, D. (2001). Traffic and related self–driven many–particle systems, *Reviews of Modern Physics* Vol. 73: 1068–1141.

Hill, T. L. (1963). *Thermodynamics of small sytems, Part I*, Benjamin.

Hill, T. L. (1964). *Thermodynamics of small sytems, Part II* Benjamin.

Hill, T. L. (1968). *Thermodynamics for Chemist and Biologist*, Addison Wesley.

Holian, B. L., Mareschal, M. & Ravelo, R. (2011). Burnett–Cattaneo continuum theory for shock waves, *Physical Review E* Vol. 83: 026703.

Holian, B. L. & Lomdahl, P. S. (1998). Plasticity Induced by Shock Waves in Nonequilibrium Molecular–Dynamics Simulations, *Science* Vol. 280: 2085–2088.

Holian, B. L., Patterson, C. W., Mareschal, M. & Salomons, E. (1993). Modeling shock waves in an ideal gas: Going beyond the Navier–Stokes level, *Physical Review E* Vol. 47: R24–R27.

Holian B. L., Hoover, W. G., Moran B. & Straub B. K. (1980). Shock–wave structure via non–equilibrium molecular–dynamics and Navier–Stokes continuum mechanics, *Physical Review A* Vol. 22: 2798–2808.

Holmes, P., Lumley, J. L. & Berkooz, G. (1998). *Turbulence, Coherent Structures, Dynamical Systems and Symmetry*, Cambridge University Press.

Hoover, Wm. G. & Hoover, C. G. (2010). Shock waves and Local Hydrodynamics; Failure of the Navier–Stokes Equations, Macias, A. & Dagdug, L. (eds.), *in* New trends in Statistical Physics: Festschrift in Honor of Leopoldo García–Colín 80^{th} Birthday, World Scientific, Singapore, pp. 15–26.

Hoover, Wm. G. & Hoover, C. G. (2010). Well–posed two–temperature constitutive equations for stable dense fluid shock waves using molecular dynamics and generalizations of Navier–Stokes–Fourier continuum mechanics, *Physical Review E* Vol. 81: 046302.

Hoover, Wm. G. (2006). *Smooth Particle Applied Mechanics: The State of the Art.*, World Scientific.

Horikoshi, M., Nakajima, S., Ueda, M. & Mukuyama, T. (2010). Measurement of Universal Thermodynamic Functions for a Unitary Fermi Gas, *Science* Vol. 327: 442–445.

Huang, K. (1964). *in* de Boer, J. & Uhlenbeck, G. E. (eds.), *Studies in Statistical Mechanics, vol. II*, North Holland, Amsterdam, pp. 2–106.

Hwa, R. C. (1974). Statistical description of hadron constituents as a basis for the fluid model of high–energy collisions, *Physical Review D* Vol. 10: 2260–2268.

Irving, J. H. & Kirkwood, J. G. (1950). The Statistical Mechanical Theory of Transport Processes. IV. The Equations of Hydrodynamics, *Journal of Chemical Physics* Vol. 18: 817–829.

Irving, J. H. & Zwanzig, R. W. (1951). The Statistical Mechanical Theory of Transport Coefficients. 6. Quantum Hydrodynamics, *Journal of Chemical Physics*, Vol. 19: 1173–1180.

Jackson, J. D. (1962). *Classical Electrodynamics*, John Wiley & Sons.

Jarzynski, C. (1997) Nonequilibrium Equality for Free Energy Differences, *Physical Review Letters* Vol. 78: 2690–2693.

Jarzynski, C. (1997) Equilibrium free–energy differences from nonequilibrium measurements: A master-equation approach, *Physical Review E* Vol 56: 5018–5035.

Jarzynski, C. (2007). *Lect. Notes Phys.* Vol. 711 201–216.

Jayannavar, A. M. & Sahoo, M. (2007). Charged particle in a magnetic field: Jarzynski equality, *Physical Review E* Vol. 75: 032102.

Jiménez-Aquino, J. I., Velasco, R. M. & Uribe, F. J. (2008). Dragging of an electrically charged particle in a magnetic field, *Physical Review E* Vol. 78: 032102.

Jiménez-Aquino, J. I., Velasco, R. M. & Uribe, F.J. (2009). Fluctuation relations for a classical harmonic oscillator in an electromagnetic field, *Physical Review E* Vol. 79: 061109.

Jiménez-Aquino, J. I, Uribe, F. J., & Velasco, R. M. (2010). Work-fluctuation theorems for a particle in an electromagnetic field, *J. Phys. A: Math. Theor.* Vol. 43: 255001.

Jiménez-Aquino, J. I. (2010). Entropy production theorem for a charged particle in an electromagnetic field, *Physical Review E* Vol. 82: 051118.

Jin, S. & Slemrod, M. (2001). Regularization of the Burnett equations for rapid granular flows via relaxation, *Physica D–nonlinear Phenomena* Vol. 150: 207-218.

Jin, S. & Slemrod, M. (2001). Regularization of the Burnett equations via relaxation, *Journal of Statistical Physics* Vol. 103: 1009–1033.

Saha, A. & Jaynnavar, A. M. (2008). Nonequilibrium work distributions for a trapped Brownian particle in a time-dependent magnetic field, *Physical Review E* Vol. 77: 022105.

Kadanoff, L. P. & Baym, G. (1962). *Quantum Statistical Mechanics*, Benjamin.

Kauzmann, W. (1966). *Kinetic Theory of Gases*, Benjamin. Khalatnikov, I. M. (1965). *Introduction to the Theory of Superfluidity*, Benjamin.

Kovtun, P., Son, D. T. & Sterinets, A. O. (2005). *Physical Review Letters* Vol. 94: 11160.

Khalatnikov, I. M. (1965). *Introduction to the Theory of Superfluidity*, Benjamin.

Kulsrud, R. M. (2005). *Plasma Physics for Astrophysics*, Princeton University Press.

Landau, Izv. Akad. Nauk. USSR 17, 51 (1953).

Landau, L. D. (1941). The Theory of Superfluidity of Helium II, *J. Phys. USSR* Vol. 5: 71–90.

Landau, L. D.(1986). *Fluid Mechanics*, Pergamon Press.

Lechner, W., Oberhofer, H., Dellago, C. & Geissier, P. L. (2006). Equilibrium free energies from fast–switching trajectories with large time steps, *Journal of Chemical Physics* Vol. 124: 044113.

London, F. (1964). *Superfluids Vol. II, Macrocopic Theory of Superfluid Helium*, Dover.

Luo, L. & Thomas, J. E. (2009). Thermodynamic Measurements in a Strongly Interacting Fermi Gas, *Journal of Low Temperature Physics* Vol. 154: 1–29.

Liphardt, J., Dumont, S., Smith, S. B., Tinoco Jr., I. & Bustamente, C. (2002). Equilibrium Information from Nonequilibrium Measurements in an Experimental Test of Jarzynski's Equality, *Science* Vol. 296: 1832–1835.

Madelung E. (1927) Quantentheorie in hydrodynamischer form, *Zeits. für Physik* Vol. 40, 322–.

McCourt, F. R. W., Beenakker, J. J. M., Köhler, W. E. & Kuščer, I. (1990). *Nonequilibrium Phenomena in Polyatomic Gases*, Clarendon Press.

Moratto, V. & García-Colín, L. S. (2011), Relaxation time for the Temperature in a dilute binary mixture from classical kinetic theory, *J. Non–equilibrium Thermodynamics* (in the press).

Mori, H., Oppenheim, I. & Ross, J. (1962). Wigner Functions and Transport Theory, *in* G. E. Uhlenbeck & J. de Boer (eds.), *Studies in Statistical Mechanics*, North Holland, Amsterdam.

Mott-Smith, H. M. (1951). The solution of the Boltzmann equation for a shock wave, *Physical Review* Vol. 82: 885–892.

Müller, I. & T. Ruggeri, T. (1993). *Extended Thermodynamics*, Springer.

Onsager, L., Unpublishd Remark at Low Temperature Conference at Shelter Island (1948). See Putterman (1974).

Pham–Van–Diep, C. G., Erwin, D. A. & Muntz, E. P. (1991). Testing continuum descriptions of low–Mach–number shock structures, *Journal of Fluid Mechanics* Vol. 232: 403–413.

Piran, T. (2004). The physics of gamma-ray bursts, *Reviews of Modern Physcis* Vol. 76: 1144–1210.

Procacci, P., Marsili, S., Barducci, A., Signorini, G. F. & Chelli, R. (2006). Crooks equation for steered molecular dynamics using a Nosé–Hoover thermostat, *Journal of Chemical Physics* Vol. 125: 164101.

Putterman, S. J. (1974). *Superfluid Hydrodynamics*, North Holland.

Richmyer, R. D. (1978). *Principles of Advanced Mathematical Physics, Vol1*, Springer–Verlag.

Reif, F. (1966). *Fundamentals of Thermal and Statistical Physics*, Mc Graw Hill.

Résibois, P. & Leener, M. D. (1977). *Classical Kinetic Theory of Fluids*, Wiley.

Ritort, F. (2009). Fluctuation in open systems, *Physics* Vol. 2: 43.

Rosenau, P. (1989). Extending hydrodynamics via the regularizations of the Chapman–Enskog expansion, *Physical Review A* Vol. 40: 7193âĂŞ7196.

Roy, D. & Kumar, N. (2008). Langevin dynamics in crossed magnetic and electric fields: Hall and diamagnetic fluctuations, *Physical Review E* Vol. 78: 052102.

Saito, K. & Dhar, A. (2007). Fluctuation Theorem in Quantum Heat Conduction, *Physical Review Letters* Vol. 99: 180601.

Saha, A., Lahiri, S. & Jayannavar, A. M. (2009). Entropy production theorems and some consequences, *Physical Review E* Vol. 80: 011117.

Salomons, E., & Mareschal, M. (1992). Usefulness of the Burnett description of strong shock–waves, *Physical Review Letters* Vol. 69: 269–272.

Searles, D. J. & Evans, D. J. (2000). Ensemble dependence of the transient fluctuation theorem, *Journal of Chemical Physics* Vol. 113: 3503–3509.

Seifert, U. (2005). Entropy Production along a Stochastic Trajectory and an Integral Fluctuation Theorem, *Physical Review Letters* Vol. 95: 040602.

Seifert, U. (2008). Stochastic thermodynamics: principles and perspectives, *Eur. Phys. J. B* Vol. 64: 423–431.

Sekimoto, K. (1988). Langevin Equation and Thermodynamics, *Prog. Theor. Phys.* Suppl. 130: 17–27.

Sela, N & Goldhirsch, I. (1998). Hydrodynamic equations for rapid flows of smooth inelastic spheres, to Burnett order, *Journal of Fluid Mechanics* Vol. 361: 41–74.

Sevick, E. M., Prabhakar, R., Williams, S. R. & Searles, D. J. (2008). Fluctuation Theorems, *Annu. Rev. Phys. Chem.* Vol. 59: 603–633.

Shargel, B. H. (2010). The measure-theoretic identity underlying transient fluctuation theorems, *J. Phys. A: Math. Theor.* Vol. 43: 135002.

Schäfer, T. & Teaney, D. (2009). Nearly perfect fluidity: from cold atomic gases to hot quak–gluon plasmas. *Rep. Prog. Phys.* Vol. 72, 126001.

Slemrod, M. (1998). Renormalization of the Chapman–Enskog expansion: Isothermal fluid flow and Rosenau saturation, *Journal of Statistical Physics* Vol. 91: 285–305.

Sone, Y. (2002). *Kinetic Theory and Fluid Dynamics*, Birkhäuser.

Spitzer, L. (1956). *The Physics of Fully Ionized Gases*, Interscience Wiley.

Struchtrup, H. (2005). *Macroscopic Transport Equations for Rarefied Gas Flows*, Springer–Verlag.

Tietz, C., Schuler, S., Speck, T., Seifert, U. & Wrachtrup, J. (2006). Thermodynamics of a Colloidal Particle in a Time–Dependent Nonharmonic Potential, *Physical Review Letters* Vol. 97: 050602.

Trepagnier, E. H., Jarzynski, C., Ritort, F., Crooks, G. E., Bustamante, C. J. & Liphardt, J. (2004). Experimental Test of Hatano and Sasa's Nonequilibrium Steady–State Equality, *Proc. Natl. Acad. Sciences* Vol. 101: 15038–15041.

Truesdell C. & Müncaster, R. G. (1980). *Fundamentals of Maxwell's Kinetic Theory of a Simple Monatomic Gas*, Academic Press.

Uribe, F. J., Hoover, Wm. G. & Hoover, C. G. (2011). Maxwell and Cattaneo's Time–Delay Ideas Applied to Shockwaves and the Rayleigh–Bénard Problem, arXiv:1102.2560v2 [physics.flu-dyn].

Uribe, F. J. (2011). The Shock Wave Problem Revisited: The Navier–Stokes Equations and Brenner's Two Velocity Hydrodynamics, *in* Gorban, A. N. & Roose, D. (eds.), *Coping with Complexity: Model Reduction and Data Analysis*, Springer, Berlin, pp. 207–229. In eqs. (11) and (14) the changes $T \to T(u)$ and $u(T) \to u$ should be made.

Uribe, F. J. (2001). Understanding dilute gases: Going beyond the Navier–Stokes equations, *in* Ramos, E., Cisneros, G., Fernández–Flores, R., Santillán–González A. (eds.), *Computational Fluid Mechanics*, World Scientific, Singapore, pp. 255–264.

Uribe, F. J., Velasco, R. M., García-Colín, L. S. & Díaz-Herrera, E. (2000). Shock wave profiles in the Burnett approximation, *Physical Review E* Vol.62: 6648–6666.

Uribe, F. J., Velasco, R. M. & García-Colín, L. S. (1998). Burnett description of strong shock waves, *Physical Review Letters* Vol. 81: 2044–2047.

Van Kampen, N. G. & Felderhof, B. U. (1967). *Theoretical Methods in Plasma Physics*, North Holland.

van Zon, R. & and Cohen, E. G. D. (2004). Extended heat-fluctuation theorems for a system with deterministic and stochastic forces, *Physical Review E* Vol. 69: 056121.

van Zon, R. & and Cohen, E. G. D. (2003). Stationary and transient work-fluctuation theorems for a dragged Brownian particle, *Physical Review E* Vol 67: 046102.

Velasco, R. M., García-Colín, L. S. & Uribe, F. J. (2011). Entropy Production: Its Role in Non-Equilibrium Thermodynamics, *Entropy* Vol. 13: 82–116.

Velasco, R. M., Uribe, F. J. & García–Colín, L. S. (2002). Inconsistencies in moment methods *Physical Review E* Vol. 66: 032103.

Villani, C. (2006). A Review of Mathematical Topics in Collisional Kinetic Theory, *in* S. Friedlander, S. & D. Serre, D. (eds.), *Handbook of Mathematical Fluid Dynamics, vol. 1*, Elsevier Science, pp. 71–261.

von Neumann, J. (1955). *Mathematical Foundations of Quantum Mechanics*, Princeton University Press.

Wang, G. M., Sevick, E. M., Mittag, E., Searles, D. J. & Evans, D. J. (2002). Experimental Demonstration of Violations of the Second Law of Thermodynamics for Small Systems and Short Time Scales, *Physical Review Letters* Vol. 89: 050601.

Wigner, E. P. (1932). On the quantum correction for thermodynamic equilibrium, *Physical Review* Vol. 40: 749–759.

Wilks, J. (1966). *The Properties of Liquid and Solid Helium*, Oxford University Press, Clarendon.

Wong, C. Y. (2008). Landau hydrodynamics reexamined, *Physical Review C* Vol. 78: 054902.

Wong, C. Y. (2010). Foundation of Hydrodynamics for Systems with Strong Interactions, *in* Dagdug, L. *et al.* (eds.), *AIP Conference Proceedings 1312, IV Mexican Meeting in Mathematical and Experimental Physics: Relativistic and Biological Physics*, AIP, USA, pp. 39–48.

Wong, C. Y. (2008). Lectures on Landau Hydrodynamics. arXiv: 0809.0517v1 [nucl–th].

Wong, C. Y. (2010). Klein–Gordon in hydrodynamical form, *Journal of Mathematical Physics*, Vol. 51: 122304.

Woosley, S. E., Heger, A., & Weaver, T. A. (2002). The evolution and explosion of massive stars, *Reviews of Modern Physics* Vol. 74: 1016–1071.

Xu, K. & Josyula, E. (2005). Multiple translational temperature model and its shock structure solution, *Physical Review E* Vol. 71: 056308.ôŔřč

Xu, K. & Li, Z. H. (2004). Microchannel flow in the slip regime: gas–kinetic BGK–Burnett solutions, *Journal of Fluid Mechanics* Vol. 153: 87–110.

Yarnell, J. L., Arnold, G. P., Bendt, P. J. & and Kerr, E. C. (1959). Exitations in Liquid Helium–Neutron Scattering Measurements, *Physical Review* Vol. 113: 1379–1386.

Zel'dovich, Ya. B. & Raizer, Yu. P. (2002). *Physics of Shock Waves and High–Temperature Hydrodynamic Phenomena*, Dover.

Zuckerman, D. M. & Wolf, T. B. (2002). Theory of a Systematic Computational Error in Free Energy Differences, *Physical Review Letters* Vol. 89: 180602.

11

Calorimetric Investigations of Non-Viral DNA Transfection Systems

Tranum Kaur[1], Naser Tavakoli[1,2], Roderick Slavcev[1] and Shawn Wettig[1]
[1]*School of Pharmacy, University of Waterloo*
[2]*School of Pharmacy and Pharmaceutical Sciences*
Isfahan University of Medical Sciences, Isfahan
[1]*Canada*
[2]*Iran*

1. Introduction

Although the structural and energetic forces involved in DNA condensation have been studied for years, this area has experienced a resurgence of interest in recent years with respect to developing gene therapy protocols to combat a variety of human diseases. Despite an intense effort to study the mechanism(s) of DNA condensation using a variety of techniques such as microscopic, light scattering, fluorescence, and calorimetric techniques the precise details of the energetics of DNA nanoparticle formation and how these complexes assemble is not well understood at present. Isothermal titration calorimetry (ITC) has become an important technique for studying the binding energetics of biological processes, including protein-protein binding, protein-carbohydrate binding, protein-lipid binding, antigen-antibody binding, DNA-protein binding, and the DNA-lipid binding that is at the heart of non-viral transfection vectors. Given the large informational content of thermodynamic data (such as binding constants, stoichiometry, enthalpies of interaction, etc.) it is not surprising that ITC is being used for the elucidation of the binding mechanism of DNA with surfactants or lipids used in non-viral gene delivery vectors. This is described in more detail in this Chapter.

1.1 Principle and experimental set up

One of the fundamental challenges in biophysical chemistry, as well as in all physicochemical events implying a solvent, is to attribute the contribution of different non-covalent interactions (electrostatic in the most general sense, solvation and hydrophocic interactions, hydrogen bonding, Van der Waals interactions) to the free energy change of a given molecule upon its interaction with a binding partner. Another challenge is to investigate how conformational changes in the three dimensional structure of a protein, DNA or RNA can modify the interaction between itself and its binding partner. Finally, the most important challenge is to relate structure (the high resolution X-ray or NMR structure of more and more proteins and nucleotides are available) to the "binding affinity" of these molecules with their binding partners. This means that the "binding affinities" have to be accurately measured for as many as possible systems to get a clear picture of structure-

activity relationships, which is particularly important for the design of new drugs or the design of gene vectors for gene therapy. Unlike any other method used to determine thermodynamic parameters associated with bimolecular interactions, calorimetery uses the direct measurement of the heat of interaction (or molar enthalpy ΔH) to probe the extent of binding between the molecules. When substances bind, heat is either generated or absorbed.

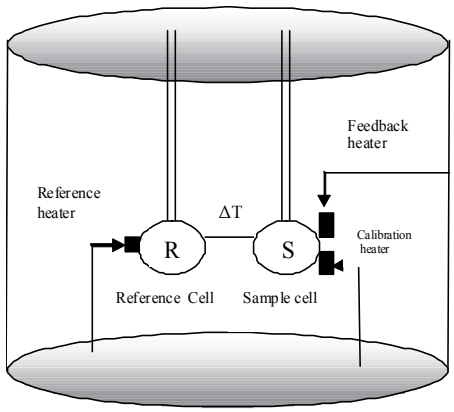

Fig. 1. Schematic diagram of an ITC instrument.

Isothermal microcalorimtery is a thermodynamic technique that directly measures the heat released or absorbed during a biomolecular binding event. Measurement of this heat allows accurate determination of binding constants, reaction stoichiometry (n), enthalpy (ΔH) and entropy (ΔS), thereby providing a complete thermodynamic profile of the molecular interaction in a single experiment. The first modern isothermal microcalorimeter was designed by Calvet (Calvet and Prat, 1963). An ITC instrument consists of two identical cells composed of a highly efficient thermal conducting material (e.g. gold) surrounded by an adiabatic jacket (Figure 1). The jacket is usually cooled by a circulating water bath. Sensitive thermopile circuits detect temperature differences between cells and the jacket, while heaters located on both cells and the jacket are activated when necessary to maintain identical temperatures between all components. In a typical ITC experiment, the macromolecule is placed into the sample cell of the calorimeter and is titrated at constant temperature with the ligand in a syringe. The reference cell contains water or buffer. Prior to injection of the titrant, a constant power (< 1 mW) is applied to the reference cell. This signal directs the feedback circuit to activate the heater located on the sample cell. This represents the baseline signal. During the injection of titrant into the sample cell, heat is taken up or evolved depending on whether macromolecular association reaction is endothermic or exothermic. For an exothermic reaction, the temperature in the sample cell will increase, and the feedback power will be deactivated to maintain equal temperature between the two cells. For endothermic reaction, the reverse will occur.

The heat released (in terms of molar enthalpy ΔH), upon interaction of the titrant is monitored over time. Each peak represents a heat change associated with the injection of a small volume of ligand solution into the ITC reaction cell. As successive amounts of the ligand are titrated into the ITC cell, the quantity of heat absorbed or released is in direct proportion to the amount of binding. When the system reaches saturation, the heat signal diminishes until only heats of dilution are observed. A binding curve is then obtained from

a plot of the heats from each injection against the ratio of ligand and binding partner in the cell. A molecular interaction between two ligands can be defined by the following equation which forms the basis for an ITC analysis:

$$\Delta G = -RT \ln K_A = \Delta H - T\Delta S \quad (1)$$

The first part of this equation implies that the change in the Gibbs free energy (ΔG) correlates with association constant K_A because R, the gas constant, and T, the absolute temperature, are constant. The dissociation constant K_D, which is commonly used to quantify the affinity between two ligands, is the inverse of K_A. The second part of this equation illustrates that the sum of enthalpy (ΔH) and entropy (ΔS) changes define the free energy (ΔG) and consequently the affinity of an interaction. A major advantage of ITC experiments is the fact that K_A and ΔH are measured in a single experiment. Having measured these two parameters the remaining variables ΔG and ΔS can be derived. In combination with structural information, the energetics of binding can provide a complete picture of the interaction and aid in identifying the most important regions of the binding interface and the energetic contribution (Pierce *et al.*, 1999).

2. Non-viral DNA transfection systems

An emerging trend in the treatment of disease is gene therapy, a broad term that includes any strategy to treat a disease by delivering exogenous gene, gene segments, or oligonucleotides into the cells of patients in order to restore normal functions to the cell. Such therapies are either DNA based (usually in the form of plasmids) or RNA based (usually in the form of small, interfering RNA or siRNA), both requiring some form of delivery system for the oligonucleotide(s) in question.

Two major classifications of delivery systems exist for DNA therapies, viral- and non-viral-based. Viral vectors typically demonstrate the highest gene transfer activity; however, they suffer from serious safety concerns particularly with respect to inflammatory and immune responses in patients. Non-viral vectors are generally comprised of a combination of cationic lipids, neutral lipids and/or cationic polymers, and have a much better safety profile compared to viral systems but suffer from low gene transfer activities. As such a great deal of effort is being expended towards the development of new non-viral vector systems with increased transfection capabilities.

Lipoplexes, complexes of liposomes with DNA, are the most investigated non-viral transfection vectors, and hold great potential application for gene delivery. They have been utilized in approximately 8% of the clinical trials for gene therapy mainly due to their advantages over viral vectors. They show low toxicity, high therapeutic gene capacity, cell-specific targeting capability, and straightforward production, modification, and functionalization procedures. A key problem in the advancement of lipoplex transfection vectors, yet to be efficiently overcome, is the above mentioned inadequacy of transfection efficiency of current cationic lipid systems, attributed to the incomplete understanding of interaction mechanisms involved. While this is driving research efforts toward the design and synthesis of novel amphiphilic cationic compounds, as well as approaches for formulation of liposomal based vectors (Giatrellis *et al.*, 2009), less effort is being directed towards better understanding the fundamental mechanism(s) by which liposome-mediated transfection occurs.

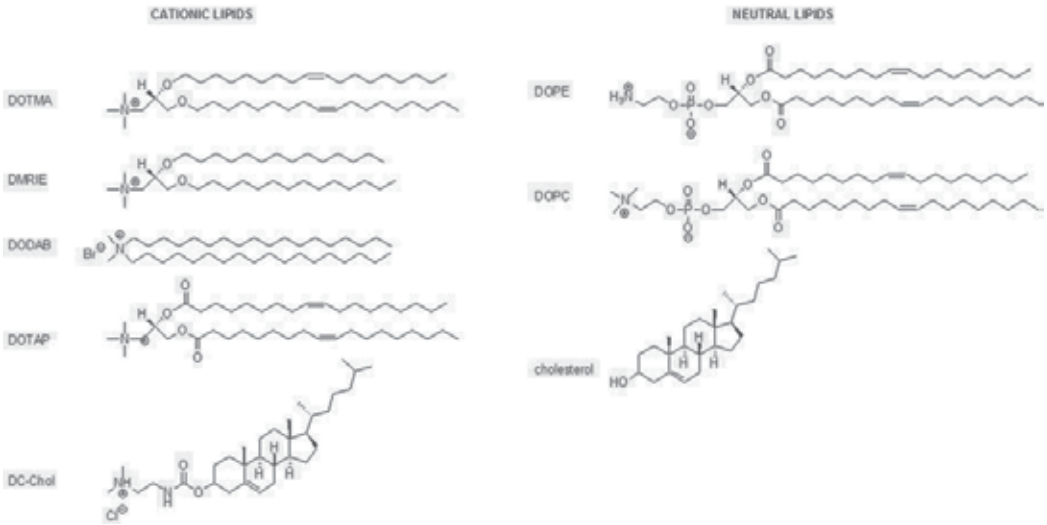

Scheme 1. Chemical structure of lipids commonly used in the formulation of DNA transfection complexes: DOTMA (1,2-di-O-octadecenyl-3-trimethylammonium propane), DMRIE (1,2-dimyristyloxypropyl-3-dimethyl-hydroxy ethyl ammonium bromide), DODAB (dioleyldimethylammonium bromide), DOTAP (1,2-dioleoyl-3-trimethylammonium-propane (chloride salt), DC-Chol (3β-[N-(N',N'-dimethylaminoethane)-carbamoyl] cholesterol hydrochloride, DOPE (1,2-dioleoyl-sn-glycero-3-phosphoethanolamine), DOPC (1,2-dioleoyl-sn-glycero-3-phosphocholine), and cholesterol.

The first reported application of cationic liposomes (or vesicles) as DNA transfection vectors was in 1987, by Felgner et al. They synthesized a cationic lipid, N-[1-(2,3-dioleyloxy)propylJ-N,N,N-trimethylammonium chloride (DOTMA), that forms small unilamellar cationic liposomes, closed bilayer membrane shells of lipid molecules, and that interact with DNA spontaneously via electrostatic attraction. These lipid-DNA complexes maintain an overall positive charge, facilitating uptake by cells again by electrostatic attraction, now between the cationic complexes and the predominantly negatively charged cellular membrane. Complexes are then internalized allowing the transfer of functional DNA into the cell followed by expression. The technique was simple, highly reproducible, and more efficient than some other, commonly used procedures such as use of polycations, calcium phosphate, microinjection, electroporation and protoplast fusion (Felgner *et al.*, 1987) .

2.1 Mechanism of DNA – lipid Interactions

Due to electrostatic interactions between negatively charged phosphate groups along the DNA back bone and the cationic head group of the lipid, they compact the DNA plasmid into small particles. This compaction serves two purposes: 1) to more easily transport the DNA across negatively charged cellular membrane(s), both in terms of eliminating electrostatic repulsion between negatively charged DNA and the cell membrane (Barreleiro et al, 2000, Safinya, 2001), and also by simply having a smaller size (relative to an uncomplexed DNA plasmid); and 2) to protect the DNA from degradation (primarily by DNAses) during the transfection process (Tranchant *et al.*, 2004;Elouahabi and Ruysschaert,

2005). The importance of the cationic lipid is however not restricted solely to the charge of its head group. (Cherezov *et al.*, 2002). Kreiss et al. believed that both the nature (or structure) of the cationic lipid as well as the DNA backbone exert a strong influence on lipid-DNA packing and complex morphology, with the formation of the lipoplexes resulting from competitive interactions between electrostatic forces of lipid-DNA and elasticity forces driven by the lipid hydrophobic moiety (Zuzzi *et al.*, 2007;Ma *et al.*, 2007;Kreiss *et al.*, 1999).
It has been suggested that lipoplex formation is an endothermic process and the repulsion force between DNA molecules as well as the release of tightly bound counterions from DNA and the lipid mainly controls the formation of cationic lipid/DNA complex (Ma *et al.*, 2007). In the course of complex formation, DNA acts as a polyanion molecule interacting with the cationic headgroups at the surface of liposomes. The neutralization of charges seems to affect both the DNA and the liposome structures. First, DNA might adopt a more compact structure, which is less accessible to intercalating dyes or nucleases. Second, neutralization might induce lipid bilayer mixing and/or aggregation resulting in fusion of liposomes and/or multilamellar structure formation. The fact that different structures are observed in the same lipoplex preparation further complicates the interpretation (Zabner *et al.*, 1995). Apart from the electrostatic interactions between positively charged lipid head groups and the negatively charged DNA phosphate backbone, variations in lipid-lipid and DNA-DNA ionic repulsive forces, attractive lipid-lipid hydrophobic interactions, hydration forces and other structural properties of the liposome and plasmid DNA can result in a wide variety of macromolecular structures that can vary not only with concentration(s) but also as a function of time. Hence, upon mixing of cationic lipid and DNA, the supramolecular organization of the two components changes considerably. Despite these changes in organization, the molecular structures of both components are generally preserved, leading to a so-called multilamellar complex, in which DNA molecules are intercalated between intact lipid bilayers and form a tightly packed grid (Smisterova *et al.*, 2001;Pitard *et al.*, 1999;Cherezov *et al.*, 2002;Radler *et al.*, 1997).

2.2 DNA / lipid complex morphologies

The most commonly complex assemblies include DNA molecules sandwiched within liposomal bilayers, DNA electrostatically adsorbed onto the vesicles outer surface, DNA encapsulated in the aqueous phase of the liposomes, and DNA coated by a monolayer of cationic lipid envelop (Felgner and Ringold, 1989;Giatrellis *et al.*, 2009). Therefore, lipoplexes have a broad range of morphologies from a hypothesized "beads on a string" arrangement proposed initially by Felgner (Felgner and Ringold, 1989) in their seminal paper, to more complicated such as spaghetti and meatballs structure (Sternberg *et al.*, 1994), map-pin structures (characterized by spheroidal heads and tapering pins)(Sternberg *et al.*, 1998)(See Figure 2), multilamellar or inverted hexagonal phase structures confirmed by high-resolution synchrotron small-angle X-ray scattering (SAXS) experiments (Safinya, 2001) and sliding columnar phase (O'Hern, 1998).
These above mentioned morphologies; however, are less common than the lamellar, "sandwich" structure (Koltover *et al.*, 1998;Sternberg *et al.*, 1994). Under lipid excess conditions there is only macroscopic heterogeneity (i.e., lipoplexes may be of different sizes) whereas the microscopic structure of lamellar cationic lipid-DNA "sandwich" is uniform as demonstrated by diffraction techniques (Radler *et al.*, 1997).

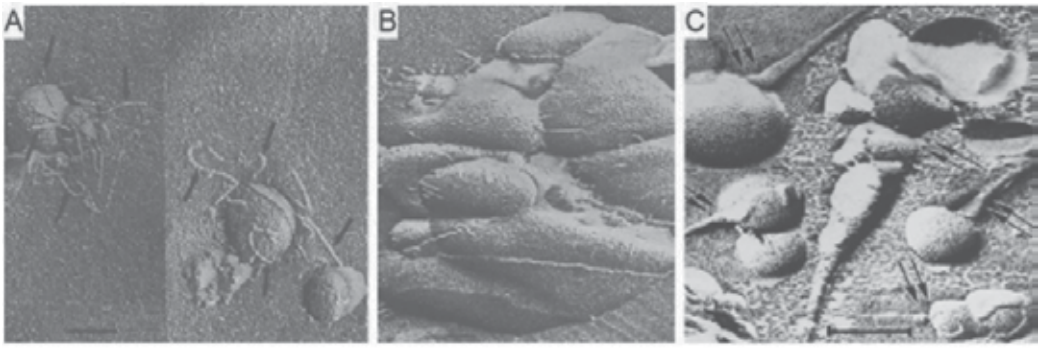

Fig. 2. A and B showing spaghetti-meatball assembly [adapted from (Sternberg *et al.*, 1994)] and C showing map-pin structures [adapted from (Sternberg *et al.*, 1998)].

2.3 Physiochemical properties, lipoplex structure, and their impact on transfection activity

Structure-activity studies suggested that biophysical properties, such as size, charge, and morphology of the resulting DNA complexes determine transfection efficiency within one class of vector. Several parameters effect transfection activity, such as structural variations of the cationic lipids (length and degree of unsaturation of the alkyl chains), the nature of the groups bound to the quaternary nitrogen, and the counterions. Variations in the lipid to DNA charge ratio and the presence or absence of helper lipids are other important formulation parameters of transfection efficiency (Lobo *et al.*, 2002;Malone *et al.*, 1989). In the majority of reported studies, lipid-DNA complexes function most effectively when a cationic lipid is mixed with a neutral or helper lipid such as DOPE (1,2-dioleoyl-sn-glycero-3-phosphoethanolamine) or DOPC (1,2-dioleoyl-sn-glycero-3-phosphocholine) (Scheme 1). DOPE is by far the most commonly used helper lipid in non-viral DNA transfection applications (Ewert *et al.*, 2008;Hui *et al.*, 1996). The inclusion of neutral or zwitterionic lipids (co-lipids), such as cholesterol, DOPE and DOPC as well as PEG lipids, other cationic lipids, and non-lipid compounds like polymers or peptides in the cationic vesicle formulations has been shown to increase the transfection efficiency of the assemblies (at least in case of DOPE) by promoting membrane fusion in different cell lines (Koynova *et al.*, 2007).

2.3.1 Size and zeta potential

In general, transfection efficiency (i) requires a positive or neutral zeta potential, (ii) is size dependent, e.g., it is higher for smaller size particles, and (iii) requires a vector that is stable in serum. The size of the DNA plays an important role in biodistribution, cellular internalization and intracellular trafficking (Pathak *et al.*, 2009). The correlation between lipoplex size and DNA transfection has been well studied; however, the most suitable size range (for transfection) still remains to be controversial. Early studies suggested the lipoplex sizes in the range of 400–1400 nm for more efficient transfection in cell culture than smaller (<400 nm) or larger (>1400 nm) aggregates (Kawaura *et al.*, 1998), but later results emphasize a smaller (<200 nm) lipoplexe size range (Zhang *et al.*, 2003). This controversy has been attributed to different size-dependent endocytic pathways involved in uptake of lipoplexes. As the gene transfection by the cationic liposomes was shown to be inhibited by wortmannin, an inhibitor of

endocytosis, it is suggested that the vesicles with moderate diameters are useful for gene transfection by endocytosis (Kawaura et al. 1998). Moreover, addition of non-lipid condensing agents such as polyethyleneimine, polylysine, protamine sulfate to the cationic lipid- DNA mixture have been reported to produce small homogeneous lipoplexes, in the range of 100 nm, more suitable to enter narrow capillaries than lipid-DNA alone. Further, the lipoplex particle size also plays a role in DNA release in which for lipoplexes with mean size of ~400–500 nm and lamellar distances of ~5–6 nm (and hence are composed of several tens of layers) extensive intermembrane interactions are required for their disassembly (Koynova, 2009). Zeta potential of lipoplexes is usually measured at different DNA/lipid ratios whereas pure cationic vesicles show a positive zeta potential of ~ 60 mV, and it decreases with addition of DNA and changes to negative at DNA/lipid charge ratio of more than 1 (Koynova *et al.*, 2007). Takeuchi et al showed that transfection efficiency of plasmid DNA (pSV2CAT) into mammalian cultured cells was consistent with the values of zeta potential of cationic liposomes containing a tertiary amino head group(Takeuchi *et al.*, 1996). Therefore, lipoplexes with a small excess of positive zeta charges favours higher transfection efficiency (Elouahabi and Ruysschaert, 2005) and *vice versa*, for lipoplex formulations containing excess amount of DNA and negatively surface charge, the release of DNA is significantly hindered compared to lipoplexes with positive zeta potential (Koynova *et al.*, 2007).

2.3.2 Structure

The role of the cationic lipid molecular structure on transfection activity of resultant lipoplexes has recently been reviewed; with the conclusion that lipids having either saturated alkyl chains with a length of ~14 carbon atoms OR longer, monounsaturated chains having trans-isomerism are generally the most effective for transfection (Koynova and Tenchov, 2009; Koynova *et al.*, 2008). It is important to note that this is only a generalization, and factors such as the stoichiometry of the cationic lipid to DNA, the ionic strength of the formulation, the temperature of the formulation (both during and after formulation), and the incubation time can all have a significant effect on the resulting structure of the lipoplex (Giatrellis *et al.*, 2009).

Association of DNA with cationic lipids in a micellar or liposomal form leads to lamellar organization with DNA molecules sandwiched between lipid bilayers. Although the lamellar phase is the common described structure, as evidenced by small-angle X-ray scattering and electron microscopy, some cationic lipid combined with a hexagonal forming lipid could also result with DNA in an inverted hexagonal structure(Barteau *et al.*, 2008). Despite all the advances in biological and biophysical characterization of cationic lipid-DNA complexes, the relationship of their structural properties to their biological activity is still not well understood. Some earlier studies, especially those carried out on lipoplexes containing DOPE, have proposed the inverted hexagonal structure (H^{C}_{II}) is more efficient in transfection than the lamellar (L^{C}_{α}) phase (See Figure 3) (Koltover *et al.*, 1998;Smisterova *et al.*, 2001). However, more recent studies have shown a general lack of correlation between lipoplex structures and transfection activity. Indeed, high lipofection not only depends on the structure and morphology of the vector assemblies, but also on other factors, (one important example of which is the type of cell being transfected; i.e. primary versus clonal, cancerous versus non-cancerous, etc.). The scope of accounting for all such factors makes it difficult for investigators to put together a comprehensive picture of effects such as variation of both cell types and cationic lipids within one study (Ma *et al.*, 2007).

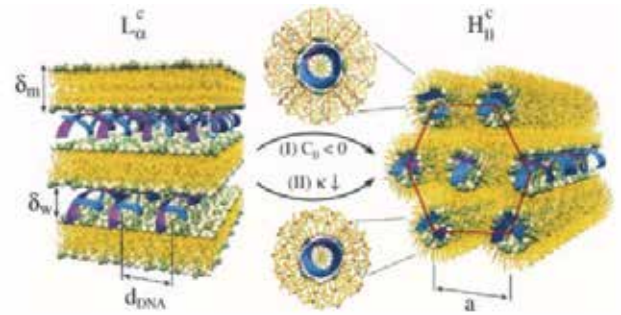

Fig. 3. Inverted hexagonal structure (H^C_{II}) phase structure and multilamellar (L^C_α) phase structures [adapted from (Koltover *et al.*, 1998)].

2.4 Thermodynamics of lipoplex formation

Self-assembly of surfactants into aggregates, such as micelles, vesicles, etc., can be induced by increasing the surfactant concentration to above the critical micelle concentration (CMC) and/or by adjusting the temperature to exceed the critical micelle temperature (CMT). In a typical calorimetry experiment, heats of dilution are recorded. Initially, the dilution of the concentrated surfactant solution (usually well above the CMC) will result in the dis-assembly of micellar aggregates into monomers, and the observed heat of dilution will contain both the heat of solution of the monomer surfactant, and the heat associated with micelle dis-assembling, which is the negative of the heat of micelle formation. As the experiment proceeds, the surfactant concentration in the measurement cell increases to above the CMC, as described in section 1, integration of the measured heats for each injection provides an observed enthalpy of dilution, from which, for a typical surfactant, the enthalpy of micellization (or aggregation), ΔH_{mic} can be obtained from the difference in the pre- and post-micellar enthalpies of dilution. The magnitude and sign (i.e., endo- or exo-thermic) of ΔH_{mic} is governed by the types and magnitude of various contributions (hydrophobic and electrostatic) arising from surfactant-surfactant interactions.

The interaction of cationic aggregates (micelles and/or lipoplexes) with DNA, while being more complex that the aggregation of the surfactants or lipids alone, is governed again by a combination of hydrophobic and electrostatic contributions. The thermodynamics of cationic lipid – DNA lipoplex formation are found to be in most cases, endothermic (Pector *et al.*, 2000;Pozharski and MacDonald, 2002). Since, for any process to be thermodynamically favoured the free energy change must be negative, an endothermic lipoplex formation must be driven by a corresponding increase in entropy (recall equation 1). The interesting question then becomes "what exactly is the source of this entropy gain upon lipoplex formation"? It is widely accepted that the major contribution to this increase in entropy arises from counterion release. Bruinsma first pointed out that lipoplex formation is not simply driven by electrostatic attraction between oppositely charged DNA polymer and lipid membrane, but that in fact the situation is more complex given that both components exist in solution with oppositely charged counterions bound to them that are released upon complex formation (Bruinsma, 1998). Release of these counterions upon complex formation results in an entropy gain that is expected to be, according to Bruinsma, ~1 kT per counterion. Both cationic lipid and DNA become partially dehydrated upon complex formation (Hirsch-Lerner and Barenholz, 1999) resulting in an additional entropy gain due to the additional degrees of freedom acquired by the released water. Hence, the entropy

based process is driven through the release of water molecules and of bound counter-ions via the ion-exchange process. It is important to note that the released counterions interact more strongly with water and restrict somewhat the mobility of the water molecules around them, an effect that must lead to some entropy loss. Additionally, the DNA and to a smaller extent the complexing lipids also experience some reduction in entropy because of loss of degrees of freedom due to increased rigidity of the complex relative to the separate components. Nevertheless, combined together the net result is entropically driven lipoplex formulation in general; however additional studies to further elucidate various contributions are still required.

As an example, Pozharski and MacDonald examined the strength of binding of DNA to the cationic lipid matrix upon lipoplex formation (Pozharski and MacDonald, 2003). In this study, the binding free energy was determined by monitoring lipoplex dissociation under conditions of increasing salt concentration. By using relatively short oligonucleotides, the investigators were able to determine the binding energy per nucleotide. A combination of calorimetry and fluorescence resonance energy transfer (FRET) was used in their work. For FRET studies a rhodamine labeled lipid was brought in proximity with carboxyfluorescein (CF) labeled DNA so that CF emission becomes quenched upon lipoplex formation. The decrease in the signal verified complex formation. A Microcal calorimeter was used to determine the cationic lipid-DNA binding enthalpy for the titration of 0.46 mM Dickerson dodecamer (5′-CGCGAATTCGCG) into 25 µM EDOPC (O-ethyldioleoylphosphocholine, cationic lipid) in HE-S buffer (of 20 mM HEPES, 0.1 mM EDTA, and 150 mM NaCl at pH 7.5). Figure 4 shows the degree of dissociation of complexes, α, plotted against NaCl concentration, and the heat absorbed at various ratios of DNA/ Lipid (D/L).

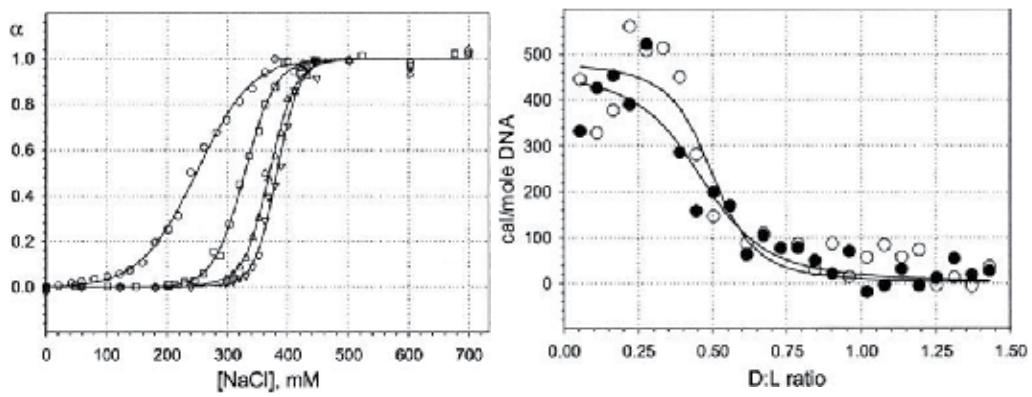

Fig. 4. DNA-EDOPC binding curves (LEFT) for lipid:DNA charge ratios of: ○2:1 ; □ 4:1 ; Δ 8:1 ; and ▼16:1 . Calorimetric profile (RIGHT) of cationic lipid-DNA binding. 460 μM of Dickerson dodecamer titrated into cationic lipid, EDOPC, suspension in HE-S buffer. Curves are from fitting to a one-site binding model; unfilled and solid circles correspond to two independent titrations. [Adapted from (Pozharski and MacDonald, 2003)].

Averaged over two runs, thermodynamic parameters of the binding were ΔG = −445 ± 20 cal/mole, and ΔH = 477 ± 42 cal/mole; it was observed that binding becomes more favorable with decreasing cationic lipid:DNA charge ratio. During lipoplex formation there is decrease of the apparent free energy with increasing length of the DNA fragment. It is suggested that there is strengthening of binding at higher lipid:DNA ratios, especially from

8:1 to 16:1, because of the continuing decrease of ΔG up to a charge ratio of 16:1. Lipoplexes with excess lipid actually have stronger lipid-DNA interactions. For example (assuming that the free bilayer is actually part of the lipoplex particle and not as separate vesicles), there may be internal edge effects such that it is easier to accommodate the boundary of DNA-covered areas when there is more lipid.

2.5 Multipoint nature of cationic lipid-DNA interactions

A DNA molecule binds to the lipid membrane at many points and the relatively small free energies of the individual charges sum to a very large binding energy for the whole molecule. The binding of an individual DNA electrostatic charge to the lipid membrane is rather weak (Pozharski and MacDonald, 2003). Hence, the size of DNA does indeed affect binding energy of lipoplex formation. Single lipid molecules cannot dissociate from the complex since they are held in bilayers by strong hydrophobic interactions and thus form a continuous matrix to which DNA can bind. DNA bases are covalently linked to each other and the stiffness of the polymer is such that a molecule only about as short as a dodecamer binds as a single unit. As a result, much more free energy is released upon a binding event and this brings the apparent dissociation constant into the micromolar range at physiological ionic strength. Longer DNA molecules bind more tightly, but their energy of interaction is also limited by their flexibility. The entropy gain upon lipoplex formation is ~1 kT per released counterion, and in general, this positive ΔS is the driving force of the lipoplex process, which is in good agreement with theoretical considerations. Moreover, very long DNA molecules will exhibit a lower tendency to remain attached throughout their length, but because the number of contact sites is high and because of their increased ability to bend, the extent of dissociation for long DNA molecules at moderate and low ionic strength is extremely small.

3. DNA – gemini surfactant systems

3.1 Unsubstituted gemini surfactants

We have recently reported the results of an isothermal titration calorimetric (ITC) study of the interaction of DNA with transfection systems based upon a family of dimeric surfactants, more commonly known as gemini surfactants (Wettig *et al.*, 2010;Yang *et al.*, 2010;Donkuru *et al.*, 2010). Gemini surfactants consist of two traditional surface active groups (i.e two hydrophobic chains and two polar headgroups) linked chemically by a spacer group. The most extensively synthesized and studied family of gemini surfactants are the N,N-bis-α,ω-alkane-diammonium dibromides, having a general structure [$C_mH_{2m+1}(CH_3)_2N^+(CH_2)_sN^+(CH_3)_2\ C_mH_{2m+1}\bullet 2Br^-$], hereafter referred as m-s-m, where m represents the carbon chain length of the alkyl tails and s the number of carbon atoms in the polymethylene spacer (See Scheme 2A). Compared to conventional surfactants having a single chain and a single head, gemini surfactants posses unique physiochemical properties, including lower critical micelle concentrations (CMCs) and better wetting properties. However, one of the most important advantages, in so far as gene therapy is concerned, is that the structure of gemini surfactants allows for expanded structural diversity through adjustment of the length of hydrophobic chains, the polarity of head groups, the structure of spacer and the counterions. The spacer length plays perhaps one of the most important roles in determining the properties of these surfactants, and therefore likely their interaction(s) with DNA. The effects of variations in the length of a polymethylene spacer group, as well

as the effects of incorporation of hydrophilic substitutents have been extensively studied and are the focus of several reviews on gemini surfactants.

It is generally observed that the chemical arrangement of gemini surfactants provide a rather rich array of aggregate morphologies and solution properties that are dependent upon the nature and size of the linking group. Our previous studies indicated that the transfection efficiency and *in vivo* cutaneous absorption was dependent on the length of the spacer between the two positively charged head groups (Foldvari et al. 2006). Gemini surfactants having a trimethylene spacer demonstrated the highest activity, with the transfection efficiencies correlating to other physical properties (such as the head group area at the air/water interface, critical micelle concentration, etc.) that depend upon the size and/or nature of the spacer group. Moreover, variation in the length of the spacer group allows for a wider variation in the distance(s) between cationic head groups, which provides flexibility for designing surfactants with an optimal match with the anionic phosphate groups on the DNA backbone thereby increasing complexation efficiency.

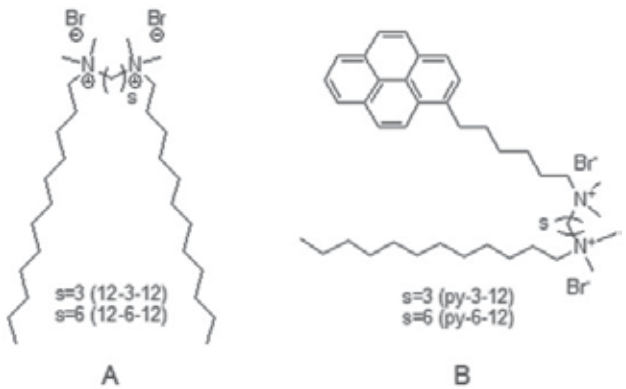

Scheme 2. Structure of the A) 12-s-12 and B) py-3-12 (see discussion below) surfactants.

Microcalorimetry studies used alone and/or along with other techniques can be very helpful in understanding the DNA-gemini interactions in the systems described above. Lipoplexes of gemini compounds, where m = 12, s = 3, 12 and m = 18 : 1(Smisterova *et al.*, 2001), s = 2, 3, 6, with DNA were investigated using isothermal titration calorimetry, dynamic light scattering (DLS), zeta potential, atomic force microscopy (AFM) and circular dichroism (CD) techniques. ITC data showed that the interaction between DNA and gemini surfactants is endothermic and the observed enthalpy *vs*. charge ratio profile depends upon the titration sequence(Wang *et al.*, 2007a). Isoelectric points (IP) of lipoplex formation were estimated from the zeta potential measurements and show good agreement with the reaction endpoints (RP) obtained from ITC. DLS data indicated that DNA is condensed in the lipoplex whereas AFM images suggested that the lipoplex morphology changes from isolated globular-like aggregated particles to larger-size aggregates with great diversity in morphology. This work has recently been extended to the study of a non-symmetric gemini surfactant in which one of the alkyl tails is a dodecyl group (i.e. m = 12) and the other has been replaced with a (pyren-6-yl)-hexyl group which has the same approximate length as a dodecyl group, but is significantly more hydrophobic in character (Wang *et al.*, 2007b). The interaction between these pyrene-based gemini surfactants (Scheme 2B) and DNA using ITC (Donkuru *et al.*, 2010), along with the 12-3-12 and 12-6-12 surfactants (for comparison), and

marked differences in the interactions with DNA were observed (Figure 5). The 2010 results for the interaction of the 12-3-12 and 12-6-12 with DNA showed a more complex interaction than that originally proposed in 2007, likely as a result of the difference in calorimeters used in the different studies. The major difference observed in the binding interaction(s) with DNA for the pyrenyl gemini surfactants lies in the ability of the pyrenyl group to intercalated between DNA base pairs; this intercalation was previously hypothesized based upon the results of fluorescence titration studies (Wang et al. 2007b).

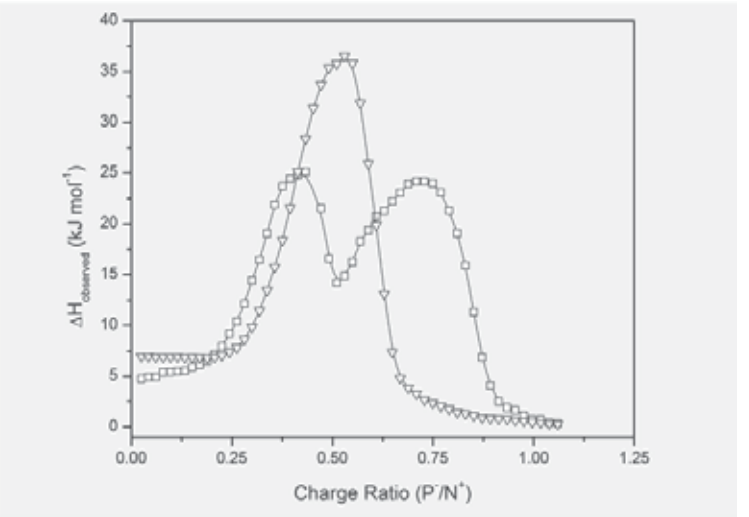

Fig. 5. Observed enthalpies for the titration of gemini surfactants with DNA: 12-3-12 at 25 °C (□) and py-3-12 at 25 °C (▽). Enthalpies are reported in kJ/mol of base pairs. [adapted from (Wettig et al., 2010)]

The double-peak feature observed in the enthalpogram for the titration of the 12-3-12 surfactant with DNA (Figure 5) is common to all of the symmetric gemini surfactants investigated (so far) by our group. The observed binding interactions have been rationalized in terms of the following steps (Wettig *et al.*, 2010):

1. An initial interaction between DNA and surfactant micelles; i.e., formation of the "beads on a string" complex – **endothermic**;
2. A significant **endothermic** contribution resulting from the disruption of the micelle-monomer equilibium by continued addition of DNA;
3. A reorganization of the "beads on a string" complex into an approximately neutral complex which gives rise to an **exothermic** contribution from both the release of structured water and binding between DNA and surfactant monomer;
4. Flocculation of the now neutral surfactant – DNA complexes – **endothermic**;
5. Precipitation of the complexes (**exothermic**) followed by no net interaction.

This interaction mechanism is depicted in Scheme 3. The major difference between this mechanism and in the original work published (Scheme 2 in Wang et al., 2007) is that the micelle-monomer equilibrium can no longer be discounted; specifically, the continued addition of DNA to the system has a substantial effect on this equilibrium and results in a significant endothermic contribution to the observed enthalpy. Interestingly a simplification of the system is observed for the pyrenyl surfactants (Scheme 2B), such that a number of

intermediate equilibria described above do not seem to occur specifically as a result of the ability for the pyrenyl groups to intercalate between the DNA base pairs.

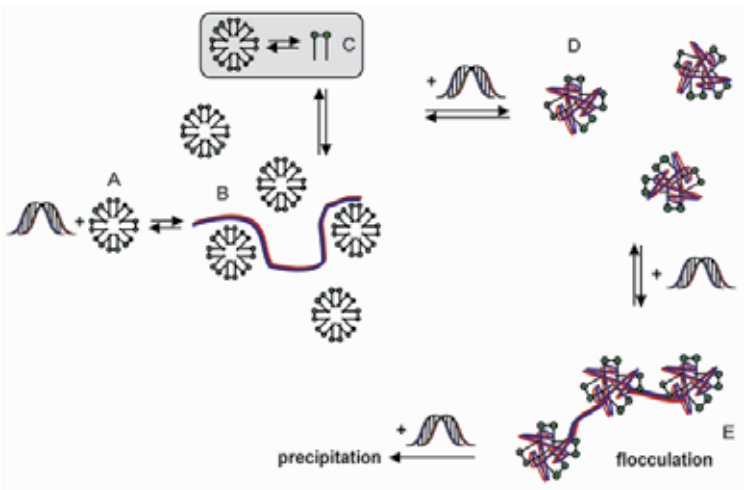

Scheme 3. Proposed interaction mechanism for m-s-m gemini surfactant – DNA systems. Initial binding of DNA to surfactant micelles (A) and formation of the beads-on a string complex (B). Continued addition of DNA results in a disruption of the monomer-micelle equilibrium (C) and the reorganization of the beads-on a string complexes into discrete DNA-surfactant aggregates (D) and eventual flocculation (E) and precipitation of these aggregates. [adapted from (Wettig et al., 2010)]

Other studies have shown that the nature of the counterion significantly affects both micellization and aggregation critical for enhanced trasnfection. The micellization of six cationic gemini surfactants with various counterions, $[C_{12}H_{25}(CH_3)_2N(CH_2)_6N(CH_3)_2C_{12}H_{25}]X_2$, designated as $C_{12}C_6C_{12}X_2$, with X = F^-, Cl^-, Br^-, Ac^-, NO_3^-, and ½ SO_4^{2-} in aqueous solutions was investigated by microcaloritmetry and conductivity measurements (Jiang *et al.*, 2004). The interaction of these surfactants with DNA in aqueous solutions was also investigated by microcalorimetry. The CMC, CAC (critical aggregation concentration) and the degree of micellar ionization, the saturation concentration of the aggregation, and the associated thermodynamic parameters were detected. Among the counterions examined, SO_4^{2-} was the most effective anion for decreasing the CMC (Koynova *et al.*, 2007). Both aggregation processes were mainly entropy-driven since the values of the entropy changes multiplied by temperature were much larger than the absolute values of the enthalpy changes. The binding of micelles to DNA was strongly dominated by the positive entropy gain on release of the small counterions from the micelles and from DNA. Further, the interaction of all of the surfactants with DNA was dependent on the DNA concentration and may be associated with each micelle interacting with more than one DNA molecule. In a another microcalorimetric study, the interaction of a series of dissymmetric gemini surfactants, (designated as $C_{(m)}C_{(6)}C_{(n)}Br_2$, with constant m+n=24, and m=12, 14, 16, and 18) with DNA in 10 mM NaCl was studied and it was found that the dissymmetry degree has a marked effect on the interaction of the $C_{(m)}C_{(6)}C_{(n)}Br_2$ surfactants with DNA since the CAC and saturation concentration tend to become smaller with increased m/n (Jiang *et al.*, 2005).

3.2 Substituted gemini surfactant systems

A more recent focus of research on gemini surfactants deals with the effect of substitution within the spacer group on the aggregation properties of the surfactant, and the rational design of surfactants with improved transfection activity (Kirby *et al.*, 2003;Wang *et al.*, 2004; Wettig *et al.*, 2002; Wettig et al., 2003; Wettig *et al.*, 2007). Transfection activity is found to depend critically upon the structural elements present (Castro *et al.*, 2004). Recently, pseudoglyceryl gemini lipids bearing an oligooxyethylene ($-CH_2-CH_2-O)_m-CH_2-CH_2-$) spacer were found to be superior gene transfecting agents as compared to those bearing polymethylene ($-CH_2)_m-$) spacers (Bajaj *et al.*, 2008). In this study, gemini lipids were found to be highly superior in gene transfer abilities as compared to their monomeric lipid and a related commercially available formulation (Bajaj *et al.*, 2008). The increased hydrophilicity of the ethoxylated spacer groups results in an increased water solubility of these compounds, and they preferentially locate at either air-water or micelle-water interface. In some cases, the efficiency of transfection has been correlated to a high extent of DNA condensation, which in turn depends heavily on the gemini spacer structure (Bombelli *et al.*, 2005). An important factor is the ability of the complexes to form polymorphic structures, which are not necessarily hexagonal. Absent from the above, is a thermodynamic characterization of the binding interaction(s) between DNA and gemini surfactants. While the determination of binding properties is complicated by the cooperative nature of the interaction between DNA and gemini surfactants, isothermal titration calorimetry has been used in a few reports.

In order to enhance gene transfection based upon structure-activity relationship, various gemini surfactants (Bombelli *et al.*, 2005) have been designed, synthesized and tested for gene delivery in our laboratory. Previously, we reported the results of a comprehensive study of the aggregation and thermodynamic properties of the 12-4-12 gemini surfactant with and without hydroxyl substitution as well as a series of ethoxylated gemini surfactants. Further, our group is using ITC to extend our work to better understand the thermodynamic properties of the complexation of DNA by the aza-, hydroxyl- and ethoxyl-gemini surfactants, specifically to examine how the binding interactions change as a result of substitution within the spacer group (Scheme 4).

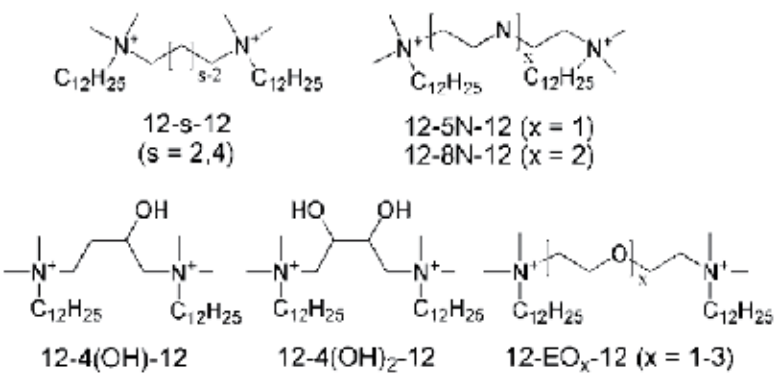

Scheme 4. Structures of the unsubstituted and substituted gemini surfactants.

Enthalpograms for the titration of 2.5 mM bp DNA into 0.5 mM gemini surfactant solutions are shown in Figure 6. The interactions between unmodified gemini surfactants (12-3-12, 12-

12-12, 18:1-2-18:1, 18:1-3-18:1, 18:1-6-18:1) (Wang *et al.*, 2007a) and pyrenyl-modified gemini surfactants (Wettig *et al.*, 2010) with DNA have been studied previously in this manner, which provides important information on the nature of the interaction(s) between surfactant micelles and DNA for conditions of excess positive charge; i.e., conditions similar to those typically used to prepare complexes for transfection studies.

The same types of interactions observed between unsubstituted gemini surfactants and DNA (described above) will occur for the various substituted gemini surfactants studied in this investigation; however, since the various substitutions are made within the head group region of the surfactant, this should result in noticeable changes in the binding interactions(s) which is indeed the case as seen in Figure 6. The maximum in ΔH_M^o for the 12-s-12 series has been attributed to energies associated with the configuration of the spacer group at the micelle–water interface. Enthalpies for the substituted gemini's in the presence of DNA were observed to decrease (becomes more exothermic), with increasing hydrophilicity of the spacer group in the order OH < EO < N (Table 1). The increased hydrophilicity of the ethoxylated spacer groups results in an increased water solubility of these compounds, and they preferentially locate at either air-water or micelle-water interface. Very recently, Anissa Bendjeriou-Sedjerar et al. (2009), from their surface tension measurements of gemini surfactants containing two quaternary ammonium groups bound by an ethylene oxide spacer chain, with x=1,3,7 and 12, reported that the hydrophilic spacer with oxyethylene moieties was not fully extended at the air-water interface. With increasing the spacer group size x = 7-10, it became sufficiently flexible to adopt a particular conformation with a loop at the water side of the interface (Benjeriou-Sedjerari *et al*., 2009). In addition, as observed for the 12-s-12 gemini surfactants, the micellization and binding process seems to be entropy driven for the 12-EOx-12 surfactants. In case of 12-8N-12 surfactant, the aza groups represent a bulkier, and perhaps more importantly, a more hydrophobic substituent as compared to oxygen for the case of the ethoxylated spacer groups. This has two direct effects on the ability of the spacer group to adopt conformations that would minimize the conformation energies: (i) steric hindrance between the aza methyl groups and the alkyl tails will not allow the spacer group to fold into the core of the micelle; and (ii) steric considerations also require that at least one of the aza methyl groups be oriented towards the aqueous phase, resulting in a net decrease in the energy associated with the transfer of the spacer from the aqueous to the micellar phase. The increase in CMC for the N-methyl subtituted series compared to the epoxy series results from increased steric repulsion, particularly with respect to packing at the surface of the micelle, and the interference between the solvation shells around nitrogen and hydrocarbon regions within the spacer (Wettig *et al.*, 2007). A hydrophilic, flexible spacer prompts micelle formation, which leads to a smaller CMC, smaller alpha, larger N, and more negative ΔG_{mic} (Wang *et al.*, 2004). One would expect that the sources of contributions to the enthalpy of binding remain the same within the series. Since the length and composition of the alkyl tails is kept constant, the contribution to $\Delta H_M°$ arising from the transfer of the alkyl tails from the bulk to the micelle should also remain constant. Therefore, the observed differences between the gemini surfactants with and without EO/aza/OH groups in the spacer must be associated with differences in hydration of the spacers of these surfactant series, when they are monomers in the bulk phase or located in the micelle/water/solution interface and when they are interacting with DNA. The initial enthalpies (ΔH_{init}) and the enthalpies at the maximum of the main peaks observed in Figure 6 (ΔH_1 and ΔH_2), along with their positions (in terms of charge ratio (P-/N+) are reported in Table 1. It is interesting to note that the

difference between the initial enthalpy (upon titration of the gemini surfactants with DNA) and the enthalpy at the first peak observed in Figure 6 (ΔH_{init} - ΔH_1) is comparable to the enthalpies of micellization for the pure surfactant compounds (Figure 7, and also ΔH_{mic} in Table 2) with a correlation of 0.72. As discussed above, one of the main differences in the mechanism proposed in our 2010 article (Wettig et al., 2010) and that originally proposed in our 2007 article (Wang et al, 2007) is the inclusion of the monomer-micelle equilibrium (Box C in Scheme 3). The monomer-micelle equilibrium is of course governed by the molecular structure of the surfactants, and therefore it is perhaps not surprising that we observe a correlation between the enthalpies of micellization and those observed upon interaction with DNA.

Surfactant	ΔH_{init} (kJ mol^{-1})	P$^-$/N$^+$	ΔH_1 (kJ mol^{-1})	P$^-$/N$^+$	ΔH_2 (kJ mol^{-1})
12-2-12	10.2	0.24	26.3	0.41	28.7
12-EO_1-12	10.5	0.53	23.8	0.80	22.0
12-EO_2-12	11.2	0.46	15.0	0.61	15.5
12-EO_1-12	11.5	0.56	15.8	0.83	17.0
12-5N-12	13.8	0.38	21.5	0.69	20.1
12-8N-12	17.7	0.31	25.0	0.60	26.1
12-4-12	6.8	0.27	20.5	0.50	24.7
12-4(OH)-12	5.8	0.24	17.5	0.37	21.4
12-4$(OH)_2$-12	4.0	0.30	18.7	0.48	19.0
12-3-12[a]	4.7	0.41	25.1	0.73	24.2
12-EO_3-12	12.1	0.42	18.9	0.68	17.6

Table 1. Thermodynamic properties for the titration of 0.5 mM gemini surfactant with DNA. [a]Data from Wettig et al., 2010.

The binding of cationic alkyammonium surfactants to DNA was studied by Matulis et al., who broke the interaction of the surfactants with DNA down into an electrostatic ($\Delta_{elec}H$) and a hydrophobic contribution ($\Delta_{h\Phi}H$; Equation 2) (Matulis *et al.*, 2002).

$$\Delta H = \Delta_{h\Phi}H + \Delta_{elec}H \quad (2)$$

The electrostatic component was estimated to be ~1.0 kJ/mol (obtained from the enthalpy of dissolution for ammonium phosphate which allowed for the determination of the hydrophobic contribution from experimental enthalpy measurements. Enthalpy titrations for the alkylammonium surfactant – DNA systems were carried out in the usual (forward) manner of adding concentrated surfactant solution to a solution of DNA, rather than the reverse manner of adding DNA to a concentrated surfactant solution used in our work above. This unfortunately precludes a more detailed analysis and comparison of our results for the substituted gemini surfactants to those for the alkylammonium surfactants (Matulis *et al.*, 2002) as well as the gemini surfactants (Bai *et al.*, 2001;Jiang *et al.*, 2005;Wang *et al.*, 2007; Pozharski and MacDonald, 2002). Forward titrations with the substituted compounds are currently underway to allow for such a comparison.

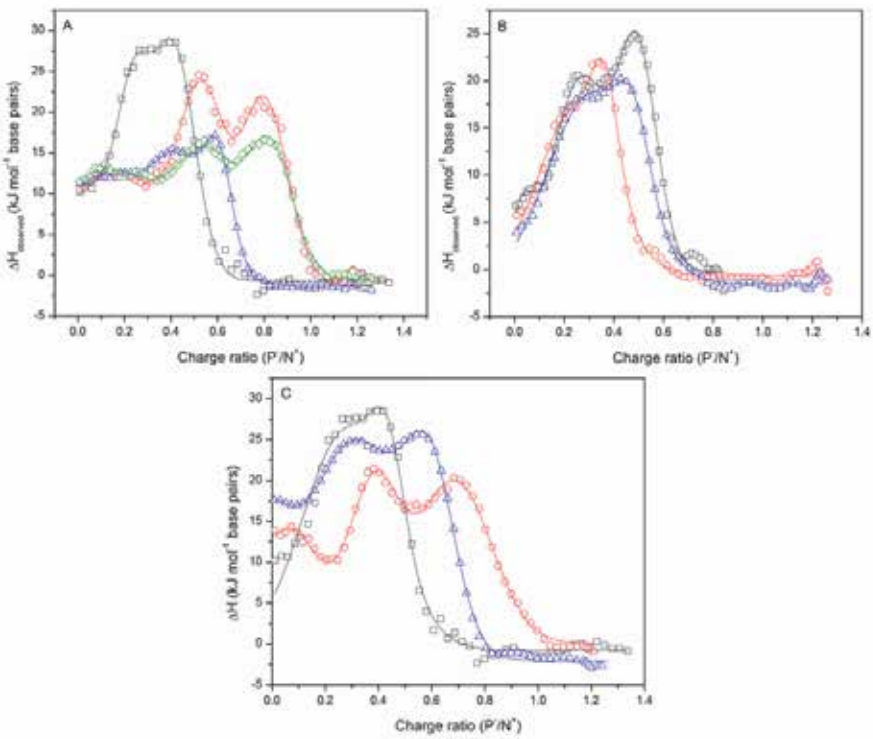

Fig. 6. Observed enthalpies for the titration of gemini surfactant solutions with DNA: A) 12-2-12 (□, black), 12-EO_1-12 (○, red), 12-EO_2-12 (△, blue) 12-EO_3-12 (◇, green); B) 12-4-12 (□, black), 12-4$(OH)_1$-12 (○, red), 12-4$(OH)_2$-12 (△, blue); C) 12-2-12 (□, black), 12-5N-12 (○, red), 12-8N-12 (△, blue). Lines represent a fit of the experimental data to a multiple Gaussian peak model.

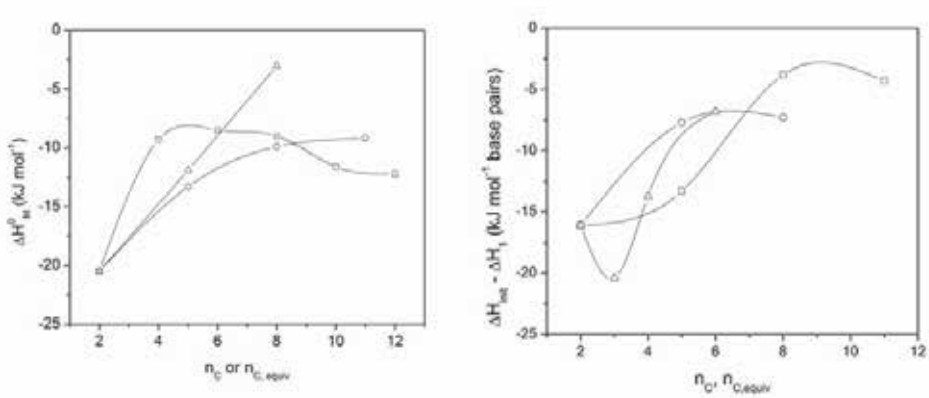

Fig. 7. Enthalpies of micellization (ΔH_{mic}) for the 12-s-12 the 12-EO_x-12 and 12-Az_X-12 gemini surfactants; and the difference in enthaply at peak 1 and the initial enthalpy (ΔH_{init} - ΔH_1) as a function of spacer length for the titration of DNA with the 12-s-12 , the 12-EO_x-12 and 12-Az_X-12 gemini surfactants.

Surfactant	ΔH_{mic} (kJ mol^{-1})	ΔH_{init} - ΔH_1 (kJ mol^{-1})
12-2-12	-20.5	-16.1
12-EO_1-12	-13.3	-13.3
12-EO_2-12	-9.9	-3.8
12-EO_3-12	-9.2	-4.3
12-5N-12	-11.9	-7.7
12-8N-12	-3	-7.3
12-4-12	-9.2[a]	-13.7
12-4(OH)-12	-12.1[a]	-11.7
12-4$(OH)_2$-12	-11.5[a]	-14.3
12-3-12	-19.3[b]	-16.1
12-6-12	-8.5[b]	-6.8

Table 2. Enthalpies of micellization for aqueous gemini surfactants and the difference in the observed peak and initial enthalpies (ΔH_{init} - ΔH_1) for the titration of gemini surfactants with DNA. [a] Data from (Wettig *et al.*, 2002); [b]Data from Wettig et al., 2010.

The advantage of the reverse titration method is that it allows for an examination of complex formation under conditions of excess lipid (Kennedy *et al.*, 2000), potentially revealing differences in binding of DNA by lipid or surfactant aggregates (vesicles, micelles, etc.) rather than with monomer lipid or surfactant molecules that would be studied in the forward titration manner. Significant differences in how the resulting complexes assemble have been noted in the comparison of forward and reverse titration methods for the EDOPC – DNA systems introduced in section 2.3 (Kennedy *et al.*, 2000), indicating the potential to control the types, or more specifically structure, of lipid-DNA complexes simply by controlling the order in which the components are added to each other. Such an explanation likely explains the very common observation that transfection efficiencies are highly dependent upon the mixing order of the various components.

4. Conclusion

Isothermal microcalorimetry plays an important role in elucidating the binding mechanism of DNA with surfactants/ lipids used in non-viral gene therapy. Measurement of heats of interaction allows accurate determination of binding constants, reaction stoichiometry (n), enthalpy (ΔH) and entropy (ΔS), thereby providing a complete thermodynamic profile of the molecular interaction in a single experiment by employing an appropriate model. Structure-activity studies suggest that biophysical properties, such as size, charge, and morphology of the resulting DNA/lipid complexes determine transfection efficiency within one class of vector. Several parameters effect transfection activity, such as structural variations of the cationic lipids (length and degree of unsaturation of the alkyl chains), the polarity of head groups, the structure of spacer, and the counterions. It is generally observed that the chemical arrangement of gemini surfactants provide a rather rich array of aggregate morphologies and solution properties that are dependent upon the nature and size of the linking group. More recently, ITC has been used to study the interaction of DNA with transfection systems based upon a family of dimeric surfactants or gemini surfactants, which consist of two traditional surface active groups linked chemically by a spacer group. ITC data shows whether the

interaction between DNA and gemini surfactants is endothermic or exothermic and the observed enthalpy *vs*. charge ratio profile depends upon the titration sequence. The magnitude and sign (i.e., endo- or exo-thermic) of ΔH_{mic} is governed by the types and magnitude of various contributions (hydrophobic and electrostatic) arising from surfactant-surfactant interactions. Since, for any process to be thermodynamically favoured the free energy change must be negative, an endothermic lipoplex formation must be driven by a corresponding increase in entropy. It is widely accepted that the major contribution to this increase in entropy arises from counterion release. The double-peak feature observed in the enthalpogram for the titration of the 12-3-12 surfactant with DNA is common to all of the symmetric gemini surfactants investigated (so far) by our group. Our group is using ITC to better understand the thermodynamic properties of the complexation of DNA by the aza-, hydroxyl- and ethoxyl-gemini substituted and unsubstituted surfactants, specifically to examine how the binding interactions change as a result of substitution within the spacer group. In addition, our group is interested in the study of a non-symmetric gemini surfactant in which one of the alkyl tails is a dodecyl group (i.e. m = 12) and the other has been replaced with a (pyren-6-yl)-hexyl group which has the same approximate length as a dodecyl group, but is significantly more hydrophobic in character. The major difference observed in the binding interaction(s) with DNA for the pyrenyl gemini surfactants lies in the ability of the pyrenyl group to intercalated between DNA base pairs. Interestingly a simplification of the system is observed for the pyrenyl surfactants (py-3-12; py-6-12), such that a number of intermediate equilibria do not seem to occur. One of the main differences in the mechanism proposed in our 2010 article (Wettig et al., 2010) and that originally proposed in our 2007 article (Wang et al, 2007) is the inclusion of the monomer-micelle equilibrium which in turn is governed by the molecular structure of the surfactants. The significance of these results remains unclear; however, forward titrations of the substituted gemini surfactants with are underway. Ultimately these results will allow for a more complete picture of the importance of head group structure of the gemini surfactants for improved DNA transfection efficiency, and the rational design of improved non-viral transfection vectors.

5. References

Bai, G., Wang, Y., Yan, H., and Thomas, R.K. (2001) Enthalpies of Micellization of Double Chain and Gemini Cationic Surfactants. *J Colloid Interface Sci* 240: 375-377.

Bajaj, A., Paul, B., Kondaiah, P., and Bhattacharya, S. (2008) Structure-activity investigation on the gene transfection properties of cardiolipin mimicking gemini lipid analogues. *Bioconjug Chem* 19: 1283-1300.

Barreleiro, P.C.A, Olofsson, G., Alexandridis, P. (2000) Interaction of DNA with cationic vesicles: A calorimetric study. *J Phys Chem B* 104: 7795-7802

Barteau, B., Chevre, R., Letrou-Bonneval, E., Labas, R., Lambert, O., and Pitard, B. (2008) Physicochemical parameters of non-viral vectors that govern transfection efficiency. *Curr Gene Ther* 8: 313-323.

Bombelli, C., Faggioli, F., Luciani, P., Mancini, G., and Sacco, M.G. (2005) Efficient transfection of DNA by liposomes formulated with cationic gemini amphiphiles. *J Med Chem* 48: 5378-5382.

Bruinsma, R. (1998) Electrostatics of DNA-cationic lipid complexes: isoelectric instability. *Eur Phys J B* 4: 75-88.

Calvet, E., and Prat, H. (1963) Recent progress in microcalorimetry. The MacMillan Company, New York.

Castro, M., Griffiths, D., Patel, A., Pattrick, N., Kitson, C., and Ladlow, M. (2004) Effect of chain length on transfection properties of spermine-based gemini surfactants. *Org Biomol Chem* 2: 2814-2820.

Cherezov, V., Qiu, H., Pector, V., Vandenbranden, M., Ruysschaert, J.M., and Caffrey, M. (2002) Biophysical and transfection studies of the diC(14)-amidine/DNA complex. *Biophys J* 82: 3105-3117.

djeriou-Sedjerari, A., Derrien, G., Charnay, C., Zajac, J., De Menorval, L.C., and Lindheimer, M. (2009) Contribution of 1H NMR to the investigation of the adsorption of cationic Gemini surfactants with oligooxyethylene spacer group onto silica. *J Colloid Interface Sci* 331: 281-287.

Donkuru, M., Badea, I., Wettig, S., Verrall, R., Elsabahy, M., and Foldvari, M. (2010) Advancing nonviral gene delivery: lipid- and surfactant-based nanoparticle design strategies. *Nanomedicine (Lond)* 5: 1103-1127.

Elouahabi, A., and Ruysschaert, J.M. (2005) Formation and intracellular trafficking of lipoplexes and polyplexes. *Mol Ther* 11: 336-347.

Ewert, K.K., Samuel, C.E., and Safinya, C.R. (2008) Lipid - DNA Interactions: Structure - Function Studies of Nanomaterials for Gene Delivery. *In: DNA Interactions with Polymers and Surfactants, R Dias & B Lindman, (Eds), John Wiley & Sons, 978-0-470-25818-7, Nj, USA*: 377-404.

Felgner, P.L., Gadek, T.R., Holm, M., Roman, R., Chan, H.W., Wenz, M. *et al.* (1987) Lipofection: a highly efficient, lipid-mediated DNA-transfection procedure. *Proc Natl Acad Sci U S A* 84: 7413-7417.

Felgner, P.L., and Ringold, G.M. (1989) Cationic liposome-mediated transfection. *Nature* 337: 387-388.

Foldvari, M., Badea, I., Wettig, S., Verrall, R., and Bagonluri, M. (2006) Structural characterization of novel gemini non-viral DNA delivery systems for cutaneous gene delivery. *Journal of Exp. Nanosci.* 1:165-176

Giatrellis, S., Nikolopoulos, G., Sideratou, Z., and Nounesis, G. (2009) Calorimetric study of the interaction of binary DMTAP/DOTAP cationic liposomes with plasmid DNA. *J Liposome Res* 19: 220-230.

Goddard, E.D. (2002) Polymer/Surfactant Interaction: Interfacial Aspects. *J Colloid Interface Sci* 256: 228-235.

Grosmaire, L., Chorro, M., Chorro, C., Partyka, S., and Zana, R. (2002) Alkanediyl-alpha, omega-bis(dimethylalkylammonium bromide) surfactants 9. Effect of the spacer carbon number and temperature on the enthalpy of micellization. *J Colloid Interface Sci* 246: 175-181.

Hirsch-Lerner, D., and Barenholz, Y. (1999) Hydration of lipoplexes commonly used in gene delivery: follow-up by laurdan fluorescence changes and quantification by differential scanning calorimetry. *Biochim Biophys Acta* 1461: 47-57.

Hui, S.W., Langner, M., Zhao, Y.L., Ross, P., Hurley, E., and Chan, K. (1996) The role of helper lipids in cationic liposome-mediated gene transfer. *Biophys J* 71: 590-599.

Jiang, N., Li, P., Wang, Y., Wang, J., Yan, H., and Thomas, R. (2004) Microcalorimetric Micellization of cationic Gemini Surfactants with various counterions ans their interaction with DNA in aqueous solution. *Journal of Physical Chemistry* 108: 15385-15391.

Jiang, N., Wang, J., Wang, Y., Yan, H., and Thomas, R.K. (2005) Microcalorimetric study on the interaction of dissymmetric gemini surfactants with DNA. *J Colloid Interface Sci* 284: 759-764.

Kawaura, C., Noguchi, A., Furuno, T., and Nakanishi, M. (1998) Atomic force microscopy for studying gene transfection mediated by cationic liposomes with a cationic cholesterol derivative. *FEBS Lett* 421: 69-72.

Kennedy, M.T., Pozharski, E.V., Rakhmanova, V.A., and MacDonald, R.C. (2000) Factors governing the assembly of cationic phospholipid-DNA complexes. *Biophys J* 78: 1620-1633.

Kirby, A.J., Camilleri, P., Engberts, J.B., Feiters, M.C., Nolte, R.J., Soderman, O. *et al.* (2003) Gemini surfactants: New synthetic vectors for gene transfection. *Angewandte Chemie-International Edition* 42: 11448-11457.

Koltover, I., Salditt, T., Radler, J.O., and Safinya, C.R. (1998) An inverted hexagonal phase of cationic liposome-DNA complexes related to DNA release and delivery. *Science* 281: 78-81.

Koynova, R., Tarahovsky, Y.S., Wang, L., and MacDonald, R.C. (2007) Lipoplex formulation of superior efficacy exhibits high surface activity and fusogenicity, and readily releases DNA. *Biochim Biophys Acta* 1768: 375-386.

Koynova, R., Wang, L., and MacDonald, R.C. (2008) Cationic phospholipids forming cubic phases: lipoplex structure and transfection efficiency. *Mol Pharm* 5: 739-744.

Koynova, R. & Tenchov, B. (2009) Cationic phospholipids: structure-transfection activity relationships. *Soft Matter* 5: 3187-3200.

Kreiss, P., Cameron, B., Rangara, R., Mailhe, P., guerre-Charriol, O., Airiau, M. *et al.* (1999) Plasmid DNA size does not affect the physicochemical properties of lipoplexes but modulates gene transfer efficiency. *Nucleic Acids Res* 27: 3792-3798.

Lobo, B.A., Rogers, S.A., Choosakoonkriang, S., Smith, J.G., Koe, G., and Middaugh, C.R. (2002) Differential scanning calorimetric studies of the thermal stability of plasmid DNA complexed with cationic lipids and polymers. *J Pharm Sci* 91: 454-466.

Ma, B., Zhang, S., Jiang, H., Zhao, B., and Lv, H. (2007) Lipoplex morphologies and their influences on transfection efficiency in gene delivery. *J Control Release* ;123: 184-194.

Malone, R.W., Felgner, P.L., and Verma, I.M. (1989) Cationic liposome-mediated RNA transfection. *Proc Natl Acad Sci U S A* 86: 6077-6081.

Matulis, D., Rouzina, I., and Bloomfield, V.A. (2002) Thermodynamics of cationic lipid binding to DNA and DNA condensation: roles of electrostatics and hydrophobicity. *J Am Chem Soc* 124: 7331-7342.

O'Hern, C.S. and Lubensky, T.C (1998) Sliding Columnar Phase of DNA-Lipid Complexes. *Physical Review Letters* 80: 4345-4348.

Pathak, A., Patnaik, S., and Gupta, K.C. (2009) Recent trends in non-viral vector-mediated gene delivery. *Biotechnol J* 4: 1559-1572.

Pector, V., Backmann, J., Maes, D., Vandenbranden, M., and Ruysschaert, J.M. (2000) Biophysical and structural properties of DNA.diC(14)-amidine complexes. Influence of the DNA/lipid ratio. *J Biol Chem* 275: 29533-29538.

Pierce, M.M., Raman, C.S., and Nall, B.T. (1999) Isothermal titration calorimetry of protein-protein interactions. *Methods* 19: 213-221.

Pitard, B., Oudrhiri, N., Vigneron, J.P., Hauchecorne, M., Aguerre, O., Toury, R. *et al.* (1999) Structural characteristics of supramolecular assemblies formed by guanidinium-cholesterol reagents for gene transfection. *Proc Natl Acad Sci U S A* 96: 2621-2626.

Pozharski, E., and MacDonald, R.C. (2002) Thermodynamics of cationic lipid-DNA complex formation as studied by isothermal titration calorimetry. *Biophys J* 83: 556-565.

Pozharski, E., and MacDonald, R.C. (2003) Lipoplex thermodynamics: determination of DNA-cationic lipoid interaction energies. *Biophys J* 85: 3969-3978.

Radler, J.O., Koltover, I., Salditt, T., and Safinya, C.R. (1997) Structure of DNA-cationic liposome complexes: DNA intercalation in multilamellar membranes in distinct interhelical packing regimes. *Science* 275: 810-814.

Safinya, C.R. (2001) Structures of lipid-DNA complexes: supramolecular assembly and gene delivery. *Curr Opin Struct Biol* 11: 440-448.

Smisterova, J., Wagenaar, A., Stuart, M.C., Polushkin, E., ten, B.G., Hulst, R. *et al.* (2001) Molecular shape of the cationic lipid controls the structure of cationic lipid/dioleylphosphatidylethanolamine-DNA complexes and the efficiency of gene delivery. *J Biol Chem* 276: 47615-47622.

Sternberg, B., Hong, K., Zheng, W., and Papahadjopoulos, D. (1998) Ultrastructural characterization of cationic liposome-DNA complexes showing enhanced stability in serum and high transfection activity in vivo. *Biochim Biophys Acta* 1375: 23-35.

Sternberg, B., Sorgi, F.L., and Huang, L. (1994) New structures in complex formation between DNA and cationic liposomes visualized by freeze-fracture electron microscopy. *FEBS Lett* 19;356: 361-366.

Takeuchi, K., Ishihara, M., Kawaura, C., Noji, M., Furuno, T., and Nakanishi, M. (1996) Effect of zeta potential of cationic liposomes containing cationic cholesterol derivatives on gene transfection. *FEBS Lett* 397: 207-209.

Tranchant, I., Thompson, B., Nicolazzi, C., Mignet, N., and Scherman, D. (2004) Physicochemical optimisation of plasmid delivery by cationic lipids. *J Gene Med* 6 Suppl 1: S24-S35.

Wang, C., Li, X., Wettig, S.D., Badea, I., Foldvari, M., and Verrall, R.E. (2007a) Investigation of complexes formed by interaction of cationic gemini surfactants with deoxyribonucleic acid. *Phys Chem Chem Phys* 9: 1616-1628.

Wang, C., Wettig, S.D., Foldvari, M., and Verrall, R.E. (2007b) Synthesis, characterization, and use of asymmetric pyrenyl-gemini surfactants as emissive components in DNA-lipoplex systems. *Langmuir* 23: 8995-9001.

Wang, X., Wang, J., Wang, Y., Yan, H., Li, P., and Thomas, R.K. (2004) Effect of the nature of the spacer on the aggregation properties of gemini surfactants in an aqueous solution. *Langmuir* 20: 53-56.

Wettig, S.D., Deubry, R., Akbar, J., Kaur, T., Wang, H., Sheinin, T. *et al.* (2010) Thermodynamic investigation of the binding of dissymmetric pyrenyl-gemini surfactants to DNA. *Phys Chem Chem Phys* 12: 4821-4826.

Wettig, S.D., Li, X.F., and Verrall, R.E. (2003) Thermodynamic aggregation properties of gemini surfactants with ethoxylated spacers in aqueous solution. *Langmuir* 19: 3666-3670.

Wettig, S.D., Nowak, P., and Verrall, R.E. (2002) Aggregation Behavior of Hydroxyl Substituted Gemini Surfactants in Aqueous Solution. *Langmuir* 18, 5354-5359.

Wettig, S.D., Wang, C., Verrall, R.E., and Foldvari, M. (2007) Thermodynamic and aggregation properties of aza- and imino-substituted gemini surfactants designed for gene delivery. *Phys Chem Chem Phys* 9: 871-877.

Yang, P., Singh, J., Wettig, S., Foldvari, M., Verrall, R.E., and Badea, I. (2010) Enhanced gene expression in epithelial cells transfected with amino acid-substituted gemini nanoparticles. *Eur J Pharm Biopharm* 75: 311-320.

Zabner, J., Fasbender, A.J., Moninger, T., Poellinger, K.A., and Welsh, M.J. (1995) Cellular and molecular barriers to gene transfer by a cationic lipid. *J Biol Chem* 270: 18997-19007.

Zhang, J.S., Li, S., and Huang, L. (2003) Cationic liposome-protamine-DNA complexes for gene delivery. *Methods Enzymol* 373: 332-342.

Zuzzi, S., Cametti, C., Onori, G., and Sennato, S. (2007) Liposome-induced DNA compaction and reentrant condensation investigated by dielectric relaxation spectroscopy and dynamic light scattering techniques. *Phys Rev E Stat Nonlin Soft Matter Phys* 76: 011925.

12

Time Evolution of a Modified Feynman Ratchet with Velocity-Dependent Fluctuations and the Second Law of Thermodynamics

Jack Denur
Electric & Gas Technology, Inc.,Garland, Texas
U.S.A.

1. Introduction

1.1 The Zhang formulation of the second law of thermodynamics, and a velocity dependent modified Feynman-ratchet model

The Zhang [1] formulation of the second law of thermodynamics (second law) states that no spontaneous momentum flow is possible in an isolated system. By *spontaneous*, it is meant [1]: not merely (a) *sustaining*, i.e., permanent; but also (b) *robust*, i.e., capable of withstanding dissipation, of surviving disturbances, and of generating (regenerating) itself if initially nonexistent (if destroyed). The Zhang [1] formulation of the second law implies that, *at thermodynamic equilibrium (TEQ)*, not even *merely sustaining* momentum flow is possible, i.e., that *no* systematic motion — most generally, *no* systematic process — is possible *at TEQ*: Systematic processes generated and maintained *spontaneously despite TEQ* violate the second law; by contrast, systematic *merely sustaining*, i.e., *non*robust *and non*dissipative — and hence *non*spontaneous — processes do not violate the second law, but merely imply that TEQ has *not* been *completely* realized [1,2]. [Given any irreversibility (e.g., friction), (*non*spontaneous) *merely sustaining* processes lose *even their sustainability* — they become *non*robust *and dissipative* — their negentropy (and hence free energy) is lost, and then TEQ *is completely* realized [1,2].]
Corollary: The Zhang [1] formulation of the second law implies that, within a system maintained at *non*-TEQ, spontaneous momentum flow and hence systematic motion — most generally systematic process — is *certain*. Said *certainty* may be *actualized* or *in potentiality*: Example: a gas constrained to within less than the total volume of its container is at *non*-TEQ and has the *potential* for systematic motion — expansion — which is *actualized* upon release of the constraint.
Feynman's classic ratchet and pawl [3] elucidates the Zhang [1] formulation of the second law: In the original classic "Ratchet and Pawl" chapter [4], it is stated, as the upshot concerning Feynman's classic system,

> "In spite of all our cleverness of lopsided design, if the two temperatures are exactly equal there is no more propensity to turn one way than the other. The moment we look at it, it may be turning one way or the other, but in the long run it gets nowhere. The fact that it gets nowhere is really the fundamental deep principle on which all of thermodynamics is based."

Recently, various formulations of the second law have been challenged, in both the quantum [5–8] and classical [5,8–10] regimes.

In this chapter [11], we show that velocity-dependent fluctuations (but not fluctuations in general) challenge the second law in the classical regime. [A digression concerning limited aspects of the quantum regime is provided in Sect. 6. Otherwise, except for the last four paragraphs of Sect. 3 (and a few very brief mentions elsewhere), this chapter deals only with the classical regime.] Our challenge is most self-evident with respect to the Zhang [1] formulation of the second law, but (as will be discussed in the last four paragraphs of Sect. 3): The Zhang [1] formulation of the second law is *maximally* strong — no other formulation thereof can be stronger [although some other(s) may be equally strong]. [Classically (with one exception [6gg] that is not applicable insofar as this present chapter is concerned) — all formulations of the second law are equivalent — but not so quantum-mechanically [6s–6ff].] Hence: A challenge to the Zhang [1] formulation of the second law is also a challenge to *all* other formulations thereof.

In this chapter [1], Feynman's ratchet [3] is modified to the minimum extent necessary to ensure that velocity-dependence of fluctuations can spontaneously break the randomness of its Brownian motion at TEQ — spontaneously superposing a *non*random walk on its Brownian motion and hence challenging the second law. This minimally-modified Feynman ratchet, illustrated in Fig. 1, will now be described.

In the right-handed Cartesian coordinate system of Fig. 1, the $+X$, $+Y$, and $+Z$ directions are to the right, into the page, and upwards, respectively. The Brownian motion of the disk 1 of mass m' (shown edge-on in Fig. 1) is constrained to be X-directional by the frictionless guide 2. The pawl 3 of mass m (whose lower tip protrudes below the disk in Fig. 1) is in a vertical groove within the $+X$ disk face, wherein — in addition to its X-directional Brownian motion in lockstep with the disk as part of the combined disk-and-pawl system (DP) — it also has Z-directional Brownian motion relative to the disk per se. The DP's total mass is $M = m' + m \gg m$. Each peg 4 is of Z-directional height H, and is separated from adjacent pegs by X-directional distance L. The pawl's altitude Z is the vertical distance of its undersurface above the $Z = 0$ level at the floor of the peg row 4, and is restricted to $Z \geq Z_{\text{min}}$ ($0 < Z_{\text{min}} < H$) by a stop within the $+X$ disk face. (A simple design for the stop: Let the vertical groove that accommodates the pawl have thinner slots extending in the $+Y$ and $-Y$ directions. These slots accommodate pins extending from the pawl in the $+Y$ and $-Y$ directions, respectively. The floors of these slots preclude Z-directional motion of the pins below the pin/slot-floor contact level, thereby restricting the pawl's altitude to $Z \geq Z_{\text{min}}$.) The *net* peg height is thus $H_{\text{net}} \equiv H - Z_{\text{min}}$ ($0 < H_{\text{net}} < H$). The entire system, including the DP, is at TEQ with equilibrium blackbody radiation (EBR) at temperature T. L is, for simplicity, taken to be large compared with the combined pawl-plus-peg X-directional thickness; yet L can easily still be small enough so that changes in the DP's X-directional Brownian-motional velocity V occur, essentially, *only at* pawl-peg bounces, and *not* via DP-EBR X-directional momentum exchanges *between* pawl-peg bounces [12]. (The frictionless guide 2, of course, has no effect on V.) A uniform gravitational field g is attractive downwards (in the $-Z$ direction). The $V = 0$ rest frame — wherein (a) the frictionless guide 2 and peg row 4 are fixed and (b) the EBR at temperature T is isotropic — is (for simplicity) taken as that of g's source [of mass $\gg M$ (or even $\ggg M$)]. Except for the EBR, our system is nonrelativistic: i.e., all speeds (except of EBR photons) are $\ll c$, and all pertinent differences in gravitational potential (e.g., gH) are $\ll c^2$.

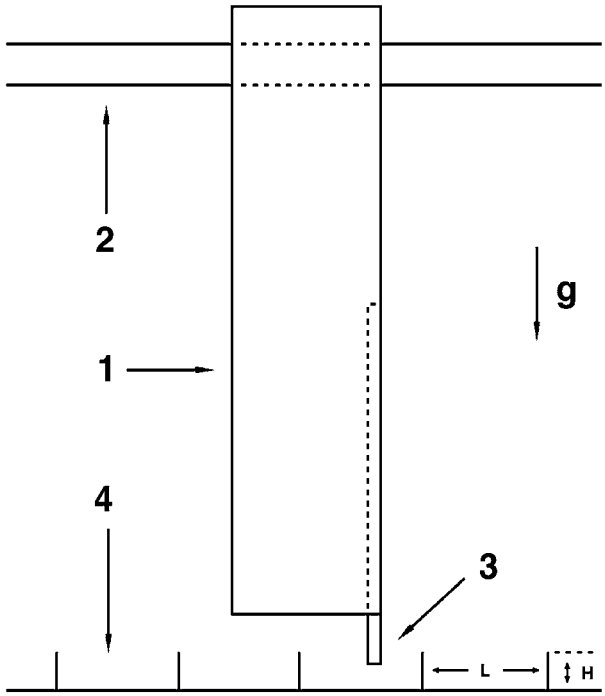

Fig. 1. Modified Feynman ratchet with velocity-dependent fluctuations

The right-handed Cartesian coordinate system described in the immediately preceding paragraph is the most appropriate one given *linear* X-directional DP Brownian motion. For transformation to *circular* X-directional DP Brownian motion, said right-handed Cartesian coordinate system can be transformed into a right-handed cylindrical coordinate system by (a) curving the X-directional axis into a circle, and (b) letting the $+X$, $+Y$, and $+Z$ directions be counterclockwise, radially outwards from the center of this circle, and upwards, respectively. Corresponding to X-directional Brownian-motional velocity V of the DP, to first order in V/c, Doppler-shifted EBR at temperature [13]

$$T_{\pm}(V,\alpha) = T\left(1 \pm \frac{V\cos\alpha}{c}\right) \tag{1}$$

impinges on the $\pm X$ disk face at angle α from the $\pm X$ direction — at a rate proportional both to the differential solid angle $2\pi\sin\alpha d\alpha$ and, by Lambert's cosine law, to $\cos\alpha$ [13]. {The pawl, being in the $+X$ disk face, "sees" EBR impinging — as per the immediately preceding sentence [including (1)] with the $+$ signs — *only* from directions with $+X$ components (except for its lower tip — of *negligible* size compared with the *entire* pawl even at maximum tip protrusion, i.e., even at $Z = Z_{\min}$ — when said tip protrudes below the disk).} Averaging over the range $0 \le \alpha \le \pi/2$ [13],

$$T_{\pm}(V) = \langle T_{\pm}(V,\alpha)\rangle = \frac{\int_0^{\pi/2} T\left(1 \pm \frac{V\cos\alpha}{c}\right)\sin\alpha\cos\alpha d\alpha}{\int_0^{\pi/2}\sin\alpha\cos\alpha d\alpha} = T\left(1 \pm \frac{2V}{3c}\right). \tag{2}$$

The DP's thermal response time is sufficiently short that $T_+(V)$ [$T_-(V)$] is the temperature, corresponding to V having a given value, of the $+X$ disk face (including the pawl) *itself* [12] [of the $-X$ disk face *itself* [12]] — *not* merely of Doppler-shifted EBR "seen" thereby [13].
The stop *within the* $+X$ *disk face* — and hence *itself* [12] at temperature, corresponding to V having a given value, of $T_+(V)$ [12,13] — restricts the pawl's altitude to $Z \geq Z_{\min}$: this prevents mechanical thermal contact [although not radiative thermal contact (which is *negligible*)] between the floor of the peg row — at elevation $Z = 0$ and temperature T — and the pawl's undersurface. (Except when the pawl's undersurface protrudes below the disk, the $+X$ disk face shields it from EBR impinging from directions with $-X$ components — and, in any case, the pawl's undersurface area is *negligible* compared with that of the *entire* pawl.) The pawl's thermal isolation within the $+X$ disk face is thereby improved — helping to ensure that $T_+(V)$ is the temperature, corresponding to V having a given value, of the pawl *itself* [12], *not* merely of Doppler-shifted EBR "seen" thereby [13].
In accordance with the Boltzmann distribution, and applying (2) with the $+$ signs, the *conditional* probability [14] $P(Z > H|V)$ that the pawl, of weight mg, can attain sufficient altitude $Z > H$ to jump the pegs — and hence *not* to impede the DP's X-directional Brownian motion — given V, is

$$\begin{aligned} P(Z > H|V) &= \exp[-mg\,(H - Z_{\min})\,/kT_+(V)] \\ &\equiv \exp[-mgH_{\text{net}}/kT_+(V)] \\ &= \exp\left\{-mgH_{\text{net}} \Big/ \left[kT\left(1 + \frac{2V}{3c}\right)\right]\right\} \\ &\equiv \exp\left[-A \Big/ \left(1 + \frac{2V}{3c}\right)\right] \\ &= \left(1 + \frac{2AV}{3c}\right) e^{-A}. \end{aligned} \tag{3}$$

The second step of (3) restates the definition (initially given near the middle of the paragraph immediately following Fig. 1)

$$H_{\text{net}} \equiv H - Z_{\min}, \tag{4a}$$

the third step of (3) is justified by (2) with the $+$ signs, the fourth step of (3) defines

$$A \equiv mgH_{\text{net}}/kT, \tag{4b}$$

and the last step of (3), which is correct to first order in V/c, is justified because V is nonrelativistic, with $|V| \ll c$ for all values of $|V|$ that have nonnegligible probabilities of being equaled or exceeded.
By (3), $P(Z > H|V)$ is slightly greater when $V > 0$ than when $V < 0$. Hence, *despite TEQ*, the *velocity-dependence* of $P(Z > H|V)$ spontaneously superposes a *non*random walk (spontaneous momentum flow [1]) in the $+X$ (Forward) direction on the DP's Brownian motion — challenging the second law.
Note that $T_\pm(V, \alpha)$, $T_\pm(V)$, Z, and $P(Z > H|V)$ manifest velocity-dependent fluctuations. By contrast, T, H, $Z_{\min}$, $H_{\text{net}} \equiv H - Z_{\min}$, L, m', m, $M = m' + m \gg m$, g, and $A \equiv mgH_{\text{net}}/kT$ are parameters, fixed in any one given (thought) experiment.

2. Markovian time evolution and challenges to the second law

The derivation of our system's time evolution will be easiest if we first consider, in (5) – (22) and the associated discussions [except in defining notation in the third paragraph of this Sect. 2, and in the last step of (7)], *only* occasions when $|V|$ happens to have any *one* given value, i.e., when $V = \pm |V|$. Subsequently, we will average over *all* $\pm |V|$ pairs, i.e., over *all* $|V|$.
By (3) and (4), we have, to first order in $|V|/c$, for the *conditional* probabilities [14] F and R of $Z > H$ obtaining given DP Brownian motion in, respectively, the Forward or $+X$ direction at $V = +|V|$ and Reverse or $-X$ direction at $V = -|V|$,

$$F \equiv P(Z > H | V = +|V|) \equiv P(>|+) = \left(1 + \frac{2A|V|}{3c}\right) e^{-A} \tag{5}$$

and

$$R \equiv P(Z > H | V = -|V|) \equiv P(>|-) = \left(1 - \frac{2A|V|}{3c}\right) e^{-A}, \tag{6}$$

respectively. The states $Z > H$, $Z < H$, $V = +|V| > 0$, and $V = -|V| < 0$ are denoted as $>$, $<$, $+$, and $-$, respectively. [Since Z and V are *continuous* random variables, the *point* values $Z = H$ and $V = |V| = 0$ each has *zero* probability measure [14a] of occurrence — and hence does not finitely contribute to any quantity integrated or averaged over any *finite* range of Z and V, respectively (e.g., over *all* Z and over *all* V, respectively).] Given $V = \pm |V|$, immediately preceding any pawl-peg interaction, the DP is in *one* of the four states $> +$, $> -$, $< +$, or $< -$; the former two states implying that this interaction will be a pawl-over-peg jump, and the latter two that it will be a pawl-peg bounce. Immediately following a jump (bounce), $\operatorname{sgn} V$ is unchanged (reversed).
We now study our system's time evolution, given $V = \pm |V|$, in discrete time-steps of $\Delta t = L/|V|$ that separate consecutive pawl-peg interactions, with time N immediately preceding the $(N+1)$ st pawl-peg interaction. If a quantity Q or an average thereof is time-dependent, then its value at time N is indicated via a subscript N. Let $\langle Q \rangle_N$ ($\langle\langle Q \rangle\rangle_N$) denote the expectation value at time N of a quantity Q over any *one* given $\pm |V|$ pair ($\langle Q \rangle_N$ *itself* subsequently averaged over *all* $|V|$). {Notes: (a) All averages in this chapter are, in this wise, either over any *one* given $\pm |V|$ pair or over *all* $|V|$, except: (i) the average $\langle T_{\pm}(V, \alpha) \rangle$ over α in (2) (denoted via enclosure within single angular brackets), and (ii) some of the averages in Sect. 6, and in the Footnotes. (b) Consistently with the fifth-to-the-last sentence (especially the last clause thereof) of the paragraph immediately following Fig. 1: The combined pawl-plus-peg X-directional thickness is $\ll L$; hence, the X-directional spatial, and temporal, intervals separating consecutive pawl-over-peg jumps are only negligibly greater [by said thickness, and (said thickness)/$|V|$, respectively] than those separating consecutive pawl-peg bounces (jump preceded or followed by bounce being the intermediate case).}
TEQ, i.e., *maximum initial total entropy*, implies that *initially*, at $N = 0$,

$$\begin{aligned} & P(+)_0 = P(-)_0 = \frac{1}{2} \\ & \iff \langle V \rangle_0 = |V| \, [P(+)_0 - P(-)_0] = 0 \implies \langle\langle V \rangle\rangle_0 = 0. \end{aligned} \tag{7}$$

The expression in (7) for $\langle V \rangle_0$ is true for *all* $\pm |V|$ pairs, hence implying that for $\langle\langle V \rangle\rangle_0$. For all $N \geq 0$,

$$\begin{aligned}\langle V\rangle_N &= |V|\,[P(+)_N - P(-)_N]\\ \iff P(\pm)_N &= \frac{1}{2}\left(1 \pm \frac{\langle V\rangle_N}{|V|}\right).\end{aligned} \tag{8}$$

The second line of (8) is justified by $P(+)_N + P(-)_N = 1$ and by (7).
Given $V = \pm|V|$ and $P(+)_N + P(-)_N = P(> |+) + P(< |+) = P(> |-) + P(< |-) = 1$, said time evolution is a two-state discrete-time Markov chain [15] with (a) states $+$ and $-$; and (b) the following *conditional* transition probabilities:

$$P[(+)_N|(+)_{N-1}] = P(> |+) = F, \tag{9a}$$

$$P[(-)_N|(-)_{N-1}] = P(> |-) = R, \tag{9b}$$

$$P[(-)_N|(+)_{N-1}] = P(< |+) = 1 - F, \tag{9c}$$

and

$$P[(+)_N|(-)_{N-1}] = P(< |-) = 1 - R. \tag{9d}$$

Note that (9) – (18) are correct not only for the *specific* F and R given by the rightmost terms of (5) and (6), respectively, but also for *general* F and R that are *at most* functions of $|V|$ *only* — and hence *constant* for any *one* given $|V|$. [Of course, (1), (2), (7), and (8) are correct *in*dependently of *any* mention of F and R.]
Applying (9a), (9d), and $P(+)_N + P(-)_N = 1$, we obtain, for all $N \geq 0$, [15]

$$\begin{aligned}P(+)_N &= FP(+)_{N-1} + (1-R)P(-)_{N-1}\\ &= FP(+)_{N-1} + (1-R)[1 - P(+)_{N-1}]\\ &= (F+R-1)P(+)_{N-1} + 1 - R\\ &= (F+R-1)[(F+R-1)P(+)_{N-2} + 1 - R] + 1 - R\\ &= (F+R-1)\{(F+R-1)[(F+R-1)P(+)_{N-3} + 1 - R]\\ &\quad + 1 - R\} + 1 - R\\ &= (F+R-1)^N P(+)_0 + (1-R)\sum_{j=0}^{N-1}(F+R-1)^j\\ &= (F+R-1)^N\left(\frac{1}{2}\right) + (1-R)\frac{1-(F+R-1)^N}{2-F-R}\\ &= \frac{2(1-R) - (F-R)(F+R-1)^N}{2(2-F-R)}\end{aligned}$$

$$\begin{aligned}\implies P(-)_N &= 1 - P(+)_N\\ &= \frac{2(1-F) + (F-R)(F+R-1)^N}{2(2-F-R)}\end{aligned}$$

$$\implies P(\pm)_N = \frac{1}{2}\left\{1 \pm \frac{(F-R)[1-(F+R-1)^N]}{2-F-R}\right\}. \tag{10}$$

The second step and third-to-the-last step of (10) are justified by $P(+)_N + P(-)_N = 1$. In the third through sixth lines of (10), a recursion relationship is developed via repeated substitution. In the seventh step of (10), we applied the first line of (7) and standard summation of the geometric series in the sixth line of (10). [If $N = 0$, then: (i) This geometric series contains no terms and hence vanishes. (ii) $(F + R - 1)^0 = 1$ is true throughout the range $-1 \leq F + R - 1 \leq 1$ of $F + R - 1$, with possible difficulty only at the *point* value $F + R - 1 = 0$. But, since $(F + R - 1)^0 = 1$ remains true even as $F + R - 1 \longrightarrow 0^{\pm}$ *infinitesimally closely* (from both above and below) — by *continuity* we take $(F + R - 1)^0 = 1$ even at the *point* value $F + R - 1 = 0$. Note that, among indeterminate forms, perhaps x^0 alone is so well-behaved, maintaining a fixed well-defined unique finite value (1) even as $x \longrightarrow 0^{\pm}$ infinitesimally closely (from both above and below) — by contrast, for example, $\frac{x}{0} \longrightarrow \pm\infty$ as $x \longrightarrow 0^{\pm}$. Hence, $\lim\limits_{x,y \longrightarrow 0} x^y = \lim\limits_{x,y \longrightarrow 0} \left(e^{\ln x}\right)^y = \lim\limits_{x,y \longrightarrow 0} e^{y \ln x} \overset{|y \ln x| \ll 1}{\longrightarrow} 1 + y \ln x \overset{|y \ln x| \ll 1}{\longrightarrow} 1$: if $x = F + R - 1$ and $y = 0$, then the last two steps immediately preceding yield *exactly* 1 — *not* merely a limiting value of 1. For perhaps the most general approach pertinent to (10) of $F + R - 1$ to 0 that is consistent with $(F + R - 1)^0 = 1$ even at the *point* value $F + R - 1 = 0$, let $x = a\,(F + R - 1)$ and $y = b\,(F + R - 1)^n = b\left(\frac{x}{a}\right)^n = \frac{b}{a^n} x^n$, where a, b, and n are arbitrary positive constants. Then $\lim\limits_{x,y \longrightarrow 0} x^y = \lim\limits_{x \longrightarrow 0} x^{\frac{b}{a^n} x^n} = \lim\limits_{x \longrightarrow 0} \left(e^{\ln x}\right)^{\frac{b}{a^n} x^n} = \lim\limits_{x \longrightarrow 0} e^{\frac{b}{a^n} x^n \ln x} = \lim\limits_{x \longrightarrow 0} \left(1 + \frac{b}{a^n} x^n \ln x\right) = 1 + \frac{b}{a^n} \lim\limits_{x \longrightarrow 0} x^n \ln x = 1 + 0 = 1$ (the last four steps immediately preceding being justified because $\lim\limits_{x \longrightarrow 0} x^n \ln x = 0$ by L'Hospital's Rule).]

Applying the first line of (8) and the last line of (10) yields, for all $N \geq 0$,

$$\begin{aligned} \langle V \rangle_N &= |V|\,[P(+)_N - P(-)_N] \\ &= |V|\,(F - R)[1 - (F + R - 1)^N]/(2 - F - R). \end{aligned} \tag{11}$$

By (11), $\langle V \rangle_N$ is antisymmetric in F and R; hence, with*out* loss of generality, we *always* take $F \geq R \implies \langle V \rangle_N \geq 0$ — e.g., as obtains for the *specific* F and R given by the rightmost terms of (5) and (6), respectively. The equality $F = R \implies \langle V \rangle_N = 0$ obtains *only* given: (a) the *point* value $V = |V| = 0$, which has *zero* probability measure of occurrence; and/or (b) $N = 0$. Our challenge to the second law requires the *strict* inequality $F > R \implies \langle V \rangle_N > 0$ *despite TEQ*, which obtains given $|V| > 0$ and $N \geq 1$.

Direct calculation of $P(+)_N$ and $P(-)_N$ via (10) can be cumbersome. However, applying the second line of (11) — and then the antisymmetry of $\langle V \rangle_N$ as per the paragraph immediately following (11) — to the last line of (10) further simplifies the already simpler expression given by the second line of (8) [restated in the first line of (12)]:

$$\begin{aligned} P(\pm)_N = P(V = \pm\,|V|)_N &= \frac{1}{2}\left(1 \pm \frac{\langle V \rangle_N}{|V|}\right) \\ \implies P(V)_N &= \frac{1}{2}\left(1 + \frac{\langle V \rangle_N}{V}\right) = P(V)_0\left(1 + \frac{\langle V \rangle_N}{V}\right). \end{aligned} \tag{12}$$

The further simplification as per the second line of (12) [wherein $P(V)_0 = \frac{1}{2}$ and $V = \pm |V|$ insofar as (5) – (22) and the associated discussions are concerned] is justified by said antisymmetry.
By (11), the final steady-state value of $\langle V \rangle_N$, i.e.,

$$\langle V \rangle_\infty = |V| (F - R)/(2 - F - R), \tag{13}$$

is reached at $N = 1$ if $F + R - 1 = 0 \iff 2 - F - R = 1$; i.e.,

$$\begin{aligned} \langle V \rangle_1 &= |V| (F - R) \text{ for } \textit{all } 0 \leq F, R \leq 1 \iff -1 \leq F + R - 1 \leq 1 \\ &= \langle V \rangle_\infty \text{ if } F + R - 1 = 0 \iff 2 - F - R = 1. \end{aligned} \tag{14}$$

Hence, $P(V)_N$ of (12) manifests similar behavior. The completion of time evolution at $N = 1$ if $F + R - 1 = 0 \iff 2 - F - R = 1$ obtains for *all* quantities studied in this chapter. [In Sect. 4, we will show that, while allowing time evolution to $N \longrightarrow \infty$ *does* maximize $\langle V \rangle_N$ and $\left| P(V)_N - \frac{1}{2} \right|$, it does *not* correspond to maximizing the force that tends to accelerate the DP in the $+X$ direction, or to our *primary* objective of maximizing its power output and hence its time rate of negentropy production.]
Now, define

$$\begin{aligned} \langle V \rangle_{N+\frac{1}{2}} &\equiv \frac{1}{2}(\langle V \rangle_N + \langle V \rangle_{N+1}) \\ &= |V| (F - R)[2 - (F + R)(F + R - 1)^N]/[2(2 - F - R)] \end{aligned} \tag{15}$$

and

$$\begin{aligned} \langle \Delta V \rangle_{N+\frac{1}{2}} &\equiv \langle V \rangle_{N+1} - \langle V \rangle_N \\ &= |V| (F - R)(F + R - 1)^N. \end{aligned} \tag{16}$$

Let f be the force that tends to accelerate the DP in the $+X$ direction. By Newton's second law and (16), at the $N \longrightarrow N + 1$ transition, i.e., at the $(N + 1)$ st pawl-peg interaction, we have

$$\begin{aligned} \langle f \rangle_{N+\frac{1}{2}} &= M \langle \Delta V \rangle_{N+\frac{1}{2}} \Big/ \Delta t \\ &= M \langle \Delta V \rangle_{N+\frac{1}{2}} \Big/ (L/|V|) \\ &= (MV^2/L)(F - R)(F + R - 1)^N. \end{aligned} \tag{17}$$

The second step of (17) is justified because consecutive pawl-peg interactions are separated in time by $\Delta t = L/|V|$. Let P^* be the DP's power output (not to be confused with probability P). Applying (15) and (17), at the $N \longrightarrow N + 1$ transition, i.e., at the $(N + 1)$ st pawl-peg

interaction, we have

$$\begin{aligned}\langle P^* \rangle_{N+\frac{1}{2}} &= \langle fV \rangle_{N+\frac{1}{2}} \\ &= \langle f \rangle_{N+\frac{1}{2}} \langle V \rangle_{N+\frac{1}{2}} \\ &= \frac{M|V|^3}{2L} \frac{(F-R)^2(F+R-1)^N[2-(F+R)(F+R-1)^N]}{2-F-R}. \end{aligned} \tag{18}$$

The second step of (18) is justified because $\langle V \rangle_{N+\frac{1}{2}}$ of (15) is *in*dependent of which of the four DP states ($> +$, $> -$, $< +$, or $< -$) — and hence of the corresponding $(N+1)$ st pawl-peg interaction (jump or bounce) — that happens to occur at the $N \longrightarrow N+1$ transition [14].
For the *specific* F and R given by the rightmost terms of (5) and (6), respectively; (11), the second lines of (12), (17), and (18), respectively become

$$\langle V \rangle_N = (2V^2/3c)A[1-(2e^{-A}-1)^N]/(e^A-1), \tag{19}$$

$$\begin{aligned} P(V)_N &= \frac{1}{2}\left\{1+\left(\frac{2V}{3c}\right)\frac{A[1-(2e^{-A}-1)^N]}{e^A-1}\right\} \\ &= \frac{1}{2}+\left(\frac{V}{3c}\right)\frac{A[1-(2e^{-A}-1)^N]}{e^A-1}, \end{aligned} \tag{20}$$

$$\langle f \rangle_{N+\frac{1}{2}} = (4M|V|^3/3Lc)Ae^{-A}(2e^{-A}-1)^N, \tag{21}$$

and

$$\langle P^* \rangle_{N+\frac{1}{2}} = \left(\frac{8M|V|^5}{9Lc^2}\right)\frac{A^2e^{-A}(2e^{-A}-1)^N[1-e^{-A}(2e^{-A}-1)^N]}{e^A-1}. \tag{22}$$

Now, consider *all* $\pm|V|$ pairs, i.e., *all* V, and hence also *all* $|V|$; especially, consider fluctuations of V among *all* possible values. TEQ, i.e., *maximum initial total entropy*, implies that *initially*, at $N=0$,

$$\begin{aligned} P(V)_0 &= P(V)_{\rm mw} \\ &= (M/2\pi kT)^{1/2}e^{-MV^2/2kT} \\ \Longrightarrow\ P(|V|)_0 &= P(|V|)_{\rm mw} \\ &= 2P(V)_0 = 2P(V)_{\rm mw} \\ &= (2M/\pi kT)^{1/2}e^{-MV^2/2kT}, \end{aligned} \tag{23}$$

$P(V)_{\rm mw}$ [$P(|V|)_{\rm mw}$] being the one-dimensional Maxwellian probability density of V [$|V|$]. Letting $P(V)_0 = \frac{1}{2} \longrightarrow P(V)_0 = P(V)_{\rm mw}$ and $V = \pm|V| \longrightarrow$ continuous V in the second line

of (12), and then applying (19), we obtain

$$\begin{aligned} P(V)_N &= P(V)_0 \left(1 + \frac{\langle V \rangle_N}{V}\right) \\ &= P(V)_{\mathrm{mw}} \left(1 + \frac{\langle V \rangle_N}{V}\right) \\ &= P(V)_{\mathrm{mw}} \left\{1 + \left(\frac{2V}{3c}\right) \frac{A[1 - (2e^{-A} - 1)^N]}{e^A - 1}\right\}. \end{aligned} \tag{24}$$

Any $\langle Q \rangle_N$, e.g., $\langle V \rangle_N$, $\langle f \rangle_{N+\frac{1}{2}}$, or $\langle P^* \rangle_{N+\frac{1}{2}}$, is defined for a given $\pm |V|$ *pair*, i.e., for a given $|V|$ — it is *un*defined and can*not* even be calculated given *only* a *single* value of V, e.g., given *only* $+|V|$ *alone* or given *only* $-|V|$ *alone*. $\langle Q \rangle_N$ can be written in the more detailed form $\langle Q(|V|) \rangle_N$; by contrast, the expression $\langle Q(V) \rangle_N$ is meaningless. Since (20) and (24) are correct to first order in V/c, by (24), $P(|V|)_N = P(+|V|)_N + P(-|V|)_N = P(|V|)_0 = P(|V|)_{\mathrm{mw}}$ to first order in $|V|/c$; hence, to first order in $|V|/c$, any average $\langle\langle Q \rangle\rangle_N$ over $P(|V|)_{\mathrm{mw}}$ equals that over $P(|V|)_N$ itself. [Of course, *initially*, at $N = 0$, $P(|V|)_N = P(|V|)_0 = P(|V|)_{\mathrm{mw}}$ *exactly*, not merely to first order in $|V|/c$; hence, any average $\langle\langle Q \rangle\rangle_0$ over $P(|V|)_{\mathrm{mw}}$ is *exact*.] The following five averages over $P(|V|)_{\mathrm{mw}}$ will be useful: $\langle\langle |V| \rangle\rangle_{\mathrm{mw}} = (2kT/\pi M)^{1/2}$, $\langle\langle V^2 \rangle\rangle_{\mathrm{mw}} = kT/M$, $\left\langle\left\langle |V|^3 \right\rangle\right\rangle_{\mathrm{mw}} = [2(kT/M)^3]^{1/2}$, $\langle\langle V^4 \rangle\rangle_{\mathrm{mw}} = 3(kT/M)^2 = 3\langle\langle V^2 \rangle\rangle_{\mathrm{mw}}^2$, and $\left\langle\left\langle |V|^5 \right\rangle\right\rangle_{\mathrm{mw}} = 8[2(kT/M)^5]^{1/2}$. [Of course, *numerically*, these five averages are identical whether taken over $P(|V|)_{\mathrm{mw}}$ or over $P(V)_{\mathrm{mw}}$. But, *conceptually*, as per the first two sentences of this paragraph — and anticipating the next paragraph — they are more correctly taken over $P(|V|)_{\mathrm{mw}}$.] Averaging over any *one* given $\pm |V|$ pair to obtain $\langle Q \rangle_N$ first, and subsequently averaging over *all* $|V|$ to obtain $\langle\langle Q \rangle\rangle_N$, is preferable to attempting to obtain $\langle\langle Q \rangle\rangle_N$ directly because, e.g.: (a) the former procedure is easier, (b) *both* $\langle Q \rangle_N$ *and* $\langle\langle Q \rangle\rangle_N$ are thus obtained, and (c) the $|V|$-dependence of $F - R$ is thus accounted for — e.g., as per application of (5) and (6) to the last terms of (11), (17), and (18) in order to obtain (19), (21), and (22), respectively.

Averaging V^2, $|V|^3$, and $|V|^5$ in (19), (21), and (22), respectively, over $P(|V|)_{\mathrm{mw}}$ (as per the immediately preceding paragraph) yields (25), (27), and (28), respectively. So that (25) – (28) are a complete set of equations, we restate the last line of (24) as (26). Thus, we obtain

$$\begin{aligned} \langle\langle V \rangle\rangle_N &= \frac{2\langle\langle V^2 \rangle\rangle_{\mathrm{mw}}}{3c} \frac{A[1 - (2e^{-A} - 1)^N]}{e^A - 1} \\ &= \frac{2kT}{3Mc} \frac{A[1 - (2e^{-A} - 1)^N]}{e^A - 1}, \end{aligned} \tag{25}$$

$$P(V)_N = P(V)_{\mathrm{mw}} \left\{1 + \left(\frac{2V}{3c}\right) \frac{A[1 - (2e^{-A} - 1)^N]}{e^A - 1}\right\}, \tag{26}$$

$$\langle\langle f\rangle\rangle_{N+\frac{1}{2}} = \frac{4M\left\langle\left\langle |V|^3\right\rangle\right\rangle_{\mathrm{mw}}}{3Lc} Ae^{-A}(2e^{-A}-1)^N$$

$$= \frac{4}{3L}\left[\frac{2(kT)^3}{Mc^2}\right]^{1/2} Ae^{-A}(2e^{-A}-1)^N, \tag{27}$$

and

$$\langle\langle P^*\rangle\rangle_{N+\frac{1}{2}} = \left(\frac{8M\left\langle\left\langle |V|^5\right\rangle\right\rangle_{\mathrm{mw}}}{9Lc^2}\right) \frac{A^2e^{-A}(2e^{-A}-1)^N[1-e^{-A}(2e^{-A}-1)^N]}{e^A-1}$$

$$= \frac{64}{9Lc^2}\left[\frac{2(kT)^5}{M^3}\right]^{1/2} \frac{A^2e^{-A}(2e^{-A}-1)^N[1-e^{-A}(2e^{-A}-1)^N]}{e^A-1}. \tag{28}$$

Note that specification to $P(V)_{\mathrm{mw}} = \frac{1}{2}P(|V|)_{\mathrm{mw}}$ is *not* required for the validity of our analyses: For example, $P(V)_{\mathrm{mw}}$ is *specifically* applied in the last two lines of (24) and in (26); and $P(|V|)_{\mathrm{mw}}$ in (25), (27), and (28). By contrast, for example, (7) – (22) and the first line of (24) are valid not only for $P(V)_0 = P(V)_{\mathrm{mw}} = \frac{1}{2}P(|V|)_{\mathrm{mw}}$, but for *any* $P(V)_0$ — whether continuous, discrete, or possessing both continuous and discrete ranges — that is symmetrical about $V = 0$. {Of course, (1) – (6) are valid for *any* $P(V)$ *whatsoever* [including, e.g., a Dirac δ-function, in which case either (5) or (6) but (unless $V = |V| = 0$) not both would obtain.]} For any *one* given value of $|V|$, i.e., for any *one* given $\pm|V|$ pair, velocity-dependent fluctuations behave identically — and break the randomness of Brownian motion identically — given *any* $P(V)_0$ that is symmetrical about $V = 0$. Note, in particular, as per (12), (20), and the first line of (24), that, for any given V, the bias of $P(V)_N$ from $P(V)_0$ is identical given *any* $P(V)_0$ that is symmetrical about $V = 0$. Considering *all* V, and hence also *all* $|V|$, $P(V)_{\mathrm{mw}} = \frac{1}{2}P(|V|)_{\mathrm{mw}}$ is the symmetrical velocity probability density — indeed, *the* velocity probability density — corresponding to maximum entropy. Hence, $P(V)_{\mathrm{mw}} = \frac{1}{2}P(|V|)_{\mathrm{mw}}$ is employed in this chapter — but with the view that generalization is possible to *any* $P(V)_0$ that is symmetrical about $V = 0$.

3. Negentropy production, and formulations of the second law

Positive values (however small) of $\langle V\rangle_N$, $\left|P(V)_N - \frac{1}{2}\right|$, $\langle f\rangle_{N+\frac{1}{2}}$, $\langle P^*\rangle_{N+\frac{1}{2}}$, $\langle\langle V\rangle\rangle_N$, $|P(V)_N - P(V)_{\mathrm{mw}}|$, $\langle\langle f\rangle\rangle_{N+\frac{1}{2}}$, and $\langle\langle P^*\rangle\rangle_{N+\frac{1}{2}}$ *despite TEQ* challenge the second law. A positive value of $\langle\langle P^*\rangle\rangle_{N+\frac{1}{2}}$ *despite TEQ* is our *primary* challenge thereto, because if $\langle\langle P^*\rangle\rangle_{N+\frac{1}{2}}$ overcomes a conservative resisting force, equal in magnitude but opposite in direction to $\langle\langle f\rangle\rangle_{N+\frac{1}{2}}$, then there obtains an uncompensated *negative* time rate of change in *total* entropy S:

$$\langle\langle P^*\rangle\rangle_{N+\frac{1}{2}} > 0 \implies dS/dt = -\langle\langle P^*\rangle\rangle_{N+\frac{1}{2}} \Big/ T < 0. \tag{29}$$

Perhaps the simplest such conservative resisting force, $Mg\sin(-\theta) = -Mg\sin\theta \doteq -Mg\theta$, is obtained by sloping our system very slightly upwards towards the $+X$ direction — as per Fig. 1 and the two immediately following paragraphs, very slightly upwards towards the right given a right-handed Cartesian coordinate system, or into a very gentle counterclockwise upward spiral given a right-handed cylindrical coordinate system — at a very small slope angle θ ($0 < \theta \ll 1$ rad; also, $0 < \theta \ll mgL/kT = AL/H_{\text{net}}$), such that $\langle\langle f \rangle\rangle_{N+\frac{1}{2}} = Mg\sin\theta \doteq Mg\theta$. (If, instead, the resisting force is frictional and hence *non*conservative, then it can be overcome at steady state indefinitely — frictional dissipation being *recycled* into power P^* — *despite TEQ*.) Generation — or regeneration via recycling — of power P^* *despite TEQ* entails spontaneous momentum flow [1] in challenge of the Zhang formulation [1] of the second law (and hence, as per the last two paragraphs of this Sect. 3, of *all* formulations thereof).

Of course, (29) is true for *all* DP power outputs, e.g., (29) is also true for the DP's Carnot-engine [17] power outputs.

But, in view of recent work concerning limitations of validity of certain formulations — especially, of *entropy*-based formulations — of the second law in the quantum regime [6s–6ff], the employment of the *entropy*-based (29) requires justification.

In the classical regime, (a) the Zhang [1] formulation of the second law (no spontaneous momentum flow in an isolated system $\implies$ no systematic motion — most generally, no systematic process — at TEQ), and (b) Thomson's formulation thereof (no extractable work at TEQ), are equivalent to (c) the formulation thereof stating that total entropy (total negentropy) can never decrease (increase), and, indeed, to (d) all other formulations of the second law. But, in the quantum regime, entropy (or, equivalently, negentropy — and hence free energy) is a difficult, non-uniquely-defined concept — as opposed to heat, and especially to work [6s–6ff]. Hence, in the quantum regime, (a) and (b) immediately above are preferable to (c) [and (d)] immediately above. This present chapter deals only with the classical regime — except for the last four paragraphs of this Sect. 3, a digression concerning limited aspects of the quantum regime in Sect. 6, and a few very brief mentions elsewhere. This present chapter is based primarily on (a) immediately above — which implies (b) immediately above *always*, and, apart from difficulties in the quantum regime [6s–6ff], also (c) [and (d)] immediately above. Nevertheless: Insofar as this present chapter is concerned, certainly outside of Sect. 6 — and, owing to the *limited* nature of said quantum aspects, probably even in Sect. 6 — (c) immediately above [which justifies the employment of *entropy* in (29)], and also (d) immediately above, still retain validity. [As an aside, note that the usual statement of (b) immediately above — no extractable work *via cyclic processes* at TEQ — is too restrictive. If a system is capable of doing work *even only on a one-time basis via a non*cyclic process — e.g., via a *one-time* isothermal expansion of a gas initially constrained to within less than the total volume of its container — then it is *not initially* at TEQ: it is at TEQ only *after* the gas has expanded to occupy the total volume of its container and hence is no longer capable of doing work. Thus, deleting "via cyclic processes" yields a more general statement as per (b) immediately above, and in accordance with the first two paragraphs of Sect. 1.]

In *both* the classical *and* the quantum regimes — but primarily in the quantum regime (particularly for *finite* quantum systems [6ee]), wherein different formulations of the second law can be *in*equivalent [6s–6ff]: The Zhang [1] formulation of the second law [(a) immediately above)] is a *maximally* strong formulation thereof, i.e., as strong a formulation thereof as is possible {some other formulation(s), e.g., the Thomson formulation [(b) immediately above], may be equally strong [6s–6dd], but no other formulation can be stronger}: Thus: A challenge

to the Zhang [1] formulation of the second law is a challenge to *all* formulations [6s–6ff] thereof — and hence a challenge to *the* second law [6dd]. By contrast (particularly in the quantum regime [6s–6ff]), a challenge to any other formulation(s) [6s–6ff] of the second law (i) may or (ii) may not be a challenge to the Zhang [1] formulation thereof, and hence to *all* formulations, thereof — and hence may be a challenge, respectively, (i) to *the* second law [6dd] or (ii) merely to *a* second law [6dd]. And a *true* challenge must be to *the* — not merely to *a* — second law.
There has recently been discovered a *classical* situation [6gg] wherein the minimal-work-principle formulation of the second law can be *in*valid. [The minimal-work-principle formulation of the second law has previously been investigated in the quantum regime (where it also can be *in*valid) [6v,6w].] But this is not applicable insofar as this present chapter is concerned, and in any case does not alter the *maximally strong status* of the Zhang [1] formulation of the second law.

4. Details of Markovian time evolution, and maximization of challenges to the second law

Time evolution is complete at $N = 1$ if $F + R - 1 = 0 \implies A = \ln 2$. This corresponds to an *overall* probability (considering *both* Forward *and* Reverse DP Brownian motion) of $\frac{1}{2}$ (correct to first order in $|V|/c$ for all $N \geq 1$ and exact at $N = 0$) that any given pawl-peg interaction is either a jump or a bounce, i.e., to $P(> |F + R - 1 = 0 \implies A = \ln 2)_N = P(< |F + R - 1 = 0 \implies A = \ln 2)_N = \frac{1}{2}$ (correct to first order in $|V|/c$ for all $N \geq 1$ and exact at $N = 0$). As $F + R - 1 \longrightarrow 1 \implies A \longrightarrow 0$, pawl-peg bounces become ever rarer, and hence time evolution becomes ever slower. As $F + R - 1 \longrightarrow -1 \implies A \longrightarrow \infty$, pawl-over-peg jumps become ever rarer, and hence time evolution becomes ever slower.
Time evolution of $\langle V \rangle_N$ and $P(V)_N - \frac{1}{2}$, and likewise of $\langle\langle V \rangle\rangle_N$ and $P(V)_N - P(V)_{\rm mw}$, towards final steady-state values as $N \longrightarrow \infty$ is monotonic and asymptotic if $0 < F + R - 1 < 1 \implies \ln 2 > A > 0$, diminishing-oscillatory if $-1 < F + R - 1 < 0 \implies \infty > A > \ln 2$, and complete at $N = 1$ if $F + R - 1 = 0 \implies A = \ln 2$.
For general F and R that [as per the sentence immediately following (9d)] are *at most* functions of $|V|$ *only*, and hence *constant* for any *one* given $|V|$ — not merely for the *specific* F and R given by the rightmost terms of (5) and (6), respectively — the functional form of any $\langle Q \rangle_N$ with respect to F, R, and N (and hence with respect to A and N) is *in*dependent of $|V|$. Thus, the values of F, R, and N (and hence of A and N) yielding maximization of any $\langle Q \rangle_N$ are also *in*dependent of $|V|$ — and thus likewise also yield maximization of the corresponding $\langle\langle Q \rangle\rangle_N$.
By inspection of (10) – (14), (19), (20), (25), and (26), $\langle V \rangle_N$ and $\left| P(V)_N - \frac{1}{2} \right|$, and likewise $\langle\langle V \rangle\rangle_N$ and $|P(V)_N - P(V)_{\rm mw}|$, are maximized by maximizing $(F - R)[1 - (F + R - 1)^N]/(2 - F - R) \implies$ maximizing $A[1 - (2e^{-A} - 1)^N]/(e^A - 1)$: maximization obtains given $0 < A \ll 1$ — implying maximization of $(1 - \frac{1}{2}A)[1 - (1 - 2A)^N]$ — which is maximized at unity by letting $A \longrightarrow 0$ and $N \longrightarrow \infty$, but with $N \longrightarrow \infty$ sufficiently faster than $A \longrightarrow 0$ such that $(1 - 2A)^N \longrightarrow 0$. We thus obtain the *absolute* maxima

$$\langle V \rangle_{N,\max} = \langle V \rangle_\infty \,|(A \longrightarrow 0) = 2V^2/3c$$
$$\implies \langle\langle V \rangle\rangle_{N,\max} = \langle\langle V \rangle\rangle_\infty \,|(A \longrightarrow 0) = 2\left\langle \left\langle V^2 \right\rangle \right\rangle_{\rm mw} \Big/ 3c = 2kT/3Mc \qquad (30)$$

and

$$\left|P(V)_N - \frac{1}{2}\right|_{\max} \Big/ \frac{1}{2} = \left|P(V|A \longrightarrow 0)_\infty - \frac{1}{2}\right| \Big/ \frac{1}{2}$$
$$= |P(V)_N - P(V)_{\rm mw}|_{\max} \Big/ P(V)_{\rm mw}$$
$$= |P(V|A \longrightarrow 0)_\infty - P(V)_{\rm mw}| \, P(V)_{\rm mw}$$
$$= 2\,|V| \,/3c. \qquad (31)$$

If $F + R - 1 \longrightarrow 1 \implies A \longrightarrow 0$, then time evolution becomes infinitely slow — requiring $N \longrightarrow \infty$ — because then pawl-peg bounces become infinitely rare. But any "practical" time evolution is limited to at most a *large but finite* number N of pawl-peg interactions. Hence, $\langle V\rangle_N$ and $\left|P(V)_N - \frac{1}{2}\right|$, and likewise $\langle\langle V\rangle\rangle_N$ and $|P(V)_N - P(V)_{\rm mw}|$, attain "practical" maxima — corresponding to *small but not infinitesimal* $1 - (F + R - 1) \implies$ *small but not infinitesimal* A and to *large but not infinite* N — that are almost but not quite as large as the *absolute* maxima given in (30) and (31) corresponding to $F + R - 1 \longrightarrow 1 \implies A \longrightarrow 0$ and to $N \longrightarrow \infty$. [This is especially true because, if pawl-peg bounces are *extremely* rare, then the DP has sufficient time *between* pawl-peg bounces so that its X-directional momentum exchanges with the EBR are no longer (as is assumed in our analyses) negligible compared with its X-directional momentum exchanges *at* pawl-peg bounces [12].]

For *small* $N \geq 1$, maximizing $\langle V\rangle_N$ and $\langle\langle V\rangle\rangle_N$ with respect to A by setting $\partial \langle V\rangle_N / \partial A = 0 \implies \partial \langle\langle V\rangle\rangle_N / \partial A = 0$ yields maxima at *moderate* A, because *small* $N \geq 1$ implies only *one or a few* pawl-peg interactions — *not* the *many* pawl-peg interactions that would be required to compensate (or overcompensate) for the *small* probability of pawl-peg bounces corresponding to *small* A. For example, $\langle V\rangle_1$ and $\langle\langle V\rangle\rangle_1$ are maximized at $A = 1$, with $\langle V\rangle_{1,\max} = \langle V\rangle_1 \,|(A = 1) = 4V^2/3ec \implies \langle\langle V\rangle\rangle_{1,\max} = \langle\langle V\rangle\rangle_1 \,|(A = 1) = 4\langle\langle V^2\rangle\rangle_{\rm mw}/3ec = 4kT/3Mec$. Note that these maxima lie in the diminishing-oscillatory regime, as per the second paragraph of this Sect. 4, and hence are larger [by a factor of $2(1 - e^{-1})$] than $\langle V\rangle_\infty \,|(A = 1) = 2V^2/[3c(e - 1)] \implies \langle\langle V\rangle\rangle_\infty \,|(A = 1) = 2\langle\langle V^2\rangle\rangle_{\rm mw}/[3c(e - 1)] = 2kT/[3Mc(e - 1)]$, [obtained by putting $N = \infty$ and $A = 1$ into (19) and (25)] — but smaller (by a factor of $2/e$) than the *absolute* maxima as per (30). [Similar results obtain for $\left|P(V)_1 - \frac{1}{2}\right| \Big/ \frac{1}{2} = |P(V)_1 - P(V)_{\rm mw}| \,/P(V)_{\rm mw}$, whose maximization at $A = 1$ yields $\left|P(V)_1 - \frac{1}{2}\right|_{\max} \Big/ \frac{1}{2} = |P(V)_1 - P(V)_{\rm mw}|_{\max} \Big/ P(V)_{\rm mw} = \left|P(V|A = 1)_1 - \frac{1}{2}\right| \Big/ \frac{1}{2} = |P(V|A = 1)_1 - P(V)_{\rm mw}|P(V)_{\rm mw} = 4\,|V| \,/3ec$.] For another example, $\langle V\rangle_2$ and $\langle\langle V\rangle\rangle_2$ are maximized at $A = \frac{1}{2}$ (< 1 as expected), but at the same values as $\langle V\rangle_1$ and $\langle\langle V\rangle\rangle_1$, respectively; and similarly for $\left|P(V)_2 - \frac{1}{2}\right| \Big/ \frac{1}{2} = |P(V)_2 - P(V)_{\rm mw}| \,/P(V)_{\rm mw}$.

By contrast, via inspection of (17), (21), and (27), $\langle f\rangle_{N+\frac{1}{2}}$ ($\langle\langle f\rangle\rangle_{N+\frac{1}{2}}$) are maximized by: (a) first, setting $\langle f\rangle_{N+\frac{1}{2}} = \langle f\rangle_{\frac{1}{2}}$ ($\langle\langle f\rangle\rangle_{N+\frac{1}{2}} = \langle\langle f\rangle\rangle_{\frac{1}{2}}$), thereby maximizing $(F + R - 1)^N$ at unity $\implies$ maximizing $(2e^{-A} - 1)^N$ at unity; and (b) then, setting $d(Ae^{-A})/dA = 0 \implies A = 1 \implies (Ae^{-A})_{\max} = e^{-1}$. We thus obtain the *absolute* maxima

$$\langle f\rangle_{N+\frac{1}{2},\max} = \langle f\rangle_{\frac{1}{2}} \Big| \,(A = 1) = 4M\,|V|^3 \,/3ecL$$
$$\implies \langle\langle f\rangle\rangle_{N+\frac{1}{2},\max} = \langle\langle f\rangle\rangle_{\frac{1}{2}} \Big| \,(A = 1) = 4M \left\langle \left\langle |V|^3 \right\rangle \right\rangle_{\rm mw} \Big/ 3ecL = \frac{4[2(kT)^3/M]^{1/2}}{3ecL}. \qquad (32)$$

Time evolution of $\langle f \rangle_{N+\frac{1}{2}}$ and $\langle\langle f \rangle\rangle_{N+\frac{1}{2}}$ towards 0 as $N \longrightarrow \infty$ is monotonic and asymptotic through positive values for all $N \geq 0$ if $0 < F + R - 1 < 1 \implies \ln 2 > A > 0$, diminishing-oscillatory through positive (negative) values at all even (odd) $N \geq 0$ if $-1 < F + R - 1 < 0 \implies \infty > A > \ln 2$, and complete at $N = 1$ if $F + R - 1 = 0 \implies A = \ln 2$.
Thus, as per (18) and (28), in order to maximize $\langle P^* \rangle_{N+\frac{1}{2}}$ ($\langle\langle P^* \rangle\rangle_{N+\frac{1}{2}}$) and hence, by Sect. 3, $-dS/dt$ — our *primary* challenge to the second law — we should *not* allow the Markovian time evolution of our DP to approach as closely as is "practical" (as per the fifth paragraph of this Sect. 4) to its *final* steady state $N \longrightarrow \infty$. Rather, we should allow this time evolution to proceed *only* to $N_{\text{opt}} + 1$, where N_{opt} is the *optimum finite* value of N; also set A at its corresponding *optimum finite* value A_{opt} (*not* $A \longrightarrow 0$); and then let the DP do work against a conservative resisting force equal in magnitude but opposite in direction to $\langle f \rangle_{N_{\text{opt}}+\frac{1}{2}}$ ($\langle\langle f \rangle\rangle_{N_{\text{opt}}+\frac{1}{2}}$) in this *imposed* steady state: N_{opt} and A_{opt} will be derived shortly. {If, instead, the resisting force is *non*conservative, e.g., friction, then $\langle P^* \rangle_{N+\frac{1}{2}}$ and $\langle\langle P^* \rangle\rangle_{N+\frac{1}{2}}$ are still thereby maximized, even though $-dS/dt$ is then dissipated as fast as it is (re)generated via recycling [recall the last two sentences of the paragraph containing (29)].} In special cases, particular optimizations may correspond to the immediately aforementioned general ones, e.g., setting $\theta = \theta_{\text{opt}}$ (with $\theta_{\text{opt}} > 0$ and finite) if $\langle\langle f \rangle\rangle_{N+\frac{1}{2}} = Mg \sin\theta \doteq Mg\theta$ as per the sentence immediately following (29).
As an aside, note that the DP's Carnot-engine [17] power outputs, *are* maximized (at $\theta = 0$) if the Markovian time evolution of our DP *is* allowed to approach as closely as is "practical" (as per the fifth paragraph of this Sect. 4) to its *final* steady state, with $A \longrightarrow 0$ and $N \longrightarrow \infty$ as per the first sentence of the paragraph containing (30) and (31) [17], corresponding (as closely as "practical") to the *absolute* maxima given by (30) and (31).
Maximizing $\langle P^* \rangle_{N+\frac{1}{2}}$ and $\langle\langle P^* \rangle\rangle_{N+\frac{1}{2}}$ with respect to N at given fixed $F + R - 1 \implies$ given fixed A, by setting

$$\partial \langle P^* \rangle_{N+\frac{1}{2}} \Big/ \partial N = 0 \implies \partial \langle\langle P^* \rangle\rangle_{N+\frac{1}{2}} \Big/ \partial N = 0, \tag{33}$$

yields, for the optimum value of N,

$$N_{\text{opt}} = -\ln(F + R)/\ln(F + R - 1) \implies N_{\text{opt}} = -\ln(2e^{-A})/\ln(2e^{-A} - 1). \tag{34}$$

Obviously, (34) is valid only if $0 \leq F + R - 1 < 1 \implies \ln 2 \geq A > 0$. Also, obviously, if (34) yields a non-whole-number value for N_{opt}, then the *actual* value of N_{opt} equals the whole-number value either immediately smaller or immediately larger than the non-whole-number value yielded by (34). If $-1 < F + R - 1 \leq 0 \implies \infty > A \geq \ln 2$, and also if $0 \leq F + R - 1 < 1 \implies \ln 2 \geq A > 0$ but with $F + R - 1$ sufficiently close to $0 \implies A$ sufficiently close to $\ln 2$ such that (34) yields N_{opt} sufficiently close to 0 as opposed to 1, then $N_{\text{opt}} = 0$.
By (34) and the three immediately following sentences: As $F + R - 1$ increases from 0 to $1 \implies A$ decreases from $\ln 2$ to 0, N_{opt} increases monotonically from 0 to ∞. (By the fifth paragraph of this Sect. 4, infinitesimally small $1 - (F + R - 1) \implies$ infinitesimally small A and infinitely large N are not "practical".) By (18), (22), and (28), the immediately preceding paragraph, and anticipating the two immediately following paragraphs: (a) If $F + R - 1 = 0 \implies A = \ln 2$, then $\langle P^* \rangle_{\frac{1}{2}} > 0$, $\langle\langle P^* \rangle\rangle_{\frac{1}{2}} > 0$, and, for all $N \geq 1$, $\langle P^* \rangle_{N+\frac{1}{2}} = \langle\langle P^* \rangle\rangle_{N+\frac{1}{2}} = 0$.

(b) If $-1 < F + R - 1 < 0 \implies \infty > A > \ln 2$, then $\langle P^* \rangle_{N+\frac{1}{2}} \longrightarrow 0$ and $\langle\langle P^* \rangle\rangle_{N+\frac{1}{2}} \longrightarrow 0$ via ever-diminishing oscillations as $N \longrightarrow \infty$, being positive (negative) at all even (odd) $N \geq 0$.
(c) If $0 < F + R - 1 < 1 \implies \ln 2 > A > 0$, then $\langle P^* \rangle_{N+\frac{1}{2}}$ and $\langle\langle P^* \rangle\rangle_{N+\frac{1}{2}}$ may reach their maxima at any $N \geq 0$.
Only for $N = 0$ can $\langle P^* \rangle_{N+\frac{1}{2}}$ and $\langle\langle P^* \rangle\rangle_{N+\frac{1}{2}}$ be maximized analytically with respect to A at given fixed N by setting

$$\partial \langle P^* \rangle_{N+\frac{1}{2}} \Big/ \partial A = 0 \implies \partial \langle\langle P^* \rangle\rangle_{N+\frac{1}{2}} \Big/ \partial A = 0. \tag{35}$$

For all $N \geq 1$, (35) must be solved numerically. [We neglect the trivial analytical solution of (35), which yields $A = 0$ and corresponds to $\langle P^* \rangle_{N+\frac{1}{2}} = \langle\langle P^* \rangle\rangle_{N+\frac{1}{2}} = 0$ for all $N \geq 0$.] Solving (35) analytically for $N = 0$ yields, for the corresponding optimum value of A,

$$A_{\text{opt}}|(N = 0) = 1, \tag{36}$$

and, for the corresponding maximum values of $\langle P^* \rangle_{\frac{1}{2}}$ and $\langle\langle P^* \rangle\rangle_{\frac{1}{2}}$,

$$\langle P^* \rangle_{\frac{1}{2},\max} = \langle P^* \rangle_{\frac{1}{2}} \Big| (A = 1) = 8M \left| V \right|^5 / [(3ec)^2 L] \tag{37}$$

and

$$\langle\langle P^* \rangle\rangle_{\frac{1}{2},\max} = \langle\langle P^* \rangle\rangle_{\frac{1}{2}} \Big| (A = 1) = \frac{8M \left\langle \left\langle |V|^5 \right\rangle \right\rangle_{\text{mw}}}{(3ec)^2 L} = \frac{64[2(kT)^5/M^3)]^{1/2}}{(3ec)^2 L}, \tag{38}$$

respectively. Note that (36) is consistent with the third sentence following (34). Equal and/or higher maxima — if any exist — of $\langle P^* \rangle_{N+\frac{1}{2}}$ and $\langle\langle P^* \rangle\rangle_{N+\frac{1}{2}}$ for $N \geq 1$ [corresponding to $A_{\text{opt}}(N)$ in the range to be given shortly by (39)], can be found numerically.
By (34) and the three immediately following sentences, corresponding to *all* maxima of $\langle P^* \rangle_{N+\frac{1}{2}}$ [$\langle\langle P^* \rangle\rangle_{N+\frac{1}{2}}$] for *all* $N \geq 1$ {whether or not any of these maxima equal or exceed $\langle P^* \rangle_{\frac{1}{2},\max}$ of (37) [$\langle\langle P^* \rangle\rangle_{\frac{1}{2},\max}$ of (38)]},

$$0 < A_{\text{opt}}|(N \geq 1) \leq [A_{\text{opt}}|(N = 1)]_{\max} < \ln 2, \tag{39}$$

where $[A_{\text{opt}}|(N = 1)]_{\max}$ is, as per the third sentence following (34), the *maximum* value of $A_{\text{opt}}(N)$ that corresponds to $N = 1$ rather than to $N = 0$. $A_{\text{opt}}(N)$ decreases monotonically and asymptotically towards 0 as $N \longrightarrow \infty$. (But note the "practical" limits as per the fifth paragraph of this Sect. 4.)
We conclude this Sect. 4 by considering [assuming, for simplicity, the *specific* F and R given by the rightmost terms of (5) and (6), respectively], the quantity

$$\begin{aligned} &F - R = 4Ae^{-A} \left| V \right| / 3c \\ &\implies \langle\langle F - R \rangle\rangle_{\text{mw}} = 4Ae^{-A} \langle\langle |V| \rangle\rangle_{\text{mw}} 3c = 4Ae^{-A} (2kT/\pi M)^{1/2} / 3c, \end{aligned} \tag{40}$$

an important measure of the degree to which the randomness of our DP's Brownian motion is broken — and maximization thereof. [Considering any *one* given $\pm |V|$ pair, $F - R$ does not involve an average, and hence is not enclosed within single angular brackets in (40) and (41).]

Maximizing $F - R$ and $\langle\langle F - R\rangle\rangle_{\mathrm{mw}}$ with respect to A, i.e., setting $d(Ae^{-A})/dA = 0 \implies A = 1 \implies (Ae^{-A})_{\max} = e^{-1}$, yields

$$(F - R)_{\max} = 4\,|V|\,/3ec$$
$$\implies \langle\langle F - R\rangle\rangle_{\mathrm{mw,max}} = 4\,\langle\langle |V|\rangle\rangle_{\mathrm{mw}}\,/3ec = 4(2kT/\pi M)^{1/2}/3ec. \tag{41}$$

Given (41), *all* other measures of the degree to which the randomness of our DP's Brownian motion is broken are also maximized immediately following the *first* step of time evolution, i.e., *all* other $\langle Q\rangle_N$ and $\langle\langle Q\rangle\rangle_N$ are also maximized at $N = 1$ (if, e.g., $Q = f$ or $Q = P^*$, at the $N = 0 \longrightarrow N = 1$ transition, i.e., at the 1 st pawl-peg interaction) and at $A = 1$. If $Q = f$, and possibly if $Q = P^*$, these maxima are absolute, i.e., not equaled or exceeded for any transition ending at $N > 1$ — in contrast with maximization if, e.g., $Q = V$. For $N > 1$ (and for transitions ending at $N > 1$), (41) does not, in general, correspond to maximization of $\langle Q\rangle_N$ and $\langle\langle Q\rangle\rangle_N$ (whether absolute or merely for the given N). [Note that, in contrast with (41) — which corresponds to maximization at $N = 1$ (or at the $N = 0 \longrightarrow N = 1$ transition, i.e., at the 1 st pawl-peg interaction) given $A = 1$ — completion of time evolution at $N = 1$ corresponds to $F + R - 1 = 0 \implies A = \ln 2$.]

5. Scaling

Assuming uniform scaling and the validity of (28) and (38), DP size $\propto L$ and $M \propto L^3$, so $\langle\langle P^*\rangle\rangle_{N+\frac{1}{2}} \propto L^{-11/2}$; and power density $\propto \langle\langle P^*\rangle\rangle_{N+\frac{1}{2}} \Big/ L^3 \propto \langle\langle P^*\rangle\rangle_{N+\frac{1}{2}} \Big/ M \propto L^{-17/2}$. Thus, $\langle\langle P^*\rangle\rangle_{N+\frac{1}{2}}$ is maximized by minimizing system size, and $\langle\langle P^*\rangle\rangle_{N+\frac{1}{2}} \Big/ L^3 \propto \langle\langle P^*\rangle\rangle_{N+\frac{1}{2}} \Big/ M$ is maximized even more strongly by both minimizing system size and maximizing the number of systems operating in parallel [18]. Also, both power and power density scale as $T^{5/2}$. As per (29), maximizing power (power density) also maximizes the time rate of the associated total negentropy production (total negentropy production density).

In correction of a previous error [19], $|T_+(V) - T_-(V)| = 4T\,|V|\,/3c$, the magnitude of the temperature difference between the $+X$ and $-X$ disk faces corresponding to $V = \pm\,|V|$ [as per (2), the two immediately following sentences, and the paragraph immediately thereafter], can*not* be reduced via *diffraction* of EBR around the disk, not even if the disk's diameter and thickness are small (linear dimensions $\lesssim hc/kT$) or even very small (linear dimensions $\ll hc/kT$) compared with the wavelength of a typical EBR photon at temperature T ($\approx hc/kT$) [20]. An EBR photon approaching the disk from, e.g., the $+X$ direction can*not*, say, be diffracted into a "U-turn" path, thence impinging on the disk from the $-X$ direction: this requires (forbidden) backwards propagation of Huygens' wavelets [20b,20c] and violates conservation of momentum [20c]! (Diffraction can, of course, occur "around a corner", but *not* into a U-turn path [20b,20c].) *Diffraction* is thereby forbidden from reducing the opacity of a small (linear dimensions $\lesssim hc/kT$) or even of a very small (linear dimensions $\ll hc/kT$) disk and hence from degrading $|T_+(V) - T_-(V)|$ [20b,20c].

Nevertheless, *diffraction* aside, a small (linear dimensions $\lesssim hc/kT$) disk, and especially a very small (linear dimensions $\ll hc/kT$) disk, typically *does* suffer from small opacity. For a typical very small (linear dimensions $\ll hc/kT$) disk, the efficiency of absorption/(re)radiation of EBR *per unit of DP volume* (and hence, assuming uniform scaling, also *per unit of DP mass*) is *in*dependent of DP size [21] — thereby rendering a very thin (thickness $\ll hc/kT$) disk

highly transparent. Said transparency degrades DP performance by (a) reduced probability of absorption/(re)radiation of any given EBR photon, and (b) rendering the pawl almost as likely to be impinged on by an EBR photon that *is* absorbed/(re)radiated emanating from the $-X$ direction as by one emanating from the $+X$ direction. Hence, typically, for such a pawl, $T_+(V) = T\left(1 + \frac{2\gamma V}{3c}\right)$, where $0 < \gamma \ll 1$, i.e., $|T_+(V) - T| = \frac{1}{2}|T_+(V) - T_-(V)|$ *is* seriously degraded in comparison with (2) — and thus DP performance *is also* seriously degraded. Since small DP size (and mass) with*out* appreciable degradation of DP performance is necessary for significant — or even measurable — power and negentropy production densities, the question arises as to whether or not said degradation in small (linear dimensions $\lesssim hc/kT$), and even very small (linear dimensions $\ll hc/kT$), DPs can be overcome.

Perhaps, it can be overcome via a DP possessing one or more of the following *un*typical properties: (a) Overlapping resonances: If the DP is comprised of atoms and/or molecules whose resonances overlap to significantly "cover" the Planck spectrum corresponding to T, then the DP might be highly opaque even if it is very small (linear dimensions $\ll hc/kT$) [22]. (b) An internal reflective shield: A nonreflective [purely absorptive/(re)radiative] nonresonant material cannot be both thin ($\lesssim hc/kT$) and opaque to EBR corresponding to T [23]. But a reflective material (even if *non*resonant) can be [24]. Therefore, a thin reflective (if *also* resonant, so much the better) midsection comprising the "center slab" of the disk separates its absorptive/(re)radiative $+X$ and $-X$ faces not only spatially, but — more importantly — thermally. [Of course, whether or not such a reflective shield is present, the $+X$ and $-X$ disk faces *themselves* must be absorptive/(re)radiative — not reflective: any purely reflective material obviously can never (re)thermalize!] (c) Alternatively, perhaps a nonrelativistic positive-rest-mass thermal background medium at temperature T might be made preponderant over the EBR [25], in which case $c \longrightarrow |U|$, with $|U|$ on the order of a typical thermal or sonic molecular speed in said medium, rather than the speed of light in vacuum — which yields the advantage, for any given DP size and mass, of $|U| \ll c \implies |V|/|U| \gg |V|/c$ [25]. A further advantage obtains if DP size and mass given a nonrelativistic positive-rest-mass thermal background medium being preponderant over the EBR can be smaller than those given the EBR being the *sole* thermal background medium. (Even given a nonrelativistic positive-rest-mass thermal background medium being preponderant over the EBR, there seems to be no advantage in "excluding" the EBR corresponding to T: such "exclusion" begins to obtain if the DP is enclosed within, say, a conducting shell of diameter $\lesssim hc/kT \approx$ wavelength of typical EBR photon at temperature T, and obtains *strongly* if said diameter $\ll hc/kT$.)

6. A digression concerning limited aspects of DP operation in the quantum regime

For brevity in notation in this Sect. 6, we first define, in the *classical* regime,

$$F \equiv \frac{1}{2}(\mu + \epsilon) \tag{42}$$

and

$$R \equiv \frac{1}{2}(\mu - \epsilon). \tag{43}$$

Note that (42) and (43) imply, and are implied by,

$$\mu \equiv F + R \tag{44}$$

and

$$\epsilon \equiv F - R. \tag{45}$$

Also, for simplicity, in this Sect. 6, we consider any *one* given $\pm|V|$ pair, i.e., any *one* given $|V|$; except for the last paragraph thereof, wherein averages over *all* $\pm|V|$ pairs, i.e., over *all* $|V|$, are briefly mentioned.

Applying (44) and (45) in the *classical* regime, we can rewrite the last line of (10), (11), (15), (16), (17), and (18), respectively, as

$$P(\pm)_N = \frac{1}{2}\left\{1 \pm \frac{\epsilon[1-(\mu-1)^N]}{2-\mu}\right\}, \tag{46}$$

$$\langle V\rangle_N = |V|\,\frac{\epsilon[1-(\mu-1)^N]}{2-\mu}, \tag{47}$$

$$\langle V\rangle_{N+\frac{1}{2}} = |V|\,\frac{\epsilon[2-\mu(\mu-1)^N]}{2(2-\mu)}, \tag{48}$$

$$\langle \Delta V\rangle_{N+\frac{1}{2}} = |V|\,\epsilon(\mu-1)^N, \tag{49}$$

$$\langle f\rangle_{N+\frac{1}{2}} = \left(\frac{MV^2}{L}\right)\epsilon(\mu-1)^N, \tag{50}$$

and

$$\langle P^*\rangle_{N+\frac{1}{2}} = \left(\frac{M|V|^3}{2L}\right)\frac{\epsilon^2(\mu-1)^N[2-\mu(\mu-1)^N]}{2-\mu}. \tag{51}$$

The ϵ-, μ-, and N-functionalities are mutually *in*dependent. At constant μ and N [except for the trivial case $N = 0$ in (46) and (47), corresponding to $\left|P(\pm)_0 - \frac{1}{2}\right| = 0$ and to $\langle V\rangle_0 = 0$, respectively], all $\langle Q\rangle_N$, as per (46) – (51), are $\propto \epsilon$ (except $\langle P^*\rangle_{N+\frac{1}{2}} \propto \epsilon^2$).

We now explore limited aspects of DP operation in the *quantum* regime, considering the pawl's quantum-mechanical tunneling through [26a] (or quantum-mechanical — as opposed to classical — jumping over [26b]) pegs when it would classically bounce, and its quantum-mechanical reflection or bouncing from pegs when it would classically jump [26]. For simplicity, we assume in this Sect. 6 — as we do throughout this chapter — (in addition to our nonrelativistic assumptions as per the last sentence of the paragraph immediately following Fig. 1): (a) that $m\langle|v|\rangle_{\rm mw}(Z - Z_{\rm min})_{\rm scale} = m(2kT/\pi m)^{1/2}(kT/mg) = (2/\pi m)^{1/2}(kT)^{3/2}/g \approx (kT)^{3/2}/m^{1/2}g \gg h$, so that the pawl's Z-directional thermal (Brownian) motion can still be treated classically; (b) that $M\langle|V|\rangle_{\rm mw} L = M(2kT/\pi M)^{1/2}L = (2kTM/\pi)^{1/2}L \approx (kTM)^{1/2}L \gg h$, so that the DP's X-directional thermal (Brownian) motion can still be treated classically; and (c) that the combined pawl-plus-peg X-directional thickness is $\ll L$, so that quantum-mechanically (as well as classically) Δt is only negligibly affected thereby.

Classically, given DP Brownian motion at $V = +|V|$, the pawl's altitude at pawl-peg interaction is $Z > H$ ($Z_{\rm min} \le Z < H$) with probability F ($1 - F$), corresponding — with *certainty* — to the interaction being a jump (bounce). By contrast, in the *quantum* regime,

the pawl can, with *non*zero probability, tunnel through [26a] (or quantum-mechanically — as opposed to classically — jump over [26b]) a peg if $Z_{\min} \leq Z < H$, and reflect or bounce from a peg if $Z > H$ [26]. Within approximations (a) and (b) as per the immediately preceding paragraph, quantum-mechanically — as classically — given DP Brownian motion at $V = +|V|$, the pawl's altitude at pawl-peg interaction is $Z > H$ ($Z_{\min} \leq Z < H$) with probability F ($1 - F$). But, quantum-mechanically [26]: (i) if $Z_{\min} \leq Z < H$, then the pawl will jump with probability $(1 - F)\tau_+$ and bounce with probability $(1 - F)(1 - \tau_+)$, where $\tau(+|V|) \equiv \tau_+$ is the quantum-mechanical probability of tunneling given $V = +|V|$, integrated over the range $Z_{\min} \leq Z < H$. And, (ii) if $Z > H$, then the pawl will jump with probability $F(1 - \rho_+)$ and bounce with probability $F\rho_+$, where $\rho(+|V|) \equiv \rho_+$ is the quantum-mechanical probability of reflection or bouncing given $V = +|V|$, integrated over the range $Z > H$. This paragraph obviously also obtains given DP Brownian motion at $V = -|V|$, as per the substitutions $V = +|V| \longrightarrow V = -|V|$, $F \longrightarrow R$, $\tau(+|V|) \equiv \tau_+ \longrightarrow \tau(-|V|) \equiv \tau_-$, and $\rho(+|V|) \equiv \rho_+ \longrightarrow \rho(-|V|) \equiv \rho_-$. Explicitly, applying (3) – (6) with $H_{\text{net}} \equiv H - Z_{\min} \longrightarrow Z - Z_{\min}$, to first order in $|V|/c$,

$$\tau_\pm \equiv \tau(\pm|V|) = \langle \tau(\pm|V|, Z) \rangle = \frac{\int_{Z_{\min}}^{H} \tau_\pm(Z) P(Z|V = \pm|V|) dZ}{\int_{Z_{\min}}^{H} P(Z|V = \pm|V|) dZ}$$
$$= \frac{\int_{Z_{\min}}^{H} \tau_\pm(Z) \left(1 \pm \frac{2mg(Z - Z_{\min})|V|}{3kTc}\right) e^{-mg(Z - Z_{\min})/kT} dZ}{\int_{Z_{\min}}^{H} \left(1 \pm \frac{2mg(Z - Z_{\min})|V|}{3kTc}\right) e^{-mg(Z - Z_{\min})/kT} dZ} \tag{52}$$

and

$$\rho_\pm \equiv \rho(\pm|V|) = \langle \rho(\pm|V|, Z) \rangle = \frac{\int_{H}^{\infty} \rho_\pm(Z) P(Z|V = \pm|V|) dZ}{\int_{H}^{\infty} P(Z|V = \pm|V|) dZ}$$
$$= \frac{\int_{H}^{\infty} \rho_\pm(Z) \left(1 \pm \frac{2mg(Z - Z_{\min})|V|}{3kTc}\right) e^{-mg(Z - Z_{\min})/kT} dZ}{\int_{H}^{\infty} \left(1 \pm \frac{2mg(Z - Z_{\min})|V|}{3kTc}\right) e^{-mg(Z - Z_{\min})/kT} dZ}. \tag{53}$$

Applying (52) qualitatively [26], for any $|V| > 0$, $\tau_+ > \tau_-$, because, given $Z_{\min} \leq Z < H$, Z is [as per (3) – (6) with $H_{\text{net}} \equiv H - Z_{\min} \longrightarrow Z - Z_{\min}$] more probably closer to H if $V = +|V|$ than if $V = -|V|$. Similarly, applying (53) qualitatively [26], for any $|V| > 0$, $\rho_- > \rho_+$, because, given $Z > H$, Z is [as per (3) – (6) with $H_{\text{net}} \equiv H - Z_{\min} \longrightarrow Z - Z_{\min}$] more probably closer to H if $V = -|V|$ than if $V = +|V|$.

Thus, letting the subscript "q" denote "quantum-mechanical", we have {as the quantum-mechanical analog of (5), (9a), and (42) [within said approximations (a) and (b)]}, for the *overall* probability, integrated over *all* $Z \geq Z_{\min}$, given DP Brownian motion at $V = +|V|$, of a pawl-over-peg jump in the $+X$ direction,

$$F_{\text{q}} = F(1 - \rho_+) + (1 - F)\tau_+. \tag{54}$$

Similarly, {as the quantum-mechanical analog of (6), (9b), and (43) [within said approximations (a) and (b)]}, the *overall* probability, integrated over *all* $Z \geq Z_{\min}$, simply via DP Brownian motion at $V = -|V|$, of a pawl-over-peg jump in the $-X$ direction is

$$R_{\mathrm{q}} = R(1-\rho_-) + (1-R)\tau_-. \tag{55}$$

All classical results in this chapter are modified in the *quantum* regime — within said approximations (a) and (b) — simply via the substitutions $F \longrightarrow F_{\mathrm{q}}$ and $R \longrightarrow R_{\mathrm{q}}$. Also, note that the correspondence principle is obeyed: *purely* classical behavior is recovered in the limits $\tau_+ \longrightarrow 0$, $\tau_- \longrightarrow 0$, $\rho_- \longrightarrow 0$, and $\rho_+ \longrightarrow 0$.
For still greater brevity in notation, we define, for the remainder of this Sect. 6,

$$\Sigma\tau \equiv \tau_+ + \tau_-, \tag{56}$$

$$\Sigma\rho \equiv \rho_- + \rho_+, \tag{57}$$

$$\Delta\tau \equiv \tau_+ - \tau_- > 0, \tag{58}$$

and

$$\Delta\rho \equiv \rho_- - \rho_+ > 0. \tag{59}$$

The inequalities in (58) and (59) are justified by the two sentences immediately following (53). Applying (42) – (45) and (54) – (59), we have, as the quantum-mechanical analogs — within said approximations (a) and (b) — of (44) and (45), respectively,

$$\begin{aligned}
\mu_{\mathrm{q}} &\equiv F_{\mathrm{q}} + R_{\mathrm{q}} \\
&= F(1-\rho_+) + (1-F)\tau_+ + R(1-\rho_-) + (1-R)\tau_- \\
&= F + R - F(\rho_+ + \tau_+) - R(\rho_- + \tau_-) + \tau_+ + \tau_- \\
&= \mu - \frac{1}{2}(\mu+\epsilon)(\rho_+ + \tau_+) - \frac{1}{2}(\mu-\epsilon)(\rho_- + \tau_-) + \tau_+ + \tau_- \\
&= \mu - \frac{\mu}{2}(\Sigma\rho + \Sigma\tau) + \frac{\epsilon}{2}(\Delta\rho - \Delta\tau) + \Sigma\tau
\end{aligned} \tag{60}$$

and

$$\begin{aligned}
\epsilon_{\mathrm{q}} &\equiv F_{\mathrm{q}} - R_{\mathrm{q}} \\
&= F(1-\rho_+) + (1-F)\tau_+ - [R(1-\rho_-) + (1-R)\tau_-] \\
&= F - R - F(\rho_+ + \tau_+) + R(\rho_- + \tau_-) + \tau_+ - \tau_- \\
&= \epsilon - \frac{1}{2}(\mu+\epsilon)(\rho_+ + \tau_+) + \frac{1}{2}(\mu-\epsilon)(\rho_- + \tau_-) + \tau_+ - \tau_- \\
&= \epsilon + \frac{\mu}{2}(\Delta\rho - \Delta\tau) - \frac{\epsilon}{2}(\Sigma\rho + \Sigma\tau) + \Delta\tau.
\end{aligned} \tag{61}$$

As per the sentence containing (46) and the two sentences immediately following (55), the *classical* (46) – (51) are modified in the *quantum* regime — within said approximations (a) and (b) — simply via the substitutions $\epsilon \longrightarrow \epsilon_{\mathrm{q}}$ and $\mu \longrightarrow \mu_{\mathrm{q}}$.
We now consider the simplest nontrivial special case, which obtains at $N = 1$ in (46) and (47), and at the $N = 0 \longrightarrow N = 1$ transition in (48) – (51). [The trivial case is: $N = 0$ in (46) and (47): recall the second sentence following (51).] In this simplest nontrivial special case, ϵ-dependence alone obtains [recall the paragraph immediately following (51)]. Can $\epsilon_{\mathrm{q}} > \epsilon$

obtain, i.e., can a quantum DP [within said approximations (a) and (b)] outperform a classical DP in this simplest nontrivial special case? Applying (45) and (61) yields

$$\begin{aligned} \epsilon_{\mathrm{q}} > \epsilon \implies & \frac{\mu}{2}(\Delta\rho - \Delta\tau) - \frac{\epsilon}{2}(\Sigma\rho + \Sigma\tau) + \Delta\tau > 0 \\ \implies & \frac{\epsilon(\Sigma\rho + \Sigma\tau)}{\Delta\tau} + \mu\left(1 - \frac{\Delta\rho}{\Delta\tau}\right) < 2. \end{aligned} \tag{62}$$

Owing to algebraic difficulty, it is unclear whether or not (62) can be fulfilled for any physically realistic values of quantities appearing therein, let alone whether or not $\epsilon_{\mathrm{q,max}} > \epsilon_{\mathrm{max}}$.
The second-simplest nontrivial special case — entailing the (mutually *in*dependent) ϵ- and μ-functionalities — obtains in the limit $N \longrightarrow \infty$ (within "practical" limits as per the fifth paragraph of Sect. 4) in (46) – (48). Applying (44), (45), (60), and (61) yields, in this second-simplest nontrivial special case, as the requirement for a quantum DP [within said approximations (a) and (b)] to outperform a classical DP,

$$\begin{aligned} & \frac{\epsilon_{\mathrm{q}}}{2 - \mu_{\mathrm{q}}} > \frac{\epsilon}{2 - \mu} \\ \implies & \frac{\epsilon + \frac{\mu}{2}(\Delta\rho - \Delta\tau) - \frac{\epsilon}{2}(\Sigma\rho + \Sigma\tau) + \Delta\tau}{2 - [\mu - \frac{\mu}{2}(\Sigma\rho + \Sigma\tau) + \frac{\epsilon}{2}(\Delta\rho - \Delta\tau) + \Sigma\tau]} > \frac{\epsilon}{2 - \mu} \\ \implies & (2 - \mu)\left[\epsilon + \frac{\mu}{2}(\Delta\rho - \Delta\tau) - \frac{\epsilon}{2}(\Sigma\rho + \Sigma\tau) + \Delta\tau\right] \\ & > \epsilon\{2 - [\mu - \frac{\mu}{2}(\Sigma\rho + \Sigma\tau) + \frac{\epsilon}{2}(\Delta\rho - \Delta\tau) + \Sigma\tau]\} \\ \implies & \left[\mu - \frac{1}{2}(\mu^2 - \epsilon^2)\right](\Delta\rho - \Delta\tau) + (2 - \mu)\Delta\tau > \epsilon\Sigma\rho \\ \implies & \mu\left(1 - \frac{1}{2}\mu\right)(\Delta\rho - \Delta\tau) + (2 - \mu)\Delta\tau > \epsilon\Sigma\rho. \end{aligned} \tag{63}$$

The last step of (63) is justified because [given the *specific* F and R as per the rightmost terms of (5) and (6), respectively, and applying (42) – (45)] $\epsilon^2 \ll \mu^2$. It is even less clear — owing to greater algebraic difficulty — whether or not (63) can be fulfilled for any physically realistic values of quantities appearing therein, let alone whether or not $[\epsilon_{\mathrm{q}}/(2 - \mu_{\mathrm{q}})]_{\mathrm{max}} > [\epsilon/(2 - \mu)]_{\mathrm{max}}$ can obtain.
Owing to still greater algebraic difficulty, we will not specifically consider the completely general case — entailing all three (mutually *in*dependent) ϵ-, μ-, and N-functionalities.
By averaging over *all* $\pm|V|$ pairs, i.e., over *all* $|V|$ — similarly as for our classical DP [as per the third paragraph and last four paragraphs of Sect. 2, and in light of the two sentences immediately following (55) and that immediately following (61)] — *overall* quantum DP behavior [within said approximations (a) and (b)] can be similarly derived.

7. Conclusion

In the original classic "Ratchet and Pawl" chapter [4], Feynman's upshot concerning the "Ratchet and Pawl" elucidates the Zhang [1] formulation of the second law:

> "In spite of all our cleverness of lopsided design, if the two temperatures are exactly equal there is no more propensity to turn one way than the other. The moment we

look at it, it may be turning one way or the other, but in the long run it gets nowhere. The fact that it gets nowhere is really the fundamental deep principle on which all of thermodynamics is based."

Feynman's ratchet (which manifests *only non*-velocity-dependent fluctuations) can operate — albeit *not* in violation of the second law — *if* negentropy (and hence free energy) is supplied thereto, i.e., at *non*-TEQ; e.g., (a) if the two temperatures are unequal, or (b) if the pawl — assumed to have a sufficiently short thermal response time — is heated (cooled) whenever the wheel turns in the Forward (Reverse) direction.

But Feynman's classic ratchet and pawl manifests asymmetry, i.e., lopsidedness, *only geometrically*, i.e., *only in coordinate space alone*. By contrast, *velocity-dependent* fluctuations — which *spontaneously* break the randomness of our DP's Brownian motion at TEQ — manifest asymmetry, i.e., lopsidedness, in *velocity or momentum space*, hence allowing operation *despite TEQ*: Velocity-dependent fluctuations execute procedure (b) as stated in the immediately preceding paragraph, but *spontaneously*, i.e., with*out* cost in negentropy (and hence in free energy). Of course, our DP is *also* asymmetrical geometrically: geometrical (coordinate-space) asymmetry plays an auxiliary yet necessary role in the case of our DP — and perhaps in general — to momentum-space-asymmetrical velocity-dependence of fluctuations in the spontaneous breaking of the randomness of Brownian motion at TEQ. But geometrical (coordinate-space) asymmetry *alone* does not *imply* the velocity- or momentum-space asymmetry that seems to be the *central* requirement for this spontaneous randomness-breaking.

If the impedance to Brownian-motional velocity V is thus an asymmetrical function of V *itself*, then can the randomness of V be spontaneously broken, thereby challenging the Zhang [1] formulation — and hence, as per the last four paragraphs of Sect. 3, *all* formulations — of the second law?

The correspondence principle requires that the following necessary — albeit, of course, not sufficient — condition must be satisfied by any *valid* new and/or generalized scientific theory: the new and/or generalized theory must reduce to any more restricted theory that is a special case thereof within the more restricted theory's (narrower) range of validity. Our theory challenging the second law via *velocity-dependence* of fluctuations *is* in accordance with the correspondence principle: it predicts that the second law and all results based thereon remain inviolate if *velocity-dependence* of fluctuations vanishes.

Of course, the five immediately preceding paragraphs do *not* preclude *un*related challenges to the second law that are *not* based on velocity-dependence of fluctuations [5–10]. Also, obviously, the five immediately preceding paragraphs do *not* imply that *every* velocity-dependent effect can spontaneously break the randomness of Brownian motion at TEQ — challenging the second law. For example, it seems unlikely that the Lorentz force — and hence, by extension, *any non*dissipative velocity-dependent force that acts perpendicularly to the velocity *itself* (i.e., to the direction of motion), and hence which can do no work — can thus challenge the second law [27]. [Note: The Zhang formulation of the second law, enunciated in Ref. [1a] (and restated in the first two paragraphs of Sect. 1, with further discussions in the last four paragraphs of Sect. 3, of this present chapter), is valid irrespective of whether or not (*non*dissipative) velocity-dependent forces acting perpendicularly to the velocity itself (i.e., to the direction of motion), and hence which can do no work — such as the Lorentz force — can challenge the second law.] Also, of course,

(in general, velocity-dependent) *dissipative* frictional forces do *not* challenge the second law — rather, friction (whether velocity-dependent or not) *manifests* the second law.

Questions that have not been addressed or answered in this present chapter imply the following: (i) resolving the challenge to the second law (pro or con) posed by our classical velocity-dependent DP model, i.e., posed by our DP per se [as developed initially in Ref. [3k] and more quantitatively both in this present chapter and in previous shorter versions [28] thereof], and posed by possible classical generalizations of our DP model; (ii) investigating alternative derivations relevant to our DP model; (iii) more thorough study of quantum-mechanical velocity-dependent models; (iv) possible generalization of source(s) of velocity-dependence — in both the classical and quantum regimes — to other than the Doppler effect, if such source(s) exist; (v) investigating whether or not geometrical asymmetry is *always* an auxiliary requirement to velocity-dependence of fluctuations for our challenge to the second law, and the issue of auxiliary requirement(s) in general (in both the classical and quantum regimes); (vi) understanding which manifestation(s) of velocity-dependence can or cannot challenge the second law in both the classical and quantum regimes — recall the last four sentences of the immediately preceding paragraph; and (vii) investigating relationship(s) to other (classical and quantum) challenges to the second law [5–10], including a search for unifying principle(s) behind challenges thereto — whether based on velocity-dependence of fluctuations or not (recall the immediately preceding paragraph).

Perhaps, in passing, it might be noted that there have also been challenges — albeit *un*related to this present chapter — to the first [29] and third [30] laws of thermodynamics.

8. Acknowledgments

Dr. Donald H. Kobe is gratefully acknowledged for many very thoughtful and extensive discussions and correspondences, hence contributing many improvements, directly concerning this present chapter and concerning the expoundment of previous shorter versions [28] thereof, as well as concerning ideas initially discussed in Ref. [3k] and in still earlier work [31] that are developed more quantitatively in this present chapter and in said shorter versions [28]. I am very thankful to Dr. Daniel P. Sheehan for insightful and detailed correspondences, including both a draft and the final version of relevant material from his new book [32], that provided an independent viewpoint concerning Refs. [3k] and [28] and hence helped to inspire new ideas for this present chapter (especially for Sect. 5); to Dr. Alexey V. Nikulov for interesting and insightful correspondences concerning the Zhang [1] formulation of the second law and various challenges thereto; to Dr. Paolo Grigolini for thought-provoking background discussions (especially those concerning temperature fluctuations and superstatistics [12]) and for helpful supplementary discussions (especially those concerning style and mathematical notation); to Dr. James H. Cooke for thoughtful and interesting discussions, correspondences, and constructive criticisms concerning Ref. [3k] but also pertinent for this present chapter; to Dr. Marlan O. Scully and to Dr. Th. M. Nieuwenhuizen for perceptive discussions concerning the second law, especially in the quantum regime; to Dr. Jacek M. Kowalski for interesting discussions concerning Markov processes; and to Dr. Richard McFee for helpful correspondences and discussions concerning Ref. [7a], and the second law in general; and to Dr. Bright Lowry, who first introduced me to Feynman's ratchet and pawl in 1972 during insightful discussions concerning the second law of thermodynamics. Grateful acknowledgments are expressed to Dr. Kurt W. Hess, Dr. Stan

Czamanski, Mr. S. Mort Zimmerman, and Mr. Robert H. Shelton for many interesting and thoughtful discussions, as well as numerous helpful suggestions and correspondences, both directly concerning this present chapter and also concerning background ideas pertaining thereto that were originally developed in Ref. [3k] and in still earlier work [31]. Additionally, thanks are expressed to Dr. Bruce N. Miller, Dr. Wolfgang Rindler, Dr. Roland E. Allen, Dr. Bruno J. Zwolinski, Dr. G. R. Somayajulu, Dr. Abraham Clearfield, Dr. Patricia H. Reiff, Dr. Paul Sheldon, Dr. Mauro Bologna, Dr. Baris Bagci, and Dr. Nolan Massey for helpful background discussions. I thank Mr. Charles M. Brown for informing me of Refs. [27e] and [27f], and (see Ref. [27g]) of a talk concerning therewith at the PQE-2006 conference (which was followed by another talk concerning therewith at the PQE-2007 conference); as well as for updating me concerning his own efforts in diode self-rectification. Finally, Dr. A. N. Grigorenko is gratefully acknowledged for very comprehensive, thoughtful, and interesting correspondences, and for constructive criticisms, concerning Ref. [3k] and related ideas.

9. List of symbols

thermodynamic equilibrium	TEQ
Cartesian coordinates in right-handed Cartesian coordinate system in 3-dimensional Euclidean space	
right-left directional axis, positive to right	X
into-page/out-of-page directional axis, positive into page	Y
vertical directional axis, positive upwards	Z
(Z-directional) height of pegs	H
Z is also used for the altitude of the pawl, which is constrained from below at $Z_{\min}$. Thus, the net height of the pegs is $H_{\text{net}} \equiv Z - Z_{\min}$.	
X-directional spatial separation between adjacent pegs	L
disk-and-pawl system	DP
mass of disk	m'
mass of pawl	m
mass of disk-and-pawl system	$M = m' + m$
X-directional velocity of disk-and-pawl system (DP)	V
gravitational acceleration	g
speed of light	c
Kelvin temperature	T
Boltzmann's constant	k
equilibrium blackbody radiation	EBR
dimensionless gravitational potential energy parameter of pawl corresponding to it just barely clearing the pegs	$A \equiv mgH_{\text{net}}/kT$
angle of impingement, away from the normal or perpendicular, of a given EBR photon on the right disk face (which includes the pawl)	α
Kelvin temperature of EBR impinging on the right disk face, including the pawl	T_+
Kelvin temperature of EBR impinging on the left disk face	T_-

probability	P
probability of the pawl clearing a peg when the DP is moving in the forward or $+X$ direction	F
probability of the pawl clearing a peg when the DP is moving in the reverse or $-X$ direction	R
time	t
time interval between consecutive pawl-peg interactions (which could be either jumps or bounces)	Δt
time step in discrete Markovian time evolution (discrete time)	N
change in V between consecutive pawl-peg interactions (which could be either jumps or bounces)	ΔV
force exerted on DP by pegs	f
power output of DP	P^*
general quantity	Q
entropy	S
angle of incline (upwards towards the right, i.e., towards the $+X$ direction)	θ
Planck's constant	h
speed of gas molecules surrounding DP if DP is not (as we usually assume) surrounded only by EBR in vacuum	U
$\mu \equiv F + R$	
$\epsilon \equiv F - R$	
quantum-mechanical probability of the pawl tunneling through a peg when it is not high enough to clear a peg classically, i.e., when $Z_{\min} \leq Z < H$	τ
quantum-mechanical probability of the pawl bouncing from a peg when it is high enough to clear a peg classically, i.e., when $Z > H$	ρ

List of subscripts

minimum	min
net	net
maximum	max
optimum	opt
Maxwellian	mw
quantum	q

10. References

1. (a) Zhang, K.; Zhang, K. Mechanical models of Maxwell's demon with noninvariant phase volume. *Phys. Rev. A* 1992, *46*, 4598–4605. [Reference [1a] is a classical rather than quantum-mechanical treatment; as is true of this present chapter (except for the last four paragraphs of Sect. 3, Sect. 6, and a few very brief mentions elsewhere, therein), and also of Refs. [3k], [28a], and [28b]; but, in contrast therewith, Ref. [1a] considers only (*non*dissipative) velocity-dependent forces that are perpendicular to the velocity

itself (i.e., to the direction of motion), and hence which can do no work (e.g., the Lorentz force).]

Reference [1a] was partially anticipated earlier by

(b) Bridgman, P. W. Note on the Principle of Detailed Balancing. *Phys. Rev.* 1928, *31*, 101–102; and, in extension, by

(c) Davies, P. C. W. *The Physics of Time Asymmetry*. University of California Press: Berkeley, 1974; Sect. 6.4 (especially the last paragraph).

Reference [1a] is summarized in

(d) Čápek, V.; Sheehan, D. P. *Challenges to the Second Law of Thermodynamics: Theory and Experiment*. Springer: Dordrecht, 2005 (Fundamental Theories of Physics Series, Vol. 146), Sect. 10.1.2.

2. Allahverdyan, A. E.; Nieuwenhuizen, Th. M. A mathematical theorem as the basis for the second law: Thomson's formulation applied to equilibrium. *Physica A* 2002, *305*, 542–552. See the first and fifth paragraphs of Sect. 5.

Note: There is no contradiction between Ref. [1a], which forbids spontaneous momentum flow at TEQ, and Ref. [2], which allows persistent currents at TEQ. Persistent currents such as those allowed by Ref. 2 at TEQ are at *zero* resistance and hence do *not* qualify as spontaneous momentum flows, which must self-maintain *despite both* TEQ *and non*zero (positive) resistance. An example of a persistent current such as is allowed by, and mentioned in, Ref. [2] is a quantum vortex, which exists in a quantum-mechanical ground state from which no energy can be extracted either dissipatively as heat or nondissipatively as work.

3. (a) Feynman's classic ratchet and pawl is discussed in Feynman, R. P.; Leighton, R. B.; Sands, M. *The Feynman Lectures on Physics: Definitive Edition*. Addison Wesley: Reading, Mass, 1963 (Pearson Addison-Wesley: San Francisco, Calif., 2006); Vol. I, Chap. 46.

More recent analyses of Feynman's classic system are developed in, for example:

(b) Parrondo, J. M. R.; Español, P. Criticism of Feynman's analysis of the ratchet as an engine. *Am. J. Phys.* 1996, *64*, 1125–1130.

(c) Magnasco, M. O.; Stolovitzky, G. Feynman's Ratchet and Pawl. *J. Stat. Phys.* 1998, *93*, 615–632.

(d) Jarzynski, C.; Mazonka, O. Feynman's ratchet and pawl: An exactly solvable model. *Phys. Rev. E* 1999, *59*, 6448–6459.

(e) Sokolov, I. M. Reversible fluctuation rectifier. *Phys Rev. E* 1999, *60*, 4446–4449.

(f) Velasco, S.; Roco, J. M. M.; Medina, A.; Hernández, A. C. Feynman's ratchet optimization: maximum power and maximum efficiency regimes. *J. Phys. D: Appl. Phys.* 2001, *34*, 1000–1006.

(g) Pesz, K.; Gabrys, B. J.; Bartkiewicz, S. J. Analytical solution for the Feynman ratchet. *Phys. Rev. E* 2002, *66*, 061103.

(h) Munakata, T; Suzuki, D. Rectification efficiency of the Feynman ratchet. *J. Phys. Soc. Japan* 2005, *74*, 550–553.

(i) Suzuki, D.; Munakata, T. Stationary probability flow and vortices for the Smoluchowski-Feynman ratchet. *Physica A* 2006, *368*, 16–24.

(j) Tu, Z. C. Efficiency at maximum power of Feynman's ratchet as a heat engine. *J. Phys. A - Math. Theor.* 2008, *41*, Article Number 312003.

(k) For a survey (as of 1989) anticipating our velocity-dependent DP, see Denur, J. Velocity-dependent fluctuations: Breaking the randomness of Brownian motion.

Phys. Rev. A 1989, *40*, 5390–5399. Erratum. *Phys. Rev. A* 1990, *41*, 3390. See Sect. I and Footnotes 1–5.

4. Reference [3a], the last paragraph of Sect. 46-2: This is the upshot of the discussions concerning Feynman's classic ratchet and pawl in Sect. 46-1 and 46-2. Said upshot is qualitatively justified on bases of (i) mechanics in Sect. 46-3 and (ii) special initial conditions in Sects. 46-4 and 46-5.
5. (a) Investigations of various formulations of the second law, various viewpoints concerning the absolute validity thereof, and challenges thereto in both the quantum and classical regimes, are given in Sheehan, D. P., Editor. *First International Conference on Quantum Limits to the Second Law, AIP Conference Proceedings (Vol. 643)*. AIP: Melville, New York, 2002. Various authors cited in Footnotes [6] – [10] also have papers published in this *AIP Conference Proceedings (Vol. 643)*. Specific topics and/or models are studied in Ref. [3k] and in the references cited in Footnotes [6] – [11] and [27]; with Refs. [31] and [3k] being precursors, and Refs. [28a] and [28b] being shorter versions, of this present chapter.

For more recent investigations concerning the topics mentioned in Ref. [5a], and related topics, see also the following book (Ref. [5b]) and three Special Issues of journals (Refs. [5c] – [5e]):

(b) Čápek, V.; Sheehan, D. P. *Challenges to the Second Law of Thermodynamics: Theory and Experiment*. Springer: Dordrecht, 2005 (Fundamental Theories of Physics Series, Vol. 146)

(c) Nikulov, A. V.; Sheehan, D. P. (Guest Editors). *Entropy* March 2004, *6 (Issue 1)*. Special Issue on Quantum Limits to the Second Law of Thermodynamics.

(d) Nieuwenhuizen, Th. M.; Keefe, D. P.; Špička, V. (Guest Editors). Proceedings of the International Conference Frontiers of Quantum and Mesoscopic Thermodynamics FQMT'04 (Prague, Czech Republic, 26–29 July 2004). *Physica E* October 2005, *29 (Issues 1–2)*.

(e) Sheehan, D. P. (Guest Editor). *Found. Phys.* December 2007, *37 (Number 12)*. Special Issue: The Second Law of Thermodynamics: Foundations and Status.

(f) To be published: Sheehan, D. P., Editor. The Second Law of Thermodynamics: Status and Challenges. AIP Conference Proceedings (Volume number to be determined). AIP: Melville, New York, 2011.

6. Viewpoints concerning the second law in systems manifesting quantum-mechanical entanglement and/or coherence range from (I) that it can be violated: for example:

(a) Čápek, V.; Bok, J. Violation of the second law of thermodynamics in the quantum microworld. *Physica A* 2001, *290*, 379–401.

(b) Čápek, V.; Frege, O. Violation of the 2nd law of thermodynamics in the quantum microworld. *Czech. J. Phys.* 2002, *52*, 679–694.

(c) Čápek, V. Zeroth and second laws of thermodynamics simultaneously questioned in the quantum microworld. *Eur. Phys. J. B* 2002, *25*, 101–113.

(d) Allahverdyan, A. E.; Nieuwenhuizen, Th. M. Breakdown of the Landauer bound for information erasure in the quantum regime. *Phys. Rev. E* 2001, *64*, 056117.

(e) Nieuwenhuizen, Th. M.; Allahverdyan, A. E. Statistical thermodynamics of quantum Brownian motion: Construction of perpetuum mobile of the second kind. *Phys. Rev. E* 2002, *66*, 036102.

(f) Allahverdyan, A. E.; Nieuwenhuizen, Th. M. Bath-generated work extraction and inversion-free gain in two-level systems. *J. Phys. A Math. Gen.* 2003, *36*, 875–882.
(g) Čápek, V. Dimer as a challenge to the second law. *Eur. Phys. J. B* 2003, *34*, 219–223. Note: Reference [6g] was Dr. V. Čápek's last paper before he passed away. Therein, Dr. V. Čápek responds to Ref. [6l], and Dr. Daniel P. Sheehan has written a tribute to Dr. V. Čápek. There is also a tribute to Dr. V. Čápek in Ref. [5d]: Špička, V.; Nieuwenhuizen, Th. M.; Keefe, D. P.; Špička, V. (Guest Editors). In memoriam: Vladislav Čápek (1943–2002). Ref. [5d], vii–viii.
(h) Nieuwenhuizen, Th. M. Thermodynamics and small quantum systems. *J. Mod. Optics* 2003, *50*, 2433–2441.
(i) Reference [5b]; Chap. 3, Sect. 4.6.
to (II) that it cannot: for example:
(j) Scully, M. O. Extracting Work from a Single Thermal Bath via Quantum Negentropy. *Phys. Rev. Lett.* 2001, *87*, 220601.
(k) Hoffmann, K. H. Quantum thermodynamics. *Ann. der Phys.* 2001, *10*, 79–88.
(l) Novotný, T. Investigation of apparent violation of the second law of thermodynamics in quantum transport studies. *Europhys. Lett.* 2002, *59*, 648–654.
(m) Linke, H. Coherent Power Booster. *Science* 2003, *299*, 841–842.
(n) Scully, M. O.; Zubairy, M. S.; Agarwal, G. S.; Walther, H. Extracting Work from a Single Heat Bath via Vanishing Quantum Coherence. *Science* 2003, *299*, 862–864.
(o) Scully, M. O.; Rostovtsev, Y.; Sariyanni, Z-E.; and Zubairy, M. S. Using quantum erasure to exorcize Maxwell's demon: I. Concepts and context. Ref. [5d], 29–39.
(p) Rostovtsev, Y.; Sariyanni, Z-E.; Zubairy, M. S.; and Scully, M. O. Using quantum erasure to exorcize Maxwell's demon: II. Analysis. Ref. [5d], 40–46.
(q) Sariyanni, Z-E.; Rostovtsev, Y.; Zubairy, M. S.; and Scully, M. O. Using quantum erasure to exorcize Maxwell's demon: III. Implementation. Ref. [5d], 40–46.
(r) A qualitative summary was given in Weiss, P. Breaking the Law. *Science News* Oct. 7, 2000 *158 (No. 15)*, pp. 234, 235, and 239.
For recent studies concerning the second law in the quantum regime, see, for example:
(s) Allahverdyan, A. E.; Balian, R; Nieuwenhuizen, Th. M. Maximum work extraction from finite quantum systems. *Europhys. Lett.* 2004, *67*, 565–571.
(t) Allahverdyan, A. E.; Balian, R; Nieuwenhuizen, Th. M. Quantum thermodynamics: thermodynamics at the nanoscale. *Journal of Modern Optics* 2004, *51*, 2703–2711.
(u) Allahverdyan, A. E.; Nieuwenhuizen, Th. M. Fluctuations of work from quantum subensembles: The case against quantum work-fluctuation theorems. *Phys. Rev. E* 2005, *71*, 066102.
(v) Allahverdyan, A. E.; Nieuwenhuizen, Th. M. Minimal work principle: Proof and counterexamples. *Phys. Rev. E* 2005, *71*, 046107.
(w) Allahverdyan, A. E.; Nieuwenhuizen, Th. M. Adiabatic processes need not correspond to optimal work. Ref. [5d], 74–81.
(x) Allahverdyan, A. E.; Nieuwenhuizen, Th. M. Explanation of the Gibbs paradox within the framework of quantum thermodynamics. *Phys. Rev. E* 2006, *73*, 066119.
General overviews of the second law in the quantum regime are given in, for example:
(y) Reference [5d], 1–28.
(z) Schröder, H.; Teifel, J.; Mahler, G. Work and work fluctuations in quantum systems. *Eur. Phys. J. Special Topics* 2007, *151*, 181–188.

(aa) Susskind, L.; Lindesay, J. *An Introduction to Black Holes, Information, and the String Theory Revolution: The Holographic Universe*. World Scientific: Singapore, 2005.

(bb) Scully, R. F. and Scully, M. O.: *The Demon and the Quantum*, Wiley-VCH: New York, 2007; especially Sects. 6.6 – 6.9 and Endnotes for Sects. 6.6 – 6.9.

The various formulations of the second law are not all of equal generality:

(cc) Various formulations of the second law are discussed in, for example: Ref. [5b], Sect. 1.2; and Ref. [6t].

(dd) Violations of *a* second law can fall short of violations of *the* second law — as per, for example: Ref. [6t], p. 2707; and Ref. [6y], the third paragraph of Sect. 1.1. According to Dr. Marlan O. Scully, private communications at the *36th Winter Colloquium on the Physics of Quantum Electronics (PQE-2006)*, January 2–6, 2006 (see Refs. [6j], [6n], [6o], [6p], and [6q]), by the time of said *Colloquium*, viewpoints seemed to be converging towards the conclusion that the work required to prepare systems with quantum-mechanical entanglement, correlations, and/or coherence that can then, say, surpass the (theoretical-maximum *classical*) Carnot efficiency, equals or exceeds the extra-Carnot-efficiency work that can thereby be obtained. (This was confirmed in later private communications from Dr. Marlan O. Scully.): Thus, the extra-Carnot-efficiency work *per se* violates *a* second law [specifically, as per Ref. [5b], pp. 4–5, the Carnot theorem formulation (and possibly also the Efficiency and/or Heat Engines formulations) of the second law], but the *overall* process — *including the preparation work* — does *not* violate *the* second law [i.e., the Zhang formulation of the second law, enunciated in Ref. [1a] (and restated in the first two paragraphs of Sect. 1, with further discussions in the last four paragraphs of Sect. 3, of this present chapter)]. Some questions concerning the validity of *the* second law — not merely *a* second law — in the quantum regime (e.g., for nonlinear systems coupled to a bath) which had been open have now been resolved in favor of the second law: See, for example: Kim, I; Mahler, G. Quantum Brownian motion and the second law of thermodynamics. *Eur. Phys. J. B* 2006, *54*, 405–414. Erratum, *Eur. Phys. J. B* 2007, *56*, 279. Also, Kim, I.; Mahler, G. "The second law of thermodynamics in the quantum Brownian oscillator at an arbitrary temperature", *Eur. Phys. J. B* 2007, *60*, 401–408. Resolution in favor of the second law is discussed in: Kim, I.; Mahler, G. Clausius inequality beyond the weak-coupling limit: The quantum Brownian oscillator. *Phys. Rev. E* 2010, *81*, 011101-1–12. Also, Bandyopadhyay, M. Does the second law hold in the quantum regime?. *Phys. Scr.* 2010, *81*, 065004-1–7. And, Kim, I. Field-induced dynamics in the quantum Brownian oscillator: An exact treatment. *Phys. Lett. A* 2010, *374*, 3828–3837.

(ee) According to Th. M. Nieuwenhuizen, private communications at the Symposium: The Second Law of Thermodynamics: Foundations and Status on June 19–20, 2006 (part of the 87th Annual Meeting of the Pacific Division of the AAAS on June 18–22, 2006): All formulations of the second law of thermodynamics are equivalent in the classical regime [with one exception that is not applicable insofar as this present chapter is concerned): see Ref. [6gg]], and also for infinite systems in the quantum regime. However, they are not equivalent for a finite quantum system, even if in thermal contact with an infinite heat bath. (For a finite quantum system in thermal contact with a finite heat bath, the deviations from classical behavior are even larger.)

(ff) Allahverdyan, A. E.; Johal, R. S.; Nieuwenhuizen, Th. M. Work extremum principle: Structure and function of quantum heat engines. *arXiv.0709.4125v1 [cond-mat-stat-mech]* 26 Sep 2007.

(gg) Allahverdyan, A. E.; Nieuwenhuizen, Th. M. Minimal Work Principle and its Limits for Classical Systems. *arXiv:cond-mat/0607579 v1* 22 Jul 2006. Also, Allahverdyan, A. E.; Nieuwenhuizen, Th. M. Minimal-work principle and its limits for classical systems. *Phys. Rev. E* 2007, *75*, 051124.

7. (a) Spontaneous rectification of thermal voltage fluctuations in diodes with very small capacitance at very low temperatures is studied in, for example, McFee, R. Self-Rectification in Diodes and the Second Law of Thermodynamics. *Am. J. Phys.* 1971, *39*, 814–820.

Spontaneous rectification based on the Little-Parks effect is investigated in, for example:

(b) Nikulov, A. V. Quantum force in a superconductor. *Phys. Rev. B* 2001, *64*, 012505.

(c) Nikulov, A. V. One of Possible Applications of High-Tc Superconductors. *arXiv:physics/0106020 v1* 6 Jun 2001.

(d) Nikulov, A. V. Perpetuum Mobile without Emotions. Ref. [5a], pp. 207–213.

(e) Dubonos, S. V.; Kuznetsov, V. I.; Nikulov, A. V. Quantum voltage oscillations observed on segments of an inhomogeneous superconducting loop. *arXiv:cond-mat/0305337 v1* 15 May 2003.

(f) Dubonos, S. V.; Kuznetsov, V. I.; Zhilyaev, I. N.; Nikulov, A. V.; Firsov, A. A. Observation of the External-ac-Current-Induced dc Voltage Proportional to the Steady Current in Superconducting Loops. *JETP Lett.* 2003, *77*, 371–375.

(g) Aristov, V. V.; Nikulov, A. V. Quantum Power Source. Putting in Order of a Brownian Motion without Maxwell's Demon. *arXiv:cond-mat/0310073 v1* 3 Oct 2003. In *Proceedings of SPIE* 2003, *Vol. 5128 "Quantum Informatics"*, 148–156.

(h) Berger, J. Noise Rectification by superconducting loop with two weak links. *Phys. Rev. B* 2004, *70*, 024524.

(i) Nikulov, A. About Peretuum Mobile without Emotions. Ref. [5a], pp. 207–212.

(j) Reference [5b], Sects. 4.2.3 and 4.4.

(k) Nikulov, A. V. Why the persistent power can be observed in mesoscopic quantum system. *arXiv:cond-mat/0404717 v1* 29 Apr 2004.

(l) Nikulov, A. V. Quantum limits to the second law and a breach of a symmetry. *Invited Lecture at the Conference: "Frontiers of Quantum and Mesoscopic Thermodynamics"*, 26–29 July 2004. Will be published In *Phys. Rev. E*. (E-print: Quantum limits to the second law and breach of symmetry. *arXiv:cond-mat/0505508 v1* 20 May 2005.) Two related papers: (i) Nikulov, A. V. Differences between application of some basic principles of quantum mechanics on atomic and mesoscopic levels. *arXiv:cond-mat/0506653 v1* 24 June 2005. (ii) Nikulov, A. Fundamental Differences between applications of some basic principles of quantum mechanics on atomic and mesoscopic levels. In Burra G. Sidearth, Antonio Alfonso-Faus, Marius J. Fullana, Editors. *Frontiers of Fundamental Physics: Eighth International Symposium. AIP Conference Proceedings (Vol. 905)*. AIP: Melville, New York, 2007; pp. 117–119. (E-print: Fundamental Differences Between Application of Basic principles of Quantum Mechanics on Atomic and Higher Levels. *arXiv:0707.0827 v1* 2007.) {Note: These two related papers investigate possible difficulties with the *purely*-dynamical law of conservation of (angular) momentum associated with (anti)*thermo*-dynamical second-law-violating

currents at *non*zero resistance in Little-Parks-effect circuits. Of course, the Little-Parks (anti)*thermo*-dynamical second-law-violating effect could still obtain even given *strict* conservation of *purely*-dynamical *total* (angular) momentum: Generation of counter-rotation in the surroundings with which a Little-Parks current's electrons interact could *strictly* conserve *total* (angular) momentum at essentially infinitesimal cost — which might be paid for by the Little-Parks effect itself — in kinetic energy imparted to said surroundings, if said surroundings are extremely massive compared with the combined masses of these electrons. A possible coupling mechanism might entail leakage of these electrons' wave packets into classically forbidden regions and hence into said surroundings, perhaps similarly to the mechanism discussed in Ref. [15] cited in *arXiv:cond-mat/0506653 v1* 24 June 2005 [Hirsch, J. E. The Lorentz force and superconductivity. *Phys. Lett. A* 2003, *315*, 474–479 (see especially, on p. 478, the second paragraph and Fig. 4)]. Even almost infinitesimally weak coupling might suffice, because the kinetic energy thus imparted to the surroundings also need be almost infinitessimal. This topic is further investigated in later papers, e.g.: Aristov, A. A.; Nikulov, A. V. Could the EPR correlation be in superconducting structures?. Possibility of experimental verification. *arXiv:cond-mat/0604566* 25 Apr 2006; Nikulov, A. V. About Essence of the Wave Function on Atomic Level in Superconductors. *arXiv:0803.1840v1 [physics.gcn-ph]* 12 Mar 2008. and Nikulov, A. V., "What is azimuthal quantum force in superconductor," *arXiv:1104.4856v1 [cond-mat.supr-con]* 26 Apr 2011.

(m) Spontaneous rectification in nanoscale RLC circuits is studied in, for example, Allahverdyan, A. E.; Nieuwenhuizen, Th. M. Testing the violation of the Claussius inequality in nanoscale electric circuits. *Phys. Rev. B* 2002, *66*, 115309.

(n) Results are discussed and various viewpoints through 2005 are summarized in Berger, J. The

Chernogolovka experiment. Ref. [5d], 100–103.

Examples of more recent work are:

(o) Nikulov, A. Fundamental Differences Between Application of Basic Principles of Quantum Mechanics on Atomic and Higher Levels. *arXiv:0707:0827* 2007. (Talk presented at the *Eighth International Symposium Frontiers of Fundamental Physics*, Madrid, October 17–19, 2006.)

(p) Gurtovoĭ, V. L.; Dubonos, S. V.; Karpii, S. V.; Nikulov, A. V.; Tulin, V. A. Contradiction between the Results of Observations of Resistance and Critical Current Quantum Oscillations in Asymmetric Superconducting Rings. *J. Exp. Thoer. Phys.* 2007, *105*, 262–267.

(q) Dubonos, S. V.; Gurtovoi, V. L.; Nikulov, A. V.; Tulin, V. A. Can dc voltage proportional to the persistent current be observed on segment of asymmetric mesoscopic ring? *arXiv:0707.0807v1 [cond-mat.supr-con]* 5 Jul 2007.

(r) Nikulov, A. V. The quantum challenge at the mesoscopic level. *arXiv:0707.4351v1 [cond-mat.supr-con]* 30 Jul 2007.

(s) Burlakov, A. A.; Gurtovoĭ, V. L.; Dubonos, S. V.; Nikulov, A. V.; Tulin, V. A. Little-Parks effect in a system of asymmetric superconducting rings. *JETP Letters* 2007, *86*, 517–521.

(t) Gurtovoĭ, V. L.; Dubonos, S. V.; Nikulov, A. V.; Osipov, N. N.; Tulin, V. A. Dependence of the Magnitude and Direction of the Persistent Current on the Magnetic Flux in Superconducting Rings. *J. Exp. Thoer. Phys.* 2007, *105*, 1157–1173.

(u) Nikulov, A. V. About Essence of the Wave Function on Atomic Level and in Superconductors.
arXiv:0803.1840v1 [physics.gen-ph] 12 Mar 2008.

(v) Burlakov, A. A.; Gurtovoi, V. L.; Dubonos, S. V.; Nikulov, A. V.; Tulin, V. A. Observation of the Little-Parks Oscillations in a System of Asymmetric Superconducting Rings. *arXiv:0805.1223v1 [cond-mat.supr-con]* 8 May 2008.

(w) Nikulov, A. V. Bohm's quantum potential and quantum force in superconductor. *arXiv:0812.4118v1 [quant-ph]* 22 Dec 2008.

(x) Gurtovoi, V. I; Il'in, A. I.; Nikulov, A. V.; Tulin, V. A. The dc voltage proportional to the persistent current observed on system of asymmetric mesoscopic loops. *arXiv:0910.5140v1 [cond-mat.supr-con]* 27 Oct 2009.

(y) Gurtovoi, V. I; Il'in, A. I.; Nikulov, A. V.; Tulin, V. A. Could dissipationless current be observed at non-zero resistance? *Proceedings of the 18th International Symposium "NANOSTRUCTURES: Physics and Technology"*, p. 277 (St. Petersburg, Russia, 2010). Also at *arXiv:1006.5346v1 [cond-mat.supr-con]* 28 Jun 2010.

(z) Gurtovoi, V. I; Il'in, A. I.; Nikulov, A. V.; et. al. Weak dissipation does not result in disappearance of the persistent current. *Low Temperature Physics* 36, 974–981 (2010).

A challenge to the second law of thermodynamics entailing thermal evaporation of electrons in capacitors at sufficiently but not excessively high temperatures is explored in:

(aa) D'Abramo, G. Thermo-charged capacitors and the Second Law of Thermodynamics. *Physics Letters A* 374, 1801-1805 (2010).

(bb) D'Abramo, G. On the exploitability of thermo-charged capacitors. *Physica A: Statistical Mechanics and its Applications* 390, 482–491 (2011).

8. (a) Proposed violations of the second law in plasma systems can be studied classically. See, for example, Sheehan D. P.; Means, J. D. Minimum requirement for second law violation: A paradox revisited. *Phys. Plasmas* 1998, *5*, 2469–2471; and references cited therein, especially those by Sheehan, D. P.

(b) An alternative (classical) viewpoint given in Cruden, B. A. On the proposed second law paradox in a nonzero floating potential. *Phys. Plasmas* 2001, *8*, 5323–5326.

This alternative viewpoint is reviewed in

(c) Reference [5b], Sect. 8.4.

(d) However, quantum-mechanical analyses may be more rigorous. See, for example, V. Čápek; Sheehan, D. P. Quantum mechanical model of a plasma system: a challenge to the second law of thermodynamics. *Physica A* 2002, *304*, 461–479; and references cited therein.

(e) Reference [5b], Chap. 8.

9. Many proposed violations of the second law in low-density gas systems can be analyzed classically. Low-density gas-systems in gravitational fields are investigated in, for example:

(a) Sheehan, D. P.; Glick, J.; Duncan, T.; Langton, J. A.; Gagliardi, M. J.; Tobe, R. Phase Space Portraits of an Unresolved Gravitational Maxwell Demon. *Found. Phys.* 2002, *32*, 441–462.

(b) Sheehan, D. P.; Glick, J.; Duncan, T.; Langton, J. A.; Gagliardi, M. J.; Tobe, R. Phase space analysis of a gravitationally-induced, steady-state nonequilibrium. *Phys. Scripta* 2002, *65*, 430–437.
(c) Sheehan, D. P. A Classical Gravitational Second Law Paradox. Ref. [5a], pp. 391–396.
(d) Reference [5b], Chap. 6.
A critique is given in
(e) Wheeler, J. C. Resolution of a Classical Gravitational Second-Law Paradox. *Found. Phys.* 2004, *34*, 1029–1062.
This critique is reviewed in
(f) Reference [5b], Sect. 6.2.5.
Field-free low-density gas systems are investigated in, for example:
(g) Miller, S. L. Insights into the Second-Law of Thermodynamics from Anisotropic Gas-Surface Interactions. Ref. [5e], 1660–1684.
(h) Denur, J. Speed-Dependent Weighting of the Maxwellian Distribution in Rarefied Gases: A Second-Law Paradox? Ref. [5e], 1685–1706. [Note: Reference [9h] considers a *speed*-dependent second-law paradox, in contrast with the *velocity*-dependent second-law challenge considered in this present chapter.)
(i) Crosignani, B. and Di Porto, P. Random Fluctuations of Diathermal and Adiabatic Pistons. Ref. [5e], 1707–1715.
10. Proposed violations of the second law in solid-state systems are understandable classically. See, for example:
(a) Sheehan, D. P.; Putnam, A. R.; Wright, J. H. A Solid-State Maxwell Demon. *Found. Phys.* 2002, *32*, 1557–1595.
A concise summary of Ref. [10a] is given in
(b) Weiss, P. Motor design flouts physical law. *Science News* Nov. 2, 2002, *162 (No. 18)*, 286.
More recent research, concerning a p-n junction solid-state oscillating motor, is discussed in
(c) Sheehan, D. P.; Wright, J. H.; Putnam, A. R.; and Perttu, E. K. Intrinsically biased, resonant NEMS-MEMS oscillator and the second law of thermodynamics. Ref. [5d], 87–99.
(d) The system investigated in Ref. [10c] is analyzed with respect to fundamental second-law considerations in Sheehan, D. P.; Gross, D. H. E. Extensivity and the thermodynamic limit: Why size really does matter. *Physica A* 2006, *270*, 461–482.
11. Reference [3k]. The analyses in this present chapter, as well as in previous shorter versions [28] thereof, are more quantitatively correct. The analyses in this present chapter (except for the last four paragraphs of Sect. 3, Sect. 6, and a few very brief mentions elsewhere, therein), as well as in Refs. [3k], [28a], and [28b], are classical.
12. (a) Reference [3k]. See especially the two paragraphs immediately following that containing Eq. (7), Appendixes A, B, and C, and Footnote 7. The references cited in Footnote 7 of Ref. [3k] provide further supplementation.
An extension of the concept of temperature fluctuations is developed in, e.g.:
(b) Beck, C. Dynamical Foundations of Nonextensive Statistical Mechanics. *Phys. Rev. Lett.* 2001, *87*, 180601.
(c) Beck, C. Superstatistics: Recent developments and applications. *arXiv:cond-mat/0502306 v1* 12 Feb 2005. Also in Zichichi, A. (Senior Editor). Beck, C.; Benedek, G.; Rapisarda, A.; Tsallis, C. (Editors). *Complexity, Metastability, and Nonextensivity*. World Scientific: Singapore, 2005; pp. 33–42.

(d) Abe, S.; Beck, C.; Cohen, E. G. D. Superstatistics, thermodynamics, and fluctuations. *Phys. Rev. E* 2007, *76*, 031102

13. See, for example:

(a) Peebles, P. J. E., *Principles of Physical Cosmology*. Princeton University Press: Princeton, N. J., 1993; pp. 134–138, 151–158, 174, and 176–181.

(b) Misner, C. W.; Thorne, K. S.; Wheeler, J. A. *Gravitation*. W. H. Freeman: New York, 1973; Sect. 22.6 [especially pp. 587–589 and most especially Exercise 22.17 (of Chap. 22) on pp. 588–589].

(c) Peebles, P. J. E.; Wilkinson, D. T. Comment on the Anisotropy of the Primeval Fireball. *Phys. Rev.* 1968, *174*, 2168.

(d) Gill, T. P. *The Doppler Effect*. Academic: New York, 1965; Chap. VIII.

14. See, for example:

(a) Kolmogorov, A. N. *Foundations of the Theory of Probability, Second English Edition*. Chelsea: New York, 1956.

(b) Ghahramani, S. *Fundamentals of Probability with Stochastic Processes, Third Edition*. Pearson Prentice Hall: Upper Saddle River, N. J., 2005.

(c) Kelly, D. G. *Introduction to Probability*. Macmillan: New York, 1994.

15. See, for example:

(a) Cox, D. R.; Miller, H. D. *The Theory of Stochastic Processes*. Chapman and Hall: London, 1965 (1990 Printing)]; Sects. 3.1, 3.2, and 3.6.

(b) Jones, P. W.; Smith, P. *Stochastic Processes, An Introduction*. Arnold: London, 2001; Chap. 4 (especially Sect. 4.3).

(c) The recursion method used in (10) is similar to that given in Hoel, P. G.; Port, S. C.; Stone, C. J. *Introduction to Stochastic Processes*. Houghton Mifflin: Boston, 1972 (reissued by Waveland: Prospect Heights, Ill., 1987); pp. 1–2, Sects. 1.1, 1.2, and 1.4.2, and pp. 47–49.

16. See, for example, Nikulov, A. V. Ref. [7c] (see especially Sect. 4.2.); and Refs. [7d] and [7l].

17. Reference [3k], Appendixes B and C.

18. See, for example, Leff, H. S.; Rex, A. F. in Leff, H. S.; Rex, A. F., Editors. *Maxwell's Demon 2: Entropy, Classical and Quantum Information, Computing*. Institute of Physics Publishing: Bristol, U. K., 2003; Sect. 1.8.4 and references cited therein. This book contains an overview of various Maxwellian demons, reprints of many important papers in the field, and much additional informative material.

19. Reference [3k], the paragraph immediately following that containing Eq. (23), and the third paragraph of Appendix D.

20. To address the error in cited Ref. [19]: *Diffraction* does *not* reduce the opacity even of a small (linear dimensions $\lesssim hc/kT$) disk, or even of a very small (linear dimensions $\ll hc/kT$) disk: Note, for example, in correction, that the temperature of Doppler-shifted EBR impinging on a body is *un*affected by *diffraction*, even if size $\lesssim hc/kT$ (or even $\ll hc/kT$), as per:

(a) Reference [13a], pp. 174 and 176–177.

(b) Hecht, E. *Optics, Fourth Edition*. Addison-Wesley: New York, 2002; Sect. 4.4.2, pp. 444–446, Sects. 10.4–10.5. (See especially p. 105 in Sect. 4.4.2.) Also: Hecht, E. Why don't Huygens' wavelets go backwards?. *Physics Teacher* 1980, *18*, 149.

(c) Dr. Patricia H. Reiff, private communications, 1999.

21. See, for example:

(a) Bohren, C. F.; Nevitt, T. J. Absorption by a sphere: a simple approximation. *Applied Optics* 1983, *22*, 774–775.
(b) van de Hulst, H. C. *Light Scattering by Small Particles*. John Wiley: New York, 1957 (corrected republication by Dover: New York, 1981); Chaps. 2, 6, and 14.
(c) Bohren, C. F.; Huffman, D. R. *Absorption and Scattering of Light by Small Particles*. John Wiley: New York, 1983 (Professional Paperback Edition, 1998); Chap. 1, Chap. 5 (especially Sects. 5.1–5.2), and pp. 287–289.
(d) Reference [13a]; pp. 151–158, 174, and 176–181 (especially p. 174, and pp. 176–181).
(e) Some general discussions are given in Bohren, C. F.; Clothiaux, E. E. *Fundamentals of Atmospheric Radiation*. Wiley-VCH: Weinheim, 2006; Sects. 1.3, 1.4, 2.9, and 3.5.
22. See, for example:
(a) Bohren, C. F. How can a particle absorb more than the light incident on it? *Am. J. Phys.* 1983, *51*, 323–327.
(b) H. Paul; R. Fisher. Comment on "How can a particle absorb more than the light incident on it?". *Am. J. Phys.* 1983 *51*, 327.
(c) Bohren, C. F.; Huffman, D. R. Ref. [21c]; Sect. 3.4 (especially p. 72), Sect. 4.7 (especially the last two paragraphs — which show that resonance can obtain if size $\lesssim hc/kT$), and Chap. 12 (in Sect. 12.1.8, the model studied in Ref. [22a] is treated again).
(d) Garbuny, M. *Optical Physics*. Academic: New York, 1965; pp. 100–101 and 268–269.
(e) Dr. Roland E. Allen, private communications, 2003.
(f) References [20a] – [22e] may further address the difficulty associated with DP size $\lesssim hc/kT$ discussed qualitatively in Ref. [3k], the two paragraphs immediately following that containing Eq. (23) — noting (as per Footnote [20]), in correction, that the temperature of Doppler-shifted EBR impinging on a body is *un*affected by *diffraction*, even if DP size $\lesssim hc/kT$ (or even $\ll hc/kT$).
23. See, for example, Ref. [21b]; Sect. 11.23 (especially pp. 182–183), and p. 269.
24. See, for example, Ref. [21b], Chap. 14.
25. Reference [3k], Appendix D.
26. See, for example:
(a) Schiff, L. I. *Quantum Mechanics, Third Edition*. McGraw-Hill: New York, 1968; pp. 100–107.
(b) Cohen, B. L. A Simple Treatment of Potential Barrier Penetration. *Am. J. Phys.* 1965, *33*, 97–98.
27. (a) A challenge to the second law based on the Lorentz force was proposed in Fu, X. Y. An Approach to Realize Maxwell's Hypothesis. *Energy Convrs. Mgmt.* 1982, *22*, 1–3.
This challenge was critiqued in:
(b) Wang,Y. R. Fu's Experiment and the Generalized Gibbs Distribution. *Energy Convrs. Mgmt.* 1983, *23*, 185–191. {Note: Reference [27b] (see especially the first two paragraphs on p. 188) seems to imply that (in the *classical* regime) an increase in entropy is *not* equivalent to the Clausius-Heat formulation of the second law as stated in Ref. [5b], p. 4: "No process is possible for which the *sole* effect is that heat flows from a reservoir at a given temperature to a reservoir at a higher temperature.": ("sole" is not italicized in original text). But: If the entropy increase associated with the second term of Y. R. Wang's unnumbered equation [that immediately following his Eq. (12)] on p. 188 equals or exceeds in magnitude the entropy decrease associated with heat flowing "uphill" as per the first term thereof, then is not the Clausius-Heat

formulation of the second law obeyed *despite* such "uphill" heat flow — since it is then *not* the only (or even the largest) effect? Does Y. R. Wang neglect the word *sole*?}

The Fu challenge seemed to be resolved in favor of the second law in:

(c) Wang, Y. Z. The Origin of the Electric Current in Fu's Experiment — An Analysis of Fu's Work on Realizing Maxwell's "Demon". *Energy Convrs. Mgmt.* 1986, *26*, 249–252.

(d) Reference [1a]. Reference [1a] considers only (*non*dissipative) velocity-dependent forces acting perpendicularly to the velocity *itself* (i.e., to the direction of motion), and hence which can do no work — of which the Lorentz force is one example.

There have been more recent attempts to revive it:

(e) Fu, X.; Fu, Z. Realization of Maxwell's Hypothesis. *arXiv:physics/0311104* 2003.

(f) Fu, X.; Fu, Z. Another Way to Realize Maxwell's Demon. *arXiv:physics/0509111* 2005.

(g) As per private communications at the *36th Winter Colloquium on the Physics of Quantum Electronics (PQE-2006)*, January 2–6, 2006: The Fu analyses (in Refs. [27a], [27e], and [27f]) through the time of this 2006 *Colloquium* neglected electrons that leave plate B towards the right in *both* of Fu's Lorentz-force systems, as per *both* Fig. 1 *and* Fig. 2 of Ref. [27f]. This seemed, *at that time*, to resolve the Fu challenge in favor of the second law more strongly than does Ref. [27c]. But Fu met this challenge with a new Lorentz-force system [private communications at the *37th Winter Colloquium on the Physics of Quantum Electronics (PQE-2007)*, January 2–6, 2007]. Nevertheless, as per other private communications at this 2007 *Colloquium*, there may still be unresolved issues concerning even Fu's new Lorentz-force system.

(h) Note: The Zhang formulation of the second law, enunciated in Ref. [1a] (and restated in the first two paragraphs of Sect. 1, with further discussions in the last four paragraphs of Sect. 3, of this present chapter), is valid irrespective of whether or not (*non*dissipative) velocity-dependent forces acting perpendicularly to the velocity itself (i.e., to the direction of motion), and hence which can do no work — such as the Lorentz force — can challenge *the* second law (or even merely *a* second law): recall the last four paragraphs of Sect. 3, and Refs. [6s] – [6ff], especially Ref. [6dd].

28. (a) Denur, J. Modified Feynman ratchet with velocity-dependent fluctuations. Ref. [5a], pp. 326–331. A revised version of Ref. [28a] is:

(b) Denur, J. Modified Feynman ratchet with velocity-dependent fluctuations. Ref. [5c], 76–86.

29. Sheehan, D. P; Kriss, V. G. Energy Emission by Quantum Systems in an Expanding FRW Metric. *arXiv:astro-ph/0411299 v1* 11 Nov 2004. See also references cited therein, especially Ref. 20 cited therein: Harrison, E. R. Mining Energy in an Expanding Universe. *Astroph. J.* 1995, *446*, 63–66. [It should be noted, however, that it may be possible to consider the loss in the cosmic background radiation's kinetic energy associated with the cosmological redshift as being compensated for by the gain in its gravitational potential energy in the universe's gravitational field as the universe expands: This is easiest to visualize in a positively-curved (curvature index $= +1$) closed universe (shell of 3-sphere) wherein said radiation is trapped. Letting ν (λ) be the frequency (wavelength) corresponding to the peak of the cosmic-background-radiation blackbody Planck distribution, and considering expansion of said 3-sphere from radius of curvature R_1 to radius of curvature R_2, $\nu(R_2)/\nu(R_1) = \lambda(R_1)/\lambda(R_2) = R_1/R_2$. This implies conservation of *total* — *kinetic plus gravitational-potential* — energy given a cosmological gravitational potential difference of $\Delta\Phi = c^2 \ln \frac{R_2}{R_1}$. (Of course, similarly, during a possible

contraction phase, it may be possible to consider the gain in the cosmic background radiation's kinetic energy associated with the cosmological blueshift as being compensated for by the loss in its gravitational potential energy in the universe's gravitational field as the universe contracts.) See, for example, Rindler, W. *Relativity: Special, General, and Cosmological, Second Edition*. Oxford: Oxford, U. K., 2006; Sect. 1.6, Exercise 1.9 (of Chap. 1) on p. 28, Chap. 9, and Sects. 12.2 and 16.4.]

30. Scully, M. O.; Aharonov, Y.; Kapale, T. K.; Tannor, D. J.; Süssmann, G.; Walther, H. Sharpening accepted thermodynamic wisdom via quantum control: or cooling to an internal temperature of zero by external coherent control fields without spontaneous emission. *J. Mod. Optics* 2002, *49*, 2297–2307.
31. (a) Denur, J. The Doppler demon. *Am. J. Phys.* 1981, *49*, 352–355.
Constructive criticisms, given in
(b) Motz, H. The Doppler demon exorcised. *Am. J. Phys.* 1983, *51*, 72–73;
and
(c) Chardin, G. No free lunch for the Doppler demon. *Am. J. Phys.* 1984, *52*, 252–253
hopefully have been addressed in Ref. [3k], and more completely in this present chapter and in previous shorter versions [28] thereof.
32. Reference [5b], Sect. 5.3.

13

Thermodynamics, Kinetics and Adsorption Properties of Some Biomolecules onto Mineral Surfaces

Özkan Demirbaş and Mahir Alkan
University of Balikesir, Faculty of Science and Literature, Chemistry Dept
Turkey

1. Introduction

Developments in biotechnology have led to an enormous increase in the exposure of proteins and enzymes (biomolecules) to non-biological solid surfaces in applications such as artificial implants, purification strategies, biosensors, and drug delivery systems. Biotechnological and biomedical applications requiring adhesion, adsorption, biocompatibility, permeability and/or other properties depend on the surface properties of the material significantly (Arica et al., 2010; Karagoz et al., 2010; Nakanishi, 2001; Luo and Andrade, 1998).

Besides the practical importance of gaining knowledge on biomolecule structures in the adsorbed state, it is also important to understand the adsorption-induced structural changes from a more fundamental view-point as rearrangements in the biomolecule structure are seen as an important driving force for adsorption to take place. The adsorption of a biomolecule to a surface usually produces a change in its physicochemical properties, which may affect the biological functioning of the molecule. Biomolecule adsorption is a complex process in which the structural stability of a biomolecule, the ionic strength and the pH of the solution and surface properties of sorbent are known to influence the affinity of a biomolecule for a given interface (Giacomelli and Norde ,2001; Norde, 2000).

Soil extracellular enzymes, like other proteins, are adsorbed on many surfaces, particularly on clay minerals, which have high specific surface areas, and so are likely to be predominantly in an adsorbed state for example, the system of bovine serum albumin (BSA) and silica particles has extensively been investigated. There are a number of studies related to the biomolecule adsorption on oxide surfaces such as silica particles, montmorillonite, hydroxyapatite, TiO_2 particles, chitosan, stainless steel surface or mica. However, understanding the mechanism of biomolecule adsorption and evaluating the impact on practical applications is very important (Kondo et al., 1992 and 1993a; Buijs et al., 1996). On the other hand, many protocols for enzyme immobilization involve irreversible binding to a functionalized support. In the reversible enzyme immobilization, the supports could be regenerated using a suitable desorption agent, and they be recharged again with a fresh enzyme. In the reversible enzyme immobilization, the supports could be regenerated using a suitable desorption agent, and they be recharged again with a fresh enzyme. On the other hand, when the covalently immobilized enzyme becomes inactivated upon use both the

enzyme and the support should be eliminated as wastes (Bayramoglu et al., 2010, Zhou, 2010; Wang et al., 2010; Bolivar et al., 2009).

Sepiolite is an oxide mineral with a unit cell formula $Si_{12}O_{30}Mg_8(OH,F)_4(H_2O)_4.8H_2O$ (Ahlrichs et al., 1975). In some aspects sepiolite is similar to other 2:1 trioctahedral silicates, such as talc, molecule formula is $Mg_3Si_4O_{10}(OH)_2$ (Rytwo et al., 2002; Grim, 1968). Sepiolites, which form an important group of clay minerals, are a magnesium silicate and currently used in a number of different applications such as many industrial, catalytic and environmental applications, most of which are similar to those of the more traditional clays. Because of their structural morphology, sepiolites have received considerable attention with regard to the adsorption of organics on the clay surfaces and to their use as support for catalysts (Frost and Ding, 2003). The abundance and availability of sepiolite mineral reserves as a raw material source and its relatively low cost guarantee its continued utilization in the future, and most of the world sepiolite reserves are found in Turkey. Sepiolite is a good adsorbent for organic species because it exhibits a variety of attractive properties such as high specific surface area, high porosity (50.8%) (Göktas et al., 1997), and surface activity. Sepiolite is therefore used in a spectrum of areas where sorptive, catalytic, and rheological properties are exploited. The sorption ability of sepiolite is mainly ascribed to its high surface area. Thus, it is commonly used in oil refining; wastewater treatment; the removal of drug, and pesticide carriers; paper and detergent; etc. (Sabah and Çelik, 2002). Investigations on sepiolite have so far focused more on its sorptive properties and attempts have been made to increase its surface area.

Caseins are frequently used as an additive in food, paint, glue etc. (Walstra and Jenness, 1984) where their amphiphilic properties are utilised to modify various types of interfaces. The main proteins in renneted milk comprise a_{s1}-, a_{s2}-, β-, and para κ-casein. Of these four caseins, para-k-casein is known to be bound closely to the surface of casein micelles. The hydrophobic plots of amino acid residues in a_{s2}- and κ-casein suggest that they have surface active properties (Dalgleish, 1993) and that these proteins may also be located on the micellar surface. This being the case, a_{s2}-, β-, and para κ-casein are likely candidates for binding to the surface of fat globules. β -casein (together with a_{S1}-casein) is the most abundant protein among the four caseins present in cow's milk (Dickinson, 1999). The biological role of casein molecules includes the sequestration of amorphous calcium phosphate to form stable complexes in milk (Holt, 1998; Holt and Sawyer, 1988; Holt et al., 1996; Walstra and Jenness, 1984). Caseins are also frequently used as additives in food, paint, glue and coating colours for paper (Walstra and Jennes, 1984). Knowledge of the mechanisms by which caseins adsorb is therefore of great interest in many colloid-related industries.

Catalase (hydrogen peroxide oxidoreductase) is an enzyme normally found in the peroxisomes of nearly all aerobic cells and serves to protect the cell from the toxic effects of hydrogen peroxide by catalyzing its decomposition into molecular oxygen and water without production of free radicals. The reaction of catalase in the decomposition of hydrogen peroxide is: $2H_2O_2 \rightarrow 2H_2O + O_2$. Herein, catalase has useful applications in various industrial fields, such as food industry, textile industry, and in the analytical field as a component of hydrogen peroxide or glucose biosensor systems (Horst et al., 2006; Jürgen-Lohmann and Legge, 2006; Yoshimoto et al., 2007). However, there are many limitations for the free enzymes. Enzymes are unstable, having a short lifetime in the circulation, and causing toxic reactions (Jiang and Zhang, 1993; Shentu et al., 2005; Özlem Alptekin et al., 2009; Ran et al., 2009). These drawbacks can be partially eliminated by immobilizing enzyme

onto solid carriers. Hence, immobilization is an indispensable step in the preparation of the biocatalyst for industrial application. It has many well known advantages, all affecting the production cost (Çetinus and Nursevin Öztop, 2003; Choi and Yiu, 2004; Liu et al., 2009). With immobilized or adsorbed enzymes, improved stability, reusability, continuous operation, possibility of better control of reactions, high purity and product yields and hence, more favorable economic factors can be expected (Kennedy and Melo, 1990).
In this study, the adsorption, electrokinetic properties of biomolecules such as casein and catalase onto sepiolite surface were studied as a function of incubation time, concentrations of biomolecules, pH of the solution and temperature. In addition, thermodynamics, some parameters of kinetics and activity of catalase were studied.

2. Material and methods

Catalase (hydrogen peroxide oxidoreductase) from bovine liver, was obtained from Sigma Chemical Co. and casein was obtained from Merck. Sepiolite was obtained from Aktas Luletasi Co. (Eskisehir, Turkey). The chemical composition of the sepiolite determined by XRF is given in Table 1. Sepiolite sample was treated before using in the experiments as follows (Alkan et al., 2006). All other chemicals used were of analytical grade. All water used was of MilliQ quality or doubly distilled.

Constituent	Percentage present
SiO_2	53.47
Al_2O	0.19
CaO	0.71
Fe_2O_3	0.16
MgO	23.55
NiO	0.43
LoI	21.49

Table 1. Chemical composition of sepiolite

The cation exchange capacity (CEC) of the sepiolite used was determined by ammonium acetate method, the density by the picnometer method (Alkan et al., 2006) and the specific surface area by BET N_2 adsorption by Micromeritics Flow Sorb II-2300 equipment. The results obtained are summarised in Table 2.

CEC (meq/100 g)	Density (g mL^{-1})	Specific surface area (m^2 g^{-1})
22	2.2	318

Table 2. Some physicochemical properties of sepiolite used in this study

2.1 Zeta potential measurements

The effects of biomolecules and concentration, pH on zeta potential were evaluated using a Zeta Meter 3.0 (Zeta Meter Inc.) equipped with a microprocessor unit (Alkan et al., 2005). The instrument automatically calculates the electrophoretic mobility of

the particles and converts it to the zeta potential using the Smoluchowski equation as follows:

$$\zeta = 4\pi V_t E/D \quad (1)$$

where E is electrophoretic mobility; V_t is viscosity of the suspending liquid; D is dielectric constant; π is constant and ζ is zeta potential. In this procedure, the solid samples were transferred to 250 mL polyethylene bottle in which 100 mL of an aqueous solution was added yielding final solid concentrations of 3 g L^{-1} for sepiolite. The samples were dispersed by a thermostatic shaker bath. The pH was measured with a combination electrode (Orion 920A pH meter calibrated with pH 4.00, 7.00 and 10.00 standards) and adjusted by dropwise addition of HCl or NaOH solutions. After shaking overnight (24 h), the samples were allowed to stand for 5 min to let larger particles settle. An aliquot taken from the supernatant was used to measure the zeta potentials. The average of 15 measurements was taken to represent the measured potential. The applied voltage during the measurements generally was varied in the range of 50–150 mV.

2.2 Adsorption experiments

Adsorption experiments were carried out by shaking 0.3 g sepiolite samples with 100 mL aqueous solution at desired concentrations of bimolecules, various pHs (3–10), ionic strengths ($1x10^{-4}$ – $2x10^{-1}$ mol L^{-1}) and sodium phosphate buffer concentrations ($1x10^{-4}$ – $2x10^{-1}$ mol L^{-1}) for 24 h (the time required for equilibrium to be reached between biomolecules adsorbed and biomolecules in solution and equilibrium pHs for the suspensions). A thermostatic shaker bath was used to keep the temperature constant. All adsorption experiments were performed at 25 ^{0}C. At the end of the adsorption period, the solution was centrifuged for 15 min at 5000 rpm and then the concentrations of the residual biomolecules, Ce, were determined by Bradford method (Bradford, 1976), using a Cary 1E UV-Visible Spectrophotometer (Varian). The amounts of biomolecules adsorbed were calculated from the concentrations in solutions before and after adsorption.

2.3 Activity of catalase

The activity of catalase was determined spectrophotometrically by direct measurement of the decrease in the absorbance of hydrogen peroxide at 240 nm due to its decomposition by the enzyme. Hydrogen peroxide solutions (40-200mM) were used to determine the activity. 0.3 g of catalase adsorbed sepiolite particles were mixed with hydrogen peroxide solution in 20 mM phosphate buffer (pH 7.0) at 22 ^{0}C. The absorbance of the reaction mixture was determined and the kinetic parameters of adsorbed catalase, K_m (Michaelis constant) and V_{max} (maximum reaction rate) for free and adsorbed catalase were determined by varying the concentration of hydrogen peroxide in the reaction medium.

3. Results and discussion

3.1 Isoelectric point (iep) of sepiolite

The potential determining ions are those ions that establish or change the surface charge of a solid. Since potential determining ions control the surface reactions, it is an important parameter for identifying the adsorption mechanisms. For silicate type minerals potential determining ions are generally H^+ and OH^- ions. In addition, the H^+ ions in solution

undergo exchange with some of the cations in the solid lattice leading to the consumption of H^+ ions in suspension.
For an oxide or clay, there is usually only one ionisable surface group, but that is amphoteric so it can take up either a proton or an OH^- ion depending on the pH (Hunter, 2002):

$$SO\text{-}H + H^+ \rightleftharpoons SOH_2^+ \quad (2)$$

$$SO\text{-}H + OH^- \rightleftharpoons SO^- + H_2O \quad (3)$$

at isoelectric point (iep),

$$[SOH_2^+] = [SO^-] \quad (4)$$

where ''S'' denotes the surface.
When pH is equal pH_{iep}, the net charge is zero. This pH corresponds to the presence of equal numbers of oppositely charged groups on the biomolecules. Such a neutral structure of charged groups is called a dipolar ion, or zwitterions. The iep of the sepiolite was determined by measuring the zeta potential as a function of pH (Fig. 1). The zeta potential is about 0 mV for sepiolite at around pH 6.6 in this studied pH range of 1.5–10.

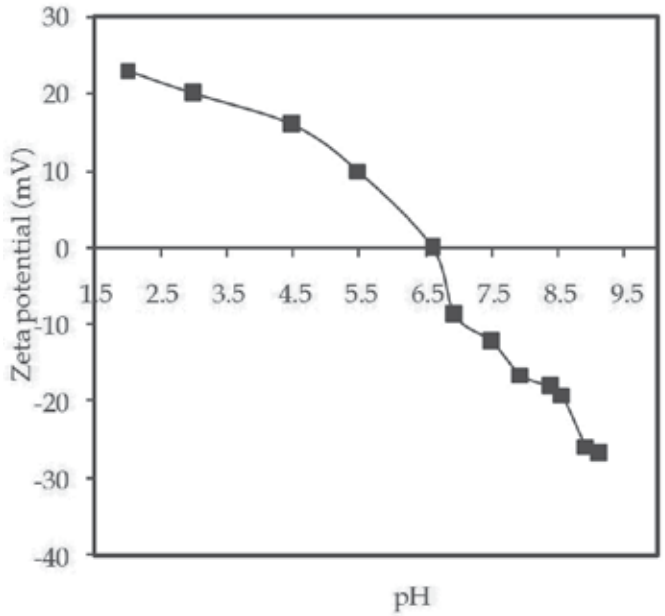

Fig. 1. The variation of zeta potential with pH of the sepiolite mineral.

3.2 Adsorption capacities as a function of incubation time of sepiolite

The adsorptions of casein and catalase on sepiolite were carried out in 0.001 M NaCl and 0.02 M sodium phosphate buffer at pH 7.0 and 22 ^{0}C. The initial concentrations of biomolecules were 1.0 mg mL^{-1} and the solid concentration was 3 g L^{-1} for sepiolite. Measuring the concentration of biomolecules in solution at different incubation times

generated in a time course of the adsorption. The results are shown in Fig. 2. According toFig. 2, the time required to reach a stationary concentration is about 10 h.

3.3 Adsorption of biomolecules onto sepiolite and zeta (ζ) - potential values

Adsorption experiments were carried out at the same conditions with zeta potential experiments in order to correlate the adsorption performance with ζ-potential of sepiolite minerals. Fig. 3 shows the variation of zeta potential with biomolecule concentrations of sepiolite minerals in 0.02 M phosphate buffer and 0.001 M NaCl at pH 7.0 and 22 ^{0}C and Fig. 4 the adsorption data obtained at the same conditions above. As seen in 4, the adsorption capacity of sepiolite has increased with increase in initial concentration of biomolecule, and the zeta potential of them has decreased with increase in initial concentration of biomolecule (less negative, see Fig.3). This means that the adsorption of biomolecules on solid increases when more biomolecules are available in solution. In fact that, the negative surfaces of solid are covered with biomolecules and they have less negative surface charge than their initial conditions. As a result, the ζ -potential of solid particles is decreased (less negative) but not positive at pH 7.0 because isoelectric points of biomolecules are lower than pH 7.0. The adsorbed biomolecules on sepiolite have negative charge so measured ζ -potential values must be negative.

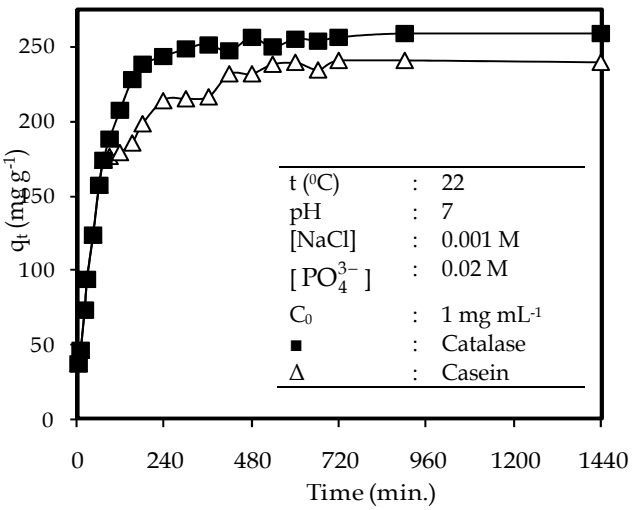

Fig. 2. The adsorption of biomolecules onto sepiolite as a function of incubation time.

Fig. 5 has shown the variation of zeta potential with equilibrium pH of various solid suspensions in 0.001 M NaCl, 0.02 M PO_3^{-4} and 1.0 mg mL^{-1} biomolecule concentrations at 22 ^{0}C, and Fig. 6 the variation of the biomolecule adsorption with equilibrium pH onto sepiolite in 0.001 M NaCl, 0.02 M PO_3^{-4} concentrations at 22 ^{0}C. Liquid phase pH has an important effect in the biomolecule adsorption on adsorbent (Patwardhan and Ataai, 1997). As seen in Fig. 6, they were found that the maximum casein and catalase adsorption

occurred at about pH 7 and pH 5.8, close to the isoelectric point of biomolecules. Since biomolecules are also negatively charged at pH values higher than about 5.8, the electrostatic repulsion between solid surface and biomolecules may prevent the binding of molecules onto sepiolite, leading to the decrease of biomolecule adsorption in the pH range of 6.0–10.0.

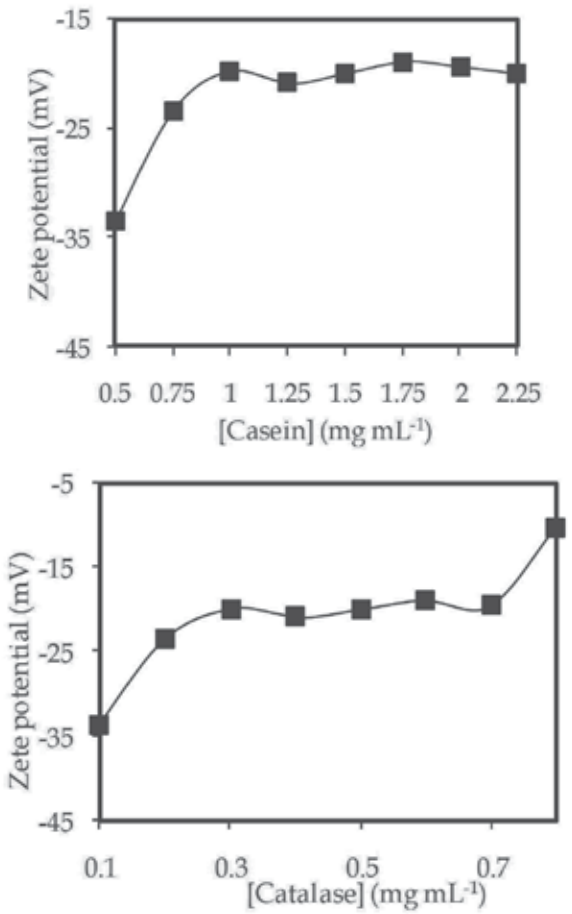

Fig. 3. The variation of zeta potential with biomolecule concentration of sepiolite minerals in aqueous solutions. (Experimental cond. 22^0C, pH 7, [PO_4^{3-}]: 0.02 M, [NaCl]: 0.001 M)

Addition of protein to the solution has a profound effect on the electrokinetic properties of solid particles (Giacomelli et al., 1997). Iep of sepiolite with catalase have been shown in Fig. 5. Catalase adsorption has caused a change in the ζ-potential or electrophoretic mobility in the entire pH range and shifted the iep of the solid particles from approximately 6.1 for sepiolite; which is the iep of catalase in solution. The casein-covered sepiolite samples have no isoelectric point in the studied pH range of 7–10. Because casein molecules doesn't solve in solution when the solution pH was acidic solutions and measure the ζ-potential or electrophoretic mobility and etc. correctly. A fairly similar trend has been reported by Giacomelli et al.,2001 and they found iep of the BSA-covered TiO_2 particles as pH 4.5; Shi et

al. investigated for the adsorption of BSA on chitosan-coated silica and found a high adsorption at pH 5.0; Sharma and Agarwal found a maximum adsorption at pH 8.0, for the adsorption of wheat germ agglutinin (pHiep 8.7) to tris(2-aminoethyl)amine-Ni(II) on Sepharose CL-6B; On the other hand, Barroug et al. reported the cooperative delivery of OH^- due to the adsorption of acidic proteins. Thus, it can be state that the increase in OH^- concentration with the increasing pH value will reduce the adsorption capacity of biomolecules.

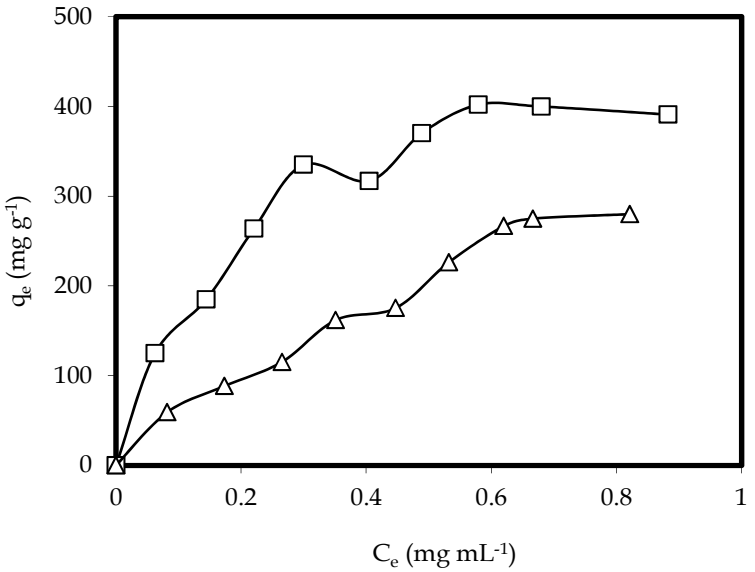

Fig. 4. The adsorption isotherms of biomolecules (Δ:casein, :catalase) onto sepiolite. (Experimental cond. 22^0C, pH 7, $[PO_4^{3-}]$: 0.02 M, [NaCl]: 0.001 M)

In the present study, the effect of temperature on adsorption was studied in the range 15 – 45 ^{0}C and the results are shown in Fig. 7 and 8, which indicate that adsorption increases from 15 to 45 ^{0}C. The amount of biomolecule adsorbed on sepiolite increased by increasing temperature. This indicated that sorption on sepiolite is not a simple physical adsorption. This observation can be explained with the help of the following facts: (i) the ongoing adsorption process is endothermic, i.e., entropically driven. (ii) Sorption with dissociation and increased availability of sites due to higher penetration of adsorbing molecules into the pores with an increase in temperature may explain this behaviour. Thus, the adsorption increases with increasing temperature. This indicates that the adsorption process becomes more favourable with increasing temperature

3.4 Adsorption isotherms

Adsorption isotherm describes a number of theories describing the adsorption equilibria. Two isotherm equations in the present study have been tested: Freundlich and Langmuir models.

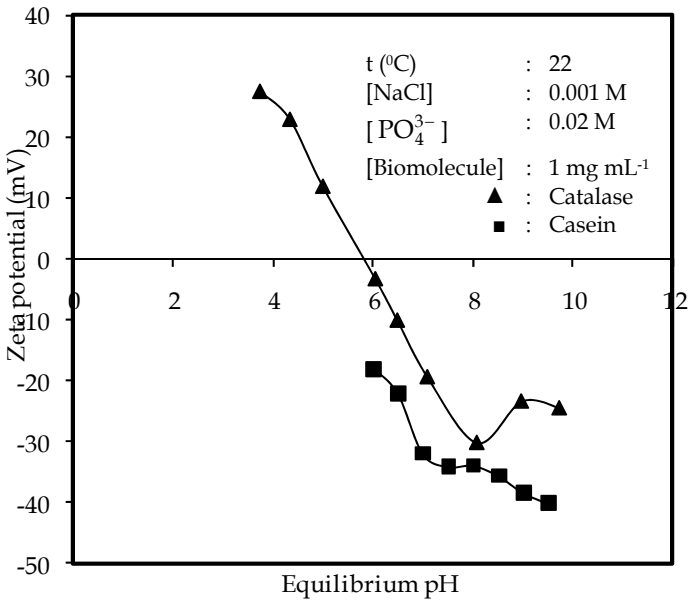

Fig. 5. The variation of zeta potential with equilibrium pH of sepiolite suspensions.

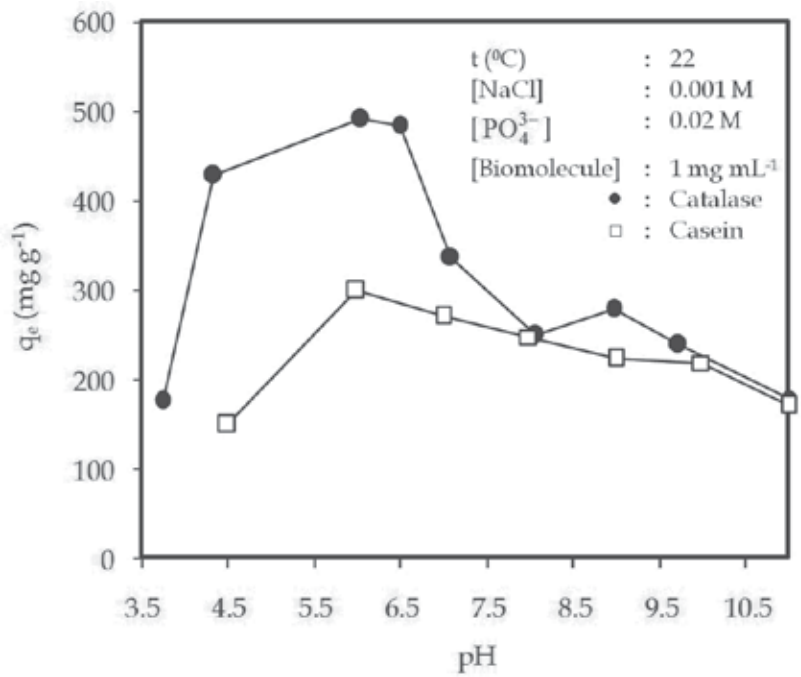

Fig. 6. The variation of biomolecule adsorption with equilibrium pH onto sepiolite.

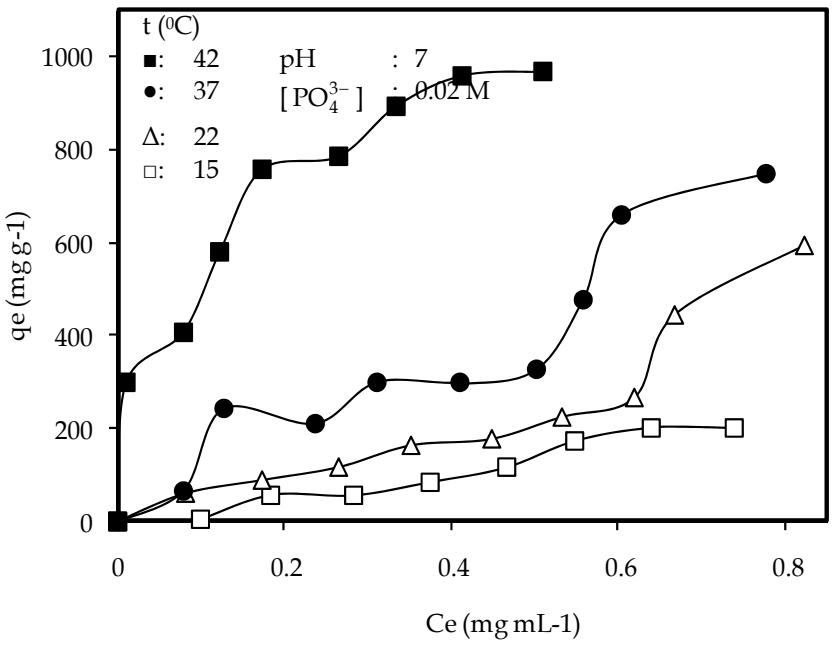

Fig. 7. The effect of temperature on casein adsorption onto sepiolite

3.4.1 Langmuir adsorption isotherm

The Langmuir isotherm theory assumes monolayer coverage of adsorbate over a homogenous adsorbent surface. Therefore, at equilibrium, a saturation point is reached where no further adsorption/desorption can occur.

The Langmuir equation is commonly expressed as (Langmuir, 1918):

$$\frac{C_e}{q_e} = \frac{1}{q_m K} + \frac{C_e}{q_m} \tag{5}$$

where C_e is the equilibrium liquid phase concentrations of protein solution (mg mL^{-1}), q_e is equilibrium protein concentration on adsorbent (mg g^{-1}), K is a direct measure for the intensity of the adsorption process, and q_m is a constant related to the area occupied by a monolayer of adsorbate, reflecting the adsorption capacity. From a plot of C_e/q_e versus C_e, q_m and K can be determined from its slope and intercept. Table 3 presents the correlation coefficient results for Langmuir isotherm, which has not a satisfactorily good correlation between the model predictions and the experimental data.

3.4.2 Freundlich adsorption isotherm

The Freundlich expression is an empirical exponential equation and therefore, assumes that as the adsorbate concentration increases so too does the concentration of adsorbate on the adsorbent surface. Theoretically, using this expression, an infinite amount of adsorption can occur (Freundlich, 1906).

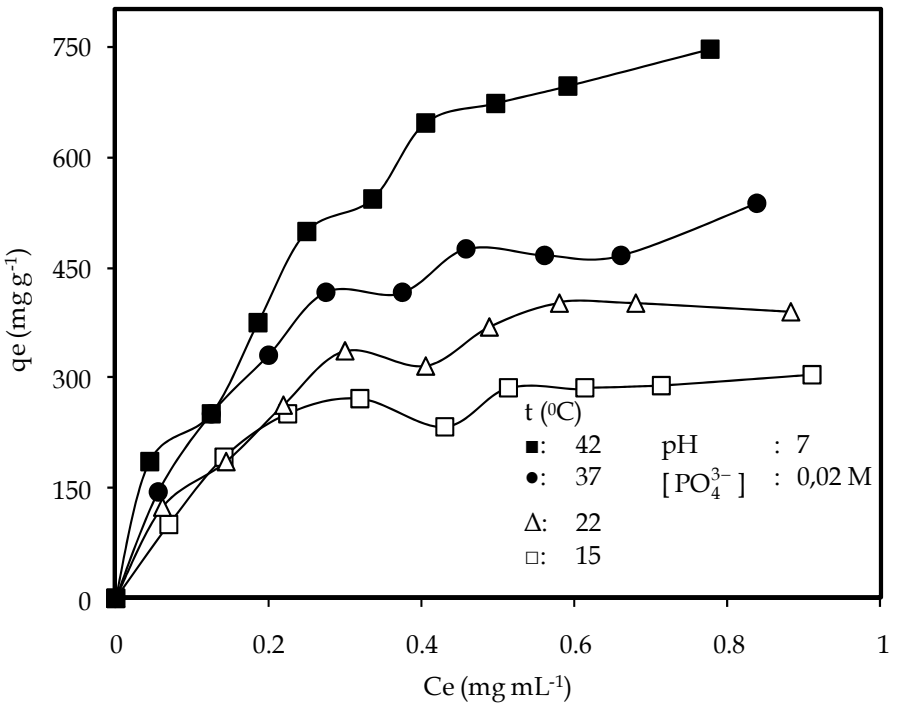

Fig. 8. The effect of temperature on catalase adsorption onto sepiolite

$$q_e = K_F C_e^{1/n} \tag{6}$$

In this equation, which is commonly given, K_F and n are the Freundlich constants. This expression is characterized by the heterogeneity factor, n, and so the Freundlich isotherm may be used to describe heterogeneous systems. To determine the constants K_F and n, the linear form of the equation (not shown) may be to produce a graph of $\ln q_e$ versus $\ln C_e$.

$$\ln q_e = \ln K_F + \frac{1}{n} \ln C_e \tag{7}$$

K_F is related to the bonding energy. K_F can be defined as the adsorption or distribution coefficient and represents the quantity of protein adsorbed onto adsorbent for a unit equilibrium concentration. The slope 1/n, ranging between 0 and 1, is a measure of adsorption intensity or surface heterogeneity, becoming more heterogeneous as its value gets closer to zero. Table 3 presents the results of the Freundlich isotherm for biomolecules adsorption on sepiolite. Freundlich isotherm appears to the experimental data better than the Langmuir isotherm, as reflected with correlation coefficients (R^2) in the range of 0.98–0.99.

3.5 Adsorption kinetics

In order to examine the controlling mechanism of sorption process, several kinetic models were used to test the experimental data. From a system design viewpoint, a lumped analysis of sorption rates is thus sufficient for practical operation.

Sample	Freundlich isotherm parameter			Langmuir isotherm parameter		
	K_F	n	R^2	q_m (mg g^{-1})	K (L mg^{-1})	R^2
Casein	2.55	2.87	0.99	595,15	5.16	0.79
Catalase	2.43	2.16	0.98	386.15	9.55	0.87

(Experimental cond. 22^0C, pH 7, $[PO_4^{3-}]$: 0.02 M, [NaCl]: 0.001 M)

Table 3. Isotherm constants for adsorption of biomolecules onto sepiolite.

3.5.1 Pseudo-first-order equation

The pseudo-first-order equation is generally expressed as follows:

$$\ln(q_e - q_t) = \ln q_e - k_1 t \tag{8}$$

where q_e and q_t are the amounts of biomolecules adsorbed at equilibrium and time t (mg g^{-1}), respectively, and k_1 is the rate constant of pseudo first-order adsorption (min^{-1}).
The half-adsorption time of the biomolecule, $t_{1/2}$, is the time required for the oxide samples to take up half as much biomolecule as it would at equilibrium. This time is often used as a measure of the rate of adsorption and given by

$$t_{1/2} = \frac{\ln 2}{k_1} \tag{9}$$

The values k_1 and $t_{1/2}$ are given in Table 4.

3.5.2 Pseudo-second-order equation

If the rate of adsorption is a second-order mechanism, the pseudo-second-order equation is expressed as

$$\frac{t}{q_t} = \frac{1}{k_2 q_e^2} + \frac{1}{q_e} t \tag{10}$$

where q_e is the amount of biomolecule adsorbed at equilibrium (mg g^{-1}) and, k_2 is the equilibrium rate constant of pseudo-second-order sorption (g(mg min)$^{-1}$).
The half-adsorption time of the biomolecule, $t_{1/2}$,

$$t_{1/2} = \frac{1}{k_2 q_e} \tag{11}$$

The values k_2 and $t_{1/2}$ are given in Table 4.

3.5.3 Intraparticle diffusion

The fractional approach to equilibrium changes according to a function of $(D_t/r^2)^{1/2}$, where r is the particle radius and D the diffusivity of solute within the particle. The initial rate of the intraparticle diffusion is the following:

$$q_t = f(t^{1/2}) \tag{12}$$

The rate parameter (kint) for intraparticle diffusion can be defined as:

$$q_t = k_{int}t^{1/2} + C \quad (13)$$

where kint is the intraparticle diffusion rate constant ($mg(g\ min^{1/2})^{-1}$) and given in Table 4.

Sample	First-order kinetic equation			$t_{1/2}$ (min)	Second-order kinetic equation			Intraparticle diffusion equation	
	$k_1 \times 10^3$ (min^{-1})	q_e (calculated) mg g^{-1}	r		k_2 g (mg min)$^{-1}$	q_e (calculated) mg g^{-1}	r	$k_{int} \times 10^2$ mg $(g\ min^{1/2})^{-1}$	r
Casein	6.1	248.2	0.99	125	0.02	285.1	0.77	10.3	0.89
Catalase	5.8	260.4	0.99	105	0.08	298.2	0.81	11.7	0.82

Table 4. Some kinetic values calculated for biomolecules adsorption onto sepiolite. (All values are not shown)

3.6 Thermodynamic parameters

Because the k_1 values have been determined, several thermodynamic parameters including the Arrhenius activation energy (E_a), activation free energy change (ΔG^*), activation enthalpy change (ΔH^*), and activation entropy change (ΔS^*) can be calculated by using the following equations and given in Table 5.:

$$\ln k_1 = \ln A - E_a/RT \quad (14)$$

$$\ln k_1 = k_b T\ K^*/h \quad (15)$$

$$\Delta G^* = -RT \ln K^* \quad (16)$$

$$\Delta H^* = E_a - RT \quad (17)$$

$$\Delta G^* = \Delta H^* - T\Delta S^* \quad (18)$$

where A is the Arrhenius factor, k_B and h are Boltzman's and Planck's constants, respectively, R is the gas constant, and K* is the equilibrium constant at temperature T. A linear plots of $\ln k_1$ versus 1/T for the adsorption of casein and catalase onto sepiolite are constructed to generate the E_a value from the slopes.

Sample	E_a ($kjmol^{-1}$)	ΔG^*($kjmol^{-1}$)	ΔH^*($kjmol^{-1}$)	ΔS^*($jmol^{-1}K^{-1}$)
Casein	40.16	248.8	38.01	-711.8
Catalase	43.12	247.1	40.67	-699.7

Table 5. The thermodynamics parameters of biomolecules onto sepiolite surface for 295K

3.7 Kinetic parameters of catalase

K_M and R_{max} are characteristic to an enzyme and are quite sensitive to the conditions under which the reaction takes place. According to the following equation, derived from Michaelis – Menten rate law:

$$\frac{1}{R} = \frac{K_M}{R_{\max}} \frac{1}{[S]} + \frac{1}{R_{\max}} \tag{19}$$

A plot of 1/R versus 1/[S], called a Lineweaver-Burk plot, would be a straight line with a slope equal to K_M/R_{max} and intercept equal to $1/R_{max}$. Kinetic constants of adsorbed and pure catalase are given in Table 6.

Kinetic constants	Pure	Adsorbed
K_m (mM)	172,09	24,21
R_{max} (mM min^{-1})	10,10	1,25

Table 6. Kinetic constants of pure and adsorbed catalase

As seen from Table 6, the K_m and R_{max} values of the adsorbed enzymes are lower than pure enzymes.

4. References

Ahlrichs, J.L., Serna, J.C., Serratosa, J.M. (1975). *Clays Clay Miner.* 23, 119–124.

Alkan, M., Demirbas, O., Dogan, M., Arslan, O. (2006). *Microporous and Mesoporous Materials* 96, 331–340.

Alkan, M., Demirbas, O., Dogan, M. (2005). *J. Colloid Interf. Sci.* 281, 240–248.

Arica, M.Y., Soydogan, H., Bayramoglu, G., 2010. *Bioprocess. Biosyst. Eng.* 33, 227–236

Barroug, A., Lernoux, E., Lemaitre, J., Rouxhet, P.G. (1998). J. Colloid Interf. Sci. 208, 147-152.

Bayramoglu, G., Yilmaz, M., Arica, M.Y., 2010. *Bioresour. Technol.* 101, 6615–6621.

Bolivar, J.M., Mateo, C., Rocha-Martin, J., Cava, F., Berenguer, J., Fernandez-Lafuente, R., Guisan, J.M., 2009 .*Enzyme Microb. Technol.* 44, 139–144.

Bradford, M.M. (1976). *Anal Biochem.* 72, 248–54.

Buijs, J., Norde, W., Lichtenbelt, J.W.T. (1996). *Langmuir* 12, 1605.

Cetinus, Senay Akkus, Nursevin Öztop, H., (2003). Immobilization of catalase into chemically crosslinked chitosan beads. *Enzyme Microb. Technol.* 32, 889–894.

Choi, Martin M.F., Yiu, Tak Pong, (2004). Immobilization of beef liver catalase on eggshell membrane for fabrication of hydrogen peroxide biosensor. *Enzyme Microb. Technol.* 34, 41–47.

Dalgleish, D. G., Hallet, F. R. (1995). Dynamic light scattering: Applications to food systems. *Food Research International*, 28(3),181–193.

Dickinson, E. (1999). Adsorbed protein layers at fluid interfaces: interactions, structure and surface rheology. *Colloids Surfaces B: Biointerfaces*, 15, 161-176.

Freundlich, H. (1906). *Phys. Chem.* 57, 384–410.

Frost, R.L., Ding, Z. (2003). Controlled rate thermal analysis and differential scanning calorimetry of sepiolites and palygorskites, *Thermochim. Acta,* 397, 119–128.

Giacomelli, C.E., Norde, W. (2001). *J. Colloid Interf. Sci.* 233, 234–240.

Giacomelli, C.E., Avena, M.J., De Pauli, C.P. (1997). *J. Colloid Interf. Sci.* 188, 387–395.

Göktas, A.A., Misirli, Z., Baykara, T. (1997). Sintering behaviour of sepiolite, *Ceram. Int.* 23, 305–311.

Grim, R.E. (1968). *Clay Minerology*, second ed., McGraw-Hill, New York.

Holt, C. (1998). Casein micelle substructure and calcium phosphate interactions studied by sephacryl column chromatography. *Journal of Dairy Science*, 81, 2994-3003.

Holt, C., & Sawyer, L. (1988). Primary and predicted secondary structure of the caseins in relation to their biological role. *Protein Engineering*, 2, 251-259.

Holt, C., Wahlgren, N. M., & Drakenberg, T. (1996). Ability of a b-casein phosphopeptide to modulate the precipitation of calcium phosphate by forming amorphous dicalcium phosphate nanoclusters. *Biochemical Journal*, 314, 1035-1039.

Horst, F., Rueda, E.H., Ferreira, M.L., (2006). Activity of magnetite-immobilized catalase in hydrogen peroxide decomposition. *Enzyme Microb. Technol.* 38 (7),1005–1012.

Hunter, R.J. (2002). *Introduction to Modern Colloid Science*, Oxford University Press, New York.

Jiang, Bo, Zhang, Yong, (1993). Immobilization of catalase on crosslinked polymeric hydrogels – effect of anion on the activity of immobilized enzyme. *Eur. Polym. J.* 29 (9), 1251–254.

Jürgen-Lohmann, Domink L., Legge, Raymond L., (2006). immobilization of bovine catalase in sol–gels. *Enzyme Microb. Technol.* 39 (4), 626–633.

Karagoz, B., Bayramoglu, G., Altintas, B., Bicak, N., Arica, M.Y., 2010. *Ind. Eng. Chem. Res.*49, 9655–9665.

Kennedy, J.F., Melo, E.H.M. (1990). Immobilized enzymes and cells. *Chem Eng Prog*. 86, 81–89.

Kondo, A., Murakami, F., Higashitani, K. (1992). *Biotechnol. Bioeng.* 40, 889.

Kondo, A., Oku, S., Murakami, F., Higashitani, K. (1993a). *Colloids Surf. B:Biointerf.* 1, 197.

Langmuir, I. (1918). *J. Am. Chem. Soc.* 40, 1361–1403.

Liu, Yong, Jia, Shaoyi, Ran, Jingyu, Wu, Songhai, (2009). Effects of static magnetic field on activity and stability of immobilized a-amylase in chitosan bead. *Catal. Commun.* 11, 364–367.

Luo, Q., Andrade, J.D. (1998). *J. Colloid Interf. Sci.* 200, 104–113.

Nakanishi, K., Sakiyama, T., Imamura, K. (2001). *J. Biosci. Bioeng.* 91, 233–244.

Norde, W. in: A. Baszkin, W. Norde (Eds.) (2000). *Physical Chemistry of Biological Interfaces*, Marcel Dekker Inc., New York, p. 115.

Özlem Alptekin, S., Tükel, Seyhan, Yildirim, Deniz, Alagöz, Dilek, (2009). Characterization and properties of catalase immobilized onto controlled pore glass and its application in batch and plug-flow type reactors. *J. Mol. Catal. B: Enzym.* 58, 124–131.

Patwardhan, A.V., and Ataai, M.M. (1997). *J. Chromatogr.* 767, 11–23.

Ran, Jingyu, Jia, Shaoyi, Liu, Yong, Wu, Songhai, (2009). Characterization of cellulose under various intensities of static magnetic fields. *Catal. Commun.* 11, 91–95.

Rytwo, G., Tropp, D., Serban, C. (2002). *Appl. Clay Sci.* 20, 273–282.

Sabah, E., Çelik, M.S. (2002). Interaction of pyridine derivatives with sepiolite, J. Colloid Interface Sci. 251, 33–38.

Sharma, S., Agarwal, G.P. (2001). *J. Colloid Interf. Sci.* 243, 61–72.

Shentu, Jingling, Wu, Jianmin, Song, Weihua, Jia, Zhishen, (2005). Chitosan microspheres as immobilized dye affinity support for catalase adsorption. *Int. J. Biol. Macromol.* 37 (30), 42–46.

Shi, Q.-H., Tian, Y., Dong, X.-Y., Bai, S., Sun, Y. (2003). *Biochem. Eng. J.* 16, 317–322.

Walstra, P., Jenness, R. (1984). *Dairy Chemistry and Physics*,Wiley-Interscience, New York.

Wang, L., Wei, L., Chen, Y., Jiang, R., 2010. *J. Biotechnol.* 150, 57–63.

Yoshimoto, Makoto, Sakamoto, Hideyuki, Yoshimoto, Noriko, Kuboi, Ryoichi, Nakao, Katsumi, (2007). Stabilization of quaternary structure and activity of bovine liver catalase through encapsulation in liposomes. *Enzyme Microb. Technol.* 41, 849–858.

Zhou, J., 2010. *J. Agric. Food Chem.* 58, 6741–6746.

14

Irreversible Thermodynamics and Modelling of Random Media

Roland Borghi
Ecole Centrale de Marseille/Laboratoire de Mécanique et d'Acoustique, CNRS
France

1. Introduction

Engineering and Nature very often are concerned with media that do contain some randomness. One particularly well known example is given by turbulent flows, where random fluctuations are the results of the growth of unstable motions from small perturbations in the initial or boundary conditions, when the velocity gradients or/and temperature gradients are too large in some place within the flow. These fluctuating motions result in effective additional friction, effective additional diffusion of species or heat, and additional energy dissipation (i.e. transfer from organized kinetic energy to turbulent kinetic energy, and finally to internal energy). Another example of random flows is seen in two-phase flows, either with particles dispersed into a liquid or gaseous continuous phase, or built with a bubbly liquid. Here, a first reason of randomness is given by the fact that the locations and velocities of the particles (or bubbles) at initial time and in entrance sections cannot be known or controlled, and the induced fluctuations are not rapidly damped with time. Generally, this randomness becomes rapidly uncorrelated with these initial conditions due to the complex interactions between the flow of the continuous phase and the moving inclusions, interactions that modify also the number and sizes of these inclusions. Consequently, the flow conditions in both phases are or become turbulent, with interconnected fluctuations of velocities. Again, the effective result of the fluctuations is additional friction, additional diffusion or dispersion, and additional energy dissipation. Two-phase or multiphase flows with a large amount of solid particles are used in the industrial devices called as "Fluidized Beds", and are encountered naturally in "Granular Flows", and in this case there are many lasting contacts between the particles. The so called "Granular Media", even without actual flow but just with some deformations or slow motions, are also subjected to randomness, due to the preparation of the medium but also to the differences between the grains shapes, and even the global properties of these media are very difficult to predict.

The properties of these kinds of media and flows have been studied since more than hundred years, and very useful prediction methods have been proposed so far, with methodologies becoming more and more clearly similar. Although all these media are showing clearly irreversible and dissipative processes, the typical reasoning of irreversible thermodynamics has never been used, at least explicitly (it might be present, but not consciously, in the brain of the authors). Our purpose here is to show that the Irreversible Thermodynamics and the "Second Principle" can justify many features of the models that

have been proposed until now for these three types of applications. It has to be emphasized that Irreversible Thermodynamics deals with the modelling of media in evolution, whatever can be this model. The usual model of classical continuous medium, where the randomness lies only at the infinitely small scale of moving molecules, is not the only one that can be addressed. The so called "Extended Irreversible Thermodynamics" (**Jou et al., 2001)** allows us indeed to build pertinent entropy functions adapted to each type of model, in particular depending of the basic variables of the model used, as we will see.

The first part of this paper deals with classical turbulent flows. The general problem of building a model for these flows, i.e. an approximate mathematical representation that could give predictions close to experiments, has in practice given rise to several solutions, which are valid in different domains, i.e. for different kinds of experimental situations. More precisely, the domains of efficiency of the different models appear to be larger and larger for models using an increasing number of variables. The basic variables that allow the building of these models are "averaged variables" (now precisely defined as statistical mean values), in a finite number, and then they do clearly constitute a truncated representation of the medium, but it is expected that these variables are sufficient for the purpose of the approximated knowledge needed. Some of these variables do satisfy balance equations, which are obtained averaging the primitive balance equations of the mechanics of continuous media, but these equations do need "closure assumptions" before to be useful in constituting a "Turbulence Model". Once the basic variables are chosen, the "Extended Irreversible Thermodynamics" allow us indeed to define an entropy function for this representation of the medium, for each of the models proposed. We will see that this entropy function is not the statistical mean value of the classical entropy for the fluid used in this turbulent flow, but has to be built taking into account the averaged form of the state equations of the fluid. Then, the Second Principle may lead to conditions concerning the ingredients of the turbulence model, conditions that are different for the different models. We will show that here simply considering two very popular models, and we will see that the usual practice does satisfy these conditions.

The second part of the chapter considers the modelling of two-phase flows. This modelling can be attacked with a similar approach and similar tools as turbulent flows: a set of averaged variables are defined; balance equations are written from the primitive equations of a piecewise continuous medium and closure assumptions are needed, to be adapted to each kind of two-phase flows. Here the closure assumptions are needed for both additional dispersion fluxes and exchange terms between the phases. These two-phase flows are again associated with irreversible effects, and again the framework of extended irreversible thermodynamics helps the modelling. We will recover again assumptions that are used in practice and supported by experiments.

The third part is devoted to granular media, with the same point of view. The approach generalizes the case of two-phase flows, because the granular medium is considered as a multiphase medium where each grain is considered as one phase, and the fluid in between as the last phase (Borghi § Bonelli, 2007). Again, the variables of the model are defined as statistically averaged grains phase and fluid phase variables, and their balance equations can be found from the primitive equations of mechanics, to be completed with closure assumptions. The approach can handle the situations where the medium is "quasi-static" as well as the ones where the medium is flowing with large velocities, giving rise to the limiting case of "Granular Gases". In both cases, Extended Irreversible Thermodynamics can be used for building entropies and giving closure assumptions, without linear laws in this case particularly. The classical models of "Granular Gases" are recovered in the limit of large velocities, with the difference that the grain size is not the single length scale to be considered.

For quasi-static situations, it is necessary to include in the model the six components of the averaged "Contact Cauchy Stress Tensor" of the grains phase. Intermediate situations can be handled as well.

2. Irreversible thermodynamics for turbulent flows models

Turbulent flows at present time are studied with models of two different types, namely Reynolds averaged Navier-Stokes (RANS) models, or Large Eddies Simulations (LES) models. We consider here for simplicity the framework of RANS models, although the extension to LES models may be not difficult. Then, the object of the study is not one given flowing medium, but an infinite number of such media, flowing submitted to initial and boundary conditions randomly perturbed. Indeed, what we call "one turbulent flow" is this ensemble of similar individual flows, because only statistical mean values calculated from this ensemble (or, at best, probability density functions) can be possibly predicted by some model.
The "mean medium" that is the subject of modelling is then described by "mean velocities", "mean densities", "mean enthalpy per unit of mass", etc.. For N realizations, one defines:

$$\overline{\rho} = \lim(N \to \infty)(\frac{1}{N}\sum_{n=1}^{N}\rho^n)$$

at each given location within the flow field, and similarly for pressure. But in the general case where the density of the fluid can vary noticeably, it has been found more interesting to consider for other variables the mean value weighted by density, and one defines:

$$\tilde{v}^\alpha = \lim(N \to \infty)(\sum_{n=1}^{N}\rho^n v^{\alpha n} / \sum_{n=1}^{N}\rho^n) \ ,$$

i.e. the mean velocity is nothing but the mean momentum divided by the mean density. Similarly for the internal energy per unit mass (or the enthalpy per unit mass), the mean values are weighted with density.
Within a turbulent flow, these quantities are defined for each location and for each time, and vary with the location and eventually with time, but these variations are much smoother than the local and instantaneous quantities measured in one single realization of the flow, and by definition they are not sensitive to perturbations of initial and boundary conditions, that are inevitably present.
Is it possible to characterize the turbulent medium by $\overline{\rho}, \tilde{e}, \tilde{v}^\alpha$ only, when a non turbulent flow of the same fluid is correctly characterized by ρ, e, v^α ? Of course, the random fluctuations do have some influence. However, in some situations, it may be possible to take into account this influence by some algebraic formulas in terms of the mean variables and their derivatives. Of course, these formulas are only approximations, with a limited domain of validity assessed by experiments.
The first invented turbulence model, called "Prandtl mixing length model", is of this type, and has been very useful in many practical cases. But a larger domain of validity can be covered taking into account additional fields variables pertinently chosen, described with their own partial differential evolution equations. There are different turbulence models of this improved type, the simplest one introduces only as additional field variable the kinetic energy of the random turbulent fluctuations, say $\tilde{k}$, the "length scale" characterizing the

two-point correlation of the fluctuations, l_t, being given with algebraic formulas. More detailed models use $\tilde{k}$ and ε, the dissipation rate of $\tilde{k}$, described by partial differential evolution equations, or $\tilde{k}$ and ω, a characteristic frequency of turbulence, or the Reynolds stress tensor components themselves and ε (Schiestel, 2006).

2.1 Basic equations

The physical basic equations corresponding to balance of mass, momentum and total energy give birth in any case to balance equations for the mean variables $\bar{\rho}, \tilde{e}, \tilde{v}^\alpha$. We write them with a tensor notation and the Einstein convention of repeated indices. We assume an orthogonal reference frame and then upper or lower indices are equivalent:

$$\frac{\partial}{\partial t}(\bar{\rho}) + \frac{\partial}{\partial x_\alpha}(\bar{\rho}\tilde{v}^\alpha) = 0 \tag{1}$$

$$\frac{\partial}{\partial t}\left(\bar{\rho}\tilde{v}^\beta\right) + \frac{\partial}{\partial x_\alpha}(\bar{\rho}\tilde{v}^\alpha\tilde{v}^\beta) = \frac{\partial}{\partial x_\alpha}(-\bar{p}\delta^{\alpha\beta} + \bar{\tau}^{\alpha\beta} - \overline{\rho v'^\alpha v'^\beta}) + \bar{\rho}g_\beta \tag{2}$$

$$\frac{\partial}{\partial t}\left(\bar{\rho}\tilde{e}_t\right) + \frac{\partial}{\partial x_\alpha}(\bar{\rho}\tilde{v}^\alpha\tilde{e}_t) = \frac{\partial}{\partial x_\alpha}(-\bar{j}_\alpha^Q - \overline{pv^\alpha} + \overline{\tau^{\alpha\beta}v^\beta} - \overline{\rho v'^\alpha e_t}) + \bar{\rho}\tilde{v}^\beta g_\beta \tag{3}$$

The total energy here comprises the internal energy, the kinetic energy of the mean motion, and the kinetic energy of turbulent fluctuations, so $\bar{\rho}\tilde{e}_t = \bar{\rho}\tilde{e} + \frac{1}{2}\bar{\rho}\tilde{v}^\alpha\tilde{v}^\alpha + \frac{1}{2}\overline{\rho v'^\alpha v'^\alpha}$. We have defined $v'^\alpha = v^\alpha - \tilde{v}^\alpha$, and so $\overline{\rho v'^\alpha} = 0$. The well known « Reynolds stress tensor » is $R_{\alpha\beta}$ such that: $\bar{\rho}R_{\alpha\beta} = \overline{\rho v'^\alpha v'^\beta}$. Similarly $e' = e - \tilde{e}$, but $p' = p - \bar{p}$. The "turbulent kinetic energy" introduced above is nothing but: $\bar{\rho}\tilde{k} = \frac{1}{2}\overline{\rho v'^\alpha v'^\alpha}$.

From (2) and (1), one obtains the equation for the kinetic energy of the mean motion:

$$\frac{\partial}{\partial t}\left(\bar{\rho}\tilde{v}^\beta\tilde{v}^\beta/2\right) + \frac{\partial}{\partial x_\alpha}(\bar{\rho}\tilde{v}^\alpha\tilde{v}^\beta\tilde{v}^\beta/2) = \frac{\partial}{\partial x_\alpha}(-\bar{p}\tilde{v}^\alpha + \tilde{v}^\beta\bar{\tau}^{\alpha\beta} - \overline{\rho v'^\alpha v'^\beta}\tilde{v}^\beta)$$

$$+(\bar{p}\delta^{\alpha\beta} - \bar{\tau}^{\alpha\beta} + \overline{\rho v'^\alpha v'^\beta})\frac{\partial\tilde{v}^\beta}{\partial x_\alpha} + \bar{\rho}\tilde{v}^\beta g_\beta \tag{4}$$

Then, from (3) and (4) we have:

$$\frac{\partial}{\partial t}\left(\bar{\rho}(\tilde{e}+\tilde{k})\right) + \frac{\partial}{\partial x_\alpha}(\bar{\rho}\tilde{v}^\alpha(\tilde{e}+\tilde{k})) = \frac{\partial}{\partial x_\alpha}(-\bar{j}_\alpha^Q - \overline{pv'^\alpha} + \overline{\tau^{\alpha\beta}v'^\beta} - \overline{\rho v'^\alpha e} - \frac{1}{2}\overline{\rho v'^\alpha v'^\beta v'^\beta})$$

$$-\bar{p}\frac{\partial\tilde{v}^\alpha}{\partial x_\alpha} + (\bar{\tau}^{\alpha\beta} - \overline{\rho v'^\alpha v'^\beta})\frac{\partial\tilde{v}^\beta}{\partial x_\alpha} \tag{5}$$

It is possible also to derive directly from the non-averaged momentum equation a balance equation for $\bar{\rho}\tilde{k} = \frac{1}{2}\overline{\rho v'^\alpha v'^\alpha}$. That is done by scalar multiplying the instantaneous (non-

averaged) momentum equation by the velocity in order to obtain an equation for the total kinetic energy, and then by subtracting the equation of the kinetic energy of the mean motion (4). One gets:

$$\frac{\partial}{\partial t}(\bar{\rho}\tilde{k})+\frac{\partial}{\partial x_\alpha}(\bar{\rho}\tilde{v}^\alpha\tilde{k})=\frac{\partial}{\partial x_\alpha}(\overline{v'^\beta\tau'^{\alpha\beta}}-\overline{v'^\alpha p}-\frac{1}{2}\overline{\rho v'^\alpha v'^\beta v'^\beta})\ -\overline{\rho v'^\alpha v'^\beta}\frac{\partial\tilde{v}^\beta}{\partial x_\alpha}+\overline{p\frac{\partial v'^\alpha}{\partial x_\alpha}}-\overline{\tau'^{\alpha\beta}\frac{\partial v'^\beta}{\partial x_\alpha}} \quad (6)$$

From (5) and (6), finally the equation for the internal energy is written:

$$\frac{\partial}{\partial t}(\bar{\rho}\tilde{e})+\frac{\partial}{\partial x_\alpha}(\bar{\rho}\tilde{v}^\alpha\tilde{e})=\frac{\partial}{\partial x_\alpha}(-\bar{j}_\alpha^Q-\overline{\rho v'^\alpha e})\ -\bar{p}\frac{\partial\tilde{v}^\alpha}{\partial x_\alpha}-\overline{p\frac{\partial v'^\alpha}{\partial x_\alpha}}+\overline{\tau'^{\alpha\beta}\frac{\partial v'^\beta}{\partial x_\alpha}}+\bar{\tau}^{\alpha\beta}\frac{\partial\tilde{v}^\beta}{\partial x_\alpha} \quad (7)$$

The last term $\overline{\tau'^{\alpha\beta}\frac{\partial v'^\beta}{\partial x_\alpha}}=\bar{\rho}\varepsilon$ of (6) is called « volumetric rate of dissipation for turbulence », due to the viscosity (and ε is the rate of dissipation by unit of mass). This term is a transfer of energy from $\tilde{k}$ to $\tilde{e}$, while the last term of (7) is the dissipation rate of kinetic energy of the mean motion, directly from $\frac{1}{2}\bar{\rho}\tilde{v}^\alpha\tilde{v}^\alpha$ to $\tilde{e}$. There is in (6) a term corresponding to a transfer from $\frac{1}{2}\bar{\rho}\tilde{v}^\alpha\tilde{v}^\alpha$: the term $-\overline{\rho v'^\alpha v'^\beta}\frac{\partial\tilde{v}^\beta}{\partial x_\alpha}$ is called the production term for $\tilde{k}$. The terms $-\bar{p}\frac{\partial\tilde{v}^\alpha}{\partial x_\alpha}-\overline{p\frac{\partial v'^\alpha}{\partial x_\alpha}}$ in (7) are also transfer terms from $\frac{1}{2}\bar{\rho}\tilde{v}^\alpha\tilde{v}^\alpha$ and $\tilde{k}$, respectively, but these terms are reversible, unlike the last terms due to the viscosity. If the medium is incompressible (i.e. $\frac{\partial v^\alpha}{\partial x_\alpha}\cong 0$), these pressure terms are vanishing. When the velocity of the flow is low, very often the two last terms can be neglected in (7) with respect to the heat flux term (Chassaing et al., 2002).

Equations (1) to (3) are able to calculate the mean variables $\bar{\rho},\tilde{e},\tilde{v}^\alpha$ if and only if the turbulent fluxes $\bar{\rho}R_{\alpha\beta}=\overline{\rho v'^\alpha v'^\beta}$ and $-\overline{pv^\alpha}+\overline{\tau^{\alpha\beta}v^\beta}-\overline{\rho v'^\alpha e_t}$, additional to the classical viscous stress and heat conduction flux, can be provided by additional closure expressions, based on theoretical or empirical grounds. Instead of (3), we can use (7), and the transfer terms from $\tilde{k}$ to $\tilde{e}$ are also to be modelled. As we have previously said, this needs to take into account additional variables that represent in some sense the turbulent fluctuations, and, at least, $\tilde{k}$ is one of these new variables. It is seen here that one balance equation for $\tilde{k}$ can be found, which can be used provided again that the correlations involving the fluctuations that appear in this equation can be given also by expressions involving only $\bar{\rho},\tilde{e},\tilde{v}^\alpha$, $\tilde{k}$ and eventually other ones…

The simplest model, the "Prandtl mixing length model", does not use a balance equation for $\tilde{k}$ but expresses it directly form the mean velocity gradient. We will see how that is done, and in addition it is postulated that turbulence involves a single (mean) turbulence length scale, l_t, which is simply related to the geometry of the turbulent flow. The second simplest turbulence model, the "Kolmogorov model", uses the balance equation (6), the unknown terms in it being conveniently modelled with closure assumptions Then, the model provides expressions for the

correlations involved in (1) to (6), in particular $R_{\alpha\beta}$, as functions of $\overline{\rho}, \tilde{e}, \tilde{v}^{\alpha}$, $\tilde{k}$, l_t and their spatial derivatives. The very popular "k-epsilon" model, instead of giving directly l_t, assume that the dissipation rate ε itself can be calculated by an additional balance equation, postulates such an equation, and writes the correlations as functions of $\overline{\rho}, \tilde{e}, \tilde{v}^{\alpha}$, $\tilde{k}$, ε and their spatial derivatives.

We will now show that the approach of irreversible thermodynamics can be of great help, once the type of model is chosen, to solve the problem of modelling. We will see that it justifies the usual choices done by researchers since 30 years, and suggests possibilities for unsolved problems.

2.2 Entropy for the Prandtl mixing length model

In this framework we expect to model the turbulent flow only with the variables $\overline{\rho}, \tilde{e}, \tilde{v}^{\alpha}$, given by their balance equations. It is assumed that the balance equation (6) for the kinetic energy of the fluctuating motion can be simplified in keeping only the production and destruction terms:

$$-\overline{\rho v'^{\alpha} v'^{\beta}} \frac{\partial \tilde{v}^{\beta}}{\partial x_{\alpha}} + \overline{p \frac{\partial v'^{\alpha}}{\partial x_{\alpha}}} = \overline{\tau^{\alpha\beta} \frac{\partial v'^{\beta}}{\partial x_{\alpha}}} \tag{8}$$

In addition, the rate of dissipation, which can be calculated through $\tilde{k}$ and l_t only, is necessarily written as $\overline{\rho}\varepsilon = C_d \tilde{k}^{3/2} / l_t$, where C_d is a non dimensional constant. This model has been initially proposed for incompressible flow, and the pressure term, with the divergence of velocity fluctuation, is totally negligible in this case, as well as the two pressure terms in (7). Then the turbulence kinetic energy is an algebraic function of the gradient of the mean velocity, and does not need to be calculated with the differential equation (6):

$$\overline{\rho} C_d \frac{\tilde{k}^{3/2}}{l_l} = -\overline{\rho v'^{\alpha} v'^{\beta}} \frac{\partial \tilde{v}^{\beta}}{\partial x_{\alpha}} \tag{9}$$

The three basic variables $\overline{\rho}, \tilde{e}, \tilde{v}^{\alpha}$ being given, the entropy function has to be searched as $\varsigma = \varsigma(\tilde{e}, 1/\overline{\rho})$ only (the velocity being a non-objective variable has not to appear), with the Gibbs and Euler-Gibbs equations classically written as:

$$\tilde{e} = \theta\varsigma - \pi\frac{1}{\overline{\rho}} + \mu\,, \qquad d\tilde{e} = \theta d\varsigma - \pi d(\frac{1}{\overline{\rho}})$$

The two functions θ, π are the partial derivatives of $\tilde{e}$ with respect to ς and $1/\overline{\rho}$, or $1/\theta$ and π/θ are the partial derivatives of ς with respect to $\tilde{e}$ and $1/\overline{\rho}$, and the relations $\theta = \theta(\tilde{e}, 1/\overline{\rho})$ et $\pi = \pi(\tilde{e}, 1/\overline{\rho})$ are the laws of state, to be found. Of course, the formula $\mu = \mu(\tilde{e}, 1/\overline{\rho})$ also can be deduced. In addition, these equations of state do satisfy necessarily the Maxwell relation: $\frac{\partial^2 \varsigma}{\partial\tilde{e}\partial(1/\overline{\rho})} = \frac{\partial(1/\theta)}{\partial(1/\overline{\rho})} = \frac{\partial^2\varsigma}{\partial(1/\overline{\rho})\partial\tilde{e}} = \frac{\partial(\pi/\theta)}{\partial\tilde{e}}$.

The fluid itself, independently of the turbulent flow, has proper equations of state, and if we assume that it is an "ideal gas", $e = C_v T + e^0, p = \rho RT$ do hold, with three constants: C_v, e^0, R. Then, we can derive $\tilde{e} = C_v\tilde{T} + e^0, \overline{p} = \overline{\rho} R\tilde{T}$, just taking the average (weighted average for the

first one, classic average for the second one). It appears that if we identify $\theta = \tilde{T}$ and $\pi = \overline{p}$, we find $\theta = \frac{\tilde{e} - e^0}{C_v}, \pi = \overline{\rho} R \frac{\tilde{e} - e^0}{C_v}$, and these relations are convenient equations of state because they satisfy the Maxwell relation : here $\frac{\partial(1/\theta)}{\partial(1/\overline{\rho})} = \frac{\partial(\pi/\theta)}{\partial \tilde{e}} = 0$. The thermodynamic description of the model is complete. From these equations of state we can derive the entropy function, similarly as in the classical case of an ideal gas: $\varsigma - \varsigma_r = C_v Ln(\frac{\theta}{\theta_r}) - RLn(\frac{\overline{\rho}}{\overline{\rho}_r})$. We emphasize that this entropy is not the statistical mean value of the entropy of the fluid $s = s(e, \rho)$. Indeed, this mean value cannot be expressed in terms of $\tilde{e}, \overline{\rho}$ only, because $s = s(e, \rho)$ is non linear, and is not usable in our modelling framework.

It has to be remarked that the previous development cannot be extended to the case of fluid satisfying a non linear Joule law $e = e(T)$. In this case, when the fluctuations are not infinitely small, it comes that $\overline{\rho}\tilde{e} = f(\overline{\rho}\tilde{T}, \overline{\rho T'^2}, \overline{\rho T'^3}, ...)$, and it is no more possible to limit the model to $\varsigma = \varsigma(\tilde{e}, 1/\overline{\rho})$. If the nonlinearity of $e(T)$ is important, we have to consider, at least, the additional variable $\overline{\rho T'^2} / \overline{\rho}$.

Once we have defined the entropy and found the equations of state, we can use the classical approach of irreversible thermodynamics for deriving some laws for the additional fluxes appearing in the mean balance equations (2) and (7).

The Gibbs-Euler equation, now written as $d\tilde{e} = \tilde{T} d\varsigma - \overline{p} d(\frac{1}{\overline{\rho}})$, allows us to obtain the balance equation for the (new) entropy, showing the term of entropy production, which has to be always positive, and zero at equilibrium. Using (1), (2), (7), (8), one gets (with the "Lagrangian" derivative of the mean motion such that $\frac{D}{Dt}(.) = \frac{\partial}{\partial t}(.) + \tilde{v}^\alpha \frac{\partial}{\partial x_\alpha}(.)$):

$$\overline{\rho}\frac{D\varsigma}{Dt} = \frac{\partial}{\partial x_\alpha}\left(-\frac{\overline{j}_\alpha^Q + \overline{\rho v'^\alpha e}}{\tilde{T}}\right) + \left(\overline{j}_\alpha^Q + \overline{\rho v'^\alpha e}\right)\frac{\partial 1/\tilde{T}}{\partial x_\alpha} + \left(\frac{\overline{\tau}^{\alpha\beta} - \overline{\rho v'^\alpha v'^\beta}}{\tilde{T}}\right)\frac{\partial \tilde{v}^\beta}{\partial x_\alpha} \tag{10}$$

The production terms are the two last terms, and in the last one the contribution due to the diagonal of the tensors is vanishing because the fluid is incompressible. It results that a simple extension of the linear classical irreversible thermodynamics is possible here, giving laws for the turbulent additional fluxes of heat and momentum.

Concerning the total friction term, a positive "total viscosity coefficient" μ_{tt} can be defined and:

$$\overline{\tau}^{\alpha\beta} - \overline{\rho v'^\alpha v'^\beta} + \frac{2}{3}\overline{\rho}\tilde{k}\delta^{\alpha\beta} = \mu_{tt}\left(\frac{\partial \tilde{v}_\alpha}{\partial x_\beta} + \frac{\partial \tilde{v}_\beta}{\partial x_\alpha}\right)$$

Considering that the fluid is Newtonian, one has already: $\overline{\tau}^{\alpha\beta} = \mu\left(\frac{\partial \tilde{v}_\alpha}{\partial x_\beta} + \frac{\partial \tilde{v}_\beta}{\partial x_\alpha}\right)$ (here $\mu = cst$ and $\tilde{v}^\alpha \cong \overline{v}^\alpha$) , and it appears for the pure turbulent contribution an "eddy viscosity coefficient" $\mu_t = \mu_{tt} - \mu$ such as:

$$-\overline{\rho v'^{\alpha} v'^{\beta}} + \frac{2}{3}\overline{\rho}\tilde{k}\delta^{\alpha\beta} = \mu_t\left(\frac{\partial \tilde{v}_\alpha}{\partial x_\beta} + \frac{\partial \tilde{v}_\beta}{\partial x_\alpha}\right) \tag{11}$$

This is the well known "Boussinesq relation" proposed for turbulent flows at the end of the 19th century.
Similarly, for the total heat flux, the linear law of irreversible thermodynamics gives:

$$-\overline{j}_\alpha^Q - \overline{\rho v'_\alpha e'} = (\lambda + \lambda_t)\frac{\partial \tilde{T}}{\partial x_\alpha} = \left(\lambda + \frac{\mu_t}{\mathrm{Pr}_t}\right)\frac{\partial \tilde{T}}{\partial x_\alpha} \tag{12}$$

This introduces the classical « turbulent Prandtl number », constant , whose value (about 0.83) has been given by many experiments.
The eddy viscosity coefficient has now to be found. Just by dimensions, it can be written as $\mu_t = \overline{\rho} C \tilde{k}^{1/2} l_t$, with (9) it comes: $\tilde{k} = \frac{C}{C_d} l_t^2 \left(\frac{\partial \tilde{v}^\alpha}{\partial x_\beta} + \frac{\partial \tilde{v}^\beta}{\partial x_\alpha}\right)\frac{\partial \tilde{v}^\beta}{\partial x_\alpha} = \frac{C}{2C_d} l_t^2 \left(\frac{\partial \tilde{v}^\alpha}{\partial x_\beta} + \frac{\partial \tilde{v}^\beta}{\partial x_\alpha}\right)\left(\frac{\partial \tilde{v}^\alpha}{\partial x_\beta} + \frac{\partial \tilde{v}^\beta}{\partial x_\alpha}\right)$,
and we get finally the well known formula of "Prandtl mixing length" :

$$\mu_t = \overline{\rho} C_{ML} l_t^2 \left(\left(\frac{\partial \tilde{v}^\alpha}{\partial x_\beta} + \frac{\partial \tilde{v}^\beta}{\partial x_\alpha}\right)\left(\frac{\partial \tilde{v}^\alpha}{\partial x_\beta} + \frac{\partial \tilde{v}^\beta}{\partial x_\alpha}\right)\right)^{1/2} \tag{13}$$

In this model, the turbulence length scale l_t, called "mixing length", is given algebraically from the geometry of the flow. The constants C_{ML} and C_d have been found actual constants when the turbulent fluctuations are well developed, and then $\mu_t \gg \mu$, but when it is not the case they vary in function of the "turbulence Reynolds number" $\mathrm{Re}_t = \mu_t / \mu$. Experiments have given such corrective functions.
The conclusion is then here that the classical approach of linear irreversible thermodynamics does justify perfectly the old empirical approach of Boussinesq and Prandtl.

2.3 Entropy for the K-epsilon model

We consider now the very popular "k-epsilon" model, where a balance equation for $\tilde{k}$, based on (6), and a balance equation for $\varepsilon^* = \varepsilon - 2\nu \frac{\partial \tilde{k}^{1/2}}{\partial x_\alpha}\frac{\partial \tilde{k}^{1/2}}{\partial x_\alpha}$, less firmly based on physics, are used. When turbulence is well established, $\varepsilon^* \cong \varepsilon$, but the additional term is not negligible close to walls, where viscosity remains playing. There are other models that use equations for l_t, or $1/\tau_t$, the inverse of a time scale of turbulence, instead of ε^*, and similar discussions could be done for these models.
In this case, the independent variables $\overline{\rho}, \tilde{e}, \tilde{k}, \varepsilon^*$ have to be taken into account in order to build an entropy function, and we have to search $\varsigma = \varsigma(\tilde{e}, 1/\overline{\rho}, \tilde{k}, \varepsilon^*)$ with:

$$\tilde{e} = \theta\varsigma - \pi\frac{1}{\overline{\rho}} - y_k\tilde{k} - y_\varepsilon\varepsilon^* + \mu\,, \quad d\tilde{e} = \theta d\varsigma - \pi d\left(\frac{1}{\overline{\rho}}\right) - y_k d\tilde{k} - y_\varepsilon d\varepsilon^*$$

Here $\theta = \theta(\tilde{e}, 1/\overline{\rho}, \tilde{k}, \varepsilon^*)$, $\pi = \pi(\tilde{e}, 1/\overline{\rho}, \tilde{k}, \varepsilon^*)$, $y_k = y_k(\tilde{e}, 1/\overline{\rho}, \tilde{k}, \varepsilon^*)$, $y_\varepsilon = y_\varepsilon(\tilde{e}, 1/\overline{\rho}, \tilde{k}, \varepsilon^*)$ are the new equations of state to be found, satisfying the six corresponding Maxwell

relations. We will have to discuss the finding of these equations of state in connexion with the discussion of the second principle. Concerning the ε^* equation, we use here the general following form, with a diffusion term and production and destruction terms:

$$\frac{\partial}{\partial t}(\bar{\rho}\varepsilon^*)+\frac{\partial}{\partial x_\alpha}(\bar{\rho}\tilde{v}^\alpha\varepsilon^*)=\frac{\partial}{\partial x_\alpha}(-J_\varepsilon^\alpha)-\bar{\rho}C_3\frac{2\varepsilon^*}{3}\frac{\partial\tilde{v}^\alpha}{\partial x_\alpha}-\bar{\rho}C_1\frac{\varepsilon^*}{\tilde{k}}R_d^{\alpha\beta}\frac{\partial\tilde{v}^\beta}{\partial x_\alpha}+C_4\frac{\varepsilon^*}{\tilde{k}}\overline{p\frac{\partial v'^\alpha}{\partial x_\alpha}}-\bar{\rho}C_2\frac{\varepsilon\varepsilon^*}{\tilde{k}} \quad (14)$$

The C's are constants (numbers, without dimension) or algebraic functions of the variables in some cases (the two first being always positive), depending of the exact version of the model used. Within the most classical k-ε model, $C_1=1.44, C_2=1.92, C_3=1.44, C_4=0$.
Using now (1), (6), (7) and (14), we can derive as in § 2.2 the balance equation for the entropy as:

$$\begin{aligned}\bar{\rho}\frac{D\varsigma}{Dt}=&\frac{\partial}{\partial x_\alpha}\left(-\frac{\bar{j}_\alpha^Q+\overline{\rho v'^\alpha e}}{\theta}-\frac{y_kJ_k^\alpha+y_\varepsilon J_\varepsilon^\alpha}{\theta}\right)+\left(\bar{j}_\alpha^Q+\overline{\rho v'^\alpha e}\right)\frac{\partial 1/\theta}{\partial x_\alpha}+\\&+J_k^\alpha\frac{\partial y_k/\theta}{\partial x_\alpha}+J_\varepsilon^\alpha\frac{\partial y_\varepsilon/\theta}{\partial x_\alpha}+\frac{1}{\theta}\left(\pi-\bar{p}-\frac{2}{3}\bar{\rho}\tilde{k}\left(y_k+\frac{C_3\varepsilon^*y_\varepsilon}{\tilde{k}}\right)\right)\frac{\partial\tilde{v}^\gamma}{\partial x_\gamma}-\\&-\frac{1-y_k-C_4\varepsilon^*y_\varepsilon/\tilde{k}}{\theta}\overline{p\frac{\partial v'^\beta}{\partial x_\beta}}-\frac{y_k+C_1\varepsilon^*y_\varepsilon/\tilde{k}}{\theta}\bar{\rho}R_d^{\alpha\beta}\frac{\partial\tilde{v}^\beta}{\partial x_\alpha}+\\&+\frac{1}{\theta}\bar{\tau}_d^{\alpha\beta}\frac{\partial\tilde{v}^\beta}{\partial x_\alpha}+\frac{1}{3\theta}\bar{\tau}^{\gamma\gamma}\frac{\partial\tilde{v}^\alpha}{\partial x_\alpha}+\frac{1-y_k-C_2y_\varepsilon\varepsilon^*/\tilde{k}}{\theta}\bar{\rho}\varepsilon\end{aligned} \quad (15)$$

We have written as $\tau_d^{\alpha\beta}$ and $R_d^{\alpha\beta}$ the deviators of the tensors $\tau^{\alpha\beta}$ and $R^{\alpha\beta}$, and $-J_k^\alpha$ is the diffusion term of (6). We recognize in this equation a diffusion term, the first on the right hand side, and all the following terms do constitute entropy production terms.
Before discussing the implications of the second principle, it is of interest to discuss the physical meaning of each term and to precise the equations of state. The first remark that has to be done is that the pressure has not to appear in the entropy production term, because it is not a source of irreversibility. Then the terms where the pressure appears have to be zero, and that implies that $\pi=\bar{p}+\frac{2}{3}\bar{\rho}\tilde{k}y_k+\frac{2}{3}\bar{\rho}C_3y_\varepsilon\varepsilon^*$ and $1-y_k-C_4\frac{\varepsilon^*}{\tilde{k}}y_\varepsilon=0$.
In addition, within the last term of (15), the directly scalar part of the entropy production, there is one contribution of the energy equation but also the contribution $-(y_k+C_2\frac{\varepsilon^*}{\tilde{k}}y_\varepsilon)$ is due to the destruction terms of the equations for $\tilde{k}$ and ε^*. Globally, this term has to be positive, but the contribution of $\tilde{k}$ and ε^* may be dangerous for that. This problem is cancelled by choosing $y_k+C_2\frac{\varepsilon^*}{\tilde{k}}y_\varepsilon=0$, and that corresponds to a "mutual equilibrium of destructions rates" for $\tilde{k}$ and ε^*. Assuming this mutual equilibrium ensures that no additional irreversibility is brought by this new kind of model.
These three relations do determine constraints on the equations of state, or on the C's. It has to be remarked that the equation (14) has been built, and most often used, for cases where

the turbulence is incompressible, then the divergence of the velocity fluctuations is vanishing, and the relation $1-y_k-C_4\frac{\varepsilon^*}{\tilde{k}}y_\varepsilon=0$ does not matter in this circumstance.

Taking into account $y_k+C_2\frac{\varepsilon^*}{\tilde{k}}y_\varepsilon=0$ and $\pi=\bar{\rho}R\tilde{T}+\frac{2}{3}\bar{\rho}\tilde{k}y_k+\frac{2}{3}\bar{\rho}C_3y_\varepsilon\varepsilon^*$, $\tilde{e}=C_v\tilde{T}+e^0$ as well as the six Maxwell relations (saying that the second partial derivatives of $\varsigma=\varsigma(\tilde{e},1/\bar{\rho},\tilde{k},\varepsilon^*)$ are identical when the derivation variables are commuted), it is possible with a few algebra to find a convenient set of four equations of state only in the case where C_3/C_2 is a constant (possibly zero). The solution is:

$$\pi=\bar{\rho}R\theta,\ \tilde{e}-e^0=C_v\theta(1-\frac{2R_k}{3R}+\frac{2R_kC_3}{3RC_2})=C_v\tilde{T},\ y_k=R_k\frac{\theta}{\tilde{k}}\ \text{and}\ y_\varepsilon=-\frac{R_k\theta}{C_2\varepsilon^*},$$

where R_k is a positive constant (with y_k chosen positive, without loss of generality). These formulas are not the unique solution of the problem, but they constitute a solution that can be supported by measurements, as approximations, at least in a certain limited range of variation of of the variables. One can remark that for keeping θ positive, which is necessary in thermodynamics, it is necessary that $1>\frac{2R_k}{3R}(1-\frac{C_3}{C_2})$.

We can now discuss in details the implications of the second principle, which prescribes that the entropy production rate, the right hand side of the following equation (16), has to be always positive, or zero at equilibrium.

$$\bar{\rho}\frac{D\varsigma}{Dt}-\frac{\partial}{\partial x_\alpha}(\frac{\bar{j}_\alpha^Q+\overline{\rho v'^\alpha e}}{\theta}+\frac{y_kJ_k^\alpha+y_\varepsilon J_\varepsilon^\alpha}{\theta})=(\bar{j}_\alpha^Q+\overline{\rho v'^\alpha e})\frac{\partial 1/\theta}{\partial x_\alpha}+J_k^\alpha\frac{\partial y_k/\theta}{\partial x_\alpha}+J_\varepsilon^\alpha\frac{\partial y_\varepsilon/\theta}{\partial x_\alpha}-$$
$$-\frac{1-y_k+y_kC_4/C_2}{\theta}\overline{p\frac{\partial v'^\beta}{\partial x_\beta}}-y_k\frac{1-C_1/C_2}{\theta}\bar{\rho}R_d^{\alpha\beta}\frac{\partial\tilde{v}^\beta}{\partial x_\alpha}+\frac{1}{\theta}\bar{\tau}_d^{\alpha\beta}\frac{\partial\tilde{v}^\beta}{\partial x_\alpha}+\frac{1}{3\theta}\bar{\tau}^{\gamma\gamma}\frac{\partial\tilde{v}^\alpha}{\partial x_\alpha}+\frac{1}{\theta}\bar{\rho}\varepsilon \quad (16)$$

We know already that $\tau^{\gamma\gamma}=\mu_v\frac{\partial v^\alpha}{\partial x_\alpha}$ and $\tau_d^{\alpha\beta}=\mu\,(\frac{\partial v^\beta}{\partial x_\alpha}+\frac{\partial v^\beta}{\partial x_\alpha}-\frac{\delta^{\alpha\beta}}{3}\frac{\partial v^\gamma}{\partial x_\gamma})$ with μ_v and μ_v positive, in such a way that $\tau^{\alpha\beta}\frac{\partial v^\beta}{\partial x_\alpha}$ is always positive, or zero if the velocity gradients are zero. We remember also that $\bar{\rho}\varepsilon=\overline{\tau^{\alpha\beta}\frac{\partial v'^\beta}{\partial x_\alpha}}$, and then the three last term can be grouped giving $\frac{1}{\theta}\overline{\tau^{\alpha\beta}\frac{\partial v^\beta}{\partial x_\alpha}}$.Then, the group of the three last term of (16) is clearly always positive, by definition, even if the two first ones are not positive, depending on the fluctuations of density.

Secondly, the term $-\frac{y_k}{\theta}(1-C_1/C_2)\bar{\rho}R_d^{\alpha\beta}\frac{\partial\tilde{v}^\beta}{\partial x_\alpha}$ concerning the influence of turbulent friction has also to be positive always, or zero. At the same time, we remember that $-\bar{\rho}R_d^{\alpha\beta}\frac{\partial\tilde{v}^\beta}{\partial x_\alpha}$ is a

production term for $\tilde{k}$ and has to be essentially positive, although not necessarily everywhere. With C_2, C_1 constant, it is implied that $1-C_1/C_2$ is necessarily positive and then the linear irreversible thermodynamics again supports the Boussinesq relation, here written for compressible flows: $-\overline{\rho}R_d^{\alpha\beta}=\mu_t(\frac{\partial\tilde{v}^\beta}{\partial x_\alpha}+\frac{\partial\tilde{v}^\beta}{\partial x_\alpha}-\frac{1}{3}\frac{\partial\tilde{v}^\gamma}{\partial x_\gamma}\delta^{\alpha\beta})$, with μ_t positive.

Here again, we have to write $\mu_t=\overline{\rho}C_l\tilde{k}^{1/2}l_t=\overline{\rho}C_\mu\tilde{k}^2/\varepsilon$, C_μ being positive, constant or function of the Reynolds number of turbulence, defined here as $\mathrm{Re}_t=\tilde{k}^2/\varepsilon\mu$, if this number is sufficiently small. This is exactly what is used in all versions of the k-epsilon model. For versions able to consider small turbulence Reynolds number, $1-C_1/C_2$ may become negative, and in this case this term has to be smaller than the three last terms corresponding to $\frac{1}{\theta}\overline{\tau^{\alpha\beta}\frac{\partial v^\beta}{\partial x_\alpha}}\approx\frac{1}{\theta}\overline{\tau^{\alpha\beta}}\frac{\partial\tilde{v}^\beta}{\partial x_\alpha}$.

The last point deals with the terms $(\overline{j_\alpha^Q}+\overline{\rho v'^\alpha e})\frac{\partial 1/\theta}{\partial x_\alpha}+J_k^\alpha\frac{\partial y_k/\theta}{\partial x_\alpha}+J_\varepsilon^\alpha\frac{\partial y_\varepsilon/\theta}{\partial x_\alpha}$. Again, we see that the modelling of $-J_k^\alpha$ and $-J_\varepsilon^\alpha$, as well as $-(\overline{j_\alpha^Q}+\overline{\rho v'^\alpha e})$ can be done in terms of $\frac{\partial\tilde{k}}{\partial x_\alpha}$, $\frac{\partial\varepsilon^*}{\partial x_\alpha}$ and $\frac{\partial\theta}{\partial x_\alpha}$, with possible coupling. No coupling has been attempted so far, however. The coefficients of diffusivity of turbulence kinetic energy, dissipation rate, and heat are all proportional to μ_t previously defined.

As previously for the Prandtl mixing length model, we see that the well known k-epsilon model can be perfectly explained in the frame work of irreversible linear thermodynamics. The constraints we have found that $C_2>C_1$ do correspond with the common practice for large turbulence. The value of C_3 is not well known, because the flows where $\frac{\partial\tilde{v}_\alpha}{\partial x_\alpha}\neq 0$ are more complex, but we have shown that we need $C_3/C_2=cst$ even if the C's are varying. Considering C_4, we have found that $1-R_k\frac{\theta}{\tilde{k}}(1-\frac{C_4}{C_2})=0$. That implies then a constraint for C_4, which is $C_4=C_2-\frac{\tilde{k}C_2}{\theta R_k}$. In case where the influence of $\tilde{k}/\theta$ is poor, $C_4=C_2$ simply. However, it remains to find an approximation for $\overline{p\frac{\partial v'^\alpha}{\partial x_\alpha}}$ when it is not negligible. In practice, this quantity plays only in flows where $\frac{\partial v'^\alpha}{\partial x_\alpha}\neq 0$, which are less well studied turbulent flows, and the experiments up to now have only confirmed that C_4 has not to be put to zero...

3. Irreversible thermodynamics for two phase flows models

The theoretical description of two-phase flows is now firmly based by describing at each instant this medium as piece-wise continuous, and then considering that the model has to

deal with statistical averages, like for turbulent flows (Drew, 1983). The randomness here is due both to the poorly known initial and limiting conditions concerning the presence of the phases, and to the existence of local perturbations permanently created by unstable phenomena within the flow, similarly to classical turbulent flows. There is again the need of defining how many mean variables are necessary, and of finding their equations. We first give here the set of variables and equations for representing the flow, without details concerning the calculations but with the relevant physical interpretation, and then we show how the Extended Irreversible Thermodynamics helps the modelling.

3.1 Variables and equations for two-phase flows modelling

The first classical attempt for representing a two-phase flow uses statistically averaged variables for volumetric mass, momentum, internal energy for the two phases, and their probability of presence, also known as the "volume fraction" of each phase. It is defined a "phase indicator" $\Phi_i(\vec{x},t)$ which is unity within the phase i and zero outside, and the statistical average $\overline{\Phi}_i(\vec{x},t)$ is nothing but the probability of presence of this phase. Of course, $\sum_{i=1,2} \overline{\Phi}_i(\vec{x},t) = 1$. For each phase, we define $\overline{\rho}_i = \overline{\Phi_i \rho_i} = \overline{\Phi}_i \overline{\rho}_i^*$, $\overline{\Phi_i \rho_i v_i^\alpha} = \overline{\rho}_i^* \overline{\Phi}_i \tilde{v}_i^\alpha$, $\overline{\Phi_i \rho_i e_i} = \overline{\rho}_i^* \overline{\Phi}_i \tilde{e}_i$.

The averaged forms of mass, momentum and energy equations can be found from the primitive equations for the piecewise continuous medium (Borghi, 2008). For momentum and energy they display additional diffusion fluxes due to the presence of local perturbations around the mean values, similarly as for the turbulent flows. We will call these terms "pseudo-turbulent" fluxes. The averaged equation for the mass of phase i is:

$$\frac{\partial}{\partial t}(\overline{\rho}_i^* \overline{\Phi}_i) + \frac{\partial}{\partial x_\alpha}(\overline{\rho}_i^* \overline{\Phi}_i \tilde{v}_i^\alpha) = -\overline{\rho_i v_{ri}^\alpha n_i^\alpha \sigma_s} \tag{17}$$

The last term on the R.H.S is the possible exchange of mass between the two phases: v_{ri}^α is the velocity of the phase i relative to the interface, non zero only when there is exchange of mass between phases (vaporization-condensation for instance) ; σ_s is the instantaneous interface area by unit of volume of the medium, mathematically defined by $-n_i^\alpha \sigma_s = \frac{\partial \Phi_i}{\partial x_\alpha}$, where n_i^α is the normal to the interface, oriented outward phase i. Of course, the gradient of the phase indicator has the structure of a Dirac peak, and σ_s is zero except on the interface (Kataoka, 1986). The averaged equation for the momentum of phase i is.

$$\frac{\partial}{\partial t}\left(\overline{\rho}_i^* \overline{\Phi}_i \tilde{v}_i^\beta\right) + \frac{\partial}{\partial x_\alpha}(\overline{\rho}_i^* \overline{\Phi}_i \tilde{v}_i^\alpha \tilde{v}_i^\beta) = \frac{\partial}{\partial x_\alpha}(\overline{\Phi}_i \overline{\sigma}_i^{*\alpha\beta} - \overline{\rho_i \Phi_i v'^\alpha_i v'^\beta_i}) + \overline{\rho}_i^* \overline{\Phi}_i g_\beta - \overline{\rho_i v_{ri}^\alpha n_i^\alpha v_i^\beta \sigma_s} + \overline{\sigma_i^{\alpha\beta} n_i^\alpha \sigma_s} \tag{18}$$

The pseudo turbulent momentum diffusion flux is $-\overline{\rho_i \Phi\, v'^\alpha_i v'^\beta_i}$. The two last terms of (18) represent the momentum given to the phase i by the other one, by exchange of mass and by the contact force, respectively. The tensor $\sigma_i^{\alpha\beta}$ is the Cauchy stress tensor within the phase i. The equation for the mean total energy of phase i is:

$$\frac{\partial}{\partial t}\left(\overline{\rho}_i^*\overline{\Phi}_i\tilde{e}_{ti}\right)+\frac{\partial}{\partial x_\alpha}(\overline{\rho}_i^*\overline{\Phi}_i\tilde{v}_i^\alpha\tilde{e}_{ti})=\frac{\partial}{\partial x_\alpha}(-\overline{\Phi}_i\overline{j_i^{Q\alpha}}^*+\overline{\Phi}_i\overline{\sigma_i^{\alpha\beta}}^*\tilde{v}_i^\beta+\overline{\Phi_i\sigma_i^{\alpha\beta}v_i'^\alpha}-\overline{\rho_i\Phi_i v_i'^\alpha e_{ti}})$$

$$+\overline{\rho}_i^*\overline{\Phi}_i\tilde{v}_i^\beta g_\beta-\overline{\rho_i v_{ri}^\alpha n_i^\alpha e_{ti}\sigma_s}+\overline{\sigma_i^{\alpha\beta}n_i^\alpha v_i^\beta\sigma_s}-\overline{j_i^{Q\alpha}n_i^\alpha\sigma_s} \tag{19}$$

The total energy is defined as $\tilde{e}_{ti}=\tilde{e}_i+\overline{\rho_i\Phi_i v_i^\alpha v_i^\alpha}/2\overline{\rho}_i=\tilde{e}_i+\tilde{v}_i^\alpha\tilde{v}_i^\alpha/2+\overline{\rho_i\Phi_i v_i'^\alpha v_i'^\alpha}/2\overline{\rho}_i$, the pseudo-turbulent energy flux is $-\overline{\rho_i\Phi\, v_i'^\alpha e_{ti}}$, and the last three terms are the exchanges of energy from the other phase, due to exchange of mass, power of contact force, and heat flux, respectively.

It is possible also to write a balance equation for the volume of phases, simply obtained from the convection equation of the field of $\Phi_i(\vec{x},t)$: $\frac{\partial}{\partial t}\Phi_i+v_s^\alpha\frac{\partial}{\partial x_\alpha}\Phi_i=\frac{\partial}{\partial t}\Phi_i+(v_i^\alpha-v_{ri}^\alpha)\frac{\partial}{\partial x_\alpha}\Phi_i=0$. When averaged, this equation gives:

$$\frac{\partial}{\partial t}\left(\overline{\Phi}_i\right)+\tilde{v}_i^\alpha\frac{\partial}{\partial x_\alpha}(\overline{\Phi}_i)=-\overline{v_i'^\alpha\frac{\partial\Phi_i}{\partial x_\alpha}}+\overline{v_{ri}^\alpha\frac{\partial\Phi_i}{\partial x_\alpha}} \tag{20}$$

The terms on the R.H.S. have to be approximated by models, the second one being only due to the exchange of mass between phases.

There are also important instantaneous interface conservation relations, linking at the interface the exchanges between the phases: first, the mass lost or gained by one phase is identical to the mass gained or lost by the other phase; second, if we neglect the surface tension phenomena, it follows that the momentum lost or gained by one phase is identical to the momentum gained or lost by the other one ; and third a similar relation holds for the total energy (Kataoka, 1986). That leads to:

$$\sum_{i=1,2}(\rho_i v_{ri}^\alpha n_i^\alpha)_s=0,\ \sum_{i=1,2}(-\rho_i v_{ri}^\alpha n_i^\alpha v_i^\beta+\sigma_i^{\alpha\beta}n_i^\alpha)_s=0,\ \sum_{i=1,2}(-\rho_i v_{ri}^\alpha n_i^\alpha e_{ti}+\sigma_i^{\alpha\beta}n_i^\alpha v_i^\beta-j_i^{Q\alpha}n_i^\alpha)_s=0 \tag{21}$$

At the interface, the tangential velocity and the temperature fields are continuous, but there are discontinuities of density, momentum and energy per unit mass. The equations (21) give "jump relations" relating the values of these quantities on both sides of the discontinuity. We will not consider further here the exchanges of mass between phases, and these relations are simplified as:

$$v_{r1}^\alpha=v_{r2}^\alpha=0,(\sigma_1^{\alpha\beta}n_1^\alpha)_s+(\sigma_2^{\alpha\beta}n_2^\alpha)_s=0,(\sigma_1^{\alpha\beta}n_1^\alpha v_1^\beta)_s+(\sigma_2^{\alpha\beta}n_2^\alpha v_2^\beta)_s=0,(j_1^{Q\alpha}n_1^\alpha)_s+(j_2^{Q\alpha}n_2^\alpha)_s=0 \tag{22}$$

The third relation of (22) is deduced from the second one because both phases have the same velocity on the interface.

The instantaneous behaviour of each phase has to be given by the knowledge of $\sigma_i^{\alpha\beta}$ and $j_i^{Q\alpha}$ as function of ρ_i, v_i^α, T_i. We will notice here $\sigma_i^{\alpha\beta}=-p_i\delta^{\alpha\beta}+\tau_i^{\alpha\beta}$ for any type of phase (but usually for a solid phase the pressure is defined by the third of the trace of $\sigma_i^{\alpha\beta}$, with an opposite sign). For a fluid phase, $\tau_i^{\alpha\beta}$ is the viscous stress tensor, which can be assumed Newtonian for instance, and an equation of state gives $p_i=p_i(\rho_i,T_i)$. For solid particles, we are not concerned with the full elasticity properties and we can limit the description as a "quasi-liquid", very viscous. For any type of phase the Fourier law for heat conduction can

be adopted and a Joule law linking the temperature to the internal energy can be considered, neglecting the energetic aspects of compressibility for liquid or solid phases. Very often it suffices to take $\rho_i = cst$.

One sees the similarities of the problem of modelling these equations with the one of modelling turbulence in single phase flows. We will show now how the irreversible thermodynamics can help this modelling task. For simplicity, we will consider in the sequel that there is no exchange of mass between the phases, this could be taken into account later.

3.2 Entropy for a simple two-phase flows model

We will consider the simple case of a model similar to the Prandtl mixing length model, where simply the variables: $\overline{\rho}_i^*, \tilde{v}_i^\alpha, \tilde{e}_i, \overline{\Phi}_i, i = 1,2$ have to be represented by their own balance equations. The development then follows the same path as § 2.2 above, but with two phases i=1, i=2.

The kinetic energies of fluctuations, namely $k_i = +\overline{\rho_i \Phi_i v_i'^\alpha v_i'^\alpha} / 2\overline{\rho}_i, i = 1,2$, follow a balance equation that can be found from the primitive equations. It writes, without exchange of mass:

$$\frac{\partial}{\partial t}(\overline{\rho}_i^* \overline{\Phi}_i k_i) + \frac{\partial}{\partial x_\alpha}(\overline{\rho}_i^* \overline{\Phi}_i k_i \tilde{v}_i^\alpha) = \frac{\partial}{\partial x_\alpha}(-\overline{\rho_i \Phi_i v_i'^\beta v_i'^\alpha v_i'^\alpha / 2} + \overline{\Phi_i v_i'^\beta \sigma_i'^{\alpha\beta}}) - \overline{\rho_i \Phi_i v_i'^\alpha v_i'^\beta} \frac{\partial \tilde{v}_i^\beta}{\partial x_\alpha}$$

$$+ \overline{p_i \Phi_i \frac{\partial v_i'^\alpha}{\partial x_\alpha}} - \overline{\rho}_i^* \overline{\Phi}_i \varepsilon_i + \overline{\sigma_i^{\alpha\beta} n_i^\beta v_i'^\alpha \sigma_s} \qquad (23)$$

We do not consider here, in the Prandtl mixing length framework, that each k_i does follow this full equation, we assume that it can be reduced to a local balance between production terms and destructions terms, giving simply that :

$$-\overline{\rho_i \Phi_i v_i'^\alpha v_i'^\beta} \frac{\partial \tilde{v}_i^\beta}{\partial x_\alpha} + \overline{p_i \Phi_i \frac{\partial v_i'^\alpha}{\partial x_\alpha}} + \overline{\sigma_i^{\alpha\beta} n_i^\beta v_i'^\alpha \sigma_s} = \overline{\rho}_i^* \overline{\Phi}_i \varepsilon_i \qquad (23')$$

The last term of (23) and (23') is due to the exchange of energy from the other phase, by the contact force.

With the point of view of the Prandtl model applied to both phases, we have to build an entropy with the variables $\overline{\rho}_i^*, \tilde{v}_i^\alpha, \tilde{e}_i, \overline{\Phi}_i, i = 1,2$, such as $\overline{\rho}\varsigma = \sum_{i=1,2} \overline{\rho}_i^* \overline{\Phi}_i \varsigma_i$, because entropy is an extensive quantity. The entropies of each phase are functions only of the variables of this phase, unlike molecular mixtures: $\varsigma_i = \varsigma_i(\overline{\rho}_i^*, \tilde{e}_i)$. As in § 2.2, we can adopt

$$\tilde{e}_i = \tilde{T}_i \varsigma_i - \overline{p}_i^* \frac{1}{\overline{\rho}_i^*} + \mu_i, \qquad d\tilde{e}_i = \tilde{T}_i d\varsigma_i - \overline{p}_i^* d(\frac{1}{\overline{\rho}_i^*})$$

Similarly, we take linear equations of state for phases, which can be averaged without needing additional variables. For a gaseous phases $\tilde{e}_i = C_{vi}\tilde{T}_i + e_i^0, \overline{p}_i^* = \overline{\rho}_i^* R_i \tilde{T}_i$, and for liquid or solid phases $\tilde{e}_s = C_s \tilde{T}_s + e_s^0, \overline{p}_s^* = K_s(\overline{\rho}_s^* - \rho_0)$, neglecting the influence of compressibility on the internal energy.

We can first show that the convective time derivative for the mean entropy of the medium is such that:

$$\overline{\rho}\frac{D\varsigma}{Dt}=\sum_i\overline{\rho}_i^*\overline{\Phi}_i\frac{D\varsigma_i}{Dt_i}-\frac{\partial}{\partial x_\alpha}(\sum_i\overline{\rho}_i^*\overline{\Phi}_i\varsigma_i(\tilde{v}_i^\alpha-\tilde{v}^\alpha)) \tag{24}$$

The convective time derivative for the medium follows the averaged velocity, while for the phases they follow the averaged velocity of each phase. Of course, the Euler-Gibbs relation is written now as:

$$\frac{D}{Dt_i}\tilde{e}_i=\tilde{T}_i\frac{D}{Dt_i}\varsigma_i-\overline{p}_i^*\frac{D}{Dt_i}(\frac{1}{\overline{\rho}_i^*}) \tag{25}$$

It is easy to verify that the equation (17) allows to write:

$\overline{\rho}_i^*\overline{\Phi}_i\frac{D}{Dt_i}(\frac{1}{\overline{\rho}_i^*})=-\frac{\overline{\Phi}_i}{\overline{\rho}_i^*}\frac{D\overline{\rho}_i^*}{Dt_i}=\overline{\Phi}_i\frac{\partial\tilde{v}_i^\alpha}{\partial x_\alpha}+\frac{D\overline{\Phi}_i}{Dt_i}$, without exchange of mass between phases. By using (20), we obtain as well:

$$\overline{\rho}_i^*\overline{\Phi}_i\frac{D}{Dt_i}(\frac{1}{\overline{\rho}_i^*})=\overline{\Phi}_i\frac{\partial\tilde{v}_i^\alpha}{\partial x_\alpha}-\overline{v'^\alpha_i\frac{\partial\Phi_i}{\partial x_\alpha}} \tag{26}$$

It is necessary then to obtain the balance equation for the mean internal energy of phases from (19), removing the kinetic energy of the mean motion by taking into account (18), and removing also the kinetic energy of the fluctuations with (23). It is found:

$$\begin{aligned}\overline{\rho}_i^*\overline{\Phi}_i\frac{D\tilde{e}_i}{Dt_i}&=\frac{\partial}{\partial x_\alpha}(-\overline{\Phi}_i\overline{j_i^{Q\alpha}}^*-\overline{\rho_i\Phi_i e_i v'^\alpha_i})-\overline{\Phi}_i\overline{p}_i^*\frac{\partial\tilde{v}_i^\alpha}{\partial x_\alpha}\\&+\overline{\Phi}_i\overline{\tau_i^{\alpha\beta}}^*\frac{\partial\tilde{v}_i^\beta}{\partial x_\alpha}-\overline{p_i\Phi_i\frac{\partial v'^\beta_i}{\partial x_\beta}}-\overline{j_i^{Q\alpha}n_i^\alpha\sigma_s}+\overline{\rho}_i^*\overline{\Phi}_i\varepsilon_i\end{aligned} \tag{27}$$

With (23'), it gives:

$$\overline{\rho}_i^*\overline{\Phi}_i\frac{D\tilde{e}_i}{Dt_i}=\frac{\partial}{\partial x_\alpha}(-\overline{\Phi}_i\overline{j_i^{Q\alpha}}^*-\overline{\rho_i\Phi_i e_i v'^\alpha_i})-\overline{\Phi}_i\overline{p}_i^*\frac{\partial\tilde{v}_i^\alpha}{\partial x_\alpha}+\overline{\Phi}_i(\overline{\tau_i^{\alpha\beta}}^*-\overline{\rho}_i^*R_i^{\alpha\beta})\frac{\partial\tilde{v}_i^\beta}{\partial x_\alpha}$$
$$-\overline{j_i^{Q\alpha}n_i^\alpha\sigma_s}+\overline{\sigma_i^{\alpha\beta}n_i^\beta v'^\alpha_i\sigma_s},$$

where $R_{id}^{\alpha\beta}$ is the deviator of the Reynolds tensor for phase i. The two last terms take into account the exchange of heat by conduction $\overline{\varphi}_i^Q=-\overline{j_i^{Q\alpha}n_i^\alpha\sigma_s}$ and the exchange of kinetic energy by contact force $\overline{\sigma_i^{\alpha\beta}n_i^\beta v'^\alpha_i\sigma_s}$, respectively, from the other phase. In the momentum balance (18) the total contact force has to be split in $\overline{\sigma_i^{\alpha\beta}n_i^\beta\sigma_s}=+\overline{p}\frac{\partial\overline{\Phi}_i}{\partial x_\alpha}+\overline{F}_{si}^{\times\beta}$. The first part is simply the influence of the variation of the volume of the phase, while $\overline{F}_{si}^{\times\beta}=\overline{\tau_i^{\times\alpha\beta}n_i^\alpha\sigma_s}$ is really the force from the other phase, and the jump condition (22) gives $\sum_{i=1,2}\overline{F}_{si}^{\times\beta}=0$. It follows that $\overline{\sigma_i^{\alpha\beta}n_i^\beta v'^\alpha_i\sigma_s}=+\overline{p}\overline{v'^\alpha_i\frac{\partial\Phi_i}{\partial x_\alpha}}+\overline{F_{si}^{\times\alpha}v'^\alpha_i}$, giving finally:

$$\overline{\rho}_i^*\overline{\Phi}_i\frac{D\tilde{e}_i}{Dt_i}=\frac{\partial}{\partial x_\alpha}(-\overline{\Phi}_i\overline{j_i^{Q\alpha}}^*-\overline{\rho_i\Phi_i e_i v'^\alpha_i})-\overline{\Phi}_i\overline{p}_i^*\frac{\partial\tilde{v}_i^\alpha}{\partial x_\alpha}+\overline{\Phi}_i(\overline{\tau_i^{\alpha\beta}}^*-\overline{\rho}_i^*R_i^{\alpha\beta})\frac{\partial\tilde{v}_i^\beta}{\partial x_\alpha}$$

$$-\overline{j_i^{Q\alpha}n_i^\alpha\sigma_s}+\overline{p}\,\overline{v'^\alpha_i\frac{\partial\Phi_i}{\partial x_\alpha}}+\overline{F_{si}^{\times\alpha}v'^\alpha_i} \tag{28}$$

Now from (24), (25), (26), (27), we obtain the entropy balance equation for the medium:

$$\overline{\rho}\frac{D\varsigma}{Dt}=\frac{\partial}{\partial x_\alpha}(-\sum_i(\overline{\rho}_i^*\overline{\Phi}_i\varsigma_i(\tilde{v}_i^\alpha-\tilde{v}^\alpha)+\frac{\overline{\Phi}_i}{\tilde{T}_i}\overline{j_i^{Q\alpha}}^*+\overline{\frac{\rho_i\Phi_i e_i v'^\alpha_i}{\tilde{T}_i}}))+\sum_i-(\overline{\Phi}_i\overline{j_i^{Q\alpha}}^*+\overline{\rho_i\Phi_i e_i v'^\alpha_i})\frac{\partial}{\partial x_\alpha}(\frac{1}{\tilde{T}_i})$$

$$+\sum_i\frac{\overline{\Phi}_i}{\tilde{T}_i}(\overline{\tau_i^{\alpha\beta}}^*-\overline{\rho}_i^*R_i^{\alpha\beta})\frac{\partial\tilde{v}_i^\beta}{\partial x_\alpha}+\sum_i\overline{\frac{F_{si}^{\times\beta}v'^\beta_i}{\tilde{T}_i}}-\sum_i\frac{\overline{p}_i^*-\overline{p}}{\tilde{T}_i}\overline{v'^\alpha_i\frac{\partial\Phi_i}{\partial x_\alpha}}+\sum_i\frac{\overline{\varphi}_i^Q}{\tilde{T}_i} \tag{29}$$

We recognize in this equation the rate of production of entropy, which has to be positive or zero in any case.

The last sum deals with the exchange of heat between the phases. As $\sum_{i=1,2}\overline{\varphi}_i^Q=0$, this term can be written as: $\overline{\varphi}_1^Q(\frac{1}{\tilde{T}_1}-\frac{1}{\tilde{T}_2})$, and the linear classical irreversible thermodynamics proposes $\overline{\varphi}_1^Q\propto(\frac{1}{\tilde{T}_1}-\frac{1}{\tilde{T}_2})$.

The second last term involves $\overline{v'^\alpha_i\frac{\partial\Phi_i}{\partial x_\alpha}}$, expression implied in the closure of (20), and we see that assuming that $\overline{p}_i^*=\overline{p}$ eliminates this term and at the same time the need of (20). Instead of this assumption, the linear irreversible thermodynamics suggests the hypotheses that $-\overline{v'^\alpha_i\frac{\partial\Phi_i}{\partial x_\alpha}}\propto(\overline{p}_i^*-\overline{p})$ and gives a closure for (20). The phase volume fraction can be calculated then with $\frac{\partial}{\partial t}(\overline{\Phi}_i)+\tilde{v}_i^\alpha\frac{\partial}{\partial x_\alpha}(\overline{\Phi}_i)=-\overline{v'^\alpha_i\frac{\partial\Phi_i}{\partial x_\alpha}}=K(\overline{p}_i^*-\overline{p})$. Such an equation is almost identical to the equation proposed by M. Baer and I. Nunziato for compressed granular medium (Baer & Nunziato, 1986).

The two first terms of the entropy production deal with the diffusion fluxes of heat and momentum. For momentum, when each phase is divergence free (which is originally the scope of Prandtl model), we find for each phase the same formulation as for a single phase turbulent flow in §2.2. Similarly, for heat diffusion, if this term is considered uncoupled with others, the classical model found in §2.2 is again obtained for each phase.

The term $\sum_i\overline{\frac{F_{si}^{\times\beta}v'^\beta_i}{\tilde{T}_i}}=\sum_i\frac{1}{\tilde{T}_i}(\overline{F_{si}^{\times\beta}v_i^\beta}-\overline{F}_{si}^{\times\beta}\tilde{v}_i^\beta)$ is connected with the exchange of momentum between phases. The "jump relations" (22), similarly as $\sum_{i=1,2}\overline{F}_{si}^{\times\beta}=0$, gives $\sum_{i=1,2}\overline{F_{si}^{\times\beta}v_i^\beta}=0$ (and gave $\sum_{i=1,2}\overline{\varphi}_i^Q=0$ previously used). Because at the interface between the phases the

velocities of phases are equal, an averaged interface velocity $\overline{v}_s^\beta$ can be defined such that $\overline{F_{si}^{\times\beta} v_i^\beta} = \overline{F}_{si}^{\times\beta} \overline{v}_s^\beta$, and the related source term of entropy can be written $\sum_i \frac{1}{\tilde{T}_i} \overline{F}_{si}^{\times\beta} (\overline{v}_s^\beta - \tilde{v}_i^\beta)$. The classical linear irreversible thermodynamics leads to $\overline{F}_{si}^{\times\beta} = K_i (\overline{v}_s^\beta - \tilde{v}_i^\beta)$, and with $\overline{F}_{s1}^{\times\beta} = -\overline{F}_{s2}^{\times\beta}$, that gives an expression for the averaged interface velocity : $\overline{v}_s^\beta = \frac{K_1 \tilde{v}_1^\beta + K_2 \tilde{v}_2^\beta}{K_1 + K_2}$.

The K_i are positive constants, depending on the characteristics of the two phases in contact, to be found with experiments. If we consider the possibility of a coupling, in agreement with the so called Curie theorem, we find that it is possible that the contact force $\overline{F}_{si}^{\times\beta}$ to the phase i is linked to the gradients of temperature within the phases. We recover here a "thermophoretic "effect.

All these discussions do justify the assumptions currently done for the modelling of two-phase flows, in a large range of applications.

4. Irreversible thermodynamics for modelling of granular media

Granular flows are nothing but two-phase flows of solid irregular particles within a gaseous or liquid phase. But the high number of particles per unit of volume, and the low velocity that may persist allow numerous and long duration contacts between the particles, unlikely to usual two-phase flows. The approach that has been presented in §3 for two phase flows can be used also, but the problem that arises immediately is that very often the solid phase, locally, is built with two or three particles (or more) in contact, and consequently the solid here is not a true solid for which behaviour laws are known. Actually, each grain is one solid, but a couple of grains does not. So, it is necessary to consider the medium as a multi-phase medium, where each grain represents one phase. This approach has been proposed recently by R.Borghi and S.Bonelli (Borghi § Bonelli, 2007), and we will develop a while its connection with Irreversible Thermodynamics.

4.1 Basic equations for granular media

For granular media, the equations (17) to (20) do hold, but we can simplify them because it is not needed to follow the motion of each grain. Considering that there are N solid grains, there are N+1 phases and N+1 $\overline{\rho}_i^*, \tilde{v}_i^\alpha$, but we are interested only in the knowledge of $\overline{\Phi}_g = \sum_{i=1,N} \overline{\Phi}_i, \overline{\rho}_g^* \overline{\Phi}_g = \sum_{i=1,N} \overline{\Phi_i \rho_i}, \overline{\rho}_g^* \tilde{v}_g^\alpha \overline{\Phi}_g = \sum_{i=1,N} \overline{\rho_i \Phi_i v_i^\alpha}$, and $\overline{\rho}_f^* \equiv \overline{\rho}_{N+1}^*, \tilde{v}_f^\alpha \equiv \tilde{v}_{N+1}^\alpha$. From (17), (18), we get the mass and momentum balance equations of the "grains phase" as:

$$\frac{\partial}{\partial t}(\overline{\rho}_g^* \overline{\Phi}_g) + \frac{\partial}{\partial x_\alpha}(\overline{\rho}_g^* \overline{\Phi}_g \tilde{v}_g^\alpha) = 0 \tag{30}$$

Here the mean intrinsic density of the grains $\overline{\rho}_g^*$ can be considered generally as known and constant. If all the grains are made with the same almost incompressible solid, $\overline{\rho}_g^*$ is the density of this solid $\overline{\rho}_g^* = \rho_s$.

$$\frac{\partial}{\partial t}\left(\overline{\rho}_g^*\overline{\Phi}_g\tilde{v}_g^\beta\right)+\frac{\partial}{\partial x_\alpha}(\overline{\rho}_g^*\overline{\Phi}_g\tilde{v}_g^\alpha\tilde{v}_g^\beta)=\frac{\partial}{\partial x_\alpha}(\sum_{i=1,N}\overline{\Phi}_i\overline{\sigma}_i^{*\alpha\beta}-\sum_{i=1,N}\overline{\rho_i\Phi_i v''^\alpha_i v''^\beta_i})+\overline{\rho}_g^*\overline{\Phi}_g g_\beta$$

$$+\sum_{i=1,N}\overline{\sigma_i^{\alpha\beta}n_i^\alpha\sigma_s^i} \qquad (31)$$

We see that the effective Cauchy stress tensor for the grains has two parts: $\overline{\sigma}_{tg}^{\alpha\beta}=\sum_{i=1,N}\overline{\Phi}_i\overline{\sigma}_i^{*\alpha\beta}-\sum_{i=1,N}\overline{\rho_i\Phi_i v''^\alpha_i v''^\beta_i}$. The first one takes into account the stresses within the grains but mainly also the influences of the lasting contacts, with friction between grains depending on pertinent laws, and we can call it "mean Cauchy stress of lasting contacts"; the second one is due to the velocity fluctuations, here defined with respect to the averaged velocity of all the grains: $v''^\alpha_i=v_i^\alpha-\tilde{v}_g^\alpha$, and is similar to the Reynolds tensor for turbulent flows, and we will call it "mean kinetic stress". It is important only when the motion of the medium is well established, but even with slow mean motion there are some large and sudden fluctuations of velocity. The modelling of both terms has to be studied with care. Without models, eq.(31) is without interest.

The last term of (31) is the influence of the fluid phase. Indeed, the contact forces between grains do compensate themselves in the summation, and only the contact force with the fluid remains. More precisely, as in §2., we have $\sum_{i=1,N}\overline{\sigma_i^{\alpha\beta}n_i^\alpha\sigma_s^i}=-\overline{\sigma_f^{\alpha\beta}n_f^\alpha\sigma_s^f}=-\overline{p}_f^*\frac{\partial\overline{\Phi}_f}{\partial x_\beta}+\overline{F_f^\beta}$, where $\overline{F_f^\beta}$ is the pure contact force of the fluid on the grains.

When the fluid is air, or any gas whose intrinsic density is very small with respect of the solid, $\overline{\rho}_f^*\ll\rho_s$, we have $\overline{\rho}_g^*\overline{\Phi}_g\simeq\overline{\rho}$ and $\overline{\rho}_g^*\overline{\Phi}_g\tilde{v}_g^\alpha\simeq\overline{\rho}\tilde{v}^\alpha$. In addition, the contact force and the gradient of fluid pressure (which is of the order of $\overline{\rho}_f^*g_\beta\ll\overline{\rho}_g^*g_\beta$) are negligible in (31). Then equation (30) is nothing but the averaged continuity equation for the entire medium, and (31) gives the averaged momentum balance for the entire medium:

$$\frac{\partial}{\partial t}\left(\overline{\rho}\tilde{v}^\beta\right)+\frac{\partial}{\partial x_\alpha}(\overline{\rho}\tilde{v}^\alpha\tilde{v}^\beta)=\frac{\partial}{\partial x_\alpha}(\sum_{i=1,N}\overline{\Phi}_i\overline{\sigma}_i^{*\alpha\beta}-\overline{\Phi}_f\overline{p}_f^*\delta^{\alpha\beta}-\sum_{i=1,N}\overline{\rho_i\Phi_i v''^\alpha_i v''^\beta_i})+\overline{\rho}g_\beta \qquad (32)$$

The averaged total energy of the grains can also be studied, following the same route, and from (19) a balance equation for the mean total energy of the grains phase can be written similarly. From this equation, by removing the kinetic energy of mean motion and the kinetic energy of fluctuating motions, we can get an equation for the mean internal energy of the grains phase, similar to (28). When the fluid is light, and has a temperature similar to the one of the grains, this equation is nothing but the mean internal energy equation for the entire medium:

$$\frac{\partial}{\partial t}\overline{\rho}\tilde{e}+\frac{\partial}{\partial x_\gamma}(\overline{\rho}\tilde{v}_\gamma\tilde{e})=\frac{\partial}{\partial x_\gamma}(-\overline{\varphi}_{Qt}^\gamma)+(\sum_{i=1,N}\overline{\Phi}_i\overline{\sigma}_i^{*\alpha\beta}-\overline{\Phi}_f\overline{p}_f^*\delta^{\alpha\beta}-\sum_{i=1,N}\overline{\rho_i\Phi_i v''^\alpha_i v''^\beta_i})\frac{\partial\tilde{v}^\beta}{\partial x_\alpha} \qquad (33)$$

We have neglected in (33) the viscous friction in the fluid phase.
The equations (32) and (33) need closure assumptions for the contact stress tensor and the Reynolds-like tensor, before being useful. The fluid pressure can be calculated with the momentum equation for the fluid phase, often reduced simply as $-\frac{\partial \overline{p}_f^*}{\partial x_\beta} + \overline{\rho}_f^* g_\beta = 0$.

The modelling of the lasting contact stress tensor $\overline{\sigma}_{cg}^{\alpha\beta} = \sum_{i=1,N} \overline{\Phi}_i \overline{\sigma}_i^{*\alpha\beta}$ has been studied in details in (Borghi & Bonelli, 2007). We will only summarize their results in the next paragraph, but we will develop the question how the irreversible thermodynamics can help this modelling. The kinetic contribution, due to the velocities fluctuations, can be modelled with the principles that have been described in the first part of this chapter, and we will discuss this point in §4.3.

4.2 The modelling of the mean Cauchy stress tensor of lasting contacts

The approach of Borghi and Bonelli gives an evolution equation for $\overline{\sigma}_{cg}^{\alpha\beta}$. The grains are assumed elastic, with small strains but large possible displacements, and the contacts are displaying partly a reversible behaviour, as proposed by B.Cambou (Cambou,1998, Emeriault & Cambou, 1996), and partly irreversible sliding. The obtained evolution equation displays the rotational objective derivative of Jaumann, without any additional assumption:

$$\frac{\partial}{\partial t}\overline{\sigma}_{cg}^{\alpha\beta} + \frac{\partial}{\partial x_\gamma}(\overline{\sigma}_{cg}^{\alpha\beta}\tilde{v}_g^\gamma) = -\frac{\partial}{\partial x_\gamma}(\overline{\sigma_{cg}^{\alpha\beta} v_g^{\prime\gamma}}) + (\overline{\underset{\sim}{\varsigma}}^e)^{\alpha\beta\gamma\delta} : \left(\overline{\Phi}_g (\frac{\partial \overline{v}_g^\delta}{\partial x_\gamma})_{sym} - \overline{\mathbf{D}}^{p\gamma\delta} - \overline{\mathbf{D}}^{f\gamma\delta} \right)$$

$$-2\left(\overline{\sigma_g^{\alpha\gamma}\omega_c^{\gamma\beta}}\right)_{sym} - 2\left(\overline{\sigma_g^{\alpha\gamma}.Q_g^{\prime\gamma\beta}}\right)_{sym} - 2\left(\overline{\sigma}_g^{\alpha\gamma}.\overline{Q}_g^{\gamma\beta}\right)_{sym} \qquad (34)$$

The first term on the R.H.S. is a classical dispersion term due to the fluctuations of the velocity and appears for any averaged quantity within a "randomly moving" medium. The appearance of the Jaumann objective derivative is justified by the last term, $\overline{Q}_g^{\gamma\beta}$ being the averaged rotation rate tensor of the medium, mainly related to $(\frac{\partial \overline{\Phi}_g \overline{v}_g^\gamma}{\partial x_\beta})_{skew}$. The tensor $\overline{\underset{\sim}{\varsigma}}^e$ (fourth order) is an effective elastic stiffness tensor of the medium, due to the elastic behaviour within the grains and also particularly of the lasting contacts. The tensor $\overline{D}^p$ is due to the irreversible sliding in the contact zone between two grains, and $\overline{D}^f$ is related to the change of shape of "void volume" between the grains. The two following terms are due to the correlations of the fluctuations of the Cauchy stress with the ones of the rotation rates of the contacts and of the medium, respectively. They are not expected to be important terms. All the details concerning the definition of these terms can be found in (Borghi & Bonelli, 2007). Similarly as for turbulent and two-phase flows previously discussed, most of these terms, even when their physical meaning is clear, are not under a closed form in this equation, because the influence of fluctuations are imbedded within them, and they have to be modelled. We can remark that both the unweighted and weighted averaged velocities appeared, but when $\overline{\rho}_g^* = \rho_s$ these two velocities are equal.

By definition $\overline{\sigma}_{cg}^{\alpha\beta}$ is an averaged quantity for solid grains, $\overline{\sigma}_{cg}^{\alpha\beta} = \sum_{i=1,N} \overline{\Phi}_i \overline{\sigma}_i^{*\alpha\beta}$, we can define as well an intrinsic mean contact stress tensor as $\overline{\Phi}_g \overline{\sigma}_{cg}^{*\alpha\beta} = \overline{\sigma}_{cg}^{\alpha\beta} = \sum_{i=1,N} \overline{\Phi}_i \overline{\sigma}_i^{*\alpha\beta}$. Equation (33), together with (30), can give an equation for $\overline{\sigma}_{cg}^{*\alpha\beta}$, and also equations for the trace and deviator of this tensor. The elastic stiffness tensor $\overline{\underline{c}}^e$ has been formally defined, but it cannot be written explicitly, only numerical calculations have been done (Emeriault & Cambou, 1996). Even its dependence on $\overline{\Phi}_g$ cannot be theoretically written**.** For a statistically homogeneous and isotropic granular medium submitted to an isotropic stress, it will result that this elastic stiffness tensor can be represented with simply an effective compression modulus and an effective shear modulus, say χ^e, G^e. These quantities are not necessarily constant, and in particular they depend on $\overline{\Phi}_g$, in an unknown manner. We will consider in the sequel this case for simplicity, but the general case can be developed as well. Then, the equation for the trace and for the deviator of $\overline{\sigma}_{cg}^{*\alpha\beta}$ are simply written in terms of χ^e, G^e. If we take into account (30), remembering that we consider $\overline{\rho}_g^* = \rho_s$ as constant and defining $\pi_g^* = -trace(\overline{\sigma}_g^*)/3$, it comes:

$$\overline{\Phi}_g \frac{d}{dt}\overline{\pi}_g^* = -\frac{\partial}{\partial x_\alpha}(\overline{\pi_g^* \Phi_g v'^\alpha_g}) - 3\chi^e \overline{\Phi}_g \frac{\partial \tilde{v}_g^\alpha}{\partial x_\alpha} + \overline{I} \tag{35}$$

The last term groups all the irreversible effects of sliding contacts, $\overline{I} = tr(\overline{\underline{c}}^e : (\overline{D}^p + \overline{D}^f))/3$.

$$\overline{\Phi}_g \frac{d}{dt}\overline{\sigma}_{cd}^{*\alpha\beta} = -\frac{\partial}{\partial x_\gamma}(\overline{\sigma_{cd}^{*\alpha\beta} \Phi_g v'^\gamma_g}) + 2G^e \overline{\Phi}_g (\frac{\partial \overline{v}_g^\beta}{\partial x_\alpha})_{sym}^d - \overline{I}_d^{\alpha\beta} - 2\overline{\Phi}_g (\overline{\sigma}_{gd}^{*\alpha\gamma} \overline{Q}_g^{\gamma\beta})_{skew} \tag{36}$$

$\overline{I}_d^{\alpha\beta}$ is a second order tensor, without trace, taking into account of all the irreversible effects resulting in production and destruction for the effective Cauchy tensor of contacts. Now the modelling of $\overline{I}$ and $\overline{I}_d^{\alpha\beta}$ has to be discussed, and the extended irreversible thermodynamics will help us a lot.

The granular medium is described by the variables $\tilde{e}, \overline{\rho}, \overline{\pi}_g^*, \overline{\sigma}_{cd}^{*\alpha\beta}, \tilde{v}^\alpha$, for which we know balance equations, although some terms remain to be closed in it. First we will consider for simplicity only the case where the medium is "quasi-static". It is possible then to neglect all terms related to the fluctuations of velocity, and we can concentrate our attention on the closure of equation for the mean Cauchy stress of contacts, again in the framework of the Extended Irreversible Thermodynamics.

In this case, the entropy is simply: $\varsigma = \varsigma(\tilde{e}, 1/\overline{\rho}, \overline{\pi}_g^*, \overline{\sigma}_{gd}^{*\alpha\beta})$, and we can writes the Euler-Gibbs relation, introducing the pertinent partial derivatives: $d\varsigma = \frac{1}{T} d\tilde{e} + \frac{p}{T} d(\frac{1}{\overline{\rho}}) - \frac{y_p}{T} d\overline{\pi}_g^* - \frac{y_d^{\alpha\beta}}{T} d\overline{\sigma}_{gd}^{*\alpha\beta}$.

The balance equation of this entropy can again be found using the balance equations of the corresponding variables, i.e. (30), (34), (35), (36). After some algebra, it is found:

$$\bar{\rho}\frac{d}{dt}\varsigma = -\frac{\partial}{\partial x_\gamma}\left(\frac{\bar{\varphi}_Q^\gamma}{T}\right) + \bar{\varphi}_Q^\gamma \frac{\partial}{\partial x_\gamma}\left(\frac{1}{T}\right) + + \frac{\bar{\rho}}{T}\frac{\bar{\sigma}_{cd}^{*\alpha\beta}}{\rho_s}\left(\frac{\partial \tilde{v}_g^\beta}{\partial x_\alpha}\right)_{sym}^d - \frac{\bar{\rho}}{T}\frac{\bar{\pi}_g^*}{\rho_s}\frac{\partial \tilde{v}_g^\alpha}{\partial x_\alpha} - \frac{1}{T}\left(\bar{\Phi}_f \bar{p}_f^* - p\right)\frac{\partial \tilde{v}_g^\alpha}{\partial x_\alpha}$$
$$-\frac{y_p}{T}\left(-3\chi^e \bar{\rho}\frac{\partial \tilde{v}_g^\alpha}{\partial x_\alpha} + \rho_s \bar{I}\right) - \frac{y_d^{\alpha\beta}}{T}\left(2G^e \bar{\rho}\left(\frac{\partial \bar{v}_g^\beta}{\partial x_\alpha}\right)_{sym}^d - \rho_s \bar{I}_d^{\alpha\beta}\right) \qquad (37)$$

The reversible terms have to be cancelled in the entropy production. That implies three relationships giving three partial derivatives of the entropy, which prescribe three of the needed equations of state:

$$p = \bar{\Phi}_f \bar{p}_f^*,\ 2G^e y_d^{\alpha\beta} = \frac{\bar{\sigma}_{cd}^{*\alpha\beta}}{\rho_s},\ 3\chi^e y_p = \frac{\bar{\pi}_g^*}{\rho_s}$$

Then, the Maxwell relations give the form of the forth needed equation of state: $\tilde{e} = \frac{(\bar{\pi}_g^*)^2}{6\chi^e \rho_s} + \frac{\bar{\sigma}_{cd}^{*\alpha\beta}\bar{\sigma}_{cd}^{*\beta\alpha}}{4G^e \rho_s} + fct(T)$.

The entropy production rate of (37) can be rewritten as:

$$\bar{\rho} P_\varsigma = \bar{\varphi}_Q^\gamma \frac{\partial}{\partial x_\gamma}\left(\frac{1}{T}\right) - \frac{\bar{\pi}_g^* \bar{I}}{3T\chi^e} + \frac{\bar{\sigma}_{cd}^{*\alpha\beta} I_d^{\alpha\beta}}{2TG^e} \qquad (38)$$

In agreement with the Curie theorem, each term separately has to be positive. That gives, first, with a linear law, that the heat flux can be represented again with a Fourier law.
Concerning the effective contact Cauchy tensor, a first linear model could give:

$$\bar{I} = -\frac{3\chi^e}{\eta_v}\bar{\Phi}_g \bar{\pi}_g^*,\ \bar{I}_d^{\alpha\beta} = \frac{2G^e}{\eta}\bar{\Phi}_g \bar{\boldsymbol{\sigma}}_{cd}^{*\alpha\beta}.$$

The coefficients η, η_v are phenomenological viscosity coefficients, necessarily positive. The result would then be very similar to the old Maxwell model for visco-elastic materials.
But a very non linear model, with a threshold, could equally be compatible with the second principle, and may appear in better agreement with experiments for granular media. For instance, we could envisage (*H* being the Heaviside step function):

$$\bar{I} = -H(\pi_c - \bar{\pi}_g^*)\frac{3\chi^e}{\eta_v}\bar{\Phi}_g \frac{\left|\partial \bar{v}_g^\alpha / \partial x_\alpha\right|}{\pi_c}\bar{\pi}_g^* \qquad (39)$$

$$\bar{I}_d^{\alpha\beta} = H\left[\left(\bar{\boldsymbol{\sigma}}_{cd}^{*\alpha\beta}\bar{\boldsymbol{\sigma}}_{cd}^{*\alpha\beta}\right)^{1/2} - \left(k + \sin\phi\left|\bar{\pi}_g^*\right|\right)\right]\frac{2G^e}{\eta}\bar{\Phi}_g \frac{\left\|\left(\partial \bar{v}_g^\beta / \partial x_\alpha\right)_{sym}^d\right\|}{k + \sin\phi\left|\bar{\pi}_g^*\right|}\bar{\boldsymbol{\sigma}}_{cd}^{*\alpha\beta} \qquad (40)$$

The physical meaning of the discontinuity involved in (39) is that when the medium is compressed (then $\bar{\pi}_g^*$ is positive) more than the positive value π_c, the medium behaves very similarly to an elastic compressed solid, but when the medium is less compressed, or expanded, the normal contacts are lost in such a way that the "contact-pressure" decreases exponentially to zero due to $\bar{I}$.

With (40), the medium will remain "quasi-elastic" below one plastic limit defined by k and the angle ϕ. The existence of this limit is strongly suggested from numerical experiments with Discrete Elements Method, and experimental finding give that the medium may experience a "solid-fluid transition". The Mohr-Coulomb law displayed here is given just as example. The appearance of the solid fraction in $\overline{I}, \overline{I}_d^{\alpha\beta}$ is expected because they involve the mean interface area between grains per unit of volume, and this quantity increases with the fraction of grains. The simple linear dependence in this quantity may be replaced by an empirically found formula.
If we consider the closures (39), (40) for the equations (35), (36), beyond the plastic limit, in the case where the last two terms are predominant and counterbalancing themselves (because $\left\| (\partial \overline{v}_g^{\beta} / \partial x_{\alpha})_{sym}^{d} \right\|$ is very large), (35) and (36) are reduced into algebraic (then local) equations, giving simply:

$$\overline{\boldsymbol{\sigma}}_{cd}^{*\alpha\beta} = \eta(k + \sin\phi \left| \overline{\pi}_g^* \right|) \frac{(\partial \overline{v}_g^{\beta} / \partial x_{\alpha})_{sym}^{d}}{\left\| (\partial \overline{v}_g^{\beta} / \partial x_{\alpha})_{sym}^{d} \right\|} \text{, and } \overline{\pi}_g^* = -\eta_v \pi_c \frac{(\partial \overline{v}_g^{\alpha} / \partial x_{\alpha})}{\left| \partial \overline{v}_g^{\alpha} / \partial x_{\alpha} \right|}$$

A similar law has been proposed in 1994 (Hutter & Rajagopal, 1994) and recently studied with numerical simulations (Frenette et al. 2002).
Before the plastic limit, the medium is purely elastic if the first terms on RHS of (34) and (35) are negligible. We can specify then that $\overline{\pi}_g^* = \overline{\pi}_e^*, \overline{\sigma}_{cd}^{*\alpha\beta} = \overline{\sigma}_{ed}^{*\alpha\beta}$ and deduce the equations for these elastic stresses.

In this case, (34) is reduced to $\frac{d}{dt}\overline{\pi}_e^* = -3\chi^e \frac{\partial \tilde{v}_g^{\alpha}}{\partial x_{\alpha}}$. As (30) gives $\frac{d}{dt}(\overline{\rho}) = -\overline{\rho}\frac{\partial \tilde{v}_g^{\alpha}}{\partial x_{\alpha}}$, it follows that $\frac{d\overline{\pi}_e^*}{dt} = \frac{3\chi^e}{\overline{\rho}}\frac{d\overline{\rho}}{dt}$ and it gives nothing but that:

$$\overline{\pi}_g^* = \int \frac{3\chi^e}{\overline{\rho}} d\overline{\rho} \tag{41}$$

That means that the effective pressure due to the contacts is directly function of the mean volumetric mass of the medium, here simply $\overline{\rho} = \rho_s \overline{\Phi}_g$. Of course, the effective compression modulus may be also function of the mean volumetric mass, and so this relationship is not simply logarithmic. Physically, the effective pressure goes to infinity when the compaction goes to the maximum possible (to be empirically known), and becomes zero when the grains do not experience lasting contacts. There is again in this case a pressure between grains due to short collisions of fluctuating grains, but this pressure is taken into account in the second part of the total mean Cauchy stress tensor, which we will consider in the following paragraph.
Similarly, (35) gives for elastic situations:

$$\frac{d}{dt}\overline{\sigma}_{ed}^{*\alpha\beta} = +2G^e\left(\frac{\partial \overline{v}_g^{\beta}}{\partial x_{\alpha}}\right)_{sym}^{d} - 2\left(\overline{\sigma}_{ed}^{*\alpha\gamma}\left(\frac{\partial \overline{v}_g^{\gamma}}{\partial x_{\alpha}}\right)_{skew}^{d}\right)_{skew} \tag{42}$$

In any situation we can define an elastic part and an irreversible part for the stresses, $\overline{\pi}_g^* = \overline{\pi}_e^* + \overline{\pi}_i^*, \overline{\sigma}_{cd}^{*\alpha\beta} = \overline{\sigma}_{ed}^{*\alpha\beta} + \overline{\sigma}_{id}^{*\alpha\beta}$, where equations (41) and (42) give the elastic parts and the total is given by (35) and (36) with (39) and (40).

4.3 The modelling of the mean kinetic stress tensor

We consider now the contribution $-\sum_{i=1,N} \overline{\rho_i \Phi_i v''^{\alpha}_i v''^{\beta}_i}$, due to the fluctuations of the local velocities within the grains with respect to the mean velocity v^{α}_g of all the grains. This term is quite similar to the Reynolds stress for the turbulent flows, and that suggests that a model similar to turbulent models can be proposed. We will study now this modelling, considering that we have left the quasi static regime, and even that the motion of the granular medium is sufficiently fast in such a way that the total mean Cauchy stress tensor is dominated by the kinetic stress.

In this case, it is clear that we can apply the irreversible thermodynamics approach developed in §3.2 for usual two-phase flows, without lasting contacts, similar to the framework of the Prandtl mixing length. The result with a linear approximation will be that again a Boussinesq relation can be proposed for the mean kinetic stress:

$$-\sum_{i=1,N} \overline{\rho_i \Phi_i v''^{\alpha}_i v''^{\beta}_i} - \rho_s \bar{\Phi}_g \frac{2}{3}\delta^{\alpha\beta} k_g = \rho_s \bar{\Phi}_g \nu^{eff}_g \left(\frac{\partial \tilde{v}^{\alpha}_g}{\partial x_\beta} + \frac{\partial \tilde{v}^{\beta}_g}{\partial x_\alpha} - \frac{2}{3}\delta^{\alpha\beta}\frac{\partial \tilde{v}^{\gamma}_g}{\partial x_\gamma}\right) \tag{43}$$

Of course, we have defined $\rho_s \bar{\Phi}_g k_g = \frac{1}{2}\sum_{i=1,N} \overline{\rho_i \Phi_i v''^{\alpha}_i v''^{\alpha}_i}$. This quantity is the kinetic energy of fluctuations for the grains, related to what is called "granular temperature" (with a relation like $k_g = R_k T_G$) in the framework of granular gases. At the same time, this quantity is directly related to the normal mean kinetic stress: $P = +2\rho_s \bar{\Phi}_g k_g$.

It remains then to find a model for the "effective kinetic viscosity coefficient" ν^{eff}_g , and following again the same path a model similar to the Prandtl mixing length is necessarily found. Similarly as in §2.2, transposing formula (13), we have:

$$\nu^{eff}_g = C_g l_t^2 \left(\left(\frac{\partial \tilde{v}^{\alpha}_g}{\partial x_\beta} + \frac{\partial \tilde{v}^{\beta}_g}{\partial x_\alpha}\right)\left(\frac{\partial \tilde{v}^{\alpha}_g}{\partial x_\beta} + \frac{\partial \tilde{v}^{\beta}_g}{\partial x_\alpha}\right)\right)^{1/2} \tag{44}$$

In addition, it is shown in §2.2 that the kinetic energy of fluctuations is:

$$k_g = C_B l_t^2 \left(\frac{\partial \tilde{v}^{\alpha}}{\partial x_\beta} + \frac{\partial \tilde{v}^{\beta}}{\partial x_\alpha}\right)\left(\frac{\partial \tilde{v}^{\alpha}}{\partial x_\beta} + \frac{\partial \tilde{v}^{\beta}}{\partial x_\alpha}\right) \tag{45}$$

C_B, C_g are constants. In a simple case of sheared granular medium, that gives for the normal and the shear stresses P, T :

$$P = \frac{1}{2} C_B \bar{\rho} l_t^2 \left(\left|\frac{\partial V}{\partial y}\right|\right)^2, T / P = C_g / (2C_B) \tag{46}$$

In 1954, R.A.Bagnold has found in his pioneering experiment, for the highly sheared regime called "grain-inertia regime", a quite similar law (even if the reliability of the experimental results is not so clear, see Hunt et al., 2002). He found the length l_t was given proportionally to the mean diameter of the grains, as $l_t = d / ((\bar{\Phi}_{g\max} / \bar{\Phi}_g)^{1/3} - 1)$, (Bagnold, 1954).

How to specify this length scale is a critical point of the modelling. The framework of the Prandtl model does not say anything about it. The experiments of Bagnold have given an empirical law linking it to the solid fraction $\bar{\Phi}_g$, and to the grain diameter, but for turbulent flow, it has been found that this length scale is only related to the size of the experimental device. That is because the flow field imposes to the fluctuations its own scale. We can suspect that this can be true also for granular flows, meaning that the fluctuations do concern not simply each grain independently of the others, but some times, in some places, do concern groups of grains, whose size depends on the geometry of the flow. In this case, the law for the mixing length would necessarily take into account this geometry, as well to the grain diameter and the solid fraction…

It is not conceptually difficult to obtain a balance equation for k_g, following the same route as for two phase flows. Here, we can continue to neglect the friction force of fluid phase, but we keep the lasting contact Cauchy stress, which is the only source of dissipation of kinetic energy. Transposing (6), and recognizing the elastic parts and irreversible parts of the mean contact stresses $\sigma_{cg}^{\alpha\beta} = \sigma_{eg}^{\alpha\beta} + \sigma_{ig}^{\alpha\beta}, \sigma_{cd}^{\alpha\beta} = \sigma_{ed}^{\alpha\beta} + \sigma_{id}^{\alpha\beta}, \pi_g = \pi_e + \pi_i$, we get:

$$\frac{\partial}{\partial t}(\bar{\rho}\tilde{k}_g) + \frac{\partial}{\partial x_\alpha}(\bar{\rho}\tilde{v}_g^\alpha \tilde{k}_g) = \frac{\partial}{\partial x_\alpha}(\overline{v''^\beta_g \Phi_g \sigma_{cd}^{\alpha\beta}} - \overline{v''^\alpha_g \Phi_g \pi_g} - \bar{\Phi}_f \overline{v''^\alpha_f p_f} - \frac{1}{2}\rho_s \overline{\Phi_g v''^\alpha_g v''^\beta_g v''^\beta_g})$$

$$- \sum_{i=1,N} \overline{\rho_i \Phi_i v''^\alpha_i v''^\beta_i} \frac{\partial \tilde{v}_g^\beta}{\partial x_\alpha} + \overline{\pi_e \Phi_g \frac{\partial v''^\alpha_g}{\partial x_\alpha}} + \overline{p_f \Phi_f \frac{\partial v_f}{\partial x_\alpha}} - \bar{\Phi}_f \bar{p}_f^* \frac{\partial \tilde{v}_g^\alpha}{\partial x_\alpha} - \overline{\sigma_{ed}^{\alpha\beta} \Phi_g \frac{\partial v''^\beta_g}{\partial x_\alpha}} - \overline{\sigma_{ig}^{\alpha\beta} \Phi_g \frac{\partial v''^\beta_g}{\partial x_\alpha}} \quad (47)$$

The last term in this equation is nothing but the dissipation rate of kinetic energy, due to the irreversible effects of the contacts, that we can note $-\bar{\rho}\varepsilon_g$. The first term on the R.H.S. is a classical dispersion term, the second one is a production term directly related to the gradient of the mean velocity, which appears classical also. The other terms are responsible for transfer of kinetic energy from the elasticity of the grains phase or the fluid phase. They are not in closed form, because they involve fluctuations, except $-\bar{\Phi}_f \bar{p}_f^* \frac{\partial \tilde{v}_g^\alpha}{\partial x_\alpha}$, and their modelling is to be studied. One can already propose that the fluid motion between the grain, with very low velocity, is divergence free, then $\overline{p_f \Phi_f \frac{\partial v_f}{\partial x_\alpha}} \simeq 0$. We can then rewrite formally:

$$\frac{\partial}{\partial t}(\bar{\rho}\tilde{k}_g) + \frac{\partial}{\partial x_\alpha}(\bar{\rho}\tilde{v}_g^\alpha \tilde{k}_g) = \frac{\partial}{\partial x_\alpha}(-j_k^\alpha) - (\sum_{i=1,N} \overline{\rho_i \Phi_i v''^\alpha_i v''^\beta_i}) \frac{\partial \tilde{v}_g^\beta}{\partial x_\alpha} +$$
$$+ \overline{\pi_e \Phi_g \frac{\partial v''^\alpha_g}{\partial x_\alpha}} - \overline{\sigma_{ed}^{\alpha\beta} \Phi_g \frac{\partial v''^\beta_g}{\partial x_\alpha}} - \bar{\Phi}_f \bar{p}_f^* \frac{\partial \tilde{v}_g^\alpha}{\partial x_\alpha} - \bar{\rho}\varepsilon_g \quad (48)$$

We see first, if we compare this equation to the one for turbulence kinetic energy, eq. (6), that applying the Prantdl mixing length approach for obtaining the Bagnold formulas (46) needs to neglect the terms $+\overline{\pi_e \Phi_g \frac{\partial v''^\alpha_g}{\partial x_\alpha}} - \overline{\sigma_{ed}^{\alpha\beta} \Phi_g \frac{\partial v''^\beta_g}{\partial x_\alpha}} - \bar{\Phi}_f \bar{p}_f^* \frac{\partial \tilde{v}_g^\alpha}{\partial x_\alpha}$ within (48). Indeed, the two

first of these terms are due to lasting contacts between grains, and they are expected to be less and less efficient when the solid fraction decreases. The term due to the fluid phase is also expected to be small when the fluid is not submitted to compression or expansion.
Second, this equation is very similar to the equation for the granular temperature in "granular gases". For instance we can take the one proposed by S. B. Savage and co-workers (Lun et al, 1984).

$$\bar{\rho}\frac{\partial}{\partial t}(\frac{3}{2}T_G)+\bar{\rho}\tilde{v}_g^\alpha\frac{\partial}{\partial x_\alpha}(\frac{3}{2}T_G)=\frac{\partial}{\partial x_\alpha}(\bar{\rho}K\frac{\partial T_G}{\partial x_\alpha}+\bar{\rho}D\frac{\partial\bar{\rho}}{\partial x_\alpha})+\Sigma_{\alpha\beta}\frac{\partial\tilde{v}_g^\beta}{\partial x_\alpha}-\bar{\rho}T_G\Gamma \tag{49}$$

The tensor $\Sigma_{\alpha\beta}$ is what we have called in §4.1 the kinetic stress, and the constitutive relation "formula" is given by the classical theory of granular gases $\Sigma_{\alpha\beta}=-(\bar{\rho}T_G(1+4\bar{\Phi}_g\eta\varphi_0(\bar{\Phi}_g))\delta_{\alpha\beta}+\bar{\rho}\eta(\frac{\partial\tilde{v}_g^\beta}{\partial x_\alpha}+\frac{\partial\tilde{v}_g^\alpha}{\partial x_\beta})-\bar{\rho}\eta_v\delta_{\alpha\beta}\frac{\partial\tilde{v}_g^\gamma}{\partial x_\gamma})$. The first diagonal contribution in this stress tensor is simply proportional to the granular temperature itself, the two last ones are linked to the mean velocity gradient with effective viscosity coefficients η,η_v, which the theory relates to the variables $T_G,d,\bar{\Phi}_g$. The first diagonal term involves a reversible contribution which is nothing but $\bar{\rho}T_G=\rho_s\bar{\Phi}_gT_G$, but involves also an irreversible contribution related to η. The coefficients K,D in (49) are also diffusion coefficients proportional to η,η_v. The last term of (49) is a destruction term due to inelastic collisions, and the classical theory gives $\Gamma=\varphi_5(\bar{\Phi}_g)\frac{T_G^{1/2}}{d}$. The functions φ_0,φ_5 are non dimensional functions of the solid fraction only.
We notice the close analogy with our equation (48) for $\bar{\rho}\tilde{k}_g$. We recognize the dispersion flux, the production term due to mean velocity gradient, and the last term is the dissipation rate. Similarly to the Prandtl model, the kinetic stress is related to the gradient of mean velocity with the Boussinesq relation, and the dissipation rate is calculated proportional to $\frac{T_G^{3/2}}{l_t}$, with the length scale l_t linked to the mean diameter of the grains. There is also a dependence on the solid fraction, which is due to the occupation of the space when there are many grains. We get in (48) additional terms due to the elastic properties of the grain phase, which are not considered in granular gases because the lasting contacts are not considered, only instantaneous collisions are supposed to play. We can then consider that (48) agrees with the classical developments of the theory of granular gases and extend their validity for granular medium where the solid fraction is sufficiently high and the global velocity is low, in such a way that the enduring contacts can no more be neglected.
The problem of finding the length scale that plays in these models, taking into account or not that there are "cooperative motions" of groups of grains, remains. We can remark that a model similar to the k-epsilon model is able to address this problem. We could follow the approach of §2.3 for the modelling of the equation for $\tilde{k}_g$ and of an equation for ε_g, from which we can extract a length scale. The irreversible thermodynamics will hep us, as shown in §2.3, for choosing the terms and the coefficients of these balance equations.

5. Conclusion

We have applied the "Extended Irreversible Thermodynamics" approach in order to built models for three examples of "random media", and we have found that this approach do justify the bases of classical models, which have been proposed without any reference to Thermodynamics. Of course, this approach gives only the shapes of the laws, and there are constants or non-dimensional functions remaining, to be determined from experiments. The approach can be applied to different models, more or less detailed, for the same kind of situation. We have shown only a few examples, and other models, in other situations can be studied with the same route.

6. References

Baer, M. & Nunziato, J. (1986). A Two-Phase Mixture Theory for the Deflagration to Detonation Transition (DDT) in Reactive Granular Materials. *Int. J. Multiphase Flow,* Vol. 12, No. 6, pp. 861-889

Bagnold, R.A. (1954). Experiments on a Gravity-free Dispersion of Large Solid Spheres in a Newtonian Fluid under Shear. *Proc. R. Soc. London,* Ser. A, 225, pp. 49-63

Borghi, R. (2008). *Les milieux continus multiphysiques hors d'équilibre et leur modélisation,* Cépaduès-Editions, ISBN 978-2-85428-757-8, Toulouse, France

Borghi, R. & Bonelli, S. (2007). Towards a Constitutive Law for the "Unsteady Contact Stress" in Granular Media, *Continuum Mechanics and Thermodynamics*, 19, pp. 329-345

Cambou, B. (1998). *Behaviour of granular Materials,* Springer Verlag, Berlin

Chassaing, P., Antonia, R. A., Anselmet, F., Joly, L., Sarkar, S. (2002). *Variable Density Fluid Turbulence,* Kluwer Academic Publishers, ISBN 1-4020-0671-3, Dordrecht, The Netherlands

Drew, D. A. (1983). *Annual Review of Fluid Mechanics,* 15, pp. 261-291

Emeriault, F. & Cambou, B. (1996). Micromechanical modelling of anisotropic non-linear elasticity of granular medium, *Int. J. Solids Structures,* Vol.33, No.18, pp. 2591-2607

Frenette, R., Zimmermann, T., Eyheramendy, D. (2002). Unified Modeling of Fluid or Granular Flows on Dam-Break Case, *J. of Hydraulic Eng.,* march 2002, pp. 299-305

Hunt, M.L., Zenit, R., Campbell, C.S., Brennen, C.E. (2002). Revisiting the 1954 suspension experiments of R.A.Bagnold, *J. Fluid Mech.,* vol. 452, pp. 1-24

Hutter, K. & Rajagopal, K. R. (1994). On flows of granular materials, *Continuum Mechanics and Thermodynamics,* 6, pp. 81-139

Jou, D., Casas-Vazquez, J., Lebon, G. (2001). *Extended Irreversible Thermodynamics,* 3rd Ed., Springer Verlag, Berlin

Kataoka, I. (1986). Local Instant Formulation of Two-Phase Flow, *Int. J. Multiphase Flow*, Vol. 12, No. 5, pp. 745-758

Lun, C. K. K., Savage, S.B., Jeffrey, D. J., Chepurniy, N. (1984). Kinetic theories for granular flows: inelastic particles in Couette flow and slightly inelastic particles in a general flowfield, *J. Fluid Mechanics*, Vol. 140, pp. 223-256

Schiestel, R. (2006). *Méthodes de modélisation et de simulation des écoulements turbulents,* Hermès-Science/Lavoisier, ISBN 2-7462-1336-2, Paris, France

15

Thermodynamic Approach for Amorphous Alloys from Binary to Multicomponent Systems

Lai-Chang Zhang
The University of Western Australia
Australia

1. Introduction

When conventional metal alloys are cooled from their molten state, atoms will quickly rearrange themselves in a long range regular and periodic manner. Therefore, conventional metallic materials have a crystalline structure in nature. The structure of amorphous alloys is very different from that of the conventional metals, where the atoms are "frozen" in a random, disordered structure when the molten liquid was cooled fast enough to frustrate the formation of crystalline structure. The first amorphous alloy, $Au_{75}Si_{25}$ (in atomic percent, at.%, throughout this chapter), was formed in 1960 (Klement et al., 1960) by using a rapid quenching technique for chilling metallic liquids at very high rate of 10^5 – 10^6 K/s. Since then, considerable effort has been devoted to form amorphous structure through kinds of rapid solidification techniques (Suryanarayana, 1980). The research on amorphous alloys have received more development momentum in the early 1970s and 1980s when the continuous casting technique was developed for commercial manufacture of metallic glasses ribbons, lines, and sheets (Chen, 1980). However, the high cooling rate has limited the geometry of amorphous alloys in the form of thin sheets and lines. Such a small physical size (less than 50 μm) has significantly limited the potential industrial/commercial applications of this new class of materials. As a result, a variety of solid-state amorphization techniques were developed in 1980s to form amorphous alloys (see two reviews as Johnson, 1986; Cahn & Zarzycki, 1991). Two terms "amorphous alloy" and "metallic glass" have been using to describe these novel materials. A widely used "amorphous alloy" is adopted in this chapter to describe any metallic alloy that does not possess crystallinity. However, this chapter still uses "metallic glass" especially for that obtained by melt quenching techniques.
The first bulk metallic glass, defined as the amorphous alloys with a dimension no less than 1 mm in all directions, was discovered by Chen and Turnbull (Chen & Turnbull, 1969) in ternary Pd-Cu-Si alloy. These ternary bulk metallic glass-forming alloys have a critical cooling rate of about 100 K/s and can be obtained in the amorphous state with thickness up to 1 mm and more. Since then, especially after the presence of new bulk metallic glasses in $La_{55}Al_{25}Ni_{20}$ (Inoue et al., 1989) and $Zr_{41.2}Ti_{13.8}Cu_{12.5}Ni_{10.0}Be_{22.5}$ (Peker & Johnson, 1993), multicomponent bulk metallic glasses which could be prepared by direct casting at low cooling rates have been drawing increasing attention in the scientific community. A great deal of effort has been devoted to developing and characterizing bulk metallic glasses with a section thickness or diameter of a few millimetres to a few centimetres. A large variety of multicomponent bulk metallic glasses in a number of alloy systems, such as Pd-, Zr-, Mg-, Ln-, Ti-, Fe-, and Ni-based

bulk metallic glasses, have been developed via direct casting method through low cooling rates of the order of 1 – 100 K/s (Inoue, 2000; Suryanarayana & Inoue, 2011). In this method, the compositions of alloys are carefully designed to have large glass-forming ability (GFA) so that "bulk" amorphous alloys can be formed at a low cooling rate. From the requirement for high cooling rates to bypass crystallization, it is clear that metallic glasses cannot be directly cast in very large sizes. The "record" size of the bulk metallic glasses is 72 mm diameter for a $Pd_{40}Cu_{30}Ni_{10}P_{20}$ bulk metallic glass (Inoue et al., 1997). Currently, amoprhous alloys have a variety of uses for sports and luxury goods, electronics, medical, and defense.

2. Alloy development strategies

Amorphous alloys have become more and more attractive because of their excellent chemical, electrical, high mechanical strength, good corrosion resistance, reduced sliding friction and improved wear resistance, excellent soft and hard magnetic properties, and unique optical or electrical properties (Johnson, 1999; Inoue, 2000; Eckert et al., 2007; Wang, 2009; Xu et al., 2010; Suryanarayana & Inoue, 2011). A very large number of amorphous alloys have been synthesized from binary to ternary, quaternary, and even higher order alloy systems in the last 50 year, no matter by direct melt cooling methods or through solid-state amorphization techniques. In order to obtain the fundamental knowledge of the glass-forming ability (GFA) of multicomponent alloy systems to search for bulk metallic glasses with larger dimensions, a great number of parameters/indicators have been proposed to evaluate the GFA of amorphous alloys produced in a large number of alloy systems. Suryanarayana and Inoue have summarized these GFA parameters (Suryanarayana & Inoue, 2011), including reduced glass transition temperature T_{rg} ($=T_g/T_l$, where T_g is glass transition temperature and T_l is liquidus temperature), supercooled liquid region ΔT_x ($=T_x-T_g$, where T_x is the onset crystallization temperature), a parameter ($=T_x/T_l$), β parameter ($=1+T_x/T_l$), γ parameter ($=T_x/(T_g+T_l)$) and so on. Although different GFA parameters were able to give a reasonably good correlation for some bulk metallic glass-forming alloy systems, not one single parameter could satisfactorily explain the glass-forming ability of all bulk metallic glass-forming alloy systems. It is noted that, all the aforementioned GFA parameters require the transformation temperatures data (i.e. glass transition temperature T_g, onset crystallization temperature T_x or liquidus temperature T_l) of an amorphous alloy. However, these transformation temperatures could be obtained only after the amorphous alloy has been formed and is reheated in thermal analysis equipment (i.e. DSC/DTA). In addition, the values of these transformation temperatures, especially the onset crystallization temperature T_x and liquidus temperature T_l are largely dependent on the heating rate that is adopted to reheat the amorphous alloys in a DSC/DTA equipment (Zhang et al., 2006).

Because of the absence of fundamental theory to predict easy glass formation, presently the search for new compositions for amorphous alloys is conducted largely by trial-and-error approach, partially guided by experimental and/or computer calculated phase diagrams and a few empirical rules. Various alloy development strategies have been proposed for multicomponent glass-forming alloys, such as Egami's volume strain criterion (Egami & Waseda, 1984; Egami, 1997, 2003; Yan et al., 2003), Inoue's three empirical rules (Inoue et al., 1990, 1992), and Miracle's topological criterion (Senkov & Miracle, 2001; Miracle & Senkov, 2003). Among them, Inoue's three empirical rules, which were formulated based on the extensive data generated on the formation of bulk metallic glasses, are the mainstay for a long time to guide the search of new bulk glass-forming alloy compositions in multicomponent

alloy systems. In fact, hundreds of multicomponent alloy compositions have been prepared in amorphous state guided by these three empirical rules. The Inoue's rules are as follows:

- The multicomponent alloy system must consist of at least three components. The formation of amorphous phase becomes easier with increasing the number of components in the alloy system.
- The atomic radius mismatch between the constituent elements must differ from each other by greater than 12%, and
- There should be large negative heats of mixing between the main components in the alloy system.

Among these criteria, the first one is based on the thermodynamic and kinetic aspects of glass formation. The increment of the number of components in an alloy will significantly increase the entropy of fusion, leading to an increase in the degree of the dense random packing of atoms. This results in a decrease in enthalpy of fusion and also an increase in the solid–liquid interface energy. As a result, these factors contribute to a decrease in the free energy of the system. The second criterion is based on the topological aspects (structure and packing of atoms), and the third one is essential for mixing of atoms (alloying to occur) and for the formation of a homogeneous amorphous phase. The combination of the significant differences in atomic sizes between the constituent elements and the negative heat of mixing is expected to result in efficient packing of clusters and consequently increase the density of random packing of atoms in the supercooled liquid state. This, in turn, leads to increased liquid–solid interface energy, and decreased atomic diffusivity, both contributing to enhanced glass formation.

Even though the Inoue's three empirical rules have received great success in the development of bulk metallic glasses, some apparent exceptions have been reported in a few alloy systems. The recently developed bulk metallic glasses in some binary alloy systems such as Ca–Al, Cu–Hf, Cu–Zr, Ni–Nb, and Pd–Si (Suryanarayana & Inoue, 2011) have apparently broken the first criterion among the Inoue's three empirical rules. Although the maximum sizes of these bulk metallic glasses in binary alloys are too small (about 1 − 2 mm), they are indeed belong to the family of bulk metallic glasses as their size is greater than the well-defined critical size of bulk metallic glass (no less than 1 mm). It is noted that the aforementioned strategies could not effectively pinpoint the chemical compositions for glass formation in multicomponent alloy systems. Therefore, the search of new compositions for bulk metallic glass-forming alloys could only rely heavily on the trial-and-error approach, which involves considerable laboratory work to find a good bulk glass-forming alloy composition. A three-dimensional search method has been developed to navigate in three-dimensional composition space for locating the best glass-forming compositions in the Mg–(Cu,Ag)–(Y,Gd) alloy system (Ma et al., 2005; Zheng et al., 2006). By combining these alloy development strategies with the knowledge of the very recently developed bulk metallic glasses, a four-step approach has been recently proposed for searching the compositions to form bulk metallic glasses in multicomponent alloy systems (Fan et al., 2010). It involves: (a) searching deep eutectic composition(s) in binary or ternary phase diagrams, (b) alloying 10-20 at.% metals showing a mutual solubility with one of the base elements, (c) selecting suitable alloying elements with large difference in atomic size and negative heat of mixing to main component, and (d) micro-alloying 1-2 at.% appropriate elements. Actually, this four-step approach is still involved in the frame of Inoue's three empirical rules.

Considering their chemical compositions, amorphous alloys are quite complex, usually containing more than 3 (mostly 4−6) constituent elements. This chemical complexity makes it very laborious to search for the best bulk glass-forming composition in each

multicomponent alloy system. Although the above-mentioned alloy development strategies have been used with some success, the search for good bulk metallic glass-forming composition guided by these strategies has not been completely satisfactory and does need tremendous laboratory work. Furthermore, phase diagrams are currently unavailable for the multicomponent alloy systems, only for up to 3 or 4 components. Since the complexity of phase diagrams increases with the component number in an alloy system, it is hard to determine the effect of the alloying elements on the existed phase diagram or the eutectic compositions (and much less about deep eutectics). It is worthy to note that the chemical compositions having the best glass-forming ability need not always lie at the eutectics and they could be located at off-eutectic compositions (Wang et al., 2005). In addition, it will be a formidable problem to determine the minimum solute content in such a high order alloy system, because the contribution of each constituent element to the volumetric strain is going to be different depending on their atomic sizes. The situation becomes more complex when one realizes that the magnitude and the sign of stress could be different for different alloying elements. Therefore, it would be great for the development of new multicomponent bulk metallic glasses if the glass-forming ability of a designated multicomponent glass-forming alloy composition could be ascertained without the necessity of doing any experiments to form the amorphous samples. It will cut down a lot of laboratory work by the current trial-and-error approach to find a good bulk glass-forming composition in a multicomponent alloy system. Therefore, a predictive approach and thermodynamic modelling (for example, through the measured or calculated heats of mixing or other thermodynamic parameters) is required to solve this problem.

3. Thermodynamic approaches based on enthalpy calculation

The thermodynamic properties of alloys are very important for the understanding of the relative stability of alloys and phases. From the laws of classic thermodynamics, the thermodynamic stability of a system at constant temperature and pressure is determined by its Gibbs free energy, G. The Gibbs free energy of a system is defined as

$$G = H - TS \tag{1}$$

where H is the enthalpy, T is the absolute temperature, S is the entropy.
Thermodynamically, a system at constant temperature and pressure will be in a stable equilibrium if it has the lowest possible value of the Gibbs free energy.
Any transformation that results in a decrease in Gibbs free energy is possible. Therefore a necessary criterion for any phase transformation is

$$\Delta G = G_2 - G_1 = \Delta H - T\Delta S < 0 \tag{2}$$

where G_1 and G_2 are the free energies of the initial and final states, respectively. The transformation need not go directly to the stable equilibrium state but can pass through a whole series of intermediate metastable states.
It can be seen from the definition of G, Equation (1), that the state with the highest stability will be that with the best compromise between low enthalpy and high entropy. Thus, at low temperature metallic crystalline solids are most stable since they have the strongest atomic bonding and therefore the lowest internal energy (enthalpy). On the other hand, liquids and gases become more stable at elevated temperatures since the $-TS$ term dominates due to high atomic vibration frequency (entropy) at elevated temperatures. Therefore, amorphous

phase becomes more "stable" when its Gibbs free energy is lower than that of the competing crystalline phase. In other words, the Gibbs free energy change ΔG (= $G_{amorphous} - G_{crystalline}$) becomes negative.

There are several ways to obtain thermodynamic properties of an alloy. One possibility is the experimental investigation. However, it is impossible for some alloys to conduct the experimental measurements due to both technological difficulties and high cost and huge time consumption. So, systematic prediction via theory is a significant and effective approach to obtain thermodynamic properties of alloys, especially for multicomponent alloys. Strictly speaking, it is the Gibbs free energy rather than the enthalpy that should be considered to determine the stability of a phase. However, the contribution from entropy is much smaller than that from enthalpy in solid compounds, and therefore the entropy contribution to the free energy term is neglected, and only the enthalpy term is regarded as an indicator of the stability of an alloy (Suryanarayana & Inoue, 2011). A number of methods, both computational and experimental, have been devised to estimate the formation enthalpies of alloys. In order to cast a wide search net for prospective alloys or alloy modifications, a rapid means of estimating the formation enthalpies would greatly speed up the discovery of the good glass formers in multicomponent alloy systems. The following four types of theoretical methods have been used to estimate the formation of amorphous structure in multicoponent alloy systems.

- First principles calculations, within the framework of density-functional theory,
- Statistical mechanics based approaches, using atomistic simulation techniques like ab-initio calculations, molecular dynamics simulations and Monte Carlo methods,
- Solution thermodynamics, based on extrapolation of experimental data, as in the CALPHAD (which stands for CALculation of PHAse Diagrams) method, and
- Semi-empirical methods like Miedema's semi-emprical model, or the BFS (Bozzolo-Ferrante-Smith) model, which is in turn based on the equivalent crystal theory.

Each of these methods has its own pros and cons (Ray et al., 2008). First-principles calculations can yield highly accurate values, however, they also have a high computing cost and require prior information on the crystal structure. There are great amounts of calculations to be performed for the prediction of the formation enthalpy of a binary alloy using the first principles, and this amount increases rapidly with increasing the number of component. Atomistic simulations of energy can be carried out using harmonic methods, which can be used only for solid phases. But, some parameters such as vibrational frequencies necessary in these methods could only be obtained from the quasiharmonic lattice theory. The CALPHAD method is based on expressing the thermodynamic variables as a polynomial function of temperature. Extensive database of these functions is largely required for multicomponent alloys. In absence of such a database the CALPHAD approach cannot be used. Amongst the semi-empirical approaches, the Miedema's approach is perhaps the most commonly used one. The Miedema's method can be adapted for extremely fast calculation of enthalpies, although theses semi-empical approaches are not as accurate as ab-initio techniques. However, in situations where a large number of alloys have to be considered in absence of a prior thermodynamic database, an approach like the Miedema's model could provide an excellent starting point.

4. Thermodynamic approach for amorphous alloys via Miedema's model

The stability of any given phase is determined by its Gibbs free energy with reference to the competing phases. Thus, an amorphous phase will be stable if its Gibbs free energy is lower

than that of the competing crystalline phase(s) in the glass-forming alloy systems. Miedema (de Boer et al., 1988; Bakker, 1998) has developed a semi-empirical method to calculate the enthalpies of the formation of liquid, solid solutions, intermetallic compounds, and amorphous phases in alloys based on the chemical, elastic, structural, and topological effects. So far, the Miedema's semi-empirical model is a simple and powerful way to calculate the mixing enthalpy of alloys. The Miedema's semi-empirical model was primary developed for binary alloy systems, and it has been subsequently extended for ternary alloy systems (Gallego et al., 1990) and for quaternary or higher order alloy systems (Zhang et al., 2007). Regarding the applications of the Miedema's model to amorphous alloys, it could be used for predicting the glass-forming ability, glass-forming composition range, onset crystallization temperature, glass transition temperature and so on. This section only gives two application examples for the predictions of the glass-forming composition range (GFR) and glass-forming ability (GFA), and the applications for others could be retrieved in literatures (for examples, de Boer et al., 1988; Bakker, 1998; Takeuchi & Inoue, 2001).

4.1 The original Miedema's model for binary alloys

In general, the formation enthalpy of an alloy consists of the following four common parts depending on the type of the alloy

$$\Delta H = \Delta H^{chemical} + \Delta H^{elastic} + \Delta H^{structure} + \Delta H^{topological} \tag{3}$$

The first part $\Delta H^{chemical}$ is the enthalpy of chemical mixing. The Miedema's model uses only three quantities, attached to each element, that determine enthalpy changes upon alloying: molar volume, electronegativity and the electron density at the boundary of the Wigner-Seitz cell. All parameters and constants used in the model are estimated and tabulated by Miedema and can be found in literatures (de Boer et al., 1988; Bakker, 1998). In Miedema's model, atoms are conceived as "blocks" of the element (de Boer et al., 1988). These blocks represent Wigner-Seitz cells or, in general, they correspond to the Voronoi or Laguerre polyhedra. In this picture, when bringing dissimilar atoms into contact, energy effects occur at the interface, where the two polyhedra are in contact, and will correspondingly be proportional to the area of this interface. Thus, for dilute solution of atoms A in an excess of atoms B, this area is proportional to $V_A^{2/3}$, where V_A is the molar volume of A.

A second quantity that plays a role in the enthalpy change upon alloying is a sort of potential that is felt by the outer electrons of the atom. It resembles the electronegativity and is denoted by φ (Pauling, 1960). The potential φ gives the energy $-e\varphi$ that is needed for bringing such an electron with negative charge e to infinity, so it has a positive sign and is expressed in Volt. This energy is proportional to $-(\varphi_A - \varphi_B)^2$, because an amount of electronic charge $\Delta Z \propto |-\varphi_A - \varphi_B|$ is transferred over this "potential" difference with a corresponding energy gain of $|\Delta Z \cdot \Delta\varphi|$. The square $-(\varphi_A - \varphi_B)^2$ is also clear from the fact that the enthalpy effect is the same. In both cases the same amount of electronic charge is transferred, no matter the electronic charge is transferred from A to B or the other way. This energy contribution is called negative part of the enthalpy upon alloying $\Delta H_{A\,in\,B}^{interfacial}$ (negative part). The actual values of the φ's, used in Miedema's model are slight modifications of measured values, within experimental error, in order to obtain a set of parameters that adequately describe the alloying behavior. A second term in the enthalpy is "the density at the boundary of the Wigner-Seitz cell" and is denoted by n_{WS}. This value is always positive and represents the positive term in the mixing enthalpy $\Delta H_{A\,in\,B}^{interfacial}$ (positive part). The origin of the positive term in the

enthalpy lies in the fact that, when solving an A atom in a B host a discontinuity in n_{WS} is created, which is not allowed so that the discontinuity should be smoothed at the boundary by bringing electrons to higher energy levels, which explains the positive sign of this contribution. The enthalpy change is proportional to $(n_{WSA}^{1/3} - n_{WSB}^{1/3})^2$ and is, for a similar reason as previously outlined, a squared difference (Bakker, 1998). The sum of positive and negative parts may be either positive or negative in sign, depending on the relative absolute values of both parts. Miedema has found in a semi-empirical way the dependence between these three quantities and the chemical (interfacial) enthalpy for solving one mole of transition metal A in an excess of transition metal B

$$\Delta H^{chemical}(A\ in\ B) = \frac{V_A^{2/3}}{(n_{WS}^{-1/3})_{average}}\{-P(\Delta\varphi)^2 + Q(\Delta n_{WS}^{1/3})^2 + R\} \tag{4}$$

where P, Q and R are empirical constants for a given group of metals. P and Q are proportionality constants, and constant R is connected with the hybridization of d-type wave functions with p-type wave functions if transition metals and non-transition metals become nearest neighbours in an alloy. The term "chemical" refers to the effects due to electron transfer and smoothing of the electron density at the boundary of the Wigner-Seitz cell.

In the case of *random*, *dilute solution* of two elements having equal molar volumes (A in B with fractions c_A and c_B correspondingly) the chemical enthalpy effect upon the formation of a alloy is

$$\Delta H^{chemical}(1\ mole\ of\ A) = c_B \Delta H^{chem}(A\ in\ B) \tag{5}$$

since the average contact of atoms A with atoms B is given by c_B.

Or, the same per 1 mole of atoms ("A plus B"):

$$\Delta H^{chemical}(1\ mole\ of\ atoms) = c_A c_B \Delta H^{chemical}(A\ in\ B) \tag{6}$$

In the case of the atoms with different sizes the surface area is also different for atoms A and atoms B. Therefore, Miedema introduced the concept of surface fraction or "surface concentration" as

$$c_A^S = \frac{c_A V_A^{2/3}}{c_A V_A^{2/3} + c_B V_B^{2/3}} \tag{7}$$

$$c_A^S + c_B^S = 1 \tag{8}$$

And in this case one obtains

$$\Delta H^{chemical}(1\ mole\ of\ atoms) = c_A c_B^s \Delta H^{chemical}(A\ in\ B) \tag{9}$$

It is clear that in an ordered compound the surface contact between atoms A and atoms B is larger than that in a completely disordered alloy. Miedema denoted the degree to which atoms A are in contact with atoms B by f_B^A. Comparison of the experimental and calculated enthalpies has shown that f_B^A could be well described by $f_B^A = c_B^s\left[1 + \gamma\left(c_A^s c_B^s\right)^2\right]$, where $\gamma = 0$ for completely disordered alloys, $\gamma = 8$ for intermetallic compounds and $\gamma = 5$ for amorphous alloys (Weeber, 1987). Therefore, the Equation (9) can be generalized and rewritten in the form

$$\Delta H^{chemical} = c_A f_B^A \frac{V_A^{2/3}}{(n_{WS}^{-1/3})_{average}} \{-P(\Delta\varphi)^2 + Q(\Delta n_{WS}^{1/3})^2 + R\} \quad (10)$$

The second term $\Delta H^{elastic}$ in Equation (3) is elastic enthalpy representing the so called size mismatch enthalpy. In solid solutions, where atoms of different sizes have to occupy equivalent lattice positions, an additional positive contribution to the alloying enthalpy arises due to lattice deformations necessary to accommodate atoms of different sizes. In order to estimate the mismatch enthalpy Miedema used continuum elastic theory of Eshelby and Friedel (Eshelby, 1956) and received the following equation for the elastic part of the enthalpy upon alloying

$$\Delta H^{elastic}(A\ in\ B) = \frac{2K_A G_B (V_A - V_B)^2}{4G_B V_A + 3K_A V_B} \quad (11)$$

where K is the bulk modulus, G is the shear modulus and V is the molar volume. Elastic enthalpy is essential for solid solutions only, when solute atoms are randomly distributed in the lattice of the solvent. In contrast, in liquids and in solid ordered equilibrium phases this energy is almost non-existent.

The $\Delta H^{structure}$ contribution appears, according Miedema, in the solid solutions and reflects the preference for the transition metals in the 3*d* series to crystallize in one of the main crystallographic structures body-centered cubic (bcc), face-centered cubic (fcc) or hexagonal closely packed (hcp), depending on Z, the number of valence elections per atom. Miedema constructed, partly on the basis of band-structure calculations, partly on empirical findings of the structural stabilities for bcc, fcc and hcp structures of metals (de Boer et al., 1988; Bakker, 1998).

Since the crystal structure of a pure transition element depends on the number of valence electrons Z of the metal, the solution of one mole of atoms A in excess of atoms B leads in fact to the transformation A to B from a structural point of view and the corresponding energy change can be written as $E_{\sigma,B} - E_{\sigma,A}$. But atoms A, which are virtually transformed into atoms B have a different number of electrons than atoms B themselves. Therefore, the total number of electrons per atom in an alloy also differs from the value of pure atoms B and the structural enthalpy will change by an amount $(Z_A - Z_B)\frac{\partial E_{\sigma,B}}{\partial Z}$. Thereby the total structural enthalpy change per mole of solvent atoms is determined by

$$\Delta H^{structure}(A\ in\ B) = (Z_A - Z_B)\frac{\partial E_{\sigma,B}}{\partial Z} + \left(E_{\sigma,B} - E_{\sigma,A}\right) \quad (12)$$

The last term $\Delta H^{topological}$ in Equation (3) is called topological enthalpy. For liquids the topological enthalpy, accounting for the difference between the crystalline state and the liquid state is the heat of fusion with the magnitude of about $R\bar{T}_m$, where R = 8.31 J K^{-1} is the gas constant and $\bar{T}_m$ is the average of the two melting temperatures.

In amorphous alloys a certain degree of relaxation towards the solid state exists, so that the enthalpy contribution will be lower. It has been proposed as (Bakker et al., 1995)

$$\Delta H^{topological} = 3.5 \times 10^{-3} \cdot \left(c_A T_{m,A} + c_B T_{m,B}\right),\ kJ\ mol^{-1} \quad (13)$$

According to this one can write the formation enthalpies of different types of alloys in the following forms

$$\Delta H^{liquid} = \Delta H^{chemical} \tag{14}$$

$$\Delta H^{solid\ solution} = \Delta H^{chemical} + \Delta H^{elastic} + \Delta H^{structure} \tag{15}$$

$$\Delta H^{compound} = \Delta H^{chemical} \tag{16}$$

$$\Delta H^{amorphous} = \Delta H^{chemical} + H^{topological} \tag{17}$$

All previous equations can be applied for only one type of concentrated binary alloys: intermetallic compounds, and for random, dilute solutions, but not for concentrated solutions. Miedema solved this problem by just averaging according to the following equations:

$$\Delta H^{chemical} = c_A c_B\left[f_B^A \Delta H^{chemical}(A\ in\ B) + f_A^B \Delta H^{chemical}(B\ in\ A)\right] \tag{18}$$

$$\Delta H^{elastic} = c_A c_B\left[c_B \Delta H^{elastic}(A\ in\ B) + c_A \Delta H^{elastic}(B\ in\ A)\right] \tag{19}$$

$$\Delta H^{structure} = E_\sigma^{struct}ure(\langle Z\rangle) - E_\sigma^{ref}(\langle Z\rangle) \tag{20}$$

where $\langle Z\rangle$ is the average number of valence electrons, $E_\sigma^{structure}(\langle Z\rangle)$ is the value of E_σ for the most stable structure with $\langle Z\rangle$ electrons per atom, $E_\sigma^{ref}(\langle Z\rangle)$ is a linear extrapolation between the lattice stabilities of the two relevant metals in their equilibrium states.

One of the well-known applications of the Miedema's model is to predict the glass-forming composition range (GFR) in glass-forming alloy systems. In general, by comparing the enthalpy difference between the formation enthalpy of the amorphous phase ($\Delta H^{amorphous}$) and that of the solid solution ($\Delta H^{solid\ solution}$) or intermetallic compounds ($\Delta H^{compund}$), the glass-forming range can be estimated. That is, if the enthalpy of the formation of the amorphous phase is lower than that of the solid solution or that of the intermetallic compounds, the amorphous phase is preferentially formed, otherwise, when considering metastable equilibrium conditions, the solid solution or intermetallic compounds are easily formed ("general method"). Or, the glass-forming range can also be estimated using the "common tangent method", *i.e.* using two common tangents between the enthalpy curves of the amorphous phase and the competitive crystalline phases such as the solid solutions and/or the intermetallic compounds (Weeber & Bakker, 1988). The compositions where the formation enthalpy curve of the amorphous phase attains the lowest absolute values then define the glass-forming composition range. In contrast, the compositions between the common tangents give an estimate for the two-phase region where the amorphous phase coexists with crystalline phases. The Miedema's model was applied to predict the glass-forming composition ranges in a series of binary alloy systems (Weeber et al., 1988), such as Cu-Ti, Ni-Ti, Ni-Zr, Ni-Nb, and so on. Fig. 1 gives an example of the calculated enthalpies of amorphous phase and that of the terminal solid solutions in the Ni-Ti binary alloy system. The predicted glass-forming composition range in the Ni-Ti system is 24 - 77 at.% Ni, which is in well agreement with the experimental glass-forming composition range (28 - 72 at.% Ni) prepared by mechanical alloying. Table 1 summarizes the predicted glass-forming composition ranges determined by applying the Miedema's model and the experimental results under mechanical alloying in several binary alloy systems. It shows that, in binary alloy systems, the determined glass-forming composition ranges by the Miedema's model are in accordance with those obtained from experimental observations.

Alloy	Predicted range	Measured range
Ni-Ti	24 - 77 at.% Ni	28 - 72 at.% Ni
Ni-Zr	24 - 83 at.% Ni	20 - 80 at.% Ni
Ni-Nb	31- 80 at.% Ni	20 - 80 at.% Ni
Cu-Ti	28 - 75 at.% Cu	10 - 87 at.% Cu
Fe-Zr	27 - 79 at.% Fe	30 - 78 at.% Fe
Pd-Ti	20 - 54 at.% Pd	15 - 58 at.% Pd
Cu-Hf	29 - 79 at.% Cu	30 - > 70 at.% Cu
Ni-Hf	25 - 84 at.% Ni	15 - 65 at.% Ni

Table 1. Some examples of the predicted glass-forming composition ranges in binary alloy systems, determined by using the Miedema's model, and the measured composition ranges under mechanical alloying. (Reprinted from Weeber et al., 1988. With permission)

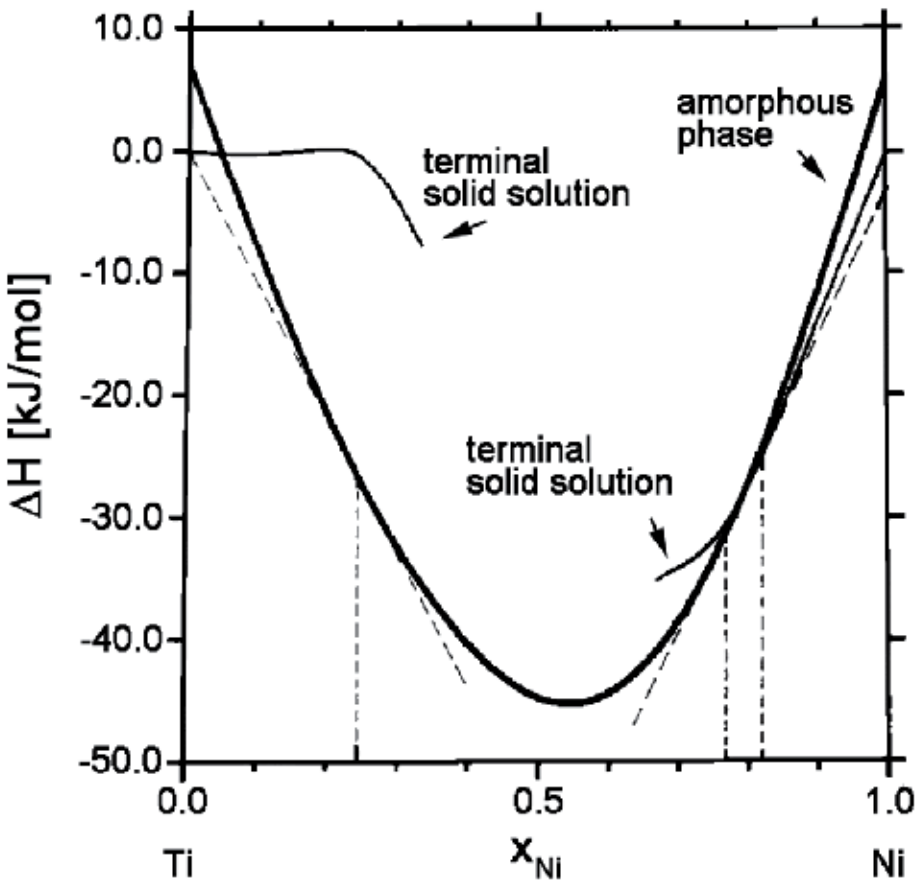

Fig. 1. Enthalpy diagram by the Miedema's model for the amorphous phase and the terminal solid solutions in the Ni-Ti system. The glass-forming composition range, defined by using double common tangents method, is 24 - 77 at.% Ni (Reprinted from Weeber et al., 1988. With permission)

Recently, by combining with a new glass-forming ability parameter, the Miedema's model has been used as a guide to searching for the best glass-forming ability composition in binary alloy systems (Xia et al., 2006a, 2006b, 2006c). It is argued that the formation of a metallic glass should involve two aspects (Xia et al., 2006a). While glass formation requires that the Gibbs free energy of the hypothetical amorphous phase is lower than that of the competing crystalline phases (mostly intermetallic compounds and sometimes solid solution depending alloy systems), the resistance to crystallization is dependent on the difference in the Gibbs free energies of the amorphous phase and intermetallic compounds. Therefore, the first aspect is the thermodynamic driving force for glass formation ($-\Delta H^{amorphous}$). The larger this value is, the easier is the glass formation. The other aspect is the resistance for glass formation against crystallization ($\Delta H^{amorphous} - \Delta H^{\text{competing phase}}$). The smaller this value is, the higher is the stability of the amorphous phase. The $\Delta H^{\text{competing phase}}$ could be $\Delta H^{solid\ solution}$ or $\Delta H^{compound}$ depending on the actual competing phases in an alloy system. Based on this, a γ* parameter was proposed as a measure of glass-forming ability of alloy systems, defined as

$$\gamma^* = GFA \propto \frac{-\Delta H^{amorphous}}{\Delta H^{amorphous} - \Delta H^{\text{competing phase}}} = \frac{\Delta H^{amorphous}}{\Delta H^{\text{competing phase}} - \Delta H^{amorphous}} \tag{21}$$

The greater is the value of γ* the higher is the glass-forming ability of the alloy. The formation enthalpy ΔH as a function of compositions for an amorphous phase and all the competing phases could be calculated by the Miedema's model. Using the aforementioned approach, one could determine the glass-forming composition ranges in which different phases are stable. Afterwards, by calculating the γ* parameter within this determined composition range in which the amorphous phase is stable, the best glass-forming composition could be estimated when the γ* parameter reaches a maximum value.

Xia et al. (Xia et al., 2006a) has applied the above method to search the best glass-forming composition in the Ni–Nb system, as shown in Fig. 2. The plots of γ* with composition indicates that the best glass former lies at the composition around $Ni_{61.5}Nb_{38.5}$, where the γ^* reaches its largest value. Experimental studies of the glass-forming ability on $Ni_{100-x}Nb_x$ alloys, at short intervals of 0.5 at.% in the composition range of x = 37.5 − 40.5 at.% Nb, have shown that the alloy $Ni_{62}Nb_{38}$ has the best glass-forming ability among the investigated compositions. The predicted composition is roughly in agreement with the experimental observations. The small difference in the experimental and predicted compositions was attributed to the fact that the entropy term was neglected in the calculations. Similar work on Cu–Hf alloys (Xia et al., 2006b) and Cu-Zr alloys (Xia et al., 2006c) have confirmed that this method is practical for predicting the best glass-forming compositions, at least in the studied binary alloy systems.

4.2 Extended Miedema's model for ternary alloys

Gallego et. al. (Gallego et al., 1990) approximated the formation enthalpy in ternary system as a sum of the formation enthalpies of the respective binary alloy systems. This extended model has been largely used in ternary alloy systems and has received considerable success. However, such an approach has neglected the role of ternary interaction parameters and the relative compositions of the individual binaries, since the partitioning coefficients need not be the same for all the binaries. A number of work has attempted to improve on this extended Miedema's approach to multicomponent glass-forming alloy systems (Goncalves & Almeida, 1996; Zhang & Jesser, 2002; Herbst, 2002; Shindo et al., 2002; de Tendler et al.,

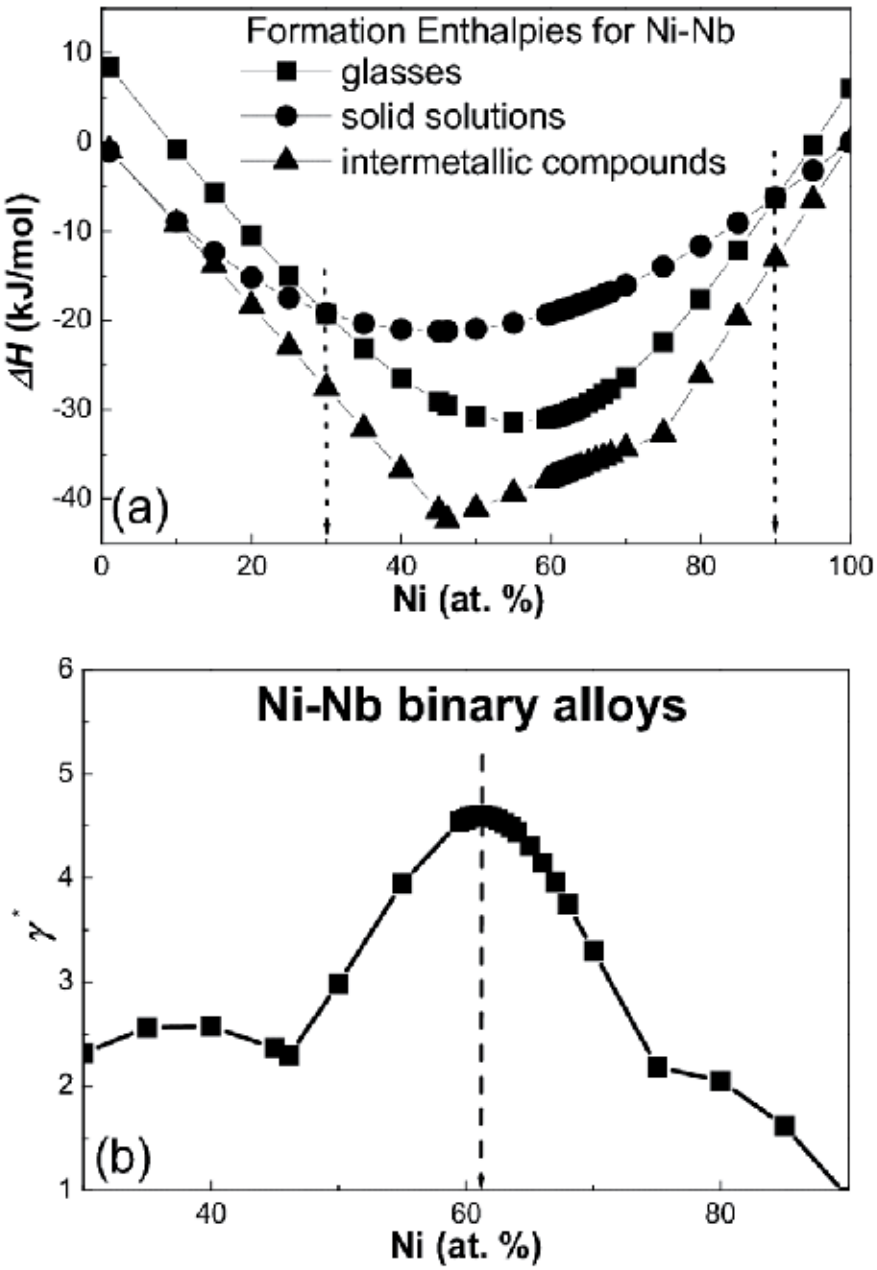

Fig. 2. (a) Plots of calculated enthalpies of the amorphous phase and competing crystalline phases in the Ni-Nb system. At any given compositions, the phase with the lowest enthalpy will be the most stable phase. The amorphous phase is stable at the compositions between the two dash lines. (b) Plot of γ^* parameter as a function of composition in the Ni-Nb system. Note that the largest value of γ^* lies at the best glass-forming composition. (Reprinted from Xia et al., 2006a. With permission)

2006; Ouyang et al., 2006a, 2006b; Zhang et al., 2007; Bera et al., 2007; Wang et al., 2007). All these amended extensions have their own pros and cons.

Goncalves and Almeida (Goncalves & Almeida, 1996) devised an ingenious approach for the estimation of enthalpies based on the relative positions of atoms. This approach was devised for $MgCu_2$, $MgZn_2$, $CaCu_5$ structure types. In principle the approach can be extended to other structure types as well, once the crystallographic information is available. However, this approach cannot be applied in absence of relevant crystallographic information. Herbst (Herbst, 2002) used an extended version of the Miedema's model to predict the hydrogen content in ternary hydrides. However, this approach had to establish and incorporate polynomial fits based on the data for a large number of hydrides. Hence this approach is not a general approach and cannot be applied directly to multicomponent glass-forming alloy systems. Zhang and Jesser (Zhang & Jesser, 2002) attempted to extend the original Miedema's model using the same approach as Gallego et. al. (Gallego et al., 1990) while incorporating an additional strain energy component. The strain energy was calculated using the Eshelby's model (Eshelby, 1956). However, the Eshelby's model is a continuum approach, devised to treat the stresses arising from inclusions and hence, strictly speaking, cannot be applied to alloying at atomistic levels. De Tendler et. al. (de Tendler et al., 2006) also adopted an approach similar to Gallego et. al. (Gallego et al., 1990) while adding an entropy component to estimate the Gibbs free energy. Ouyang et al. (Ouyang et al., 2006a, 2006b) used a geometric approach similar to Toop's approach (Saunders & Miodownik, 1998). However, it is known that Toop's approach is largely applicable to ionic solids rather than metallic materials. Bera et al. (Bera et al., 2007) estimated the formation enthalpies using a pseudo-binary approach. However, their approach was based on crystallography and hence cannot be used in absence of crystallographic information. Among all these amended extensions, the extended method by Gallego et. al. (Gallego et al., 1990) has so far received the most success for ternary alloy systems. Therefore, this chapter only describes the extended method by Miedema's model by Gallego et. al. (Gallego et al., 1990).

In a ternary alloy system A-B-C, the formation enthalpies of each phase could be defined as:

$$\Delta H_{ABC} = \Delta H_{AB} + \Delta H_{AC} + \Delta H_{BC} \tag{22}$$

As a result, the formation enthalpies the amorphous phase are given by the equations:

$$\Delta H_{ABC}^{amorphous} = \Delta H_{ABC}^{chemical} + \Delta H_{ABC}^{topoligical} \tag{23}$$

$$\Delta H_{ABC}^{chemical} = \Delta H_{AB}^{chemical} + \Delta H_{AC}^{chemical} + \Delta H_{BC}^{chemical} \tag{24}$$

$$\Delta H_{ij}^{chemical} = c_i \cdot c_j \left(c_j \cdot \Delta H_{i\ in\ j}^{interface} + c_i \cdot \Delta H_{j\ in\ i}^{interface} \right) \tag{25}$$

$$\Delta H^{topological} = 3.5 \times 10^{-3} \cdot \sum_{i=1}^{3} c_i \cdot T_{m,i}\ ,\ kJ\ mol^{-1} \tag{26}$$

where $\Delta H^{amorphous}$ is the formation enthalpy of the amorphous phase, $\Delta H_{ABC}^{chemical}$ is the enthalpy of chemical mixing defined by Equations (24) and (25), $\Delta H^{topological}$ is defined by Equation (26), where c_i is the composition of the i^{th} components whose melting temperatures are $T_{m,i}$. The factor $\{1 + \gamma \cdot (c_i^s \cdot c_j^s)^2\}$ needs to be multiplied to Equation (25) as previously in binary alloy systems when short-range order (SRO) exists in the amorphous phase (Weeber, 1987) (γ is called an SRO parameter, $\gamma = 5$ is the usual case), where c_i^s is the surface fraction of the cell. Here, c_i^s is developed for a multicomponent alloy system as

$$c_i^S = \frac{c_i \cdot V_i^{2/3}}{\sum_i c_i \cdot V_i^{2/3}} \tag{27}$$

where V_i is the molar volume of the component. These values were taken from the literature (Niessen et al., 1983).
Based on the formation enthalpy of intermetallic compound in a binary alloy system (Equation 16) and the enthalpy of chemical mixing in ternary alloy system (Equation 24) the formation enthalpy of intermetallic compound in a ternary alloy system is defined as:

$$\Delta H^{compound} = \Delta H_{AB}^{chemical} + \Delta H_{AC}^{chemical} + \Delta H_{BC}^{chemical} \tag{28}$$

The structural contribution to the enthalpy of solid solution, arising from the difference between the valences and crystal structures of the solute and the solvent, is expected to have only a minor effect and can be almost negligible in determining the glass-forming composition range (Lopez et al., 1987; Bakker, 1998) when compared with the elastic energy contribution. Also, it is difficult to calculate this structural contribution in multicomponent alloy systems and so it was not considered in the calculations. Hence, the formation enthalpies of a solid solution phase can be derived from

$$\Delta H_{ABC}^{solid\ solution} = \Delta H_{ABC}^{chemical} + \Delta H_{ABC}^{elastic}(solid\ solution) \tag{29}$$

where $\Delta H_{ABC}^{chemical}$ is the enthalpy of chemical mixing, as shown in Equation (24). $\Delta H_{ABC}^{elastic}(solid\ solution)$ is the elastic enthalpy arising from the atomic size mismatch, expressed as Equations (30) - (32)

$$\Delta H_{ABC}^{elastic}(solid\ solution) = \Delta H_{AB}^{elastic} + \Delta H_{AC}^{elastic} + \Delta H_{BC}^{elastic} \tag{30}$$

$$\Delta H_{ij}^{elastic} = c_i \cdot c_j\left(c_j \cdot \Delta H_{i\ in\ j}^{elastic} + c_i \cdot \Delta H_{j\ in\ i}^{elastic}\right) \tag{31}$$

$$\Delta H_{i\ in\ j}^{elastic} = \frac{2K_i G_j \left(V_i^* - V_j^*\right)^2}{3K_i V_j^* + 4G_j V_i^*} \tag{32}$$

Here, K_i is the bulk modulus of the solute, G_j is the shear modulus of the solvent, and V_i^* and V_j^* are the modified molar volumes of the solute and the solvent, respectively, corrected for charge transfer effects (Bakker, 1985):

$$\Delta V_i = \frac{P_0 V_i^{2/3}\left(\emptyset_i^* - \emptyset_j^*\right)}{\left(n_{WS}^i\right)^{-1/3} + \left(n_{WS}^j\right)^{-1/3}} \cdot \left|\left(n_{WS}^i\right)^{-1} - \left(n_{WS}^j\right)^{-1}\right| \tag{33}$$

V_i is the molar volume of pure component i, the $\emptyset^*$ parameters are the electronegativity (in volts) and the n_{WS} parameters are the electron densities at the Wigner-Seitz cell boundary (in density units). The parameter P_0 has been found empirically to be 1.5 (Bakker, 1985). All numerical values of the parameters are available in the literature de Boer et al., 1998.
In order to verify the applicability of this extended Miedema's model, Gallego et. al. (Gallego et al., 1990) has compared the glass-forming composition ranges in the Co-rich region in Co-Zr-M (M = Nb, W, Mo, V and Cr) ternary alloys. The calculated composition ranges by the extended Miedema's model are close to the values of the minimum solute concentrations for glass formation derived from the Ueno-Waseda equation.
Murty et al. (Murty et al., 1992) applied this extended model to the ternary Ti-Ni-Cu alloy system to calculate the glass-forming composition range, as shown in Fig. 3. The calculated glass-forming composition ranges in this ternary alloy system are x = 0 - 30 and 58 - 60 for

$Ti_{40}Ni_{60-x}Cu_x$, x = 0 - 24 and 49 - 50 for $Ti_{50}Ni_{50-x}Cu_x$ and x = 0 - 15 for $Ti_{60}Ni_{40-x}Cu_x$. These calculated results are in general agreement with those experimental observations by mechanical alloying.

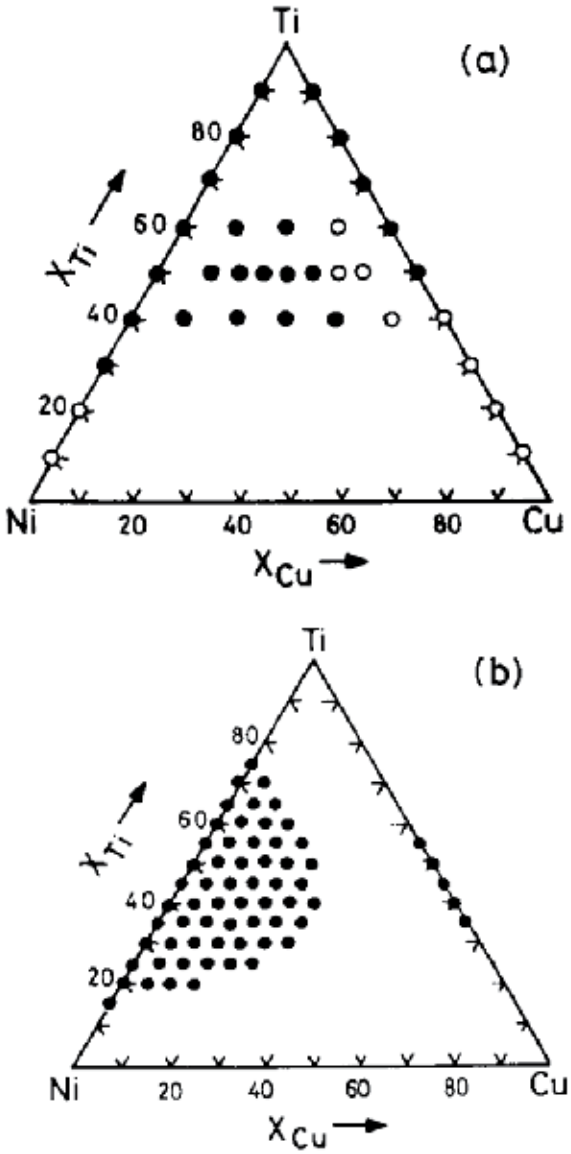

Fig. 3. Comparison of (a) experimental and (b) calculated glass-forming composition ranges in Ti-Ni-Cu alloy system (Reprinted from Murty et al., 1992. With permission)

Takeuchi and Inoue (Takeuchi & Inoue, 2001) used the Miedema's model to determine the stability of the amorphous phase and estimate the glass-forming composition range. By carrying out the calculations for 335 glass-forming ternary alloy systems except for Al-Cu-Fe, Al-Mo-Si and Au-Ge-Si, it is showed that the calculated results are in agreement with the

experimental data for Cu-Ni- and Al-Ti- based ternary alloy systems. An example is shown in Fig. 4 (a). But, the calculated glass-forming composition ranges in Zr-, La-, Fe-, and Mg-based ternary alloy systems were overestimated, as shown in Fig. 4 (b), because of the simplification inherent in their model. The authors has also noted that the factors that influence the glass-forming composition range are $\Delta H^{interface}$, $\Delta H^{elastic}$, T_{m}, viscosity, diffusion, short-range order, intermediate phases, and so on. They have compared the glass forming composition ranges obtained by considering and those obtained by ignoring the short-range order factor in amorphous phase, which is expressed as the $\{1 + \gamma \cdot (c_i^s \cdot c_j^s)^2\}$. Figs. 4 (c) and (d) show an example of the effect of short-range order factor on the glass-forming composition range. By considering the short-range order factor, the calculated glass-forming ranges in the Al-Ni-Zr system are much closer to the experimental observations, especially for the compositions near the Al-rich corner and the Al-Zr binary subsystem. It is interesting to note that the short-range order has different influences on the glass formation in different alloy systems. For examples, the short-range order has little change in the glass forming range in the B-Fe-Zr and La-Mg-Ni systems. In contrast, ignoring the short range order factor has led to the absence in the glass-forming range in the Ni-P-Pd system.

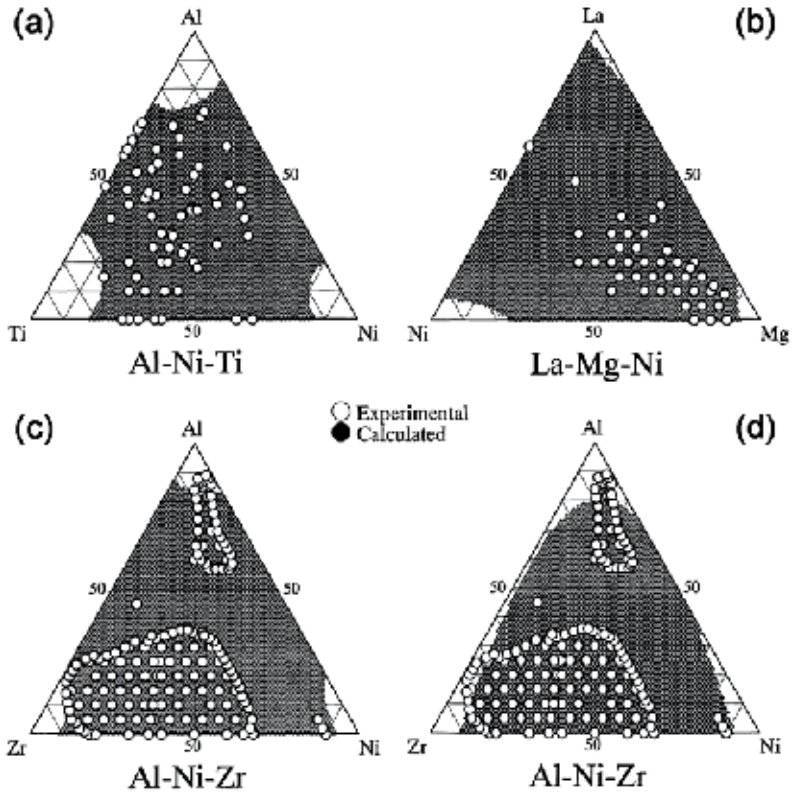

Fig. 4. Experimental and calculated glass-forming composition ranges for different alloy systems under the conditions where the short-range is (a)-(c) considered and (d) ignored. It is noted that the short-range order factor has different influences on the calculated glass-forming composition range. (Reprinted from Takeuchi & Inoue, 2001. With permission)

4.3 Extended Miedema's model for quaternary and more complex alloy systems

From the aforementioned alloy development strategies for multicomponent amorphous alloys in Section 2, one finds that the fourth and later alloying elements, take only about 1-2 at.% in the alloy, which are actually dilute solution in a ternary alloy. In addition, the components in all the multicomponent glass-forming alloy systems could be divided into three types of elements based on their atomic size and chemical affinity (Takeuchi & Inoue, 2001). Therefore, the quaternary or higher order alloy systems could be regarded as pseudo-ternary or occasionally as pseudo-quaternary alloy systems. As a result, the extended Miedema's model could be applied to quaternary or higher order alloy systems, as long as such high order alloy systems are discreetly conceived as pseudo-ternary alloy systems based on the chemical affinity of the components.

Zhang et al. (Zhang et al., 2007) has successfully presented this pseudo-ternary solution method to the Ti-Zr-Nb-Cu-Ni-Al multicomponent alloy system consisting of 6 constituent elements. It is suggested to divide the elements in the alloy system into three groups based on their chemical affinity and afterwards to calculate the formation enthalpy of the alloys using the Miedema's formula for ternary alloys in Section 4.2. As an example, the Ti-Zr-Nb-Cu-Ni-Al alloy system can be considered as a pseudo-ternary alloy system, where (Ti,Zr,Nb) may be regarded as A, (Cu,Ni) as B and Al as C, respectively. The corresponding parameters of each pseudo-component (*i.e.* A, B, and C) can be calculated using the confusion principle, as the elements in each pseudo-component are infinite soluble each other. According to the experimental observations (Zhang et al., 2007), the competitive crystalline phases in the course of the formation of the amorphous phase in this high order alloy system are only solid solutions (*i.e.* Cu and (Nb,Zr) solid solutions). Therefore, the formation enthalpies of the amorphous phase and the solid solutions are calculated to determine the glass-forming range, as shown in Fig. 5. Comparing with the formation enthalpies of the solid solution and that of the amorphous phase in this (Ti,Zr,Nb)-(Cu,Ni)-Al pseudo-ternary alloy system, the calculated glass-forming composition range corresponds to a (Ti,Zr,Nb) content of about from 21 to 51 at.% using the double tangent method (see GFR A in Fig. 5). In contrast, when using the general method, the calculated glass-forming composition range is estimated as 12 - 63 at.% (Ti,Zr,Nb) (see GFR B in Fig. 5). From the experiments, an amorphous phase was formed by mechanical alloying for the powder mixtures with a (Ti,Zr,Nb) content of 20 - 60 at.%. Both calculated glass-forming ranges are comparable to the experimental results. Therefore, the Miedema's model can be successfully applied to calculate the glass-forming composition range in complex alloy systems composed of more than four components, as long as by appropriately regarding the complex alloy systems as pseudo-ternary alloy systems.

Due to the complexity of ternary and higher order multicomponent alloy systems, the calculations may be not precisely in agreement with the experimental observations. On the other hand, it is expensive and time-consuming to experimentally measure the formation enthalpy of such complex alloys. Therefore, there is a significant need for simple and reliable theoretical calculation. Because of more complexity arising from large component number in multicomponent alloy systems, the extended Miedema's model becomes definitely more complex than the original binary one. The larger the component number in an alloy is, the more complex is the extended Miedema's model and at the same time the less accurate is the calculation. The extended Miedema's model by Gallego et. al. (Gallego et al., 1990) has neglected the third and subsequent interaction parameter and the relative composition of the individual binaries and calculated the formation enthalpy as a sum of corresponding binary alloys (such as the Equation 22 in the Section 4.2). As previously

described at the beginning in the Section 4.2, there exist some other proposed extensions of the Miedema's model for multicomponent alloy systems. The values of the formation enthalpy from these extensions deviate more or less from the experimental observations (Kokotin 2010), which will significantly influence the precision when applying the extended Miedema's model to higher order alloy systems.

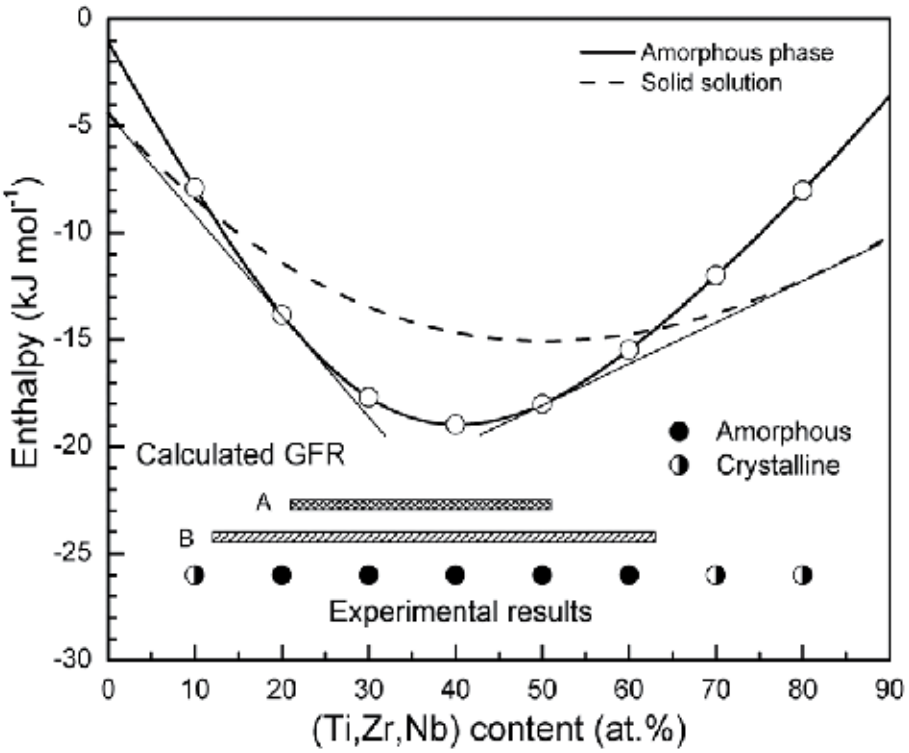

Fig. 5. Calculated enthalpy diagrams of the pseudo-ternary $(Ti,Zr,Nb)_x(CuNi)_{90-x}Al_{10}$ alloy system. The calculated glass-forming composition range (GFR) and the experimentally determined GFR are plotted together for comparison. GFR A and B are estimated using the common tangent method and the general method, respectively. Both calculated glass-forming composition ranges are in agreement with the experimental observations. It proves that the Miedema's model can be successfully applied to complex alloy systems composed of more than four components. (Reprinted from Zhang et al., 2007. With permission)

5. Conclusions

Due to complexity arising from large component number, the fundamental understanding of the formation, structure and properties becomes more and more difficult with increasing the component number in the multicomponent glass-forming alloy systems. The Miedema's semi-empirical model enables us to make fast predictions for values of several effects in alloys, such as for glass-forming ability and for glass forming composition range from binary to ternary and higher order multicomponent alloy systems. The calculated results are well agreement with the experimental observations. By supplemented by suitable

parameters and/or procedures, the application of the Miedema's semi-empirical model and extensions to estimate the formation enthalpies would greatly speed up the search for prospective alloys or alloy modifications for multicomponent glass-forming alloys.
Various Miedema's model extensions could lead to deviations of the calculated values of the formation enthalpy from the experimental data. These deviations will reduce the precision when application the model is incorporated with other parameters/procedures for multicomponent glass-forming alloy systems. From this reason, more suitable modification and justification of the Miedema's semi-empirical model is needed, especially for multicomponent alloy systems.

6. Acknowledgments

The author is grateful to J. Eckert, K.B. Kim, H.B. Lu, P. Yu, W.Y. Zhang, and M. Calin for their stimulating discussions. Financial support provided by Research Services of The University of Western Australia (through UWA Research Development Award Scheme) is gratefully acknowledged.

7. References

Bakker, H. (1985). Fast Metal Impurity Diffusion in Metals and The Miedema Model. *Journal of the Less-Common Metals*, Vol. 105, No. 1, (January 1985), pp. 129-138, ISSN 0022-5088

Bakker, H., Zhou, G.F., & Yang, H. (1995). Mechanically Driven Disorder and Phase Transformation in Alloys. *Progress in Materials Science,* Vol. 39, No. 3, (July 1995), pp. 159-241, ISSN 0079-6425

Bakker, H. (1998). *Enthalpies in Alloys: Miedema's Semi-empirical Model*, Trans Tech Publication Ltd, ISBN 0-87849-783-8, Switzerland

Bera, S., Mazumdar, S., Ramgopal, M., Bhattacharyya, S., & Manna, I. (2007). Prediction of Enthalpy of Formation and Gibbs Energy Change in Pseudo-Binary (Ti-Zr)(Fe-Cr)(2) and Pseudo-Ternary (Ti-Zr)(Fe-Cr)(2)-H System Using Extended Miedema Model. *Journal of Materials Science*, Vol. 42, No. 10, (May 2007), pp. 3645-3650, ISSN 0022-2461

Bozzolo, G., Ferrante, J., & Smith, J.R. (1992). Method for Calculating Alloy Energetics. *Physical Review B*, Vol. 45, No. 1, (January 1992), pp. pp. 493-496, ISSN 1098-0121

Cahn, R.W., & Zarzycki, J. (1991). *Glasses and Amorphous Materials*, Vol. 9 of *Materials Science and Technology: A Comprehensive Treatment*. Wiley, John, & Sons Incorporated, ISBN 783527268221, Weinheim, Germany

Chen, H.S. (1980). Glassy Metals. *Reports on Progress in Physics*, Vol. 43, No. 4, (January 1980), pp. 353-432, ISSN 0034-4885

Chen, H.S., & Turnbull, D. (1969). Formation, Stability and Structure of Palladium-Silicon Based Alloy Glasses. *Acta Metallurgica*, Vol. 17, No. 8, (August 1969), pp. 1021-1031, ISSN 0001-6160

Cocco, G., Soletta, I., Enyo, S., Magini, M., & Cowlam N. (1990). On The Amorphisation Reactions of CuTi by Mechanical Alloying. *Journal de Physique Colloques*, Vol. 51, No. C4, (July 1990), pp. 181-187, ISSN 0449-1947

de Boer, F.R., Boom, R., Mattens, W.C.M., Miedema, A.R., & Niessen A.K. (1988). *Cohesion in Metals: Transition Metal Alloys*, Elsevier, ISBN 0-444-87098-9, North-Holland, Amsterdam

de Tendler, R.H., Soriano, M.R., Pepe, M.E., Kovacs, J.A., Vicente, E.E., & Alonso, J.A. (2006). Calculation of Metastable Free-Energy Diagrams and Glass Formation in The Mg–Cu–Y Alloy and Its Boundary Binaries Using The Miedema Model. *Intermetallics*, Vol. 14. No. 3, (March 2006), pp. 297-307, ISSN 0966-9795

Dinsdale, A.T. (1991). SGTE Data for Pure Elements. *Calphad*, Vol. 15, No. 4, (October-December 1991), pp. 317-*425*, ISSN 0364-5916

Eckert, J., Das, J., Pauly, S., & Duhamel, C. (2007). Mechanical Properties of Bulk Metallic Glasses and Composites. *Journal of Materials Research*, Vol. 22, No. 2, (February 2007), pp. 285-301, ISSN 0884-2914

Egami, T., & Waseda, Y. (1984). Atomic Size Effect on The Formability of Metallic Glasses. *Journal of Non-Crystalline Solids*, Vol. 64, No. 1-2, (April 1984), pp. 113–134, ISSN 0022-3093

Egami, T. (1997). Universal Criterion for Metallic Glass Formation. *Materials Science and Engineering A*, Vol. 226-228, No. 1-2, (June 1997), pp. 261-267, ISSN 0921-5093

Egami, T. (2003). Atomistic Mechanism of Bulk Metallic Glass Formation. *Journal of Non-Crystalline Solids*, Vol. 317, No. 1-2, (March 2003), pp. 30–33, ISSN 0022-3093

Eshelby, J.D. (1956). The Continuum Theory of Lattice Defects, In: *Solid State Physics Vol. 3: Advances in Research and Applications*, Seitz, F., & Turnbull, D., pp. 79-144, Academic Press, ISBN 9780126077032, New York, USA

Fan, G.J., Zhao, J.C., & Liaw, P.K. (2010). A Four-Step Approach to The Multicomponent Bulk-Metallic Glass Formation. *Journal of Alloys and Compounds*, Vol. 497, No. 1-2, (May 2010), pp. 24-27, ISSN 0925-8388

Gallego, L.J., Somoza, J.A., & Alonso, J.A. (1990). Glass-Formation in Ternary Transition-Metal Alloys. *Journal of Physics-Condensed Matter*, Vol. 2, No. 29, (July 1990), pp. 6245-6250, ISSN 0953-8984

Goncalves, A.P., & Almeida, M. (1996). Extended Miedema Model: Predicting The Formation Enthalpies of Intermetallic Phases with More Than Two Elements. *Physica B*, Vol. 228, No. 3-4, (November 1996), pp. 289-294, ISSN 0921-4526

Herbst, J.F. (2002). On Extending Miedema's Model to Predict Hydrogen Content in Binary and Ternary Hydrides. *Journal of Alloys and Compounds*, Vol. 337 No. 1-2, (May 2002), pp. 99-107, ISSN 0925-8388

Hohenberg, P., & Kohn, W. (1964). Inhomogeneous Electron Gas. *Physical Review*, Vol. 136, No. 3B, (Novemeber 1964), pp. B864-B871, ISSN 0163-1829

Inoue, A., Kita, K., Zhang, T., & Masumoto, T. (1989). An Amorphous $La_{55}Al_{25}Ni_{20}$ Alloy Prepared by Water Quenching. *Materials Transactions JIM*, Vol. 30, No. 9, (September 1989), pp. 722-725, ISSN 1345-9678

Inoue, A., Yamaguchih, H., Zhang, T., & Masumoto. T. (1990). Al-La-Cu Amorphous-Alloys with A Wide Supercooled Liquid Region. *Materials Transactions JIM*, Vol. 31, No. 2, (Feburary 1990), pp. 104-109, ISSN 1345-9678

Inoue, A., Nakamura, T., Nishiyama, N., & Masumoto, T. (1992). Mg-Cu-Y Bulk Amorphous-Alloys with High-Tensile Strength Produced by A High-Pressure Die-

Casting Method. *Materials Transactions JIM*, Vol. 33, No. 10, (October 1992), pp. 937-945, ISSN 1345-9678

Inoue, A., Nishiyama, N., & Kimura, H. (1997). Preparation and Thermal Stability of Bulk Amorphous $Pd_{40}Cu_{30}Ni_{10}P_{20}$ Alloy Cylinder of 72 mm in Diameter. *Materials Transactions JIM*, Vol. 38, No. 2, (February 1997), pp. 179-183, ISSN 1345-9678

Inoue, A. (2000). Stabilization of Metallic Supercooled Liquid and Bulk Amorphous Alloys. *Acta Materialia*, Vol. 48, No. 1, (Janurary 2000), pp. 279-306, ISSN 1359-6454

Inoue, A., & Takeuchi, A. (2002). Recent Progress in Bulk Glassy Alloys. *Materials Transactions*, Vol. 43, No. 8, (August 2002), pp. 1892-1906, ISSN 1345-9678

Johnson, W.L. (1986). Thermodynamic and Kinetic Aspects of The Crystal to Glass Transformation in Metallic Materials. *Progress in Materials Science*, Vol 30, No. 2, (January 1986), pp. 81–134, ISSN: 0079-6425

Johnson, W.L. (1999). Bulk Glass-Forming Metallic Alloys: Science and Technology. *MRS Bulletin*, Vol. 24, No. 10, (October 1999), pp. 42-56, ISSN 0883-7694

Klement, W., Willens, R.H., & Duwez, P. (1960). Non-crystalline Structure in Solidified Gold-Silicon Alloys. *Nature*, Vol. 187, No. 4740, (September 1960), pp. 869-870, ISSN 0028-0836

Kokotin, V. (2010). *Polyhedra-Based Analysis of Computer Simulated Amorphous Structures*. PhD thesis, Technical University Dresden, Germany

Lopez, J.M., Alonso, J.A., & Gallego, L.J. (1987). Determination of The Glass-Forming Concentration Range in Binary-Alloys from A Semiempirical Theory - Application to Zr-Based Alloys. *Physical Review B*, Vol. 36, No. 7, (July 1987), pp. 3716-3722, ISSN 1098-0121

Ma, H., Shi, L.L., Xu, J., Li, Y., & Ma E. (2005). Discovering Inch-Diameter Metallic Glasses in Three-Dimensional Composition Space. *Applied Physics Letters*, Vol 87, No. 18, (October 2005), pp. 181915, ISSN 0003-6951

Miedema, A.R., de Chatel, P.F., & de Boer, F.R. (1980). Cohesion in Alloys - Fundamentals of A Semi-Empirical Model. *Physica B, & C*, Vol. 100, No. 1, (January 1980), pp. 1-28, ISSN 0378-4371

Miracle, D.B., & Senkov, O.N. (2003). Topological Criterion for Metallic Glass Formation. *Materials Science and Engineering A*, Vol. 347, No. 1-2, (April 2003), pp. 50–58, ISSN 21-5093

Murty, B.S., Ranganathan, S., & Rao, M.M. (1992). Solid-State Amorphization in Binary Ti-Ni, Ti-Cu and Ternary Ti-Ni-Cu System by Mechanical Alloying. *Materials Science Engineering A*, Vol. 149, No. 2, (January 1992), pp. 231-240, ISSN 0921-5093

Niessen, A.K., de Boer, F.R., Boom, R., de Chatel, P.F., Matterna, W.C.M., & Miedema, A.R. (1983). Model Predictions for The Enthalpy of Formation of Transition Metal Alloys II. *Calphad*, Vol. 7, No. 1, (January-March 1983) pp. 51-70, ISSN 0364-5916

Ouyang, Y.F., Zhong, X.P., Du, Y., Feng, Y.P., & He, Y.H. (2006a). Enthalpies of Formation for The Al–Cu–Ni–Zr Quaternary Alloys Calculated via A Combined Approach of Geometric Model and Miedema Theory. *Journal of Alloys and Compounds*, Vol. 420, No. 1-2, (August 2006), pp. 175-181, ISSN 0925-8388

Ouyang, Y.F., Zhong, X.P., Du, Y., Jin, Z.P., He, Y.H., Yuan, Z.H. (2006b). Formation Enthalpies of Fe–Al–RE Ternary Alloys Calculated with A Geometric Model and Miedema's Theory. *Journal of Alloys and Compounds*, Vol. 416, No. 1-2, (June 2006), pp. 148-154, , ISSN 0925-8388

Pauling, L. (1960). *The Nature of The Chemical Bond*, 3rd Edition, Cornell University Press, ISBN 0-8014-0333-2, Ithaca, USA

Peker, A., & Johnson, W.L. (1993). A Highly Processable Metallic Glass: $Zr_{41.2}Ti_{13.8}Cu_{12.5}$-$Ni_{10.0}Be_{22.5}$. *Applied Physics Letters*, Vol 63, No. 17, (October 1993), pp. 2342–2344, ISSN 0003-6951

Politis, C., & Johnson, W.L. (1986). Preparation of Amorphous $Ti_{1-x}Cu_x$ ($0.10 < x < 0.87$) by Mechanical Alloying. *Journal of Applied Physics*, Vol. 60, No. 3, (August 1986), pp. 1147-1151, ISSN 0021-8979

Ray, P.K., Akinc, M., & Kramer, M.J. (2008). Estimation of Formation Enthalpies Using An Extended Miedema Approach. *Proceeding of 22nd Annual Conference on Fossil Energy Materials*, Pittsburgh, PA, USA, July 2008

Ray, P.K., Akinc, M., & Kramer, M.J. (2010). Applications of An Extended Miedema's Model for Ternary Alloys. *Journal of Alloys and Compounds*, Vol. 489, No. 2, (January 2010), pp. 357-361, ISSN 0925-8388

Rickman, J.M., & LeSar, R. (2002). Free-Energy Calculations in Materials Research. *Annual Review of Materials Research*, Vol. 32, No. 1, (January 2002) pp. 195-217, ISSN 1531-7331

Saunders, N., & Miodownik, A.P. (1998). *CALPHAD: Calculation of Phase Diagrams – A Comprehensive Guide*, Pergamon, ISBN 0-08-042129-6, New York, USA

Schwarz, R.B., Petrich, R.R., & Saw, C.K. (1985). The Synthesis of Amorphous Ni-Ti Alloy Powders by Mechanical Alloying. *Journal of Non-Crystalline Solids*, Vol. 76, No. 2-3, (December 1985), pp. 281-302, ISSN 0022-3093

Senkov, O.N., & Miracle, D.B. (2001). Effect of The Atomic Size Distribution on Glass Forming Ability of Amorphous Metallic Alloys. *Materials Research Bulletin*, Vol. 36, No. 12, (October 2001), pp. 2183-2198, ISSN 0025-5408

Shindo, T., Waseda, Y., & Inoue, A. (2002). Prediction of Glass-Forming Composition Ranges in Zr-Ni-Al alloys. *Mateirlas Transactions*, Vol. 43, No.10, (October 2002), pp. 2502-2508, ISSN 1345-9678

Smith, J.R., & Banerjea, A. (1987). New Approach to Calculation of Total Energies of Solids with Defects - Surface-Energy Anisotropies. *Physical Review Letters*, Vol. 59, No. 21, (November 1987), pp. 2451-2454, ISSN 0031-9007

Suryanarayana, C. (1980). *Rapidly Quenched Metals - A Bibliography 1973–1979*. Plenum, ISBN 0904357228, New York, USA

Suryanarayana, C., & Inoue, A. (2011). *Bulk Metallic Glasses*. CRC Press, ISBN 978-1-4200-8597-6, Boca Raton, London, New York

Takeuchi, A., & Inoue, A. (2001). Calculations of Amorphous-Forming Composition Range for Ternary Alloy Systems and Analyses of Stabilization of Amorphous Phase and Amorphous-Forming Ability. *Materials Transactions*, Vol. 42, No. 7, (July 2001), pp. 1435-1444, ISSN 1345-9678

Wang, D., Tan, H., & Li, Y. (2005). Multiple Maxima of GFA in Three Adjacent Eutectics in Zr–Cu–Al Alloy System - A Metallographic Way to Pinpoint The Best Glass Forming Alloys. *Acta Materialia*, Vol. 53, No. 10, (June 2005), pp. 2969-2979, ISSN 1359-6454

Wang, W.C., Li, J.H., Yan, H.F., & Liu, B.X. (2007). A Thermodynamic Model Proposed for Calculating The Standard Formation Enthalpies of Ternary Alloy Systems. *Scripta Materialia*, Vol. 56, No. 11, (June 2007), pp. 975-978, ISSN 1359-6462.

Wang, W.H. (2009). Bulk Metallic Glasses with Functional Physical Properties. *Advanced Materials*, Vol. 21, No. 45, (December 2009), pp. 4524-4544, ISSN 0935-9648

Weeber, A.W. (1987). Application of The Miedema Model to Formation Enthalpies and Crystallization Temperatures of Amorphous Alloys. *Journal of Physics F Metal Physics*, Vol. 17, No. 4, (April 1987), pp. 809-813, ISSN 0305-4608

Weeber, A.W., & Bakker, H. (1988). Extension of the Glass-Forming Range of Ni-Zr by Mechanical Alloying. *Journal of Physics F Metal Physics*, Vol. 18, No. 7, (July 1988), pp. 1359-1369, ISSN 0305-4608

Weeber, A.W., Loeff, P.I., & Bakker, H. (1988). Glass-Forming Range of Transition Metal-Transition Metal Alloys Prepared by Mechanical Alloying. *Journal of the Less-Common Metals*, Vol. 145, (December 1988), pp. 293-299, ISSN 0022-5088

Xia, L., Li, W.H., Fang, S.S., Wei. B.C., & Dong, Y.D. (2006a). Binary Ni-Nb Bulk Metallic Glasses. *Journal of Applied Physics*, Vol 99, No. 2, (January 2006), pp. 026103, ISSN 0021-8979

Xia, L., Ding, D., Shan, S.T., & Dong, Y.D. (2006b). The Glass Forming Ability of Cu-Rich Cu-Hf Binary Alloys. *Journal of Physics-Condensed Matter*, Vol. 18, No. 15, (April 2006), pp. 3543-3548, ISSN 0953-8984

Xia, L., Fang, S.S., Wang, Q., Dong, Y.D., & Liu, C.T. (2006c). Thermodynamic Modeling of Glass Formation in Metallic Glasses. *Applied Physics Letters*, Vol. 88, No. 17, (April 2006), pp. 171905, ISSN 0003-6951

Xu, J., Ramamurty, U., & Ma E. (2010). The Fracture Toughness of Bulk Metallic Glasses. *JOM*, Vol. 62, No. 4, (April 2010), pp. 10-18, ISSN 1047-4838

Yan, Z.J., Li, J.F., He, S.R., & Zhou, Y.H. (2003). Evaluation of The Optimum Solute Concentration for Good Glass Forming Ability in Multicomponent Metallic Glasses. *Materials Research Bulletin*, Vol. 38, No. 4, (March 2003), pp. 681-689, ISSN 0025-5408

Zhang, B.W., & Jesser, W.A. (2002). Formation Energy of Ternary Alloy Systems Calculated by An Extended Miedema Model. *Physica B*, Vol. 315, No. 1-3, (April 2002), pp. 123-132, ISSN 0921-4526

Zhang, L.C., Xu, J., & Ma, E. (2006). Consolidation and Properties of Ti-based Bulk Amorphous Alloy by Equal Channel Angle Extrusion. *Materials Science and Engineering A*, Vol. 434, No. 1-2, (October 2006), pp. 280-288, ISSN 0921-5093.

Zhang, L.C., Kim, K.B., Yu, P., Zhang, W.Y., Kunz, U., & Eckert, J. (2007). Amorphization in Mechanically Alloyed (Ti, Zr, Nb)-(Cu, Ni)-Al Equiatomic Alloys. *Journal of Alloys and Compounds*, Vol. 428, No. 1-2, (January 2007), pp. 157-163, ISSN 0925-8388

Zheng, Q., Ma, H., Ma, E., & Xu, J. (2006). Mg–Cu–(Y, Nd) Pseudo-Ternary Bulk Metallic Glasses: The Effects of Nd on Glass-Forming Ability and Plasticity. *Scripta Materialia*, Vol. 55, No. 6, (September 2006), pp. 541-544, ISSN 1359-6462

16

Equilibria Governing the Membrane Insertion of Polypeptides and Their Interactions with Other Biomacromolecules

Aisenbrey Christopher and Bechinger Burkhard
University of Strasbourg / CNRS, Institut de chimie, Strasbourg
France

1. Introduction

Many biological processes are governed by chemical equilibria and the conventional thermodynamic formalisms apply. In particular the association of ligands to macromolecules, such as enzymes to large supramolecular structures, to large assemblies of proteins and/or nucleic acids (e.g. the ribosome) or to membranes has important consequences for the regulation of many biological activities and a quantitative understanding of these processes is of utmost importance for basic biological sciences and even more so for applied biomedical research. As the macromolecules involved can participate in many such regulatory interactions and these interactions are interconnected it is often necessary to describe such interaction networks by systems biology approaches. Here we illustrate the underlying thermodynamic principles by taking as an example a family of peptides that exhibit antimicrobial and cell penetrating activities which are potentially at the center for the transport of nucleic acids into cells, a property that is useful for some of state-of-the art medical treatments using highly-specific small interfering RNA or DNA molecules. The thermodynamic concepts will be illustrated by focusing on the interactions of these peptides, namely their partitioning into lipid membranes and the association of such peptides with nucleic acids, and we conclude with more detailed presentations of some of the methods that have been used for their investigation.

2. Observations on the membrane interactions of amphipathic helical peptides

Amphipathic helical peptides adopt a variety of alignments in lipid membranes. Membrane-active peptides are produced in nature, such as alamethicin and melittin (Bechinger, 1997), or are created by design (Lear et al., 1988; Bechinger, 1996; Killian et al., 1996) and their study by biophysical approaches has provided valuable insight into their lipid interactions as well as their mechanisms of membrane permeabilization. Of the peptides occurring in nature the dodecameric peptide alamethicin causes well-characterized voltage-dependent conductance changes of the membrane and therefore these peptides have early on served as a paradigm for large voltage- or ligand-gated channel proteins (reviewed e.g. in (Sansom, 1993; Bechinger, 1997; Leitgeb et al., 2007)). The open alamethicin pore is thought to consist

of a 'transmembrane helical bundle' in which the individual helices are grouped with their more hydrophilic side facing the water-filled pore (Sansom, 1993). Such barrel shaped pores may be less regular and more asymmetric than the first models suggested (Unwin, 2005). Similar transmembrane helical bundle arrangements have been observed for a variety of membrane proteins (Long et al., 2007; Traaseth et al., 2007; Cady et al., 2010).

Although a strong propensity for transmembrane alignments (TM) of the very hydrophobic alamethicin is indeed observed (Salnikov et al., 2009) a variety of biophysical approaches including oriented solid-state NMR and CD spectroscopies (cf. 4.5) indicate that alamethicin can also adopt in-planar (IP) alignments (Salnikov et al., 2010). Possibly, the in-planar state of alamethicin is an intermediate during membrane association and channel gating (Sansom, 1993; Bechinger, 1997) and a series of subsequent equilibria govern the polypeptide interactions within the membrane (in-plane ↔ transmembrane ↔ TM oligomers, cf. Figure 1). Various models for the molecular mechanism of alamethicin pore-formation are based on interactions of its helix dipole with the TM electric field, where reorientation of the dipole, enhanced partitioning of alamethicin into the bilayer and/or membrane insertion of the N-terminus results in the voltage-gating of the channel structure (reviewed in Sansom, 1993; Bechinger, 1997). As other shorter peptaibols, i.e. peptides of amino acid composition, hydrophobicity and amphipathicity closely related to alamethicin, are predominantly found oriented parallel to the membrane surface the hydrophobic matching between the membrane thickness and the peptide helix has been found to be an important parameter governing this equilibrium (Bechinger et al., 2001; Salnikov et al., 2009; Salnikov & Bechinger, 2011).

Another class of amphipathic peptides that are found in nature protects the producing host organism from pathogenic infections. The best studied of these sequences are the cationic amphipathic polypeptides magainin, cecropin and melittin. These antimicrobial compounds were first isolated from frogs and insects and when compared to alamethicin and related peptides it is noteworthy that they carry several positive charges on their hydrophilic faces. As a consequence magainins and ceropins stably intercalate into the membrane with the helix axis oriented parallel to the membrane surface (Bechinger, 1999). By interacting with the membranes of bacteria and/or fungi these peptides are capable to disturb their bilayer integrity and/or enter the cell interior and thereby develop their antimicrobial activities (Bechinger, 1999; Brogden, 2005).

The alignment of the magainin helices parallel to the membrane surface places their hydrophobic region about 10 Å above the bilayer centre in agreement with the amphipathic distribution of polar-charged and hydrophobic residues (Matsuzaki et al., 1994). Notably, in this manner the peptides have pronounced effects on the membrane structure including the disruption of the fatty acyl chain packing (Salnikov et al., 2009), membrane thinning (Ludtke et al., 1995), pore formation (Gregory et al., 2008) and macroscopic phase transitions of the peptide-lipid assemblies (Bechinger, 2009). All of these modifications are associated with changes in the enthalpy and entropy of the system and merit consideration in a thermodynamic analysis.

When added to pre-formed bilayers magainins and melittin have been shown to partition into the membranes within tens of seconds (Mozsolits et al., 2001; Papo & Shai, 2003). The partitioning of magainin 2 into the membrane interface is characterized by a coefficient of about 1000 M^{-1} in the presence of zwitterionic but overall neutral membranes (Wieprecht et al., 1999), a value that apparently increases by orders of magnitude for negatively charged surfaces (Wenk & Seelig, 1998). This is explained by an augmentation of the local

concentration of positively charged peptides next to the anionic membrane surface (illustrated in Bechinger, 2004). Furthermore, these cationic peptides have been shown to preferentially interact with the negatively charged phospholipids in mixed model membranes resulting in their segregation into domains rich in anionic phospholipids and cationic peptides (Mason et al., 2006). Therefore, electrostatic interactions not only control the membrane association of cationic amphiphiles, but they also have a pronounced effect on the lateral distribution of the lipids within mixed bilayers.

The different examples mentioned above show that membrane-active peptides can occur in many different alignments and the predominant topology depends on a number of factors such as lipid composition, peptide-to-lipid ratio, hydration, temperature, pH and the presence of additional membrane components (Bechinger, 1996; Huang, 2000; Vogt et al., 2000; Tremouilhac et al., 2006; Salnikov & Bechinger, 2011). The membrane alignment of several peptides has been investigated by biophysical approaches such as circular dichroism or ^{15}N solid-state NMR spectroscopy (cf. 4.5), where the peptides have been reconstituted into oriented and more recently also non-oriented membranes (Wu et al., 1990; Bechinger & Sizun, 2003; Prongidi-Fix et al., 2007). The transitions between such states have been characterized by equilibria such as those shown in Figure 1.

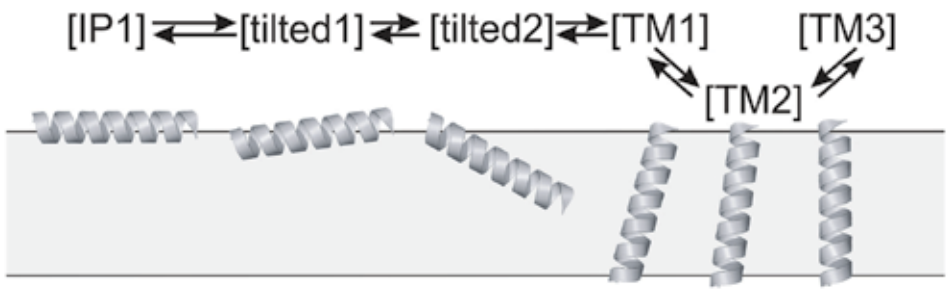

Fig. 1. Shows a selection of the equilibria that interconnect the many different membrane topologies.

The different TM states could represent, for example, different tilt angles such as those observed for the antimicrobial peptide PGLa (Salnikov & Bechinger, 2011) and/or oligomerisation states, and the possibility exists that the IP topology is also to be diversified into additional sub-states (Figure 1). The thermodynamic treatment of the in-plane to transmembrane transition will be presented in section 3.2.

When added to lipid bilayers amphipathic peptides induce alterations in the lipid macroscopic phase properties that in many ways resemble changes observed in the presence of detergents (Bechinger, 1999; Bechinger, 2005). Indeed, a decrease in the order parameter of lipid bilayers due the presence of magainins and other amphipathic peptides has been monitored in solid-state NMR measurements (Dvinskikh et al., 2006; Mason et al., 2007; Salnikov et al., 2009). As a consequence the bilayer packing is disturbed within an estimated radius of approximately 50 Å (Chen et al., 2003; Mecke et al., 2005). These effects have been explained by taking into consideration the molecular shapes of the lipids and peptides. Whereas cylindrical molecules, which equally fill the membrane interior and the interface, form stable bilayer structures amphipathic molecules that occupy a much larger space at the interface than in the hydrophobic part of the membranes cause positive curvature strain,

and lipids with very small head groups have the opposite effect (Israelachvili et al., 1980; Bechinger, 2009). Therefore the consequences of peptide association with the membrane are dependent on the ensemble of peptide molecular properties but also the size and shape of the lipid head groups, i.e. the membrane lipid composition (Bechinger, 2009). Notably, when added at high enough concentrations the peptides can even cause membrane disintegration (Dufourc et al., 1986; Hallock et al., 2002; Bechinger, 2005). The many possible outcomes of this plasticity of phospholipid membranes when interacting with peptides is best described by phase diagrams where the wide range of structures, configurations and morphologies are shown as a function of peptide-to-lipid ratio, the detailed membrane composition, temperature, hydration and buffer composition (Bechinger, 1999; Bechinger & Lohner, 2006). Within such representations regions exists where the bilayers are only slightly perturbed or even stabilized due to the presence of polypeptide, whereas at the other extreme the membrane undergoes lysis. Furthermore, conditions where membrane openings form in a more regular manner can be found and these are probably the ones that are most interesting for a formal thermodynamic treatment. The peptide-induced phase alterations can be transient and local, or they can affect the supramolecular assembly as a whole (Bechinger, 2009).

3. The LAH4 family of peptides

The so called LAH4 sequences were designed to test if peptides in a predominantly in-planar configuration can indeed cause pore formation and the antimicrobial activities which have been described for many amphipathic sequences. The polar face of the helical LAH4 peptides consists of histidines and the hydrophobic region of alanines and leucines (Figure 2). Two lysines at each terminus have been added to increase the solubility of the peptides in aqueous environments. The histidines exhibit pK_a values around 6 and these residues can therefore be used to tune the hydrophobic moment of these sequences merely by changing the pH (Georgescu & Bechinger, 2010). The LAH4 peptides interact with membranes (Bechinger, 1996) and they exhibit antimicrobial activities (Vogt & Bechinger, 1999; Mason et al., 2009; Bechinger, 2011). Interestingly, more recent investigations show that derivatives of LAH4 exhibit potent antimicrobial action against a number of pathogens found in clinical environments, and these activities are quite pronounced when the peptides occur in orientations parallel to the membrane surface (Mason et al., 2006). Furthermore the LAH4 sequences are also capable to transport big hydrophilic cargo such as DNA and RNA across the hydrophobic interior of membranes and thereby exhibit potent transfection capacities (Kichler et al., 2003; Langlet-Bertin et al., 2010; Bechinger et al., 2011). Because of these important biological activities the thermodynamics of the peptides' interactions with membranes and nucleic acids were investigated in considerable detail and these investigations shall be presented in the following.

3.1 Membrane topology of LAH4 peptides

The interactions of LAH4 peptides with oriented phospholipid bilayers were analysed using solid-state NMR and ATR-FTIR spectroscopies (cf. 4.5). Whereas an alignment parallel to the bilayer surface was observed at pH < 6 when the histidines are cationic, transmembrane orientations are found when the histidines are discharged (Bechinger, 1996; Bechinger et al., 1999). Furthermore CD- and multidimensional solution NMR spectroscopies are indicative

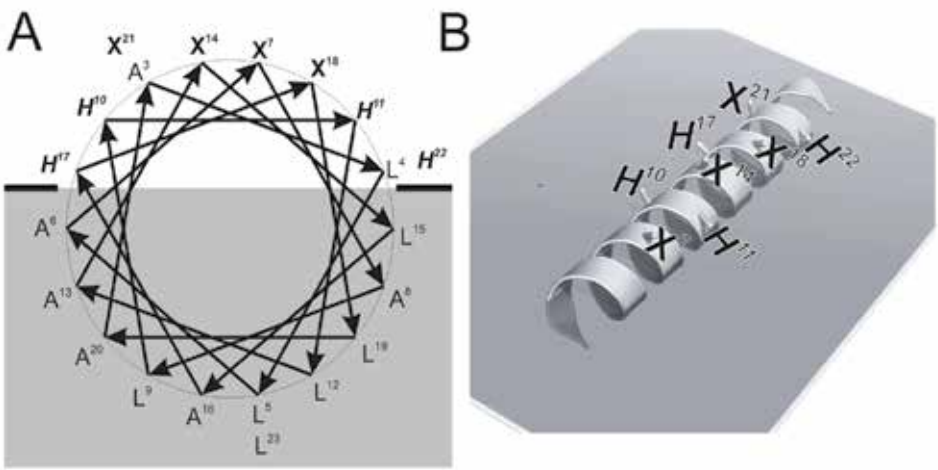

Fig. 2. Helical wheel representation of LAH4X4 (Aisenbrey et al., 2006), a sequence of the LAH4 family, obtained by viewing the arrangement of residues as a projection along the helix long axis (left) and top view onto the structure (right). An amphipathic distribution of residues becomes apparent when considering that the leucine (L) and alanine (A) residues exhibit a hydrophobic character (exposed to the membrane interior shaded in grey). In contrast, the histidines (H), are polar or charged, depending on the pH of the solvent. Variation of the character of the residues labelled X allows one to modulate the driving forces for membrane insertion and thereby the transmembrane alignment of the helical peptide. The N- and C-terminal lysines, two at each end, have been omitted for clarity.

that these histidine-rich peptides exhibit a high degree of α-helical conformations in micellar environments (Vogt & Bechinger, 1999; Georgescu & Bechinger, 2010). Remarkably, the outlines of the α-helical structures are pH dependent and shift from a C-terminal (encompassing residues 9-24 at pH 4.1) to a more N-terminal position (residues 4-21 at pH 7.8). At intermediate pH two short helices are interconnected by a hinge region of residues 10-13 (Georgescu & Bechinger, 2010). This flexible domain probably facilitates the transition from in-plane to transmembrane alignments. Notably, although aqueous solutions of the peptide appear transparent by eye dynamic light scattering measurements indicate that the peptides form small α-helical aggregates at neutral pH (Marquette et al., 2008). In contrast the hydrodynamic radii measured at acidic pH agree with an extended monomer. On a functional level the members of the LAH4 family exhibit membrane pore-formation in model membranes (Marquette et al., 2008) and antimicrobial action at both neutral and acidic pH (Vogt & Bechinger, 1999). These observations indicate that a well-defined transmembrane channel structure is not required for biological action.

Notably the transition between in-planar and transmembrane alignments is reversible, a requirement to evaluate the transfer energy of amino acid side chains from the membrane interface to the membrane interior using equilibrium thermodynamics. A direct measurement of these transition energies has been achieved to our knowledge for the first time by modulating the composition of the polar face through amino acid replacements (Figure 2) and by analysing the resulting shifts in the transition pH (Aisenbrey et al., 2006;

Aisenbrey et al., 2006). In order to achieve this goal it was necessary to develop the thermodynamic formalism presented in the next section.

3.2 Formalism to describe the membrane topological transitions of amphipathic peptides

In order to describe the in-plane to transmembrane transition of membrane-associated LAH4 peptides a series of consecutive equilibria connecting subsequent states is considered: $IP^{ch} \leftrightarrow IP^{o} \leftrightarrow TM$ (Aisenbrey et al., 2006; Aisenbrey et al., 2006). The in plane configuration (IP) of the helices, can occur with the histidines charged (ch) or neutral (o) and TM represents the transmembrane inserted state (Figure 3). This model can be extended by also considering peptides that are dissolved in the aqueous buffer and which are in exchange with the surface-associated state IP^{ch}.

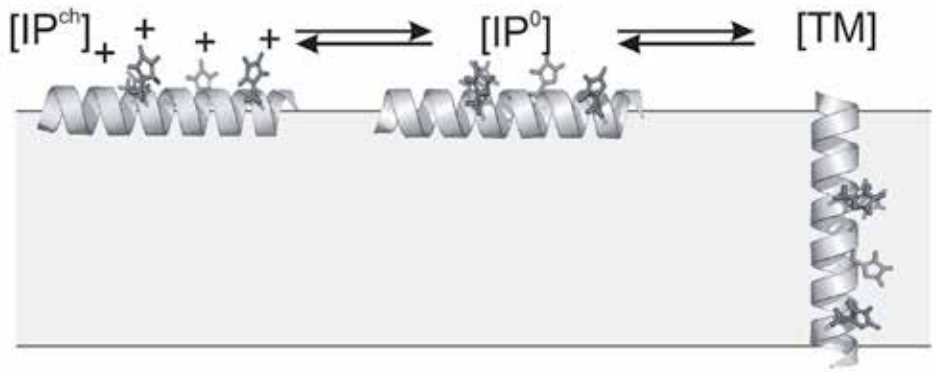

Fig. 3. Model of LAH4 in the lipid membrane. The transmembrane state is in thermodynamic equilibrium with in-planar alignments and uncharged histidines. Notably, two in-planar states are considered namely one where the histidines are neutral and another one where these side chains are protonated. The charges carried by the histidines strongly depend on the pH of the surrounding medium.

The energy contributions that govern the in-plane → transmembrane reorientation process include the interactions of hydrophobic and polar amino acids in different environments but also contributions such as van der Waals, steric or entropic contributions that change upon disruption of the lipid packing and are different when peptides partition to the membrane interface or when they insert in a transmembrane fashion (reviewed in Bechinger, 1996). Furthermore, according to the model presented in Figure 3 only uncharged histidines are capable to insert into the membrane interior and their discharge is a prerequisite for LAH4 transmembrane alignments. Therefore, peptides carrying charged histidine side chains remain at the membrane surface and adopt in-plane orientations.

However, even at pH values smaller or around the pK_a the histidine side chains can be neutralized (Bechinger, 1996; White & Wimley, 1999) thereby permitting membrane insertion at lower energetic cost than when placing a charged residue into the hydrophobic membrane interior (Israelachvili et al., 1980). The required energy of discharge must derive from other driving forces that are associated with changes in the peptide topology including for example favourable 'hydrophobic' contributions. As a consequence the transmembrane-insertion, conformational changes that are associated with membrane-association and the

discharge of side chains are often tightly connected processes (Liu et al., 1996; Aisenbrey et al., 2006) and if this is the case a direct equilibrium between the transmembrane uncharged peptide and the in-planar charged peptide can be established ($IP^{ch} \leftrightarrow TM$).
On the other hand, when additional polar amino acids (other than the histidines) favourably interact with the water phase even the complete neutralisation of the histidines is insufficient to promote the transmembrane insertion, therefore the in-planar state remains strongly populated even when the histidines are uncharged (IP^{o}). When the pH of the sample is augmented the four histidines of LAH4 and related sequences become neutral in a gradual manner and close to the pK_a values of the histidines, only a fraction of these side chains are cationic. Therefore, under such conditions a transmembrane uncharged state (TM), an uncharged in-planar state (IP^{o}) and in-planar states carrying a variable number of charges have all to be taken into consideration (IP^{1+}, IP^{2+}, IP^{3+}, IP^{4+}).
Standard thermodynamic relationships allow one to calculate the equilibrium constant for the IP to TM transition from the Gibb's free energy ΔG associated with the transition of the peptide from the interface into the membrane interior (or vice versa). Whereas the in-plane alignment occurs on both sides of the lipid bilayer two possible orientations exist for the transmembrane peptide. Therefore, the equilibrium constant is calculated according to

$$k_{TM} = \frac{[TM]}{[IP^{o}]} = \mathrm{e}^{\frac{-\Delta G}{RT}} \tag{1}$$

Furthermore, the uncharged in-planar configuration (IP^{o}) is in equilibrium exchange with the series of charged in-planar states (IP^{ch}). Assuming that none of these charged states inserts into the membrane in a transmembrane fashion, they combine to $[IP^{ch}] = [IP^{1+}]+[IP^{2+}]+[IP^{3+}]+[IP^{4+}]$. The reciprocal of the constant (k_{ch}) for the transition $IP^{o} \leftrightarrow IP^{ch}$ is expressed as a sum of the reciprocals of the individual constants:

$$1/k_{Ch} = \frac{[IP^{ch}]}{[IP^{o}]} = \sum 1/k_j \text{, with } k_j = \frac{[IP^{o}]}{[IP^{j+}]} \tag{2}$$

Where k_j depends on the free energy difference by charging j histidines, which is statistically possible in $\varepsilon_j = \binom{4}{j}$ different ways. The constants are given by:

$$k_j = \frac{[IP^{o}]}{[IP^{j}]} = \frac{1}{\varepsilon_j}\mathrm{e}^{-2.3\,j\,(pH-pK_a)} \tag{3}$$

Combining equations [2] and [3] gives

$$1/k_{Ch} = \frac{[IP^{ch}]}{[IP^{o}]} = \sum_{j=1}^{4}\binom{4}{j}\left(\mathrm{e}^{2.3\,(pH-pK_a)}\right)^{j} = \left(1+\mathrm{e}^{2.3(pK_a-pH)}\right)^{4} - 1 \tag{4}$$

The ratio of the transmembrane over total peptide concentration, p_{TM}, which can be determined by various experimental methods (cf. 4.5), is:

$$p_{TM} = \frac{[TM]}{[TM] + [IP^o] + [IP^{ch}]} = \frac{1}{1 + e^{\frac{\Delta G}{RT}\left(1 + e^{2.3(pK_a - pH)}\right)^4}} \tag{5}$$

Equation [5] is graphically represented in Figure 4. The simulations show that the steepness of the transition depends on ΔG, being steeper for the more favoured transitions (i.e. negative ΔG). In contrast, if the overall driving force approaches zero or for positive ΔG the transmembrane state is only partly populated regardless of pH. Figure 4 also illustrates that for ΔG near zero or at positive values, the transition mid-point is shifted towards pH values higher than the pK_a of the histidines. This shift arises from the degeneracy of the in-planar states where statistically the configurations carrying one to three charges is possible in multiple (ε_j) ways.

Through addition of hydrophobic residues at the X-positions (Fig. 2) ΔG << 0 and the transition takes place at pH < pK_a. Under such conditions an approximation for the fraction of transmembrane peptide is obtained by

$$p_{TM} \approx \frac{1}{1 + e^{4 \cdot 2.3\left(pK_a + \frac{\Delta G}{2.3 \cdot 4\,RT} - pH\right)}} \tag{6}$$

The resulting curve is sigmoidal with the transition at $pK_a - \frac{\Delta G}{4 \cdot 2.3\,RT}$, a result also obtained by considering a simple model where the transition is described by the equilibrium $IP^{4+} \leftrightarrow TM$ as described before (Bechinger, 1996). In this simpler case the midpoint of transition occurs at pH_{50}, the pH value where 50% of the molecules are in transmembrane state (p_{TM}=1/2). Using equation [5] one obtains:

$$p_{TM} = \frac{[TM]}{[TM] + [IP^o] + [IP^{ch}]} = \frac{1}{1 + e^{\frac{\Delta G}{RT}\left(1 + e^{2.3(pK_a - pH)}\right)^4}} \tag{7}$$

When peptides of moderate or low hydrophobicity are studied a better description of the transition is obtained when measuring $p_{1/2}$, which indicates the pH where 50% of the maximal p_{TM} is reached ($p_{1/2}$=1/2 p_{TM}^{max} cf. Figure 4). With

$$p_{TM}^{max} = \frac{1}{1 + e^{\frac{\Delta G}{RT}}} \tag{8}$$

$pH_{1/2}$ can be expressed as

$$pH_{1/2} = pK_a - \frac{1}{2.3} \ln\left(\left(e^{\frac{\Delta G}{4RT}} + 2\right)^{\frac{1}{4}} - 1\right) \tag{9}$$

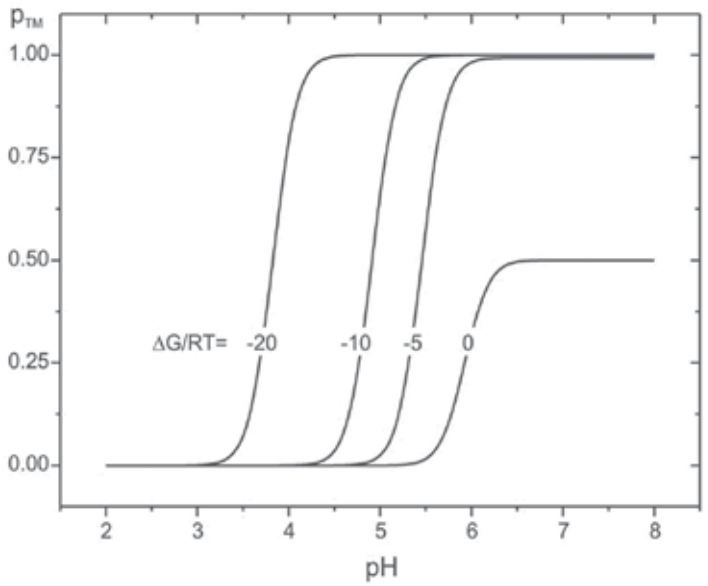

Fig. 4. Graphical representations of equation [5]. The pH-dependent transmembrane fraction of histidine-rich amphipathic peptides (LAH4 family) is shown as a function of the Gibb's free energy of the IP → TM transition.

Finally we should note that the local pH close to the membrane surface or in the proximity of other charges and dipoles can exhibit significant differences when compared to the proton activity in bulk solution. As a consequence when the the pK_a values of LAH4 and related peptides associated to DPC detergent micelles were determined using NMR spectroscopy the titration curves appeared less steep than expected from the Henderson-Hasselbach equation (Bechinger, 1996; Georgescu & Bechinger, 2010). Therefore, in order to take into account attractive or repulsive interactions at the biomolecular surfaces a correction parameter c was introduced and equation [5] modified:

$$p_{TM} = \frac{1}{1 + e^{\frac{\Delta G}{RT}\left(1 + e^{2.3\ c\left(pK_a - pH\right)}\right)^4}} \tag{10}$$

By fitting the pH-dependent ^{1}H NMR chemical shifts of the indol 4H positions of LAH4 (and related peptides) average values of c=0.8 and pK_a=6.0 are obtained (Aisenbrey et al., 2006; Aisenbrey et al., 2006).

The formalism introduced in this section was used in previous publications to follow the membrane topological changes of LAH4 and other amphipathic peptides using solid-state NMR and ATR-FTIR spectroscopies on oriented phospholipid bilayers (Bechinger, 1996; Bechinger et al., 1999; Vogt et al., 2000; Bechinger, 2001). Notably this has allowed to directly measure the energies that are associated with the transition of amino acid residues from a membrane interfacial location to the membrane interior (Aisenbrey et al., 2006; Aisenbrey et al., 2006) and to compare these values with calculations where this transition has been part of a thermodynamic cycle (White & Wimley, 1999). Interestingly when amino acid residues

are compared to each other the preferences are somewhat different when the transitions from the interface → membrane interior are compared to those from the aqueous phase → membrane interior. In particular the alanine residues that are considered 'hydrophobic' on the latter scale have an equal preference for interfacial and inner positions (Bechinger, 2001; Aisenbrey et al., 2006). Furthermore, the measurements indicate that tyrosine, tryptophan and valine exhibit a tendency to remain associated with the membrane interface (Aisenbrey et al., 2006).

When considering the interaction contributions that govern IP to TM transitions of helical peptides as a whole, $\Delta G_{IP \Leftrightarrow TM}$, changes in the environment of amino acid side chains have to be considered as discussed in the previous paragraph (White & Wimley, 1999; Bechinger, 2000; Aisenbrey et al., 2006). In addition the ensemble of contributions that arise from changes in the packing of the phospholipid membrane, hydrophobic mismatch and peptide-peptide interactions are relevant to dissect the energy contributions governing these equilibria (Bechinger, 1996; Harzer & Bechinger, 2000). The hydrophobic mismatch contributions have been found particularly important when the topologies of the antimicrobial peptide PGLa (Salnikov & Bechinger, 2011) or that of peptaibols, such as the 15 residue zervamicin II or ampullosporin A were studied (Bechinger et al., 2001; Salnikov et al., 2009). Although the data indicate that hydrophobic mismatch has a pronounced influence on the peptide topology, it was also found that the peptaibols adopt transmembrane alignments only within bilayers that are thinner than one would expect from their hydrophobic length alone. Therefore, in order to explain such differences other interactions need to be taken into consideration as well. Furthermore, more recent studies indicate an interfacial localisation of alamethicin, a hydrophobic peptide generally found to adopt transmembrane alignments, is stabilized in the presence of phosphatidylethanolamine. This lipid carries a relatively small head group and it is thought that the alamethicin helix relieves some of the packing frustration in a bilayer environment by occupying space at the bilayer interface (Salnikov et al., 2010).

Finally it should be mentioned that amphipathic sequences such as cationic antimicrobial peptides or LAH4 also dissolve in the aqueous phase surrounding the membranes. Therefore an additional reversible equilibrium merits thermodynamic analysis namely the transition from the water phase to the membrane-associated state. The membrane-association of these peptides has been quantitatively analysed by centrifugation assays where the residual amount of peptide in the aqueous phase in the presence of increasing amounts of lipids is determined by following the changes in spectroscopic signals such as for example the tryptophan fluorescence (cf. 4.1), or by performing a full thermodynamic analysis using isothermal titration calorimetry (Wenk & Seelig, 1998; Seelig, 2004). Notably, many of these methodologies do not differentiate between various membrane associated states and therefore include all of the topological possibilities discussed in the previous sections.

3.3 Interactions of LAH4 peptides with DNA

In addition to the pronounced antimicrobial properties that were discussed in section 3.1 (Vogt & Bechinger, 1999; Mason et al., 2006; Mason et al., 2007; Mason et al., 2009) the LAH4 peptides also exhibit potent DNA transfection activities (Kichler et al., 2003). Furthermore, it was recently shown that they are potent siRNA delivery vehicles with efficiencies that are higher than those of several well-established compounds such as Lipofectamine, DOTAP and polyethylenimine (Langlet-Bertin et al., 2010). In our laboratory a number of biophysical

investigations have been performed, supported by many biochemical studies by our long-standing collaborators, which aimed at understanding the mechanisms of these transfection activities. Indeed, the ensemble of data has allowed to modify the initial LAH4 sequence in such a manner to obtain considerably improved transfection activities (Kichler et al., 2006; Mason et al., 2006; Mason et al., 2007; Mason et al., 2007). Interestingly, in some of the hereditary diseases, such as cystic fibrosis, the patients suffer from increased infection rates and augmented sensibility to some highly pathogenic species. Therefore, the simultaneous antimicrobial and DNA transfection activities of the LAH4-transfection complexes are of potential interest for multimodal applications (Kichler et al., 2003).

Gel shift and biochemical experiments indicate that large peptide-DNA complexes form when the peptide and the nucleic acids are mixed at neutral conditions and this complexation is required for the entry into cells via an endosomal pathway (Kichler et al., 2003; Kichler et al., 2007). However, efficient transfection also requires that the information carried by the nucleic acids is made available at their cytoplasmic or nuclear destination, respectively. It is therefore essential that at their destination these macromolecules are liberated from their carrier, which requires that the interactions are reversible and not too tight. Therefore, the association/dissociation equilibria of the LAH4-DNA transfection complexes have been investigated as a function of pH using isothermal titration calorimetry (ITC), a method that provides a full thermodynamic analysis of binding constant, number of binding sites, ΔG, ΔH and ΔS (cf. 4.4).

The ITC analysis of the LAH4-DNA interactions indicate that under saturating conditions and at pH 7.5 one peptide is associated with about 2 base pairs of DNA. Association occurs in the μM range and the thermodynamic signature suggests that under these conditions is driven by electrostatic interactions. As the histidine side chains are probably uncharged at neutral conditions (Bechinger, 1996) the data have been suggestive that the cationic lysine termini of LAH4 interact with the negatively charged phosphates of the DNA, a conclusion that was recently confirmed by solid-state NMR distance measurements (Bechinger et al., 2011). Indeed only the lysine side chain nitrogens show close-by contacts with the DNA phosphates (< 8 Å). Condensation of the DNA strands into compact globular structures can therefore be explained by interactions of the anionic phosphates with two lysine side chains at each terminus of the peptide thereby enabling the cross-linking of distant parts of the extended DNA molecule, as well as of different DNA strands.

At pH < 6, such as it occurs in the endosomal compartment, the four histidine side chains become positively charged thereby doubling the overall charge of the peptide. As a consequence about half of the peptides are released from the transfection complex (Prongidi-Fix et al., 2007). At the same time the thermodynamic signature of the ITC experiments are indicative of structural arrangements as hydrophobic and van der Waals contacts also become important and complement the electrostatic interactions. Importantly the peptides liberated from the complex at low pH are readily available to interact with the endosomal membranes.

4. Methods for the quantitative measurement of thermodynamic quantities

4.1 Peptide-association with lipid vesicles using tryptophan fluorescence spectroscopy

The adsorption of peptides to lipid membranes can be measured by any physical property that changes upon the process and following the fluorescence signal of tryptophan (Musse

et al., 2006) or circular dichroism spectroscopy (cf. 4.2) are widely used methods. A mayor advantage of tryptophan fluorescence spectroscopy is the natural occurrence of this amino acid residue within the sequence of many proteins and peptides (Lakey et al., 1993). As the diameter of the vesicles is of similar size as the wave length of the emitted light recording of such spectra has to be done with care and precautions need to be taken during the processing of the experimental data (Ladokhin et al., 2000). The tryptophan fluorescence signal is highly dependent on its environment (Fig. 5A-C). Whereas the spectral intensities are quenched (reduced) and red shifted in polar environments, an increased and blue-shifted emission spectrum is observed in more apolar solvents (Sun et al., 2010). This effect is used, for example, in the stopped-flow kinetic analysis of protein folding, where tryptophan moieties tend to move from the polar aqueous buffer into the hydrophobic interior of the protein. In the presence of lipid vesicles an increased fluorescence signal is an indication for the insertion of this amino acid side chain into the less polar interface or into the apolar interior of the membrane (Musse et al., 2006).

An essay for the membrane-association of polypeptides has been established where an increasing amount of small unilamellar phospholipid vesicles is titrated in a step-wise manner into a peptide solution of given concentration. This leads to a series of continuously changing spectra, and the alterations are used to follow polypeptide association and to calculate the association parameters. The use of small vesicles in such experiments (ca. 100 nm in diameter) avoids extensive scattering artefacts in the UV spectral range, which is typically used to monitor the tryptophan fluorescence.

Provided that during membrane-association the changes in the environment of the tryptophan side chains can be approximated by a transition between two distinct states, each being characterized by a sufficiently different fluorescence signal, a relatively simple analysis of the titration experiment is possible. In such a case the peptide simply transfers between 'free in solution' and 'associated with the membrane' (Fig. 5C). Notably, the two-state approximation is also possible if different configurations of the polypeptide, such as different aggregation states, result in equivalent fluorescence signals. For example, together the monomeric and the dimeric state of a polypeptide in solution would be considered as the 'water soluble protein fraction' as long as the tryptophan fluorescence is not affected by the association.

In such cases the fluorescence intensities of the polypeptide in aqueous buffer (0% bound) and in the presence of an excess of lipid membranes (100% bound) serve as reference for the analysis of the titration experiment. Provided that complete adsorption for the highest lipid concentration is reached the normalized change in signal intensity (or peak maximum) correspond directly to the fraction of bound peptide since all spectra are linear combinations of the two reference spectra. In order to obtain the binding curve with the highest accuracy possible the frequency with the biggest difference between the free and adsorbed state is generally used. However the normalized intensity change at any other frequency should lead to the same result except if additional equilibria need to be taken into consideration. In the latter case the data are analysed by a more sophisticated approach (Aisenbrey et al., 2008).

4.2 Titration experiments using circular dichroism spectroscopy

Circular dichroism spectroscopy is a relatively fast and inexpensive tool to estimate the secondary structure composition of proteins and peptides (Sreerama & Woody, 1993; Lees et

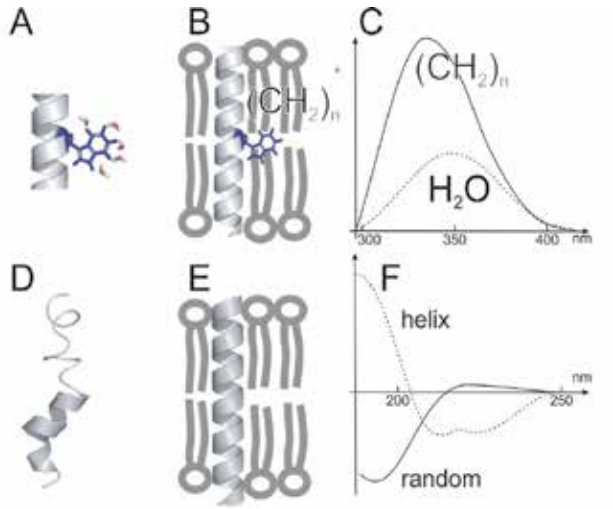

Fig. 5. Illustrates the principle of adsorption measurements by fluorescence and circular dichroism spectroscopies. Whereas the tryptophan fluorescence is quenched and red shifted in the polar aqueous environment (A) the fluorescence quantum yield increases upon transfer into the apolar environment of the membrane (B). As a consequence the fluorescence signal is increased and blue shifted in a hydrophobic environment (C solid line) when compared to those obtained in aqueous buffers (C, dotted line). Peptides that are mostly random coil in aqueous solution (D) often adopt helical structures when membrane-associated (E). Concomitant with this structural transition are CD spectral changes from random coil (F, solid line) to helical signatures (F, dashed lines).

al., 2006). It is based on the chirality of the peptide bond with its adsorption maximum in the range of 214 nm, therefore, circular dichroism spectrometers with a powerful light source in the UV spectral range are needed for these measurements. Provided that the peptide changes its secondary structure upon adsorption to lipid membranes the concomitant spectral changes can be used to follow the adsorption isotherm (Fig. 5F). Most commonly small unilamellar vesicles are titrated to a given concentration of peptide. In titration experiments using circular dichroism spectroscopy a good indication for the presence of a two-state transition is the presence of an isosbestic point. In this case similar considerations apply for the analysis of these experiments as those outlined for titrations using fluorescence spectroscopy (4.1).

4.3 Analysis of binding data in the case of more than two states

In the case of the presence of three states the relation between the concentrations (c_i of state i) and the measured signals S_{CD} and S_{fluo} is given by the following matrix, where S_{CD}^i and S_{fluo}^i are the CD and fluorescence signal intensities of state I, respectively.

$$\begin{pmatrix} S_{CD} \\ S_{fluo} \\ C_{peptide} \end{pmatrix} = \underbrace{\begin{pmatrix} S_{CD}^A & S_{CD}^B & S_{CD}^C \\ S_{fluo}^A & S_{fluo}^B & S_{fluo}^C \\ 1 & 1 & 1 \end{pmatrix}}_{SC} \begin{pmatrix} C_A \\ C_B \\ C_C \end{pmatrix} \tag{11}$$

The third line in the matrix assures the conservation of the masses. If the matrix elements of SC are known the concentrations can be calculated from the experimental fluorescence and circular dichroism signals by matrix inversion. This works only when the two optical techniques provide complementary information, i.e. the fluorescence change should not parallel exactly the CD transitions. If both methods provide redundant information the inverse matrix cannot be calculated. To determine the matrix elements it is necessary to measure the CD- and fluorescence signals of the pure states A, B and C, or to make some assumption that can resolve this issue. Such an assumption could be, that the polypeptide does not change its average secondary structure even though the tryptophans are in different chemical environments.
Even though the previous sections were dedicated to (tryptophan-)fluorescence and circular dichroism the principles of data analysis remain valid for other experimental methods as long as a change in the signal parallels the binding isotherm.

4.4 Measurement of enthalpy and free energy of binding by isothermal titration calorimetry

Isothermal titration calorimetry is based on the measurement of the reaction enthalpy when molecular interactions occur. The experiment is performed in such a manner that a ligand is added to a substrate in a step-wise manner and the heat of reaction measured with high precision during each injection of the ligand into the solution with the substrate (Fig. 6). The free energy of binding (the binding constant) is obtained by fitting a thermodynamic model to the resulting titration curve. The beginning of a titration experiment is characterized by an excess of substrate (Figure 6 A, red ¾ circles) and provided that the substrate has been made available at high enough concentrations all of the injected ligands bind to one of the substrates (Figure 6, green ¼ circles). Thus the reaction enthalpy per injected ligand is directly obtained. At the end of the experiment the binding sites of the substrate molecules are saturated and no further heat is released or consumed upon further addition of ligand (Figure 6B). If the binding constant is high with respect to the concentrations used in the experiment, the binding reaction abolishes in a sudden manner once all the binding sites are occupied (Fig. 7). For smaller binding constants this transition occurs more smoothly (Fig. 7). Therefore the shape of the titration curve is used to determine the binding constant (and thereby the free energy of binding).

4.4.1 A possible model to analyse ITC traces and its mathematical consequences

In a simple case the ligand (L) binds to the substrate (S) following the chemical equation $S+L \leftrightarrow SL$.
After correction for the dilution of the substrate concentration upon injection of the ligand the measured enthalpy per injection is directly proportional to the amount of newly formed complexes after each injection. Therefore knowing the concentration of the complex after each injection of substrate provides access to the binding constant k. With S being the total concentration of the substrate (both free and bound), L the total concentration of ligand added, [S] the concentration of free substrate, [L] the concentration of unbound ligand and [SL] the concentration of complex one finds:

$$\frac{[S][L]}{[SL]} = k; \quad [S]+[SL] = S; \quad [L]+[SL] = L$$
$$\Rightarrow [SL] = \tfrac{1}{2}\left((S+L+k) - \sqrt{(S+L+k)^2 - 4SL}\right) \tag{12}$$

The reaction enthalpy of one injection is calculated by considering the difference in the concentration [SL] before and after the injection. Thus for a ligand concentration of L before injection and a ligand concentration of L+ΔL after the injection the measured enthalpy is proportional to $[SL]_{(L+\Delta L)}$ - $[SL]_{(L)}$. The envelope of the injection profile corresponds to the derivative:

$$\frac{\partial[SL]}{\partial L} = \tfrac{1}{2} - \frac{S+L+k-2S}{2\sqrt{(S+L+k)^2 - 4SL}} \tag{13}$$

The thermodynamic parameters are obtained from the integration of the injection enthalpies (ΔH) and include the binding constant k = exp(-ΔG/RT) (Figure 7), the number of binding sites from the concentration of ligand and the substrate at the transition mid point, and finally the entropy ΔS from ΔG=ΔH-TΔS. Additional insights in the thermodynamics of the system are obtained from measuring the association curves at different temperatures (Seelig, 2004).

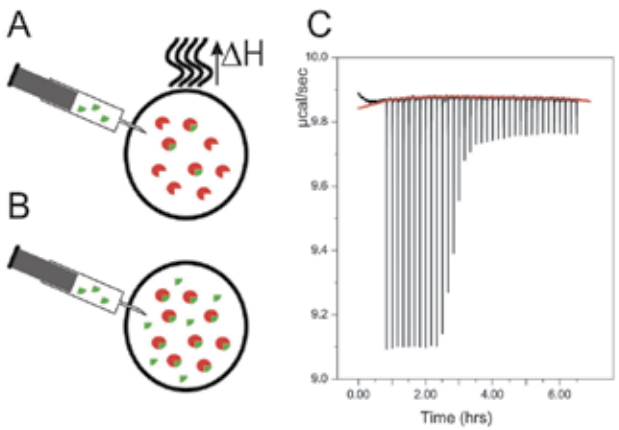

Fig. 6. Illustrates the principles of ITC measurements. A: During the initial phases of a titration the substrate molecules (red 3/4 circles) are in excess and all ligand molecules (green 1/4 circles) associated with a substrate molecule provided that the binding constant is high enough with respect to the substrate concentration. B. At the end of the experiment all substrate molecules are saturated with ligand and no further binding reaction occurs. C. shows the measured heat from individual injections which occur at regular intervals.

4.5 Characterization of topological states by solid-state NMR and ATR-FTIR spectroscopies

The methods presented in sections 4.1-4.4 provide some structural information on the polypeptide-lipid interactions such as the overall secondary structure composition of the peptides and proteins (CD spectroscopy) or about the environment of the tryptophan residues (fluorescence spectroscopy). The spectral changes during membrane association are used to determine e.g. the membrane association constants. Additional and more detailed structural information about the membrane-associated states is obtained from solid-state NMR and attenuated total reflection Fourrier transform infra-red (ATR FTIR) spectroscopies.

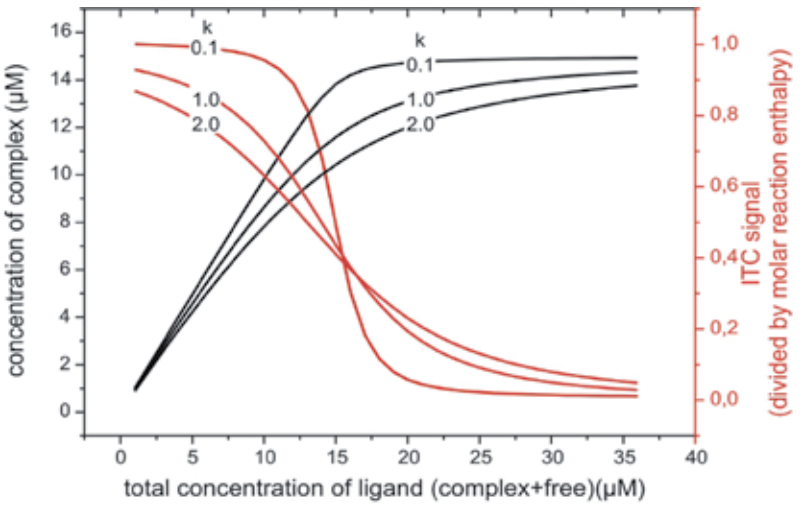

Fig. 7. Simulations of ITC experiments. The concentration of the complex (black line) and the relative heat of reaction as a function of ligand concentration are shown for three different ITC experiments in the presence of 15µM of substrate at binding constants k of 0.1, 1 and 2 µM.

Whereas in solution fast reorientational motions average the alignment dependence of all NMR interactions and only the isotropic values are obtained this is not the case in solid or semi-solid samples, such as lipid bilayer assemblies, where the resonance positions are strongly dependent on the orientation of the molecules relative to the magnetic field of the spectrometer (B_o). Therefore, in solid-state NMR spectroscopy chemical shifts, quadrupolar and dipolar splittings are all anisotropic and are routinely used to derive angular information relative to B_o. For example in membranes that are uniaxially aligned with their normal parallel to B_o the ^{15}N chemical shift of a peptide bond exhibits an anisotropy between 50 and 230 ppm (Bechinger & Sizun, 2003). Due to the particular properties of the ^{15}N chemical shift interaction with the magnetic field (which is described by a second rank tensor) ^{15}N labelled sites within helical peptides exhibit chemical shifts around 200 ppm when transmembrane and < 100 ppm when oriented along the surface (Fig. 8). Therefore, the approximate tilt angle of a membrane-associated peptide can be determined directly from this measurement (Bechinger & Sizun,

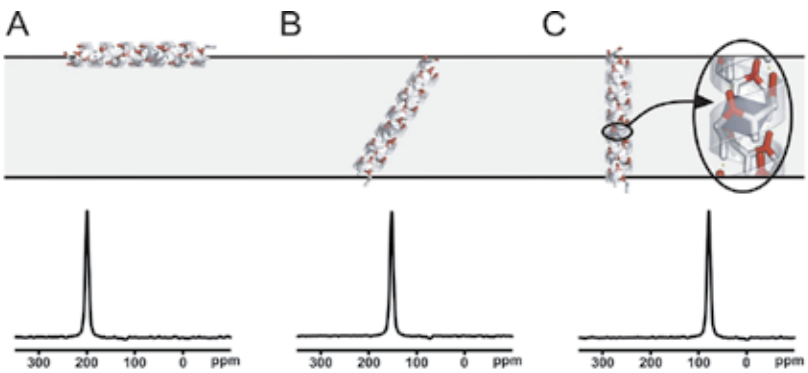

Fig. 8. Illustrates how the ^{15}N chemical shift measured from a ^{15}N labelled peptide bond within a helical domain correlates with the helix tilt angle for an in-planar (A), a tillted (B) or a transmembrane orientation (C).

2003). Accurate information on the tilt and the rotational pitch angles is obtained when other measurements such as the ^{2}H quadrupolar splitting of methyl-deuterated alanines is also taken into consideration (Bechinger et al., 2011). More recently it has also been shown that for peptides that undergo fast rotational diffusion of the membrane normal the partially averaged spectral line shapes of non-oriented samples provides similar information about the helix alignment (Prongidi-Fix et al., 2007).

ATR-FTIR spectroscopy of uniaxially oriented samples provides structural information on membrane-associated polypeptides. Whereas the resonance frequency of the amide I band is a reliable indicator of the secondary structure composition (Goormaghtigh et al., 1994), the dichroic ratio R^{ATR}, that is obtained by comparing the ATR-FTIR intensities when the sample is irradiated with light of polarization parallel and perpendicular to the surface, is an indicator of the membrane topology (Bechinger et al., 1999). In contrast to solid-state NMR spectroscopy where the in-plane and transmembrane alignments result in two distinct resonances of very different chemical shift (Fig. 8), and therefore exchange processes can also be studied, the FTIR signal of the two states results in the same resonance position albeit with different dichroic ratio (Fig. 9). Therefore the fraction of transmembrane alignment p_{TM} is evaluated from

$$R^{ATR} = \frac{2p_{TM}(R_a^{ATR} - R_b^{ATR}) + R_b^{ATR}(R_a^{ATR} + 2)}{p_{TM}(R_b^{ATR} - R_a^{ATR}) + R_a^{ATR} + 2} \tag{14}$$

where R_a^{ATR} and R_b^{ATR} are the dichroic maxima and minima, respectively (Bechinger et al., 1999). Oriented CD spectroscopy, which is not discussed in detail here, provides a third method to analyse the topology of membrane-associated polypeptides (Wu et al., 1990).

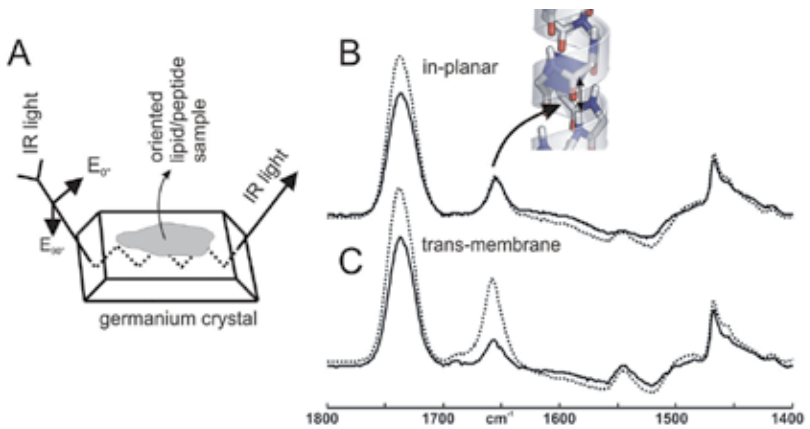

Fig. 9. A The experimental setup for attenuated total reflection infrared spectroscopy (ATR-FTIR) using linear polarized light. Infrared light is sent trough a germanium crystal in such a manner that several total reflections occur at the inner surface. The absorption spectrum is due to the evanescent field along the surface of the germanium crystal and thereby also penetrated the oriented lipid/peptide membrane. The intensities shown correspond to the carboxyl stretching motion of the peptide backbone. Dashed lines are recorded with 90° polarized light and solid lines are recorded with 0° polarized light. In the in-planar conformation the carboxyl stretching vibration has similar intensities for both polarizations (B), whereas the 90°polarized spectrum exhibits a significant higher intensity for transmembrane alignments (C).

5. Conclusion

A number of biophysical approaches have been developed for the thermodynamic analysis of the association of and the interactions between biological macromolecules and/or supramolecular systems. These techniques allow one to quantitatively describe the association constants and number of binding sites but also other thermodynamic quantities such as reaction enthalpy and entropy. This data is important to understand the regulatory mechanisms that govern life and which are key for health and disease.

6. Acknowledgment

Much of the work presented in this paper has only been possible through collaborations with many other teams and the many previous and present co-workers of our own laboratory. Of the former we would like to mention in particular the fruitful interactions with Antoine Kichler, Erick Goormaghtigh, Jean-Marie Ruysschaert, Gilles Guichard, Bernard Desbat, Marie-Hélène Metz-Boutigue and Gilles Prévost. We gratefully acknowledge the financial support over the years by Vaincre la Mucoviscidose, the Agence Nationale de la Recherche, the European Commission, the Alsace region, the CNRS, the French ministry of research and the University of Strasbourg.

7. References

Aisenbrey, C., Bechinger, B., Grobner, G. (2008) Macromolecular crowding at membrane interfaces: adsorption and alignment of membrane peptides. *J Mol Biol,* 375, 2, pp. 376-85

Aisenbrey, C., Goormaghtigh, E., Ruysschaert, J.M., Bechinger, B. (2006) Translocation of amino acyl residues from the membrane interface to the hydrophobic core: Thermodynamic model and experimental analysis using ATR-FTIR spectroscopy. *Molecular Membrane Biology,* 23, pp. 363-74

Aisenbrey, C., Kinder, R., Goormaghtigh, E., Ruysschaert, J.M., Bechinger, B. (2006) Interactions involved in the realignment of membrane-associated helices: An investigation using oriented solid-state NMR and ATR-FTIR spectroscopies topologies *Journal of Biological Chemistry,* 281, pp. 7708-16

Bechinger, B. (1996) Towards membrane protein design: pH dependent topology of histidine-containing polypeptides. *J.Mol.Biol.,* 263, 5, pp. 768-75

Bechinger, B. (1997) Structure and Functions of Channel-Forming Polypeptides: Magainins, Cecropins, Melittin and Alamethicin. *Journal of Membrane Biology,* 156, pp. 197-211

Bechinger, B. (1999) The structure, dynamics and orientation of antimicrobial peptides in membranes by solid-state NMR spectroscopy. *Biochimica et Biophysica Acta,* 1462, pp. 157-83

Bechinger, B. (2000) Understanding peptide interactions with lipid bilayers: a guide to membrane protein engeneering. *Curr.Opin.Chem.Biol.,* 4, pp. 639-44

Bechinger, B. (2001) Membrane insertion and orientation of polyalanine peptides: A 15 N solid-state NMR spectroscopy investigation. *Biophys.J.,* 82, 4, pp. 2251-6

Bechinger, B. (2001) Solid-state NMR investigations of interaction contributions that determine the alignment of helical polypeptides in biological membranes. *FEBS Lett.,* 504, pp. 161-5

Bechinger, B. (2004) Membrane-lytic peptides. *Crit.Rev.Plant Sci.,* 23, pp. 271-92

Bechinger, B. (2005) Detergent-like properties of magainin antibiotic peptides: A 31P solid-state NMR study. *Biochimica et Biophysica Acta,* 1712, pp. 101-8

Bechinger, B. (2009) Rationalizing the membrane interactions of cationic amphipathic antimicrobial peptides by their molecular shape. *Current Opinion in Colloid and Interface Science, Surfactants,* 14, pp. 349-55

Bechinger, B. (2011) Insights into the mechanisms of action of host defence peptides from biophysical and structural investigations. *J Pept Sci,* pp. 306-314

Bechinger, B., Lohner, K. (2006) Detergent-like action of linear cationic membrane-active antibiotic peptides. *Biochim Biophys Acta,* 1758, pp. 1529-39

Bechinger, B., Resende, J.M., Aisenbrey, C. (2011) The structural and topological analysis of membrane-associated polypeptides by oriented solid-state NMR spectroscopy: Established concepts and novel developments. *Biophys Chem,* 153, pp. 115-25

Bechinger, B., Ruysschaert, J.M., Goormaghtigh, E. (1999) Membrane Helix Orientation from Linear Dichroism of Infrared Attenuated Total Reflection Spectra. *Biophys.J.,* 76, pp. 552-63

Bechinger, B., Sizun, C. (2003) Alignment and structural analysis of membrane polypeptides by 15N and 31P solid-state NMR spectroscopy *Concepts in Magnetic Resonance,* 18A, pp. 130 -45

Bechinger, B., Skladnev, D.A., Ogrel, A., Li, X., Swischewa, N.V., Ovchinnikova, T.V., O'Neil, J.D.J., Raap, J. (2001) 15 N and 31 P solid-state NMR investigations on the orientation of zervamicin II and alamethicin in phosphatidylcholine membranes. *Biochemistry,* 40, 31, pp. 9428-37

Bechinger, B., Vidovic, V., Bertani, P., Kichler, A. (2011) A new family of peptide-nucleic acid nanostructures with potent transfection activities. *J Pept Sci,* 17, 2, pp. 88-93

Brogden, K.A. (2005) Antimicrobial peptides: pore formers or metabolic inhibitors in bacteria? *Nat.Rev.Microbiol.,* 3, 3, pp. 238-50

Cady, S.D., Schmidt-Rohr, K., Wang, J., Soto, C.S., Degrado, W.F., Hong, M. (2010) Structure of the amantadine binding site of influenza M2 proton channels in lipid bilayers. *Nature,* 463, 7281, pp. 689-92

Chen, F.Y., Lee, M.T., Huang, H.W. (2003) Evidence for membrane thinning effect as the mechanism for Peptide-induced pore formation. *Biophys J,* 84, 6, pp. 3751-8

Dufourc, E.J., Smith, I.C., Dufourcq, J. (1986) Molecular details of melittin-induced lysis of phospholipid membranes as revealed by deuterium and phosphorus NMR. *Biochemistry,* 25, 21, pp. 6448-55

Dvinskikh, S., Durr, U., Yamamoto, K., Ramamoorthy, A. (2006) A high-resolution solid-state NMR approach for the structural studies of bicelles. *J.Am.Chem.Soc.,* 128, 19, pp. 6326-7

Georgescu, J., Bechinger, B. (2010) NMR structures of the histidine-rich peptide LAH4 in micellar environments: membrane insertion, pH-dependent mode of antimicrobial action and DNA transfection. *Biophys J,* 99, 8, pp. 2507-15

Goormaghtigh, E., Cabiaux, V., Ruysschaert, J.M. (1994) Determination of soluble and membrane protein structure by Fourier transform infrared spectroscopy. III. Secondary structures. [Review]. *Sub-Cellular Biochemistry,* 23, pp. 405-50

Gregory, S.M., Cavenaugh, A., Journigan, V., Pokorny, A., Almeida, P.F.F. (2008) A quantitative model for the all-or-none permeabilization of phospholipid vesicles by the antimicrobial peptide cecropin A. *Biophys.J.,* 94, 5, pp. 1667-80

Hallock, K.J., Lee, D.K., Omnaas, J., Mosberg, H.I., Ramamoorthy, A. (2002) Membrane composition determines pardaxin's mechanism of lipid bilayer disruption. *Biophys J,* 83, 2, pp. 1004-13

Harzer, U., Bechinger, B. (2000) The alignment of lysine-anchored membrane peptides under conditions of hydrophobic mismatch: A CD, 15 N and 31 P solid-state NMR spectroscopy investigation. *Biochemistry,* 39, pp. 13106-14

Huang, H.W. (2000) Action of antimicrobial peptides: Two-state model. *Biochemistry,* 39, 29, pp. 8347-52

Israelachvili, J.N., Marcelja, S., Horn, R.G. (1980) Physical principles of membrane organization. *Q.Rev.Biophys.,* 13, 2, pp. 121-200

Kichler, A., Leborgne, C., Danos, O., Bechinger, B. (2007) Characterization of the gene transfer process mediated by histidine-rich peptides. *J Mol Med.,* 85, 2, pp. 191-201

Kichler, A., Leborgne, C., MÑrz, J., Danos, O., Bechinger, B. (2003) Histidine-rich amphipathic peptide antibiotics promote efficient delivery of DNA into mammalian cells. *Proc.Natl.Acad.Sci.U.S.A.,* 100, 4, pp. 1564-8

Kichler, A., Mason, A.J., Bechinger, B. (2006) Cationic amphipathic histidine-rich peptides for gene delivery. *Biochimica et Biophysica Acta,* 1576, pp. 301-7

Killian, J.A., Salemink, I., de Planque, M.R.R., Lindblom, G., Koeppe, R.E., II, Greathouse, D.V. (1996) Induction of nonbilayer structures in diacylphosphatidylcholine model membranes by transmembrane ‡-helical peptides: Importance of hydrophobic mismatch and propose role of tryptophans. *Biochemistry,* 35, pp. 1037-45

Ladokhin, A.S., Jayasinghe, S., White, S.H. (2000) How to measure and analyze tryptophan fluorescence in membranes properly, and why bother? *Anal Biochem,* 285, 2, pp. 235-45

Lakey, J.H., Duche, D., Gonzalez-Manas, J.M., Baty, D., Pattus, F. (1993) Fluorescence energy transfer distance measurements. The hydrophobic helical hairpin of colicin A in the membrane bound state. *J.Mol.Biol.,* 230, 3, pp. 1055-67

Langlet-Bertin, B., Leborgne, C., Scherman, D., Bechinger, B., Mason, A.J., Kichler, A. (2010) Design and evaluation of histidine-rich amphipathic peptides for siRNA delivery. *Pharm Res,* 27, 7, pp. 1426-36

Lear, J.D., Wasserman, Z.R., DeGrado, W.F. (1988) Synthetic amphiphilic peptide models for protein ion channels. *Science,* 240, 4856, pp. 1177-81

Lees, J.G., Miles, A.J., Wien, F., Wallace, B.A. (2006) A reference database for circular dichroism spectroscopy covering fold and secondary structure space. *Bioinformatics,* 22, 16, pp. 1955-62

Leitgeb, B., Szekeres, A., Manczinger, L., Vagvolgyi, C., Kredics, L. (2007) The history of alamethicin: a review of the most extensively studied peptaibol. *Chem Biodivers.,* 4, 6, pp. 1027-51

Liu, L.P., Li, S.C., Goto, N.K., Deber, C.M. (1996) Threshold hydrophobicity dictates helical conformations of peptides in membrane environments. *Biopolymers,* 39, 3, pp. 465-70

Long, S.B., Tao, X., Campbell, E.B., MacKinnon, R. (2007) Atomic structure of a voltage-dependent K+ channel in a lipid membrane-like environment. *Nature,* 450, 7168, pp. 376-82

Ludtke, S., He, K., Huang, H. (1995) Membrane thinning caused by magainin 2. *Biochemistry,* 34, pp. 16764-9

Marquette, A., Mason, A.J., Bechinger, B. (2008) Aggregation and membrane permeabilizing properties of designed histidine-containing cationic linear peptide antibiotics. *J Pept.Sci,* 14, 4, pp. 488-95

Mason, A.J., Bechinger, B., Kichler, A. (2007) Rational design of vector and antibiotic peptides using solid-state NMR. *Mini.Rev.Med.Chem.,* 7, 5, pp. 491-7

Mason, A.J., Gasnier, C., Kichler, A., Prevost, G., Aunis, D., Metz-Boutigue, M.H., Bechinger, B. (2006) Enhanced membrane disruption and antibiotic action against pathogenic bacteria by designed histidine-rich peptides at acidic pH. *Antimicrob.Agents Chemother.,* 50, 10, pp. 3305-11

Mason, A.J., Leborgne, C., Moulay, G., Martinez, A., Danos, O., Bechinger, B., Kichler, A. (2007) Optimising histidine rich peptides for efficient DNA delivery in the presence of serum. *J Control Release,* 118, 1, pp. 95-104

Mason, A.J., Marquette, A., Bechinger, B. (2007) Zwitterionic phospholipids and sterols modulate antimicrobial peptide-induced membrane destabilization. *Biophys J,* 93, 12, pp. 4289-99

Mason, A.J., Martinez, A., Glaubitz, C., Danos, O., Kichler, A., Bechinger, B. (2006) The antibiotic and DNA-transfecting peptide LAH4 selectively associates with, and disorders, anionic lipids in mixed membranes. *FASEB J.,* 20, 2, pp. 320-2

Mason, A.J., Moussaoui, W., Abdelrhaman, T., Boukhari, A., Bertani, P., Marquette, A., Shooshtarizaheh, P., Moulay, G., Boehm, N., Guerold, B., Sawers, R.J.H., Kichler, A., Metz-Boutigue, M.H., Candolfi, E., Prevost, G., Bechinger, B. (2009) Structural determinants of antimicrobial and antiplasmodial activity and selectivity in histidine rich amphipathic cationic peptides. *Journal of Biological Chemistry,* 284, pp. 119-33

Matsuzaki, K., Murase, O., Tokuda, H., Funakoshi, S., Fujii, N., Miyajima, K. (1994) Orientational and Aggregational States of Magainin 2 in Phospholipid Bilayers. *Biochemistry,* 33, pp. 3342-9

Mecke, A., Lee, D.K., Ramamoorthy, A., Orr, B.G., Banaszak Holl, M.M. (2005) Membrane thinning due to antimicrobial peptide binding: an atomic force microscopy study of MSI-78 in lipid bilayers. *Biophys.J.,* 89, 6, pp. 4043-50

Mozsolits, H., Wirth, H.J., Werkmeister, J., Aguilar, M.I. (2001) Analysis of antimicrobial peptide interactions with hybrid bilayer membrane systems using surface plasmon resonance. *Biochim Biophys Acta,* 1512, 1, pp. 64-76

Musse, A.A., Wang, J., Deleon, G.P., Prentice, G.A., London, E., Merrill, A.R. (2006) Scanning the membrane-bound conformation of helix 1 in the colicin E1 channel domain by site-directed fluorescence labeling. *J Biol Chem,* 281, 2, pp. 885-95

Papo, N., Shai, Y. (2003) Exploring peptide membrane interaction using surface plasmon resonance: differentiation between pore formation versus membrane disruption by lytic peptides. *Biochemistry,* 42, 2, pp. 458-66

Prongidi-Fix, L., Bertani, P., Bechinger, B. (2007) The membrane alignment of helical peptides from non-oriented 15 N chemical shift solid-state NMR spectroscopy. *J.Am.Chem.Soc.,* 129, pp. 8430-1

Prongidi-Fix, L., Sugewara, M., Bertani, P., Raya, J., Leborgne, C., Kichler, A., Bechinger, B. (2007) Self-promoted uptake of peptide/ DNA transfection complexes. *Biochemistry,* 46, pp. 11253-62

Salnikov, E., Aisenbrey, C., Vidovic, V., Bechinger, B. (2010) Solid-state NMR approaches to measure topological equilibria and dynamics of membrane polypeptides. *Biochim. Biophys. Acta* 1798, pp. 258-65

Salnikov, E., Bechinger, B. (2011) Lipid-mediated peptide-peptide interactions in bilayers: Structural insights into the synergistic enhancement of the antimicrobial activities of PGLa and magainin 2. *Biophysical J.* pp. 1473-1480

Salnikov, E.S., Friedrich, H., Li, X., Bertani, P., Reissmann, S., Hertweck, C., O'Neil, J.D., Raap, J., Bechinger, B. (2009) Structure and alignment of the membrane-associated peptaibols ampullosporin A and alamethicin by oriented 15 N and 31 P solid-state NMR spectroscopy. *Biophys.J.,* 96, pp. 86-100

Salnikov, E.S., Mason, A.J., Bechinger, B. (2009) Membrane order perturbation in the presence of antimicrobial peptides by 2 H solid-state NMR spectroscopy. *Biochimie,* 91, 734, pp. 743

Sansom, M.S. (1993) Alamethicin and related peptaibols--model ion channels. *Eur.Biophys.J.,* 22, 2, pp. 105-24

Seelig, J. (2004) Thermodynamics of lipid-peptide interactions. *Biochim Biophys Acta,* 1666, 1-2, pp. 40-50

Sreerama, N., Woody, R.W. (1993) A self-consistent method for the analysis of protein secondary structure from circular dichroism. *Anal.Biochem.,* 209, 1, pp. 32-44

Sun, F., Zong, W., Liu, R., Chai, J., Liu, Y. (2010) Micro-environmental influences on the fluorescence of tryptophan. *Spectrochim Acta A Mol Biomol Spectrosc,* 76, 2, pp. 142-5

Traaseth, N.J., Verardi, R., Torgersen, K.D., Karim, C.B., Thomas, D.D., Veglia, G. (2007) Spectroscopic validation of the pentameric structure of phospholamban. *Proc.Natl.Acad.Sci.U.S.A,* 104, 37, pp. 14676-81

Tremouilhac, P., Strandberg, E., Wadhwani, P., Ulrich, A.S. (2006) Conditions affecting the re-alignment of the antimicrobial peptide PGLa in membranes as monitored by solid state 2H-NMR. *Biochim Biophys Acta,* 1758, 9, pp. 1330-42

Unwin, N. (2005) Refined structure of the nicotinic acetylcholine receptor at 4A resolution. *J Mol Biol,* 346, 4, pp. 967-89

Vogt, T.C.B., Bechinger, B. (1999) The interactions of histidine-containing amphipathic helical peptide antibiotics with lipid bilayers: The effects of charges and pH. *Journal of Biological Chemistry,* 274, pp. 29115-21

Vogt, T.C.B., Ducarme, P., Schinzel, S., Brasseur, R., Bechinger, B. (2000) The topology of lysine-containing amphipathic peptides in bilayers by CD, solid-state NMR and molecular modelling. *Biophys.J.,* 79, 5, pp. 2644-56

Wenk, M., Seelig, J. (1998) Magainin 2 amide interaction with lipid membranes: Calorimetric detection of peptide binding and pore formation. *Biochemistry,* 37, pp. 3909-16

White, S.H., Wimley, W.C. (1999) Membrane protein folding and stability: Physical principles. *Annu.Rev.Biophys.Biomol.Struct.,* 28, pp. 319-65

Wieprecht, T., Beyermann, M., Seelig, J. (1999) Binding of antibacterial magainin peptides to electrically neutral membranes: Thermodynamics and structure. *Biochemistry,* 38, pp. 10377-8

Wu, Y., Huang, H.W., Olah, G.A. (1990) Method of oriented circular dichroism. *Biophysical Journal,* 57, pp. 797-806

Edited by Juan Carlos Moreno Piraján

Thermodynamics is one of the most exciting branches of physical chemistry which has greatly contributed to the modern science. Being concentrated on a wide range of applications of thermodynamics, this book gathers a series of contributions by the finest scientists in the world, gathered in an orderly manner. It can be used in post-graduate courses for students and as a reference book, as it is written in a language pleasing to the reader. It can also serve as a reference material for researchers to whom the thermodynamics is one of the area of interest.

ISBN 978-953-51-6056-4

Photo by kennjin / iStock

IntechOpen